Title

Nuclear Chemistry Division Annual Report, 1967

Authors

Cunningham, B B
Reynolds, F L
Stephens, F S

Publication Date

1968

UCRL-17989

Cy. 1

NUCLEAR CHEMISTRY
Annual Report 1967

Lawrence Radiation Laboratory
University of California Berkeley

DISCLAIMER

UCRL-17989
UC-4 Chemistry
TID-4500 (51st Ed.)

UNIVERSITY OF CALIFORNIA
Lawrence Radiation Laboratory
Berkeley, California

AEC Contract No. W-7405-eng-48

NUCLEAR CHEMISTRY DIVISION ANNUAL REPORT, 1967

January 1968

I. Perlman, Director, Nuclear Chemistry Division
Editors: B. B. Cunningham, F. L. Reynolds, and F. S. Stephens

Work done under the auspices of the U. S. Atomic Energy Commission

Printed in the United States of America
Available from
Clearinghouse for Federal Scientific and Technical Information
National Bureau of Standards, U. S. Department of Commerce
Springfield, Virginia 22151
Price: Printed Copy $3.00; Microfiche $0.65

NUCLEAR CHEMISTRY DIVISION ANNUAL REPORT, 1967*

Contents

*Preceding Annual Reports: UCRL-17299, UCRL-16580.

NUCLEAR CHEMISTRY DIVISION ANNUAL REPORT, 1967

Lawrence Radiation Laboratory
University of California
Berkeley, California

January 1968

A. NUCLEAR SPECTROSCOPY

1. NUCLEAR SPECTROSCOPY STUDIES ON ^{237}Np

E. Browne and F. Asaro

We have studied the alpha spectrum of ^{237}Np with 17-keV full-width-at-half-maximum (FWHM) resolution and have made studies of the γ-ray spectrum in coincidence with α particles of given energy and with other γ rays. The relatively high efficiency of the surface-barrier Au-Si detectors led to a more accurate determination of some alpha group intensities. Some discrepancies with respect to earlier studies of this isotope with magnetic spectrographs were found.[1,2] Table A.1-I gives our alpha energies, intensities, and hindrance factors.

The ^{237}Np singles γ-ray spectrum had been measured in detail previously by M. Holtz.[3] About 25 γ rays were observed in our work in a variety of singles and coincidence experiments. The most interesting of these was a 94.7-keV γ ray found in coincidence with the (unresolved) α-particle groups which populate the 103.8- and 107.8-keV states. Thus a possible state at 94.7 keV was indicated. This γ ray was also observed in γ-γ coincidence experiments with the 143.3- and 117.4-keV γ rays as gates. The FWHM was 2.4 keV at 122 keV for this last experiment. A transition of about 88 keV from the 94.7-keV level to the 1/2 spin state of the ground-state band would have been masked by the high-intensity 86.6-keV γ ray in this latter measurement. Even with a resolution (FWHM) of 1.1 keV in our singles spectrum the ≈ 88-keV γ ray was not observed. Some indication of this γ ray, however, had been seen by M. Holtz[3] in a γ-ray spectrum of ^{233}Th. If ^{233}Th has a considerably lower population to the 86.6-keV level of ^{233}Pa than ^{237}Np, it should reduce the relative intensity of the 86.6-keV γ ray, thus enhancing the possibility of observing the ≈ 88-keV γ ray.

We irradiated 5 mg of ^{232}Th in the Berkeley Research Reactor for 2 min. The gamma spectrum was measured about 10 min after the end of the irradiation with a very-high-resolution (0.84 keV FWHM at 122 keV) Ge detector. Gamma rays of 86.6, 88.1 and 94.7 keV as well as others were found which decayed with a half life of about 20 min, the half life of ^{233}Th. No significant amount of ^{233}Pa was detected. In order to confirm the position of the 88.1-keV γ ray, γ-γ coincidence measurements were made with the 143.3-keV γ ray of ^{237}Np as the gate at a resolution (FWHM) of 0.89 keV at 122 keV. The 88.1-keV transition was observed in this measurement, and hence goes from the 94.7-keV state to the 1/2 spin member of the ground-state rotational band.

A partial-decay scheme of ^{233}Pa based on our experimental data is shown in Fig. A.1-1. The 94.7-keV state is probably the 3/2(651) Nilsson state, and the level at 86.6 keV is probably the 5/2 member of the same rotational band. The previous assignment of the 5/2(642) Nilsson level to the 86.6-keV state very likely should apply instead to the 237.9-keV state. This latter state would then receive the favored alpha decay. The high alpha population to the 86.6-keV level could be due to a Coriolis admixture with the favored rotational band. The unusual energy spacing and inversion of the 3/2 and 5/2 rotational members of the 3/2(651) Nilsson state could be due to a Coriolis interaction with the 5/2(642) and 1/2(660) Nilsson states.

References

1. F. Asaro, F. S. Stephens, Jr., and I. Perlman (Lawrence Radiation Laboratory), unpublished results, 1956-58.
2. S. A. Baranov et al., Soviet Phys.—JETP 14, 1232 (1962).
3. M. Holtz (Lawrence Radiation Laboratory), unpublished results, 1966.

Table A. 1-I. Alpha groups of ^{237}Np.

α-Particle energy[a] (MeV)	Excited state (keV)	Intensity (%)	Hindrance factor
4.865 ± 0.003	0	2.6 ± 0.2	3.0×10^2
4.857 ± 0.003	≈ 9	0.3 ± 0.1	3.3×10^3
4.809 ± 0.002	57	2.93 ± 0.44	1.1×10^2
4.792 ± 0.006	≈75	≈3	9×10
4.781 ± 0.002	86	48 ± 9	4.4
4.763 ± 0.003	104	31 ± 9	5.1
4.703 ± 0.003	165	1.30 ± 0.17	4.5×10
4.688 ± 0.004	180	0.37 ± 0.15	1.2×10^2
4.658 ± 0.002	211	3.54 ± 0.11	7.74
4.633 ± 0.002	237	6.46 ± 0.13	2.78
4.591 ± 0.003	279	0.39 ± 0.04	2.4×10
4.570 ± 0.003	300	0.4 ± 0.04	1.6×10
4.507 ± 0.004	365	0.04 ± 0.02	5×10

a. All alpha energies relative to Kondrat'ev's value of 4.781 MeV for α_{86}.

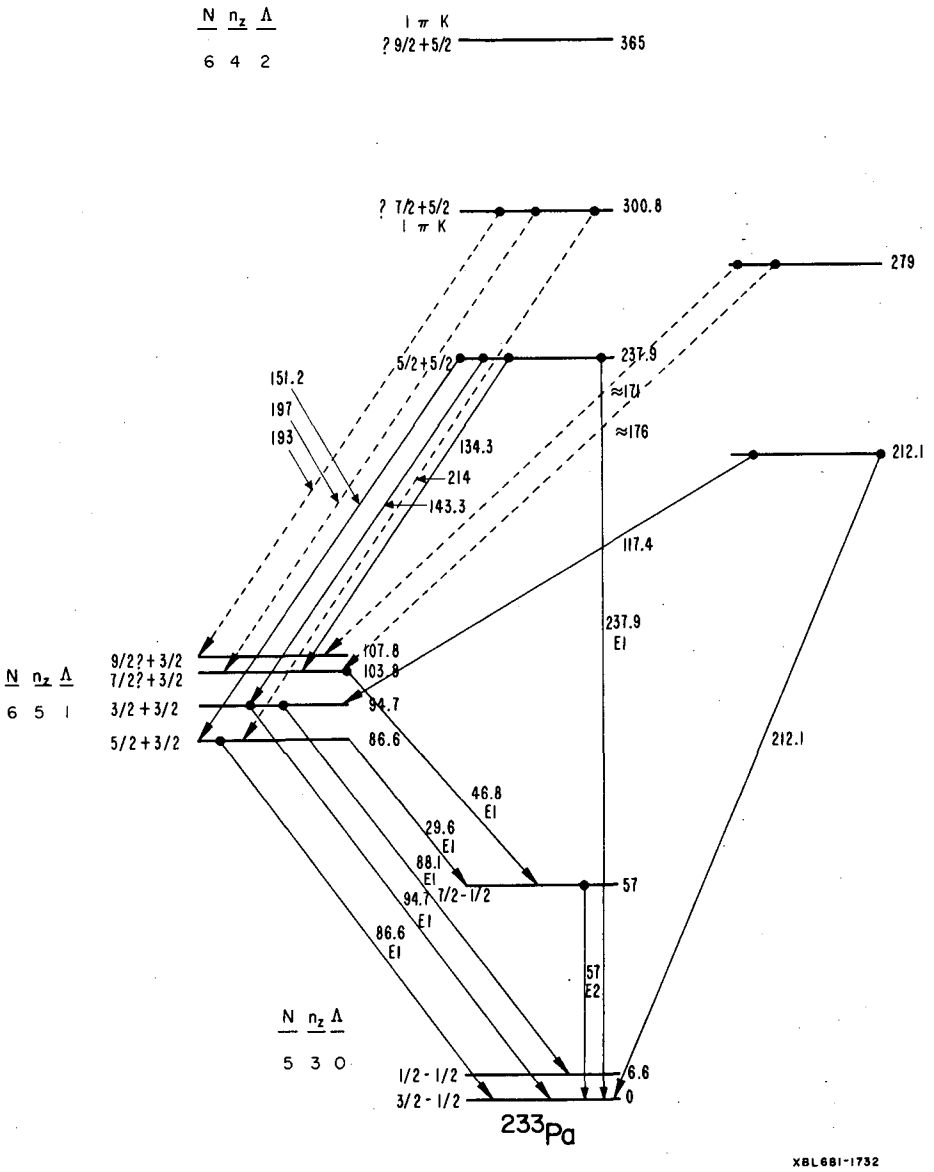

Fig. A. 1-1. Partial-decay scheme of ^{233}Pa.

2. INFLUENCE OF CORIOLIS COUPLING, PAIRING, AND OCTUPOLE VIBRATION-PARTICLE COUPLING ON $\Delta K = -1$ E1 TRANSITIONS IN $^{177}Hf^{\dagger}$

F. M. Bernthal and J. O. Rasmussen*

The strong influence of Coriolis-admixed components on the $\Delta K = \pm 1$ electric dipole transitions in odd-mass deformed nuclei is now well recognized. [1, 2] Several authors have considered the effects of Coriolis mixing in attempting to explain anomalies in experimentally observed branching ratios of E1 radiation. Although considerable success has been realized in predicting and accounting for E1 branching ratios that strongly violate Alaga's rules, relatively poor agreement with experiment has resulted from all attempts to explain quantitatively the absolute E1 transition strengths.

The 16 E1 transitions arising from the decay of 161-day ^{177m}Lu to high-spin members in ^{177}Hf provide an exceptionally rigorous experimental test for theoretical study of $\Delta K = -1$ E1 transitions. Singles spectra of the decay of ^{177m}Lu have been taken with the anti-Compton Ge(Li) spectrometer at Livermore (7 cm^3, resolution 1.1 keV at 122 keV) and a high-resolution (0.77 keV at 122 keV) Ge(Li) crystal in our Laboratory. In Fig. A. 2-1 we display for reference the now well established decay scheme of ^{177m}Lu. With the exception of the three transitions added from this work and the slightly altered half-life of ^{177m}Lu, [3] the scheme is the same as reported and modified by earlier workers.

Table A. 2-I shows the composite relative intensity data for the 14 E1 transitions observed to date. Also shown are the derived experimental values of B(E1). The lifetime of the 321-keV level has been measured by Berlovich et al. [4] and found to be $\tau_{1/2} = (6.9 \pm 0.3) \times 10^{-10}$ sec. By use of this value and the M2/E1 mixing ratio 0.18 for the 321-keV E1, [5] it is possible from relative intensity measurements to calculate directly the reduced strengths of the three E1's leading from the 9/2+[624] band head. All other values of B(E1) have been derived by using the rotational model of Bohr and Mottelson, assuming $Q_0 = 6.85$ barns. In contrast to the similar analysis first performed for ^{177}Hf by Alexander et al., [6] which neglected the effects of Coriolis mixing in the 9/2+[624] band, we have now taken into account the contributions of Coriolis-mixed components to the intraband transition strengths. The Nilsson wave amplitudes [7] for the Coriolis-mixed components originating from the $i_{13/2}$ shell model state were obtained by Holtz in a matrix diagonalization. [8]

It has been shown by Grin and Pavlichenkov [1] and by Vergnes and Rasmussen, [2] using analyses equivalent in their conclusions, that a simple first-order perturbation treatment that regards the principal and Coriolis-mixed ^{177}Hf E1 matrix elements as two adjustable parameters can explain quite successfully the observed E1 branching ratios. In Fig. A. 2-2 we show the results of such an analysis applied to the ^{177}Hf E1 intensities from this work.

As indicated in Ref. 1, the terms which should be considered up to first order in the analysis of the ^{177}Hf E1's are the following: (a) the principal 9/2+[624] → 7/2-[514] component; (b) the Coriolis-admixed (K = 7/2+) → 7/2-[514] components; (c) the 9/2+[624] → (K = 9/2-) Coriolis-admixed components. We have obtained an estimate of the wave-function coefficient for the Coriolis-mixed 7/2+[633] component in the 9/2+[624] band from the band-fit matrix diagonalization mentioned earlier. The mixing of K = 9/2- components into the 7/2-[514] band was estimated by a simple first-order perturbation treatment. Use of the normalized initial and final wave functions and treatment of the E1 matrix elements as three adjustable parameters yielded a fit to within 20% of the experimental absolute E1 transition strengths. Figures A. 2-3 and A. 2-4 show the normalized three-parameter fit in comparison with the simple two-parameter treatment and with experiment.

Recent developments [8, 9] in the theoretical interpretation of the collective octupole vibrational mode in deformed nuclei and its apparent application to the $\Delta K = 0$ class of E1 transitions [10, 11] have suggested a similar important influence on $\Delta K = 1$ E1's, all of which apparently have relatively large $\Delta K = 0$ Coriolis-mixed components.

In our calculations we have followed the approach of Faessler et al., [12] who suggest the vibration-particle coupling Hamiltonian

$$H_{vp} = -\hbar\omega_0 a_{30} r^2 Y_{30}(\theta, \phi),$$

which for $\Delta K = 0$ E1 transitions mixes the octupole band of the final state with the initial state, and vice versa. The only other quantities needed for the calculation are the octupole transition amplitude, $\langle a_3 \rangle = \hbar/\sqrt{2B_3E_3}$, and the collective E1 strength associated with the octupole vibration, $B_{coll}(E1)$. The recent publication of Donner and Greiner[10] offers estimates of the collective dipole and octupole strengths in this region. The pertinent relation given in Ref. 13 is

$$\frac{B(E1)}{B_{sp}(E1)} = 5.74\times10^{-2}\, A\, C_0^2\, (I_i\, 100 | I_f 0), \qquad (1)$$

where C_0 is the giant dipole wave function admixture coefficient for the $(K_i = 0^- \rightarrow K_f = 0^+)$, $|K_i - J_3| = 0$ class of E1's.

We have thus calculated the reduced transition strengths in ^{177}Hf taking into account pairing reduction, the influence of the Coriolis RPC (rotation particle coupling) perturbation, and the second-order vibration-particle perturbation which mixes the initial and final states of the $\Delta K = 0$ E1 components. Since the relative phases of the collective E1 components are not known, we allowed that these be arbitrary. It was found that a single phase of the same sign as the 7/2+[633] → 7/2-[514] single-particle component gave the most satisfactory results. We have allowed variation of only the single parameter $\langle a_3 \rangle$, the octupole amplitude. Pairing reduction factors have been calculated assuming λ, the chemical potential, to be at or near the energy ϵ_j of the ground-state 7/2-[514] Nilsson orbital.

Table A. 2-II shows the results of our calculations for ^{177}Hf, together with the values of B(E1) calculated using the simple three-parameter fit described earlier. Absolute values of B(E1) obtained for the appropriate choice of $\langle a_3 \rangle$ in several cases of interest are displayed. Column 1 (NC) under 'microscopic theory' shows the results obtained when all assumptions with regard to Coriolis mixing and pair reduction are taken into account and the calculations are performed within the Nilsson model, but no octupole mixing is assumed. Columns 2 and 3 (NCO and NCO') show the results for a calculation similar to that in column 1, but with inclusion of the octupole-particle coupling influence. In column 4 we include a tabulation of the results obtained using pair reduction factors calculated by Vergnes and Rasmussen [2] from the BCS wave functions for N = 105.

The general applicability of the interpretation of $|\Delta K| = 1$ E1 transitions in terms of Coriolis coupling, pairing, and vibration-particle coupling remains to be shown, but the results of our calculations for the nucleus ^{177}Hf indicate that the theoretical basis for the quantitative interpretation of E1 transitions in odd-mass deformed nuclei is established.

Prior to publication of this paper we received a copy of the thesis of R. Piepenbring (University of Strassburg) wherein the influence of collective octupole components on $|\Delta K| = 1$ E1 transitions is discussed. That work and also the earlier published letter of Monsonego and Piepenbring[13] independently suggested the importance of the collective octupole components in interpreting E1 transitions in odd-mass deformed nuclei.

Footnotes and References

†Condensation of the paper in Nucl. Phys. A101, 513 (1967).

*Department of Chemistry, University of California, Berkeley, California.

1. Yu. T. Grin and I. M. Pavlichenkov, Nucl. Phys. 65, 686 (1965).
2. M. N. Vergnes and J. O. Rasmussen, Nucl. Phys. 62, 233 (1965).
3. D. R. Nethaway and B. Mendoza, The Half-Life and Formation Cross Section of ^{177m}Lu, Lawrence Radiation Laboratory Report UCRL-70048, Sept. 1966.
4. E. E. Berlovich, Yu. K. Gusev, V. V. Il'in, and M. K. Nikitin, Soviet Phys.-JETP 43, 1625 (1962).
5. H. I. West, Jr., L. G. Mann, and R. J. Nagle, Phys. Rev. 124, 527 (1961).
6. P. Alexander, F. Boehm, and E. Kankeleit, Phys. Rev. 133, B284 (1964).
7. S. G. Nilsson, Kgl. Danske Videnskab. Selskab, Mat.-Fys. Medd. 29, No. 16 (1954).
8. M. D. Holtz (Lawrence Radiation Laboratory), private communication.
9. V. G. Soloviev, Nonrotational Collective States of Deformed Even-Even Nuclei, JINR P-1973 1966.
10. W. Donner and W. Greiner, Z. Physik 197, 440 (1966).
11. G. Monsonego and R. Piepenbring, Nucl. Phys. 78, 265 (1966).
12. A. Faessler, T. Udagawa, and R. K. Sheline, Nucl. Phys. 85, 670 (1966).
13. G. Monsonego and R. Piepenbring, Phys. Letters 21, 180 (1966).

Table A. 2-I. Experimental relative intensities and derived reduced transition strengths for ^{177}Hf E1's.

Initial spin	Final spin	E_γ (keV)	Intensity[a]	B(E1) (MeV-F^3) $\times 10^5$
9/2	7/2	321.3	8.8(5)	0.034(4)
9/2	9/2	208.3	524(21)	9.2(6)
9/2	11/2	71.7	7.2(4)	3.1(2)
11/2	9/2	313.7	10.0(5)	0.66(5)
11/2	11/2	177.0	27.8(1.2)	10.3(7)
11/2	13/2	(17.2)		
13/2	11/2	305.5	14.2(6)	2.32(13)
13/2	13/2	145.8	7.7(5)	11.6(9)
15/2	13/2	299.0	12.6(7)	4.3(3)
15/2	15/2	117.2	2.0(2)	11.5(1.3)
17/2	15/2	291.4	8.4(8)	7.0(7)
17/2	17/2	88.4	0.32(8)	9.4(2.4)
19/2	17/2	292.5	6.7(7)	8.9(9)
19/2	19/2	69.2	0.088(30)	8.6(2.9)
21/2	19/2	283.4	2.9(5)	11.0(2.0)
21/2	21/2	(41.0)		

a. Normalized to 105.4-keV γ ray = 100.

Table A. 2-II. Theoretical values of B(E1) for ^{177}Hf.

Spin		Reduced strength B(E1) (MeV-F^3) $\times 10^5$					
Initial K=9/2+	Final K=7/2-	Three parameter fit	Microscopic theory				Experiment
			NC[a]	NCO[b]	NCO'[c]	NCOBCS[d]	
9/2	7/2	0.034	3.4	0.031	0.038	0.034	0.034(4)
9/2	9/2	7.5	0.74	10.0	6.3	2.4	9.2(6)
9/2	11/2	3.5	0.05	6.5	3.9	1.6	3.1(2)
11/2	9/2	0.69	2.1	0.69	0.42	0.70	0.66(5)
11/2	11/2	9.7	0.87	12.4	7.8	2.9	10.3(7)
11/2	13/2	7.6	0.006	11.5	6.9	3.1	
13/2	11/2	2.6	1.3	3.5	2.3	2.3	2.32(13)
13/2	13/2	10.1	0.77	11.9	7.4	2.8	11.6(9)
15/2	13/2	5.0	0.74	7.0	4.6	4.4	4.3(3)
15/2	15/2	9.7	0.59	10.4	6.4	2.3	11.5(1.3)
17/2	15/2	7.3	0.34	10.7	7.2	6.8	7.0(7)
17/2	17/2	8.9	0.40	8.6	5.2	1.9	9.4(2.4)
19/2	17/2	8.2	0.14	13.6	9.2	9.1	8.9(9)
19/2	19/2	7.9	0.24	6.8	4.0	1.4	8.6(2.9)
21/2	19/2	11.0	0.01	16.3	11.2	11.8	11.0(2.0)
21/2	21/2	6.9	0.10	5.1	2.9	0.93	

a. Calculations in the Nilsson model, including Coriolis mixing and pair-reduction factors. Assumes $\lambda = \tilde{\epsilon}_{7/2-[514]}$, $\langle a_3 \rangle = 0$, and $R_0 = (U_{9/2+[624]} U_{7/2-[514]} - V_{9/2+[624]} V_{7/2-[514]}) = 0.42$.

b. Nilsson model, Coriolis coupling, pair reduction and octupole-particle coupling included in calculations. Assumes $\lambda = \tilde{\epsilon}_{7/2-[514]}$, $\langle a_3 \rangle = 0.170$, $R_0 = 0.42$.

c. Assumes $\lambda = \tilde{\epsilon}_{7/2-[514]} + 60$ keV, $\langle a_3 \rangle = 0.142$, $R_0 = 0.34$.

d. Assumes $\lambda = \tilde{\epsilon}_{7/2-[514]} + 70$ keV, BCS solution, $\langle a_3 \rangle = 0.142$, $R_0 = 0.16$.

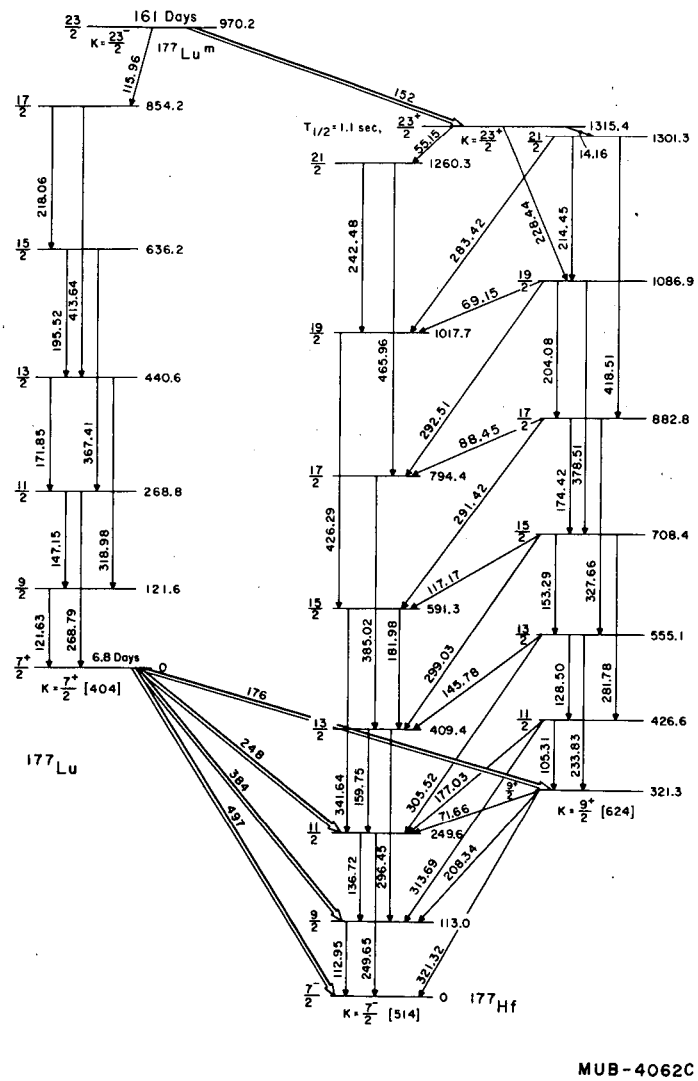

Fig. A. 2-1. The decay scheme of ^{177m}Lu with additions from this work.

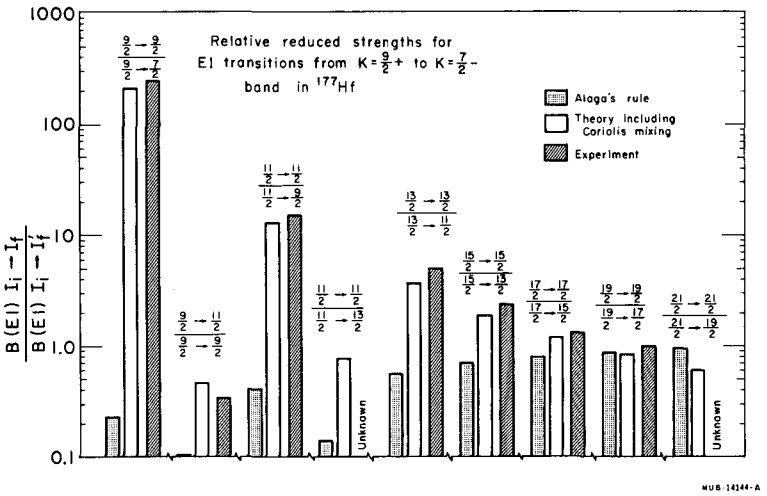

Fig. A. 2-2. Diagram of the E1 branching ratios in ^{177}Hf from the data in Table A. 2-I and the simple two-parameter theory of Refs. 1 and 2.

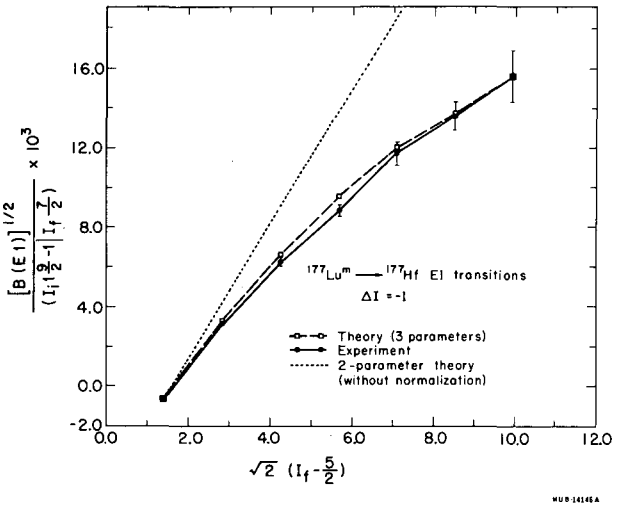

Fig. A. 2-3. The normalized three-parameter fit of absolute reduced E1 strengths in ^{177}Hf for the $\Delta I = -1$ class of transition. Derived from the form $B(E1) = [M_0(I_i\ 1\ 9/2\text{-}1 | I_f\ 7/2) + M_1\sqrt{I_i(I_i+1)-(9/2)(7/2)}\ (I_i\ 1\ 7/2\ 0 | I_f\ 7/2) + M_2\sqrt{I_f(I_f+1)-(7/2)(9/2)}\ (I_i\ 1\ 9/2\ 0 | I_f\ 9/2)]^2$, with $M_0 = 5.5\times10^{-3}$, $M_1 = 3.4\times10^{-2}$, and $M_2 = -4.5\times10^{-4}$.

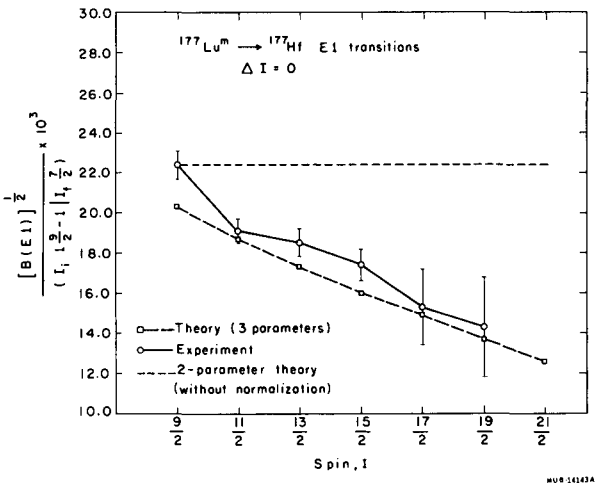

Fig. A. 2-4. Normalized three-parameter fit of the reduced E1 strengths in ^{177}Hf for the $\Delta I = 0$ class of transition.

3. ^{3}He ACTIVATION ANALYSIS FOR FLUORINE

D. M. Lee, J. F. Lamb, and S. S. Markowitz

A rapid, nondestructive method for determination of fluorine by ^{3}He activation has been developed. Preliminary work suggests a wide range of application to both organic and inorganic samples. The absolute excitation function for production of ^{20}F by the reaction ^{19}F(^{3}He, 2p)^{20}F is also given.

Targets of LiF, vacuum evaporated onto platinum foil and covered with thin tantalum foil, were used to measure the absolute excitation function shown in Fig. A. 3-1. Irradiation was performed at the Hilac at ^{3}He ion beam energies of 2 to 25 MeV, adjusted by use of aluminum degraders. The beam intensity was about 0.5 μA. The decay of the 10.7-sec ^{20}F activity induced in the target was followed by measuring the associated 1.63-MeV γ ray, using a NaI(T1) detector coupled to a multichannel analyzer operated as a 400-channel scaler. The irradiation chamber, rapid sample-recovery system, and counting procedures have been previously described.[1] Also shown in Fig. A. 3-1 is the absolute excitation function for production of ^{18}F by the reaction ^{19}F(^{3}He, α)^{18}F. The data shown agree very well with values previously published.[2, 3]

Fluorine analysis by ^{3}He activation using the induced ^{20}F activity is relatively free from interferences caused by other activities which might be induced in the sample. The only obvious interference would be ^{20}F activity induced in any ^{18}O present in the sample. However, the ^{18}O content of natural oxygen is only 0.2%. Other interferences could result from induced activities having an associated γ ray in their decay close to 1.63 MeV. Usually spectrum and decay-curve analyses allow separation of such activities. An analysis based upon the production of ^{18}F is also feasible in some cases, but the chances for interference are much greater because the activity can be measured nondestructively only by following the decay of the 511-keV β^{+} annihilation radiation. Since β^{+} emitters are most common among the products of ^{3}He-induced reactions, the decay curves obtained by following the 511-keV photopeak may be quite complicated for many types of samples. Samples containing oxygen could not be analyzed by following ^{18}F decay because of the high cross section for ^{18}F production from ^{16}O.[4]

A number of targets were analyzed nondestructively for fluorine to test the accuracy of the method. The results are shown in Table A. 3-I. All targets except the Teflon foils and the last three in the table were prepared by vacuum evaporation. The last three were prepared by homogenizing small amounts of PbF_2 with precipitated platinum (approx. 200 mg/cm^2) and pressing the mixture into a thin foil. These samples approximated "thick target" analysis for trace fluorine. The error values shown in Table A. 3-I are based on counting statistics only.

The sensitivity[5] of the nondestructive analysis, estimated from the excitation function in Fig. A. 3-1, is about 0.5 μg/cm^2 F. For a target such as calcium, assuming a negligible background under the 1.63-MeV photopeak, this corresponds to about 18 ppm fluorine. For these calculations a beam intensity of 1 μA, counting efficiency of 1%, irradiation time of 1 half-life, and a counting interval sufficiently short that the decay of ^{20}F could be followed were assumed. The sample thickness was calculated[6] with the restriction that the cross section vary by only 5% as the sample is traversed. More thorough investigations of interference and sensitivity are now in progress.

Footnotes and References

1. J. F. Lamb, D. M. Lee, and S. S. Markowitz, Simultaneous Determination of O^{18} and O^{16} Isotopes by He^{3} Activation Analysis, UCRL-17812, Oct. 1967.

2. O. D. Brill', Soviet J. Nucl. Phys. 1, 37 (1966).

3. John D. Mahony, Reactions of He with Light Elements: Applications to Activation Analysis (Ph. D. Thesis), UCRL-11780, Jan. 1965.

4. S. S. Markowitz and J. D. Mahony, Anal. Chem. 34, 329 (1962).

5. Sensitivity is defined here as the μg/cm^2 of F whose induced ^{20}F activity would result in detection such that σ is 10% of the photopeak counts, where

$$\sigma = \sqrt{\sigma^2_{\text{peak}} + \sigma^2_{\text{background}}} \ .$$

6. C. Williamson, J. P. Boujot, and J. Picard, Tables of Range and Stopping Power of Chemical Elements for Charged Particles of Energy 0.05 to 500 MeV, Centre D'Etudes Nucléaires de Saclay, Report CEA-R 3042, 1966.

Table A. 3-I. ^{3}He activation of fluorine.

Sample	F present (mg/cm^2)	F found (mg/cm^2)
LiF #13	1.68	standard
LiF #14	1.24	1.16 ± 0.01
LiF #16	0.82	0.82 ± 0.01
LiF #21	0.77	0.72 ± 0.02
LiF #19	0.53	0.53 ± 0.02
LiF #22	0.25	0.23 ± 0.03
LiF #12	1.03	1.02 ± 0.01
Teflon (CF_2) #1	1.85	1.90 ± 0.01
Teflon #2	0.93	0.90 ± 0.02
PbF_2 #1	0.28	0.25 ± 0.05
PbF_2 #2	0.22	0.20 ± 0.05
Pt+PbF_2 #1	1.53	standard
Pt+PbF_2 #2	0.32	0.32 ± 0.06
Pt+PbF_2 #3	1.28	1.22 ± 0.02

^{3}He ion beam energy = 17.5 MeV.
Beam current = 0.5 μA.
Irradiation time = 10 sec.

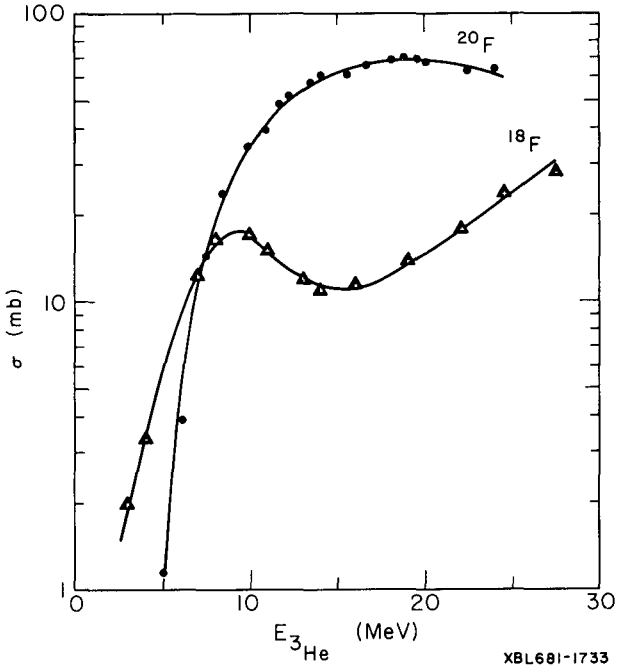

Fig. A. 3-1. Excitation functions for production of ^{20}F and ^{18}F from ^{19}F.

4. EXCITATION FUNCTIONS FOR NUCLEAR REACTIONS INDUCED IN ^{16}O BY BOMBARDMENT WITH 3- TO 20-MeV $^{3}He^{++}$ IONS

D. M. Lee, J. F. Lamb, and S. S. Markowitz

Bombardment of ^{16}O with $^{3}He^{++}$ ions of energies up to 20 MeV produces a number of nuclear reactions with reasonably large cross sections. Among the products of these reactions are ^{17}F(66 sec), ^{14}O(71 sec), ^{15}O(124 sec), ^{11}C(20.3 min), and ^{18}F(110 min). Each of these nuclides decays by positron emission or by a combination of positron emission and electron capture to the ground state of a stable daughter with the exception of ^{14}O, whose β^+ decay leads almost entirely to a 2.31-MeV first excited level. The excitation functions for total production of several of these nuclides by bombardment of ^{16}O with ^{3}He have been studied previously.[1-3] Our present work is to extend this data to higher energies and to measure those excitation functions which have not been previously reported. This more complete picture will facilitate a better choice of irradiation and counting procedures for ^{3}He activation analysis of oxygen. The sensitivity and detection limits for analysis of oxygen in several materials have been estimated, based upon several of these reactions under specific conditions and at a fixed ^{3}He energy.[4] The complete set of excitation functions will allow more flexibility in analysis of samples which may produce interferences which vary as a function of ^{3}He energy.

The oxygen targets were prepared by anodic oxidation of tantalum foils[5] with natural H_2O in the electrolyte. Irradiations were performed at the Hilac, with aluminum foil degraders used to adjust the beam energy. The activities of the irradiated samples were determined by using a 3×3 in. (diam) NaI(Tl) scintillation detector coupled to a multichannel analyzer to follow the decay of the photopeak resulting from β^+ annihilation. The resulting complex decay curves were computer-resolved by use of a least-squares code.

The absolute excitation functions measured are shown in Fig. A. 4-1. The functions for 66-sec ^{17}F and 71-sec ^{14}O were not resolvable in the β^+ annihilation radiation decay curves

because of the similarity in half-lives and are therefore shown as a composite curve in the figure. Data are not yet complete for the pure $^{16}O(^{3}He, \alpha n)^{14}O$ function as measured by following the 2.31-MeV photopeak from ^{14}O decay.

References

1. S. S. Markowitz and J. D. Mahony, Anal. Chem. 34, 329 (1962).
2. O. D. Brill', Soviet J. Nucl. Phys. 1, 37 (1966).
3. R. L. Hahn and E. Ricci, Phys. Rev. 146, 650 (1966).
4. E. Ricci, R. L. Hahn, J. E. Strain, and F. F. Dyer, in Proceedings of International Conference On Modern Trends in Activation Analysis, 1965, p. 200.
5. J. F. Lamb, D. M. Lee, and S. S. Markowitz, in Nuclear Chemistry Annual Report, UCRL-17299, Jan. 1967, p. 242.

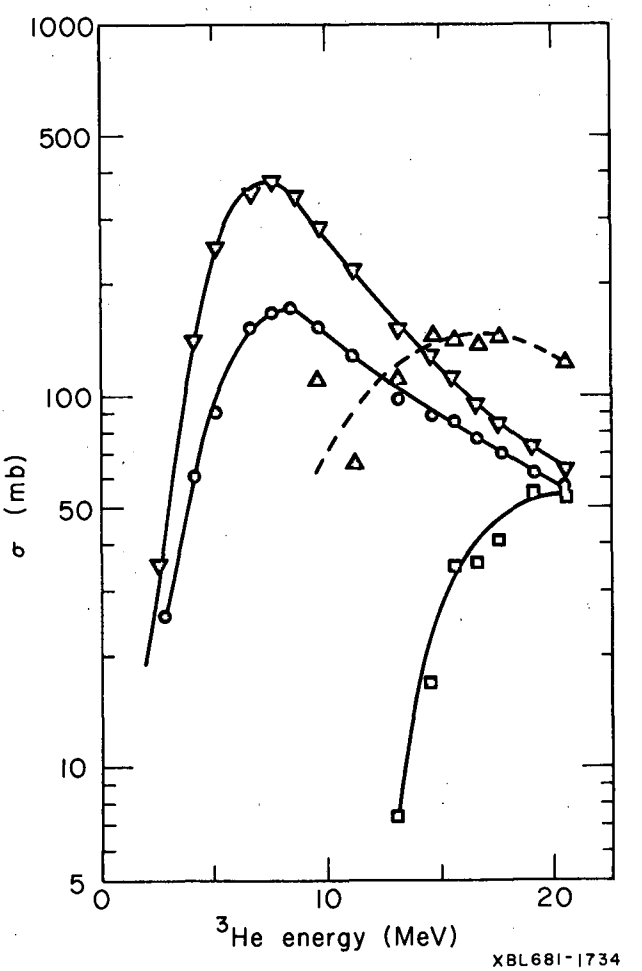

Fig. A. 4-1. Excitation functions for the production of ^{15}O, ^{11}C, ^{18}F, and $^{17}F + {}^{14}O$ from ^{16}O.

- ○ $^{16}O(^{3}He, \alpha)^{15}O$
- □ $^{16}O(^{3}He, 2\alpha)^{11}C$
- ▼ $^{16}O(^{3}He, p)^{18}F + {}^{16}O(^{3}He, n)^{18}Ne$
- △ $^{16}O(^{3}He, d)^{17}F + {}^{16}O(^{3}He, n\alpha)^{14}O$

5. EVAPORATION OF THREE TO EIGHT NEUTRONS IN REACTIONS BETWEEN ^{12}C AND VARIOUS URANIUM NUCLIDES†

Torbjorn Sikkeland, Jaromir Maly, and Donald F. Lebeck

A good fit has been obtained to the peaks of measured cross section curves for (^{12}C, xn) reactions with ^{233}U, ^{234}U, ^{235}U, ^{236}U, and ^{238}U as targets. The fit involved (i) calculation of the compound nucleus cross section by the use of the parabolic approximation to the real part of the optical model, (ii) modification of Jackson's formula for P_x to include fission and angular momentum effects, (iii) use of the Γ_n/Γ_f formula by Fujimoto and Yamaguchi. A typical fit is shown in Fig. A. 5-1 with ^{238}U as target, and the results of the Γ_n/Γ_f analysis are summarized in Table A. 5-I.

The latter two formulas are based on the assumptions that the temperature is independent of excitation energy, that the temperature for fission is equal to that for neutron evaporation, and that Γ_n/Γ_f is independent of angular momentum. This internal consistency between these formulas is only qualitative. The value of the temperature (as used in the formula for P_x) is 1.20 ± 0.05 MeV, which is significantly higher than 0.59 ± 0.05 MeV, which was found to fit the Γ_n/Γ_f data.

In the analysis we obtained a value of 4.5 keV for the quantity $\hbar^2/2\Im$. It is interesting to note that for a spherical rigid nucleus with A = 250 the value of that quantity is 3.6 keV, and deformed nuclei, in this region of the periodic table, have $\hbar^2/2\Im$ values (as deduced from the rotational energies near ground state) of about 7 keV.

Similar good fits to the shapes of experimental curves were obtained with modifications to the Jackson formula in which T is proportional to the square root of the excitation energy. And we have not ruled out the possibility that Γ_n/Γ_f varies with angular momentum and excitation energy.

It therefore appears that the good fit of the formulas for P_x and Γ_n/Γ_f is fortuitous. However, their usefulness should be evident. They have few adjustable parameters and they are relatively easy to use. They can be used in mass assignments and in the prediction of cross sections in nucleosynthesis.

We have a few remarks regarding the conclusion drawn by Donets et al. that Γ_n/Γ_f increases with increasing bombarding energy.[1] They used the unmodified Jackson formula, and values for σ_{CN} were taken from those calculated by Thomas using the square well model.[2] These values are too high at the barrier.[3] This error decreases with increasing E_i. This results in experimental Γ_n/Γ_f values that are too high for the lowest x, i. e., for the lowest excitation energies, and thus give the apparent effect that Γ_n/Γ_f increases with E_i. We believe that a variation of Γ_n/Γ_f with E_i has not yet been experimentally demonstrated for nuclei in the heavy-element region.

We thank Dr. Albert Ghiorso for help in the experiments and the Hilac crew for furnishing excellent beams of ^{12}C ions. One of us (J. M.) expresses his gratitude to the International Atomic Energy Agency, Vienna, Austria, for a research grant.

Footnote and References

†Abstract from article submitted to Phys. Rev. (UCRL-17588, May 1967).

1. E. D. Donets, V. A. Schegolev, and V. A. Ermakov, Soviet J. Nucl. Phys. 2, 1015 (1965).
2. T. D. Thomas, Phys. Rev. 116, 703 (1959).
3. V. E. Viola, Jr., and T. Sikkeland, Phys. Rev. 128, 767 (1962).

Table A.5-I. Results of the analysis of experimental maximum cross sections obtained in U(^{12}C, xn)Cf reactions. Symbols not defined in the text are, A_t = mass number of target nucleus, A_p = mass number of the product nucleus. The calculated values for $(\sigma_{CN}P_x)_{max}$ and $\overline{\Gamma_n/\Gamma_f}$ were obtained by the use of the formulas by Jackson and Fujimoto and Yamaguchi, respectively.

A_t	x	A_p	$E_{i,max}$ (MeV)	$\sigma_{x,max}$ (μb)	ΔE	$(\sigma_{CN}P_x)_{max}$ (mb)	A_{av}	$\overline{\Gamma_n/\Gamma_f}$ (exp)	$\overline{\Gamma_n/\Gamma_f}$ (calc)
238	4	246	67.5	62	2.0	26	248.5	0.28±0.03	0.30
238	5	245	73.5	100	1.5	260	248	0.26±0.01	0.25
238	6	244	83.5	15	0	400	247.5	0.22±0.01	0.23
238	7	243	≈95	3.0	0.5	550	247	0.21±0.01	0.20
238	8	242	≈115	0.29	1.0	520	246.5	0.20±0.01	0.17
236	3	245	67.5	2.5	0	1.5	247	0.13±0.03	0.19
236	4	244	70	22	0	48	246.5	0.17±0.02	0.17
236	5	243	77.5	9.8	0	300	246	0.15±0.01	0.14
236	6	242	88	2.1	1.0	420	245.5	0.15±0.01	0.13
235	3	244	67.5	1.5	0	0.75	246	0.14±0.04	0.15
235	4	243	70.5	8.8	0	80	245.5	0.11±0.02	0.13
235	5	242	77.5	5.0	-0.5	270	245	0.13±0.01	0.12
234	4	242	72	4.0	1.0	90	244.5	0.089±0.009	0.098
233	3	242	67	0.37	-1.0	2.0	244	0.060±0.016	0.087

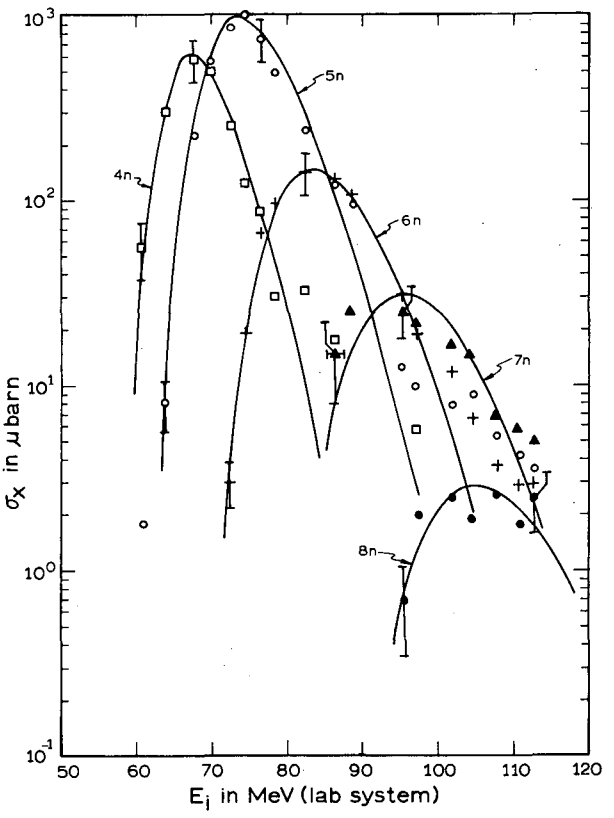

Fig. A.5-1. Experimental cross sections, σ_x, plotted versus ^{12}C energy, E_i, for ^{238}U(^{12}C, xn)$^{250-x}$Cf reactions. The symbols and corresponding values for x for the experimental points are, □, 4n; O, 5n; +, 6n; ▲, 7n; ●, 8n. The curves represent the function $\sigma_{CN}P_x$ (modification I), normalized at the peak to the experimental points. The energy scales for the curves are displaced ΔE MeV relative to that of the figure. Values for ΔE are given in Table A.5-I.

6. ON-LINE α SPECTROSCOPY OF NEUTRON-DEFICIENT ACTINIUM ISOTOPES

Kalevi Valli, William J. Treytl,* and Earl K. Hyde

In the Nuclear Chemistry Division Annual Report 1966 we reported preliminary results[1] of a study on neutron-deficient actinium isotopes. The study has been completed and a detailed description is given in UCRL-17405.

The actinium study is an extension of our previous work on the neutron-deficient isotopes of polonium and astatine,[2] radon,[3] francium,[4] and radium.[5] Actinium isotopes ^{209}Ac through ^{215}Ac were studied at the heavy-ion linear accelerator by bombardment of ^{197}Au with ^{20}Ne, ^{203}Tl with ^{16}O, ^{205}Tl with ^{16}O, and ^{209}Bi with ^{12}C. The on-line techniques were essentially the same as in the previous studies:[2] reaction products recoiling from a thin target were slowed down in a helium atmosphere, swept through a small nozzle onto a catcher foil in an adjacent vacuum chamber, and detected with a Si(Au) surface-barrier detector. However, the short half-lives made some improvements necessary. To decrease the transport time of the activity the volume of the helium-filled chamber was greatly reduced, the helium pressure was increased, and the gas flow was directed in a more linear, nonturbulent way. Figure A.6-1 shows a schematic diagram of the present apparatus.

Half-lives and accurate alpha energies were measured for the actinium isotopes. Excitation functions were determined both for the actinium isotopes and for their alpha-active daughters in the four target-projectile combinations. The assignments of the actinium isotopes are based on these curves, on systematic trends in alpha-decay properties, and on half-life data.

Some typical alpha spectra from the reaction ^{203}Tl(^{16}O;xn)$^{219-x}$Ac are shown in Fig. A.6-2. Some excitation functions from the reactions ^{203}Tl(^{16}O;xn)$^{219-x}$Ac and ^{197}Au(^{20}Ne;xn)$^{217-x}$Ac are shown in Figs. A.6-3 and A.6-4, respectively.

Footnote and References

*Present address: U. S. Naval Radiological Defense Laboratory, San Francisco, California.

1. Nuclear Chemistry Division Annual Report 1966, UCRL-17299, Jan. 1967, p. 23.
2. William Treytl and Kalevi Valli, Nucl. Phys. A97, 405 (1967).
3. Kalevi Valli, Matti J. Nurmia, and Earl K. Hyde, Phys. Rev. 159, 1013 (1967).
4. Kalevi Valli, Earl K. Hyde, and William Treytl, J. Inorg. Nucl. Chem. 29, 2503 (1967).
5. Kalevi Valli, William Treytl, and Earl K. Hyde, Phys. Rev. 161, 1284 (1967).
6. R. D. Griffioen and R. D. Macfarlane, unpublished results, 1961.

Table A.6-I. Present results compared with previous reports. Following α-energy standards were used: ^{212}Po 8.7854 MeV, ^{215}Po 7.3841 MeV, ^{219}Rn 6.8176 MeV, ^{211}Bi 6.6222 MeV.

	This work			Griffioen and Macfarlane (Ref. 6)		
Isotope	Alpha energy (MeV)	Half-life (sec)	%	Alpha energy (MeV)	Half-life (sec)	%
^{215}Ac	7.602±0.005	0.17±0.01				
^{214}Ac	7.212±0.005	8.2±0.2	52±2	7.24	12	33
				7.18	12	33
	7.080±0.005	8.2±0.2	44±2	7.12	12	33
	7.000±0.015[a]	8.2±0.5	4±1			
^{213}Ac	7.362±0.008	0.80±0.05		7.42	≈ 1	
^{212}Ac	7.377±0.008	0.93±0.05				
^{211}Ac	7.480±0.008	0.25±0.05				
^{210}Ac	7.462±0.008	0.35±0.05				
^{209}Ac	7.585±0.015	0.10±0.05				

a. This peak is probably complex.

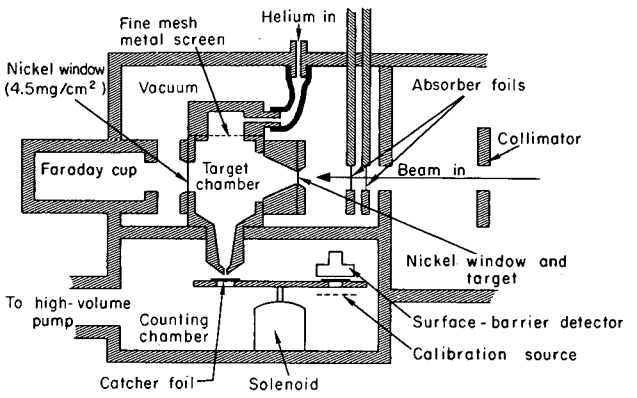

XBL677-3552

Fig. A.6-1. Schematic diagram of the apparatus. For $^{197}Au + ^{20}Ne$ reactions the following values were used: chamber depth from target to back window 3.6 cm, absolute helium pressure 1.7 atm, helium flow rate 90 cm^3/sec. For other reactions the helium pressure was varied to obtain maximum yields.

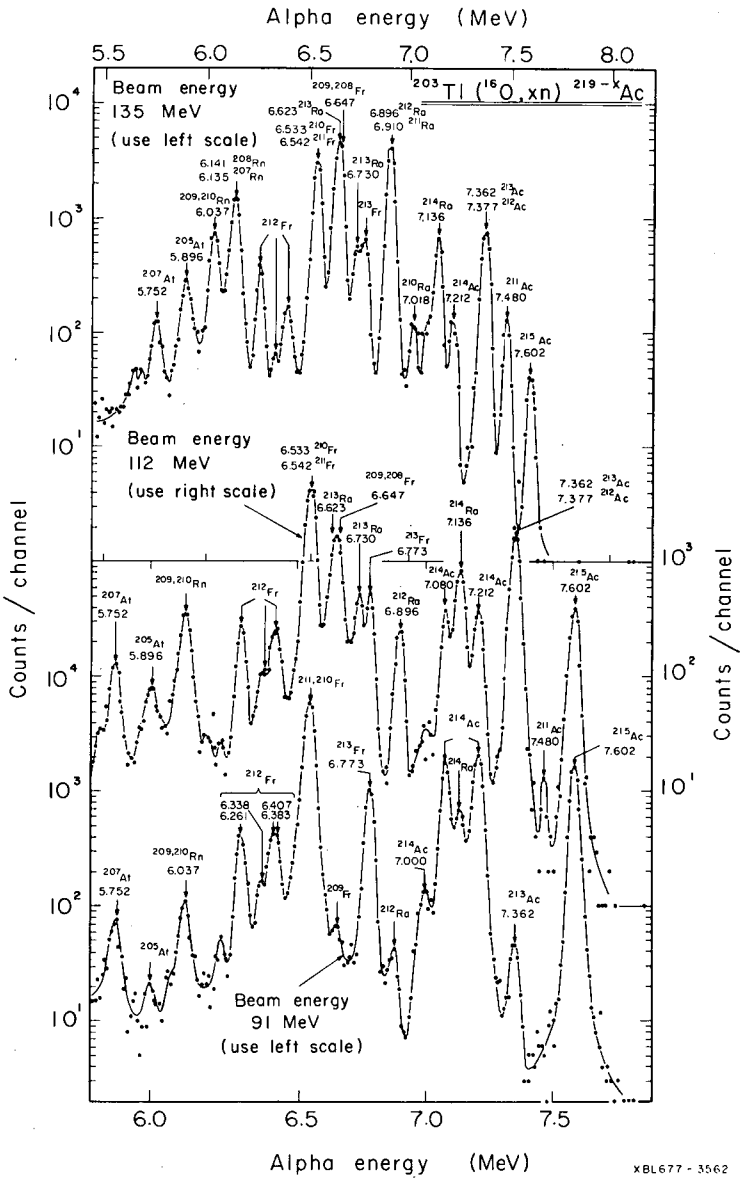

XBL677-3562

Fig. A.6-2. Three alpha spectra showing actinium and daughter activities from the $^{203}Tl(^{16}O, xn)^{219-x}Ac$ reactions. Note that the alpha energy scale of the spectrum at 135 MeV ion energy is different from the other two spectra.

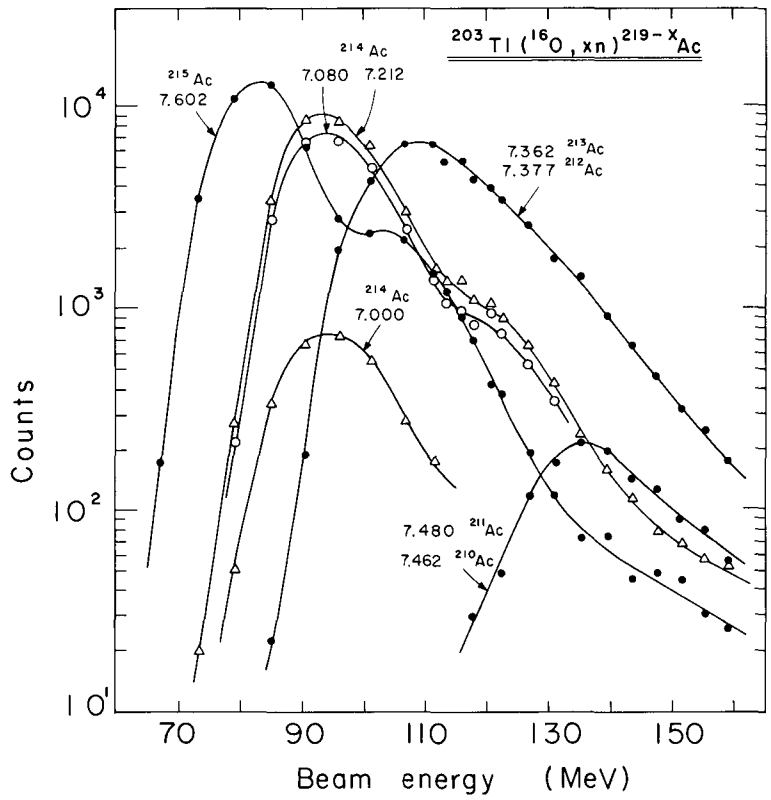

XBL677-3558

Fig. A.6-3. Excitation functions for the actinium isotopes produced in the ^{203}Tl(^{16}O, xn)$^{219-x}$Ac reactions. The second maxima come from the 11.8% ^{205}Tl present in the target.

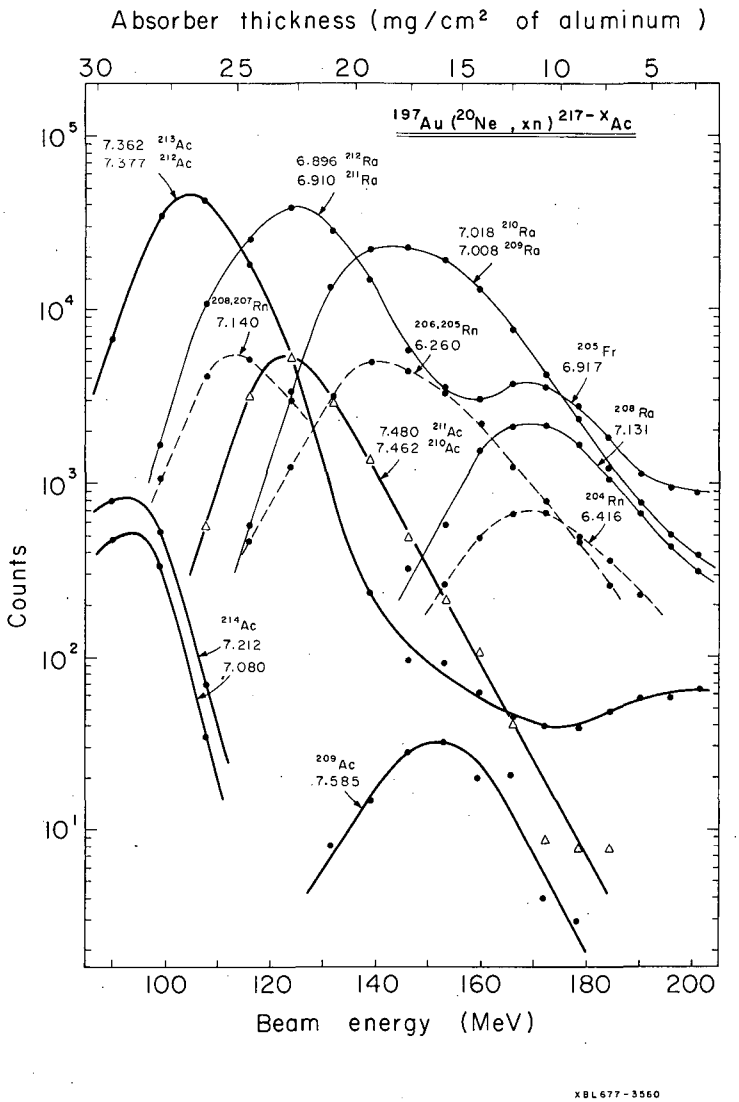

Fig. A.6-4. Excitation functions of the actinium, radium, and radon activities produced in the $^{197}Au(^{20}Ne, xn)^{217-x}Ac$ reactions.

7. NEUTRON-DEFICIENT THORIUM ISOTOPES

Kalevi Valli and Earl K. Hyde

We have almost completed a study of light throium isotopes as a further extension of our work* on neutron-deficient isotopes of several elements in the region above lead. We have produced thorium isotopes ^{213}Th through ^{217}Th by bombardment of ^{206}Pb with ^{16}O at the heavy-ion linear accelerator.

Our previous studies* have shown that other reactions compete with the regular compound-nucleus reactions and that this competition becomes increasingly important as the atomic number of the compound nucleus increases. In the work reported here, formation cross sections for the alpha-emitting thorium isotopes produced by $^{206}Pb(^{16}O;xn)^{222-x}Th$ are severely reduced by fission and by direct reactions that produce great amounts of actinium, radium, francium, and lighter elements "directly."

Because of the low production rates and the short half-lives of the thorium isotopes it was necessary to make additional improvements on the performance of the apparatus shown in Fig. A.6-1. The target chamber was made still smaller, the nozzle was replaced by a capillary, and the flipping wheel was abandoned in most experiments. Instead, the activity was collected directly onto the front surface of an alpha detector, or on a surface close to an alpha detector. The average transfer time of the activity was a few milliseconds; activities with shorter half-lives (^{216}Ac, 0.4 msec) could be seen in reduced intensities.

A summary of our thorium results is given in Table A.7-I. The assignments are based on excitation functions of the thorium isotopes and of their daughters. The α-particle energies of the four new thorium isotopes are shown in Fig. A.7-1 and compared with isotopes of lighter elements with 126 or fewer neutrons.

A detailed description of this work will be given in UCRL-18026, in preparation.

Footnote

*See references in the preceding report A.6.

Table A.7-I. Summary of Th results.

Isotope	Alpha energy (MeV)	Half-life (sec)	%
^{216}Th	7.921±0.008	0.028±0.002	
^{215}Th	7.522±0.008	1.2 ± 0.2	40±3
	7.393±0.008	1.2 ± 0.2	52±3
	7.331±0.010	1.2 ± 0.5	8±3
^{214}Th	7.680±0.010	0.125±0.025	
^{213}Th	7.690±0.010	0.150±0.025	
^{217}Th	9.250±0.010	< 0.5 msec	

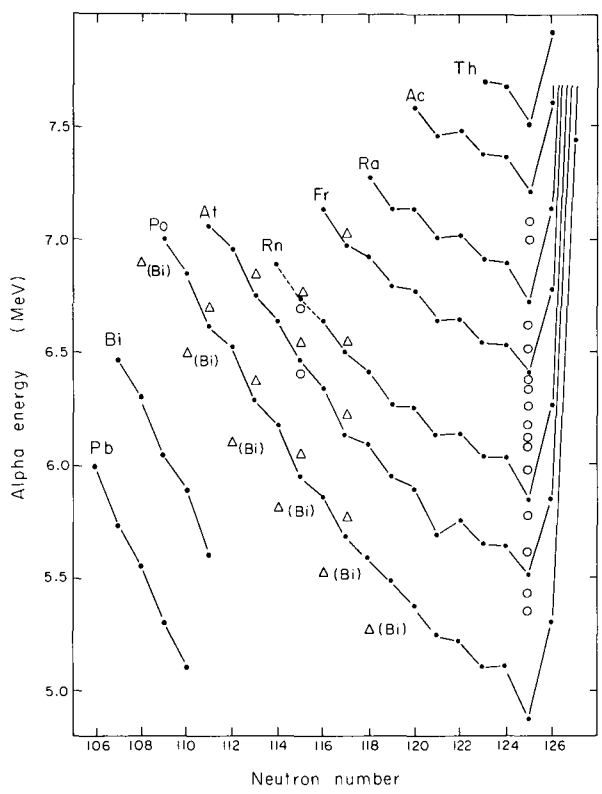

Fig. A.7-1. Alpha-decay energies of the four new thorium isotopes plotted versus neutron number and compared with isotopes of lighter elements. Solid circles indicate ground-state decay, open circles represent decay to excited states of the daughter nucleus, and triangles represent isomeric states.

8. COULOMB EXCITATION OF ^{235}U

F. S. Stephens, M. D. Holtz, R. M. Diamond, and J. O. Newton

The ^{235}U nucleus has been studied by Coulomb excitation, using ^{4}He, ^{16}O, and ^{40}Ar projectiles. Three collective bands based on the 7/2-[743] ground band were observed. These include the K_0+2(11/2-) and K_0-2(3/2-) gamma vibrational bands and the 7/2- beta vibrational band. In addition two single-particle rotational bands (5/2-[752] and 9/2-[734]) were also observed. These two bands, together with the ground band, are components of the $j_{15/2}$ orbital, which provides all the negative parity levels in the 126–184 shell. Because of their expected purity and the high j value these levels lent themselves to a detailed Coriolis calculation, which will be discussed shortly. B(E2) values for excitation of the strongest electron and γ-ray lines were measured. The proposed level scheme is shown in Fig. A. 8-1. In these experiments, 0.003- to 0.05-cm-thick foils, 92% ^{235}U and 8% ^{238}U by mass, were bombarded with projectiles of various energy at the Hilac. The electron spectra were taken on a small wedge-gap spectrometer, and the γ-ray spectra were taken with Ge(Li) detectors. Generally ^{238}U foils were also bombarded under the same conditions to aid in the analysis. These spectra were taken during the beam bursts (5 msec beam pulses 40 times per second), while a second spectrum of equivalent length was usually taken between the bursts and subtracted from the former to eliminate the γ radiation from ^{235}U radioactive decay.

In order to see the greatest number of rotational states 0.01-cm-thick ^{235}U foils were bombarded with 182-MeV ^{40}Ar ions. ^{4}He and ^{16}O projectiles were used for the B(E2) measurements and also for the electron and γ-ray energy measurements of singly excited lines. Some examples of these spectra are shown in Figs. A. 8-2 and A. 8-3.

By using the ^{40}Ar spectra, levels up to spin 25/2 could be identified in the ground band, up to 13/2 in the 5/2-[752] band, and up to 13/2 in the 9/2-[734] band. All these levels were fitted to within 0.5 keV with a three-parameter Coriolis calculation. This calculation also accounted for the admixed amplitudes between the 5/2-7/2 and 7/2-9/2 pairs of bands as indicated by the absolute B(E2) values, and for all the relative E2 and M1 transition probabilities observed. In this calculation all the states arising from the $j_{15/2}$ orbital were included. Where the bands were not observed we used the Nilsson energies[1] at deformation $\eta = 5.5$. All the rotational energy calculations were done in nth-order perturbation theory by use of the computer program BETABLE, written by T. Clements. This program repeatedly solves the secular determinants for all the I values involved, simultaneously adjusting all the parameters until a best least-squares fit to the experimental data is made. The results of this calculation are best shown graphically. By use of the usual rotational formula the energy difference between two consecutive states in a rotational band can be written

$$\frac{E_I - E_{(I-1)}}{2I} = 2I^2B + \frac{\hbar^2}{2\Im} \quad .$$

Thus a plot of $[E_I - E_{(I-1)}]/2I$ vs $2I^2$ should give a straight line with slope B and intercept $\hbar^2/2\Im$. The three-parameter fit is shown in Fig. A. 8-4. The oscillations are due to the influence of the K = 1/2 band. In this calculation $\hbar^2/2\Im$ is a variable as well as the Coriolis matrix elements between the K = 3/2 and 5/2 bands and between the K = 5/2 and 7/2 bands. The ratio obtained from the relative B(E2) values experimentally observed is used to set the matrix element between the K = 7/2 and 9/2 bands at three quarters of the K = 5/2 to 7/2 value. This program gives a very reasonable rotational constant of 6.5 keV while cutting the 3/2-5/2 matrix element by 20% and the 5/2-7/2 matrix element by 46%.

Of the five bands excited in ^{235}U, we ascribe basically collective character to three. These three have more or less the expected properties for such bands, and a detailed examination of these properties has been given in a fuller report[2] of this work. The other two excited bands together with the ground band are basically single-particle states, and their properties seem to be adequately given by Coriolis-admixed Nilsson wave functions.

References

1. S. G. Nilsson, Kgl. Danske Videnskab. Selskab Mat. -Fys Medd. 29, No. 16 (1955).

2. F. S. Stephens, M. D. Holtz, R. M. Diamond, and J. O. Newton, Coulomb Excitation of ^{235}U (UCRL-17976, Dec. 1967), to be submitted to Nucl. Phys.

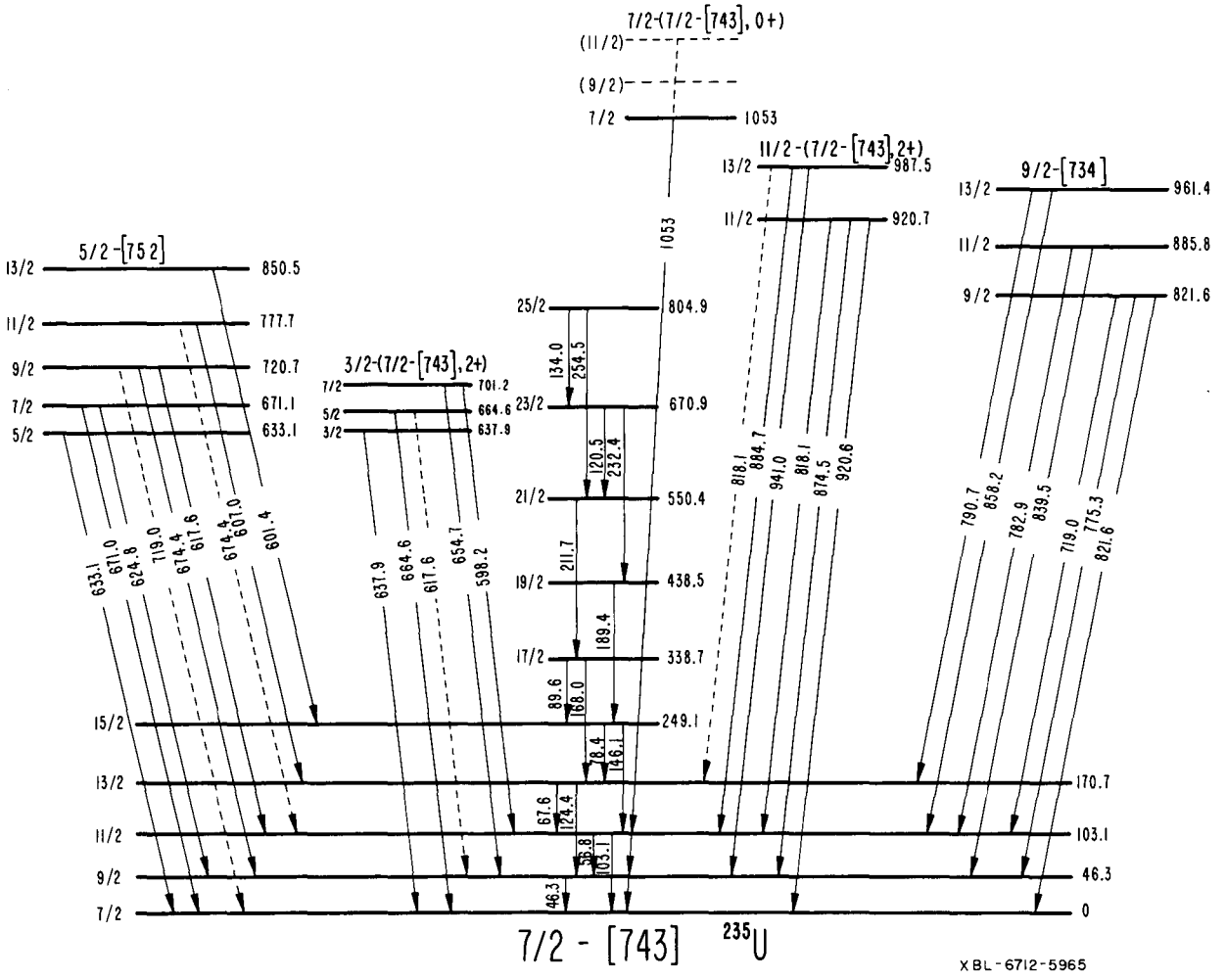

Fig. A. 8-1. Levels Coulomb excited in ^{235}U.

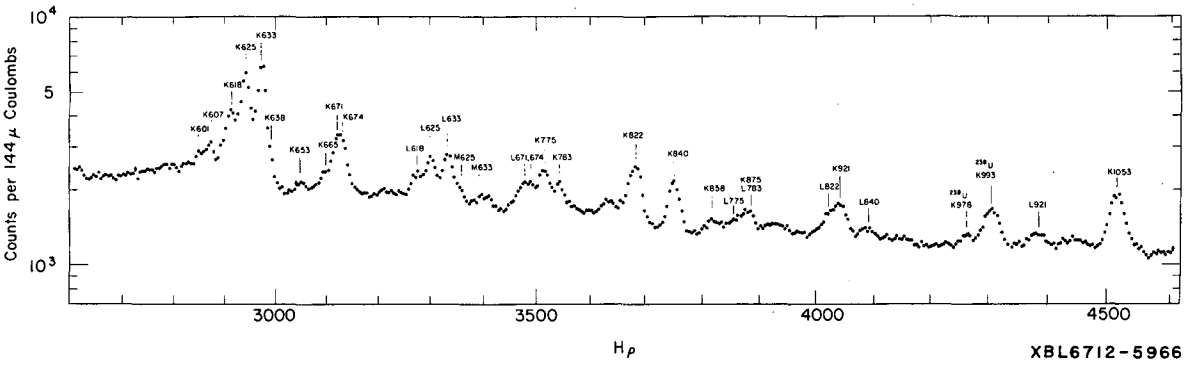

Fig. A. 8-2. Electron spectrum of ^{235}U Coulomb excited by 78-MeV ^{16}O projectiles.

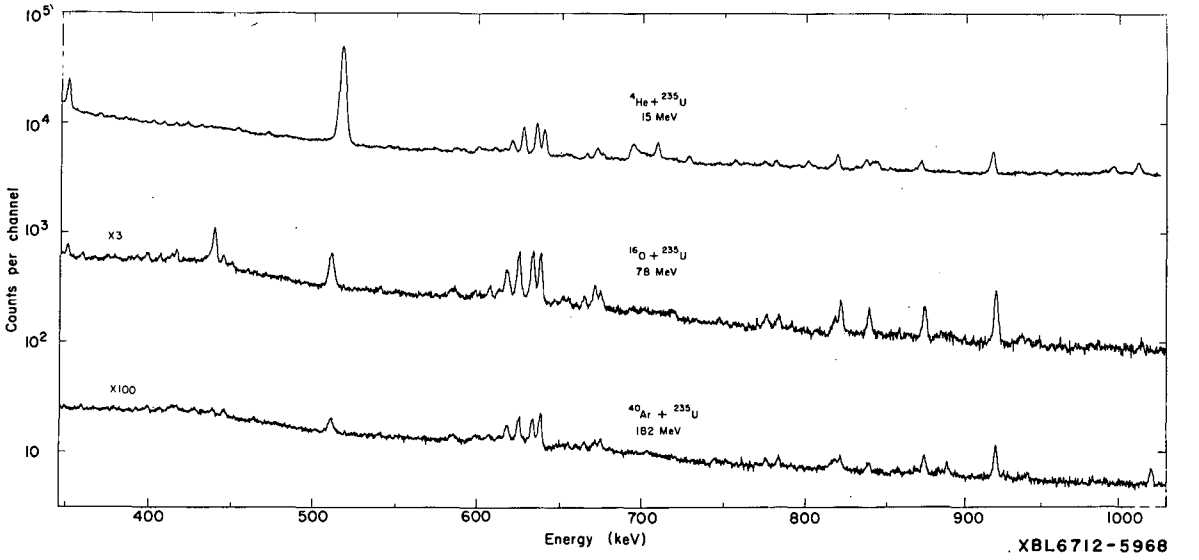

Fig. A. 8-3. Gamma-ray spectra of ^{235}U in the region 400 to 1000 keV. The three spectra correspond to Coulomb excitation by ^{4}He, ^{16}O, and ^{40}Ar projectiles, as indicated on the figure.

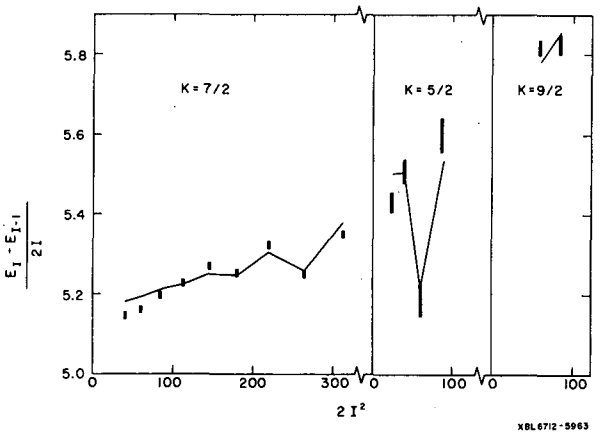

Fig. A. 8-4. Rotational spacings of bands in ^{235}U. The points are the experimental data, with the height of a point indicating the error limits, and the lines are those corresponding to the three-parameter Coriolis calculation.

9. ENERGY LEVELS IN ^{154}Dy

M. Neiman† and David Ward

The γ rays associated with the β decay of ^{154}Ho have been studied by use of a Li-Ge detector. The reaction ^{148}Sm(^{11}B, 5n)^{154}Ho at 75 MeV bombarding energy was employed. The beam was provided by the Berkeley Hilac. Counts were recorded in the time interval between beam bursts of the machine, and the spectrum is shown in Fig. A. 9-1. The half-life of the activity was found to be 3.25 ± 0.1 minutes, and γ rays assigned to ^{154}Dy on the basis of their half-life are shown in Table A. 9-I. A γ-γ coincidence measurement using two Li-Ge detectors was also performed. Spectra are shown in Fig. A. 9-2.

The "in-beam" spectrum of ^{154}Dy in the reaction ^{139}La(^{19}F, 4n)^{154}Dy at 86 MeV has also been studied. The prominent transitions of the ground-state quasi-rotational band are indicated in Fig. A. 9-3. The anisotropy of the angular distribution of the γ rays with respect to the beam direction was also determined. The results are tabulated in Table A. 9-I.

A level scheme is proposed in Fig. A. 9-4, based on the results of the "in-beam" work, coincidence data, and consideration of the energy sums and intensity balance. Previous work has shown that the $2^+ \rightarrow 0^+$ transition is at 335 keV; however, no level scheme was proposed.[1, 2] That the levels 906.0, 1252.4, and 1659.4 keV have spins 2^+, 4^+, and 6^+ is suggested mainly by the strong resemblance of the level scheme to those of the other 88-neutron nuclei ^{150}Sm and ^{152}Gd.[3] In Table A. 9-I the classifications A and B denote reasonably certain and tentative assignment respectively.

It is possible that the levels given tentatively as $2^{+\prime}$, $4^{+\prime}$, and $6^{+\prime}$ form a quasi beta-vibrational band,[4] the $0^{+\prime}$ level which would be expected at around 600 keV being undetected in the experiments described here (viz, ^{150}Sm and ^{152}Gd). The β decay of ^{154}Ho offers interesting possibilities for the detailed study of collective levels in ^{154}Dy, since rarely does β decay populate levels of such high angular momentum. It is clear that the decaying level in ^{154}Ho must have an unusually high spin. Recently Hahn et al.[5] have assigned an α decay of half-life 11.8 ± 1.0 minutes to ^{154}Ho--whether this level, or the β-decaying level observed in these experiments in the ground state, can not be decided from the present experiments. Further study of the levels in ^{154}Dy would involve spectroscopy of the conversion electrons; in particular, the transitions $J' \rightarrow J$ should have strong E_0 admixtures if the levels J' have characteristics of a β-vibrational band.

Footnote and References

†Current address: Rutgers University, New Jersey.

1. P. Lagarde, J. Treherne, A. Gizon, and J. Valentin, J. Physique 27, 116 (1966).
2. H. Morinaga and P. E. Gugelot, Nucl. Phys. 46, 210 (1963).
3. Table of Isotopes, C. M. Lederer, J. M. Hollander, and I. Perlman (1967).
4. M. Sakai, Nucl. Phys. A104 [2], 301 (1967).
5. R. L. Hahn, K. S. Toth, and T. H. Handley, Phys. Rev. 163, 1291 (1967).

Table A. 9-I. Gamma rays assigned to ^{154}Dy.

Decay of $^{154}Ho \xrightarrow{\beta} {}^{154}Dy$		$^{139}La(^{19}F, 4n)^{154}Dy$				
Transition energy (keV)	Relative intensity	Transition energy (keV)	Relative intensity	Anisotropy	Assignment	
159.7 ± 0.2	3.9 ± 0.3					
289.2 ± 0.2	4.3 ± 0.3					
295.8 ± 0.2	12.8 ± 0.3	295.8 ± 0.3	7 ± 2	-0.4 ± 0.15		
310.3 ± 0.25	3.0 ± 0.3					
334.7 ± 0.25	100	334.7 ± 0.25	100	0.53 ± 0.08	$2^+ \rightarrow 0^+$	A
346.5 ± 0.3	12.5 ± 0.7				$4^{+\prime} \rightarrow 2^{+\prime}$	B
407.0 ± 0.3	24.5 ± 0.7	406.8 ± 0.4	9 ± 3	0.8 ± 0.3	$6^{+\prime} \rightarrow 4^{+\prime}$	B
412.5 ± 0.3	84 ± 3	412.5 ± 0.3	100 ± 5	0.6 ± 0.1	$4^+ \rightarrow 2^+$	A
434.9 ± 0.4	2.5 ± 0.3				$6^{+\prime} \rightarrow 6^+$	B
		439.8 ± 0.5	29 ± 4	-0.36 ± 0.05		
444.2 ± 0.4	5.1 ± 0.3					
		448.0 ± 0.5	8 ± 3	2.0 ± 1		
471.9 ± 0.6	2.5 ± 0.4					
477.4 ± 0.4	56 ± 2	477.6 ± 0.4	85 ± 5	0.8 ± 0.1	$6^+ \rightarrow 4^+$	A
		488.0 ± 0.5	11 ± 2	0.2 ± 0.2		
505.2 ± 0.4	16.2 ± 0.5				$4^{+\prime} \rightarrow 4^+$	B
523.8 ± 0.4	16 ± 0.4	524.1 ± 0.4	73 ± 5	0.7 ± 0.1	$8^+ \rightarrow 6^+$	A
		557.3 ± 0.4	45 ± 5	0.6 ± 0.15	$10^+ \rightarrow 8^+$	A
570.6 ± 0.5	10 ± 2				$2^{+\prime} \rightarrow 2^+$	B
		589.0 ± 1	30 ± 5	0.3 ± 0.15		
		616.0 ± 1	22 ± 4	0.3 ± 0.15		
		637.0 ± 1	21 ± 4	0.8 ± 0.3		
726.5 ± 0.7	13 ± 2				$(7^{\pm}, 8^+) \rightarrow 8^+$	B
815 ± 0.7	13 ± 3				$(7^{\pm}, 8^+) \rightarrow 6^{+\prime}$	B
906 ± 1	1.5 ± 0.5				$2^{+\prime} \rightarrow 0^+$	B
1249.5 ± 1	16 ± 2				$(7^{\pm}, 8^+) \rightarrow 6^+$	B

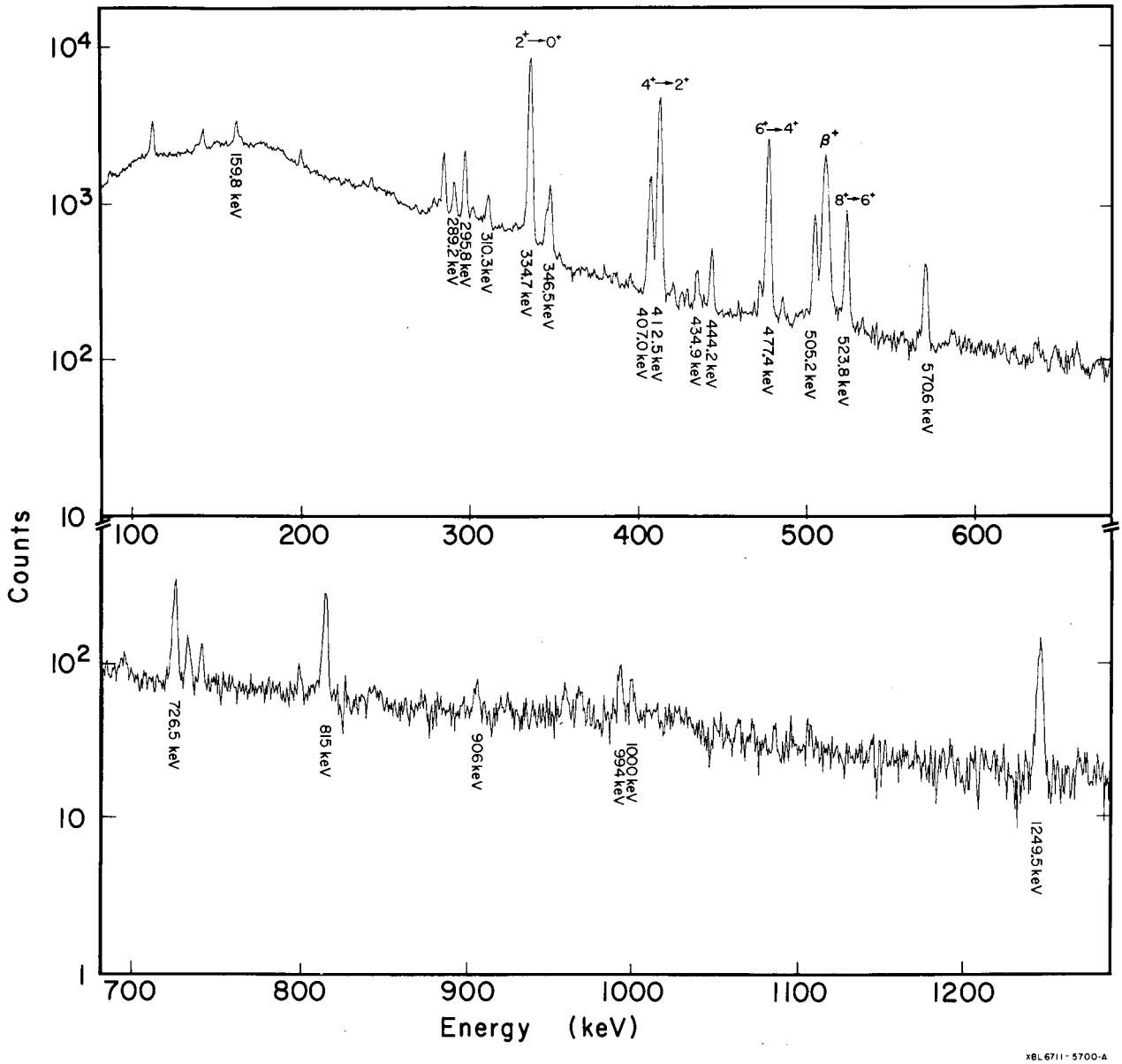

Fig. A. 9-1. Gamma spectrum of the decay $^{154}Ho \xrightarrow{\beta} {}^{154}Dy$ following the reaction $^{148}Sm(^{11}B, 5n)^{154}Ho$ at 75 MeV.

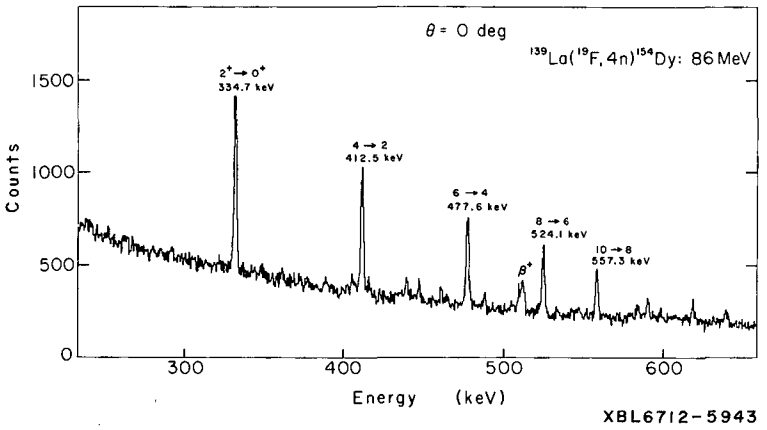

Fig. A. 9-2. Gamma-ray coincidence spectra of the decay ^{154}Ho $\xrightarrow{\beta}$ ^{154}Dy.

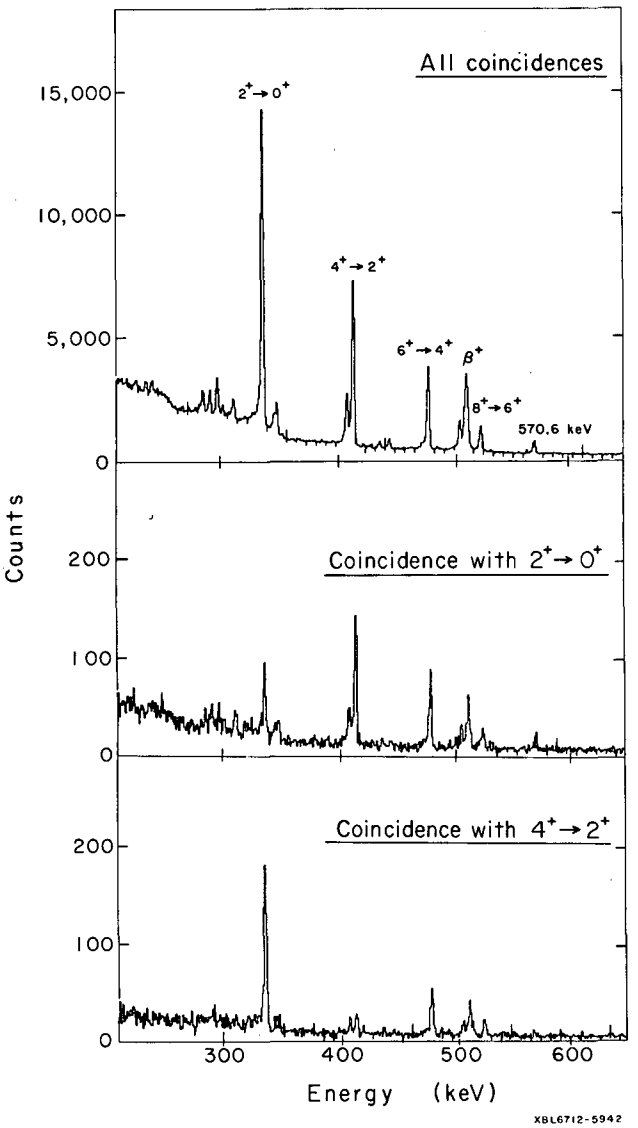

Fig. A. 9-3. Gamma rays during the reaction ^{139}La(^{19}F, 4n)^{154}Dy at 86 MeV.

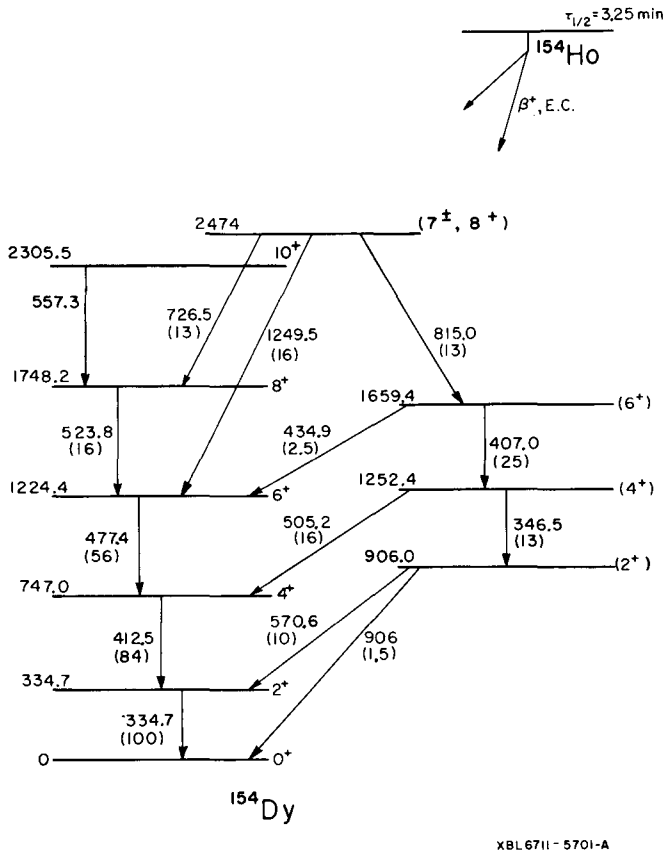

Fig. A. 9-4. Level scheme for ^{154}Dy.

10. NUCLEAR SPECTROSCOPY FOLLOWING ^{40}Ar, xn REACTIONS†

David Ward, F. S. Stephens, and J. O. Newton*

We have studied the γ rays emitted as the final step in the deexcitation of ^{40}Ar, xn reaction products. Previous studies of this type have used projectiles ranging from protons to ^{19}F ions.[1-3] The advantages of using very heavy projectiles are: (i) considerably greater linear and angular momentum are imparted to the compound system; (ii) accessibility is provided to regions of the periodic table that cannot easily be reached with lighter ions, and (iii) the very neutron-deficient compound systems can usually be produced with lower excitation energy, resulting in greater product specificity.

That it is feasible to make spectroscopic measurements following ^{40}Ar, xn reactions is shown in Fig. A. 10-1, where spectra resulting from $^{124, 122, 120}$Sn(^{40}Ar, 4n)$^{160, 158, 156}$Er reactions are shown. We have also made the 88-, 90-, and 92-neutron Yb isotopes by bombarding separated Te targets, and the rotational transitions thus identified are shown in Table A-10-I.

The peak cross sections (at ≈ 160 MeV) for the ^{40}Ar, 4n reactions were measured on the assumption that the 4+→2+ transition represents the entire cross section for producing the 4n product. This seems very likely, as there is essentially no drop in the rotational transition intensities until much higher in the bands. Our preliminary estimate is that the ^{40}Ar, 4n cross sections peak around 200 mb, and, adding an empirical correction for the 3n and 5n reactions, we obtain ^{40}Ar, xn cross sections of ≈ 400 mb. This means that angular momenta up to about 50 ħ are contributing to the xn reactions. This implies that the upper limit to the observed

ground-band rotational spectra depends on the nuclear energy levels rather than being a limitation imposed by the available angular momentum.

We also have an estimate of the cross section for evaporated α particles from ^{40}Ar reactions on ^{124}Sn and ^{130}Te at 160 MeV, and find them to be around 100 mb. Thus it appears that most of the total reaction cross section for ^{40}Ar on Sn and Te targets at this energy still goes into compound nucleus formation and subsequently into neutron emission. Even if a considerably smaller fraction of the total reaction cross section goes into these reactions, it seems likely that spectroscopic studies will be possible following xn reactions with considerably heavier ions.

Footnotes and References

†Paper presented at International Conference on Nuclear Structure, Tokyo, Japan, September 7-13, 1967 (UCRL-17568, June 1967).

*Department of Physics, University of Manchester, Manchester 13, England.

1. H. Morinaga and P. E. Gugelot, Nucl. Phys. 46, 210 (1963).
2. G. B. Hansen, B. Elbek, K. A. Hagemann, and W. F. Hornyak, Nucl. Phys. 47, 529 (1963).
3. F. S. Stephens, N. L. Lark, and R. M. Diamond, Nucl. Phys. 63, 82 (1965).

Table A. 10-I. Rotational transition energies.

	N = 92		N = 90		N = 88	
Transition	^{160}Er	^{162}Yb	^{158}Er	^{160}Yb	^{156}Er	^{158}Yb
2 → 0	126.2	166.5	192.7	243.0	344.4	357.9
4 → 2	264.3	320.2	335.7	395.3	452.9	476.0
6 → 4	376.3	436.2	443.8	508.8	543.2	548.3
8 → 6	464.6	521.2	523.8	588.7	618.2	
10 → 8	532.1	569.4	579.7	~636	~675	
12 → 10	579.4		608.7			

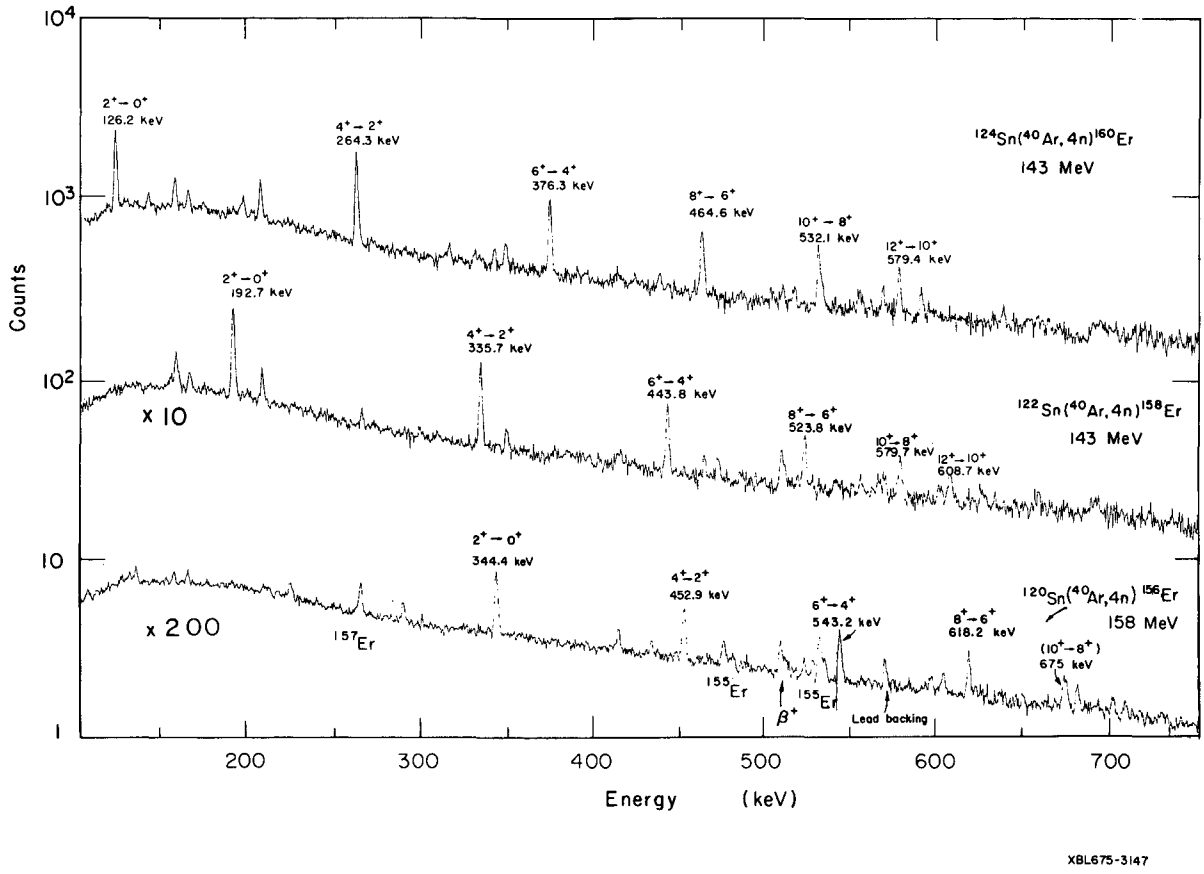

Fig. A. 10-1. Gamma-ray spectra following ^{40}Ar, 4n reactions, taken with a 6 cm^2×0.8-cm-deep Ge(Li) detector.

11. COLLECTIVE LEVELS IN NEUTRON-DEFICIENT EVEN CERIUM NUCLEI

David Ward, F. S. Stephens, and R. M. Diamond

The γ-ray spectra of $^{136, 134, 132, 130, 128}$Ce have been studied during HI, 4n reactions, in which a given cerium nucleus was the final product. The reactions (^{20}Ne, 4n) on $^{116, 114, 112, 110}$Cd, and (^{16}O, 4n) on $^{124, 122, 120, 118, 116}$Sn, were employed. Heavy-ion beams were provided by the Berkeley Hilac. Excitation functions and angular distributions of the γ rays were measured, and in the cases $^{136, 132, 128}$Ce, γ-γ coincidence experiments using two Li-Ge counters were performed. These measurements enabled us to assign the transitions of the ground-state quasi-rotational band with considerable confidence. Typical spectra are shown in Figs. A. 11-1 and A. 11-2, and the partial level schemes in Fig. A. 11-3; the results are tabulated in Tables A. 11-I and A. 11-II.

As would be expected from the work of Clarkson et al.[1] on the isotopes of Ba and Xe, these light Ce isotopes show increasingly collective behavior as the neutron number is decreased. This is evident from the drop in the energy of the first 2+ level, and the increase in the ratio E4:E2 with decreasing N.

We were not able to assign the γ rays of ^{126}Ce from the reaction ^{110}Cd(^{20}Ne, 4n)^{126}Ce, and we conclude that the intermediate nuclei involved in this system are sufficiently neutron-deficient that the evaporation of charged particles is of probability comparable to that for neutrons. This is evidenced by the products of ^{20}Ne, α2n and ^{20}Ne, 2p2n reactions shown in Fig. A. 11-2. We also note that the peak cross section for the ^{20}Ne, 4n reaction on ^{112}Cd (215 millibarns) is considerably less than that for the same reaction on ^{114}Cd (310 mb). It seems likely that the use of other techniques will be necessary to study systems as neutron-deficient as ^{126}Ce. For example, the reaction HI, α2n appears to offer further possibilities, such as ^{100}Ru(^{32}S, α2n)^{126}Ce. The techniques could be extended to taking γ spectra in coincidence with the evaporated α particles.

The energy levels have been analyzed by using the Harris equation,[2]

$$E_J = \frac{1}{2}\omega^2 (I_0 + 3C\omega^2), \qquad J(J+1) = \omega^2 (I_0 + 2C\omega^2)^2 .$$

The results are shown in Table A. 11-III. The spacings differ considerably from those of the rotational model: $E_J = AJ(J+1)$, and it will be seen that the effective moment of inertia, $(E_J - E_{J-2})/(4J-2)$, decreases rapidly with increasing spin. This is probably due to several effects, such as centrifugal stretching[3] and the Coriolis anti-pairing effect.[4] The Harris-model parameters I_0 and C are a convenient meeting point between the data and theoretical calculations including these effects. Such calculations have recently been performed for nuclei at the end of the rare earth region,[5] and it would be of interest to extend them to the cerium region. In this cerium region the deviations of the level spacing from the rotational model are much larger than in the rare earths; however, the Harris equations give fits of a comparable quality.

References

1. J. E. Clarkson, R. M. Diamond, F. S. Stephens, and I. Perlman, Nucl. Phys. A93, 272 (1967).
2. S. M. Harris, Phys. Rev. 139, B770 (1965).
3. R. M. Diamond, F. S. Stephens, and W. J. Swiatecki, Phys. Letters 11, 315 (1964).
4. B. R. Mottelson and P. G. Valatin, Phys. Rev. Letters 5, 511 (1960).
5. T. Udagawa and R. K. Sheline, Phys. Rev. 147, 671 (1966).
6. J. O. Newton, F. S. Stephens, R. M. Diamond, K. Kotajima, and E. Matthias, Nucl. Phys. A95, 357 (1967).

Table A. 11-I. Energies E, relative yields I, and anisotropies A, for the ground-band transitions. (The anisotropy should generally lie in the range 0.33 to 0.75 for stretched E2 transitions--Ref. 6.)

		Transitions				
		2 → 0	4 → 2	6 → 4	8 → 6	10 → 8
^{136}Ce	E	552.0	761.6	(899.0)		
$^{124}Sn(^{16}O, 4n)$	I	100.0	99.0	19.0		
	A	0.25 ± 0.04	0.19 ± 0.06	0.05 ± 0.2		
^{134}Ce						
$^{122}Sn(^{16}O, 4n)$	E	409.2	639.3	813.9	946.5	
	I	100.0	89.0	62.0	40.0	
	A	0.42 ± 0.04	0.47 ± 0.08	0.63 ± 0.15	0.45 ± 0.15	
^{132}Ce	E	325.4	533.5	683.8	787.8	
$^{120}Sn(^{16}O, 4n)$	I	100.0	97.0	73.0	52.0	
$^{116}Cd(^{20}Ne, 4n)$	A	0.61 ± 0.03	0.53 ± 0.07	0.43 ± 0.1	0.72 ± 0.15	
^{130}Ce	E	254.1	456.7	613.4	729.0	
$^{118}Sn(^{16}O, 4n)$	I	100.0	86.0	82.0	61.0	
$^{114}Cd(^{20}Ne, 4n)$	A	0.40 ± 0.04	0.49 ± 0.07	0.57 ± 0.1	0.87 ± 0.15	
^{128}Ce	E	207.3	399.9	550.6	662.5	(725.5)
$^{116}Sn(^{16}O, 4n)$	I	100.0	73.0	72.0	59.0	24
$^{112}Cd(^{20}Ne, 4n)$	A	0.41 ± 0.03	0.60 ± 0.1	0.59 ± 0.15	0.59 ± 0.15	

Table A. 11-II. Prominent non-ground-band transitions.

Nucleus	Energy (keV)	Relative intensity	Anisotropy
^{136}Ce	664.8	75	-0.05 ± 0.04
^{134}Ce	907.0	24	0.9 ± 0.2
^{132}Ce	570.5	28	0.79 ± 0.16
	802.0	16	0.44 ± 0.15
	828.7	28	1.2 ± 0.3
^{130}Ce	503.3	29	0.53 ± 0.1
	756.3	30	0.50 ± 0.12

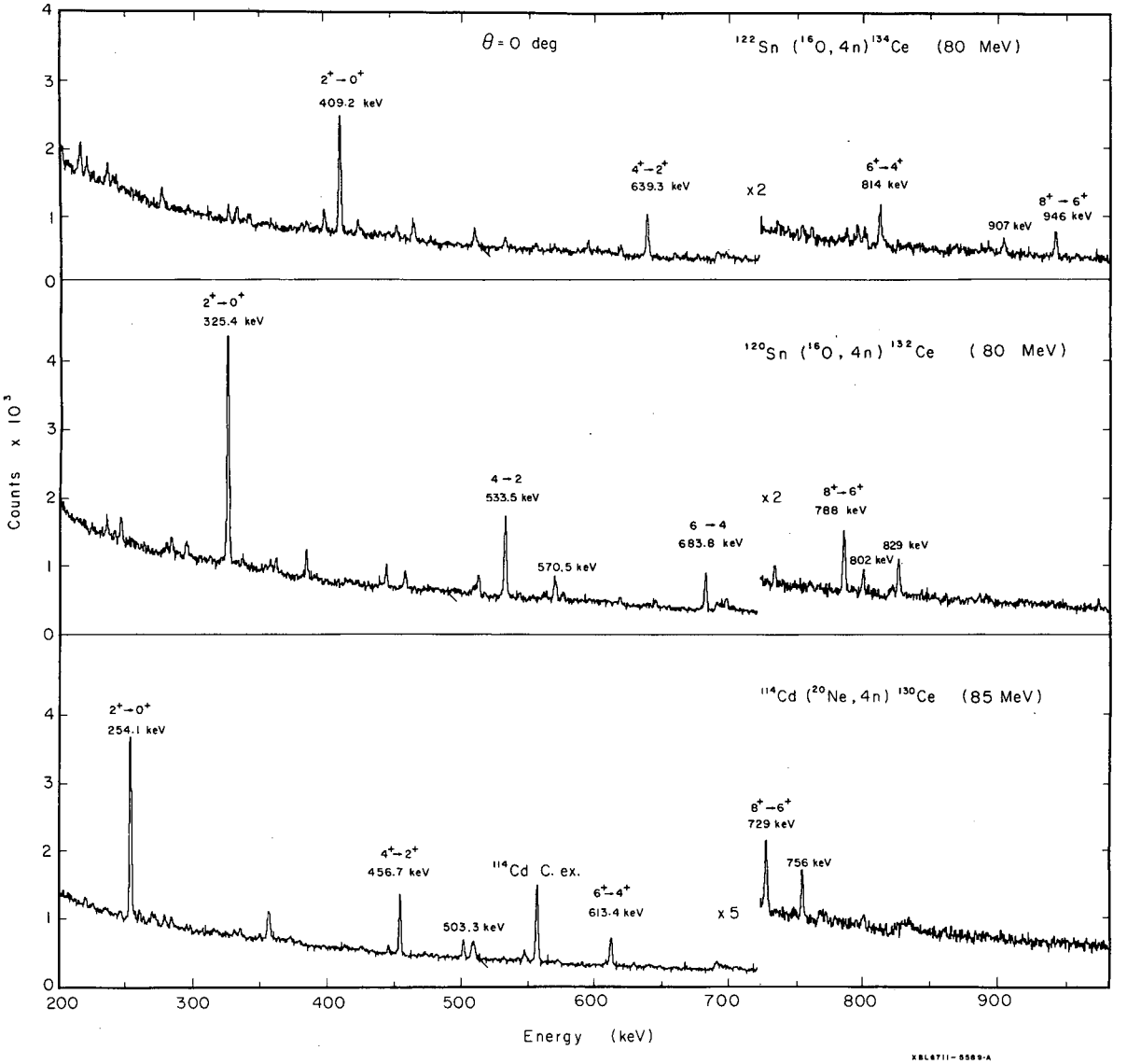

Fig. A. 11-1. Gamma spectra of $^{134, 132, 130}$Ce.

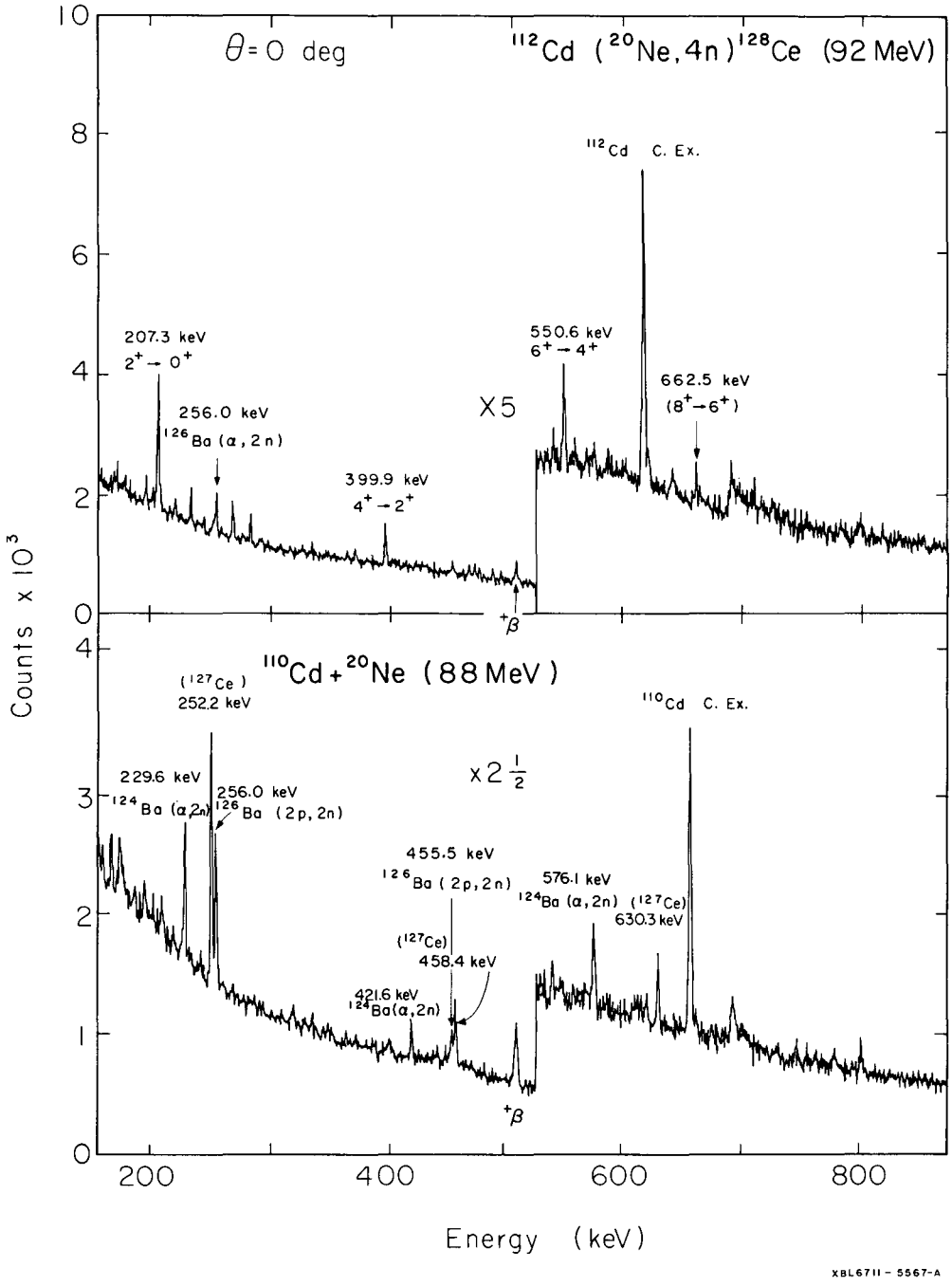

Fig. A. 11-2. Gamma spectra of ^{128}Ce, and competing reactions in the system ^{110}Cd + ^{20}Ne at 88 MeV.

Table A. 11-III. Harris-model fits.

Nucleus		Energy levels (keV)						Parameters		rms Deviation
		2^+	4^+	6^+	8^+	10^+	12^+	I_0 ($\times 10^3$)	C ($\times 10^8$)	(%)
^{136}Ce	Expt.	552.0	1313.6	2213.0						
	Theory	552.1	1312.6	2214.0	3224	4325	5503	1.947	2.533	0.17
^{134}Ce	Expt.	409.2	1048.6	1862.0	2809					
	Theory	407.2	1060.1	1864.0	2783	3796	4889	5.018	2.682	0.92
^{132}Ce	Expt.	325.4	858.9	1542.7	2331					
	Theory	324.1	866.0	1542.6	2321	3182	4114	6.898	4.095	0.51
^{130}Ce	Expt.	254.1	710.7	1324.1	2053					
	Theory	252.7	719.4	1325.0	2035	2830	3699	10.25	4.311	0.81
^{128}Ce	Expt.	207.3	607.3	1157.8	1820	(2573)				
	Theory	205.7	613.8	1162.3	1818	2561	3379	13.43	4.389	0.64

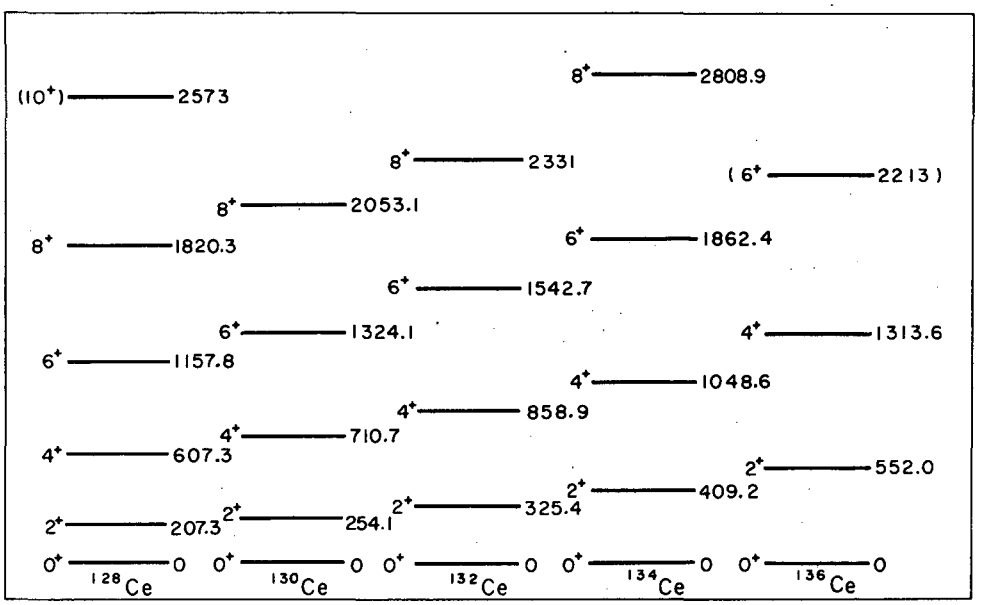

Fig. A. 11-3. Energy levels of the ground-state quasi-rotational band in the light even cerium nuclei.

12. SYSTEMATICS OF ENERGY LEVELS IN EVEN NUCLEI

David Ward, F. S. Stephens, and R. M. Diamond

Recent results in the field of HI, xn γ-ray spectroscopy[1] show that the 88- to 90-neutron discontinuity between vibrational and rotational behavior, which is very noticeable for Z = 62 and 64, tends to diminish for higher Z, and is scarcely present at Z = 70. This is shown in Fig. A. 12-1. A similar behavior has been previously noted in the Z = 76 to 78 region of the periodic table.[2]

Mallmann has plotted $E_J/E2$ against $E4/E2$ for the ground-state rotational bands of even nuclei, and concluded that the levels exhibit a smooth behavior between the rotational and vibrational limits.[3] We have prepared a similar plot, shown in Fig. A. 12-2, with considerably more data. We have plotted here only the data up to spin eight; the higher spin values contain fewer data points and are very similar to those shown. In this type of plot a one-parameter relationship can be represented by a point, as indicated by the rotational and harmonic oscillator (vibrational) points shown, and a two-parameter relationship gives a line. We have shown five such lines: (i) the two-term series expansion in I(I+1) (labeled A+B), which is quite bad except for the very good rotors; (ii) the centrifugal stretching models[4-6] (labeled D. C.); (iii) the recent relationship due to Sood[7] based on treatments of molecular rotation; (iv) the remarkably simple empirical relationship used by Ejiri[8] and others,[9] $E_I = kI(I+1) + aI$ or $E_I = AI(I+N)$; and (v) the equations of Harris,[10] $E_J = (1/2)\omega^2(\Im_0 + 3c\omega^2)$, $J(J+1) = \omega^2(\Im_0 + 2c\omega^2)^2$. We draw several conclusions from this plot: (a) the data fall remarkably closely on a single line between the rotational and harmonic oscillator limit, as previously noted by Mallman, (b) for the reasonably good rotors ($E_4/E_2 > 3$) the relationship of Sood gives the best fits, and (c), considering the whole region, it appears that the Harris equations give the best fit.

This plot serves as an objective comparison of these models with regard to their capability of reproducing the energy-level spacings. Because the models vary so widely in their complexity and physical content we feel that this comparison, although useful for a number of purposes, is not to be considered an evaluation of their worth or validity. More information is needed to determine what is really happening in the nucleus as the angular momentum is increased in the ground-state band.

References

1. David Ward, F. S. Stephens, and J. O. Newton, Phys. Rev. Letters 19, 1247 (1967).
2. J. Burde, R. M. Diamond, and F. S. Stephens, Nucl. Phys. 85, 481 (1966).
3. C. A. Mallman, Phys. Rev. Letters 2, 507 (1959).
4. A. S. Davydov and A. A. Chaban, Nucl. Phys. 20, 499 (1960).
5. S. A. Moszkowski, in Handbuch der Physik 39, ed. by F. Flügge; in Proceedings of the Summer Study Group on Physics of Emperor Tandem van de Graaff Region, BNL 948 (C-46).
6. R. M. Diamond, F. S. Stephens, and W. J. Swiatecki, Phys. Letters 11, 315 (1964).
7. P. C. Sood, Phys. Rev. (to be published).
8. H. Ejiri, University of Tokyo, Institute for Nuclear Study, report INS-J 101 (1966).
9. See O. Nathan and S. G. Nilsson, in Alpha-, Beta-, and Gamma-Ray Spectroscopy, ed. by K. Siegbahn (North-Holland Publishing Co., Amsterdam, 1965).
10. S. M. Harris, Phys. Rev. 139, B770 (1965).

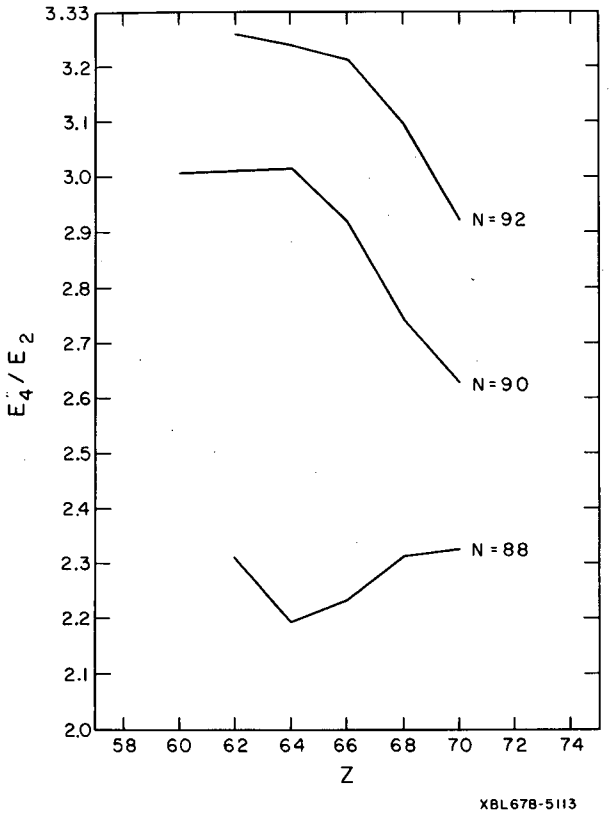

Fig. A. 12-1. The ratio of the energy of the 4+ member of the ground-state collective band to that of the 2+ member plotted as a function of the Z of the nucleus. The lines connect points with constant N.

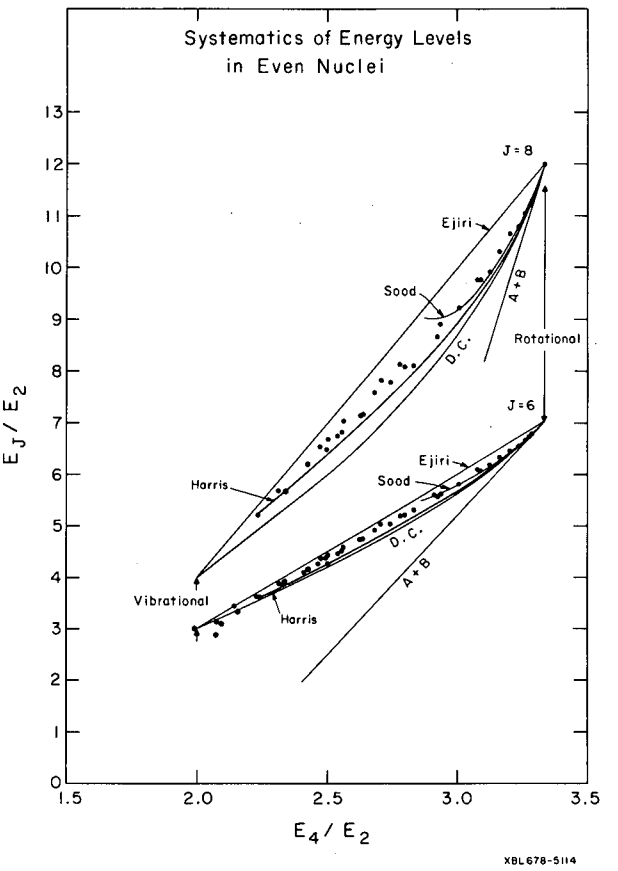

Fig. A. 12-2. The ratio E_J/E_2 plotted for J = 6 and 8 against E_4/E_2 for a number of nuclei (dots), and the predictions of five two-parameter relationships for these ratios, shown as lines (see text). All the data we could find having $2 < E_4/E_2 < 3$ are shown; however, only a few representative points with $E_4/E_2 > 3$ have been included.

13. POTENTIAL-ENERGY EFFECTS IN HEAVY-ION TRANSFER REACTIONS†

R. M. Diamond, A. Poskanzer, F. S. Stephens, W. J. Swiatecki, and D. Ward

Nucleon transfer reactions have been rather extensively studied with light projectiles ($Z \leq 2$) on a wide variety of targets. With heavy projectiles ($Z > 2$), however, these studies have been carried out mostly with light targets.[1] The few studies made using both heavy projectiles and medium or heavy targets have been done radiochemically, and have been mainly concerned with neutron transfers.[1-3] Recently, however, the reaction (^{12}C, ^{13}N), which transfers a proton from the target to the projectile, has been studied radiochemically with of heavy targets,[4] and the results yielded much lower cross sections than expected from the neutron transfer cases. Also, in a recent radiochemical study of ^{12}C and ^{14}N on ^{115}In, it has been found[5] that the loss of two protons by the target appeared to be much less probable than the corresponding gain of two protons by the target.

In the present work, using a power-law-type particle identifier system with semiconductor detectors,[6] we have studied the proton transfers in both directions, using five targets between Ni and Au, and four projectiles between ^{10}B and ^{14}N.

From spectra such as those shown in Fig. A. 13-1, we could easily integrate the total yield of a given element, as the separations between different elements were quite good. However, it was more difficult to integrate accurately the isotopes of a given element, and we estimate an average uncertainty of around 30% in the ratio due to this effect, although in one or two cases with poor statistics it could be as large as a factor of two. Although it is clear that these reactions are complex, we found a general trend that the transfer of a proton from a heavy target to the projectile is less favored than the transfer in the other direction.

The quantitative interpretation of these transfer reactions would undoubtedly be difficult. As with any dynamical process it would involve several steps, of which the first would be an analysis of the potential energies of the relevant nuclear configurations, in particular the energies of the target and projectile in close proximity before and after transfer. Indeed, it has been recognized for some time that the masses--or more precisely the Q-values--affect the yields of the products of transfer reactions. The Q-values refer, however, to the masses of infinitely separated nuclei, and the relevant energy in transfer reactions must also include the Coulomb interaction energy. If one considers the target and projectile as two spheres in close proximity, one can easily write down the expression for their electrostatic interaction energy and, using the same separation distance, also for the interaction energy following the transfer of particles. It is apparent that systems in which the projectile loses protons are favored by the Coulomb interaction energy, since $(Z_t + 1)(Z_p - 1) < (Z_t - 1)(Z_p + 1)$. Here Z_t and Z_p are the atomic numbers of target and projectile.

To test these energy considerations we have plotted in Fig. A. 13-2 the ratio of yields (projectile + p)/(projectile - p) against (a) the difference in Q-values for the reactions, ΔQ, and (b) that difference plus the difference in Coulomb interaction energy, $\Delta Q + \Delta E_c$. We calculated interaction energies using projectile-target distances deduced from the experimental conditions themselves (bombarding energy and θ); the results do not differ significantly from what would be obtained by assuming tangent spheres whose sizes were given by a radius parameter equal to about 1.4 F.

The correlation in Fig. A. 13-2b is rather good, in that the ^{10}B, ^{11}B, and ^{14}N results fall approximately on a single curve which goes through the point of equal yields for $\Delta Q + \Delta E_c = 0$. The points for ^{12}C, although lying on a different curve (for a reason that is not obvious to us) also confirm the existence of a correlation between yield ratios and potential energy differences. Moreover this curve also passes approximately through the neighborhood of the equal yield point when $\Delta Q + \Delta E_c = 0$. There is considerable scatter of the points in Fig. A. 13-2, part of which may be due to experimental error, but which may also reflect real effects not included in this simple treatment. It is apparent, however, that the correlation in Fig. A. 13-2b is a great improvement over that in Fig. A. 13-2a, where Coulomb interaction energy is not included.

More extensive experiments will be necessary to determine the extent of validity of the correlation between yields of transfer reactions and the relevant potential energy changes of two nuclei in close proximity. Since such a correlation is, however, not at all unexpected from first principles, we believe it may not be premature to point out some of the consequences of the existence of this correlation.

For any given pair of nuclei the most direct method of estimating the potential energy or mass is to add to the experimental masses of the nuclei the electrostatic interaction energy. Insofar as the average trends of nuclear masses are known to be reproduced by the liquid drop model,[7] it should be possible to predict what the gross average trends of transfer reaction yields should be, based on a study of the elementary problem of two tangent charged polarizable spheres. The results have been discussed briefly in the full report of this work.†

What we have proposed specifically here is that the asymmetry in the direction of proton transfers, as well as the apparent gross differences in proton and neutron transfers, can be understood by considering the relevant potential energies of the systems. These energies have been approximated by the masses at infinite separation (Q values) plus a Coulomb interaction energy term. The latter term is important when heavy projectiles and targets are involved, and its inclusion brings the proton data into reasonable accord with expectations. A convenient qualitative way to view the energetics of the proton transfer process is to realize that most

projectiles in contact with a heavy target nucleus constitute a proton-rich region compared with the target nucleus. This (for most projectiles) provides a driving force for the transfer of protons into the target nucleus rather than out of it, and the effect is the larger the greater the difference in the charge densities (i.e., neutron/proton ratios) of the target and projectile.

Footnotes and References

†UCRL-18013, Jan. 1968, submitted to Phys. Letters.

1. A. Ghiorso, R. M. Diamond, and H. E. Conzett, eds., Proceedings of the Third Conference on Reactions Between Complex Nuclei (University of California Press, Berkeley, California, 1963), Sessions B and C, pp. 81-198.
2. W. E. Frahn and R. H. Ventner, Nucl. Phys. 59, 651 (1964), and references therein.
3. A. G. Artyukh, V. V. Volkov, and T. Kwiecinska, J. Nucl. Phys. (USSR) 4, 1165 (1966).
4. V. V. Volkov and J. Wilczynski, Nucl. Phys. A92, 495 (1967).
5. P. M. Strudler, I. L. Priess, and R. Wolfgang, Phys. Rev. 154, 1126 (1967).
6. J. Cerny, S. W. Cosper, G. W. Butler, H. Brunnader, R. L. McGrath, and F. S. Goulding, Nucl. Instr. Methods 45, 337 (1966).
7. For the energy of two uniformly charged spheres see S. Frankel and N. Metropolis, Phys. Rev. 72, 914 (1947). A formula for the optimum charges on two polarizable tangent spheres is given on p. 43, H. Marshall Blann, Fission of Gold with 112-MeV C^{12} Ions: A Yield-Mass and Charge-Distribution Study (Ph. D. thesis), UCRL-9190, May 1960 (unpublished). There is a misprint in the expression for $F(\lambda)$, which should read

$$F(\lambda) = (1-\lambda)\left[\frac{6}{5}(1+\lambda)^2 - 1-\lambda-\lambda^2\right](1+\lambda)^{-1}(1+\lambda^3)^{-5/3} .$$

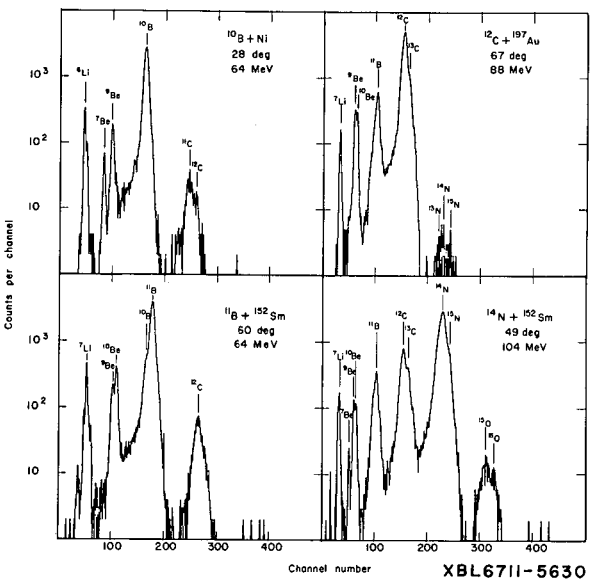

Fig. A. 13-1. Some representative particle spectra resulting from bombardment of various thin foils with heavy ions; bombarding conditions are indicated. The two spectra in each vertical pair were taken without changes in either the counter telescope or the particle-identifier system.

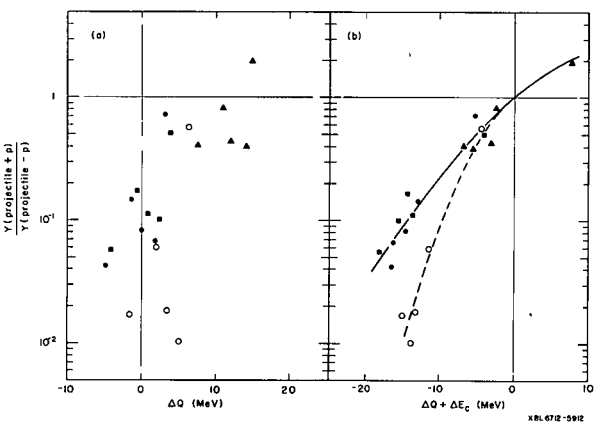

Fig. A. 13-2. The ratio of the yield for the projectiles picking up a single proton to that for the projectiles losing a single proton plotted versus (a) the difference in Q values for the two reactions and (b) the difference in Q values plus the difference in Coulomb interaction energies. The shape of the symbol indicates the projectile: □, ^{10}B; △, ^{11}B; ○, ^{14}N; and ○, ^{12}C.

14. THE $^{54}Fe(p, p'\gamma)^{54}Fe$ REACTION

J. Moss, D. L. Hendrie, D. Landis, and R. H. Pehl

A powerful tool in assigning spins to nuclear levels consists of observing the angular distribution of γ rays in coincidence with nuclear reaction particles emitted at 180 deg.[1] The usefulness of this method has, heretofore been limited because of the necessity of using poor-resolution NaI gamma detectors in order to obtain good counting efficiency.

The advent of large-volume germanium detectors coupled with the development of a high-count-rate amplifier system[2] enables us to extend this method to a wide range of new problems.

The $^{54}Fe(p, p')^{54}Fe$ reaction was chosen for the first experiment because ^{54}Fe is a single closed shell nucleus with comparatively little spectroscopic information available about its excited states. The bombarding energy was chosen to be 9 MeV to remain below the threshold for the (p, n) reaction.

The γ rays were detected by a germanium counter of ≈ 40 cm^3 intrinsic volume. It was made from a 3.4-cm-diameter pulled crystal by drifting lithium into a 5-cm-long piece from five of its six sides to a distance of 13 mm. The measured capacity of this detector at 2000 V bias was 34 pF. No noise increase was observed up to 2000 V; measurements at higher bias have not yet been made. The protons were detected by an annular lithium-drifted silicon counter placed on the beam axis at 180 deg; it intercepted particles scattered from 166 to 172 deg, subtending a solid angle of 0.115 steradian. The full-energy peak efficiency at our distance from the target of about 3 in. for the germanium counter ranged from 0.18% at 412 keV to 0.019% at 3160 keV. An abbreviated electronic schematic is shown in Fig. A. 14-1. The outputs from the preamplifiers were fed into high-rate linear amplifier systems described in Ref. 2 This system utilizes pole-zero cancelation to restore the pulse tail to the base line, and includes a pile-up rejector which insures that any pulse that is passed through the linear gate is not within 10 μsec of another pulse. The high-rate amplifiers have a fast and a slow output; the former is used for fast timing and the latter for energy analysis. A time-to-amplitude converter was used to make the fast coincidence; this allowed us to collect a large number of chance events for correction to the true coincidence spectrum by observing events in which the proton γ rays were generated in different cyclotron beam pulses. The gated particle and gamma energy signals were fed into an analog multiplexer and subsequently into a 4096-channel successive-approximation analog-to-digital converter (ADC).[3] The ADC also accepted six logic signals, two of which selected the real and random portions of the time spectrum and the rest of which were used for displaying gamma spectra in coincidence with different particle groups. The events were stored in a 1250-event buffer and then written on IBM compatible tape. The data are then finally analyzed on a CDC-6600 computer.

Figure A. 14-2 shows a single spectrum of 9-MeV protons scattered from ^{54}Fe. Figures A. 14-3 and A. 14-4 show the spectra of γ rays in coincidence with protons scattered from the states at 3.299 to 3.344 MeV (unresolved in proton spectrum) and 3.829 MeV respectively. These spectra, which are representative of a strongly excited state and a weakly excited state, respectively, were obtained after 15 hours of counting at $\theta = 55$ deg. There are 2322 counts in the 759-keV peak in Fig. A. 14-3 and 298 counts in the 2421-keV peak in Fig. A. 14-4.

Complete angular distributions are not yet available; however, some idea of the statistical precision required to assign spins may be obtained from Fig. A. 14-5, which shows the angular distributions of γ rays from the states for which spectra are shown.

Although experiments will be more difficult when working above other reaction thresholds, we believe that it is presently possible to deduce spins of the stronger excited states by this method, using germanium counters. Branching ratios may be obtained for even weaker states, since the statistical precision required is not so great.

References

1. A. E. Litherland and A. J. Ferguson, Can. J. Phys. 39, 788 (1961).
2. F. S. Goulding, D. A. Landis, and R. H. Pehl, The Design and Performance of a High-Resolution High-Rate Amplifier System for Nuclear Spectrometry, UCRL-17560, May 1967.
3. L. Robinson, F. Gin, and F. S. Goulding, A High-Speed 4096-Channel Analog-to-Digital Converter for Pulse-Height Analysis, UCRL-17419, February 1968.

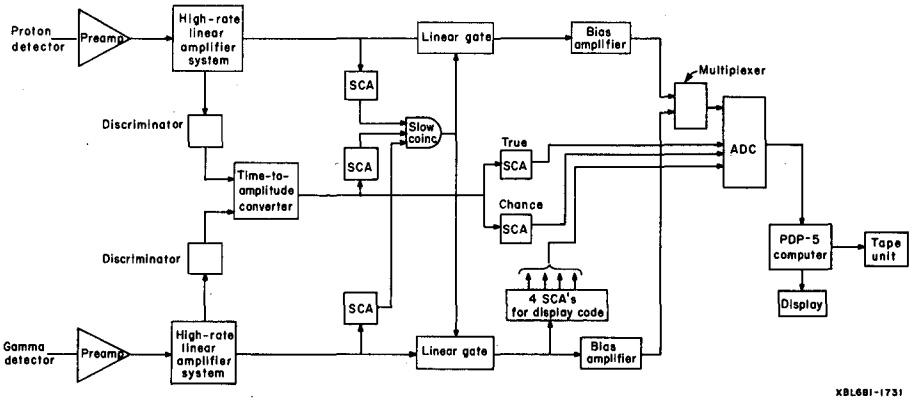

Fig. A. 14-1. Electronics block diagram for $^{54}Fe(p, p'\gamma)^{54}Fe$ experiment.

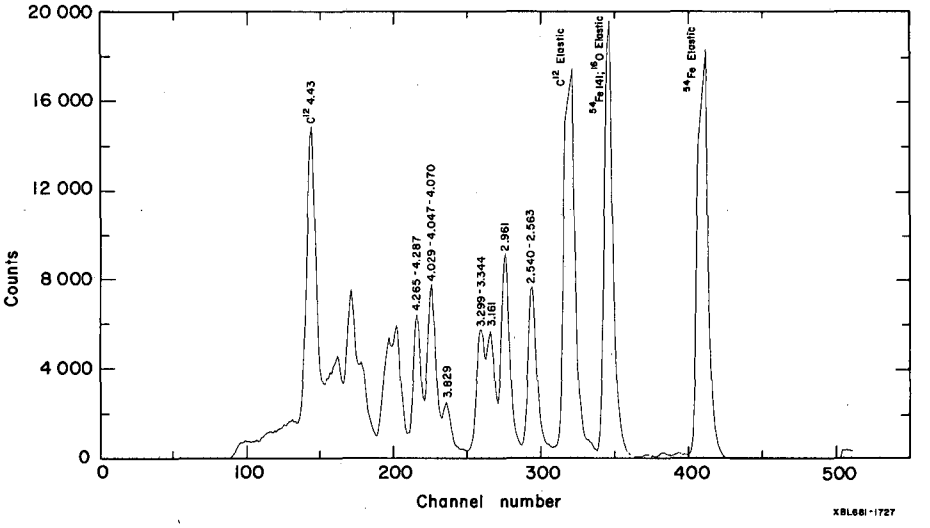

Fig. A. 14-2. Single spectrum of protons scattered from ^{54}Fe at 9 MeV.

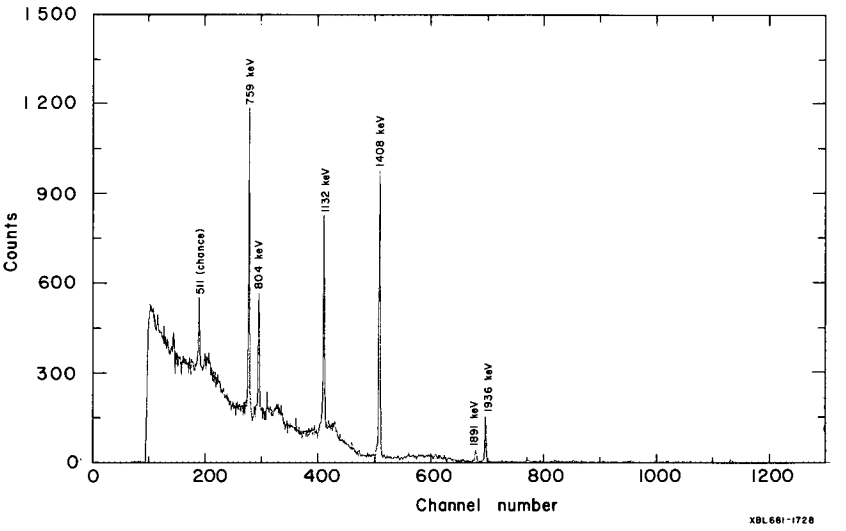

Fig. A. 14-3. Spectrum of γ rays in coincidence with the 3.291- to 3.340-MeV states in ^{54}Fe.

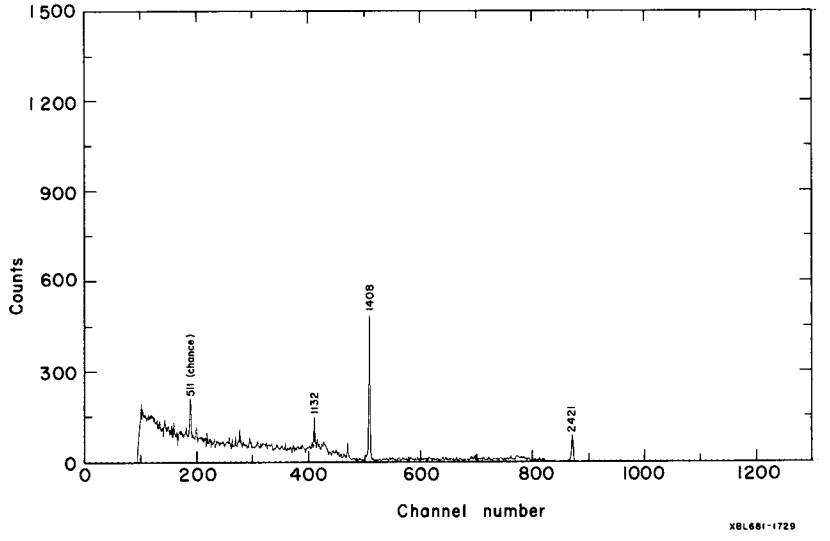

Fig. A. 14-4. Spectrum of γ rays in coincidence with the 3.829-MeV state in ^{54}Fe.

Fig. A. 14-5. Partial angular distributions of γ rays from 3.291 (▲)-, 3.340 (□)-, and 3.829 (○)-MeV state in ^{54}Fe.

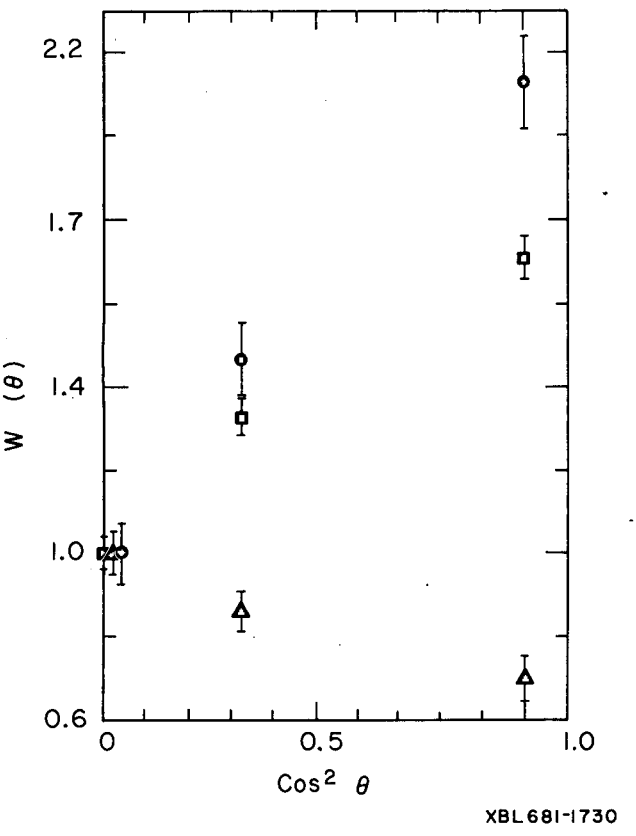

B. NUCLEAR REACTIONS AND SCATTERING

1. THE EMISSION OF α PARTICLES IN BOMBARDMENTS OF HEAVY ELEMENTS WITH α PARTICLES

G. Chenevert,† I. Halpern,† B. G. Harvey, and D. L. Hendrie

It has been observed in bombardments of heavy elements with α particles between 40 and 50 MeV that a broad spectrum of α particles is emitted.[1,2] At the more forward angles this spectrum is quite flat from energies in the neighborhood of the Coulomb barrier height to energies near the elastic scattering peak. As one goes backward in angle the α-particle spectrum begins to fall off more and more with increasing α-particle energy. The integral of the cross section over energy also drops off rapidly at backward angles. This last feature indicates that the inelastic particles are mainly the products of a direct reaction. It is not clear, however, which nuclear degrees of freedom are being excited in these scatterings, especially when the residual nuclei are left in very highly excited states. It was decided to pursue this problem by making use of the higher incident α-particle energies that are available at the 88-inch cyclotron.

Targets of tantalum, gold, and lead were bombarded at energies of 42, 50, 65, and 90 MeV, and α-particle spectra were observed at angles between 20 and 160 deg, generally in 20-deg steps. It was found that the distributions at forward angles resemble those that had been seen at the lower bombarding energies. Thus at 30 deg the observed inelastic spectrum is still quite flat ($\approx$ 1 mb/sr MeV) at a bombarding energy of 90 MeV. This implies, for example, that there is a considerable probability for a high-energy α particle to lose almost all of its available energy (and essentially all of its orbital angular momentum) in collision with a heavy nucleus.

Figure B. 1-1 shows a typical set of spectra observed at 65 MeV. It was not possible to obtain useful data forward of 30 deg because of backgrounds due to slit scattering. It is hoped that with improvements in beam optics and in counter design it will be possible to make such observations. It would be of interest, for example, to see whether the cross section passes through a maximum at some forward angle, as one would expect from elementary models for the (α, α') reaction.

Although the observed spectra are more or less featureless, a few gross structures are apparent. For example, the forward-angle spectra of lead show a prominent bump at excitation energies between 10.0 and 24.0 MeV (Fig. B. 1-1). This bump is most conspicuous at 65 MeV bombarding energy. At 42 MeV bombarding energy there is a significant depression in the spectra of Ta, Pt, and Au at about 8 MeV excitation energy. The meanings of these structures are not yet understood.

The bump which appears near $E_{\alpha'} \approx 20$ MeV at 160 deg becomes increasingly prominent as the bombarding energy is increased. Such bumps appeared for all the targets and are isotropic for backward angles. These features suggest that the bumps represent evaporated α particles. This suggestion is confirmed by quantitative estimates of α-particle evaporation rates, made by using conventional statistical theory.

Before discussing the analysis of the data, it is worth calling attention to one uncommon feature of the observed evaporation spectra. They correspond to evaporations which take place from nuclei excited to a fairly narrow band of excitation energies and are therefore particularly suited to theoretical analysis. This narrowness can be appreciated from the data shown in Fig. B. 1-2. The steepness of the excitation function for α-particle evaporation implies that after one or two neutrons are evaporated the chance to emit an α particle becomes much smaller than it is to start with. It is easy to understand why α (and other) particles which are not normally evaporated at low energy become increasingly probable at higher energies. The relative chance of evaporating a particle goes roughly as $\exp(-\Delta E/T)$, where T is the nuclear temperature and ΔE is the extra energy cost of emitting the particle in question compared with the cheapest particle, the neutron. For large ΔE, a function of this form grows rapidly with increasing T. Because of the high Coulomb barrier for α particles and heavy targets ΔE is large, and α-particle evaporation is therefore severely inhibited until the higher excitation energies available in the experiment presented here.

In analyzing the results, statistical theory was used to predict (i) the shape of the evaporation spectrum, (ii) its absolute magnitude, and (iii) its rate of growth with increasing bombarding energy. It was found that the major uncertainties in computed cross sections ($d^2\sigma/dEd\Omega$) were associated with uncertainties in (a) the parameter "a" in the commonly used level density formula for nuclei, [3] (b) the so-called inverse cross section for 20-MeV α particles striking a heavy nucleus, and (c) the difference in α-particle and neutron binding energies to the initial compound nucleus. It was found that with normally accepted values for these parameters, it was possible to fit the observations quite well. There were some slight discrepancies, which can in part be accounted for by refinements of the simple theoretical formulation used. A paper discussing the observed evaporation spectra and their implications is being prepared.

Footnote and References

†University of Washington, Seattle, Wash.

1. George Merkel, Energy and Angular Distributions of (α, α') and (d, α) Reactions (Ph. D. thesis), UCRL-9898, Nov. 1961.
2. University of Washington Annual Progress Report 1965, p. 32.
3. T. Ericson, Phil. Mag. Suppl. 9, [36], 425 (Oct. 1960).

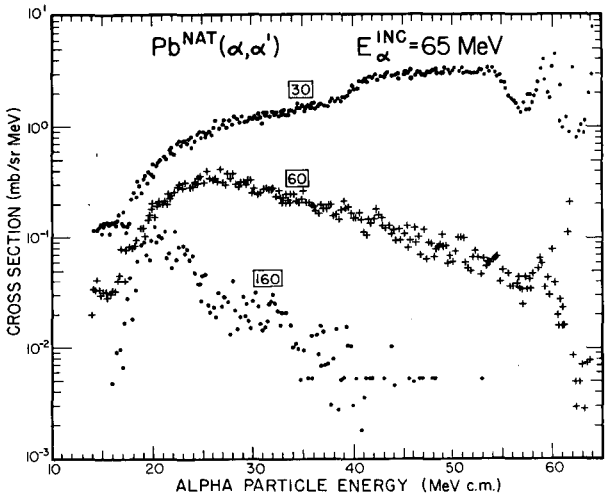

Fig. B. 1-1. Alpha spectra from $^{Nat}Pb(\alpha, \alpha')$ reaction for 30, 60, and 160 deg.

XBL 681-102

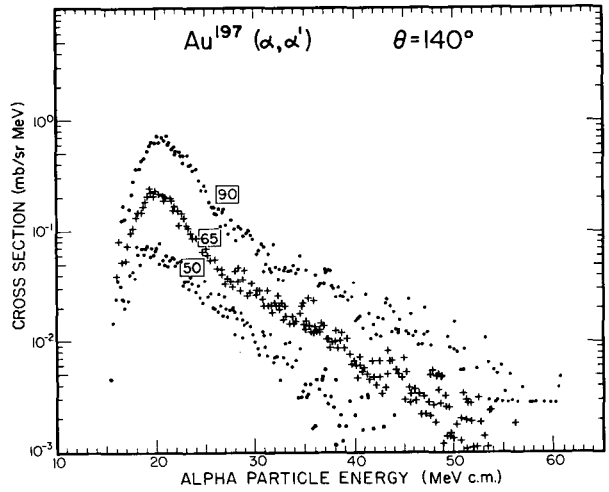

Fig. B. 1-2. 140-deg Alpha-particle spectra from the bombardment of gold with 50-, 65-, and 90-MeV particles.

XBL 681-103

2. DETERMINATION OF Y_{40} AND Y_{60} COMPONENTS IN THE SHAPES OF RARE EARTH NUCLEI†

D. L. Hendrie, Norman K. Glendenning, B. G. Harvey, O. N. Jarvis,* H. H. Duhm,‡ J. Saudinos,†† and J. Mahoney

The rotational spectra of nuclei in the rare earth (A = 152 to ≈ 190) and actinide (A = 220 to 250) regions, implying large permanent deformations, have been long known. The electric quadrupole moments of these deformed nuclei have been accurately determined by several methods. It is certainly associated largely with a Y_2 component in the nuclear radius. The knowledge about possible higher components Y_4 and Y_6, however, has been very tenuous up to now. Although calculations have predicted a Y_4 component in the uranium region, [1, 2] the evidence from alpha-decay studies is ambiguous. [3] Inelastic deuteron scattering near the Coulomb barrier has

provided evidence for the existence of such moments in the rare earth nuclei, but the magnitudes and even signs of the moments were not well determined.[4] Here we report a systematic study of the shape of deformed nuclei in the rare earth region through excitation of the ground-state rotational band by alpha particles.[5] We scattered a well-collimated and analyzed beam of 50-MeV α particles on several metallic foils of isotopically pure elements in the rare earth region. Angular distributions were taken with a cooled lithium-drifted multiple counter array. Special care was taken to keep backgrounds low and to maintain resolutions of about 50 keV. Since we have measured the differential cross sections to the various rotational levels of the ground state up to the 6+ and sometimes 8+ we are in a position to determine the shape up to Y_6 of the nuclear field produced by the ground state.

In our analysis of the data we assume that the alpha-nucleus interaction can be represented by a deformed complex optical potential and that the nucleus is a perfect rotor, at least up to the 8+ state. We calculate the cross section to members of the ground-state band by solving numerically the coupled differential equations that follow from this picture, without further assumptions.[6] Coulomb excitation effects were found to be significant and were treated on an equal basis with the nuclear excitation. The multipole expansion of the interaction, the number of partial waves, and the number of coupled channels were all carried to convergence, so that we have an exact numerical solution of the scattering model.

Since we treat explicitly the rotations, the optical potential should be essentially the same as that in the neighboring spherical region, since in both cases it must carry only the effects of the omitted intrinsic excitations.[6,7] Therefore, the same optical potential was used with only minor adjustments throughout the region from the spherical nucleus ^{148}Sm through the deformed region to ^{178}Hf. This means that essentially only the shape parameters of the optical potential had to be determined in the analysis. We parameterize the shape according to

$$R = R_0(1 + \beta_2 Y_{20} + \beta_4 Y_{40} + \beta_6 Y_{60}).$$

Figure B. 2-1 shows the data and calculation for ^{154}Sm. Notice that the only agreement occurs for $\beta_4 = +0.05$, and that the experimental data are reproduced in detail, including location of diffraction peaks, absolute magnitude of the cross sections, and even depths of the minima of the various states. The dashed and dotted curves show the disagreement with the data that is obtained when β_4 is respectively 0.0 and -0.05. We see in this way that the value of β_4 is quite precisely determined.

The agreement is somewhat improved for almost all the nuclei by including a small negative β_6 term. This term has been included in the best-fit curves shown for three of our target nuclei in Fig. B. 2-2. Here we easily see such changes in the data as shifts in the position of maxima, and smaller amplitudes of oscillation which, we find, imply a change in the sign of β_4 with increasing target mass.

Our results are summarized in Table B. 2-I and Fig. B. 2-3. From a preliminary exploration of deeper potentials it is already indicated clearly that our deformation parameters scale as βr_0 as has been suggested.[8] Accordingly in the presentation of our results we quote values of βr_0, or more precisely $\beta(r_0/1.2)$. To see whether the values of β_4 determined by our analysis can be understood in terms of the single-particle structure of nuclei, we have calculated this component in the shape by a simple method due to Harada.[2] These calculated values are compared in Fig. B. 2-3 with the values determined from the analysis of the data. It is gratifying that this simple model reproduces very well the observed trend characterized by larger positive β_4 deformations near the beginning of the deformed region, decreasing to large negative values at the end, and agrees well with a more realistic calculation by Nilsson and his co-workers.[9]

We thank Claude Ellsworth for the fabrication of the targets and Noel Brown for his efforts on the computer program.

Footnotes and References

†Work reported in D. L. Hendrie, N. K. Glendenning, B. G. Harvey, O. N. Jarvis, H. Duhm, J. Mahoney, and J. Saudinos, Inelastic α-Particle Scattering in the Rare Earth Region, and Determination of β_4 (UCRL-17547, July 1967), contribution to the International Conference on Nuclear Structure, Tokyo, Japan, September 7-13, 1967, and in full version of this paper (UCRL-17890, Nov. 1967), Phys. Letters, to be published.

*Permanent address: AERE, Harwell, Berkshire, England.

‡Permanent address: Max Planck Institut für Kernphysik, Heidelberg, Germany.
††Permanent address: CEN Saclay, Gif-sur-Yvette, S.-et-O., France.

1. K. Kjällquist, Nucl. Phys. 9, 163 (1958).
2. K. Harada, Phys. Letters 10, 80 (1964).
3. P. O. Fröman, Kgl. Danske Videnskab. Selskab Mat.-Fys. Skr. 1[3] (1957); M. G. Huber, Phys. Letters 13, 242 (1964); H. J. Mang and J. O. Rasmussen, Kgl. Danske Videnskab. Selskab Mat.-Fys. Skr. 2 [3] (1962).
4. B. Elbek, M. Kregar, and P. Vedelsby, Nucl. Phys. 86, 385 (1966).
5. Some of the experimental results were reported by B. G. Harvey, D. L. Hendrie, O. N. Jarvis, J. Mahoney, and J. Valentin, Phys. Letters 24B, 43 (1967); the possibility of establishing a Y_4 component by proton scattering was suggested by R. C. Barrett, Phys. Rev. Letters 14, 535 (1965).
6. Norman K. Glendenning, Lectures, Inelastic Scattering and Nuclear Structure, UCRL-17503, Aug. 1967, to be published in the Proceedings of the International School of Physics "Enrico Fermi," course XL, 1967 (Academic Press, Inc., New York).
7. Norman K. Glendenning, D. L. Hendrie, and O. N. Jarvis, Relation Between the Optical Potential for Spherical and Deformed Nuclei, UCRL-17935, Nov. 1967.
8. N. Austern and J. S. Blair, Ann. Phys. 33, 32 (1965); it should be noted, however, that quadrupole excitations at energies below the Coulomb barrier must scale as $\beta_2 R_c^2$.
9. P. Möller, B. Nilsson, and S. G. Nilsson, private communication.

Table B.2-I. Deformation parameters, $\bar{\beta} = (r_0/1.2)\beta$, obtained by our analysis of 50-MeV alpha scattering. The optical potential parameters used were about V = 65.9, W = 27.3, r_0 = 1.44, a = 0.637, with only very slight adjustments to individual nuclei.

	^{152}Sm	^{154}Sm	^{158}Gd	^{166}Er	^{174}Yb	^{176}Yb	^{178}Hf
$\bar{\beta}_2$	0.246	0.270	0.282	0.276	0.276	0.276	0.246
$\bar{\beta}_4$	0.048	0.054	0.036	0.0	-0.048	-0.054	-0.072
$\bar{\beta}_6$	-0.012	-0.018	-0.018	-0.018	0.0	-0.006	0.0

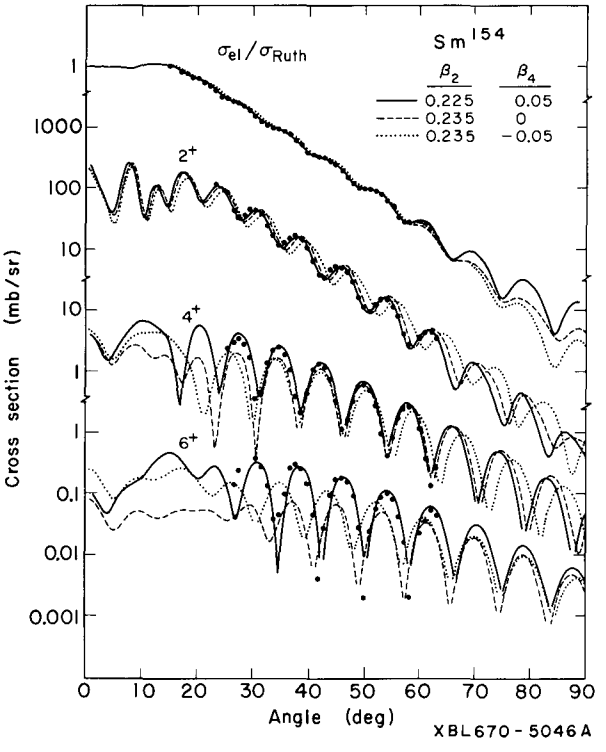

Fig. B.2-1. Differential cross sections for 50-MeV α particles scattered from ^{154}Sm. The coupled-channel calculations corresponding to values of β_4 equal to +0.05, 0.0, and -0.05 are compared. In the latter two cases the optical potential radius and β_2 were readjusted so as to achieve the best possible agreement with the 0^+ and 2^+ state. These results illustrate the extreme sensitivity to β_4, especially since differences in the 4^+ and 6^+ cross sections of an order of magnitude appear at certain angles.

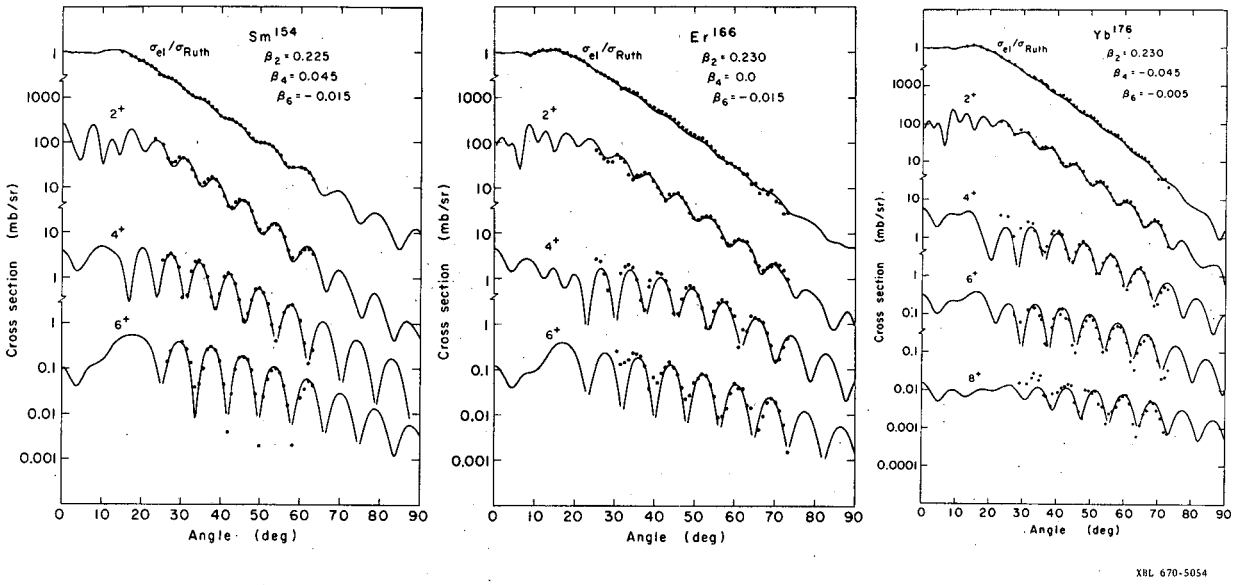

Fig. B. 2-2. Coupled-channel calculations of the differential cross sections for 50-MeV α particles of three nuclei exhibiting respectively +, 0, and - values of β_4 are compared with the data. The shape parameters in each case are exhibited in the figures.

Fig. B. 2-3. Calculated and measured values of β_4. Solid lines indicate the values of β_4 calculated in first-order perturbation theory based on the Nilsson scheme. The values of β_4, multiplied by $(r_0/1.2)$, that were obtained from an analysis of the scattering data are shown by solid dots. The error bars indicate our feeling of the precision with which the parameters can be extracted.

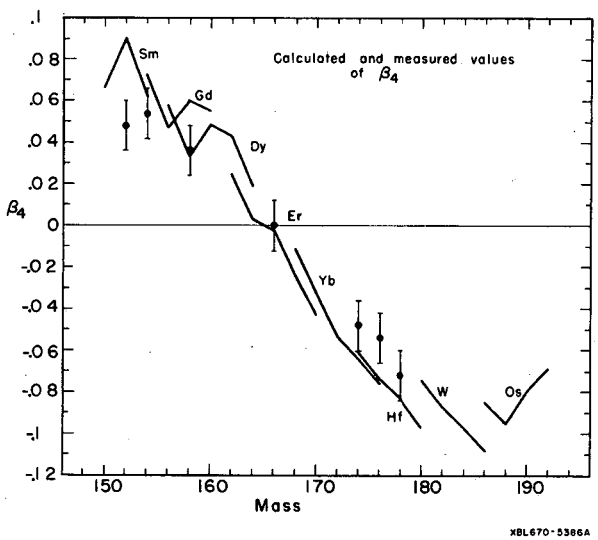

3. COMPARISON OF ^{3}He AND α SCATTERING BY USE OF DWBA ANALYSIS

H. H. Duhm,† B. G. Harvey, D. L. Hendrie, J. Saudinos,*
J. Mahoney, W. Parkinson,‡ and O. N. Jarvis††

In order to utilize the DWBA method of analyzing nuclear reaction results, one must obtain the distorted waves which describe the incoming and outgoing particles. The most commonly used procedure is to utilize the wave functions derived from an optical-model analysis of elastic scattering of the corresponding particle at an appropriate energy from the relevant (or nearly neighboring) nucleus. The ^{24}Mg(d, t)^{23}Mg, ^{24}Mg(d, ^{3}He)^{23}Na, and ^{24}Mg(^{3}He, α)^{23}Mg reactions reported separately induced us to study the elastic scattering of 35- and 47.5-MeV ^{3}He's from ^{24}Mg. Moreover, comparison of ^{3}He and α elastic and inelastic scattering results provides further information on the differences between the nuclear interactions of the two projectiles, and yields a further check on the ^{24}Mg(α, α') result reported previously.[1] Spectra from the two reactions are shown in Fig. B. 3-1.

As expected, the results are similar for the two projectiles. The 4.12-MeV 4+ level and 5.22-MeV 3+ level are well described as higher members of rotational bands.[2] They are not expected to be, and are not, able to be fit with the first-order DWBA approach. The success of a DWBA fit to the 6.00-MeV 4+ state, especially with the α-particle results, implies an addition $\ell = 4$ contribution beyond that expected from a collective rotational model.

In Table B. 3-I we see some sample optical parameters for the various reactions. Two differences are noted, which persist for all the many ambiguous optical potentials that were located. Whereas only four parameters (V, W, r_0, a) were needed to fit the alpha data, it was always necessary to use independent imaginary radius (r_w) and diffuseness (a_w) to fit ^{3}He data. In addition, the ^{3}He results always required a more diffuse well than the α results, indicating a less well-defined interaction radius[3] for the ^{3}He's.

The optical-model and DWBA fits are shown in Figs. B. 3-2 and B. 3-3. The transition strengths for several levels derived from these fits are shown in Table B. 3-II. Transition strengths derived from the other potentials found are very similar, provided one uses complex coupling and compares $\beta \times r_0$ and not β alone. However, comparison between the strengths determined from alpha and ^{3}He scattering seem to be less consistent. Whether a spin-flip process available to the ^{3}He only, or a full coupled-channel treatment of the reaction can resolve the difference is still under investigation.

Footnotes and References

†Permanent address: Max Planck Institut für Kernphysik, Heidelberg, Germany.
*Permanent address: CEN Saclay, Gif-sur-Yvette, S.-et-O., France.
‡Permanent address: University of Michigan, Ann Arbor, Michigan.
††Permanent address: AERE Harwell, Berkshire, England.

1. D. L. Hendrie, B. G. Harvey, J. Mahoney, and J. R. Meriwether, Bull. Am. Phys. Soc. 12, 912 (1967).
2. M. F. Reed, B. G. Harvey, and D. L. Hendrie, Bull. Am. Phys. Soc. 12, 912 (1967), and this report.
3. A. Springer, M. Chabre, D. L. Hendrie, and H. G. Pugh, Phys. Letters 20, 397 (1966).

Table B. 3-I. Typical optical-model parameters obtained in the elastic scattering from ^{24}Mg.

	E	V	r_0	a	W	r_w	a_w
^{3}He	35.0	116.4	1.02	0.87	16.1	1.76	0.812
^{3}He	47.5	116.0	1.02	0.87	16.6	1.76	0.812
α	49.2	196.6	1.34	0.58	53.5	-	-

Table B. 3-II. Comparison of deformation parameters from ^{3}He and ^{4}He inelastic scattering from ^{24}Mg.

Level		$\beta \times r_0$		
E_{ex} (MeV)	J^π	49.2-MeV α	35-MeV ^{3}He	47.5-MeV ^{3}He
1.37	2+	1.68	1.77	1.77
4.23	2+	0.49	0.55	
6.00	4+	0.68	0.49	0.48
7.60	3-	0.65	0.60	
8.35	3-	0.79	0.61	

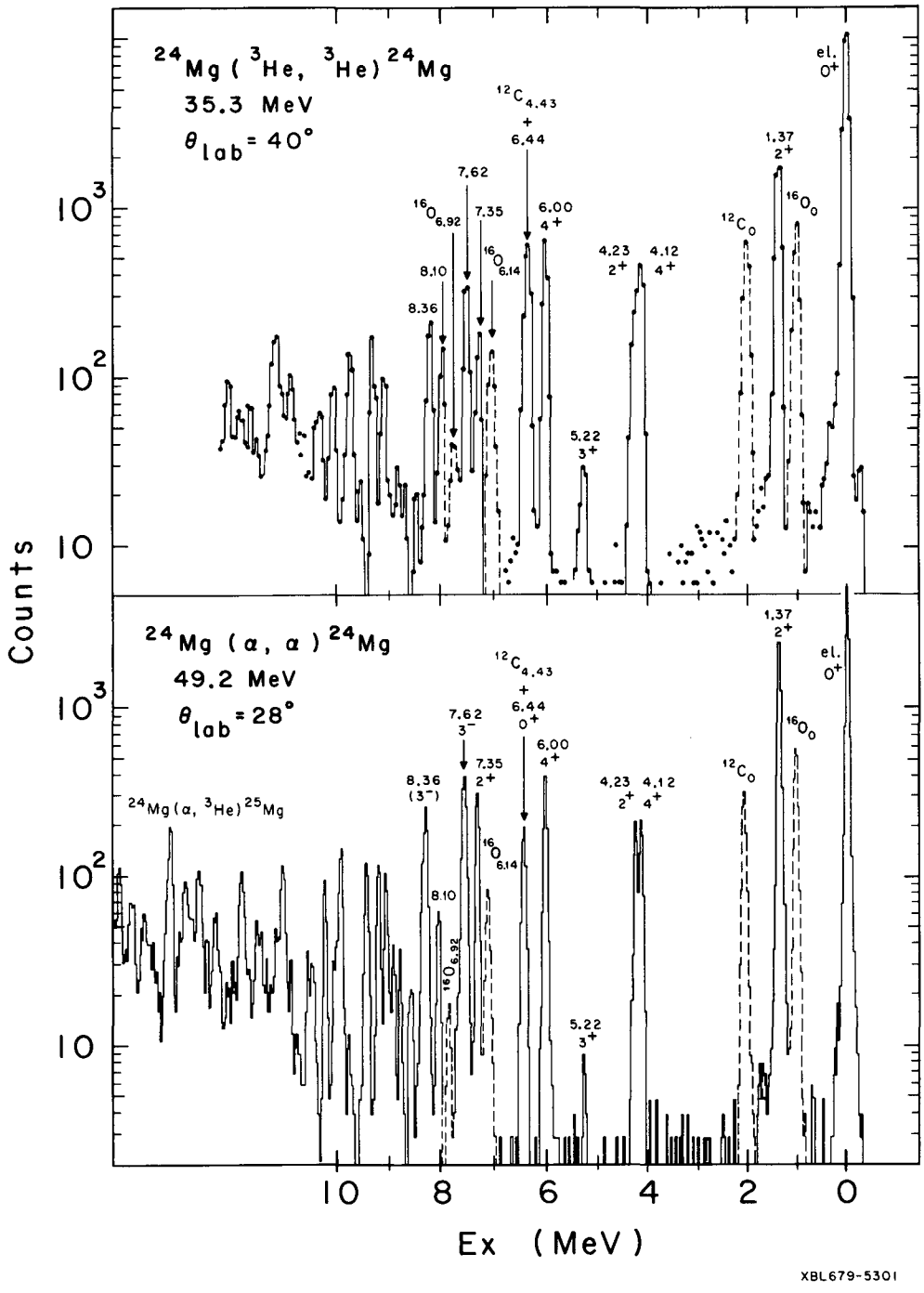

Fig. B. 3-1. Sample spectra from the ^{24}Mg(α, α') and ^{24}Mg(^{3}He, ^{3}He') reactions, indicating the relative strengths of the levels and the experimental resolution, backgrounds, and contaminants.

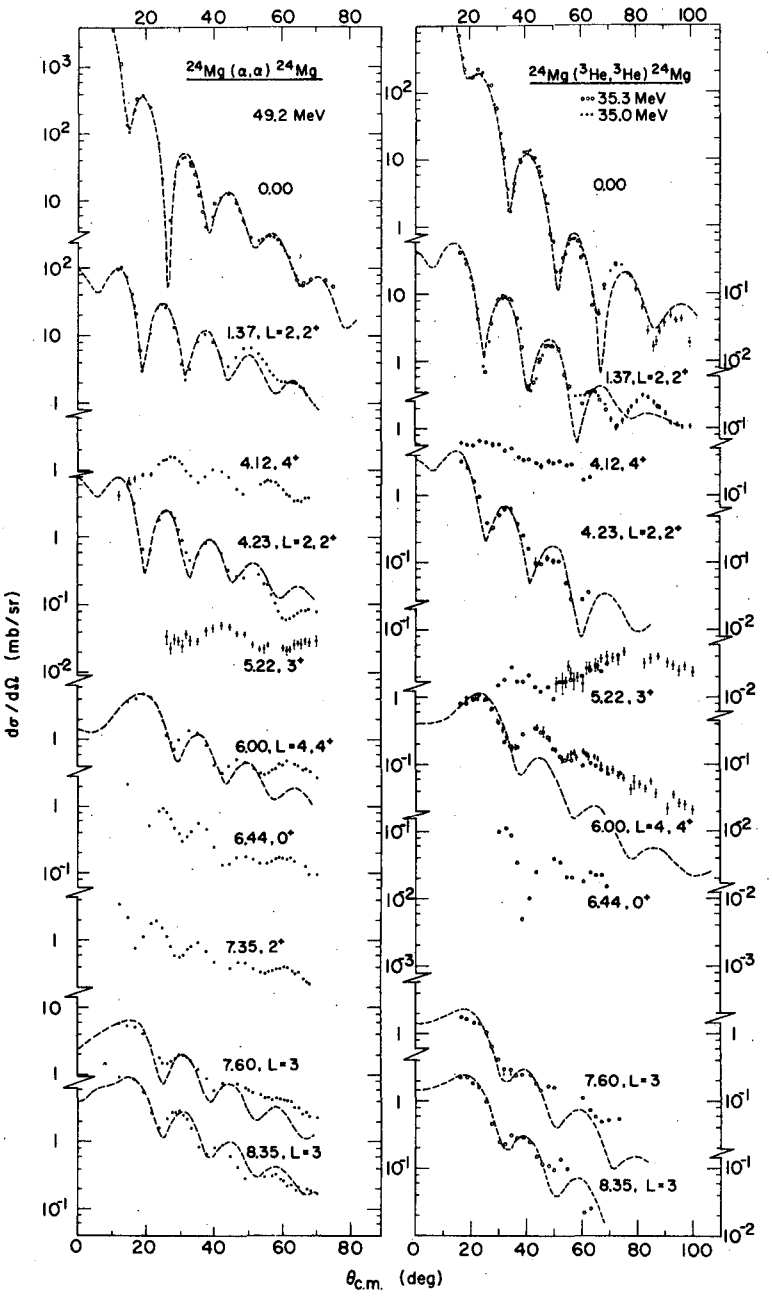

XBL 679-5304

Fig. B. 3-2. Data for optical-model and DWBA fits for the ^{24}Mg(α, α') reaction and the ^{24}Mg(^{3}He, ^{3}He') reaction at 35 MeV.

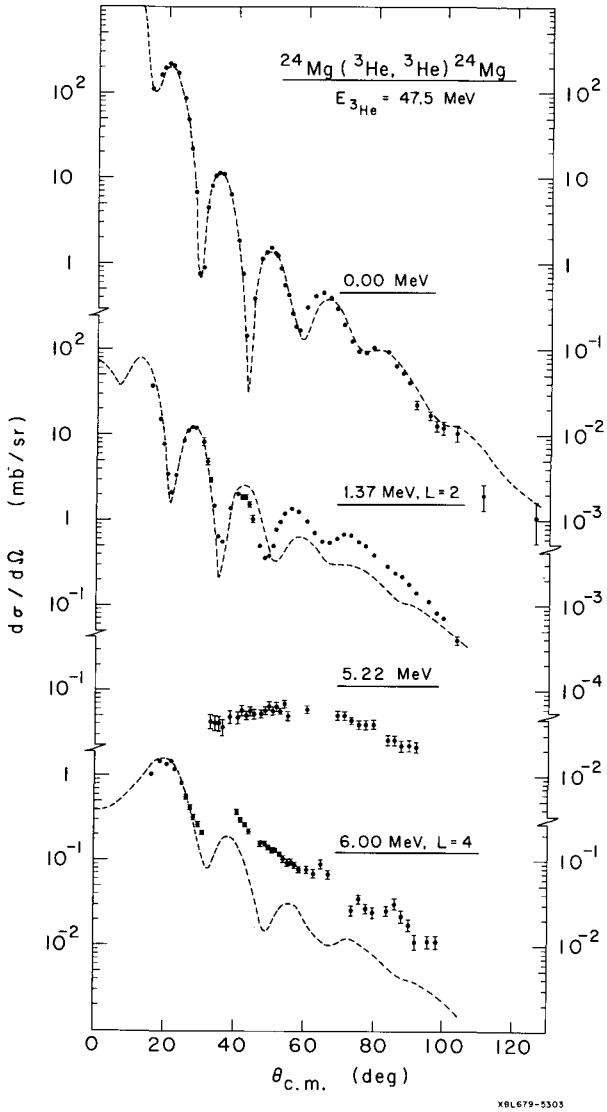

Fig. B. 3-3. Data for optical-model and DWBA fits for the ^{24}Mg(^{3}He, ^{3}He') reaction at 47.5 MeV.

4. EXCITATION FUNCTIONS AND ANGULAR DISTRIBUTIONS OF ALPHA PARTICLES SCATTERED FROM ^{12}C, ^{24}Mg, AND ^{58}Ni

J. R. Meriwether, C. Glasshauser, B. G. Harvey, D. L. Hendrie, J. Mahoney, L. Marquez, E. A. McClatchie, H. G. Pugh, and J. Thirion

The differential cross section for elastic scattering and inelastic scattering to the first excited state of ^{12}C, ^{24}Mg, and ^{58}Ni was measured as a function of angle and incident energy.

Sixteen lithium-drifted-silicon detectors were arranged at 6-deg intervals from 20 to 110 deg. The output from each detector was individually amplified and routed into 256 channels of a ND-160 4096-channel pulse-height analyzer. The counting rate into the analyzer was reduced by

discriminating against all but the high energy portion of each energy spectrum. After a sufficient number of events were accumulated in each of the sixteen spectra the data were transferred to a PDP-5 computer, where the appropriate alpha groups were integrated and the cross sections determined.

At each incident energy between 24.25 and 40.0 MeV the spectra from the counters were obtained for both ^{24}Mg and ^{58}Ni. The entire assembly of counters was then rotated 3 deg so that spectra could be obtained from 23 to 113 deg. This resulted in angular distributions with 32 points at 3-deg intervals. The incident energy was then changed by 250 keV and the entire procedure repeated. The ^{12}C data were obtained in a similar manner, but only from 25.5 to 33.0 MeV.

These data points define a surface whose properties are determined by the variation of the differential cross section as a function of the scattered particle angle and the incident energy. The large amount of data obtained is indicated by the fact that there are about 2000 points in the surface determined by the data from the elastic scattering by ^{24}Mg.

Some typical results are shown in Figs. B. 4-1 through B. 4-3, where the cross section as a function of energy is plotted at specific angles. The broad structure (best seen in Fig. B. 4-3) is due to the shift of the diffraction pattern with energy. The sharp fluctuations seen for ^{12}C and ^{24}Mg are as yet unexplained. ^{58}Ni does not show any of this latter structure.

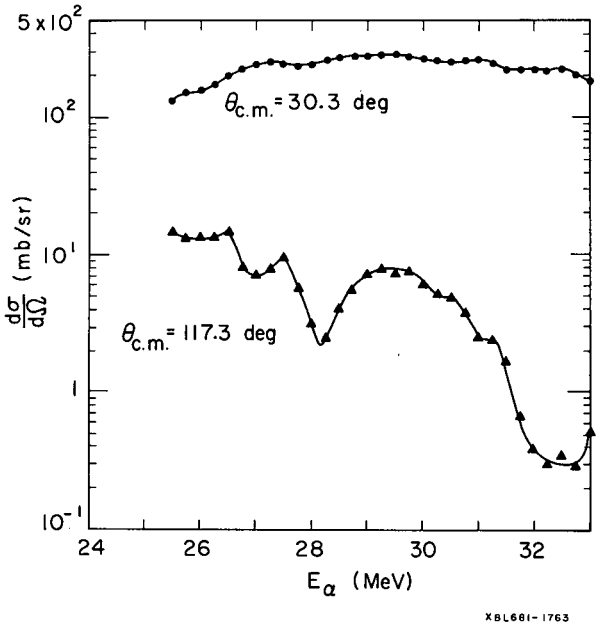

Fig. B. 4-1. Excitation function of elastically scattered α particles on ^{12}C from 25.5 to 33 MeV.

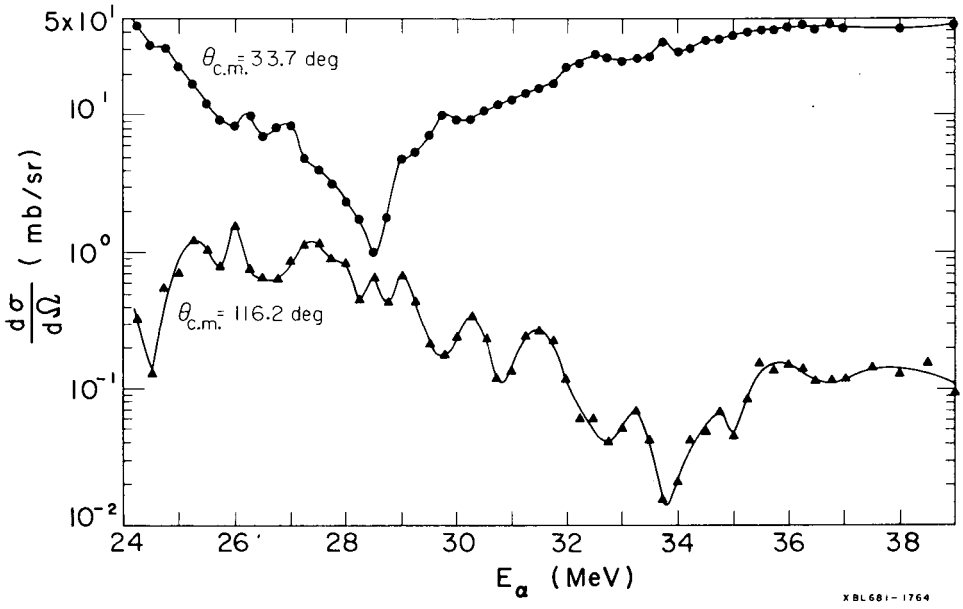

Fig. B. 4-2. Excitation function of elastically scattered α particles on ^{24}Mg from 24.25 to 39 MeV.

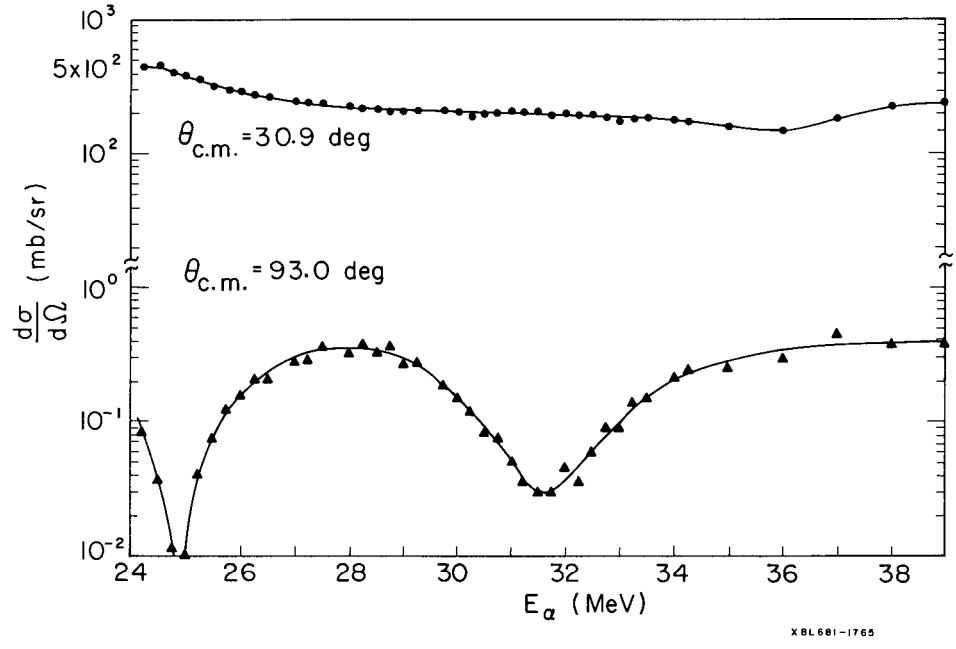

Fig. B. 4-3. Excitation function of elastically scattered α particles on ^{58}Ni from 24.25 to 39 MeV.

5. SCATTERING OF 17.8-MeV PROTONS FROM ^{58}Ni, AND ^{60}Ni SPIN AND PARITY ASSIGNMENTS FOR LEVELS OF ^{58}Ni

O. N. Jarvis,† B. G. Harvey, D. L. Hendrie, and Jeannette Mahoney

The purpose of the experimental work presented here was to provide data for comparison with the microscopic description of inelastic scattering formulated by Glendenning[1] and Glendenning and Veneroni.[2] The results of this comparison have been presented elsewhere.[1,3] In this paper the experimental results are compared with DWBA calculations using collective form factors. The proton energy of 17.8 MeV was chosen because elastic polarization data (but no cross sections) were already available for the two nickel isotopes.[4] For comparison of theoretical predictions with experimental level energies and with scattering results, it is necessary to know the spins and parities of the nuclear levels. Several new assignments were made for ^{58}Ni by a study of the scattering of 50-MeV α particles.

Experiments were performed with momentum-analyzed beams from the 88-inch cyclotron. Scattered particles were detected in cooled (-25°C) Si(Li) counters, giving energy resolutions of about 30 keV (FWHM) for protons and 60 keV for α particles.

The energy level scheme for ^{58}Ni is shown in Table B. 5-I. We discuss here only those spin and parity assignments resulting from this work. The 2.773-MeV level gives an (α, α') angular distribution in phase with the elastic angular distribution at large angles, indicating either negative parity or double excitation. It seems most unlikely that a negative parity state could lie so low in energy. Since other evidence[5] suggests a spin of 2 or 3, we conclude that it is probably the 2+ member of the two-phonon triplet.

The 2.900-MeV level is very weakly excited by (α, α'); it has previously been assigned a spin of 1.[5] We therefore conclude that it must be 1+ rather than 1-.

A strong assignment of spin 0 can be made for the 2.940-MeV level by comparison of its (p, p') angular distribution with that for the well-known 0+ level of ^{60}Ni at 2.286 MeV. Its weak excitation by (α, α') is consistent with this assignment. It is the only candidate for the 0+ member of a two-phonon triplet.

The 3.414-MeV level has previously been assigned a spin of 2 or 3.[5] Because of its weak (α, α') excitation, we prefer 3+. By the same argument, the 3.588-MeV level--previously assigned a spin of 1 or 2 (Ref. 6)--is probably 1+. The 3.773-MeV level has been assigned spin 3; the weak (α, α') excitation implies positive parity. Finally, comparison of the angular distributions for the 4.103-, 4.405-, and 5.59-MeV levels with DWBA calculations strongly suggests spins 2+, 4+, and 4+ respectively.

Optical model analyses were made both for the elastic differential cross sections and for the polarization data (for ^{58}Ni and ^{60}Ni). The final optical model parameters are given in Table B. 5-II. The angular distribution and polarization fits for ^{58}Ni are shown in Fig. B. 5-1. Similar results were obtained for ^{60}Ni. It was found necessary to simultaneously fit the cross section and polarization data for consistent results.

Distorted-wave Born-approximation calculations, using both real and complex deformed potentials, were made. The use of complex deformed potentials gave better agreement with the experimental results. (The spin-orbit part of the potential could not be deformed, but this is expected to have little effect upon the results.) The calculations included Coulomb excitation as a possible excitation mode. The β_2 and β_3 values obtained for the first 2+ and first 3- levels of ^{58}Ni and ^{60}Ni are shown in Table B. 5-III. The results of the (p, p') and (α, α') experiments for ^{58}Ni agree very well. For both ^{58}Ni and ^{60}Ni the particle scattering results are in excellent agreement with electromagnetic measurements of β_2. (Since the quantity actually measured in scattering experiments is $\beta_I R$, where R is the interaction radius, rather than β_I alone, the results shown in Table B. 5-III have all been renormalized to a radius $R = 1.25\ A^{1/3}$ F.

A more complete account of this work may be found in O. N. Jarvis, B. G. Harvey, D. L. Hendrie, and Jeanette Mahoney, The Inelastic Scattering of 17.8-MeV Protons from ^{58}Ni, ^{60}Ni, and ^{120}Sn, and the Determination of Spin and Parity Assignments for ^{58}Ni from α Particle Scattering (UCRL-17352, Jan. 1967), Nucl. Phys., in press.

Footnote and References

†Permanent address: AERE Harwell, Berkshire, England.

1. N. K. Glendenning, Phys. Letters 21, 549 (1966).
2. N. K. Glendenning and M. Veneroni, Phys. Letters 8, 334 (1964).
3. N. K. Glendenning, B. G. Harvey, D. L. Hendrie, O. N. Jarvis, and J. Mahoney, in Proceedings of the International Conference on Nuclear Physics, Gatlinburg, Sept. 1966 (to be published).
4. D. J. Baugh, G. W. Greenlees, J. S. Lilley, and S. Roman, Nucl. Phys. 65, 33 (1965).
5. L. W. Swenson and R. K. Mohindra, Phys. Rev. 150, 877 (1966).
6. P. F. Hinricksen, G. T. Wood, and S. M. Shafroth, Nucl. Phys. 81, 449 (1966).
7. S. F. Eccles, H. F. Lutz, and V. A. Madsen, Phys. Rev. 141, 1067 (1966).
8. N. R. Roberson and H. O. Funsten, Bull. Am. Phys. Soc. 9, 93 (1964), and private communication.
9. M. P. Fricke and G. R. Satchler, Phys. Rev. 139, B567 (1965).
10. P. H. Stelson and L. Grodzins, Nuclear Data (Section A) 1, 21 (1965).

Table B. 5-I. Level scheme of ^{58}Ni.

Energy (MeV)	Spin and parity
0	0+
1.456	2+
2.458	4+
2.773	2+
2.900	1+
2.940	0+
3.035	2+
3.260	2+
3.414	3+
3.524	4+
3.615	4+
3.773	3+
3.895	2+
4.103	2
4.291	?
4.35	?
4.405	?
4.472	3-
4.519	?
4.540	?
4.75	4+
4.90	?
4.95	?
5.07	?
5.10	?
5.45	?
5.59	4+

Table B. 5-II. Optical-model parameters for proton scattering at about 17.8 MeV.

Isotope	V	a_v	r_v	W_1	a_w	r_w	V_s	a_s	r_s	σ_R (mb)	χ^2_σ/N_σ	χ^2_π/N_π
^{58}Ni	46.94	0.781	1.25	10.90	0.432	1.304	4.39	0.530	1.202	1078	21.9	9.8
^{60}Ni	46.45	0.846	1.25	11.90	0.465	1.279	5.48	0.502	1.253	1185	17.3	11.6
^{58}Ni	47.21	0.770	1.25	10.98	0.434	1.289	4.04	a_v	r_v	1072	28.4	19.5
^{60}Ni	47.42	0.843	1.25	12.60	0.448	1.282	4.74	a_v	r_v	1185	22.5	29.5
^{58}Ni	46.75	0.678	1.25	13.07	0.389	1.259	9.06	a_v	r_v	958	4.2	
^{60}Ni	46.59	0.754	1.25	14.19	0.422	1.261	8.89	a_v	r_v	1090	3.0	

Note: Potential depths are given in MeV, lengths in F.

Fig. B. 5-1. Results of the optical-model calculations for protons scattered from ^{58}Ni at 17.7 MeV. The cross-section data are presented as ratios to the Rutherford scattering cross sections. The solid lines are the best fits to cross-section and polarization results, the dotted lines were obtained from parameters chosen to fit only the cross-section data.

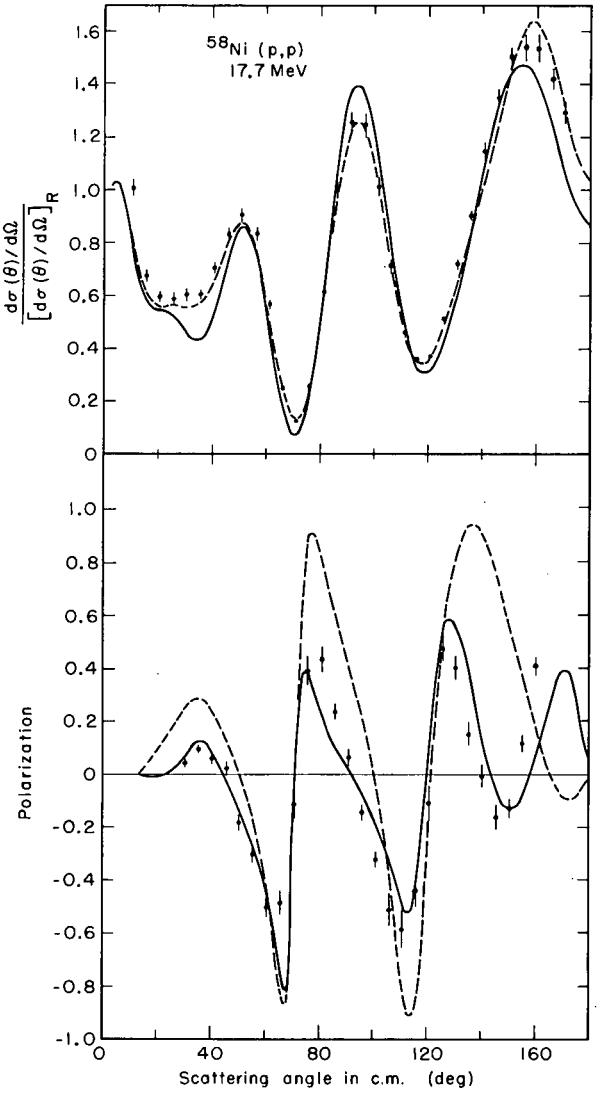

XBL671-409

Table B. 5-III. Values of the deformation parameters for the collective levels derived from the present data compared with other results.

Target	Jπ	Q (MeV)	1 Complex (σ+P)	2 Complex σ	3 Real (σ+P)	4 Real σ	5 18.6 MeV(p, p') DWBA	6 18.6 MeV(p, p') C. C.	7 17.5 MeV (p, p')	8 40 MeV (p, p')	9 C. E.	10 50 MeV (α, α')
^{58}Ni	2+	-1.456	0.21(0.20)	0.24(0.20)	0.22(0.20)	0.25(0.22)	0.24	0.21	0.21	0.18	0.18±0.01	0.21
	3-	-4.472	0.16(0.15)	0.17(0.16)	0.15(0.15)	0.17(0.16)	0.19		0.15	0.18		0.15
^{60}Ni	2+	-1.332	0.21(0.20)	0.25(0.20)	0.24(0.195)	0.24(0.22)	0.30	0.26	0.21	0.21	0.20±0.01	
	3-	-4.038	0.17(0.17)	0.18(0.17)	0.15(0.145)	0.16(0.15)	0.22		0.17	0.16		

Notes: Present (p, p') results are given in the first four columns. (σ+P) denotes results from optical model potential which fitted both cross-section and polarization data, etc. "Complex" and "Real" refer to the interaction form factor. The first column contains our preferred (p, p') set. The values for β_L contained within parentheses were obtained without Coulomb excitation as a possible excitation mode.

Columns 5 and 6 show the results of Eccles et al. (Ref. 7) using DWBA and coupled-channels calculations.
Columns 7 and 8 show the (p, p') results of Roberson and Funsten (Ref. 8) and of Fricke and Satchler (Ref. 9).
Column 9 gives the averaged results obtained in electron scattering and Coulomb excitation work (Ref. 10).
Column 10 gives our (α, α') results.
The results quoted in columns 8-10 have been corrected to $R = 1.25\ A^{1/3}$ (see text).

6. THE EXCITATION OF UNNATURAL-PARITY STATES BY INELASTIC α SCATTERING

Mary F. Reed, David L. Hendrie, Bernard G. Harvey, and Norman K. Glendenning

In previous α-scattering experiments on ^{24}Mg, approximately constant shapes were found for the angular distributions for the elastic and natural-parity states at different incident α-particle energies when compared on QR plots.[1] However, for the 3+ unnatural-parity state, two wide peaks appear at low incident α-particle energies and move to smaller values of QR as the energy is increased. Alpha-scattering experiments were carried out at the 88-inch cyclotron to see whether the 2- unnatural-parity states in ^{20}Ne and ^{16}O behave in the same way.

Figure B. 6-1 shows the experimental angular distributions for the 2- unnatural-parity state in ^{20}Ne. These results and those for the elastic and natural-parity states are similar to those found for ^{24}Mg, except only one broad peak is present in the unnatural-parity state angular distributions for ^{20}Ne. Figure B. 6-2 shows the experimental results for the 2- unnatural-parity state in ^{16}O. In this case the angular distributions for the 2- state behave more like those of the natural-parity states. Thus the wide peaks found for the ^{24}Mg and ^{20}Ne cases do not seem to be characteristic of unnatural-parity states in general.

^{24}Mg and ^{20}Ne are deformed nuclei whose low-lying levels are usually described as members of rotational bands with strong coupling between the different states in the bands. ^{16}O, on the other hand, is spherical in its ground state, and its level structure is usually described in terms of the shell model with only weak coupling between the excited states. These differences in level structure and coupling strengths may give rise to the observed differences in behavior found in the ^{24}Mg and ^{20}Ne angular distributions as compared with those for ^{16}O. To test this hypothesis we are planning experiments to investigate a 4- state in the spherical nucleus ^{208}Pb.

The reaction mechanisms in the two cases above may be different. Simple direct mechanisms involving a single excitation with a well-defined transfer of angular momentum are not allowed in the excitation of unnatural-parity states by α particles.[4] Allowed mechanisms are compound nucleus formation and decay, excitations through an intermediate state, and a coupling of the orbital angular momentum of the incoming α particle with a spin flip of one or more of the target nucleons. Theoretical investigations of the compound nucleus and cascade mechanisms have been carried out for the 3+ state in ^{24}Mg at incident α-particle energies of 50 and 81 MeV. No theory has yet been formulated for the spin-flip mechanism.

A Hauser-Feshbach computer code[5] was used to generate angular distributions, assuming the compound nucleus mechanism. The very small cross sections obtained allowed us to conclude that this mechanism does not play an important role in the excitations at these energies.

The cascade or multiple excitation mechanism was investigated by means of a coupled-channel computer code.[6] The coupled-channel formalism corresponds to the physical situation in which a nuclear level is produced by both single excitations, if allowed, and all the possible combinations of multiple excitations. The 2- states in ^{16}O and ^{20}Ne may be made by $\ell = 3$ plus $\ell = 2$ double excitation, while the 3+ in ^{24}Mg may be $\ell = 2$ plus $\ell = 2$ excitation. In these calculations a modification of the program SEEK[7] is used to fit the elastic angular distributions and obtain the starting optical-model parameters--V, W, $r = r_i$, r_c, and $a = a_i$. These parameters as well as the nuclear shape parameters were then put into the coupled-channel program and adjusted as necessary to give the best overall fit to both the shapes and magnitudes of the experimental angular distributions. The results obtained for 50 MeV are shown in Fig. B.6-3. The values of the parameters used are given in the figure. A search of parameter space complete enough to give good fits to all the ^{24}Mg levels has not been completed; nevertheless the shape and magnitude for the 3+ angular distribution are fitted well enough to suggest very strongly that, in this case at least, a multiple excitation mechanism can account for the experimental results. Whether this will be true for ^{16}O and ^{20}Ne remains to be investigated. Similar results were obtained in a comparison of coupled-channel calculations with our 81-MeV data for this reaction. Vincent, Boschitz, and Priest[8] have also used this formalism to calculate angular distributions for comparison with their 42-MeV α-scattering results on ^{24}Mg and found fairly good agreement. Thus, these results allow us to conclude that the multiple excitation process may account for the excitation of the unnatural-parity state in ^{24}Mg at these α-particle energies.

References

1. M. F. Reed, B. G. Harvey, and D. L. Hendrie, Nuclear Chemistry Annual Report, 1966 UCRL-17299, Jan. 1967, p. 127.
2. B. G. Harvey, J. R. Merriwether, J. Mahoney, A. Bussière de Nercy, and D. J. Horen, Phys. Rev. 146, 712 (1966).
3. B. G. Harvey, E. J. M. Rivet, A. Springer, J. R. Merriwether, W. B. Jones, J. H. Elliott, and P. Darriulat, Nucl. Phys. 52, 465 (1964).
4. W. W. Eidson and J. G. Cramer, Phys. Rev. Letters 9, 497 (1962).
5. W. R. Smith, The Hauser-Feshbach Nuclear Scattering Computer Code LIANA, Oak Ridge National Laboratory Report ORNL-TM-1234, 1965.
6. N. K. Glendenning, Inelastic Scattering and Nuclear Structure, Lectures for International School of Physics "Enrico Fermi," UCRL-17503, Aug. 1967.
7. M. A. Melkanoff, J. Raynal, and T. Sawada, SEEK: A Fortran Program for Automatic Searches in Elastic Scattering Analyses with the Nuclear Optical Model, UCLA Report 66-10, 1966.
8. J. S. Vincent, E. T. Boschitz, and J. R. Priest, Phys. Letters 25B, 81 (1967).

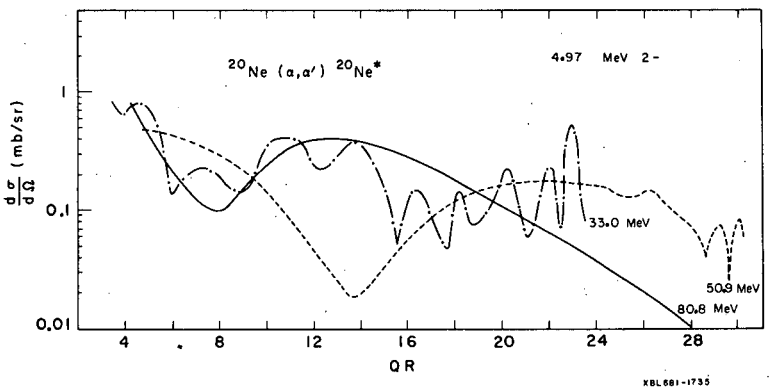

Fig. B.6-1. The ^{20}Ne 2- unnatural-parity angular distributions plotted versus momentum transfer, Q, times R for E_α = 33, 50.9, and 80.8 MeV.

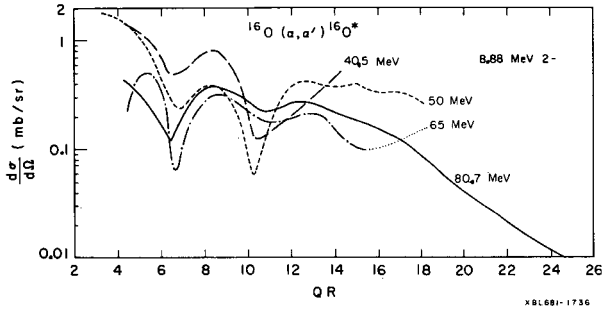

Fig. B. 6-2. The ^{16}O 2- unnatural-parity angular distributions for E_α = 40.5 (Ref. 2), 50, 65 (Ref. 3), and 80.7 MeV.

Fig. B. 6-3. Angular distributions for the $^{24}Mg(\alpha,\alpha')^{24}Mg^*$ reaction at 50 MeV. The optical model and shape parameters used to generate these fits are given.

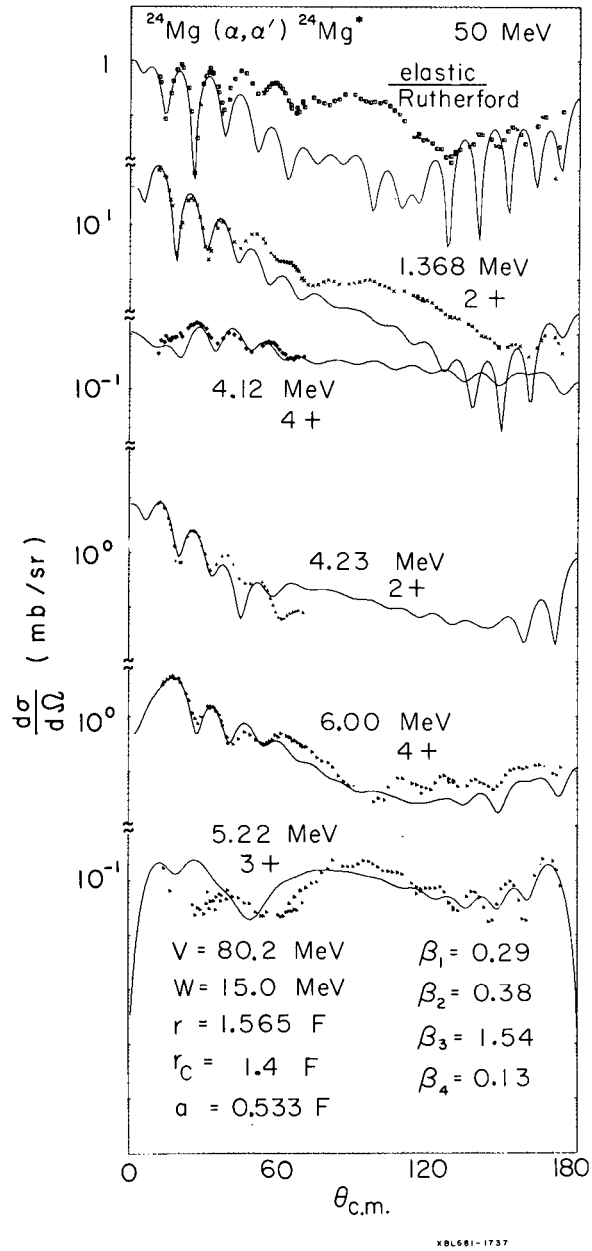

7. THE ^{208}Pb(d, t) AND (d, ^{3}He) REACTIONS WITH 50-MeV DEUTERONS

W. C. Parkinson,† D. L. Hendrie, H. Duhm,* J. Mahoney, and J. Saudinos‡

Considerable evidence has accumulated recently that in heavy nuclei the radius of the proton distribution is somewhat smaller than the radius of the neutron distribution. It is of interest to determine whether the effect is observable in a comparison of neutron and proton pickup reactions. The (d, t) and (d, ^{3}He) reactions on ^{208}Pb are favorable ones to study, since in each case the particle is presumably picked up from reasonably pure single-particle states, and a change of 10% in the radii or the diffuseness of the nuclear surface should result in a factor-of-two difference in the cross section.

The absolute differential cross sections of the six lowest-lying levels of ^{207}Pb and the four lowest-lying levels of ^{207}Tl, excited by the ^{208}Pb(d, t) and (d, ^{3}He) reactions respectively, have been measured for 50 MeV incident deuteron energy. In addition, the absolute differential cross section has been measured for the elastic scattering of 47.5-MeV ^{3}He ions on ^{208}Pb. The excitation energies and level assignments in both ^{207}Pb and ^{207}Tl are in agreement with previous measurements.[1] The measured differential cross sections are being compared by use of a DWA analysis. The analysis is being carried out in cooperation with G. R. Satchler of Oak Ridge, using optical-model parameters determined from the measured ^{3}He elastic scattering data, and from deuteron elastic scattering data at 52 MeV.[2]

References

†Permanent Address: University of Michigan, Ann Arbor, Michigan.
*Permanent Address: Max Planck Institute für Kernphysik, Heidelberg, Germany.
‡Permanent Address: CEN, Saclay, France.

1. G. Muehllehner, A. S. Poltorak, W. C. Parkinson, and R. H. Bassel, Phys. Rev. 159, 4 (1967); S. Hinds, R. Middleton, J. H. Bjerregaard, O. Hansen, and O. Nathan, Nucl. Phys. 83, 17 (1966).
2. G. Wagner (Max Planck Institute, Heidelberg, Germany), private communication.

8. HIGH SPIN PROTON-NEUTRON TWO-PARTICLE LEVELS IN THE MEDIUM-MASS ($54 \leq A \leq 70$) REGION

C.-C. Lu, M. S. Zisman, and B. G. Harvey

Previous experiments with (α, d) reactions in light nuclei have shown a greater tendency for capture of the two particles in high-spin levels of the $(J)^2$ configuration[1, 2] than in low-spin levels. The search has been extended to the medium-mass region by using the 50-MeV α-particle beam of the Berkeley 88-inch cyclotron.

The (α, d) and (α, t) reactions were carried out simultaneously on separated isotope targets ^{52}Cr, $^{54, 56}$Fe, ^{59}Co, $^{58, 60, 62}$Ni, ^{63}Cu, and $^{64, 66, 68}$Zn at four angles to search for levels of $(g\ 9/2)^2_{9+}$ configuration. Identification of the deuterons and tritons was accomplished with a Goulding-Landis-type particle identifier.[3] Excitation energies of the strongly populated levels in the (α, d) reaction are given in Table B. 8-I. A typical energy spectrum is shown in Fig. B. 8-1.

A plot of the -Q value of formation of the most strongly excited levels, $-Q_f$, as a function of $A_{residual}$, Fig. B. 8-2, shows a regular decrease with increasing A, which indicates that the levels chosen are probably of similar configuration, possibly $(g\ 9/2)^2_{9+}$. It was found, however, that in ^{54}Mn and ^{56}Co it was necessary to choose the second most strongly populated level in order to obtain a smoothly varying plot of $-Q_f$ vs $A_{residual}$. This is not unreasonable, since the (α, t) spectra (see Fig. B. 8-3) show that f 7/2 single-particle proton capture predominates over the g 9/2 single-particle capture in these nuclides, and thus we might expect large levels with f 7/2 protons to appear in the (α, d) reaction in addition to the $(g\ 9/2)^2$ levels. In the higher-mass region the g 9/2 proton capture is predominant, and here we find that the most strongly populated level should be chosen.

For the two odd-A targets, ^{59}Co and ^{63}Cu, there are no strongly populated levels in the (α, d) spectra. This is consistent with previous results. For a target with ground-state spin $J_c \neq 0$ a multiplet of $(2J_c + 1)$ states can be formed from vector coupling J_c to the total J of the captured pair. In the present case, the ground-state spins are ^{59}Co(J_c = 7/2-) and ^{63}Cu(J_c = 3/2-), and we expect that the capture strength will be distributed over many states in the allowed multiplet. This has the effect of decreasing the strength of the high-spin level relative to the other states made in the reaction, and a single strongly excited level is no longer observed.

Due to the large angular momentum transfer in the (α, d) reaction we expect to populate levels with high spin. In the medium-mass region, using a simple shell-model picture, we might expect levels with $(f\,5/2)^2_{5+}$, $(f\,5/2, g\,9/2)_{7-}$, and $(g\,9/2)^2_{9+}$ configurations to appear. The $(f\,5/2)^2_{5+}$ level should not appear strongly in the high-A region (e.g., ^{68}Zn), where we have a largely filled f 5/2 neutron shell. Since the $-Q_f$ vs $A_{residual}$ plot shows no discontinuity at higher A, the $(g\,9/2)^2_{9+}$ or $(f\,5/2, g\,9/2)_{7-}$ configuration may be indicated. Further work will be required in order to establish the configuration of these states.

The residual interaction energies for the neutron-proton pair in the well-known $(d\,5/2)^2_{5+}$ level in ^{14}N and the $(f\,7/2)^2_{7+}$ level in ^{34}Cl have been determined from the single-particle energies and the excitation energies of the two-particle states. The experimental results are in agreement with shell-model calculations (see Table B.8-II) based on the potential of True,[4] using the Talmi integrals to evaluate the diagonal matrix elements as discussed by Moshinsky and Brody.[5] Calculations for the $(g\,9/2)^2_{9+}$ configuration are in progress.

Footnotes and References

1. E. Rivet, R. H. Pehl, J. Cerny, and B. G. Harvey, Phys. Rev. 141, 1021 (1966).
2. C. C. Lu and B. G. Harvey, in Nuclear Chemistry Annual Report, 1966, UCRL-17299, Jan. 1967, p. 95.
3. F. S. Goulding, D. A. Landis, J. Cerny, and R. H. Pehl, Nucl. Instr. Methods 31, 1 (1964).
4. W. W. True, Phys. Rev. 130, 1530 (1963).
5. M. Moshinsky and T. A. Brody, Tables of Transformation Brackets, Monografías del Instituto de Física, Mexico, 1960.
6. The empirical diagonal matrix element for the $(d\,5/2)^2$, J = 5, T = 0 state was calculated in Ref. 2. The empirical diagonal matrix element for the $(f\,7/2)^2$, J = 7, T = 0 state was calculated and presented in graphical form by D. M. Kim, J. Phys. Soc. Japan 21, 2445 (1966). We used the same method in our calculations.

Table B.8-I. High spin [probably $(g\,9/2)^2_{9+}$] levels in the (α, d) reactions.

Final nucleus	Energy level (MeV)	Q_f (MeV)
^{54}Mn	9.47 ± 0.05	-20.04
^{56}Co	8.92 ± 0.03	-19.85
^{58}Co	6.79 ± 0.03	-18.27
^{60}Cu	5.99 ± 0.03	-18.58
^{62}Cu	4.75 ± 0.03	-17.12
^{64}Cu	4.57 ± 0.03	-16.60
^{66}Ga	2.99 ± 0.03	-16.00
^{68}Ga	2.88 ± 0.03	-15.40
^{70}Ga	2.88 ± 0.03	-14.69

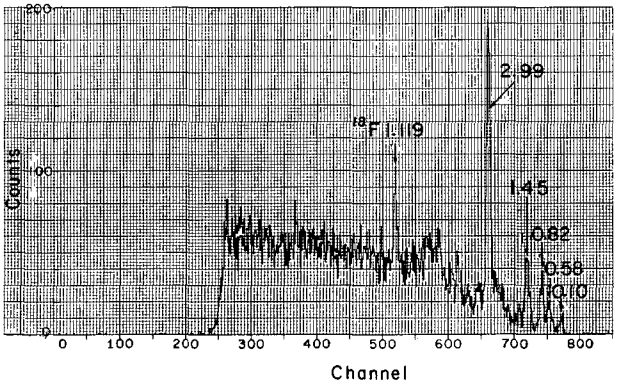

Fig. B.8-1. Deuteron energy spectrum for the reaction ^{64}Zn$(\alpha, d)^{66}$Ga at θ(lab) = 20 deg, with E(α) = 50 MeV.

XBL681-1761

Table B. 8-II. Diagonal matrix elements.

Matrix element	Levels (MeV)	Empirical[a] (MeV)	Calculated (MeV)
$[(d\,5/2)^2 J=5,\ T=0 \mid V \mid (d\,5/2)^2 J=5,\ T=0]$	^{14}N 8.963	4.05	
			4.17
	^{18}F 1.119	3.89	
$[(f\,7/2)^2 J=7,\ T=0 \mid V \mid (f\,7/2)^2 J=7,\ T=0]$	^{26}Al 8.27	3.56	
	^{30}P 7.03	2.92	
	^{34}Cl 5.2	3.1	2.61
	^{40}Sc 0.60	2.62	

a. Ref. 6.

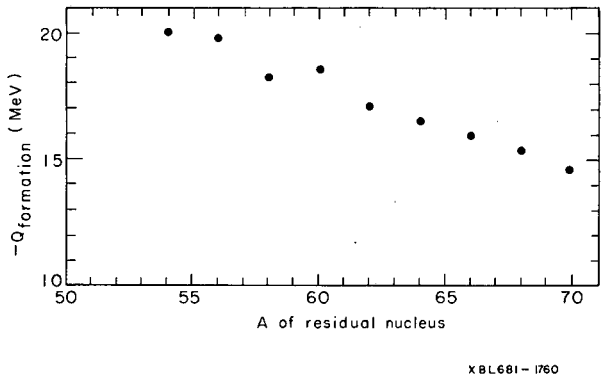

Fig. B. 8-2. Relationship between the mass number A of the product nucleus and the Q value of formation of the levels [probably $(g\,9/2)^2_{9+}$] strongly populated by the (α, d) reaction.

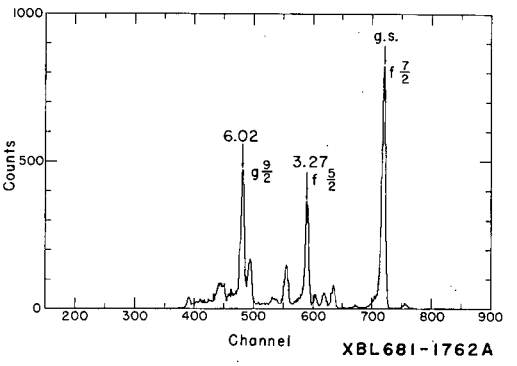

Fig. B. 8-3. Triton energy spectrum for the reaction ^{54}Fe(α, t)^{55}Co at θ(lab) = 14 deg, with E(α) = 50 MeV.

9. THE UNBOUND NUCLIDE ^{7}B†

Robert L. McGrath, Joseph Cerny, and Edwin Norbeck*

The mass and width of the ground state of the T_z = -3/2 unbound nuclide ^{7}B have been measured by using the ^{10}B(^{3}He, ^{6}He)^{7}B reaction. These data, together with those recently reported[1] on ^{7}He, complete the mass-seven isospin quartet in which all members are unbound with respect to T = 3/2 particle-decay modes.

A 50-MeV ^{3}He beam generated by the Berkeley 88-inch cyclotron was used to bombard a 280-μg/cm^2 carbon-backed ^{10}B target, and reactions induced on a 300-μg/cm^2 ^{11}B target were used for energy calibrations. Since (^{3}He, ^{6}He) reactions on light targets typically have laboratory-system cross sections of $\approx$ 1 to 4 μb/sr, a particle identification system for low-yield nuclear reactions was employed. This system utilizes two four-counter semiconductor telescopes, and has been previously described.[2] The ^{6}He energy spectra taken at 14.1 deg (lab) arising from bombardment of both ^{10}B and ^{11}B targets are shown in Fig. B. 9-1. The original data were summed over ten channels to improve the statistics; the overall resolution was about 230 keV. Because of a 7% ^{11}B impurity in the ^{10}B target, there is a small peak in the upper spectrum of Fig. B. 9-1 that corresponds to the ^{8}B ground state.

The close similarity of the Q values and kinematics of the $^{10}B(^{3}He, ^{6}He)^{7}B$ and $^{11}B(^{3}He, ^{6}He)^{8}B$ reactions made the latter useful for energy calibrations. The reported ^{8}B level structure[3] consisted of the ground, 0.78-, and 2.17-MeV states. Since a 2.17-MeV excitation for the ^{8}B second excited state appeared inconsistent with the $^{11}B(^{3}He, ^{6}He)^{8}B$ data, the $^{10}B(p, t)^{8}B$ reaction was investigated at six angles with 43.7-MeV protons. Triton peaks corresponding to the ^{10}C and ^{14}O ground states, due to ^{12}C and ^{16}O target contaminants, offered excellent energy calibrations. The excitation and width (FWHM) of this ^{8}B state were found to be 2.33 ± 0.04 MeV and 390 ± 40 keV; this new excitation was adopted in establishing the ^{7}B mass.

Figure B. 9-2 shows a ^{6}He energy spectrum constructed by summing data from both telescopes placed at 14.1 deg and subtracting the ^{8}B impurity spectrum; the cutoff at 26.2 MeV corresponds to the lowest energy that could be reliably counted in both systems. The $^{4}He + 3p$, $^{6}Be + p$, and $^{5}Li + 2p$ thresholds are marked along the energy axis; the broad peak at about 29.8 MeV is attributed to the unbound ground state of ^{7}B. Expected shapes of three-, four-, and five-body phase-space distributions are indicated by the dashed, solid, and dot-dashed lines, respectively. The data suggested that the ^{7}B peak is superimposed on a continuum background composed of the $^{5}Li + 2p$ or the $^{4}He + 3p$ phase-space distributions (or both); the peak in the inset is the result of subtracting from the raw spectrum the $^{5}Li + 2p$ distribution normalized as shown in the figure. Spectra at two other angles, 10 and 19.65 deg (lab), were obtained in order to check the kinematical behavior of the peak shown in Fig. B. 9-2. At both angles the energy and width of the observed peak were consistent with the ^{7}B assignment. The mass excess [$^{12}C = 0$] of ^{7}B was found to be 27.94 ± 0.10 MeV. Its width was determined to be 1.6 MeV with no background subtraction, and 1.3 or 1.4 MeV, respectively, with the $^{5}Li + 2p$ or $^{4}He + 3p$ distributions normalized as shown in Fig. B. 9-2 subtracted from the data. A representative width for the ^{7}B ground state of 1.4 ± 0.2 MeV may be taken from these results.

It is of interest to test the ability of the isobaric multiplet mass equation (IMME)[4] to relate the masses of members of an unbound quartet. One can predict the ^{7}B mass using the known datum[1] on ^{7}He and revised excitations for the ^{7}Li and ^{7}Be members acquired from both a reanalysis of previously published data[5] from the $^{9}Be(p, ^{3}He)^{7}Li$ and $^{9}Be(p, t)^{7}Be$ reactions and an analysis of new data on these reactions utilizing a 45-MeV proton beam. Our final values show the lowest ^{7}Li $T = 3/2$ state to lie at 11.28 ± 0.04 MeV, while the lowest ^{7}Be $T = 3/2$ state lies at 10.97 ± 0.4 MeV. The resulting ^{7}B mass excess is predicted to be 27.76 ± 0.17 MeV, which is seen to be in good agreement with experiment. This agreement is interesting, since the members of the quartet become increasingly unbound to allowed decay modes in moving from ^{7}He to ^{7}B so that their wave functions could be quite different. Unfortunately, no theoretical estimates are available concerning the magnitude of expected deviations from the IMME in such multiplets.

Footnotes and References

†Condensed from Phys. Rev. Letters 19, 1442 (1967).

*Department of Physics, University of Iowa, Iowa City, Iowa. Supported in part by the National Science Foundation.

1. R. H. Stokes and P. G. Young, Phys. Rev. Letters 18, 611 (1967); R. H. Stokes and P. G. Young, in Proceedings of the International Conference on Nuclear Structure, Tokyo, Japan, September 7-13, 1967 (to be published).

2. F. S. Goulding, D. A. Landis, J. Cerny, and R. H. Pehl, IEEE Trans. Nucl. Sci. NS-13[3], 514 (1966).

3. T. Lauritsen and F. Ajzenberg-Selove, Nucl. Phys. 78, 1 (1966).

4. E. P. Wigner and E. Feenberg, Rept. Progr. Phys. 8, 274 (1941); S. Weinberg and S. B. Treiman, Phys. Rev. 116, 465 (1959); D. H. Wilkinson, Phys. Letters 12, 348 (1964).

5. C. Detraz, J. Cerny, and R. H. Pehl, Phys. Rev. Letters 14, 708 (1965).

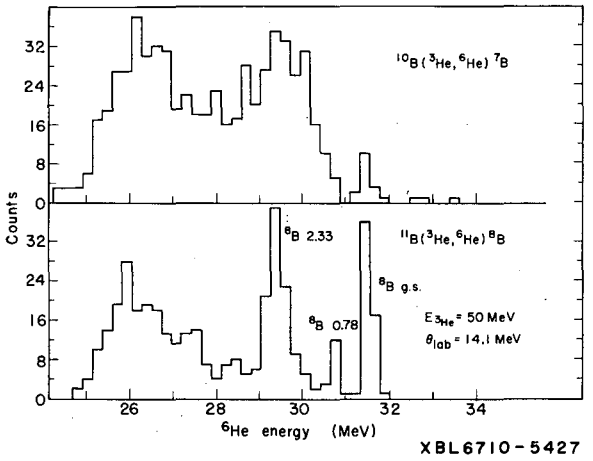

Fig. B.9-1. ^{6}He energy spectra from the $^{10}B(^3He,^6He)^7B$ (top) and $^{11}B(^3He,^6He)^8B$ (bottom) reactions. The upper spectrum contains weak ^8B groups due to a 7% ^{11}B target impurity.

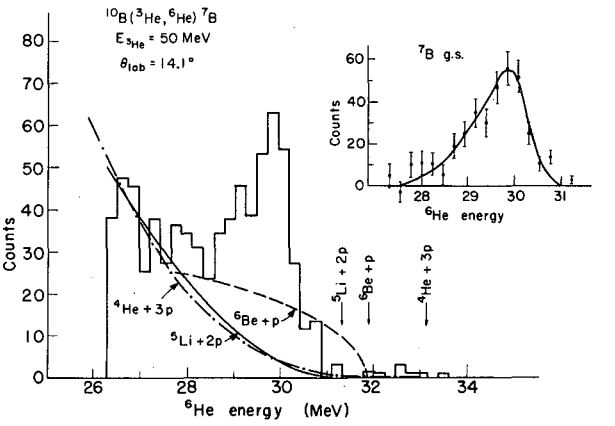

Fig. B.9-2. A composite $^{10}B(^3He,^6He)^7B$ energy spectrum obtained by summing data from two counter telescopes at 14.1 deg (lab) and subtracting the ^8B impurity spectrum. Particle thresholds are marked along the energy axis and the shapes of three-, four-, and five-body phase-space distributions are given by the dashed, solid, and dot-dashed lines, respectively. The four-body curve has been subtracted from the spectrum to obtain the peak in the inset, which is attributed to the ground state of ^{7}B.

10. MASS AND SPECTROSCOPIC MEASUREMENTS IN THE COMPLETED MASS 21 AND 37 ISOSPIN QUARTETS†

Gilbert W. Butler, Joseph Cerny, S. W. Cosper,* and Robert L. McGrath

The measurement of masses of nuclei far from stability permits one to evaluate the various theoretical approaches toward prediction of the limits of particle stability.[1] In addition, mass measurements, in conjunction with other data, permit a further study of the isobaric multiplet mass equation[2] (IMME): $M(A, T, T_z) = a(A, T) + b(A, T)T_z + c(A, T)T_z^2$. Since this equation relating the masses of members of an isospin multiplet contains three coefficients, its validity can be independently checked only if four or more members of such a multiplet with $T \geq 3/2$ are known.

The mass 21 and mass 37 isospin quartets (the former includes ^{21}F, ^{21}Ne, ^{21}Na, and ^{21}Mg, the latter ^{37}Cl, ^{37}Ar, ^{37}K, and ^{37}Ca) have been studied in a series of nuclear reaction experiments at the 88-inch cyclotron. Whereas the $T = 3/2$ states in the $T_z = -1/2$ and $+1/2$ nuclei were readily located by one- and two-nucleon transfer reaction investigations (discussed later)—and the masses of both ^{21}F and ^{37}Cl ($T_z = +3/2$) were already known—in order to complete the quartets it was necessary to employ the three-neutron transfer reaction (^{3}He, ^{6}He) to measure the masses of the $T_z = -3/2$ nuclei ^{21}Mg and ^{37}Ca via the $^{24}Mg(^3He,^6He)^{21}Mg$ and $^{40}Ca(^3He,^6He)^{37}Ca$ reactions.

Due to the low (^{3}He, ^{6}He) cross sections [≤ 1 μb/sr (lab) for $A > 16$], an improved particle-identification system employing two transmission ΔE detectors and an E detector has been developed[3] to permit their measurement. Pulses from these detectors were amplified and fed to a triple-counter particle identifier, which has been discussed in detail in Ref. 3.

A residual background in the ^{6}He region of the particle-identifier spectrum of this improved system arose from the fact that the chance coincidence of a ^{3}He particle and a deuteron traversing the counter telescope within the resolving time of the system could produce an energy loss and hence an identification signal very similar to that of a ^{6}He particle. Two approaches were followed in order to reduce these chance coincidences. First, a pile-up rejector[3] was designed so that events which consisted of two particles traversing the counter telescope spaced in time by ≤ 47 nsec were rejected—thus restricting all chance coincidence events to those occurring in a single cyclotron beam burst. Second, the two ΔE pulses together with the E_{total} and particle-identifier pulses for each event in any desired region of the identifier spectrum were recorded in an on-line PDP-5 computer and were later individually analyzed by using the known detector thicknesses and range-energy relations in silicon. This procedure both rejected some coincidence events and enabled us to attach a higher degree of reliability to the "good" events.

Data from the ^{37}Ca experiment are presented in more detail, since it had a considerably lower yield than the ^{21}Mg experiment. The mass of ^{37}Ca was determined via the ^{40}Ca(^{3}He, ^{6}He)^{37}Ca reaction at 55.9 MeV, and Fig. B.10-1 presents a triple-counter particle-identifier spectrum from this experiment. Corrected ^{6}He energy spectra from two independent observations of the ^{40}Ca(^{3}He, ^{6}He)^{37}Ca reaction are shown in Fig. B.10-2. Each ^{6}He spectrum contains two sharp states which correspond to the ground and first excited states of ^{37}Ca. An average cross section for the ^{37}Ca ground-state transition at 11.2 deg (lab) was 0.175 μb/sr, and the Q-value was determined to be -24.27 ± 0.05 MeV, which corresponds to a ^{37}Ca mass excess of -13.24 ± 0.05 MeV (^{12}C = 0). The first excited state of ^{37}Ca appears at an excitation energy of 1.62 ± 0.03 MeV.

The mass of ^{21}Mg was determined by the ^{24}Mg(^{3}He, ^{6}He)^{21}Mg reaction at 55.9 MeV. An average differential cross section for the ^{21}Mg ground-state transition at 14.1 deg (lab) was 0.84 μb/sr, and the average Q-value was determined to be -27.22 ± 0.12 MeV, which corresponds to a ^{21}Mg mass excess of 10.62 ± 0.12 MeV. Four excited levels of ^{21}Mg were observed with average excitations of 0.22 ± 0.03, 1.27 ± 0.06, 1.62 ± 0.04, and 1.89 ± 0.04 MeV.

The ^{22}Ne(d,t)^{21}Ne and ^{22}Ne(d, ^{3}He)^{21}F reactions were studied simultaneously at a bombarding energy of 40 MeV in order to characterize the T = 3/2 states in ^{21}Ne. An energy level at 8.92 ± 0.040 MeV was determined to be the lowest T = 3/2 state in ^{21}Ne on the basis of angular distribution and energy systematics. The ^{23}Na(p,t)^{21}Na reaction was studied at 42 MeV in order to locate T = 3/2 levels in ^{21}Na. A ^{21}Na energy level with an excitation energy of 8.92 ± 0.03 MeV was presumed to be the lowest T = 3/2 level, since this excitation agreed with the value of 8.90 ± 0.04 MeV reported earlier.[4] Finally, the ^{39}K(p,t)^{37}K and ^{39}K(p, ^{3}He)^{37} Ar reactions at 45 MeV were used to locate the lowest T = 3/2 levels in ^{37}K and ^{37}Ar, which were found at excitation energies of 5.035 ± 0.025 and 5.010 ± 0.030 MeV in ^{37}K and ^{37}Ar, respectively.

The completion of the mass 21 and mass 37 isospin quartets permits two further independent tests of the parabolic character of the isobaric multiplet mass equation (IMME), since the coefficients can be determined from three of the members of a quartet and then used to predict a mass for the fourth member. A list of the $T_z = -3/2$ nuclei whose mass excesses have been measured, together with the coefficients and the predictions of the IMME for the four isospin quartets which have been completed to date, is presented in Table B.10-I. In all four of the completed isospin quartets there is very good first-order agreement between the predicted and experimental mass excesses, within the relatively large experimental errors, which indicates that the IMME is accurate over a fairly large variation in atomic number. An apparent discrepancy in the much more accurate mass 9 quartet data[5] was interpreted as indicating a possible need for the inclusion of a higher-order term $d(A,T)T_z^3$ in the IMME, but unfortunately no explicit theoretical estimate of the magnitude of such a coefficient is available. It is clear from Table B.10-I that such a d(A, T) coefficient is no greater than $\langle Z \rangle \alpha c$, where $\langle Z \rangle$ is the average atomic number of an isospin quartet and α is the fine-structure constant. Theoretical predictions of the magnitude of the expected second-order corrections would be quite valuable.

Footnotes and References

†Condensation of article Phys. Rev., Feb. 20, 1968.

*Present address: Physics Department, University of Southwestern Louisiana, Lafayette, Louisiana.

1. V. I. Goldansky, Nucl. Phys. 19, 482 (1960); J. Jänecke, Nucl. Phys. 61, 326 (1965); I. Kelson and G. T. Garvey, Phys. Letters 23, 689 (1966).

2. E. P. Wigner and E. Feenberg, Rept. Progr. Phys. 8, 274 (1941); E. P. Wigner, in Proceedings of the Robert A. Welch Foundation Conference on Chemical Research, 1957, Vol. I, ed. by W. O. Milligan (The Robert A. Welch Foundation, Houston, 1958), p. 67; S. Weinberg and S. B. Treiman, Phys. Rev. 116, 465 (1959); D. H. Wilkinson, Phys. Letters 12, 348 (1964).
3. F. S. Goulding, D. A. Landis, J. Cerny, and R. H. Pehl, IEEE Trans. Nucl. Sci. NS-13[3], 514 (1966).
4. J. C. Hardy and R. E. Bell, Can. J. Phys. 43, 1671 (1965) and references therein.
5. C. A. Barnes, E. G. Adelberger, D. C. Hensley, and A. B. McDonald, in Proceedings of International Conference on Nuclear Physics, Gatlinburg, Tennessee, September 1966 R. L. Becker, et al., Eds. (Academic Press, New York and London, 1967) p. 261.

Table B.10-I. Isobaric multiplet mass equation predictions and calculated coefficients.

Isobaric multiplet mass equation:

$$M(A, T, T_z) = a(A, T) + b(A, T)T_z + c(A, T)T_z^2 [+ d(A, T)T_z^3]$$

$T_z = -3/2$ Nucleus	Mass excess Experimental (MeV)	Mass excess Predicted (MeV)	b(A, T) (MeV)	c(A, T) (keV)	[d(A, T)] (keV)	$\langle Z \rangle \alpha c$ (keV)
^{9}C	28.99(70)[a, b]					
^{9}C	28.916(5)[c]	28.961(29)	-1.332(7)	278(11)	7(5)	9
^{13}O	23.11(70)[b]	23.10(49)	-2.180(16)	254(15)	-1(14)	12
^{21}Mg	10.62(120)	10.59(152)	-3.545(51)	154(43)	-5(32)	12
^{37}Ca	-13.24(50)	-13.24(118)	-6.176(39)	176(33)	1(21)	24

a. All errors are in parentheses and are given in keV.
b. See J. Cerny, R. H. Pehl, G. Butler, D. G. Fleming, C. Maples, and C. Détraz, Phys. Letters 20, 35 (1966).
c. See Ref. 5.

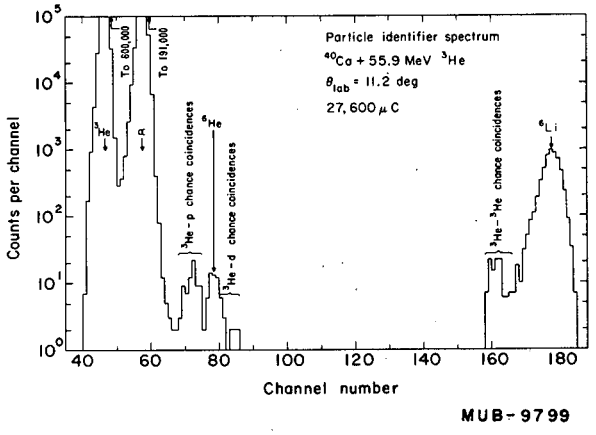

Fig. B.10-1. Triple-counter particle-identifier spectrum from 55.9-MeV ^{3}He ions incident on a ^{40}Ca target.

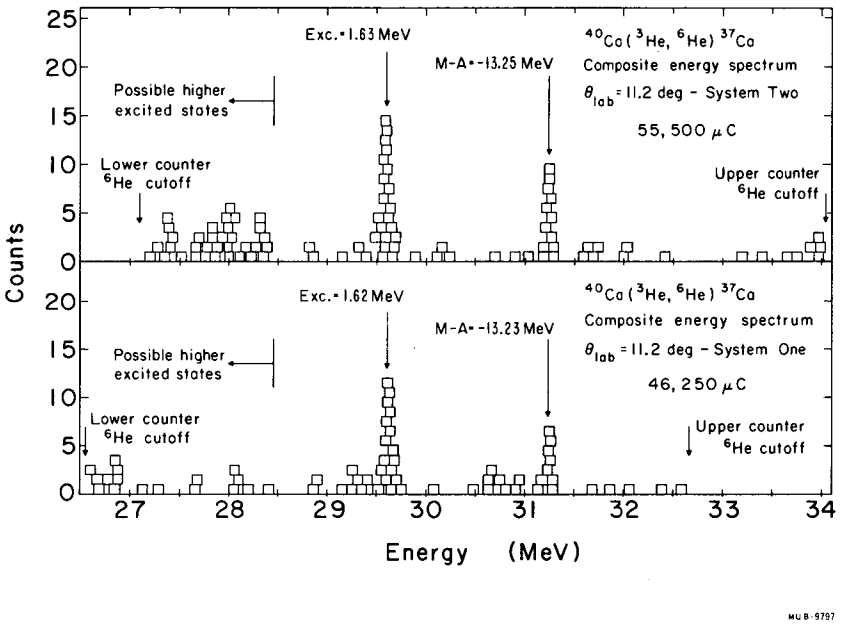

Fig. B. 10-2. Two independent ^{6}He energy spectra from the ^{40}Ca(^{3}He, ^{6}He)^{37}Ca reaction at 55.9 MeV; the data from both systems were kinematically corrected to 11.2 deg. Each block represents one count and the block width is 100 keV.

11. A SEARCH FOR T = 3/2 STATES IN ^{5}Li, ^{5}He, AND ^{5}H†

Robert L. McGrath, Joseph Cerny, and S. W. Cosper*

The problem of the existence of the ^{5}H isotope has been the subject of numerous investigations.[1] Since (p, t) and (p, ^{3}He) reactions readily populate analog states,[2] one can also attempt to study the T = 3/2 states in ^{5}He and ^{5}Li to obtain information on this multiplet. However, a previous unsuccessful search[3] for the mass five T = 3/2 states utilizing these two-nucleon transfer reactions has already been reported.

We have performed several further experiments, attempting to locate T = 3/2 states in various mass-5 nuclei. The first was a repeat of the ^{7}Li(p, t)^{5}Li reaction with improved counting statistics; no new reasonably narrow states were observed, which is an indication that the T = 3/2 state(s) must lie at fairly high excitation (probably above 20 MeV) and be broad.

Secondly, data on coincidences between tritons, ^{3}He's, and alphas (see below) resulting from reactions of p + ^{7}Li have been collected in order to study the decay properties of intermediate ^{5}He and ^{5}Li states. Three- or four-particle final states, resulting from a nuclear reaction, are distinguished by the kinematics if the momenta of two particles are determined.[4] Available T = 3/2 decay modes for both ^{5}He and ^{5}Li intermediate states lead to four-particle final states, whereas T = 1/2 decay modes yield either three- or four-particle final states. Consequently, coincidence data between tritons or ^{3}He particles corresponding to formation of ^{5}Li or ^{5}He states, and triton, ^{3}He, or α particles corresponding to particle decay of these states, can provide a sensitive probe for the location of T = 3/2 states. Six two-dimensional energy arrays consisting of coincidence events between the above particle types were obtained by using two ΔE-E semiconductor telescopes together with an on-line computer.

A typical coincidence array is shown in Fig. B. 11-1, in which tritons were counted at 40 deg and and ^{3}He's at -70 deg. The three- and four-particle final states are cleanly separated in the figure, and the kinematic curves for these final states are shown in the arrays. Projections of

both the three- and four-particle events onto each energy axis are given; the phase-space volume is given by the dotted lines for comparison with the data. Qualitatively the remaining triton-^{3}He data are similar to those shown in Fig. B. 11-1. Data were collected at two pairs of angles (50, -60 deg) and (40, -70 deg) so that triton-^{3}He projections at four angles were obtained. Projections of the four-particle ^{5}He-^{3}He and triton-triton data are shown in Fig. B. 11-2, where the four-particle spectra have been transformed to the recoil ^{5}He or ^{5}Li coordinate systems. In general the four-particle spectra in both figures simply rise with increasing excitation energy and possess no well-defined peak structure which might be associated with the sought analog states. Calculated four-particle phase-space distributions have been fitted by eye to the spectra in Fig. B. 11-2 for comparison. The fits approximate rather well the shapes of the spectra extending from the experimental cutoffs up to about 27 MeV excitation energy in both ^{5}He and ^{5}Li. There appears to be no indication of mass-5 T = 3/2 states in these four-particle data, implying again that the sought analog states are very broad.

A third experiment was the observation of ^{8}B ions from reactions of α particles on ^{9}Be targets, which permits direct examination of the ^{5}H system. A 129-MeV α-particle beam was used to bombard a self-supporting 650-μg/cm^2 ^{9}Be target. Signals from two four-counter telescopes were fed to two triple-counter particle identifiers, which have been previously described.[5] Figure B. 11-3 presents the ^{8}B spectra; no sharp states are evident in the data from either telescope. Instead, the spectra rise rather smoothly above the threshold for ^{5}H particle stability (relative to decay into t + n + n). We have attempted to fit the spectra with arbitrary combinations of three- and four-particle phase-space distributions, but with little success. Both spectra exhibit a residual "peak" extending from near the threshold to about 20 MeV excitation in ^{5}H, peaking in both cases at 11.6 MeV excitation above threshold. This peak can certainly not be associated with a single state of ^{5}H. Whether it results from several broad states or angular momentum or both, or other effects not considered in the phase-space calculations, is not clear. It is possible to set an upper limit on the cross section of a well-defined state of ^{5}H. If the state is narrower than about 1 MeV and lies lower than 1.5 MeV above the threshold, it would have been obvious in the data if it possessed an average cross section at the two angles larger than 22 nb/sr or, in other words, larger than 1/25 the cross section for the ^{12}C(α, ^{8}B)^{8}Li g. s. reaction. If ^{5}H is just bound, then it would be apparent in the data if the average cross section were about 1/88 that of ^{8}Li g. s. reaction.

We find no evidence for mass-5 states having the expected T = 3/2 decay properties. In the vicinity of 20-MeV excitation in ^{5}Li (the region of interest with respect to the particle stability of ^{5}H) cross-section upper limits for well-defined T = 3/2 states can be estimated which are substantially smaller than (p, t), (p, ^{3}He) cross sections for formation of T = 3/2 states in other nuclei. Further, the ^{9}Be(α, ^{8}B)^{5}H data exhibit no peaks which can be associated with sharp ^{5}H states. Therefore we conclude from these data that the lowest mass-5 T = 3/2 states exist at relatively high excitation above the relevant three-particle decay thresholds, and hence are quite broad. These results are qualitatively consistent with the theoretical predictions[6] that ^{5}H is unbound by at least several MeV.

Footnotes and References

†Condensed from Phys. Rev. 165, 1126 (1968).

*Present address: Physics Department, University of Southwestern Louisiana, Lafayette, Louisiana.

1. T. Lauritsen and F. Ajzenberg-Selove, Nucl. Phys. 78, 1 (1966).

2. J. Cerny and R. H. Pehl, Phys. Rev. Letters 12, 619 (1964); J. Cerny, R. H. Pehl, and G. T. Garvey, Phys. Rev. Letters 12, 234 (1964); C. Détraz, J. Cerny, and R. H. Pehl, Phys. Rev. Letters 14, 708 (1965); J. Cerny, R. H. Pehl, G. Butler, D. G. Fleming, C. Maples, and C. Détraz, Phys. Letters 20, 35 (1966).

3. J. Cerny, C. Détraz, and R. H. Pehl, Phys. Rev. 152, 950 (1966).

4. Č. Zupančič, Nuclearni Inštitut Jožef Stefan Report No. R-429, 1964 (unpublished).

5. F. S. Goulding, D. A. Landis, J. Cerny, and R. H. Pehl, IEEE Trans. Nucl. Sci. 13, 514 (1966).

6. F. C. Barker (The Australian National University, Canberra, Australia), private communication, 1965; T. I. Kopaleishvili (Tbilisi State University, Tbilisi, U.S.S.R.), private communication, 1967; R. F. Fraser and B. M. Spicer, Australian J. Phys. 19, 893 (1966).

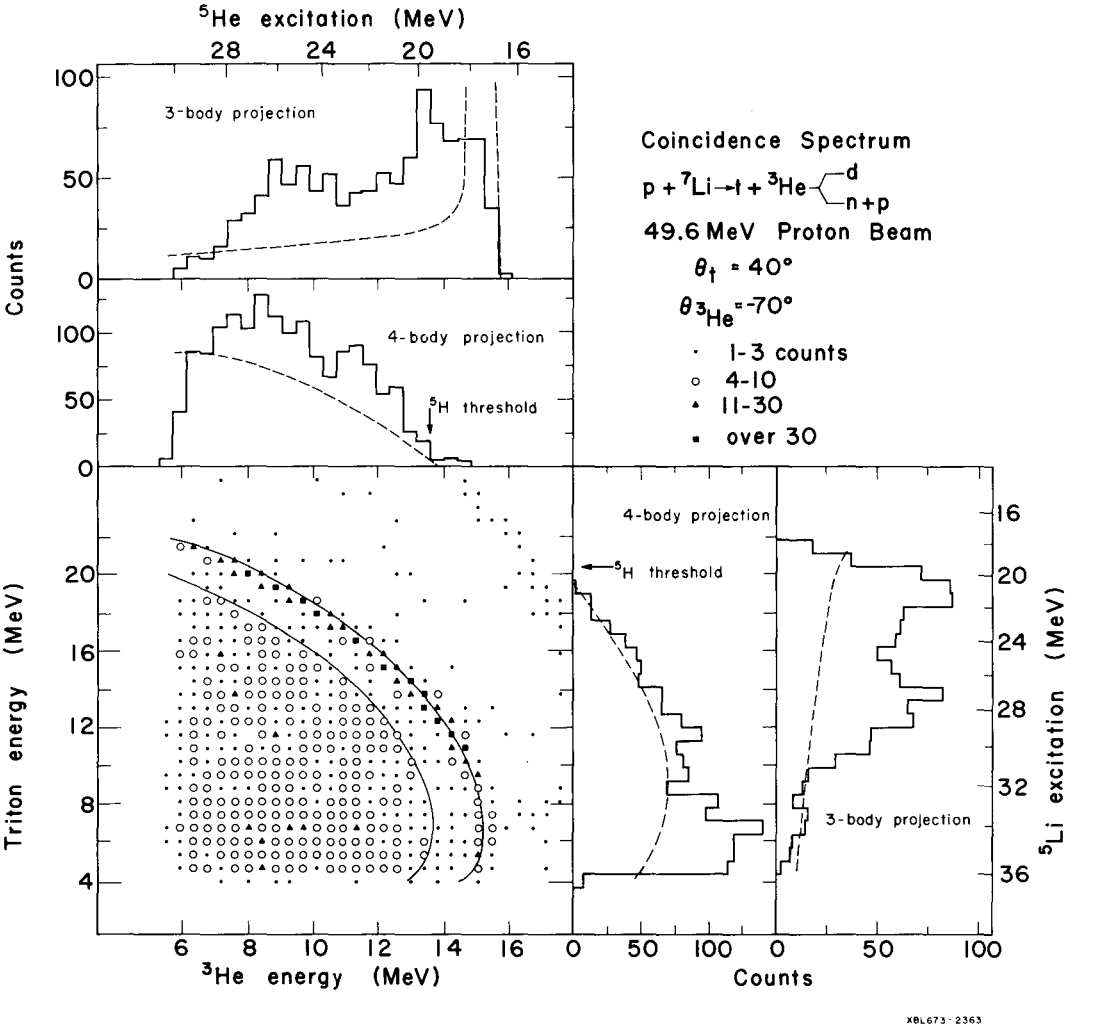

Fig. B. 11-1. A triton (40 deg) ^{3}He (-70 deg) coincidence spectrum. The solid lines in the two-dimensional array are the three- and four-particle final-state kinematic curves. Projections of the data onto both energy axes are shown; the phase-space distributions are given by the dashed lines for comparison. If ^{5}H is bound, the excitation of the lowest $T = 3/2$ state of either ^{5}He or ^{5}Li is less than ≈ 19.5 MeV, which is indicated by the arrow in the four-particle spectra.

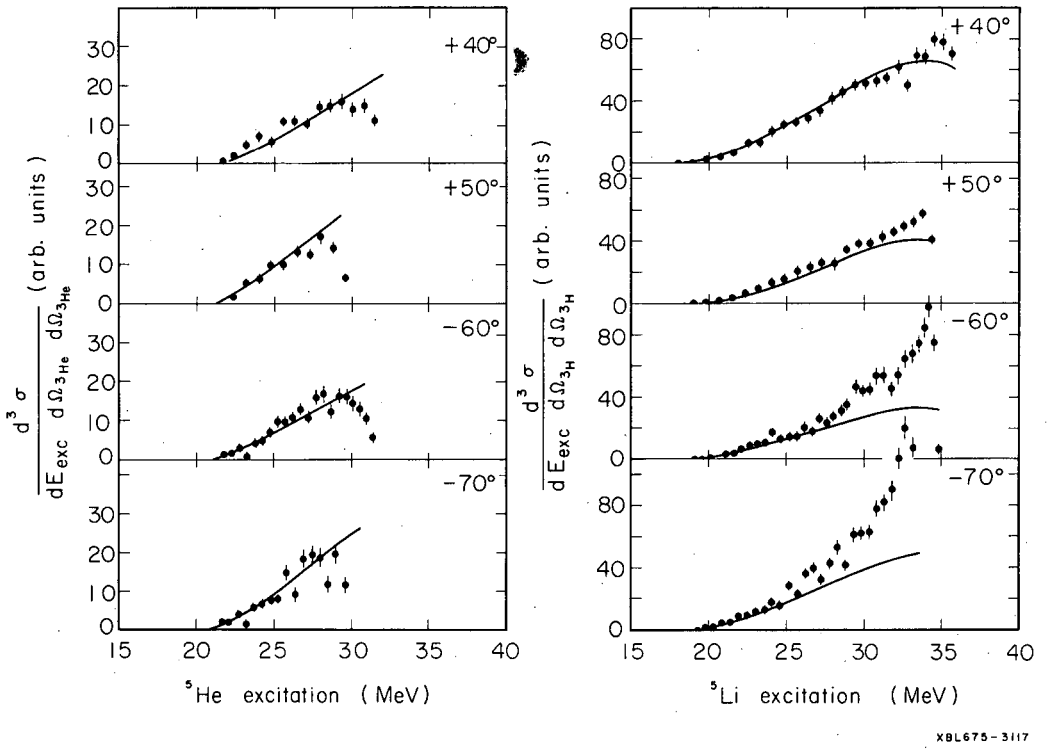

Fig. B. 11-2. Projections of the ^{3}He-^{3}He four-particle final-state coincidence data are shown on the left and projections of the triton-triton four-particle final-state data on the right after transformation to the ^{5}He and ^{5}Li recoil systems, respectively. The solid lines are phase-space fits to the spectra.

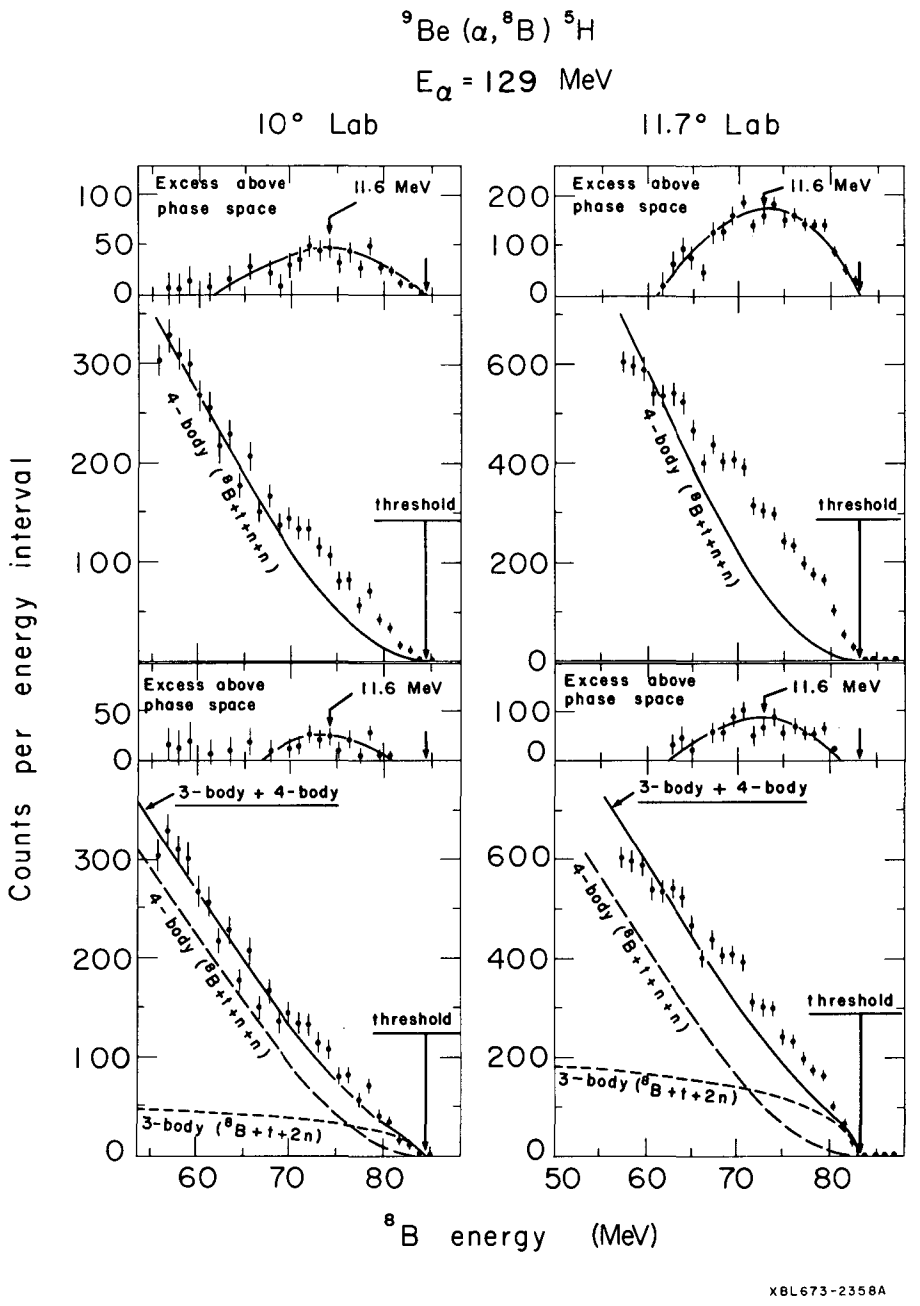

Fig. B. 11-3. The ^{9}Be(α, ^{8}B)^{5}H energy spectra at 10 and 11.7 deg (lab). The spectra are fitted with four-particle (^{8}B+t+n+n) phase-space distributions in the upper half of the figure and with a sum (solid line) of three-particle (^{8}B+t+2n) and four-particle (^{8}B+t+n+n) phase-space distributions (dashed lines) in the lower half of the figure.

12. THE LOCATION AND DECAY MODES OF THE LOWEST $J^\pi = 1/2^-$, $T = 3/2$ STATES IN ^{11}B AND ^{11}C

S. W. Cosper, Robert L. McGrath, Joseph Cerny, C. C. Maples,
Donald G. Fleming, and George W. Goth

The simultaneous observation of tritons and ^3He particles resulting from the proton bombardment of p-shell $T_z = +1/2$ target nuclei has been shown to be an effective method for locating low-lying $T = 3/2$ states in the $T_z = -1/2$ and $T_z = +1/2$ nuclei produced by these reactions.[1] We wish to report the observation of low-lying $T = 3/2$ states in ^{11}C and ^{11}B which have been located by use of the $^{13}C(p, t)^{11}C$ and $^{13}C(p, ^3He)^{11}B$ reactions. These states have been assigned $T = 3/2$ on the basis of angular distributions and cross section ratios. As an additional test of the isospin purity of these states, their decay schemes have been investigated through coincidence measurements between the tritons or ^3He particles forming the $T = 3/2$ states and energetically allowed charged-particle decays.

Triton and ^3He energy spectra and angular distributions were obtained in two separate experiments using 43.7- and 50.5-MeV proton beams from the 88-inch cyclotron. A 3-in.-diameter target gas cell, covered with 0.1-mil Havar, contained methane enriched to 93% in ^{13}C. Signals from two independent three-detector telescopes--each consisting of a 149μ ΔE detector, a 3060μ E detector, and a 510μ E-reject (anticoincidence) detector--were amplified and fed to power-law-type particle identifiers.[2] Gating signals generated by the four channels of the particle identifier routers were used to route the total energy signals into the appropriate 1024-channel quadrant of the pulse-height analyzers.

Figure B. 12-1 presents energy spectra of tritons and ^3He particles resulting from 50.5-MeV proton bombardment of ^{13}C. The insets in each section of the figure are an expanded graph of that portion of the complete spectrum bracketed by arrows from which the $T = 1/2$ continuum background, indicated by the dashed line, has been subtracted. Each inset contains a rather large broad peak, located at 12.47 ± 0.06 MeV in the (p, t) and 12.94 ± 0.05 MeV in the (p, ^3He) spectra, with widths of 550 ± 50 and 350 ± keV, respectively. The angular distributions of these two states at $E_p = 50.5$ and 43.7 MeV are shown in Fig. B. 12-2. The (p, t) and (p, ^3He) differential cross sections are identical within counting and background subtraction statistics, as expected for transitions to $T = 3/2$ states.

Intermediate coupling calculations by Cohen and Kurath[3, 4] and by Boyarkina[5] predict that the lowest p-shell $T = 3/2$ state in ^{11}B should lie between 12.5 and 13.7 MeV excitation; a simple Coulomb calculation predicts 12.78 MeV excitation for the ^{11}B $T = 3/2$ state based on the ^{11}Be first excited state. These predictions are all consistent with the measured excitation of 12.94 ± 0.05 MeV for the relatively large peak in the (p, ^3He) energy spectrum in Fig. B. 12-1. In addition, the angular distributions of these two states in ^{11}C and ^{11}B exhibit the characteristic $L = 0$ behavior expected. For the above reasons, the $^{11}B^*$ (12.94 MeV) and $^{11}C^*$ (12.47 MeV) states are assigned $T = 3/2$, and are the analogs of a low-lying state in ^{11}Be. Since the parity of the ^{11}Be ground state is positive[6] and the second excited state of ^{11}Be lies at 1.78 MeV, these $T = 3/2$ states are analogs of the first excited state of ^{11}Be at 0.32 MeV.

Reference to Fig. B. 12-3 shows that the ^{11}B 12.94-MeV state and the ^{11}C 12.47-MeV state each have only one open $T = 3/2$ particle decay mode, i. e., via emission of an $L = 1$ proton to the ^{10}Be g. s. and to the ^{10}B 1.74-MeV $T = 1$ state, respectively. Except for the isospin selection rule, these states might decay via a number of other modes illustrated in the figure. Thus a test of the isospin purity of these mass-11 states is achieved by determining the fraction of isospin-allowed decays. Coincidence events between triton and ^3He particles forming these states and the charged-particle decay modes shown in the figure were obtained by using two ΔE-E counter telescopes located at +30 and -85 deg in conjunction with an on-line computer. Fractional branching ratios for decay of the $T = 3/2$ states were calculated by comparing the number of coincidence events corresponding to the various residual states shown in Fig. B. 12-3 with the number calculated on the basis of the triton or ^3He singles counts recorded in the +30-deg telescope and the geometry of the -85-deg telescope (since the $T = 3/2$ states have spin 1/2, their decay is isotropic in the mass-11 coordinate system). We obtain 70 ± 25% for decay of the ^{11}B state to the ^{10}Be ground state, and 92 ± 25% for decay of the ^{11}C state to the ^{10}B 1.74-MeV $T = 1$ state. Qualitatively, these results support the $T = 3/2$ assignment. Further support for the conclusion that these $T = 3/2$ states decay predominantly via emission of an $L = 1$ proton to the mass-10 $T = 1$ states comes from the calculated ratio of $^{11}C/^{11}B$ penetrabilities of 1.33, which agrees with the experimental width ratio of (550 ± 50)/(350 ± 50) = 1.57 ± 0.27.

References

1. C. Détraz, J. Cerny, and R. H. Pehl, Phys. Rev. Letters 14, 708 (1965); and J. Cerny, R. H. Pehl, G. W. Butler, D. G. Fleming, C. Maples, and C. Détraz, Phys. Letters 20, 35 (1966).
2. F. S. Goulding, D. A. Landis, J. Cerny, and R. H. Pehl, Nucl. Instr. Methods 31, 1 (1964).
3. D. Kurath, Phys. Rev. 101, 216 (1956).
4. S. Cohen and D. Kurath, Nucl. Phys. 73, 1 (1965).
5. A. N. Boyarkina, Akad. Nauk USSR 28, 255 (1964).
6. D. E. Alburger, C. Chasman, K. W. Jones, J. W. Olness, and R. A. Ristinen, Phys. Rev. 136, B916 (1964).

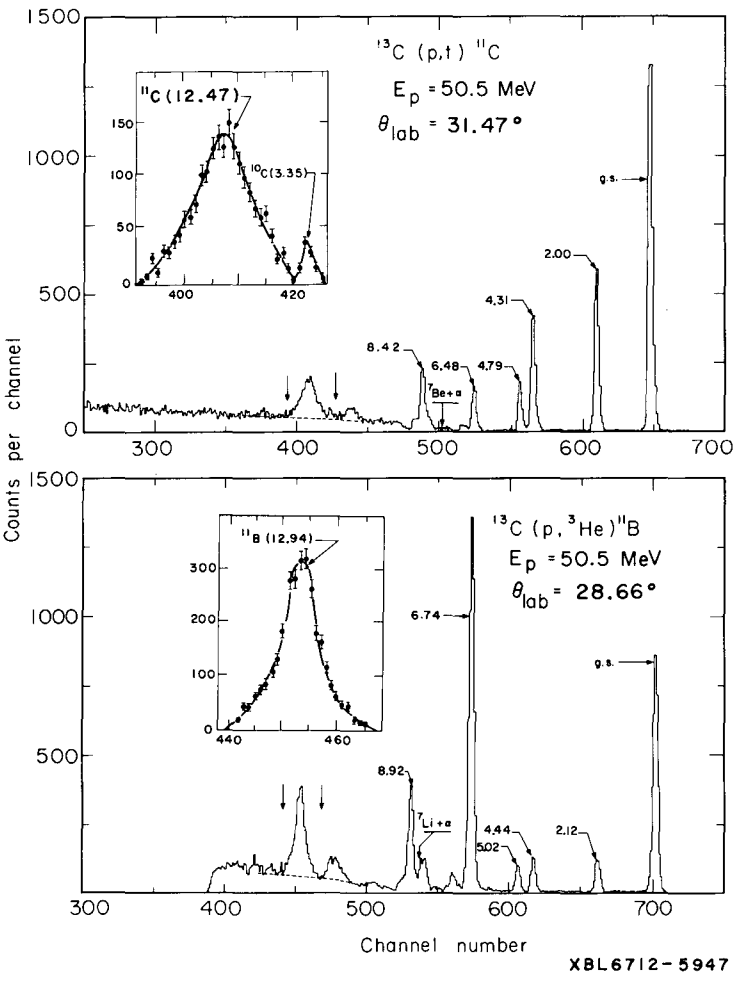

Fig. B. 12-1. Energy spectra of tritons and ^{3}He particles resulting from 50.5-MeV proton bombardment of ^{13}C.

Fig. B. 12-2. Angular distributions of tritons and ^{3}He particles forming the 12.47-MeV ^{11}C and 12.94-MeV ^{11}B states.

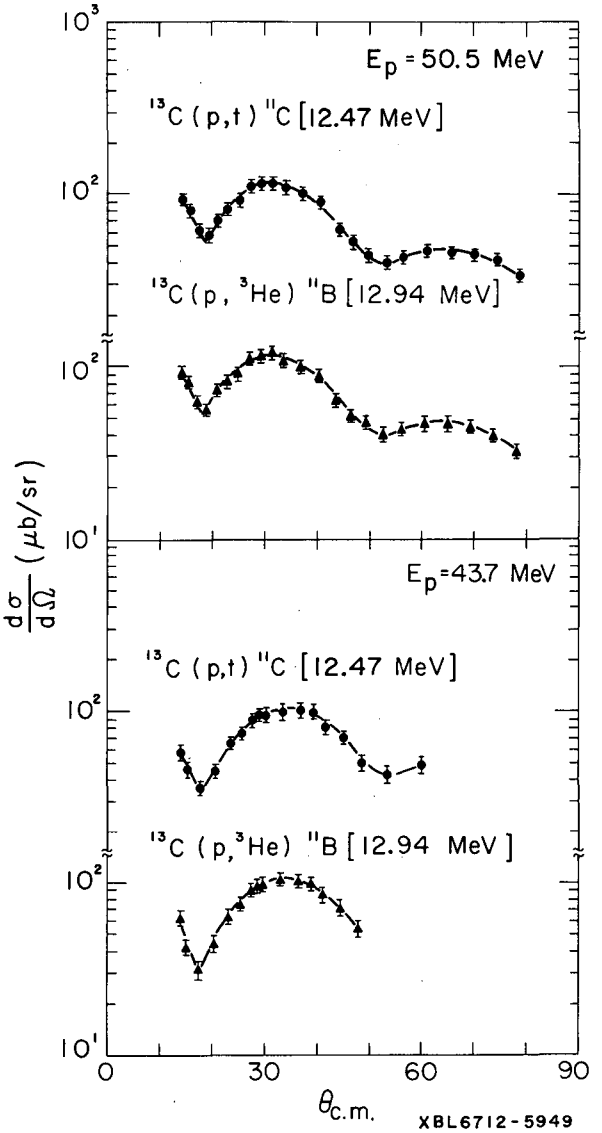

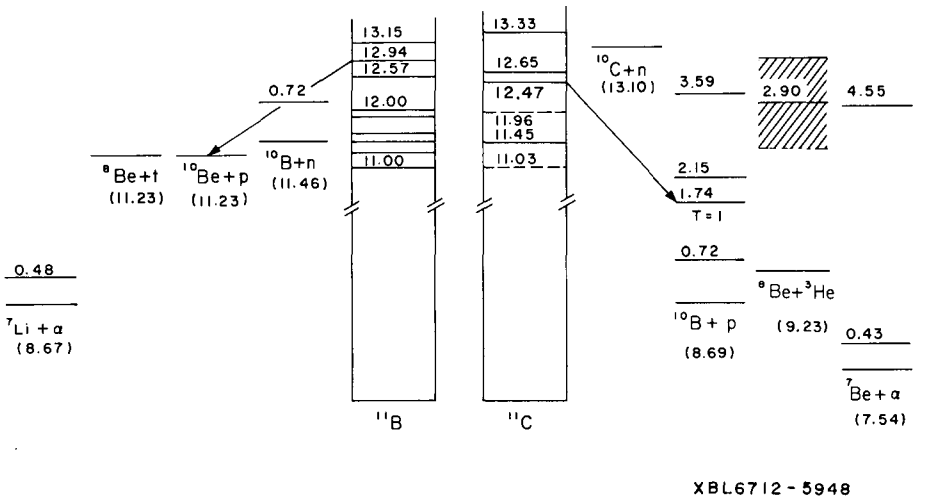

Fig. B. 12-3. Partial energy-level scheme for ^{11}B and ^{11}C showing various particle thresholds.

13. ISOSPIN-FORBIDDEN DECAY OF THE ^{24}Mg 15.43-MeV 0+ T = 2 STATE†

Robert L. McGrath, S. W. Cosper, and Joseph Cerny

Even though the locations (and very large upper limits on the widths) of many 0+ T = 2 states in T_z = 0 nuclei are known,[1,2] no further information on their properties is available. Since in general no T = 2 particle-decay channels are open for these T = 2 states, they are expected to be relatively sharp. Their isospin-forbidden particle decays are of particular interest, since they provide a sensitive measure of the isospin impurity admixed into these states by charge-dependent forces (Coulomb plus nuclear). Although attempts to determine the particle-decay properties and total widths of these states through their observation as "twice T-forbidden" compound nucleus resonances in proton scattering have been made--a technique successfully applied to T = 3/2 states[3,4]--solely negative results were obtained.[3,5,6]

In order to be certain that a typical T = 2 state does indeed possess a total particle width comparable to its gamma width ($\Sigma\Gamma_{particle} \gtrsim \Gamma_\gamma$), and to sufficiently establish its decay properties to ascertain whether its exploration by compound resonance techniques is feasible, the isospin-forbidden particle decay of the ^{24}Mg 0+ T = 2 state populated in the isospin-allowed ^{26}Mg(p, t)^{24}Mg reaction has been investigated. This particular T = 2 state was chosen because previous searches for it in resonance experiments were unsuccessful[3,6] and because its low proton-decay energy makes it accessible to standard electrostatic accelerators.

Figure B. 13-1 shows all the probable[7] decay modes open to the ^{24}Mg T = 2 state. Utilizing the 42.1-MeV proton beam of the Berkeley 88-inch cyclotron, we have measured coincidences between tritons forming this state at 15.43 ± 0.07 MeV excitation and decay protons [E_{max}(lab) = 3.9 MeV] or α particles [E_{max}(lab) = 6.1 MeV] leading to the ^{23}Na or ^{20}Ne levels indicated by heavy lines in the figure. Figure B. 13-2 presents the layout of the three three-counter telescopes employed; E-reject detectors were used to reduce background. Tritons leading to the T = 2 state were identified[8] in system 1 placed at the L = 0 peak angle of 22.4 deg lab. Fast and slow coincidences were required between tritons and (a) identified protons in system 2 or 3 or identified α particles in system 2 (solid angles of 3.5×10^{-3} sr) or (b) particles stopping in the ΔE detector of system 3 (solid angle of 8.0×10^{-3} sr). Because of the small solid angles of systems 2 and 3, arising from the need for particle identification, the low cross section for tritons populating the T = 2 state ($d\sigma/d\Omega \approx 100$ μb/sr), and a counting rate limitation of 30 000 cps in the system 1 E-detector, an average of only two coincidence events per hour in both systems from the decay of

this state was obtainable. Forty hours of coincidence data were recorded in four 512×512 arrays on magnetic tape, utilizing an on-line PDP-5 computer; the cumulative triton singles data were stored in a 1024-channel pulse-height analyzer. The spin-zero property of the T = 2 state ($\Gamma \leq 35$ keV[9]) guaranteed an isotropic decay with respect to the ^{24}Mg c. m. system--thus detailed angular correlation measurements were not required to extract decay widths.

Data from several coincidence arrays are presented in Fig. B. 13-3 through B. 13-5. Figure B. 13-3 shows the triton coincidences with particles stopping in the ΔE detector of system 3; coincident particles which lost more than 1.8 MeV in this detector were required by kinematics to be α particles. Alpha decays leading to the ^{20}Ne ground and first excited states lie inside the two bands on the figure. These bands are established from the curve given by three-body kinematics adjusted for finite counter geometry, energy losses in the target, and electronic resolution. (Events corresponding to energy losses of less than 1.8 MeV in the ΔE detector are probably due to triton-proton coincidences.) Figure B. 13-4 shows the array arising from triton coincidences with identified protons in system 3. The bands encompass decays to the ground and first excited states of ^{23}Na.

A triton singles spectrum is shown at the top of Fig. B. 13-5; the resolution (FWHM) of the T = 2 peak is about 180 keV. Below this spectrum are displayed projections of bands from three of the coincidence arrays onto the triton axis. The ^{23}Na ground and 0.44-MeV state projections contain data from systems 2 and 3; data for the other ^{23}Na levels come only from system 2. The ^{20}Ne + α data are obtained from system 3.[10]

Counts attributed to the decay of the T = 2 state were obtained by summing the projected spectra over the appropriate triton energies and subtracting (a) the chance background and (b) the "real" continuum background. The continuum was assumed smooth, and was calculated by interpolating the projected count level averaged over 15 channels on both sides of the T = 2 peak. Fractional decay widths for each observable decay mode were obtained by comparing its net coincidence counts to the number predicted from the triton singles data after the isotropic decay of the T = 2 state in ^{24}Mg had been transformed from the c. m. system to lab, assuming 100% decay via that particular mode.

The sum of all fractional widths for decay to the six lowest ^{23}Na levels and the lowest two levels of ^{20}Ne is $1.3_0 \pm 0.2_0$. This sum should be ≤ 1.0; although the discrepancy is outside one standard deviation, it is considered to be statistical. There is, of course, no way to be certain that a small state does not lie underneath the T = 2 state[11] and, perhaps, decay anisotropically. Further, from the nature of the projected data in Fig. B. 13-5, such a state would more probably α-decay. However, since the major peaks in the projected spectra associated with the T = 2 decays center precisely about the relevant triton energy, and since the triton singles peak shape coupled with an absolute comparison of the ^{26}Mg(p, t)^{24}Mg(T = 2) with the ^{26}Mg(p, ^{3}He)^{24}Na(T = 2) angular distribution data[12] implies < 10% "contamination," we consider a significant contribution from such a small state to be improbable. In any event, no such problem could affect the conclusion that the major decay mode of the ^{24}Mg T = 2 state is via proton decay to the ^{23}Na g. s., making it possible for compound resonance experiments to explore this state. Figure B. 13-1 presents our data on the decay of the T = 2 state.

Footnotes and References

†Condensed from Phys. Rev. Letters 18, 243 (1967).

1. G. T. Garvey, J. Cerny, and R. H. Pehl, Phys. Rev. Letters 12, 726 (1964).

2. J. Cerny, R. H. Pehl, and G. T. Garvey, Phys. Letters 12, 234 (1964); J. Cerny and G. T. Garvey, Isobaric Spin in Nuclear Physics, ed. by J. D. Fox and D. Robson (Academic Press, New York, 1966), pp. 514 and 517; and C. A. Barnes, discussion in Proceedings of the International Conference on Nuclear Physics, Gatlinburg, Tennessee, 1966 (Academic Press, New York, 1967).

3. D. J. Bredin, O. Hansen, G. M. Temmer, and R. Van Bree, Isobaric-Spin in Nuclear Physics, ed. by J. D. Fox and D. Robson (Academic Press, New York, 1966), p. 472.

4. G. M. Temmer and R. Van Bree, in Proceedings of the International Conference on Nuclear Physics, Gatlinburg, Tennessee, 1966 (Academic Press, New York, 1967).

5. G. M. Temmer, discussion in Proceedings of the International Conference on Nuclear Physics, Gatlinburg, Tennessee, 1966 (Academic Press, New York, 1967).

6. B. Titleman, G. T. Garvey, and G. M. Temmer, private communication.

7. The only other open decay mode, ^{12}C + ^{12}C + 1.5 MeV, would be strongly inhibited by the Coulomb barrier. The ^{23}Na level scheme is taken from A. R. Poletti and D. F. H. Start,

Phys. Rev. 147, 800 (1966) and references therein; the ^{20}Ne data come from T. Lauritsen and F. Ajzenberg-Selove, in Nuclear Data Sheets--1962, compiled by K. Way, et al., NRC 61-5, 6.

8. F. S. Goulding, D. A. Landis, J. Cerny, and R. H. Pehl, Nucl. Instr. Methods 31, 1 (1964).

9. A. B. McDonald, E. G. Adelberger, and C. A. Barnes, private communication.

10. Only α particles corresponding to transitions to the ^{20}Ne g. s. were cleanly observed in system 2 due to the ΔE counter thickness. The fewer coincidence counts resulting from the smaller solid angle of this system were in agreement with the data from system 3, but were not incorporated.

11. It is of some interest to note that the ^{22}Ne(^{3}He, n)^{24}Mg reaction near this excitation populates only the T = 2 state at 15.43 MeV and an additional level at 15.54 MeV (unobserved in these results) with a FWHM of about 380 keV (Ref. 9).

12. J. Cerny and G. T. Garvey, unpublished data.

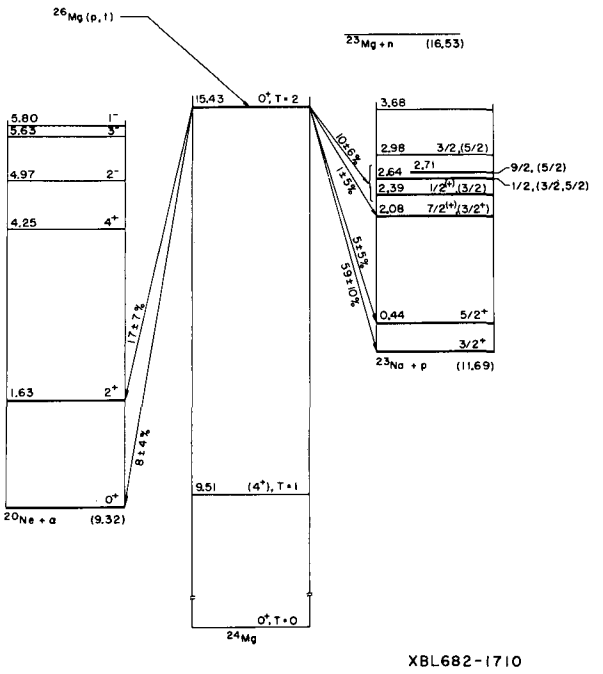

Fig. B. 13-1. Level diagram showing the ^{24}Mg, 15.43 MeV, 0+, T = 2 state and its possible particle-decay modes. Observed transitions are indicated with arrows, along with their percentage branching ratios.

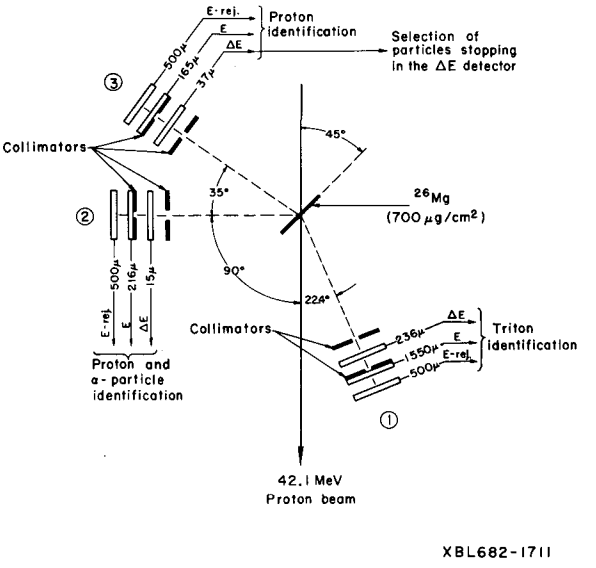

Fig. B. 13-2. Schematic representation of the experimental setup, showing the arrangement of the three telescopes and target with respect to the incident beam. Thicknesses of the phosphorus-diffused or lithium-drifted silicon detectors are indicated.

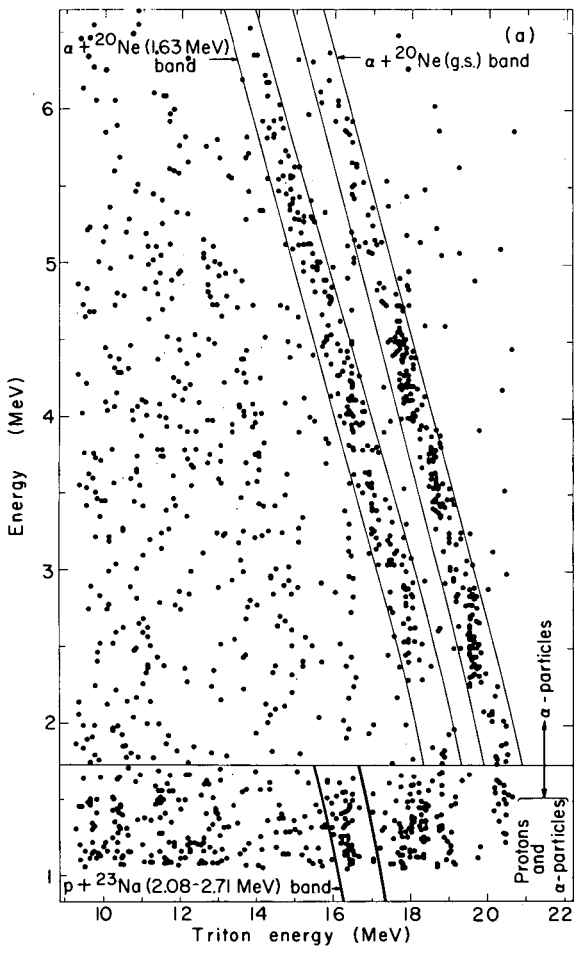

Fig. B. 13-3. A two-dimensional spectrum of individual events of tritons from system 1 in coincidence with particles stopping in the ΔE detector of system 3.

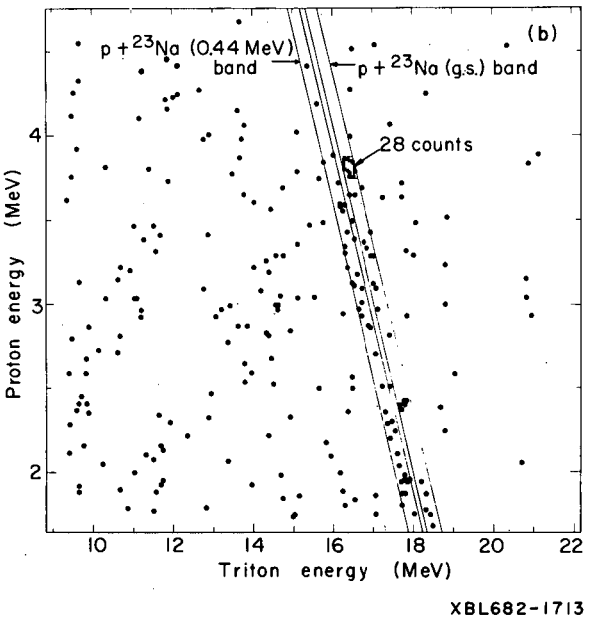

Fig. B. 13-4. A two-dimensional spectrum of individual events of tritons from system 1 in coincidence with protons from system 3. The pronounced peak corresponds to decays from the ^{24}Mg T = 2 state to the ^{23}Na g. s.

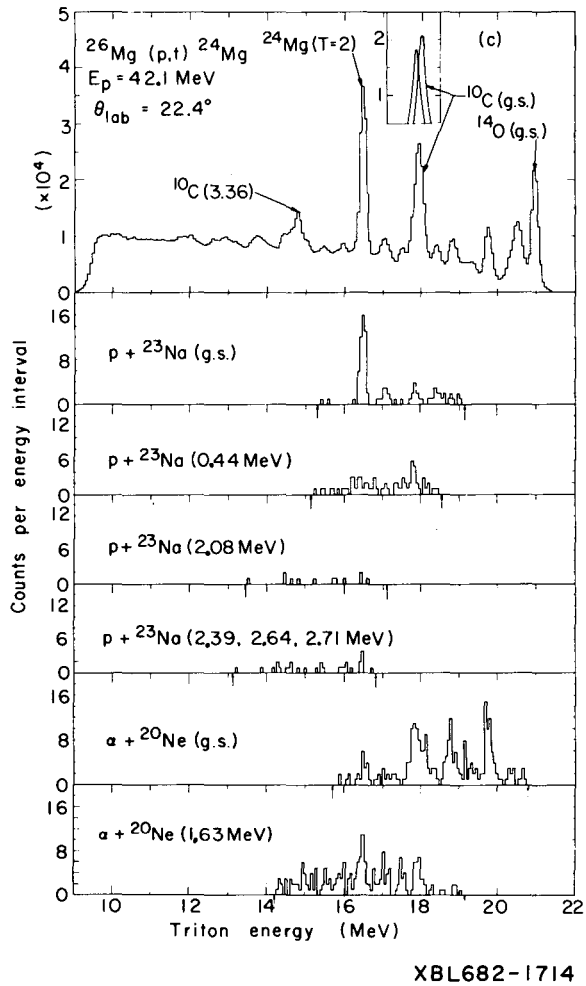

Fig. B. 13-5. The upper spectrum presents the triton singles data. The lower spectra are projections of the bands in the coincidence data onto the triton axis; the arrows in these spectra indicate the energy cutoffs required by kinematics.

14. THE ^{15}N(p, t)^{13}N AND ^{15}N(p, ^{3}He)^{13}C REACTIONS AND THE SPECTROSCOPY OF LEVELS IN MASS 13†

Donald G. Fleming,* Joseph Cerny, Creve C. Maples, and Norman K. Glendenning

The nuclear spectroscopy of the mass-13 nuclei may be examined by comparison of the ^{15}N(p, t)^{13}N and ^{15}N(p, ^{3}He)^{13}C reactions populating mirror final states. Little work on comparisons of these reactions to final states other than isobaric analogs has been reported.[1] We attempt to fit both the shapes and magnitudes of the (p, t) and (p, ^{3}He) transitions with distorted-wave Born approximation (DWBA) calculations,[2,3] thereby testing the mass-13 wave functions of Cohen and Kurath[4] over 15 MeV of excitation.

These reactions were induced by a 43.7-MeV proton beam from the 88-inch cyclotron on a 99% $^{15}N_2$ gas target. The particles were detected by a (dE/dx-E-E_{rej}) counter telescope system which fed a particle identifier.[5] Figure B. 14-1 presents energy spectra of the ^{15}N(p, t)^{13}N and ^{15}N(p, ^{3}He)^{13}C reactions taken at 15 deg, and indicates the spin and parity of the observed levels together with their excitations. Typical energy resolutions (FWHM) of 150 and 180 keV were ob-

tained for tritons and helium-3, respectively. Levels were observed up to 15 MeV of excitation in both ^{13}N and ^{13}C, and angular distributions were obtained for all the observed levels between $\theta_{c.m.} \approx 10$ to 90 deg (except for levels of ^{13}C above 12 MeV, which were seen only to 70 deg). Figure B. 14-2 presents an energy level diagram for ^{13}N and ^{13}C with dotted lines connecting mirror states.

Since appropriate elastic scattering data were not available in either the entrance or exit channel, the optical-model parameters were obtained from an examination of the "best fit" parameters available in the literature. The best overall potential combination was determined from fitting the $^{15}N(p,t)^{13}N$ transitions alone, since only single L transfers are allowed. A triton potential utilizing a sum of single-nucleon potentials with surface absorption (derivative Saxon-Wood) gave the best overall fits to the data. The exit channel parameters were taken to be the same for tritons and ^{3}He.

Considerable theoretical interest has been concentrated on nuclei in the 1p shell within the framework of the intermediate coupling model. Two-nucleon structure factors[3] (G_{NLSJT}) have been calculated for all the $^{15}N(p,t)^{13}N$ and $^{15}N(p,{}^{3}He)^{13}C$ transitions by using coefficients of fractional parentage derived from Cohen and Kurath's complete intermediate-coupling wave functions.[4] Harmonic oscillator wave functions were assumed for the single-particle states in the nuclear structure calculation, and the oscillator parameter ν was taken to be $0.32\ F^{-2}$, in accord with the value used by True in his shell-model calculation of the 1p levels in ^{14}N.[6]

The following new spin and parity assignments have been made: (i) the 7.38-MeV level in ^{13}N was confirmed as $5/2^-$ and the mirror level in ^{13}C was found at 7.55 MeV; (ii) the 8.93-MeV level in ^{13}N is known to be $1/2^-$ and the mirror level in ^{13}C was found at 8.86 MeV; (iii) the mirror to the 9.48-MeV $3/2^-$ in ^{13}N was found at 9.52 MeV in ^{13}C, although the analysis indicated that this level is probably not composed primarily of a $(1p)^9$ configuration, and hence is not predicted by intermediate coupling calculations; (iv) a new level was seen in ^{13}N at 10.78 MeV, and is thought to be $1/2^-$ with its mirror in ^{13}C at 11.09 MeV; (v) the 11.88-MeV level in ^{13}N was confirmed as $3/2^-$ and the 11.80-MeV level in ^{13}C is thought to be the mirror; and (vi) a level was found at 12.40 MeV in ^{13}C and assigned as $7/2^-$.

An attempt was made to utilize the two-nucleon transfer theory[3] to account for the relative cross sections found in the $^{15}N(p,t)^{13}N$ reaction. Relatively good agreement was obtained between theory and experiment, although adjustment of the oscillator parameter, ν, of bound state wave functions for excited states was necessary.[7] As our adjustment of ν does not markedly affect the amplitudes of the wave functions of Cohen and Kurath,[4] these wave functions must be regarded as giving a good description of the final states populated in the $^{15}N(p,t)^{13}N$ reaction.

Footnotes and References

†Condensed from Phys. Rev., Feb. 20, 1968.

*Now at the Nuclear Structure Laboratory, University of Rochester, Rochester, New York.

1. J. Cerny, C. Détraz, and R. H. Pehl, Phys. Rev. 152, 950 (1966).
2. N. K. Glendenning, Ann. Rev. Nucl. Sci. 13, 191 (1963).
3. N. K. Glendenning, Phys. Rev. 137B, 102 (1965).
4. S. Cohen and D. Kurath, Nucl. Phys. 73, 1 (1965), and D. Kurath, private communication.
5. F. S. Goulding, D. A. Landis, J. Cerny, and R. H. Pehl, Nucl. Instr. Methods 31, 1 (1964).
6. W. M. True, Phys. Rev. 130, 1530 (1963).
7. D. G. Fleming, J. Cerny, C. C. Maples, and N. K. Glendenning, journal version of this report; Donald G. Fleming, A Comparative Study of (p, t) and (p, ^{3}He) Reactions on Light Nuclei (Ph. D. thesis), UCRL-17790, Aug. 1967.

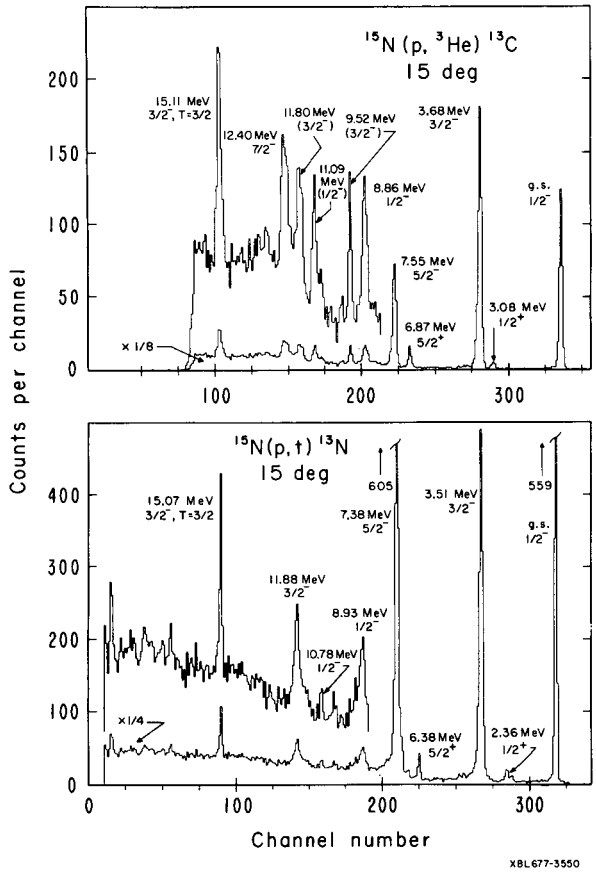

Fig. B. 14-1. Energy spectra for the $^{15}N(p,t)^{13}N$ and $^{15}N(p,{}^{3}He)^{13}C$ reactions. The spectra have been adjusted to match channels for the $5/2^-$ transitions, showing a slight nonlinearity in the triton spectrum at the higher energies.

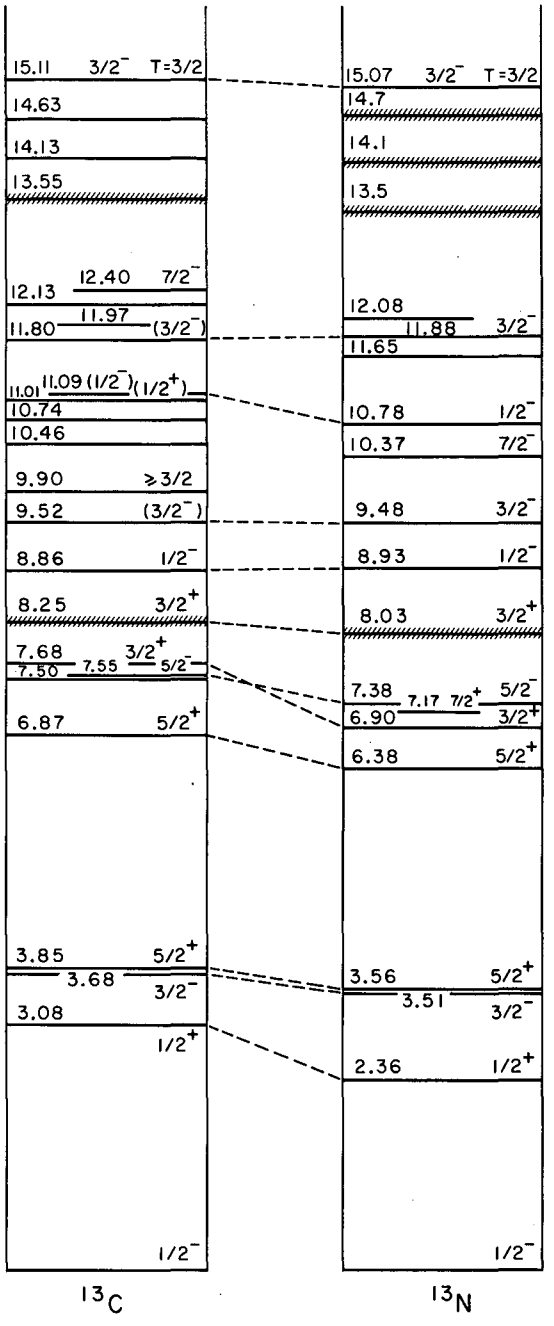

Fig. B. 14-2. Energy level diagram for ^{13}N and ^{13}C.

15. ENERGY DEPENDENCE OF $^{26}Mg(p,t)^{24}Mg$ AND $^{12}C(p,t)^{10}C$ L = 0 AND L = 2 ANGULAR DISTRIBUTION SHAPES†

S. W. Cosper,* H. Brunnader, Joseph Cerny, and Robert L. McGrath

During a recent experiment[1] in which the lowest T = 2 (15.43 MeV; 0^+) state in ^{24}Mg was populated via the $^{26}Mg(p,t)$ reaction, it was noted that the typical L = 0 triton angular distribution of this state[2] showed a marked magnitude and shape deterioration when the incident proton energy was lowered from 38.7 to 32.5 MeV. That both the magnitude and shape of this angular distribution could undergo such a drastic change with only a 6-MeV change in incident proton energy near $E_p \approx 35$ MeV appeared to be of considerable interest for three reasons: (a) Most other L = 0 and L = 2 (p,t) angular distributions, primarily involving relatively high c.m. energy tritons, had shown a nearly static shape which changed slowly with target mass number (compare Refs. 3 and 4)--a fact which had been used to assign L = 0 or L = 2 transfer to unknown (p,t) and (p, ^{3}He) angular distributions; (b) this magnitude and shape deterioration, if not predicted by current two-nucleon transfer theory, could cause uncertainties in the spectroscopic information extracted from some (p,t) reaction data; and (c) any experiments directed toward establishing the location[2] or decay properties[1] of $T = |T_z| + 2$ states via (p,t) investigations would require knowledge of the conditions under which the cross section to these high isospin states was a maximum.

In order to obtain further data concerning this phenomenon, proton beams of various energies from the Berkeley 88-inch cyclotron were used to bombard targets of ^{26}Mg and ^{12}C. The resulting tritons were identified by means of a ΔE-E detector telescope and a power-law-type particle identifier.[5] Angular distributions of tritons leaving ^{24}Mg in its ground, 1.37-MeV (2+), and 15.43-MeV (0+, T = 2) states, as well as angular distributions from the $^{12}C(p,t)^{10}C$ ground and 3.35-MeV (2+) states, were investigated. The L = 0 (p,t) data are shown in Fig. B. 15-1 and the L = 2 data in Fig. B. 15-2. In both figures the solid curves represent two-nucleon transfer[6] distorted-wave Born approximation (DWBA) fits to the data, where each fit has been individually normalized. Real and imaginary well depths were allowed to vary smoothly with energy; the actual values of the parameters used followed quite closely the approximate expressions presented in Fig. B. 15-1. The two-nucleon transfer DWBA clearly reproduces the general features of the observed shape variation of these (p,t) angular distributions with incident proton energy.

The magnitude and shape deterioration of the angular distribution of the 15.43-MeV ^{24}Mg state at low energies is readily apparent in Fig. B. 15-1. The first maximum, beyond zero deg, of the characteristic L = 0 shape, clearly seen from 50.0 down to 38.7 MeV, has disappeared at $E_p = 32.5$ MeV—the cross section in that angular region having decreased by almost a factor of 8. The other two L = 0 distributions in Fig. B. 15-1 also show comparable magnitude and shape deterioration at the lower incident proton energies. Further, the L = 2 angular distributions shown in Fig. B. 15-2 also tend to deteriorate at lower proton energies.

Figure B. 15-3 presents a summary of these data and their DWBA fits. Noting this figure, one sees that the most striking property of the three L = 0 transitions is that they all seem to reach a maximum integrated and first maximum cross section at E_t (c.m.) $\approx 17 \pm 2$ MeV. The L = 2 transition to the ^{10}C (3.35 MeV) state also shows this behavior. In contrast, both the integrated and first maximum cross sections for the ^{24}Mg (1.37 MeV) state are still rising at E_t (c.m.) ≈ 8 MeV. An intercomparison of Figs. B. 15-1, B. 15-2, and B. 15-3 shows that the characteristic (p,t) L = 0 and 2 shapes begin to deteriorate below E_t (c.m.) ≈ 10 MeV. Hence assignment of L-transfer values to unknown (p,t) transitions by comparing their angular distribution shapes to known transitions could possibly be misleading if the incident energy is such that E_t (c.m.) ≤ 10 MeV. Since the DWBA appears to reproduce the observed energy dependence of these (p,t) cross sections quite well, spectroscopic information extracted from (p,t) reaction data using the DWBA should not be affected by this observed strong energy dependence.

Footnotes and References

†Condensed from Phys. Letters 25B, 324 (1967).

*Present address: Physics Department, University of Southwestern Louisiana, Lafayette, Louisiana, 70501.

1. R. L. McGrath, S. W. Cosper, and J. Cerny, Phys. Rev. Letters 18, 243 (1967).
2. G. T. Garvey, J. Cerny, and R. H. Pehl, Phys. Rev. Letters 12, 726 (1964).
3. J. Cerny, C. Détraz, and R. H. Pehl, Phys. Rev. 152, 950 (1966).

4. G. Bassani, N. M. Hintz, and C. D. Kavaloski, Phys. Rev. 136, B1006 (1964); and G. Bassani, N. M. Hintz, C. D. Kavaloski, J. R. Maxwell, and G. M. Reynolds, Phys. Rev. 139, B830 (1965).
5. F. S. Goulding, D. A. Landis, J. Cerny, and R. H. Pehl, Nucl. Instr. Methods 31, 1 (1964).
6. N. K. Glendenning, Phys. Rev. 137, B102 (1965).

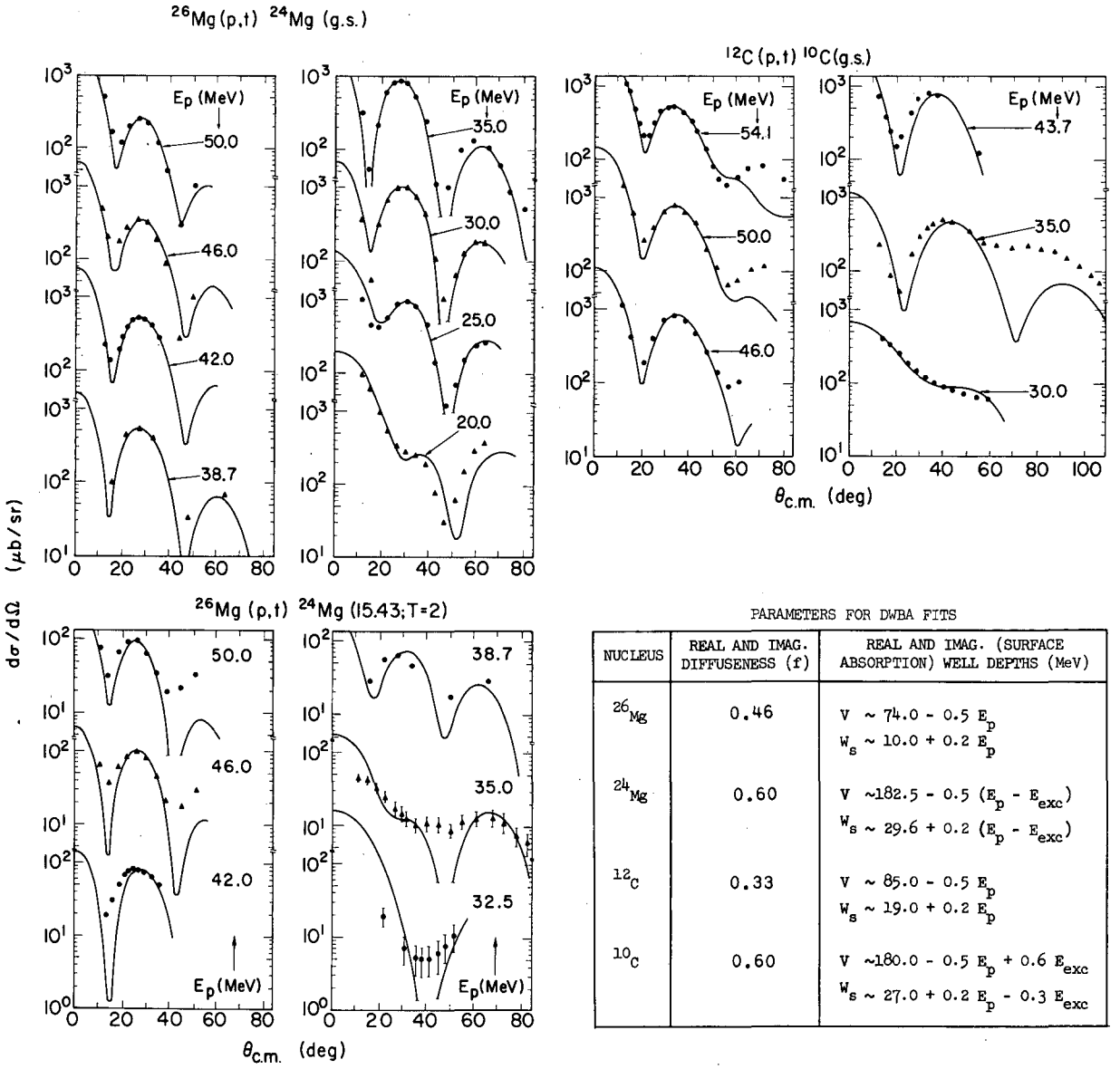

PARAMETERS FOR DWBA FITS

NUCLEUS	REAL AND IMAG. DIFFUSENESS (f)	REAL AND IMAG. (SURFACE ABSORPTION) WELL DEPTHS (MeV)
^{26}Mg	0.46	V ~ 74.0 - 0.5 E_p W_s ~ 10.0 + 0.2 E_p
^{24}Mg	0.60	V ~182.5 - 0.5 (E_p - E_{exc}) W_s ~ 29.6 + 0.2 (E_p - E_{exc})
^{12}C	0.33	V ~ 85.0 - 0.5 E_p W_s ~ 19.0 + 0.2 E_p
^{10}C	0.60	V ~180.0 - 0.5 E_p + 0.6 E_{exc} W_s ~ 27.0 + 0.2 E_p - 0.3 E_{exc}

XBL 677-3577

Fig. B.15-1. Some L = 0 triton angular distributions resulting from the proton bombardment of ^{26}Mg and ^{12}C at various incident energies. The solid curves are two-nucleon transfer DWBA fits which were generated by using the parameters shown in the figure plus proton radii of 1.15 F (for ^{26}Mg) and 1.04 F (for ^{12}C) and triton radii of 1.25 F in both cases. (E_p and E_{exc} are the incident proton energy and the excitation of the state being fitted in MeV, respectively.) Each fit has been independently normalized to the data.

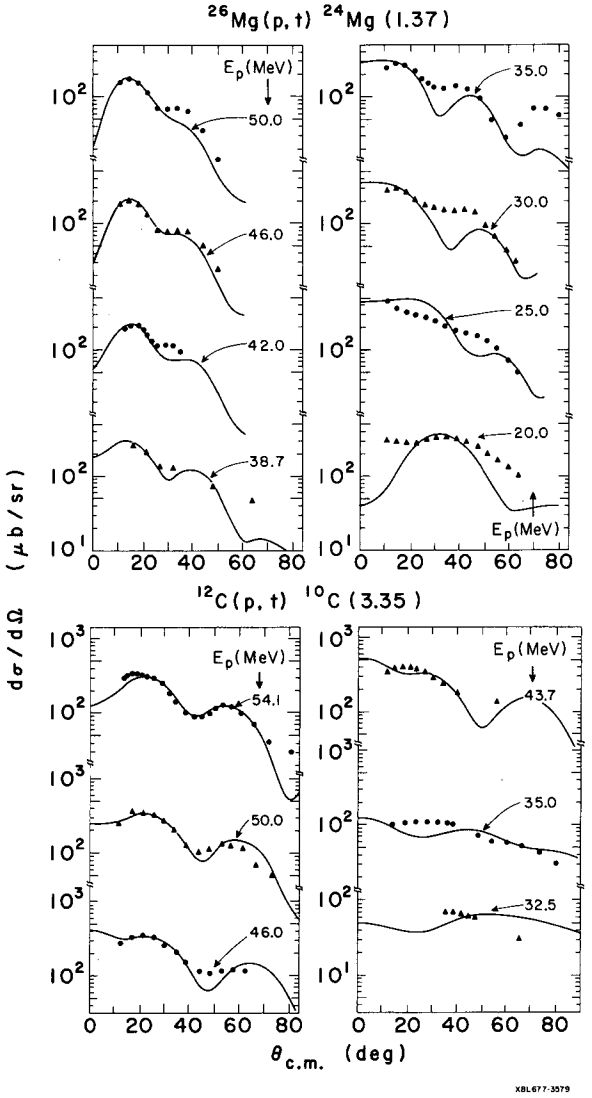

Fig. B. 15-2. Some L = 2 triton angular distributions from the ^{26}Mg(p, t) and ^{12}C(p, t) reactions at various incident proton energies. See legend of Fig. B. 15-1.

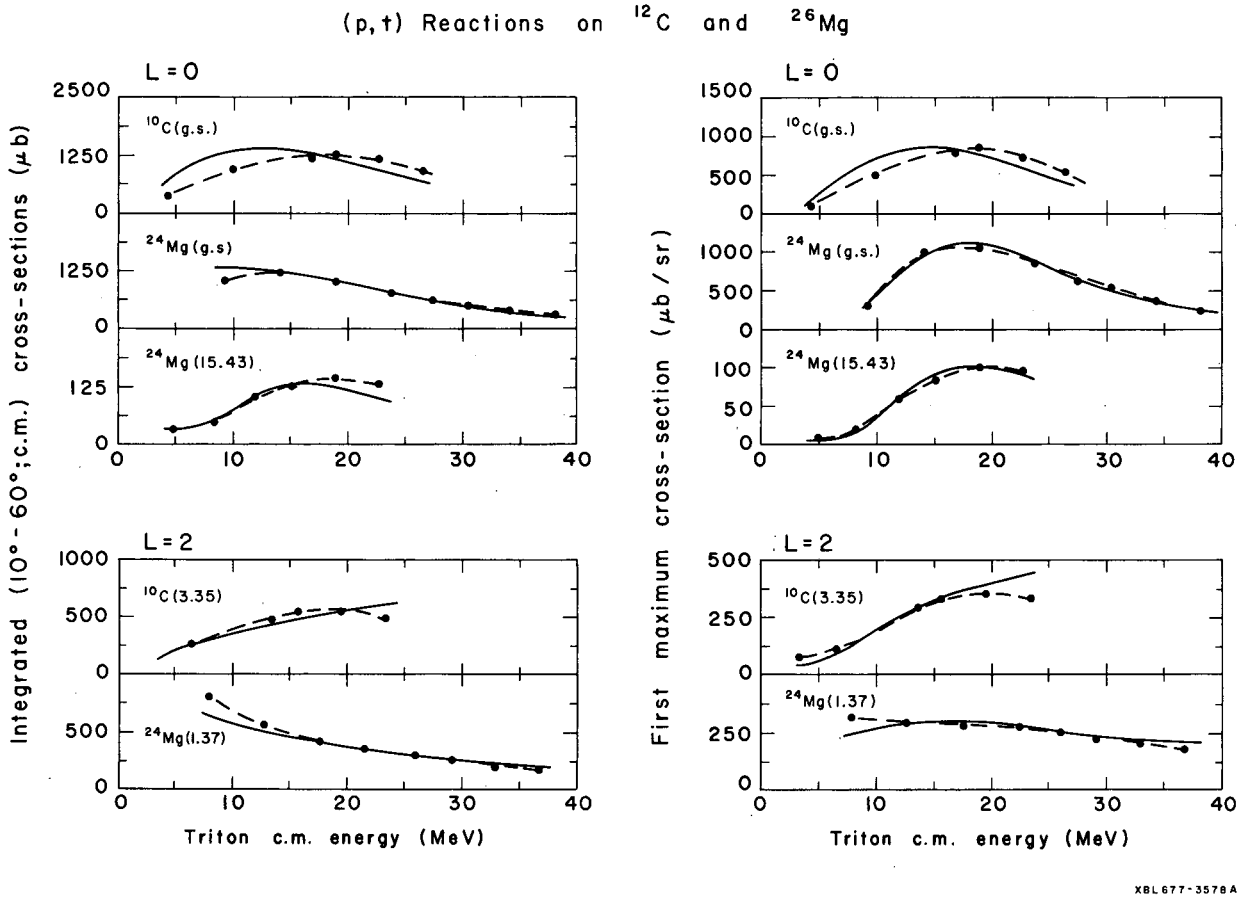

Fig. B.15-3. Integrated (10 to 60 deg c.m.) and first maximum (past 0 deg) peak cross sections plotted versus triton c.m. energy for some L = 0 and L = 2 (p,t) transitions to states in ^{24}Mg and ^{10}C. The data points are connected with dashed lines; the solid curves are DWBA predictions. All DWBA values for a given state have the same normalization.

16. HIGH-RESOLUTION FAST-NEUTRON SPECTROSCOPY OF THE REACTION $^{9}Be(p,n)^{9}B$ AT 20 MeV†

R. J. Slobodrian, H. Bichsel,* J. S. C. McKee,‡ and W. F. Tivol

The reaction $^{9}Be(p,n)^{9}B$ was studied at 14.1 MeV laboratory energy by Saji[1] with a proton recoil neutron spectrometer operating typically at 5% resolution. We have measured neutron spectra produced in this reaction by 20-MeV protons. Figure B.16-1 shows a drawing of our detector assembly. It consists of a suitable collimation system, a radiator of protons (recoils from a thin film of polyethylene), and a solid-state detector telescope consisting of two detectors ($\Delta E, E$). The electronics includes low-noise preamplifiers, amplifiers, particle identifier circuits,[2] and multichannel analyzers.

The direct application of solid-state detectors to neutron spectroscopy has been recently studied and discussed.[3,4] The (n,α) reactions in silicon are so numerous that such use is at present impractical for spectroscopic purposes.[4] Birk et al.[3] considered the spectroscopy of 6-MeV neutrons detecting proton recoils from a proton radiator using a single silicon detector. Such a method becomes impractical at higher neutron energies due to the (n,α) reactions in silicon. At higher energies the proton recoil detection with silicon detectors depends vitally on the coincidence requirement between the ΔE and E detectors.[1,5] A refinement is achieved by means of a

particle identification system.[2] A detailed description of our spectrometer and possible improvements will be published elsewhere.[6]

Considerable effort has been vested in the search for a state in ^{9}B analog to the 1.7-MeV state in ^{9}Be. A state at about 1.4 MeV in ^{9}B was first reported by Marion et al.[7] and was also weakly seen at some angles by Saji[1] in his $^{9}Be(p, n)^{9}B$ experiment. More recent work on ^{9}B was carried out through reactions in which a charged particle was detected, like $^{12}C(p, \alpha)^{9}B$,[8,9] $^{10}B(^{3}He, \alpha)^{9}B$,[10] and $^{10}B(d, t)^{9}B$.[11,12] Symons and Treacy[8] observed a broad peak in the spectrum of the reaction $^{12}C(p, \alpha)^{9}B$ at a channel energy of approximately 1.4 MeV. They calculated a fit to the observed peak, using the notation and procedure of Barker and Treacy[13] with a channel radius of 4.35 F and an energy of 1.7 MeV. Bauer et al.[9] reached states of ^{9}B through the reactions $^{12}C(p, \alpha)$, $^{9}Be(p, n)$, and $^{6}Li(\alpha, n)$, using α particles between 12.7 and 18.3 MeV and protons at 6.3 and 7.4 MeV. They concluded that there was no state of ^{9}B at 1.7 MeV. However, it should be noted that a broad peak with barycenter at about 1.4 MeV is visible in the spectra of Bauer et al.[9] from $^{12}C(p, \alpha)^{9}B$ at 12.7 MeV, as well as in the other reactions they studied, in agreement with the results of Symons and Treacy.[8]

Our experiment was performed at 20 MeV lab energy, with protons from the Berkeley 88-inch variable-energy cyclotron. To reduce background the beam was accelerated as 40-MeV H_2^+. Figure B. 16-2 contains some sample spectra, showing evidence for a peak at about 1.4 MeV in the neutron spectra. In addition the state assigned an energy of 3.07 MeV by Saji[1] is seen completely resolved in our spectra, and we assign to it an energy of 3.16 ± 0.07 MeV. The $^{9}Be(p, n)^{9}B$ time-of-flight spectra of Bauer et al.[9] at 7.4 MeV and 15 deg lab angle show a peak at about 3.1 MeV, and the same is true for the $^{6}Li(\alpha, n)$ spectra at 14.4 MeV at several angles. Figures B. 16-2b and B. 16-2c show also indications of peaks at 2.8 and 1.7 MeV, but further experimental work is needed in this regard.

Some comments are in order concerning the 1.4-MeV peak in the spectra of the ^{9}B nucleus. It seems reasonable to relate it to the threshold of the channel $^{5}Li + \alpha$, located at 1.685 MeV (Ref. 14) in the ^{9}B system. The relation between thresholds and states has been discussed by Baz,[15] Inglis,[16] and others. The conclusions indicate that it is more probable to observe states near thresholds than elsewhere.

The 3.16-MeV peak appears consistently in the neutron spectra reaching ^{9}B through reactions $X(x, n)^{9}B$, but it is absent in charged particle spectra.

We gratefully acknowledge the help of T. M. Chan with the design of the neutron spectrometer assembly; J. Meneghetti, who supervised its construction; and R. Lothrop, who made the Si detectors. The cooperation of the 88-inch cyclotron crew and supporting personnel is highly appreciated.

Footnotes and References

†Phys. Rev. Letters 19, 595 (1967).

*On leave from the University of Southern California, Los Angeles, California.

‡On leave from University of Birmingham, England.

1. Y. Saji, J. Phys. Soc. Japan 15, 367 (1960).

2. F. S. Goulding, D. A. Landis, J. Cerny, and R. H. Pehl, Nucl. Instr. Methods 31, 1 (1964).

3. M. Birk, G. Goldring, and P. Hillman, Nucl. Instr. Methods 21, 197 (1963), and references therein.

4. J. A. Shannon and J. B. Trice, Nucl. Instr. Methods 41, 255 (1966), and references therein.

5. A Si detector telescope with three detectors and a triple coincidence requirement may further improve the performance, particularly at higher energies.

6. R. J. Slobodrian, J. S. C. McKee, and H. Bichsel, High-Resolution Fast Neutron Recoil Spectrometer (in preparation).

7. J. B. Marion, C. F. Cook, and T. W. Bonner, Phys. Rev. 94, 807 (1954); J. B. Marion and J. S. Levin, Phys. Rev. 115, 144 (1959).

8. G. D. Symons and P. B. Treacy, Phys. Letters 2, 175 (1962).

9. R. W. Bauer, J. D. Anderson, and C. Wong, Nucl. Phys. 56, 117 (1964).

10. L. G. Earwaker, J. G. Jenkins, and E. W. Titterton, Nucl. Phys. 46, 540 (1963); J. G. Patterson, J. M. Poate, and E. W. Titterton, Proc. Phys. Soc. 85, 1085 (1965).

11. G. D. Symons, Phys. Letters 18, 142 (1965).

12. K. Bähr, W. Fitz, R. Jahr, and R. Santo, Phys. Letters 21, 686 (1966).
13. F. C. Barker and P. B. Treacy, Nucl. Phys. 38, 33 (1962).
14. T. Lauritsen and F. Ajzenberg-Selove, Nucl. Phys. 78, 1 (1966), and references therein.
15. A. J. Baz, Zh. Eksptl. i Teor. Fiz. 33, 923 (1958) [Engl. Transl. Soviet Phys. --JETP 6, 709 (1958).]
16. D. R. Inglis, Nucl. Phys. 30, 1 (1962).

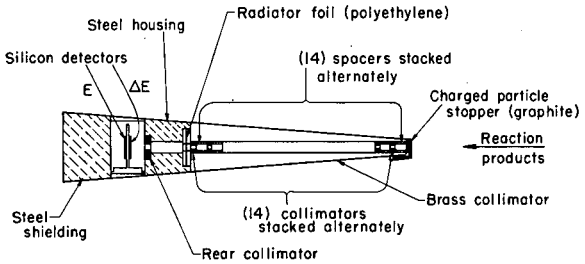

Fig. B.16-1. Schematic of the collimator, radiator and detector telescope assembly of the neutron spectrometer.

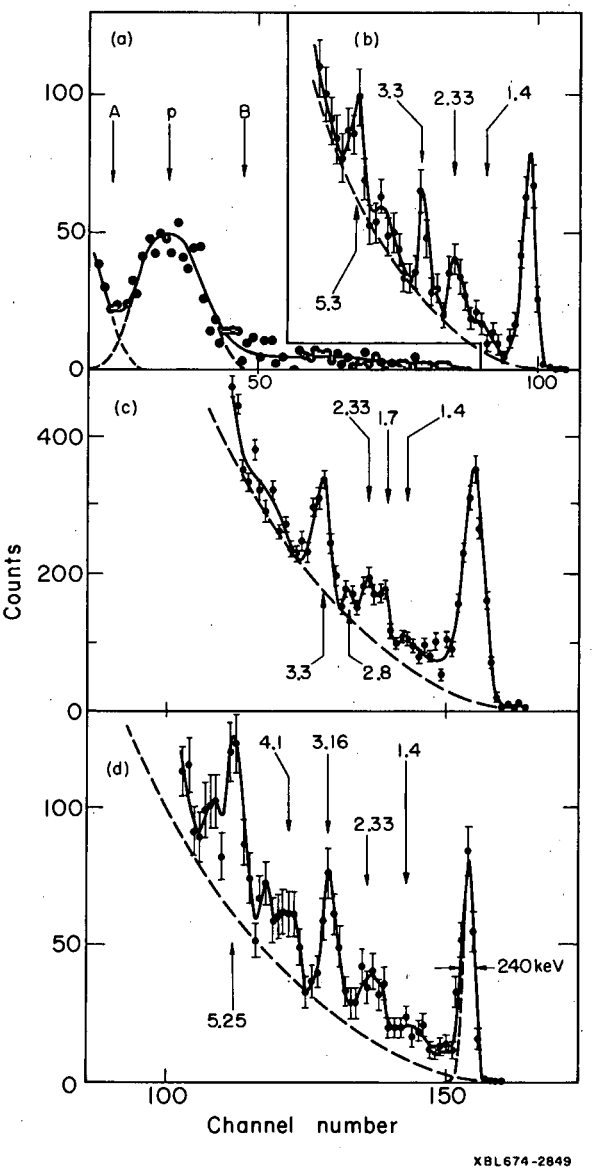

Fig. B.16-2. Sample spectra obtained in this experiment. The n-p cross section has not been unfolded, as it does not alter the spectroscopic content appreciably. Solid lines have been drawn to help the eye. The energy labels on the peaks result from conversions of pulse height to energy.
(a) Particle identifier spectrum. Discriminators were normally located at A and B to select the proton recoils. However, a display of the energy spectrum of pulses above B did not show any structure.
(b) Spectrum at 9 deg lab, using a ^{9}Be target of 18.8 mg cm^{-2} with ΔE-E coincidence requirement and no particle identification. The radiator thickness was approximately 0.08 mm.
(c) Spectrum at 12 deg lab, same target as (b) with coincidence requirement and particle identification. At this angle we find evidence for the 2.8-MeV state and indications of a peak at 1.7 MeV.
(d) Spectrum at 17 deg lab, obtained with a 4.70-mg cm^{-2} ^{9}Be target and detection conditions as in (c). The structure of the spectrum near 2.33 MeV is consistent with the 12-deg spectrum of (c), although the statistics is poorer. The resolution of our neutron spectrometer, unfolding the target thickness effect, was 200 keV near 18 MeV, i.e., 1.1%.

17. A SEARCH FOR EXCITED STATES OF ^{3}He†

R. J. Slobodrian, J. S. C. McKee,* D. J. Clark,
W. F. Tivol, and T. A. Tombrello‡

The possible existence of a bound trineutron[1] has stimulated the search for states of the three-nucleon systems, although conflicting evidence has been reported recently with respect to the original experiment.[2] Kim et al.[3] have investigated the reaction p + ^{3}He at 30.2 MeV lab energy, and have observed peaks in the proton spectra at 8.2, 10.2, and 12.6 MeV excitation. Such peaks were observed at two laboratory-system angles and were interpreted as a possible indication of states of the ^{3}He nucleus. The cross section for excitation of the 10.2-MeV state was estimated to be about 2×10^3 μb/sr at θ_{lab} = 15 deg, and somewhat lower values were obtained for the other two states. In contrast, at 25 MeV lab energy Austin et al. observed no peaks in the p + ^{3}He interaction[4] and established a limit of 250 μb/sr for the cross section for such states of ^{3}He, from this reaction.

On the other hand Baldin[5] has predicted the existence of a state within the energy region investigated.

Warner et al.[6] have investigated the ^{4}He + ^{3}He reaction, and their conclusion was that no peaks (attributable to unbound T = 1/2 levels of ^{3}He) were observed down to a cross section of about 300 μb/sr.

We have investigated the ^{3}He + ^{3}He interaction at 44 and 53 MeV lab, using the ^{3}He beam of the Berkeley 88-inch isochronous cyclotron. The ^{3}He spectra were detected by using Si detector telescopes together with an electronic particle identifier circuit,[7] over a wide angular range from 5 to 42 deg lab angles. Calibration spectra were obtained from the reaction ^{14}N(^{3}He, ^{3}He')^{14}N*. The identified ^{3}He energy spectra were recorded by use of a 4096-channel analyzer. Figure B. 17-1 exhibits the general features of the measured spectra, and Fig. B. 17-2 shows for comparison a spectrum obtained under identical experimental conditions from ^{14}N + ^{3}He. The analysis of our spectra is consistent with the absence of sharp peaks to a limit of about 120 μb/sr, and up to about 30 MeV excitation for the smallest angle measured.

In conclusion, the ^{3}He + ^{3}He interaction can reach both T = 1/2 and T = 3/2 states, and our results indicate that no such states are excited down to cross section values much lower than those mentioned by Kim et al.[3] for the p + ^{3}He interaction.

We acknowledge the assistance of D. Landis with the electronic equipment, J. Meneghetti with the mechanical part of the experiment, and R. Lothrop, who made the Si detectors.

Footnotes and References

†Condensed from Nucl. Phys. A101, 109 (1967).
*On leave from University of Birmingham, England.
‡Summer visitor from California Institute of Technology.

1. V. Ajdačić, M. Cerineo, B. Lalović, G. Paić, I. Slăus, and P. Tomaš, Phys. Rev. Letters 14, 444 (1965).
2. S. T. Thornton, J. K. Bair, C. M. Jones, and H. B. Willard, Phys. Rev. Letters 17, 701 (1966).
3. C. C. Kim, S. M. Bunch, D. W. Devins, and H. H. Forster, Phys. Letters 22, 314 (1966).
4. S. M. Austin, W. Benenson, and R. A. Paddock, Bull. Am. Phys. Soc., Ser. II 12, 16 (1967).
5. A. M. Baldin, Phys. Letters 17, 47 (1965).
6. R. E. Warner, J. S. Vincent, and E. T. Boschitz, Phys. Letters 24B, 91 (1967).
7. F. S. Goulding, D. A. Landis, J. Cerny III, and R. H. Pehl, IEEE Trans. Nucl. Sci. NS-11, 388 (1964).

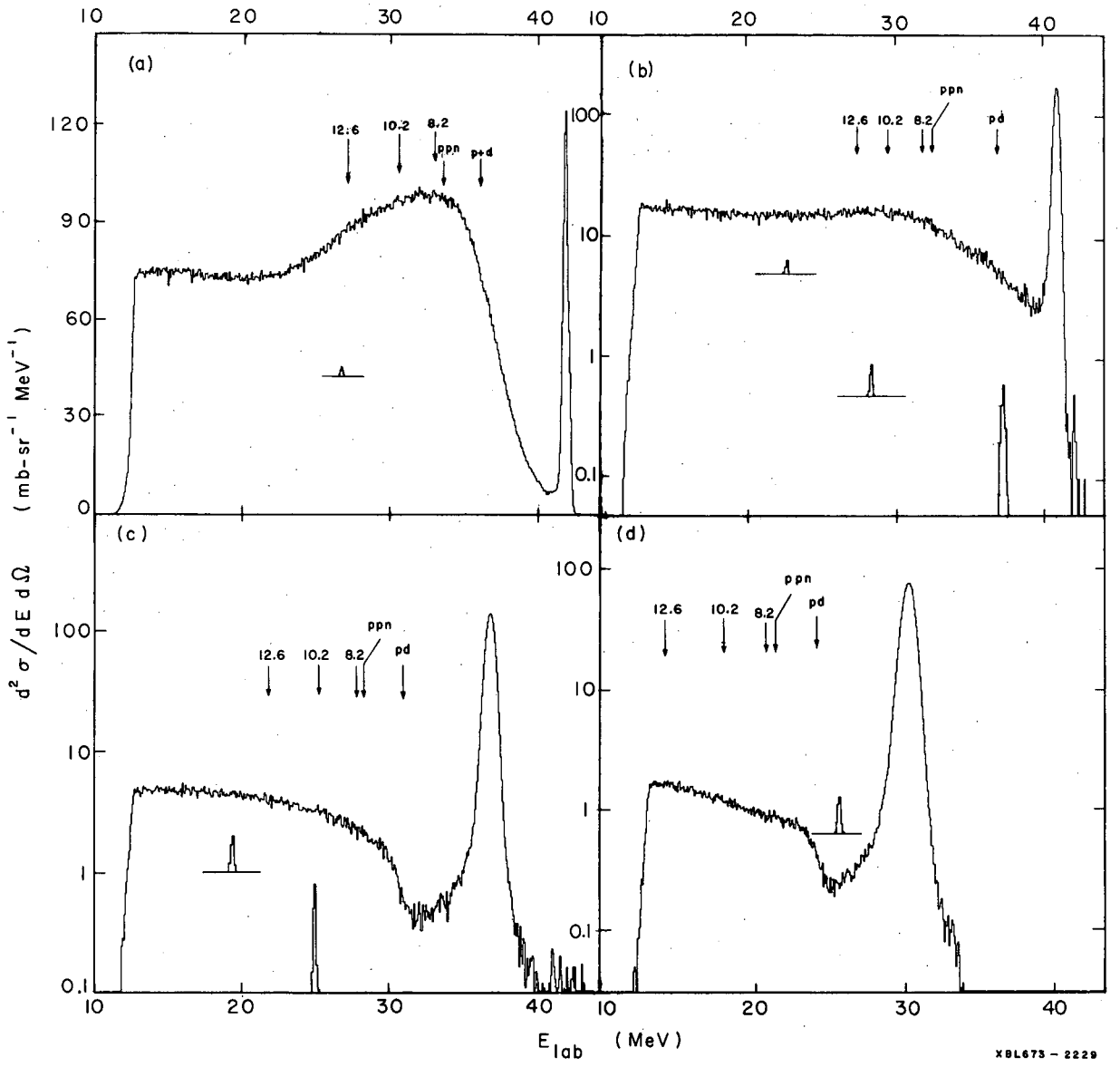

Fig. B.17-1. Sample spectra at 44 MeV. Peaks corresponding to a cross section of 120 μb-sr^{-1} are drawn for comparison. The low-energy cutoff is due to the ΔE detector thickness of the telescope. Thresholds and "states" are indicated by arrows. (a) 5 deg lab, (b) 10 deg lab, (c) 20 deg lab, (d) 31 deg lab. Spectra (a) and (b) show an electronically attenuated elastic group.

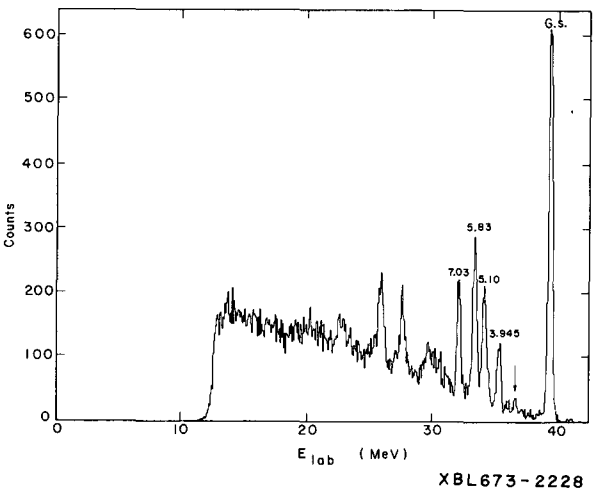

Fig. B. 17-2. Comparison spectrum from $^{14}N(^3He, ^3He)^{14}N^*$ at θ_{lab} = 15 deg, taken under identical experimental conditions. The arrow points to a peak of cross section 90 μb/sr.

18. THE 2p FINAL-STATE INTERACTION IN THE $^3He(^3He, \alpha)2p$ REACTION†

R. J. Slobodrian, J. S. C. McKee,* W. F. Tivol, D. J. Clark, and T. A. Tombrello‡

Recent letters[1, 2] have reported on the $^3He(^3He, \alpha)2p$ reaction at 26 MeV[1] and at 11.96 MeV lab energy,[2] bearing evidence for the p-p interaction. The spectra at 26 MeV have not been analyzed theoretically. A fit using the Watson-Migdal formalism[3] was produced for the 11.96-MeV spectra,[2] but the agreement is partially obscured by the pα interaction (^5Li), prominent at the angles investigated.

There is interest in reactions leading to the $^1S_0$ state of two nucleons with regard to the determination of the scattering parameters of the n-n interaction.[4] The usefulness of the deuteron breakup reaction nd → nnp for such purpose has been questioned, and the Watson theory seems to be misleading in this interaction.[5] The existing data on the mirror reaction pd → ppn indicate that the pn interaction obscures the effects of the pp interaction.[6, 7] On the other hand the peaks observed in angular correlation measurements are sharper than predicted by the Watson-Migdal formalism.[8] This would explain the discrepancy between the value for the nn scattering length a_n from the $d(\pi^-, \gamma)2n$ (Ref. 9) or the $^3H(d, ^3He)2n$ reactions,[4] and the values obtained from the nd experiments.[10, 11] It should be noted that the scattering lengths required to fit the spectra from the $p(^3He, d)2p$, $^2H(^3He, t)2p$ (Ref. 12), and $^3H(n, d)2n$ (Ref. 13) reactions seem larger than the currently accepted values of these quantities. The reaction $^2H(t, ^3He)2n$ may also require a large value of a_n, but no data are presently available. The physical fact is that such reactions lead asymptotically to three particles in the final state, and this is true for Breit-Wigner resonances between pairs of particles, as well as for virtual or antibound "states." Thus, neither the Breit-Wigner resonances nor the virtual states are true quantum mechanical states. The Eisenbud interpretation[14] of a rapidly increasing phase shift as a time delay leads to the definition of a physical lifetime for resonant and virtual states, and both manifest themselves by peaks in the energy spectra of the third particle. They can be interpreted in terms of poles in the scattering amplitude of two particles, and the question is how well can one extract the pole parameters from the spectrum shape (or "line" shape) of the third particle. Hence reactions leading to the 2p system and a third particle are useful to test a given theoretical formalism, if there is dominance of the pp pole.

We have studied the $^3He(^3He, \alpha)2p$ reaction at 43.7 and 54.0 MeV lab energy (at target center), using the ^3He beam of the Berkeley 88-inch variable-energy cyclotron. The experimental techniques were basically the same as described elsewhere.[4] The large positive Q is quite helpful for the detection of the ^4He spectra over a sizable angular range, between 5 and 42 deg lab (10 to 90 deg c.m.). A prominent peak near the high-energy end of the α-particle spectra was observed (Fig. B. 18-1a and c). Its angular distribution follows a pronounced diffraction pattern with minima (Fig. B. 18-1b) deeper than usual even for particle transfers leading to particle-

bound states or long-lived resonances. The angular distributions at both energies are shown in Fig. B. 18-2a and b together with fits based on a diffraction picture of the reaction mechanism.[15] The PWBA is inadequate in fitting the relative values of successive maxima or the positions of the minima. The "interaction radii" r_i in excess of 4 F lend support to a peripheral picture of the reaction mechanism, consisting of an $\ell = 0$ nucleon tranfer. More complicated processes, like charge exchange, are excluded. The energy spectra are compared with the Watson-Migdal formalism predictions, using the formulae contained in Ref. 4 and the known pp scattering length, excluding the vacuum-polarization correction, $a_p = -7.7$ F.[16] Figure B. 18-3 contains sample spectra showing a good agreement between the theory and the experimental results, over a considerable angular range. Hence the study of the reaction $^3H(t, \alpha)2n$ should prove relevant in obtaining additional information on the nn interaction. It should be interesting to ascertain whether the $^3H(t, \alpha)2n$ reaction yields a scattering length in agreement with the $^3H(d, ^3He)2n$ reaction,[4] and thus also with the π^-d experiment.[9] If there is agreement, then properly chosen reactions, with an outgoing third particle having a sharply defined boundary, may allow a more precise and complete determination of the $^1S_0$ nn scattering parameters.

We gratefully acknowledge the support of D. Landis with the electronic equipment, of R. Lothrop, who made the solid-state detectors, and of J. Meneghetti for his part with the mechanical setup of the experiment.

Footnotes and References

†Phys. Letters 25B[1], 19 (1967).
*On leave from the University of Birmingham, England.
‡Summer visitor from California Institute of Technology

1. K. P. Artjomov, V. I. Chuev, V. Z. Goldberg, A. A. Ogloblin, V. P. Rudakov, and J. N. Serikov, Phys. Letters 12, 53 (1964).
2. T. A. Tombrello and A. D. Bacher, Phys. Letters 17, 37 (1965).
3. K. M. Watson, Phys. Rev. 88, 1163 (1952); A. B. Migdal, Zh. Eksp. i Teor. Fiz. 28, 3 (1955), Soviet Phys. JETP 1, 2 (1955).
4. E. Baumgartner, H. E. Conzett, E. Shield, and R. J. Slobodrian, Phys. Rev. Letters 16, 105 (1966), and references therein.
5. R. Aaron and R. D. Amado, Phys. Rev. 150, 857 (1966), and references therein.
6. B. V. Rybakov, V. A. Sidorov, and V. A. Vlasov, Nucl. Phys. 23, 491 (1961).
7. J. L. Friedes and M. K. Brussel, Phys. Rev. 131, 1194 (1963).
8. W. D. Simpson, J. D. Bronson, W. J. Jackson, and G. C. Phillips, Rev. Mod. Phys. 37, 523 (1965); G. C. Phillips, in International Conference on Nuclear Physics, Gatlinburg, Tennessee, September 1966, paper 9-A.
9. R. P. Haddock, R. M. Salter, Jr., M. Zeller, J. B. Czirr, and D. R. Nygren, Phys. Rev. Letters 14, 318 (1965).
10. M. Cerineo, K. Ilakovac, J. Slaus, P. Tomas, and V. Valković, Phys. Rev. 133, B948 (1964).
11. V. K. Voitovetskii, I. L. Korsunskii, and V. F. Pazhin, Phys. Letters 10, 109 (1964) and Nucl. Phys. 64, 513 (1965).
12. B. J. Morton, M. P. Fricke, R. O. Ginaven, E. E. Gross, J. J. Malanify, and A. Zucker, Bull. Am. Phys. Soc. Ser. II 12, 16 (1967).
13. V. Ajdacić, M. Cerineo, B. Lalović, G. Paić, I. Slaus, and P. Thomaś, Phys. Rev. Letters 14, 442 (1965).
14. L. Eisenbud, Thesis, 1948, Princeton University; M. L. Goldberger and K. M. Watson, Collision Theory (John Wiley and Sons, Inc., New York, 1964).
15. A. Dar, Nucl. Phys. 55, 305 (1964), and references therein.
16. R. J. Slobodrian, Nuovo Cimento 40, 443 (1965).

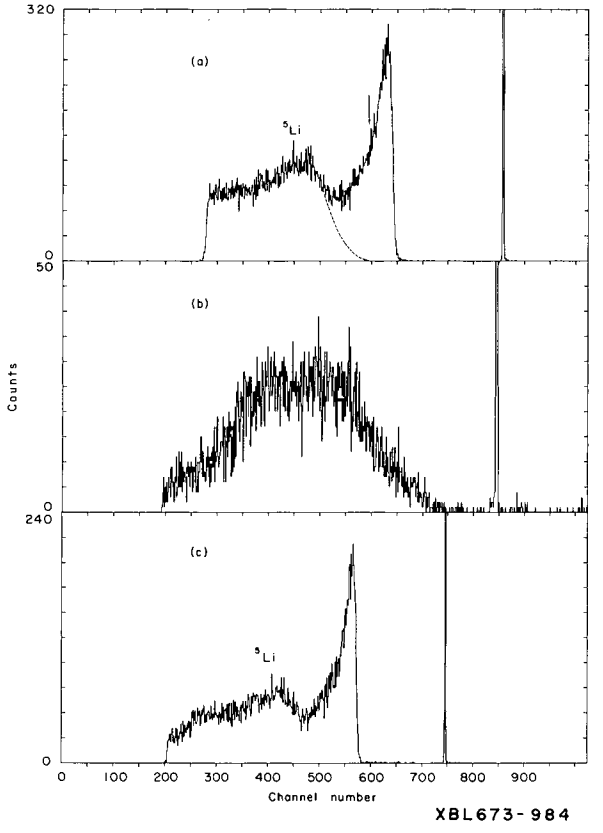

Fig. B. 18-1. ^{4}He spectra from the reaction ^{3}He + ^{3}He → ^{4}He + 2p. A pulser group is seen at the far right. (a) At 17 deg lab with 43.7 MeV bombarding energy. The arrow indicates the interval expanded in Fig. B. 18-3b. (b) At 10 deg lab (near the first minimum of the 2p enhancement), with 43.7 MeV bombarding energy. (c) At 16 deg lab with 53.0 MeV bombarding energy.

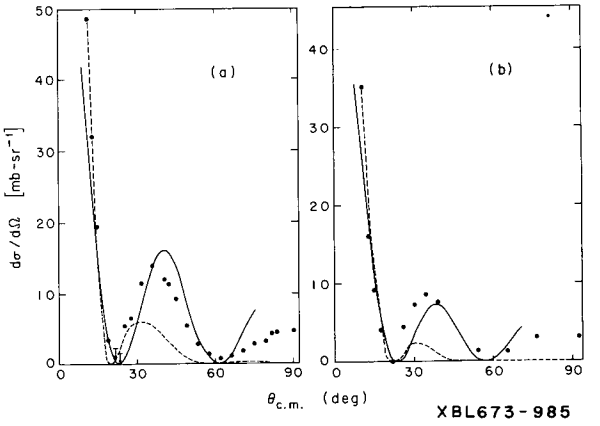

Fig. B. 18-2. Angular distribution of the ^{3}He + ^{3}He → ^{4}He + 2p peaks integrated to a value at which they drop to 1/e of the value at the maximum. The solid line corresponds to a fit with $J_0^2(q, r_i)$, the dashed line is the PWBA fit. (a) Data at 43.7 MeV. The $J_0^2(q, r_i)$ fit was calculated with r_i = 4.6 F. The PWBA fit was obtained with r_i = 5.5 F. (b) Data at 53.0 MeV. The interaction radii are respectively r_i = 4.2 F and r_i = 5.0 F for the $J_0^2(q, r_i)$ and PWBA fits.

Fig. B. 18-3. The solid lines are fits to the ^{4}He energy spectra obtained with the Watson-Migdal formalism using a_p = -7.7 F, after folding in the energy resolution and the effect of the finite angular resolution of the detector (approximately ± 0.3 deg. The solid dots are the experimental points. (a) Spectrum at θ_{lab} = 5 deg and 43.7 MeV bombarding energy. (b) Spectrum at θ_{lab} = 17 deg and 43.7 MeV bombarding energy. (c) Spectrum at θ_{lab} = 5 deg and 53.0 MeV bombarding energy.

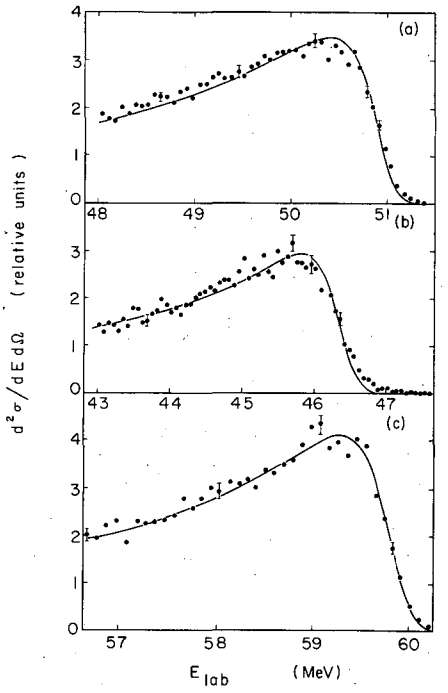

XBL673-996

19. HIGH-PRECISION MEASUREMENT OF PROTON-PROTON POLARIZATION BETWEEN 10 AND 20 MeV†

R. J. Slobodrian, J. S. C. McKee,* H. Bichsel,‡ and W. F. Tivol

There are few measurements of polarization in pp scattering below 30 MeV. The measurement by Alexeff and Haeberli[1] at 3.3 MeV resulted in small positive values. However, Knecht et al.[2] have concluded that there is no way to reproduce such values with any combination of S-, P-, and D-phase shifts, and hence that they must be in error. There is also a measurement at 16.2 MeV (Ref. 3) at 50.2 deg c.m. that produced a value 0.006 ± 0.007, and another at 17.5 MeV (Ref. 4) at 45 deg c.m. with a value 0.0125 ± 0.02. Clearly both experiments were not inconsistent with a very small polarization (positive or negative).

High-precision measurements at about 45 deg c.m. have been performed recently in the region at and above 30 MeV.[5] The polarization is consistently positive, and becomes zero at about 30 MeV. At low energies the polarization is an effect of higher order with respect to the spin correlation parameters.[6] Most recent efforts have dealt with measurements of the latter.[7] However, at 11.4 MeV the scattering is overwhelmingly singlet, and thus the spin correlation measurement ceases to yield useful information.

A high-precision measurement of the polarization in the range between 10 and 20 MeV may be helpful to the numerous groups that have carried out analyses of nucleon-nucleon scattering below 30 MeV (Refs. 5, 7-11). We have measured the polarization asymmetry in proton-proton scattering at 9.6, 15.6, and 19.7 MeV, using the variable-energy polarized beam facility of the Berkeley 88-inch cyclotron.

The proton beam is produced with nearly 100% polarization by scattering of α particles from a liquid-nitrogen-cooled high pressure hydrogen target. The energy of the beam was determined by measuring its range in aluminum. The beam was aligned by first mapping it with a slit mounted on a remotely controlled ionization chamber, and subsequently orienting the scattering table on

the beam line, using a telescope. Thereby an alignment to ±0.05 deg is accomplished. A similar accuracy is obtained in the alignment of the detector collimators. A spin precession solenoid was used to reverse the spin of the proton beam. To restore the beam barycenter a magnet was used in conjunction with a split ionization chamber that was permanently monitoring the beam direction. In order to minimize and compensate possible effects due to the spin precession solenoid it was operated half the time precessing the spin clockwise, and half the time counterclockwise. Careful tests indicate that no asymmetry is produced by the spin precession solenoid.

The hydrogen target was a cell with a continuous aluminum window 0.0019 in. thick, operated at about 3 atmospheres at room temperature. The gas was 99.99% pure. The detection was effected with two pairs of CsI(Tl) scintillator detector telescopes and associated electronics, as shown in Fig. B.19-1(a). At 20 MeV the ΔE crystals were 0.010 in. thick at forward angles and 0.005 in. near 45 deg lab. At lower energies the spectra were very clean, without the coincidence requirement of the telescopes, and therefore the ΔE detectors were not used. The spectra were measured by setting the detectors at symmetrical angles with respect to the beam. Short runs were taken, monitoring the total beam with a second ionization chamber coupled to an electrometer integrating circuit and recycling unit. Our procedure has proven in empirical tests to provide asymmetries free of systematic errors down to about ±0.1%. Figure B. 19-1(b) shows the geometrical layout of the experiment.

The 20-MeV data seem to be consistent with the trend as a function of energy established by the recent measurements at 30 and 50 MeV (Ref. 5) and the Harvard results.[12] The implications of our polarization results can be explored in terms of S, P, and D waves. The reader is referred to Ref. 9, where the effect of including F waves is shown to be small at 23.6 MeV. Figure B. 19-2 summarizes our results (tabular values are available upon request).

In the light of our analysis we can state that the OPE assumption seems to be inadequate to account for the observed values of the polarization, and that a sizable amount of spin-orbit interaction is necessary to account for the observed node in the polarization. However, the data at 9.6 and 15.6 MeV cannot exclude the usual OPE assumption, and further experimental work carried out in the small-angle region, below 15 deg lab, done with high precision, may provide a final answer to the questions posed in the work reported here.

Footnotes and References

†Phys. Rev. Letters 19, 704 (1967).
*On leave from University of Birmingham, England.
‡On leave from University of Southern California, Los Angeles, California.
1. I. Alexeff and W. Haeberli, Nucl. Phys. 15, 609 (1960).
2. D. J. Knecht, P. F. Dahl, and S. Messelt, Phys. Rev. 148, 1031 (1966).
3. W. A. Blanpied, Phys. Rev. 116, 738 (1959).
4. K. W. Brockman, Phys. Rev. 110, 168 (1958).
5. C. J. Batty, R. S. Gilmore, and G. H. Stafford, Nucl. Phys. 45, 481 (1963), and references therein.
6. J. Raynal, Nucl. Phys. 28, 220 (1961).
7. H. P. Noyes, P. Signell, N. R. Yoder, and R. M. Wright (SLAC-PUB-269, February 1967 , Phys. Rev. to be published), and references therein.
8. G. Breit and R. D. Haracz, in High Energy Physics, edited by E. H. Burhop (Academic Press, New York, 1967), and references therein.
9. S. I. Bile'kaya, Yu. M. Kazarinov, F. Lehar, and Z. Janout, Yadern. Fiz. 4, 892 (1966); English translation: Soviet J. Nucl. Phys. 4, 635 (1967).
10. R. A. Bryan and R. A. Arndt, Phys. Rev. 150, 1299 (1966).
11. R. A. Arndt and M. H. MacGregor, Phys. Rev. 154, 1549 (1967).
12. J. N. Palmieri, A. M. Cormack, N. F. Ramsey, and R. Wilson, Ann. Phys. 5, 299 (1958).

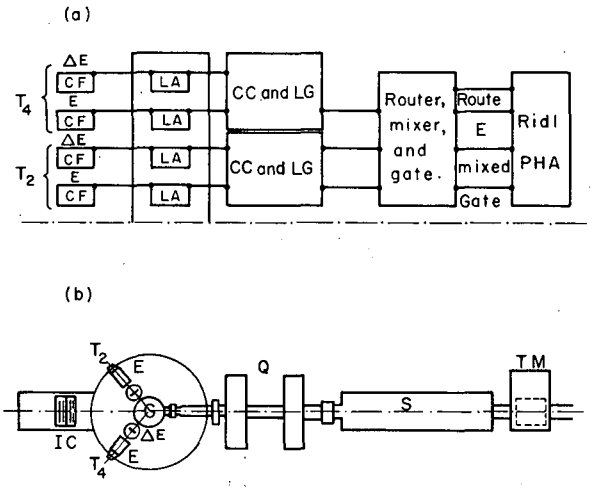

XBL677-3511

Fig. B. 19-1. Schematic drawing of the electronics and geometrical layout of the experiment.
(a) Block diagram of the electronics. CF: cathode follower; LA: linear amplifier, CC: double coincidence, LG: linear gate; T_i: detector telescope.
(b) Schematic drawing of the experimental apparatus. IC: ionization chamber; T_i: detector telescopes; Q: quadrupole lens; S: spin precession solenoid; TM: tickling magnet (for the restoration of the beam barycenter).

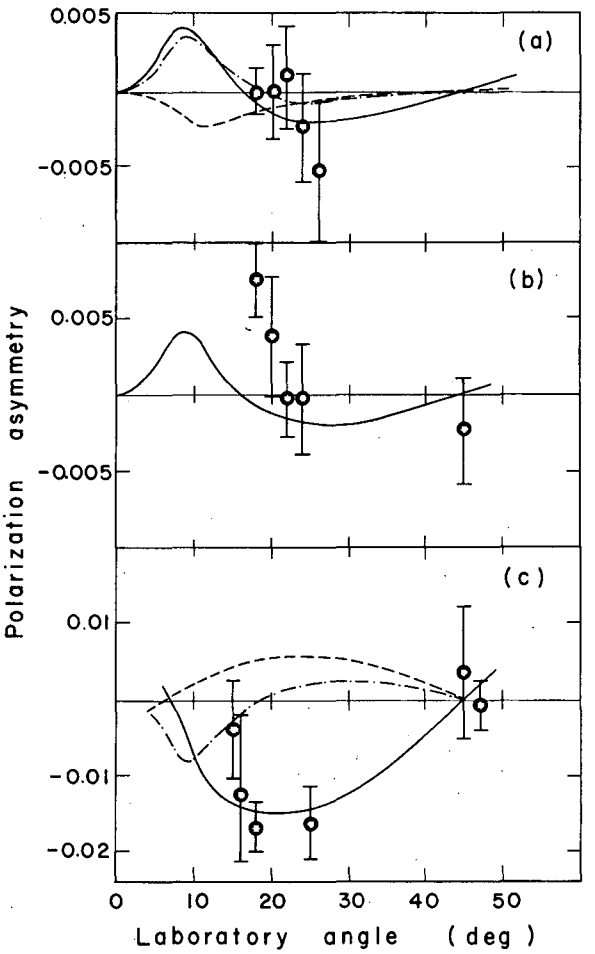

XBL677-3510

Fig. B. 19-2. Summary of experimental polarization asymmetry. The "theoretical" curves were calculated with programs adapted for the CDC 6600 computer, with slight changes from the originals of D. J. Knecht (Ref. 2).
(a) Data at 9.6 MeV. The solid line corresponds to $^3P_0$ = 3.71 deg, $^3P_1$ = 1.71 deg, $^3P_2$ = -2.29 deg, $^1D_2$ = 0.20 deg. The dash-dot line corresponds to 2.75, 1.25, -1.75, and 0.13 deg, in the same order. The dashed line corresponds to 4.23, -2.07, 0.45, and 0.14 deg; it gives the pattern typical of OPE.
(b) Data at 15.6 MeV. The solid line corresponds to $^3P_0$ = 4.2 deg, $^3P_1$ = 2.0 deg, $^3P_2$ = -2.0 deg, and $^1D_2$ = 0.3 deg.
(c) Data at 19.7 MeV. The solid line corresponds to $^3P_1$ = 7.73 deg, $^3P_1$ = 4.23 deg, $^3P_2$ = -2.77 deg, $^1D_2$ = 1.19 deg. The dash-dot line corresponds to the phases 9.04, -2.96, 1.84, and 0.8 deg, consistent with OPE. The dashed line is obtained from the Dubna phases (Ref. 9) up to and including the D wave.

20. SMALL-ANGLE BEHAVIOR OF THE POLARIZATION IN p-d ELASTIC SCATTERING†

J. S. C. McKee,* A. U. Luccio, R. J. Slobodrian, and W. F. Tivol

Recent data from this Laboratory[1] on the polarization of protons elastically scattered from deuterium in the energy range from 11.0 to 19.1 MeV indicated the development of a negative polarization close to the known minimum in the elastic scattering cross section at 120 deg c. m.

A negative polarization was also observed at the lowest angles investigated in the data obtained at 11.0 and 13.2 MeV, in contrast to Wisconsin measurements[2] in the same energy interval.

The experiment presented here was carried out as an investigation into the small-angle behavior of the polarization, and results are shown in Fig. B. 20-1. Part (a) of the figure shows previous data from this Laboratory at 11.0 MeV, Part (b) shows the present data obtained at 11.6 MeV, and Part (c) shows the previous results for an energy of 13.2 MeV.

The context of the small-angle points in Fig. B. 20-1(b) is such as to indicate a minimum in the observed asymmetry distribution at around 29 deg c. m. angle, for this energy. These data interpolate well between the results shown in Parts (a) and (b) of the figure. Comparison with the earlier results indicates that the minimum moves forward with increasing energy.

The experiment presented here was carried out by using the polarized beam facility of the 88-inch variable-energy cyclotron at Berkeley, which provides protons of approximately 100% polarization.

For measurement of the asymmetry distribution in pd scattering at large angles (greater than 22 deg lab), the equipment used was similar to that already described.[1]

The target pressure was 3 atm absolute, and pulses from all telescopes were routed to quadrants of a Nuclear Data 4096-channel pulse-height analyzer. At forward angles extended counter arms were used to support small-geometry collimators and additional ΔE counters of 0.004-in. CsI(Tl). The coincidence requirement between pulses from E and ΔE counters produced very clean spectra. The E counters were 0.030 in. thick for small-angle work, and the collimation system defined an angular acceptance of $\theta_{lab} \approx 1$ deg. A spin precession solenoid was used to reverse the spin of the incident proton beam at each angle investigated. Background from sources other than charged particles was found to be entirely negligible.

The study of pd interactions is experimentally the simplest of the nuclear three-body systems. Nonetheless, there is as yet no adequate theory to describe the interactions involved, and no predictions of pd polarizations are presently available below 40 MeV. In the nd case, however, the theoretical work of Purrington[3] including tensor forces suggests a negative polarization for angles forward of 45 deg c. m., at 10.0 MeV neutron energy. The inclusion of Coulomb and spin orbit effects in the pd case might well add an oscillatory behavior to the present form of this distribution. An interesting observation can be made from an examination of small-angle pd elastic scattering data in the energy range from 9.7 to 13.9 MeV,[4-6] and near the minimum seen in Fig. B. 20-1. Rodberg[7] has pointed out that there may be a relation between the zeros of polarization and the maxima and minima in cross-section data. He has discussed observed polarization in terms of the optical model, and found that a spin-orbit interaction when introduced as a small additional part to the real central potential can reasonably predict observed asymmetries.

The present results have been examined from this point of view, and data on elastic scattering and polarization at 90 deg c. m. are used to predict a value for the depth of the spin orbit potential (V_{so}) when an interaction radius of 1.56 F and a value of -43 MeV (Ref. 8) are used for the real part of the central interaction (V_c).

The value obtained for V_{so} is 1.0 MeV for an incident nucleon energy of 11.6 MeV. When this value is further used to predict the polarization in pd scattering at 30 deg c. m., a result of 0.014 is obtained, in reasonable agreement with our observed results. The position of the two zeros in polarization at small angles is also well reproduced from a study of the shape of the elastic scattering cross section in this angular region. Our results are thus consistent with spin orbit effects in the pd interaction.

Footnotes and References

†UCRL-17755, 1967, submitted to Nucl. Phys.
*On study leave from the University of Birmingham, England.

1. J. S. C. McKee, D. J. Clark, R. J. Slobodrian, and W. F. Tivol, Phys. Letters 24B, 608 (1967).
2. T. B. Clegg and W. Haeberli, Nucl. Phys. A95, 608 (1967).
3. R. D. Purrington, Ph. D. Thesis, Texas A and M University, 1966 (we learned of this work through a private communication from J. D. Seagrave, for which we are grateful.)
4. J. C. Allred, A. H. Armstrong, R. O. Bondelid, and L. Rosen, Phys. Rev. 88, 433 (1952).
5. S. Kikuchi, J. Sanada, S. Suwa, I. Hayashi, K. Nisimura, and K. Fukunaga, J. Phys. Soc. (Japan)15, 9 (1960).
6. W. T. H. Van Oers and K. W. Brockman, Jr., Nucl. Phys. 21, 189 (1960).
7. L. S. Rodberg, Nucl. Phys. 15, 72 (1959).
8. F. Bjorklund and S. Fernbach, Phys. Rev. 109, 1295 (1958).

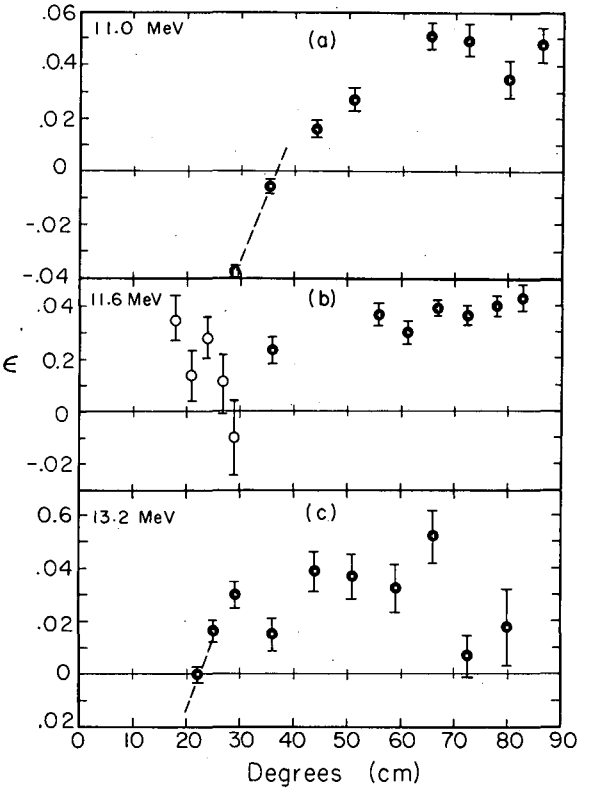

XBL678-3696

Fig. B. 20-1. Data obtained at three energies, 11.0, 11.6, and 13.2 MeV, for the asymmetry (ϵ) in pd scattering. Parts (a) and (c) are previous data contained in Ref. 1; part (b) is the data from this experiment. The open circles are obtained by using the small-angle collimation and coincidence system; all other data are obtained by the methods of Ref. 1. Errors shown are statistical. The dashed lines indicate comparable positions for a zero in polarization at each energy.

C. NUCLEAR STRUCTURE THEORY

1. POSSIBLE OBSERVATION OF VACUUM POLARIZATION EFFECTS IN THE $^1S_0$ pp STATE†

R. J. Slobodrian

Vacuum polarization effects (VPE) have in the past provided remarkable confirmation of predictions of quantum electrodynamics (QED), like the correction of the Lamb shift.[1] More recently, however, the validity of QED at small distances was questioned by experiment.[2] Later work by the collaboration Hamburg-Columbia[3] proved to be in contradiction with the work of Ref. 2 and confirmed the validity of QED to momentum transfers up to 400 MeV/c.

The VPE on pp scattering, and hence on pp interaction, have been calculated in the past by Foldy and Eriksen[4] and also by Heller.[5] Both calculations are in agreement except for minor differences due to the alternative methods used in the computation. The absolute accuracy or validity of the corrections due to the VPE on pp interaction has not been established yet.[6] This point is important for the determination of the shape parameters of the effective range expansion, or equivalently for a proper choice of a potential describing the S-wave interaction. Very-low-energy scattering experiments (below 300 keV in the laboratory system) may provide clues concerning this point. However, no accurate data exist at present and the experimental difficulties are considerable.

Recent experiments have shown that reactions involving two protons and a third particle in the final state are dominated by the $^1S_0$ nucleon-nucleon interaction. This is the case for ^{3}He(d, t) 2p (Ref. 7, 8) or ^{3}He(^{3}He, α) 2p (Ref. 9). So far a reasonable agreement has been found in fitting the spectra with formulas based on the Watson-Migdal final-state interaction theory.[10, 11] The center-of-mass spectra are given by

$$\frac{d^2\sigma}{dE_0 d\Omega} = |g(\phi)|^2 \quad \frac{C(\eta)\,\rho(E_0)}{C^2(\eta)E_{2p} + (\hbar^2/M_p)[-1/a_p - h(\eta)/R + \gamma_p E_{2p}]^2}\,, \tag{1}$$

where $C(\eta) = 2\pi\eta/(e^{2\pi\eta} - 1)$ and $h(\eta) = \mathrm{Re}\left[\frac{\Gamma'(-i\eta)}{\Gamma(-i\eta)}\right] - \ln(\eta)$, $\eta = e^2/\hbar v$ (v is the relative velocity of the pp system, E_{2p} the relative energy), $\gamma_p = r_e M_p/\hbar^2$ (r_e is the effective range), $\rho(E_0)$ is the phase space factor, $|g(\phi)|^2$ is a reaction-mechanism-dependent factor, function of the momentum transfer. The factorization of the transition matrix element into terms dependent on the nucleon-nucleon pole and the momentum transfer pole is valid for direct or peripheral nucleon transfer reactions, as it corresponds to the assumptions of the Watson-Migdal theory. Expression 1 does not include VPE, as it is simply obtained from the linearized effective-range expansion of the function

$$K = RC^2(\eta)\,k\,\mathrm{cotan}\;\delta_0 + h(\eta), \tag{2}$$

where $R = \hbar^2/M_p e^2$, δ_0 is the $^1S_0$ phase shift. Foldy and Eriksen[4] calculated the corrections ΔK on the basis of first-order perturbation theory,

$$\Delta K = M_p C^2(\eta)\, R/\hbar^2 \int_0^\infty V_{vp}(r) u^2(r) dr, \tag{3}$$

where V_{vp} is the vacuum polarization potential. The corrections are highly nonlinear at low relative energies. Using the values of ΔK of Foldy and Eriksen,[4] one can correct the "line shape"

of the $^1S_0$ state of two protons for VPE, including a term $\Delta K/R$ in the effective range expansion. Figures C.1-1 and C.1-2 summarize the results of the computation and its application to the ^{3}He(d, t)2p reaction. Laboratory spectra are shown for obvious practical considerations.

Some discussion is in order concerning the actual observability of the effect. A spectrum shape measured with high statistical accuracy (0.1%) and high energy resolution and precision (down to a few keV) should provide a good test of the correctness of the calculated VPE. However, it is not yet known if the third-particle spectra are described theoretically to that accuracy by expression 1. If such accurate investigation proved to depart from both the corrected and uncorrected line shape, it may be due to the neglect of other interactions, but not necessarily due to a breakdown of QED. The following more lengthy experimental path may then prove useful to further pursue the point. The reactions T(d, ^{3}He)2n and T(T, ^{4}He)2n performed with the same degree of experimental accuracy could provide the spectrum shape when the electrostatic field is switched off. Subsequently, turning on the electrostatic interactions, and properly handling the electromagnetic corrections,[12] one can calculate the spectrum of the mirror reactions both with and without VPE.

Clearly, agreement would mean another brilliant confirmation of QED, disagreement could be blamed on its failure or to other unknown factors related to charge asymmetry of nuclear forces.

Footnote and References

†Phys. Letters 25B, 89 (1967).

1. E. E. Salpeter, Phys. Rev. 89, 92 (1953).
2. R. P. Blumenthal, D. C. Elm, W. L. Faissler, P. M. Joseph, L. M. Lanzerotti, F. M. Pipkin, and D. G. Stairs, Phys. Rev. 144, 1199 (1966).
3. J. G. Asbury, W. K. Bertram, U. Becker, P. Joos, M. Rohde, J. S. Smith, S. Friedlander, C. Jordan, and C. C. Ting, Phys. Rev. Letters 18, 65 (1967).
4. L. L. Foldy and E. Eriksen, Phys. Rev. 98, 775 (1955).
5. L. Heller, Phys. Rev. 120, 627 (1960).
6. R. J. Slobodrian, Nuovo Cimento 40, 443 (1965).
7. E. Baumgartner, H. E. Conzett, E. Shield, and R. J. Slobodrian, Phys. Rev. Letters 16, 105 (1966), and references therein.
8. B. J. Morton, E. E. Gross, J. J. Malanify, and A. Zucker, Phys. Rev. Letters 18, 1007 (1967).
9. R. J. Slobodrian, J. S. C. McKee, W. F. Tivol, D. J. Clark, and T. A. Tombrello, Phys. Letters 25B [1], 19 (1967).
10. K. M. Watson, Phys. Rev. 88, 1163 (1952).
11. A. B. Migdal, Zh. Eksperim. i Teor. Fiz. 28, 3 (1955) [translation: Soviet Phys.-JETP 1, 2 (1955)].
12. R. J. Slobodrian, Phys. Rev. 145, 766 (1966), and references therein.

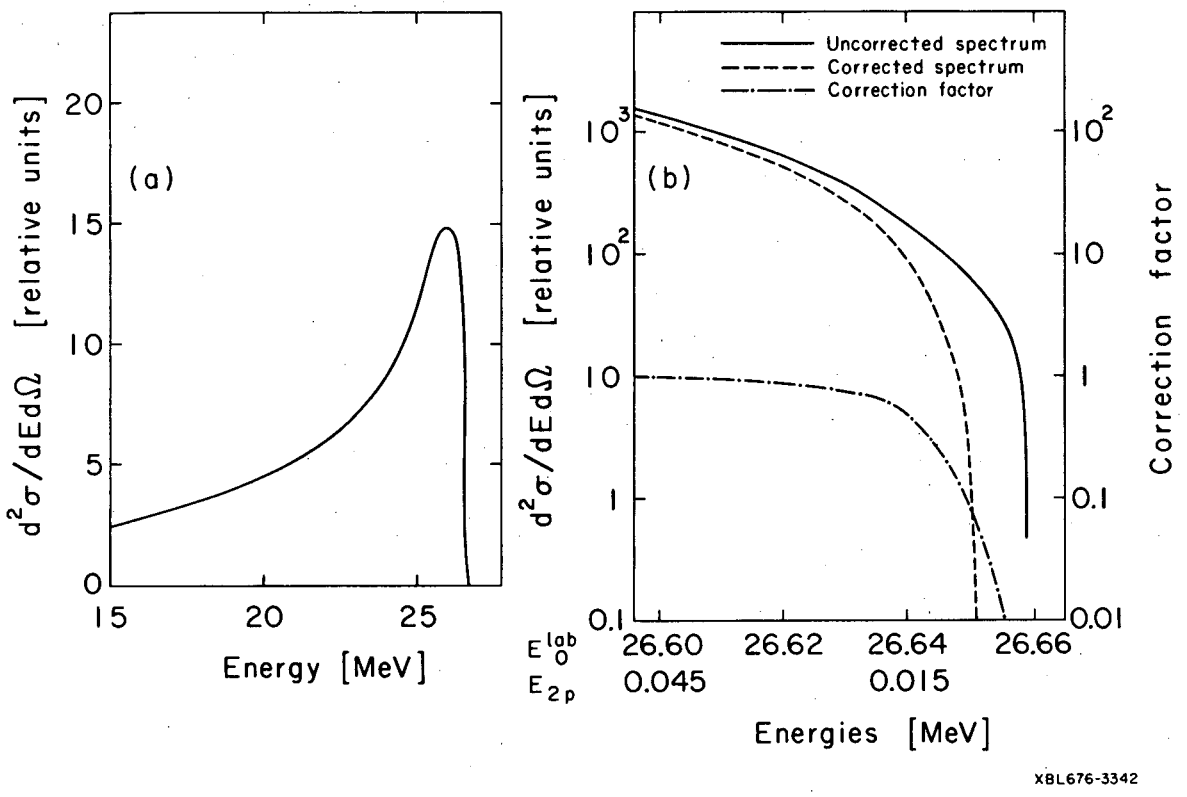

Fig. C. 1-1. (a) Line shape due to $^1S_0$ pp state. The calculation corresponds to the ^{3}He(d, t) 2p reaction near 30 MeV at 8 deg. (b) Highly expanded view of the high-energy end of the spectrum and correction factor calculated as described in the text. Note the shift of about 10 keV of the spectrum end point.

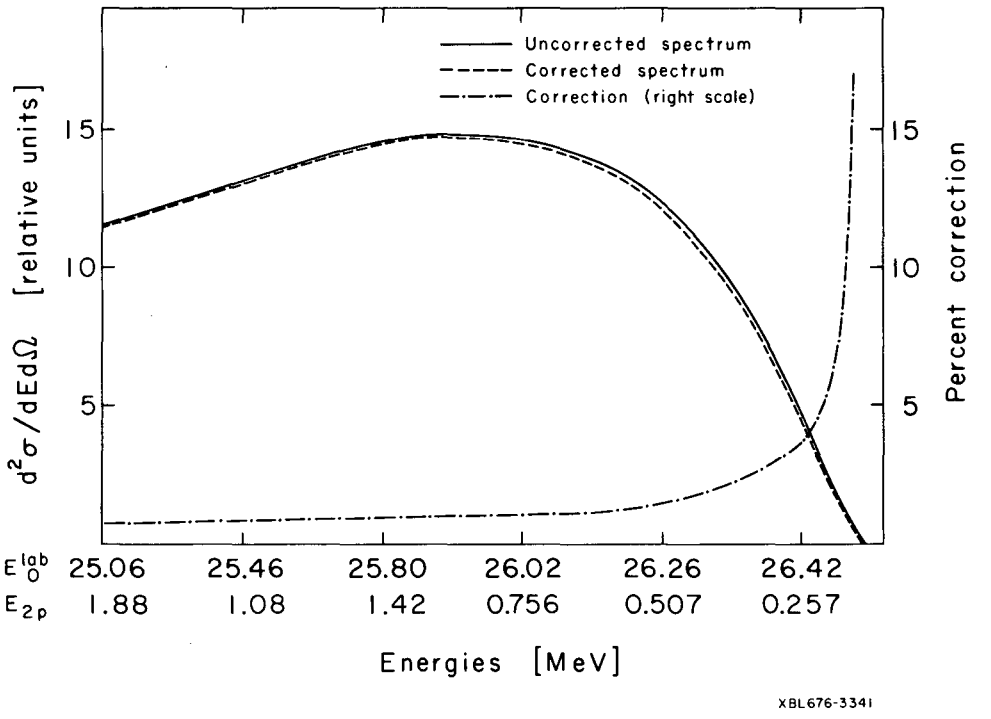

Fig. C. 1-2. Overall view of the corrections of the line shape and correction factor. Note the sizable range over which the correction is nonlinear.

2. A VIRTUAL BOUND STATE IN ^{8}Be †

H. E. Conzett

The observed asymmetric peak in the ^{7}Li(p, α)α reaction at 5.6 MeV has been interpreted in terms of two resonances corresponding to two levels in ^{8}Be at excitations near 22.1 and 22.5 MeV.[1] Also, the 800-keV resonance in the ^{6}Li(d, α)α reaction[2] has been assumed to correspond to the 22.5-MeV level.[3] The tentative assignments of J = 2^+ to both levels by Jeronymo et al.[3] have been supported by more complete analysis of the data,[4] and the recent study of ^{6}Li(d, α)α reaction at 600 keV with polarized deuterons confirms the 2^+ assignment of the 22.5-MeV level.[5]

Since the ^{6}Li + d threshold corresponds to a ^{8}Be excitation of 22.28 MeV, it seems possible to explain the experimental results in terms of a single 2^+ state near 22.1 MeV. If it has some ^{6}Li + d parentage, as can be expected so near threshold, its deuteron reduced width would require its decay via the ^{6}Li + d channel in addition to its known decay into the open alpha, proton, and neutron channels. Hence it could be an excellent example of a virtual bound state; that is, it is bound by some 150 to 200 keV in the ^{6}Li + d channel but can decay via the open channels. The resultant width (near 1 MeV) provides a large energy overlap of the state with the deuteron channel, so that without the barrier penetrability factors the ^{6}Li(d, α)α cross section would show a Breit-Wigner resonance behavior corresponding, however, to a negative resonance energy. Thus, it would display only part of the high-energy side of the resonance peak. The barrier penetrability factors would reduce the cross section to zero at threshold, providing a resulting peaking in accord with that observed experimentally.

This virtual bound state could also account for the asymmetry of the peak in the ^{7}Li(p, α)α cross section at 5.6 MeV. That is, the total width, $\Gamma = \Gamma_\alpha + \Gamma_p + \Gamma_n$, is the sum of the partial alpha, proton, and neutron widths below the deuteron threshold (assuming negligible decay via the ^{3}He and triton channels). Above threshold it is augmented by the deuteron partial width, Γ_d, so this

region of the resonance peak should show a broadening due to the increase in the total width. Again, this is in qualitative agreement with the observed behavior.

In addition to the obvious advantage of describing the experimental results in terms of a single 2^+ state rather than two, the identification of a nuclear virtual bound state should have considerable intrinsic interest because of its rarity. The analogous strange-particle resonance, the $Y_0^*(1405)$, has received considerable attention as a virtual bound state.[6]

References

†Paper for the International Conference on Nuclear Structure, Tokyo, Japan, September 7-13, 1967.

1. I. G. Han and N. P. Heydenburg, Bull. Am. Phys. Soc. 6, 415 (1961).
2. N. P. Heydenburg et al., Phys. Rev. 74, 405 (1948).
3. J. M. F. Jeronymo et al., Nucl. Phys. 38, 11 (1962).
4. R. M. Freeman and G. S. Mani, Proc. Phys. (London) Soc. 85, 267 (1965).
5. H. Bürgisser et al., Helv. Phys. Acta 40, 185 (1967).
6. R. H. Dalitz and T. C. Wong, Phys. Rev. 153, 1617 (1967) and references therein.

3. INADEQUACY OF THE SIMPLE DWBA TREATMENT OF COMPARATIVE (p, t) AND (p, ^{3}He) TRANSITIONS†

Donald G. Fleming,* Joseph Cerny, and Norman K. Glendenning

We have tested current theories of direct two-nucleon transfer reactions by comparing (p, t) and (p, ^{3}He) transitions on odd-mass nuclei leading to mirror final states. In particular our data on proton-induced reactions on ^{15}N at 43.7 MeV and on ^{13}C at 49.6 MeV as well as the data of Hardy and Skyrme[1] on the p + ^{31}P reaction at 40 MeV have been investigated. Many mirror transitions have been analyzed with DWBA calculations[2] in an attempt to fit both angular distributions and cross-section ratios. As an example, Fig. C.3-1 shows the fits obtained for the ^{15}N(p, t)^{13}N g.s. and ^{15}N(p, ^{3}He)^{13}C g.s. transitions with a spin-independent nucleon-nucleon interaction, $A^S = A^T$ (the singlet-even strength of the two-body potential is denoted by A^S and the triplet-even strength by A^T); in general, good results for the shapes of the angular distributions are obtained with this interaction. However, agreement between theory and experiment for the cross-section ratios of mirror (p, t) to (p, ^{3}He) transitions improves in every case with the inclusion of a strongly spin-dependent force ($A^S = 0.3\ A^T$) in the nucleon-nucleon interaction (see Ref. 3). An example of this can be seen in Fig. C.3-2, dealing again with the above transitions.

The inclusion of this strongly spin-dependent force, however, does not produce satisfactory agreement in all cases, as can be seen from the data in Table C.3-I. The (p, t) transitions are still found to be generally stronger than expected, relative to the (p, ^{3}He) transitions. Further, three transitions (denoted by a in the table) have been observed in which the experimental ratio of these cross sections exceeds the theoretical upper limit of 4/1 which arises if both transitions proceed solely via S = 0 transfer of the nucleon pair. Two possibilities, both of which introduce coherent effects, may account for this result: (i) interference terms arising through a spin-orbit interaction in the optical potential,[4] or (ii) interference terms between a direct reaction contribution and a core-excitation contribution to the cross section. The former explanation is somewhat preferred, especially when one notes (Table C.3-I) that the examples that are outside this limit arise from highly populated final states—the strongest transition in the ^{15}N(p, t)^{13}N data and the second and third strongest in the ^{13}C(p, t)^{11}C data.

Footnotes and References

†Condensed from Phys. Rev. 165, 1153 (1968).

*Now at the Nuclear Structure Laboratory, University of Rochester, Rochester, New York.

1. J. C. Hardy and D. J. Skyrme, in Isobaric Spin in Nuclear Physics, J. D. Fox and D. Robson, eds. (Academic Press, New York, 1966), p. 701.

2. N. K. Glendenning, Ann. Rev. Nucl. Science 13, 191 (1963); N. K. Glendenning, Phys. Rev. 137B, 102 (1965).
3. J. C. Hardy and I. S. Towner, Phys. Letters 25B, 98 (1967).
4. G. R. Satchler, Nucl. Phys. 55, 1 (1964).

Table C.3-I. Mass 13 and mass 11 experimental and theoretical integrated cross sections.

Final state J^π	$^{15}N(p,t)^{13}N$ σ_T (μb) (10 to 90 deg) c.m.	$^{15}N(p,^3He)^{13}C$ σ_T (μb) (10 to 90 deg) c.m.	$R_{exp} = \frac{\sigma_T(p,t)}{\sigma_T(p,^3He)}$	R_{theory} $A^S = A^T$	R_{theory} $A^S = 0.3\ A^T$
$1/2^-$	941	308	3.16	0.635	1.46
$3/2^-$	652	573	1.14	0.686	1.50
$5/2^-$	1271	270	4.72[a]	1.71	2.72
Final state J^π	$^{13}C(p,t)^{11}C$ σ_T (μb) (10 to 80 deg) c.m.	$^{13}C(p,^3He)^{11}B$ σ_T (μb) (10 to 80 deg) c.m.	$R_{exp} = \frac{\sigma_T(p,t)}{\sigma_T(p,^3He)}$	R_{theory} $A^S = A^T$	R_{theory} $A^S = 0.3\ A^T$
$3/2^-$	1320	359	3.68	1.34	2.44
$1/2^-$	310	63	4.92[a]	1.51	2.74
$5/2^-$	425	90	4.72[a]	0.402	1.01
$3/2^-$	167	58	2.88	0.875	1.84

[a] Transitions in which the experimental ratio exceeds the theoretical upper limit for both transitions proceeding solely via S = 0 transfer of the nucleon pair (see text).

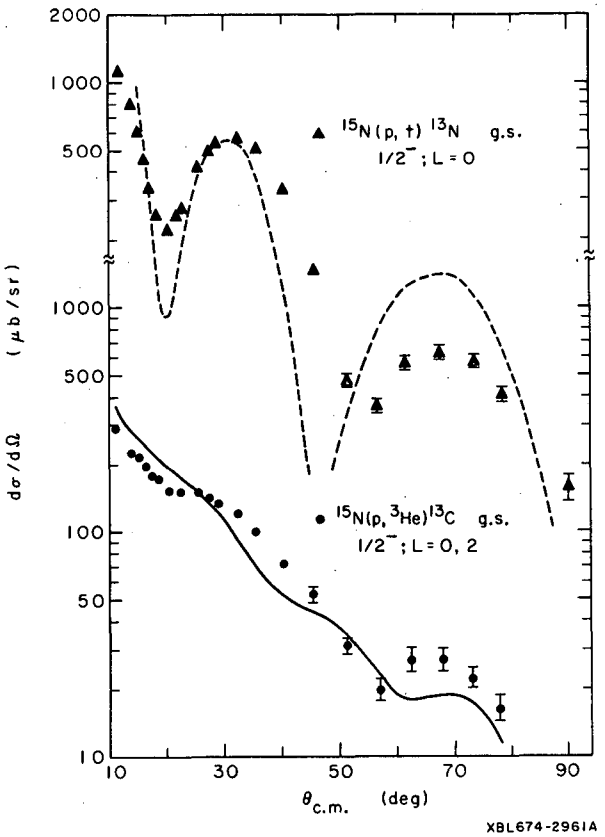

Fig. C.3-1. Angular distributions for transitions to the ground states of ^{13}N and ^{13}C populated in the $^{15}N(p, t)$ and $^{15}N(p, ^3He)$ reactions, respectively. The curves are DWBA fits to the data for a spin-independent nucleon-nucleon interaction, $A^S = A^T$. The theoretical curves have been separately and arbitrarily normalized to the data at forward angles. The optical model parameters used are discussed in the original UCRL report.

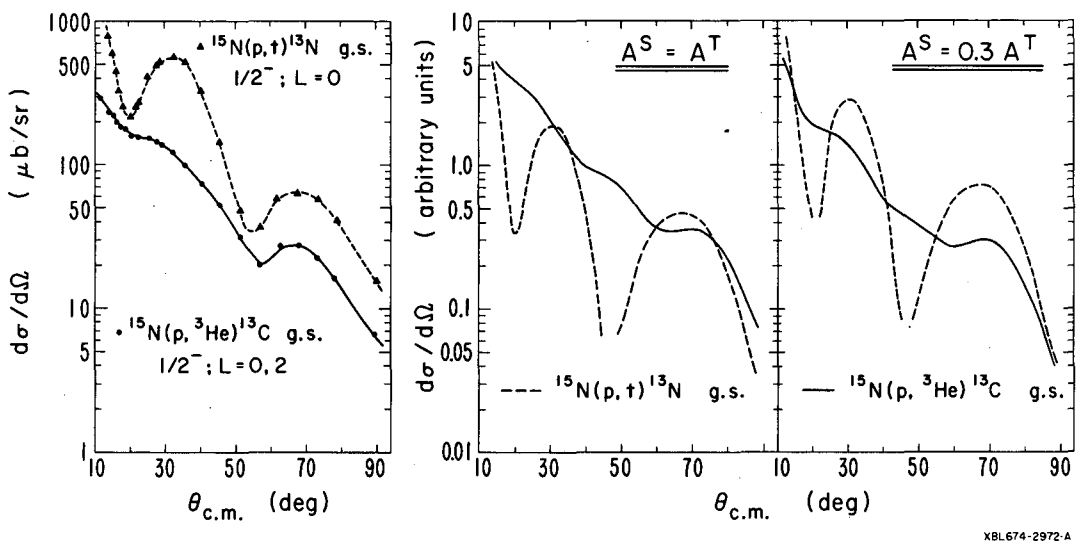

Fig. C.3-2. (a) $^{15}N(p, t)^{13}N$ and $^{15}N(p, ^3He)^{13}C$ ground state ($1/2^-$) angular distributions. The curves are drawn through the experimental points and have no theoretical significance. (b) Theoretical cross sections for a spin-independent ($A^S = A^T$) nucleon-nucleon interaction. The dashed line represents the $^{15}N(p, t)^{13}N$ g. s. transition and the solid line the $^{15}N(p, ^3He)^{13}C$ transition. The cross sections are given in the same arbitrary units and have <u>not</u> been normalized to each other. (c) As in (b), but with the chosen spin-dependent ($A^S = 0.3\, A^T$) nucleon-nucleon interaction.

4. SURFACE-DELTA-INTERACTION MODEL FOR NUCLEAR STRUCTURE ANALYZED BY PROTON INELASTIC SCATTERING†

Amand Faessler,* Norman K. Glendenning, and A. Plastino‡

As is well known, the S-wave phase shift for nucleon-nucleon scattering decreases with increasing relative energy until it eventually becomes negative around 115 MeV, reflecting the repulsion at short distance. Inside the nucleus, the relative energy of two interacting nucleons is on the average rather high, so that a reduction in their interaction energy may be expected. At the surface, however, the relative energy is low enough that there will be a net attraction in the S states. Of course this behavior is not automatically reproduced by the phenomenological forces with which it is convenient to work in nuclear-structure calculations. Moszkowski and Green[1] were thus led to introduce a phenomenological force with the above surface localization assured by the inclusion of a delta function, which allows the force to be effective only when the interacting particles are at the nuclear surface. This they called a surface delta interaction (SDI). The zero range and sharp localization are naturally simplifying assumptions which it is hoped will simulate an authentic phenomenon.

The SDI has been applied in a number of situations and in particular to the nickel isotopes,[1] where also a conventional residual interaction, of finite range and effective throughout the nuclear volume, has been employed.[2] In both cases the so-called two-quasi-particle Tamm-Dancof approximation was made in solving the many-body problem.

In this paper we calculate inelastic proton cross sections to a number of states in the nickel isotopes, thus subjecting the above nuclear descriptions to a test. The scattering problem was treated by numerically solving the relevant coupled differential equations.

Scattering Theory

Since the nuclear states are here described in terms of their nucleonic structure, the interaction of the scattered particle with the nucleus is by way of a two-nucleon potential rather than the one-body deformed potential used in macroscopic treatments. For the form of the interaction between nucleons we use

$$V(r, r_i) = (V_0 + V_1 \sigma \cdot \sigma_i) \exp\left[-\left(\frac{|r - r_i|}{\rho}\right)^2\right],$$

where r, σ are the position and spin coordinates of the scattered particle, and r_i, σ_i of the ith nucleon in the nucleus. The spin scalar and vector parts V_0 and V_1 depend in general on the isospin so that, as noted previously,[3] neutrons and protons may be expected to scatter differently in exciting the same nuclear state (except when the excitation is characterized by $T = 0$).

If we use some simple ideas about the free two-nucleon potential, we find that for protons scattering from states described by neutron correlations, the spin-dependent part V_1 is small compared with V_0.[3] Recent evidence from the analysis of scattering on the zirconium isotopes also supports this conclusion.[4] Nevertheless, the direct interaction that should be used may be very different from the vacuum interaction, as discussed qualitatively elsewhere,[3,5] and may quite likely depend upon the region of the periodic table and the details of the nuclear description. This is so because, in practice, both the structure and scattering calculations are carried out in truncated spaces of the basic states. This causes the interaction within the truncated spaces to be modified from the free interaction by terms referring to the eliminated part of the space. It may therefore be referred to as an effective interaction—effective within a prescribed subspace of basic states. Its structure may be very complicated, since, in principle, it can be both nonlocal and complex-valued. Our approach corresponds to parameterizing it, assuming for simplicity that its off-diagonal matrix elements may be parameterized, as above, as a real local central potential of Gaussian shape. For the range we take 1.85 F, such as has often been used in shell-model calculations. For most of our calculations $V_1 = 0$, but the effect of spin dependence was examined for ^{60}Ni.

The diagonal elements of the effective interaction are not calculated in the same way, but instead are represented by a spherical optical potential. There are two reasons for this departure from a strict microscopic description. The first is that the elastic scattering, represented by the diagonal parts, is a highly coherent process (every nucleon must recoil) and is therefore hard to calculate accurately. The second is that there may be important contributions from channels that are not explicitly treated. Such contributions can be accounted for approximately in the optical potential. This makes a phenomenological treatment of the diagonal parts desirable even if the first difficulty could be surmounted.

Results

Two-quasi-particle states

Proton cross sections for the coupled system comprising two 0^+, four 2^+, and one 4^+ state in the nickel isotopes of mass 58, 60, and 62 were calculated by use of the two-quasi-particle description of these isotopes. Two nuclear descriptions were used, one based on the surface-delta-interaction calculation of Faessler and Plastino,[1] and one on the volume finite-range interactions calculation (referred to for brevity as VFI) of Arvieu, Salusti, and Veneroni.[2] A sample result of the coupled-channel calculations for ^{60}Ni obtained by using these microscopic descriptions can be compared in Fig. C.4-1, where the experimental data[6] are also shown.

The parameters of the calculation consist of those describing the optical-model potential and the direct interaction between nucleons. The optical-model parameters are essentially fixed by the elastic scattering and therefore are not available for adjustment of the excited-state cross sections. The scalar form factor of the collective 2^+ state is dominant over its vector form factor, so that V_0 can be determined by adjusting it to obtain agreement in magnitude with this level. The angular distributions based on both structure calculations are seen to be in quite good agreement with experiment. The strength V_1 of the spin-dependent part of the interaction is relevant only for those higher-lying states whose vector form factor (giving rise to spin-flip transitions) is comparable to the scalar form factor. Since the wave functions of these states are not established, we cannot use them to determine V_1. As remarked earlier, there is some reason to believe that $V_1 << V_0$. We therefore have performed most of our calculations with $V_1 = 0$. In comparing the results for the higher-lying levels with experiment it should therefore be kept in mind that no adjustment of parameters was made.

In Fig. C.4-2 we do show the effect of taking various values for V_1, including a repulsive value. The cross section of the collective 2_1^+ state is insensitive to any of these variations, as are several of the others. The 2_4 level, which has a vector form factor of magnitude comparable to its scalar, is quite sensitive to the value of V_1, especially the polarization. However, there are no data available on this level, which lies presumably in the region above 3 MeV. The excited 0^+ level, which cannot be excited directly by the spin-flip interaction, nonetheless is fairly sensitive to V_1, especially the polarization due to its coupling to other excited states. There are no polarization data, and the computed differential cross section is not in good agreement with the data.

Two-phonon states

The available experimental evidence concerning so-called two-phonon states indicates considerable departures from the pure harmonic vibrational model. The evidence consists of the sometimes large splittings between the members of the two-phonon triplet, deviations from the predicted intensity rules for E2 radiation, and the finite static quadrupole moment of the two-phonon 2^+ state in those nuclei for which the measurements have been made. Nevertheless, some of the two-phonon character is expected to persist, though it may be shared by other neighboring states. The type of nuclear-structure calculation described by the two-quasi-particle TDA does not produce two-phonon states, because they involve four-quasi-particle configurations which were not included. However, we can use the coherent operator that produces the 2_1^+ state to generate a "two-phonon" triplet of wave functions. Presumably these are not eigenfunctions of the problem, and would mix with neighboring two-quasi-particle states, but we can consider them as an extreme limit. The form factors by which each member of the triplet is connected to the collective 2_1^+ state can be obtained easily upon using the quasi-boson commutation rules for the two-quasi-particle operators. The coupled equations for proton scattering on a model nucleus having excited states consisting of two 2^+ states calculated in the two-quasi-particle model, including the collective one, plus a triplet of states built on the latter, were solved, and the results are shown in Fig. C.4-3.

Discussion

We take the point of view that the reaction calculation has been handled well enough to allow conclusions to be drawn about the nuclear description by comparing calculated cross sections with the data. It is true that the direct interaction is subject to considerable uncertainty as discussed earlier. Assuming a real central potential with a fixed range about that of the vacuum interaction, the one well depth V_0 was determined by the collective 2_1^+ state. Variation of the remaining parameter V_1 was not successful in achieving an over-all agreement for all the remaining levels. The effective interaction may be more complicated than the one used, so that our criticism of the nuclear description of these nuclei is somewhat blunted. Nevertheless, we reach the tentative conclusion that aside from the fair success with the collective 2^+ state, the two-quasi-particle method has not so far provided, and possibly cannot provide, a very satisfactory description of the states that are weakly coupled to the ground. Some of the angular distributions are not bad, but often the absolute cross sections are in error by a factor of 2 to 3.

Footnotes and References

†Abbreviated version of Phys. Rev. 159, 846 (1967).
*University of Freiburg, Freiburg, Germany.
‡University of California, Los Angeles, California.
1. A. Plastino, R. Arvieu, and S. A. Moskowski, Phys. Rev. 145, 837 (1966).
2. R. Arvieu and M. Veneroni, Compt. Rend. 250, 992 (1960); 252, 670 (1960); R. Arvieu, Ann. Phys. (Paris) 8, 407 (1963); R. Arvieu, E. Salusti, and M. Veneroni, Phys. Letters 8, 334 (1964).
3. N. K. Glendenning and M. Veneroni, Phys. Rev. 144, 839 (1966).
4. G. R. Satchler (unpublished).
5. N. K. Glendenning, Lectures, Inelastic Scattering and Nuclear Structure at International School of Physics "Enrico Fermi," Course XL (UCRL-17503, Aug. 1967).
6. O. N. Jarvis, B. G. Harvey, D. L. Hendrie, and Jeannette Mahoney, UCRL-17352, Jan. 1967. We are indebted to these authors for transmitting their data before publication.

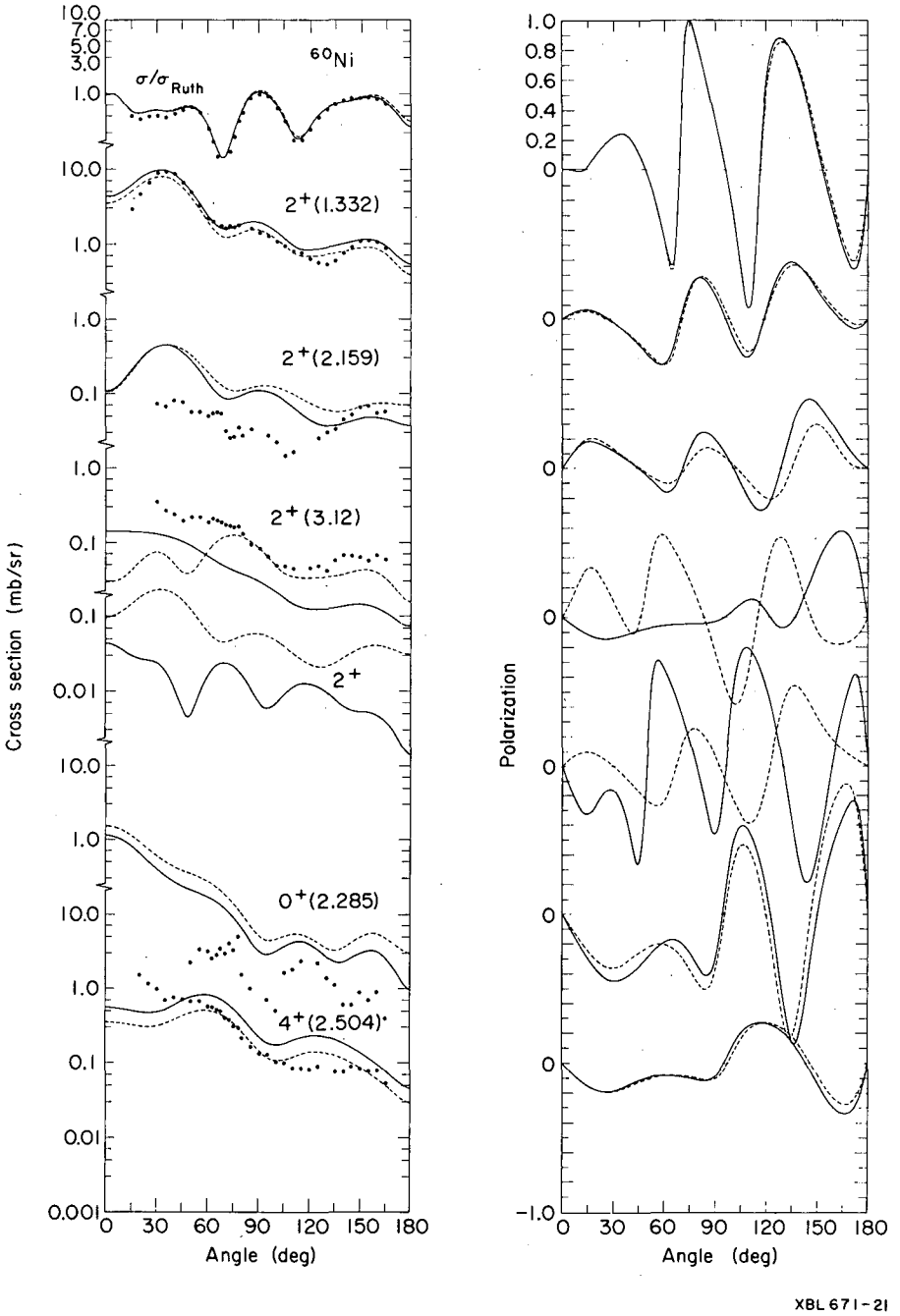

Fig. C.4-1. Differential cross sections and polarizations for 17.8-MeV protons on ^{60}Ni. Curves represent coupled-equation calculations using the microscopic descriptions of the nucleus mentioned in the text; solid line corresponds to the SDI and dashed to the VFI structure calculation. The direct interaction had the parameters $V_0 = -55$ MeV, $V_1 = 0$, $\rho = 1.85$ F. Data are from Ref. 6.

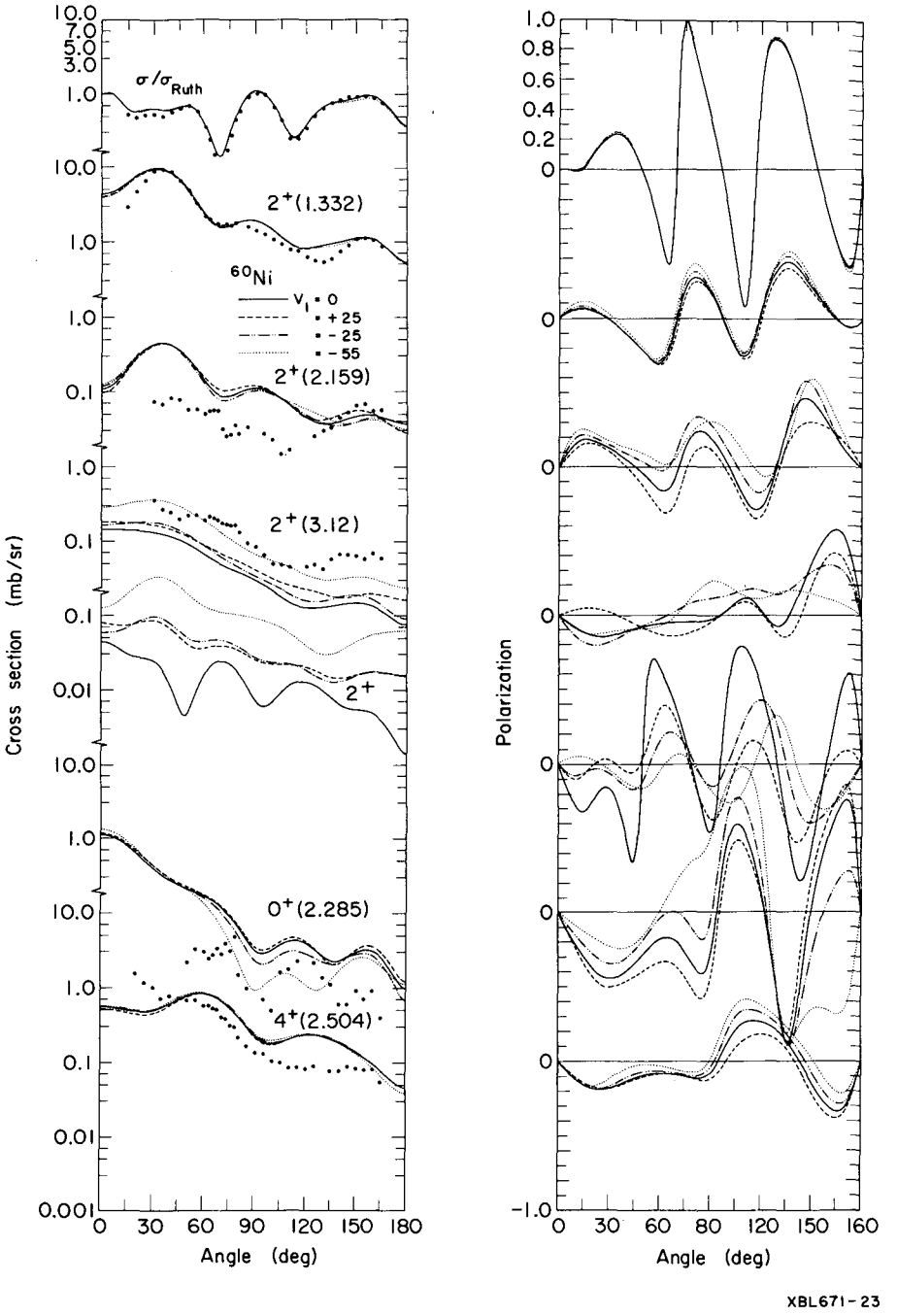

Fig. C.4-2. Differential cross sections and polarizations for 17.8-MeV protons on ^{60}Ni. Curves illustrate effect of different values for the spin-dependent part V_1 of the direction interaction computed by solving the coupled equations by use of the microscopic wave functions of the SDI structure calculation. Other direct-interaction parameters are $V_0 = -55$ MeV, $\rho = 1.85$ F.

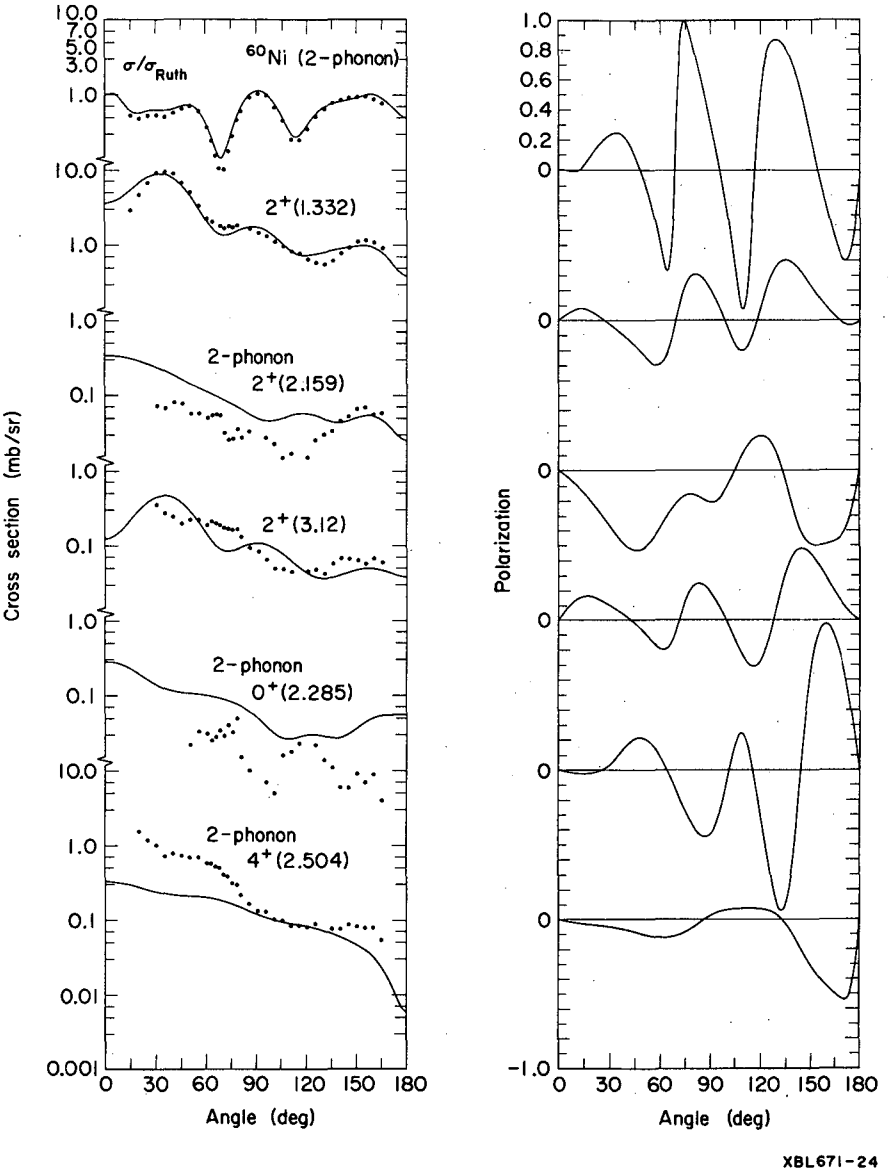

Fig. C.4-3. Protons on ^{60}Ni at 17.8 MeV. Calculation includes two-phonon states described in terms of their microscopic structure as set forth in text, as well as two-quasiparticle states generated by the SDI model of which the lowest 2_1^+ is the collective one. Direct interaction as in Fig. C.4-1.

5. RELATION BETWEEN THE OPTICAL POTENTIAL FOR SPHERICAL AND FOR DEFORMED NUCLEI†

Norman K. Glendenning, D. L. Hendrie, and O. N. Jarvis*

The elastic scattering cross sections of spherical and deformed nuclei are qualitatively different even for such close neighbors as ^{148}Sm (spherical) and ^{154}Sm (deformed). This is illustrated for 50-MeV α particles[1] in Fig. C.5-1. The slope is steeper and the amplitude of the oscillations smaller for the deformed nuclei. This difference reflects the stronger coupling to the excited states in the deformed nucleus. The optical potential (Table C.5-I) that reproduces the elastic scattering accordingly must be, and is, quite different in the two cases.

Conceptually, the optical potential was introduced to reduce an infinite-channel problem to a one-channel problem (the usual optical model for elastic scattering) or a few-channel problem (the optical model and coupling between a few low-lying levels). By construction it carries implicitly the effects of all the eliminated channels on those that are treated explicitly.[2] The eliminated channels include the intrinsic excitations which are present in all nuclei, as well as rotations in the case of deformed nuclei. It is mainly the rotations which give rise to the difference in the elastic optical potentials, as we now show.

To discuss conveniently the difference between the two cases, we introduce Feshbach's expression[3] for the optical potential,

$$U_{el} = \langle 0|V|0\rangle + \sum_{C} \langle 0|V|C\rangle \frac{1}{E-E_C+i\epsilon} \langle C|V|0\rangle, \tag{1}$$

where the sum C is over all the omitted channels, or in the case of the elastic optical potential, over all channels save the elastic. Except for those states which couple strongly to the ground state, such as collective levels, the sum will be dominated by the region of high level density in the nucleus. We can think of breaking the sum up into two parts, therefore, consisting of the sum over the low-lying collective states, and the sum over all others,

$$U_{el} = U_s + \sum_{\text{Collective}} \langle 0|V|C\rangle \frac{1}{E-E_C+i\epsilon} \langle C|V|0\rangle. \tag{2}$$

The sum over noncollective states U_s is now dominated by the high excitation region of the nucleus because of the high level density there, and should be essentially the same for all nuclei in a broad range of mass; the subscript s then denotes its smooth behavior. The more enhanced the collective states are, the larger the second term will be and hence the more the elastic optical potential will deviate from the smooth behavior we attribute to U_s.

We can easily test this division of the optical potential into a part which is peculiar to each nucleus due to the particular nature of its collective states, and a part which is slowly varying from nucleus to nucleus. This can be done by solving the coupled system comprising the elastic and collective channels. Once the collective channels are treated explicitly, they no longer contribute to the effective interaction. In other words, the second term of Eq. 2 is removed from the optical potential of the coupled system. We search empirically for a parameterization of the remaining interaction.

As an example of a deformed nucleus we choose ^{154}Sm, which we treat as a rigid rotor and include explicitly the levels of the ground-state rotational band up to and including the 6^+ state.[4] We treat explicitly the collective vibrational 2^+ state in the spherical ^{148}Sm nucleus, employing the macroscopic description. After a search for the potential parameters we find that a single potential gives rise to the excellent agreement shown in Fig. C.5-2. In fact the same potential can be used, with only minor adjustments, from the spherical ^{148}Sm throughout the deformed region up to ^{178}Hf. We identify this potential as U_s. It is given on the second line of Table C.5-I. We note that it is quite similar to the elastic potential U_{el} for the spherical nucleus. This is understood in view of our discussion following Eq. 2 and the weaker collectivity of the spherical nucleus. They differ in W and a in just the way expected.

This understanding of the optical potential has two important consequences. We are interested in determining the nuclear shape in the deformed region by analysis of inelastic alpha scattering through a solution of the coupled system.[5] Whereas it may have been assumed that the parameters of the problem include the optical parameters as well as the shape parameters β_2, β_4, $\cdots$, we have shown that the former are essentially determined by the scattering on a neighboring spherical nucleus, and that the same potential can be used throughout the deformed region with only very slight adjustments.

A second consequence concerns the search for systematics in elastic optical potentials. It is clear that whenever strong collective states exist, the elastic potential will be anomalous. Only when the contribution of the collective states to the optical potential is removed will the systematics appear, since it is U_s that is smoothly behaved.

Footnotes and References

†Condensed from UCRL-17935, Nov. 1967, submitted to Phys. Letters.

*Permanent address: AERE, Harwell, Berkshire, England.

1. The experimental results are due to B. G. Harvey, D. L. Hendrie, O. N. Jarvis, H. H. Duhm, J. Saudinos, J. Valentin, and J. Mahoney. Similar systematic differences have been found in proton scatterings by P. Stoler, M. Slagowitz, M. Makofske, and T. Kruse, Phys. Rev. 155, 1334 (1967).

2. For a fuller discussion of this see N. K. Glendenning, Inelastic Scattering and Nuclear Structure, to be published in Proceedings of the International School of Physics "Enrico Fermi," Course XL (Academic Press, New York, 1967).

3. H. Feshbach, Ann. Phys. (N. Y.) 19, 287 (1967).

4. For details see Ref. 2.

5. See Paper B.2, this report.

Table C.5-I. Optical-model parameters corresponding to Woods-Saxon shape and a uniform charge distribution with a correct quadrupole moment.

	V	W	r	a
^{148}Sm elastic only	65.5	29.8	1.427	0.671
Coupled channels	65.9	27.3	1.440	0.637
^{154}Sm elastic only	34.6	29.4	1.404	0.819

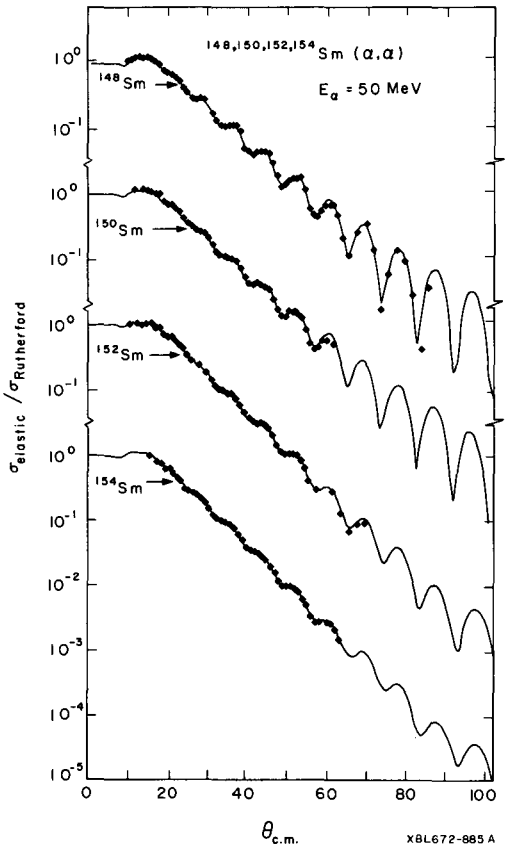

Fig. C.5-1. The elastic scattering of 50-MeV α particles from samarium isotopes which span the spherical (A=148) to deformed (A=154) region. Note the systematic trend to weaker oscillations and steeper slope of the envelope of maxima with increasing collectivity. Solid lines are elastic optical-model calculations of the cross section. The data are from Ref. 1.

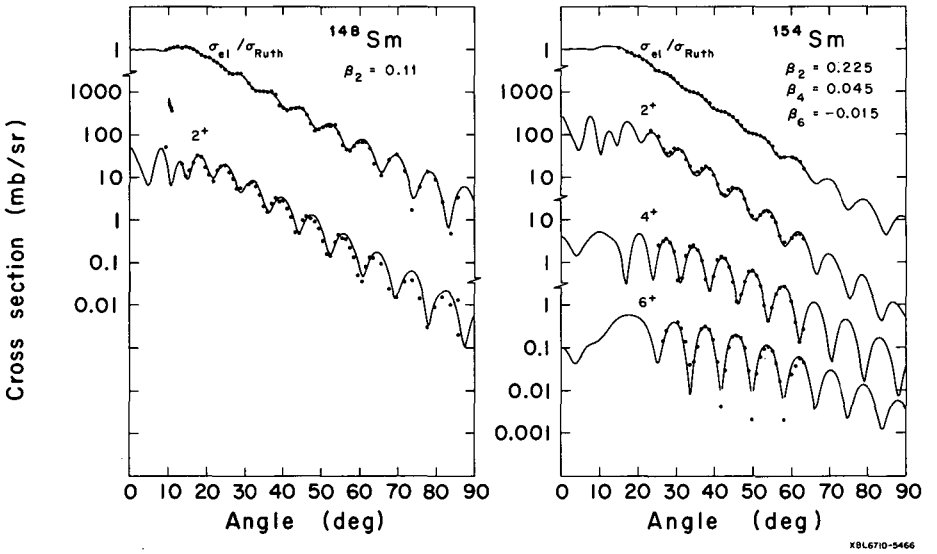

Fig. C.5-2. Elastic and inelastic scattering of 50-MeV α particles by the spherical ^{148}Sm and deformed ^{154}Sm nucleus. Solid curves are coupled-channel calculations description of 148 and a rotational description of 154. In each case the same optical potential was used (Table C.5-I) even though the elastic cross sections are different. Shape parameters β_λ for each nucleus are indicated on the figure.

6. CALCULATIONS OF THE FLATTENING OF IDEALIZED NUCLEI DURING HEAD-ON COLLISIONS†

Jaromír Malý and James Rayford Nix

When two nuclei closely approach each other they tend to flatten as a result of their mutual electrostatic forces. The amount they flatten depends upon the relative magnitudes of the electrostatic interaction (which is a function of their charges and separation) and of three of their fundamental nuclear properties: (i) stiffnesses against deformation, (ii) inertias with respect to deformations, and (iii) viscosities. If the electrostatic interaction is large enough, and each of these three properties is sufficiently small, the nuclei will flatten appreciably; otherwise, they will remain essentially spherical. Since the liquid-drop model represents the average trends of nuclear masses in the periodic table,[1] liquid-drop stiffnesses are expected to also represent an average,[2-4] and a calculation of the flattening of colliding nuclei on the basis of the liquid-drop model should give the average flattening of nuclei throughout the periodic table. We therefore study the flattening that would be experienced by nonviscous idealized liquid drops in head-on collisions.

In Fig. C.6-1 the total c.m. kinetic energy E required during head-on collisions to bring two such idealized nuclei within range of their effective nuclear forces is plotted as a function of the atomic mass number A of the target (or projectile), for three choices of projectile (or target). [The target (or projectile) atomic number Z is taken to be related to A approximately according to the course of the line of beta stability.] The kinetic energy E is given in units of the energy V that would be required to bring two spherical drops (corresponding to infinite stiffnesses, infinite inertias, or infinite viscosities) within range of their nuclear forces, viz.,

$$V = Z_1 Z_2 e^2/[(R_1 + t) + (R_2 + t)].$$

In this equation Z_1 and Z_2 are the targets and projectile atomic numbers, e is the electronic charge, R_1 and R_2 are the target and projectile radii, and t is the distance beyond the nuclear radius to which nuclear forces are effective. The five values chosen for t span the range of distances relevant to firm and gentle contacts. The ratio of the surface-energy constant to the Coulomb-energy constant, which enters these calculations, is taken from Green's analysis.[5] It is seen from the figure that the energy required to bring together two nonviscous idealized heavy nuclei is increased as a result of flattening by as much as 35% (about 200 MeV).

Measurements of the flattening experienced during head-on collisions between pairs of nuclei throughout the periodic table would yield directly information concerning a certain combination of nuclear stiffnesses, inertias, and viscosities. Although estimates of the viscosity coefficient are available,[6] less is known about this quantity than about the other two. Existing information concerning stiffnesses[3,4] and inertias[4] could therefore be used in conjunction with data on flattening to infer a value for the coefficient of nuclear viscosity. Although the accurate determination of this quantity would require calculations that use shell-affected stiffnesses and inertias, the present liquid-drop results may nevertheless prove useful in the study of transition nuclei (nonmagic spherical nuclei), whose stiffnesses are expected to equal approximately those of liquid drops.[2-4]

Footnotes and References

†Resumé of Contribution No. 7.20 to International Conference on Nuclear Structure, September 7-13, 1967, Tokyo, Japan (UCRL-17541, June 1967).

1. W. D. Myers and W. J. Swiatecki, Arkiv Fysik 36, 343 (1967).
2. Although the liquid-drop model gives the correct average behavior of stiffnesses (Refs. 3, 4), it predicts inertias that are systematically too small (Ref. 4). This deficiency is important for many purposes but may not be too serious here, since the flattening is not an extremely sensitive function of the inertia.
3. T. Honda, Progr. Theor. Phys., Suppl. 37 and 38, 451 (1966).
4. K. Alder et al., Rev. Mod. Phys. 28, 432 (1956).
5. A. E. S. Green, Phys. Rev. 95, 1006 (1954).
6. L. Wilets, Theories of Nuclear Fission (Clarendon, Oxford, 1964), pp. 99-100.

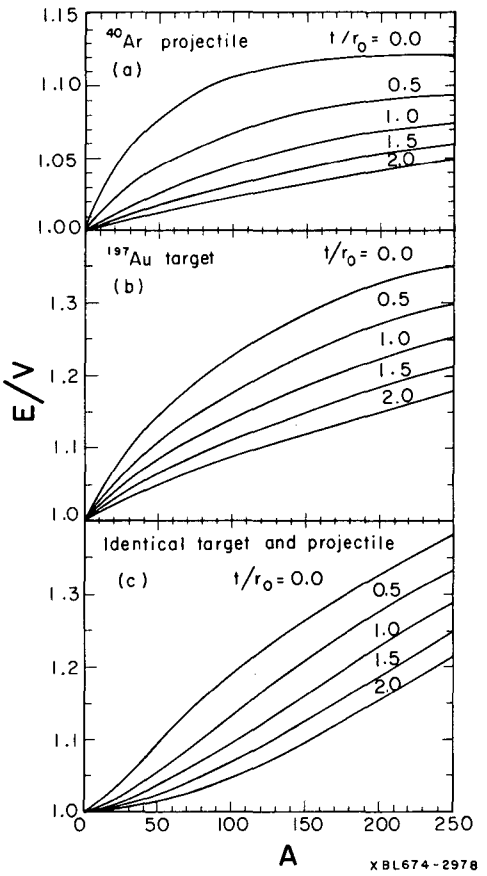

Fig. C. 6-1. The energy required to bring together the nuclear fields of two nonviscous idealized nuclei.

7. REALISTIC NUCLEAR SINGLE-PARTICLE HAMILTONIANS AND THE PROTON SHELL 114†

Heiner Meldner*

A simple ansatz for a dominating one-body operator in a realistic nuclear Hamiltonian is made and compared with similar attempts. The proposed model represents single-particle wave functions as self-consistent solutions of an integro-differential equation. Thus, all information about the single-particle part of a nuclear many-body system is expressed by a kernel, which contains a total of five physical parameters. In this way (see Table C. 7-I) it is possible to obtain a fit to

(a) nuclear charge density distributions, including isotope effects,
(b) 1s proton levels as measured in (e,e' p) scattering, and
(c) total binding energies or nuclear mass defects, while
(d) reproducing the shell-model spin assignments and mass structure.

Unlike local potential or non-self-consistent models, the present Hamiltonian allows a calculation of the eigenvalue spectrum as well as nuclear masses for different occupation functions. Hence orbital rearrangement energies can be estimated.[1] In the presence of fluctuating rearrangement energies, a gap in the eigenvalue spectrum does not necessarily lead to a physical shell effect (magic number) in the masses as a function of nucleon numbers. However, in this realistic model, the partial derivative $\partial E/\partial Z$ of the total binding energy (mass) changes considerably at the proton number $Z = 114$. Table C. 7-II shows that this shell effect has about the same magnitude as the observed ones at established magic numbers close to the line of beta stability. This confirms an earlier suggestion made by this author[2] on the basis of a gap in the proton eigenvalue spectrum at $Z = 114$.

Footnotes and References

†Shortened version of Paper (UCRL-17801, Sept. 1967) to be submitted to Phys. Rev.
*NATO Fellow. On leave from Freie Universität Berlin, West Berlin, Germany.

1. H. Meldner, Nuclear Orbital Rearrangement Energy, UCRL-17782, Aug. 1967.
2. Ref. 23 in W. D. Myers and W. J. Swiatecki, Nucl. Phys. 81, 1 (1966); H. Meldner, Arkiv Fysik 36, 593 (1967).

Table C.7-I. Experimental and calculated binding energies of some nuclei close to the line of beta stability.

Nucleus	Binding energy (MeV) Exp.	Calc.
^{44}Ca	380.9	380.3
^{88}Sr	768.5	777.5
^{118}Sn	1004.8	1017.9
^{140}Ce	1172.8	1189.0
^{208}Pb	1636.4	1636.4
$^{300}114$		2140.5

Additional comparisons with experimental data give, e.g., 1s proton level in ^{40}Ca: experimental 77±14 MeV, calculated 79 MeV; rms charge radius for ^{40}Ca: experimental 3.35±0.1 F, calculated 3.14 F; and rms charge radius for ^{208}Pb: experimental 5.42±0.03 F, calculated 5.44 F.

Table C.7-II. Experimental and calculated mass differences at closed shells ± one nucleon for the established magic numbers and for Z = 114.

Magic number	Nuclei	Mass differences (MeV) Exp.	Calc.
N = 20	$^{41}Ca - ^{40}Ca$	8.4	8.4
	$^{40}Ca - ^{39}Ca$	15.6	15.3
Z = 20	$^{41}Sc - ^{40}Ca$	1.1	1.1
	$^{40}Ca - ^{39}K$	8.3	8.0
N = 28	$^{49}Ca - ^{48}Ca$	5.0	0
	$^{48}Ca - ^{47}Ca$	10.1	13.3
Z = 28	$^{63}Cu - ^{62}Ni$	6.1	2.7
	$^{62}Ni - ^{61}Co$	11.1	13.9
N = 50	$^{89}Sr - ^{88}Sr$	6.8	5.3
	$^{88}Sr - ^{87}Sr$	11.1	11.7
Z = 50	$^{119}Sb - ^{118}Sn$	5.2	2.3
	$^{118}Sn - ^{117}In$	9.9	10.7
N = 82	$^{141}Ce - ^{140}Ce$	5.5	3.3
	$^{140}Ce - ^{139}Ce$	9.1	8.6
Z = 82	$^{209}Bi - ^{208}Pb$	3.8	3.3
	$^{208}Pb - ^{207}Tl$	8.0	5.5
N = 126	$^{209}Pb - ^{208}Pb$	3.9	3.2
	$^{208}Pb - ^{207}Pb$	7.4	5.4
Z = 144	$^{287}115 - ^{286}114$		0
	$^{286}114 - ^{285}113$		3.4
	$^{301}115 - ^{300}114$		0.1
	$^{300}114 - ^{299}113$		5.2

The pairing correction is assumed to be $15/A^{1/2}$ MeV. Additional comparisons with experimental data give, e.g., for relative rms charge radius differences $(\Delta R/R) \times 3A$, for $^{41}Sc - ^{40}Ca$: experimental 1.8 ± 1.8, calculated 2.0; for $^{209}Bi - ^{208}Pb$: experimental 1.2 ± 0.4, calculated 0.9.

8. NUCLEAR ORBITAL REARRANGEMENT ENERGY†

Heiner Meldner*

On the basis of self-consistent calculations, orbital rearrangement energies are estimated to be comparable to level differences in nuclear potential wells. Hence it is an unjustified simplification to identify such level spacings with mass differences observed, e.g., in nucleon transfer reactions.

Although it seems to be a common procedure to fit energy eigenvalues in static Woods-Saxon or oscillator potentials to the spectra of nucleon transfer reactions,[1,2] the "agreement" achieved this way is of little significance, since mass differences can be compared quantitatively with the energy eigenvalues in a given well only if further simplifications are possible. For example, one must assume that orbital rearrangement energies are small compared with the observed mass differences. It is quite obvious from this investigation that these rearrangment energies can be large and can be rather different for different orbitals.

The examples shown in Fig. C.8-1 indicate that for the first hole states in ^{47}Ca, ^{207}Pb, and ^{207}Tl the level spacings are respectively 7.6, 2.0, and 1.5 MeV in the ground state and 6.0, 1.7, and 0.5 MeV in the excited state, whereas the calculated mass differences are 2.5, 1.6, and 1.2 MeV. The experimental mass differences are 2.6, 0.57, and 0.35 MeV.[3] This kind of discrepancy indicates also that a reasonable calculation has to take into account residual two-body interactions. Hence eigenvalue differences of single-particle Hamiltonians, rearrangement energies, and level shifts due to residual two-body forces all seem to be of the same order of magnitude.

Therefore, it is also futile to infer, for example,[4] an anomalous effective mass around the Fermi level by simply identifying level spacings with mass differences, i.e., by completely neglecting rearrangements and residual interactions.

Footnotes and References

†Shortened, slightly modified version , Nuovo Cimento 53[1], 195 (1968).

*NATO Fellow. On leave from Freie Universität Berlin, West Berlin, Germany.

1. See, e.g., R. Woods, P. D. Barnes, E. R. Flynn, and G. J. Igo, Phys. Rev. Letters 19, 453 (1967); R. O. Ginaven, A. M. Bernstein, R. M. Drisko, and J. B. McGrory, Phys. Letters 25B, 206 (1967); D. Eccleshall, and M. L. Yates, Phys. Letters 19, 301 (1965); E. Rost, University of Colorado preprint COO-535-570.

2. G. E. Brown, Unified Theory of Nuclear Models and Forces (North-Holland Publishing Co., Amsterdam, 1967), p. 20.

3. C. M. Lederer, J. M. Hollander, and I. Perlman, Table of Isotopes, 6th Ed. (John Wiley and Sons, New York, 1967).

4. G. E. Brown, J. H. Gunn, and P. Gould, Nucl. Phys. 46, 598 (1963).

5. L. R. B. Elton, Phys. Letters 25B, 60 (1967).

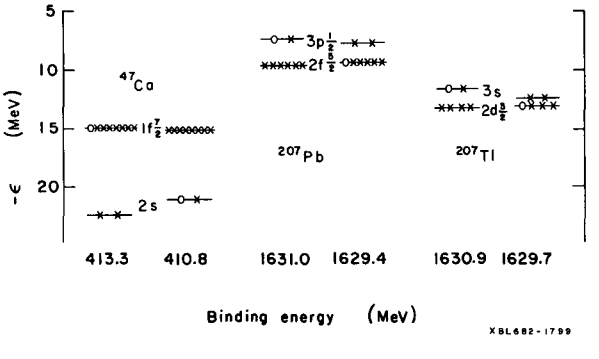

Fig. C.8-1. Binding energies and single-particle levels for the ground state and the first excited one-hole state in three doubly magic nuclei. For medium and heavy nuclei this model reproduces surprisingly well rms radii, 1s proton levels as observed in (e, e'p) reactions, and total binding energies (see paper C. 7). The above examples are expected to estimate lower limits, since orbital rearrangement is likely to be least for nuclei with one hole in a closed shell (Ref. 5).

9. NEUTRON SEPARATION ENERGIES AND THE SUPERMULTIPLET THEORY

Martin G. Redlich

In Wigner's supermultiplet theory of nuclear structure[1,2] the consequences of the assumption of the neglect of spin-dependent two-nucleon interactions upon the wave function $\Psi(1, \cdots, A)$ of a nucleus with mass number A are investigated. An early, remarkable success of this theory is the differentiation between allowed favored and unfavored β transitions. In recent years, there have been indications[3,4] from nuclear masses that the wave functions of the supermultiplet theory, which is an LS coupling theory, may be rather accurate even for heavy nuclei. In view of the success of the j-j coupling shell theory, it seems important to examine further the consequences of the supermultiplet theory's mass formula.

This formula is obtained[2] with the additional assumption of "uniform nuclear matter." It is just

$$E(A, \xi) = a(A) + \frac{1}{2} b(A)\, X(\xi). \tag{1}$$

Here, E is the binding energy and $\xi = (P, P', P'')$ is a set of numbers[2] which specify the symmetry of the wave function; X is a simple function of ξ. The functions a(A) and b(A) should vary smoothly with A, but are not otherwise determined by the theory. For the ground state of a nucleus, ξ can be obtained from A and the neutron number N. From Eq. 1 it is easy to derive a formula for the neutron separation energy $S_n(A, N)$ and for the difference between the neutron separation energies of two isobars with neutron numbers N and N_0. This difference is

$$D(A, N) = S_n(A, N) - S_n(A, N_0).$$

D(A, N) depends upon b(A), but not upon a(A). Here, b(A) is assumed to be a single constant for each N_0. It is determined approximately by the experimental D(A, N) values for N_0. For $A < 108$, the value of b(A) assumed here is approximately the one of the curve of Fig. 2 of Franzini and Radicati;[3] for larger A, it can be considered as representing an extrapolation of their curve.

In the upper part of Fig. C.9-1, the solid circles give the theoretical values of D(A, N) for $N_0 = 57$. Thus D(A, 57) = 0. The points are connected by two parallel broken lines, reflecting the even-odd difference in S_n. For other N_0, similar lines are obtained, but with different slopes for different values of b(A). All values of D(A, N) that can be obtained from experimental data[5] are shown by crosses. In general, there are several crosses for each N, corresponding to different A. In the lower part of Fig. C.9-1, the quantity

$$\Delta = \Delta(N) = \overline{D(A, N)_{\text{exp't}} - D(A, N)_{\text{theory}}}$$

is plotted. The bar indicates an average over all values of A for which data are available.

In Fig. C.9-2 there are curves of Δ vs N for $N_0 = 55$ and 51. There is a sharp drop after N = 50 for both curves. Such a drop can be expected from the j-j coupling shell theory. The 50th neutron is exceptionally strongly bound (has a large S_n) compared with either the 51st or the 55th neutron. Similar curves are obtained for neighboring values of N_0. An examination of the data available for $N > 30$ shows that rather good agreement with the supermultiplet theory's prediction is generally obtained, except near N = 50, 82, and 126. For $N < 30$, there are considerable fluctuations both in b(A) and in Δ.

It may well be that a wave function specified by the supermultiplet theory is quite a good approximation for the ground state of nearly all those nuclei which are not in small "islands of j-j coupling" near the magic neutron or proton numbers. The effect of the spin-dependent part of the two-nucleon interaction upon the wave function may normally be rather small.

References

1. E. P. Wigner, Phys. Rev. 51, 106 (1937).
2. E. Feenberg and E. P. Wigner, Repts. Progr. Phys. 8, 274 (1941).
3. P. Franzini and L. A. Radicati, Phys. Letters 6, 322 (1963).
4. G. T. Garvey and I. Kelson, Phys. Rev. Letters 16, 197 (1966).
5. J. H. E. Mattauch , W. Thiele, and A. H. Wapstra, Nucl. Phys. 67, 32 (1965).

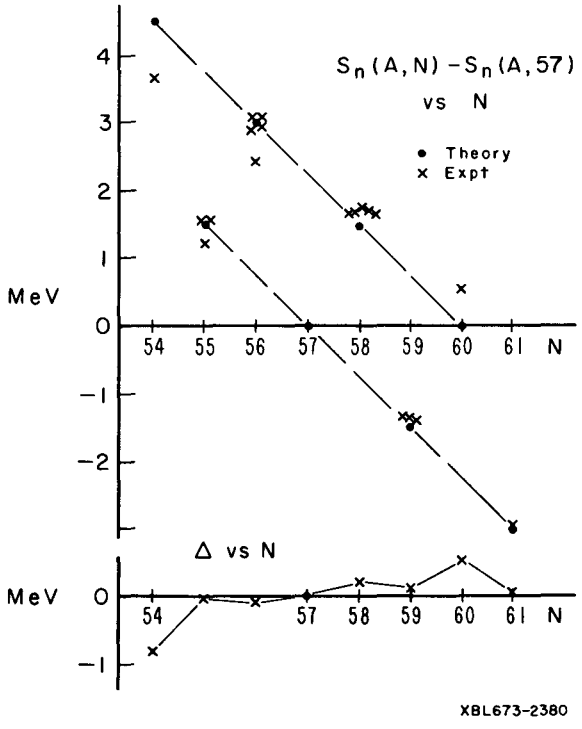

Fig. C. 9-1. The upper part shows the prediction by the supermultiplet theory for D(A, N) with $N_0 = 57$. The theoretical points are connected by the two parallel broken lines. The experimental points for each N correspond to different values of A. The bottom part shows the average deviation Δ between experiment and theory.

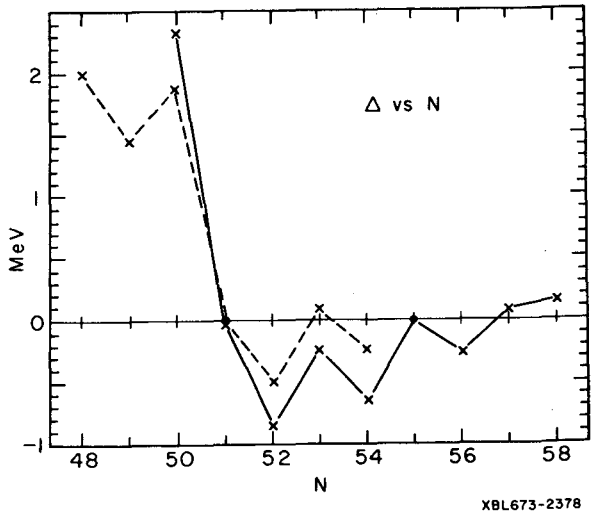

Fig. C. 9-2. The average deviation Δ between experimental and theoretical values of D(A, N) is plotted against N. There are two curves, the solid one for $N_0 = 55$ and the broken one for $N_0 = 51$.

10. NUCLEAR STRUCTURE, FISSION, AND ELEMENT 114

S. G. Nilsson

Single-particle energies have been calculated[1] for a deformed well of the type

$$V = \frac{1}{2}\hbar\omega_0 \rho^2(1 - \frac{2}{3}\epsilon P_2 + 2\epsilon_4 P_4) - 2\kappa\left[(\vec{\ell}_t \cdot \vec{s}) - \mu(\rho^4 - \langle\rho^4\rangle_N)\right],$$

where ρ and $\vec{\ell}_t$ are expressed in "stretched coordinates" so that

$$\rho^2 = \frac{M}{\hbar}\left[\omega_\perp(x^2 + y^2) + \omega_z z^2\right],$$

and where $\langle\rho^4\rangle_N$ denote the average value of $\langle\rho^4\rangle$ as evaluated over an N_t shell.

The total energy is expressed essentially as a sum of the corresponding single-particle energies with a pairing energy added according to the usual BCS prescription. To this is then added the Coulomb energy of a homogeneously charged body of a shape given by the equipotential surfaces of the potential proportional to ρ^2.

The total energy is studied as function of ϵ and ϵ_4. The superimposed condition of the conservation of volume of enclosed equipotential surfaces is enough to assure an equilibrium distortion, in agreement with experimental findings as to both quadrupole and hexadecapole moments. In Fig. C. 10-1 the β_4 deformations[2] of the potential are compared with empirical results for rare earth nuclei as obtained from inelastic alpha scattering analysis.[3] Similar calculations are exhibited for actinide nuclei in Fig. C. 10-2. Also the total deformation energy appears in rough agreement with the mass-data systematics.

However, in determining fission barrier energies the potential chosen fails at large distortions, which fact may be connected with some insufficiencies in the ρ^4 term or in its treatment (only couplings within every N_t shell are included).

To improve on this point and possibly to be able to make predictions about lifetimes of isotopes of $Z = 114$ (Fig. C. 10-3) we have started, in cooperation with R. Nix of this Laboratory, a program which essentially amounts to normalizing the results based on the nuclear potential so as to correspond on the average to the liquid-drop theory. This is ffected with the help of an averaging procedure due to Strutinsky.[4] By the latter procedure the shell correction energy, δE_{corr}, is calculated as the energy obtained by the straightforward application of the model energy levels minus the corresponding energy obtained from smeared single-particle levels. This quantity δE_{corr} is then added to the liquid-drop energy. Preliminary results of calculation following this program (S. G. Nilsson and R. Nix) are encouraging.

References

1. C. Gustafson, I. L. Lamm, B. Nilsson, and S. G. Nilsson, Arkiv Fysik 36, 613 (1967); see also S. G. Nilsson, in Lectures at the International School of Physics "Enrico Fermi," Varenna, 1967 (to be published).
2. P. Möller, S. B. Nilsson, S. G. Nilsson, A. Sobiczewski, Z. Szymanski, and S. Wycech, Phys. Letters, to be published March 1968.
3. D. L. Hendrie, N. K. Glendenning, B. G. Harvey, O. N. Jarvis, H. H. Duhm, J. Mahoney, and J. Saudinos, Phys. Letters 26B, 127 (1968).
4. V. M. Strutinsky, Nucl. Phys. A95, 420 (1967).
5. K. Kjällquist, Nucl. Phys. 9, 163 (1959/1960).
6. K. Harada, Phys. Letters 10, 80 (1964).

Fig. C. 10-1. Hexadecapole deformation β_4 in the rare earth region compared with experimental and theoretical values of Ref. 3. Recent reevaluation of the data has resulted in a small increase in the experimental Sm β_4 values and a small decrease in the Yb and Hf values. The theoretical β_4 values of W and Os are somewhat uncertain, as they are based on too small a number of grid points.

●——● present theory; ---- theory (polarization and Coulomb scattering neglected (Ref. 3); ⊡ experimental, Ref. 3).

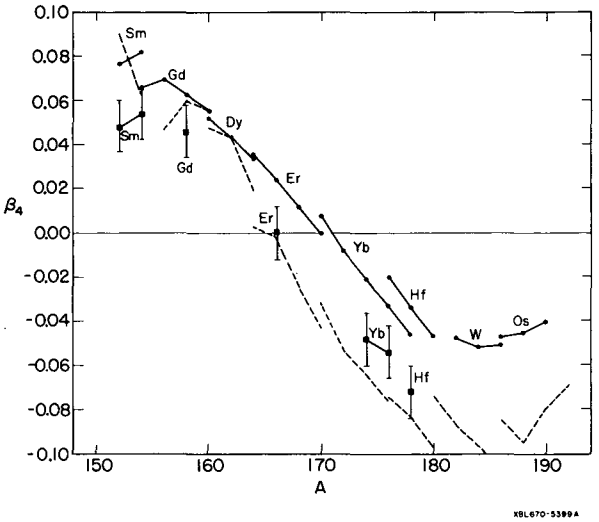

Fig. C. 10-2. Hexadecapole deformation β_4 in the actinide region compared with the theoretical calculations of Refs. 5 and 6.

●——● present theory (polarization, pairing, and Coulomb effects included); —·— theory, Harada; ----- theory, Kjällquist.

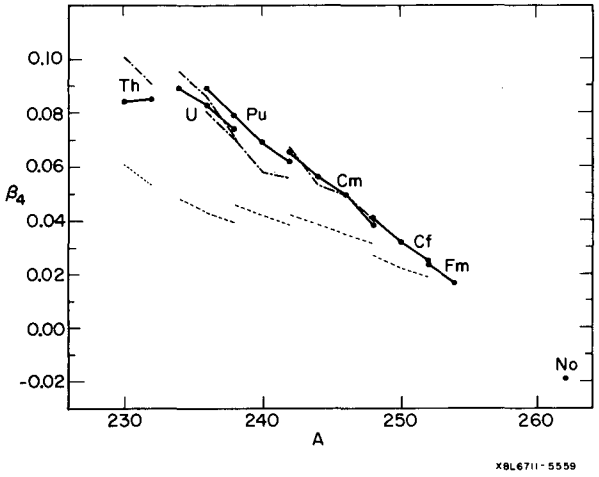

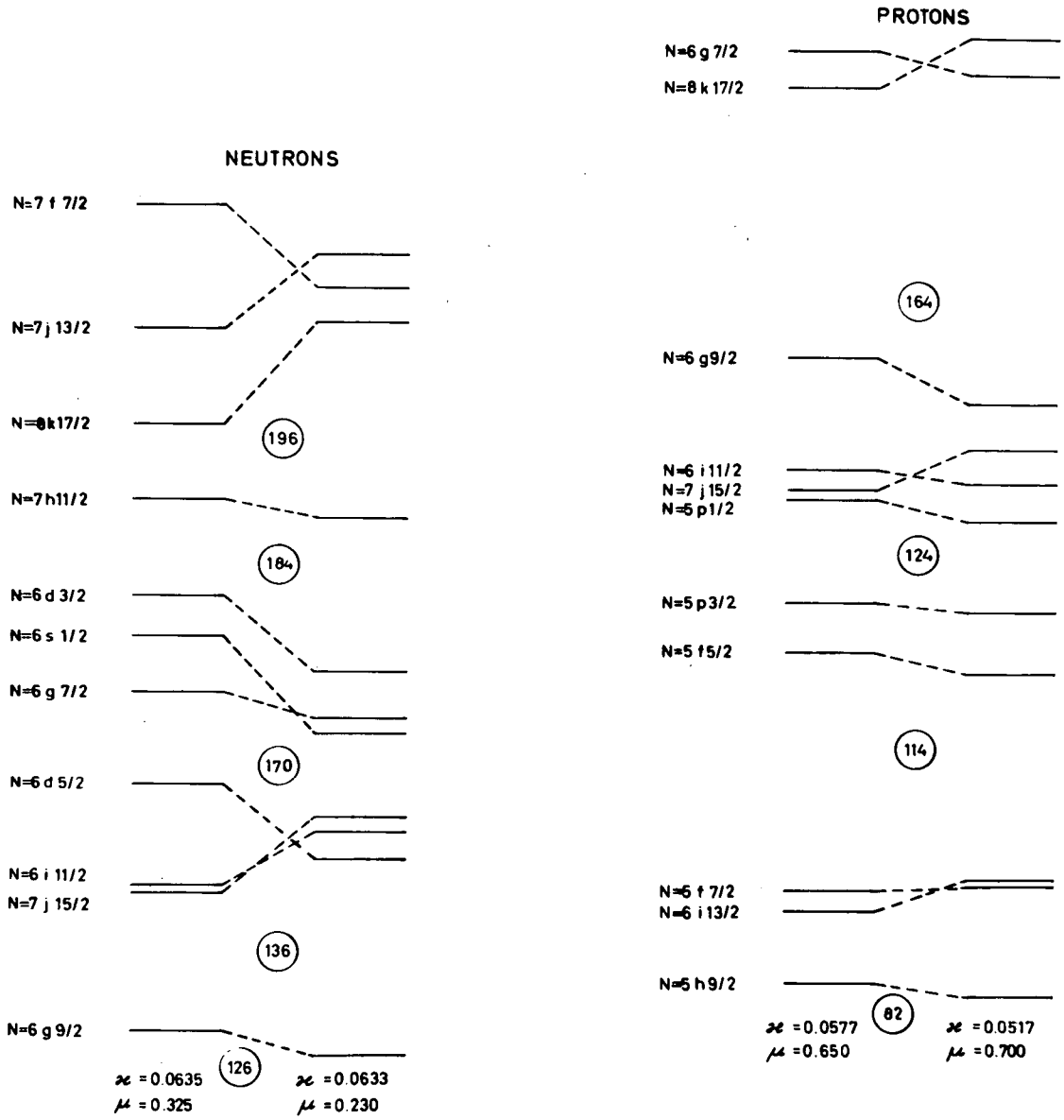

XBL 678-4665

Fig. C. 10-3. Spherical neutron and proton orbitals above Z = 82 and N = 126 for A≈ 250 parameters and for extrapolated A≈ 300 parameters as indicated in the figure.

D. FISSION

1. ELECTRON-INDUCED FISSION IN ^{238}U, ^{209}Bi, AND ^{181}Ta †*

H. R. Bowman, R. C. Gatti, R. C. Jared, G. Kilian, L. G. Moretto,‡ S. G. Thompson, M. R. Croissiaux,††** J. H. Heisenberg,††‡‡ R. Hofstadter,†† L. M. Middleman,†† and M. R. Yearian††

Electron-induced fission of ^{238}U,[1] ^{209}Bi, and ^{181}Ta produced by electrons of energy 250 and 500 MeV from the Stanford Mark III Linear Accelerator has been observed. The fission events were produced in thin targets placed in a standard scattering chamber,[2] and the fragments were detected by using the mica technique.[3] In the ^{238}U targets, the fissions were also observed with semiconductor counters, and preliminary results on the energy spectra of the fragments were obtained. The conditions of the experiments and the measured cross section results are indicated in Table D.1-I.

The pulse-height distribution of fission fragments from electron-induced fission of ^{238}U along with the spectrum obtained (by using the same experimental conditions) from spontaneous fission of ^{252}Cf are shown in Fig. D.1-1. Both these spectra are distorted as a result of the severe electronic pulse clipping (20 nsec) which was required for these measurements. The ^{238}U spectrum is probably displaced upward in pulse height by the residual background of low-energy pulses detected in coincidence with the fission fragments. It can be seen, however, that the spectrum from ^{238}U contains two peaks and therefore seems to indicate the predominantly asymmetric fission mode which is characteristic of excitation energies less than about 40 MeV for this isotope.

The electron beam was found to be relatively free of bremsstrahlung radiation, the latter being separated in the beam transport system[2] by deflecting the electron beam twice before it enters the heavily shielded target area. However, in order to be certain that the fission events observed as described above were, in fact, produced by electrons and not by background radiations, four independent checks were carried out in the following manner:

(i) The fission background in ^{238}U induced by bremsstrahlung associated with the 250-MeV electron beam was measured with both mica and fission counters after the electron beam had been deflected 2.5 cm away from the target while the target itself was maintained in its standard position. The fission rates observed by both methods were less than 1% of the rates observed when the electron beam impinged on the target.

(ii) The dependence of the fission rate in the ^{238}U target on thickness of aluminum radiator placed in front of the target was measured by using a solid state detector. The results obtained with a 250-MeV electron beam are shown in Fig. D.1-2. The point at zero thickness represents the effect of the electron beam itself without the addition of any absorber, and the horizontal line therefore represents the electron-induced fission rate. The increase in fission yield corresponding to points above this line is due to bremsstrahlung-induced fission. The increase in yield observed on introducing the thinnest aluminum radiator is in approximate agreement with a calculation based on known photofission cross sections.[4]

(iii) The general background in the region ≈ 5 cm from the target was measured by placing pieces of ^{238}U, ^{235}U, and ^{232}Th clamped between sheets of mica in this location during the 250-MeV electron bombardments and counting the tracks produced in the mica. Under these conditions the fission rates were much less than 1% of those observed from the ^{238}U targets during the comparable electron bombardments.

(iv) The effect of the bremsstrahlung generated by the electron beam within the ^{238}U and ^{209}Bi targets has been evaluated by means of the known bremsstrahlung fission cross sections and found to contribute less than 1% to the measured electron-induced fission cross sections. As far as the tantalum measurement is concerned, no bremsstrahlung fission cross section was available, so that the photofission contribution could not be calculated; therefore, the measured cross section for Ta should be considered only as an upper limit.

Preliminary measurements of the angular distributions of fission fragments from ^{238}U bombarded with 250-MeV electrons were made by using both the mica technique and semiconductor fragment detectors. The distributions showed less than 10% deviation from isotropy, such a deviation being within the expected errors.

We note that the cross sections for fission induced by electrons as given in Table D.1-I are more than an order of magnitude below the bremsstrahlung-induced fission cross sections at comparable maximum energies.[4] Although the quantitative explanation of the large decrease in cross sections in going to lighter elements is a subject for more detailed analysis, it can be understood in a rough qualitative way in terms of excitation through the giant resonance. The fission barrier for ^{238}U (6 MeV) is below the giant resonance, while for ^{209}Bi (24 MeV) and ^{181}Ta (28 MeV) the fission barriers[5] lie higher than the maximum of the giant resonance peak, and absorption in the latter cases must take place from the high-energy tail of this peak.

The results reported above are only preliminary. It is of interest to extend the cross-section measurements over a much larger energy range, to measure some mass distributions, and to confirm the evidence that the fragment angular distributions are isotropic. It should also be possible to determine whether excitations other than the giant resonance absorption are responsible for the excitation of the nuclei.

Electron-induced fission, besides being interesting in itself, has a built-in energy discriminator (the fission barrier) of very wide range (5 to 50 MeV) that allows a simple differential analysis of the energy transfer in electromagnetic processes. Experimentally, the detection of fission fragments, with mica or electronic devices, is simple and very efficient, so that it can be used with great advantage in the experiments with medium or heavy elements.

Footnotes and References

†Slightly modified version of UCRL-17864, Oct. 1967, to be published in Phys. Rev. Letters.
*Work partially supported by the U. S. Office of Naval Research, Contract [Nonr 225(67)].
‡On leave from Laboratorio di Radiochimica, Università di Pavia, Pavia, Italy.
††Department of Physics and High Energy Physics Laboratory, Stanford University, Stanford, California.
**Present address: Institut de Recherches Nucléaires, Université de Strasbourg, Strasbourg, France.
#Work supported in part by the "Bundesministerium für Wissenschaft und Forschung," Germany.

1. Yu. N. Ranyuk and P. V. Sorokin, Physics Express 9[4], 14 (1967); [condensed from Yadern. Fiz. 5, 531 (1967)].
2. T. Janssens, R. Hofstadter, E. B. Hughes, and M. R. Yearian, Phys. Rev. 142, 922 (1966).
3. P. B. Price and R. M. Walker, J. Appl. Phys. 33, 2625-2628, 3407 (1962).
4. J. A. Jungerman and H. M. Steiner, Phys. Rev. 106, 585 (1957).
5. W. D. Myers and W. J. Swiatecki, Nucl. Phys. 81, 1 (1966).

Table D.1-I. Experimental results.

Target	Thickness	Method used	Fission cross section	
			250-MeV e^-	500-MeV e^-
$_{92}^{238}U$ [a]	$85\,\mu g/cm^2$	Mica	$(6.0 \pm 1.2) \times 10^{-27} cm^2$	$(9.4 \pm 1.9) \times 10^{-27} cm^2$
$_{92}^{238}U$	$162\,\mu g/cm^2$	Counter	$(5.0 \pm 1.0) \times 10^{-27} cm^2$	$(7.0 \pm 1.4) \times 10^{-27} cm^2$
$_{83}^{209}Bi$	$1\,mg/cm^2$	Mica	$(2.3 \pm 0.5) \times 10^{-29} cm^2$	$(1.4 \pm 0.3) \times 10^{-28} cm^2$
$_{73}^{181}Ta$	$4\,mg/cm^2$	Mica		$3.9 \times 10^{-31} cm^2$ [b]

a. $^{235}U/^{238}U = 1.12 \times 10^{-4}$ in target sample.
b. Not corrected for photofission contribution [see (iv) in text].

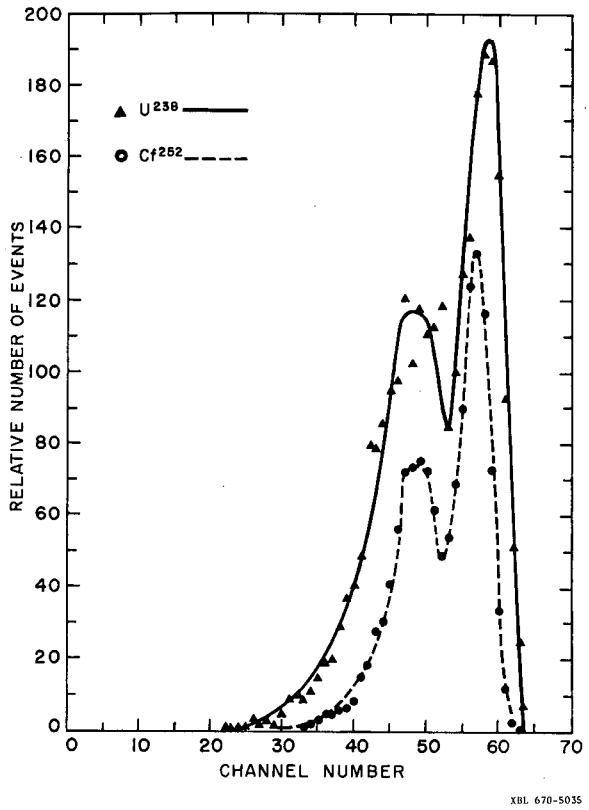

Fig. D.1-1. Pulse-height spectrum of fission fragments.

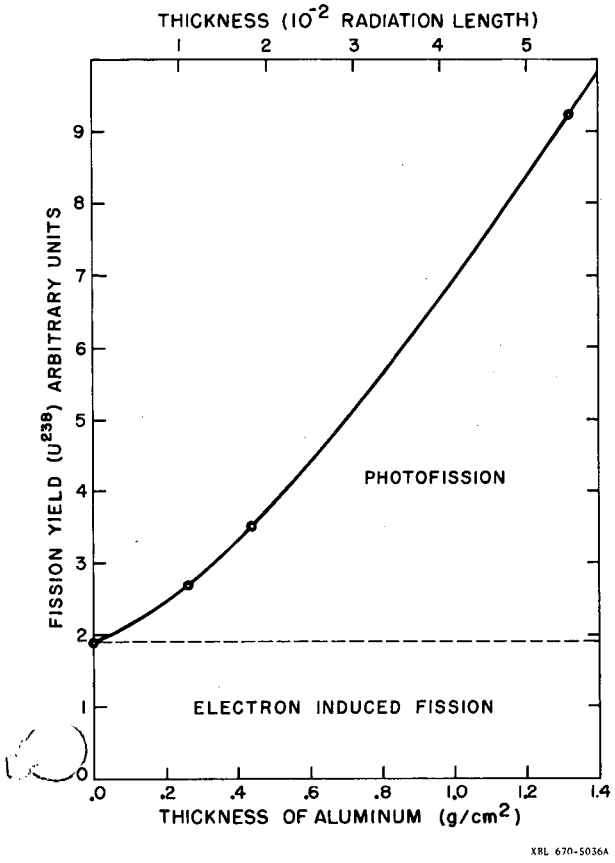

Fig. D.1-2. Dependence of fission rate on radiator thickness.

2. K x-RAY YIELDS OF PRIMARY ^{252}Cf FISSION PRODUCTS†

R. L. Watson,* H. R. Bowman, and S. G. Thompson

Several recent investigations have resulted in measurements of the yields of K x rays and conversion electrons arising from the nuclear deexcitation of primary (pre-beta-decay) fission products.[1-4] In these studies, the x-ray and electron yields were measured in association with the fragment masses, and the resulting distributions have provided new information about the general features of nuclear structure in the fission product region.

This study was undertaken with the purpose of measuring the intensities of both the light and heavy primary fission product K x rays by taking advantage of the suitability of semiconductor detectors for coincidence applications. One value of such a study is that the results can be directly compared with the bent-crystal spectrometer measurements[5,6] to shed additional light on the origin of the observed even-odd effect. In addition, a direct comparison can be made between this determination of primary K x-ray yield as a function of atomic number and the previous determinations of primary K x-ray and conversion electron yields as functions of mass.

The energy spectrum of K x rays (measured with a 0.6-mm^2 × 3-mm lithium-drifted silicon detector) arising from primary ^{252}Cf fission products is shown in Fig. D.2-1. Since the x-ray groups contributing to this spectrum were not fully resolved, it was necessary to resort to a

least-squares peak-fitting procedure in order to determine accurate values of the x-ray intensities for each element.

A computerized peak-fitting procedure was devised in which the four x-ray components comprising the K x-ray group for a given element (i.e., the $K\alpha_2$, $K\alpha_1$, $K\beta_1$, and $K\beta_2$ components) were represented by four Gaussian functions. Each Gaussian function of every x-ray group was rigidly defined by specifying its first moment, standard deviation, and area relative to the area of the Gaussian function representing the $K\alpha_1$ x-ray component. A fit to the experimental data points was then achieved by varying, in combination, the areas of the various groups of Gaussian components, utilizing the method of least squares.

The final fitted x-ray distribution associated with the heavy fission products (Sn through Sm) is shown in Fig. D.2-2. As may be seen, the fit is quite good, and the fact that only one variable parameter was needed adds considerable confidence to the results.

The yields of K x rays per fission are shown in Fig. D.2-3, plotted as a function of atomic number, and listed in Table D.2-I. Several noteworthy features are apparent; namely (a) a pronounced even-odd fluctuation for atomic numbers 52 through 57, (b) a surprisingly low yield for xenon (Z = 54), (c) a maximum in heavy fission product x-ray yield occurring at cesium (Z = 55), and (d) a fairly smooth decrease in x-ray yield on either side of the maximum in the light-product x-ray yield, which occurs at technetium (Z = 43). Hence, it is found that two of the characteristics observed by John et al.[6] and Canty et al.[5] in the total (primary plus secondary) x-ray spectrum (i.e., the even-odd fluctuation and low xenon x-ray yield) are characteristic of the primary x-ray spectrum as well. It is noted, however, that the even-odd fluctuation arising from the primary fission products extends over a much more restricted region.

In order to estimate the x-ray yields per fragment, the independent fission yield of each isotope formed in the spontaneous fission of ^{252}Cf was calculated by using the prescription given by Wahl et al.[7] By summing the calculated independent yields of all isotopes having the same atomic numbers over mass,

$$Y(Z) = \sum_{M=1}^{n} Y_{I_M}(Z) \ , \qquad (1)$$

the element yields, Y(Z), were then computed. By dividing the x-ray yields per fission by these element yields, the x-ray yields per fragment were obtained, and are shown in Fig. D.2-4, plotted as a function of atomic number.

It is interesting to compare Fig. D.2-4 with Fig. D.2-5, taken from Kapoor et al.,[2] in which is plotted the K x-ray yield per fragment versus fragment mass. For the most part, the general structural features are quite similar. Both figures exhibit sharp peaks in the light fission-product regions with slight discontinuities to the right of the yield maxima, low yields in the vicinity of the doubly closed proton (Z = 50) and neutron (N = 82) shells, and a rather abrupt rise in yield in the heavy fission-product region. One striking feature in Fig. D.2-5 which seems to be missing in Fig. D.2-4 is the sudden drop in yield to the right of the maximum yield in the heavy fission-product region.

Most of the error in these determinations will most likely be restricted to the even mass chains, since the x-ray fluctuations are probably most pronounced between adjacent even-even and odd-odd products. In fact, if the fluctuation between these pairs is fairly systematic, then the x-ray yield measurements may average out in such a way as to give Z_p values which do not deviate appreciably from the true values after all. It is especially significant, in connection with these considerations, to note that in the data given by Kapoor et al.[2] the largest deviations between the Z_p values of complementary light and heavy fragments from a sum of 98 ($Z_{p_{lt}} + Z_{p_{hy}} = 98$) occur for heavy-fragment Z_p values of 52.8, 55.4, and 56.1. The deviations for these values were 0.4, 0.4, and 0.3 units respectively.

Footnotes and References

†Resumé of Phys. Rev. 162, 1169 (1967).
*Present address: Department of Chemistry, Texas A & M University, College Station, Texas.

1. L. E. Glendenin and J. P. Unik, Phys. Rev. 140, B1301 (1965).
2. S. S. Kapoor, H. R. Bowman, and S. G. Thompson, Phys. Rev. 140, B1310 (1965).
3. R. A. Atneosen, T. D. Thomas, W. M. Gibson, and M. L. Perlman, Phys. Rev. 148, 1206 (1966).
4. R. L. Watson, A Study of the Internal Conversion Electrons Emitted Within Three Nanoseconds After the Spontaneous Fission of ^{252}Cf (Ph. D. Thesis), UCRL-16798, July 1966.
5. J. E. Canty, C. D. Coryell, L. Leifer, and N. C. Rasmussen, Bull. Am. Phys. Soc. 10, 481 (1965).
6. W. John, R. Massey, and B. G. Saunders, Phys. Letters 24B, 336 (1967).
7. A. C. Wahl, R. L. Ferguson, D. R. Nethaway, D. E. Troutner, and K. Wolfsberg, Phys. Rev. 126, 1112 (1962).

Table D.2-I. K x-ray yields of primary ^{252}Cf fission products.

Element	K x-rays per fission ($\times 10^2$)
$_{38}$Sr	0.33 ± 0.10
$_{39}$Y	0.54 ± 0.07
$_{40}$Zr	1.37 ± 0.09
$_{41}$Nb	1.80 ± 0.11
$_{42}$Mo	2.66 ± 0.16
$_{43}$Tc	5.36 ± 0.32
$_{44}$Ru	3.77 ± 0.23
$_{45}$Rh	1.76 ± 0.11
$_{46}$Pd	1.82 ± 0.12
$_{47}$Ag	0.84 ± 0.07
$_{48}$Cd	0.24 ± 0.10
$_{49}$In	< 0.10
$_{50}$Sn	0.18 ± 0.07
$_{51}$Sb	0.48 ± 0.07
$_{52}$Te	0.48 ± 0.07
$_{53}$I	3.54 ± 0.22
$_{54}$Xe	1.64 ± 0.11
$_{55}$Cs	7.45 ± 0.45
$_{56}$Ba	4.35 ± 0.26
$_{57}$La	6.11 ± 0.37
$_{58}$Ce	4.15 ± 0.25
$_{59}$Pr	3.96 ± 0.25
$_{60}$Nd	2.50 ± 0.17
$_{61}$Pm	1.67 ± 0.14
$_{62}$Sm	0.97 ± 0.16

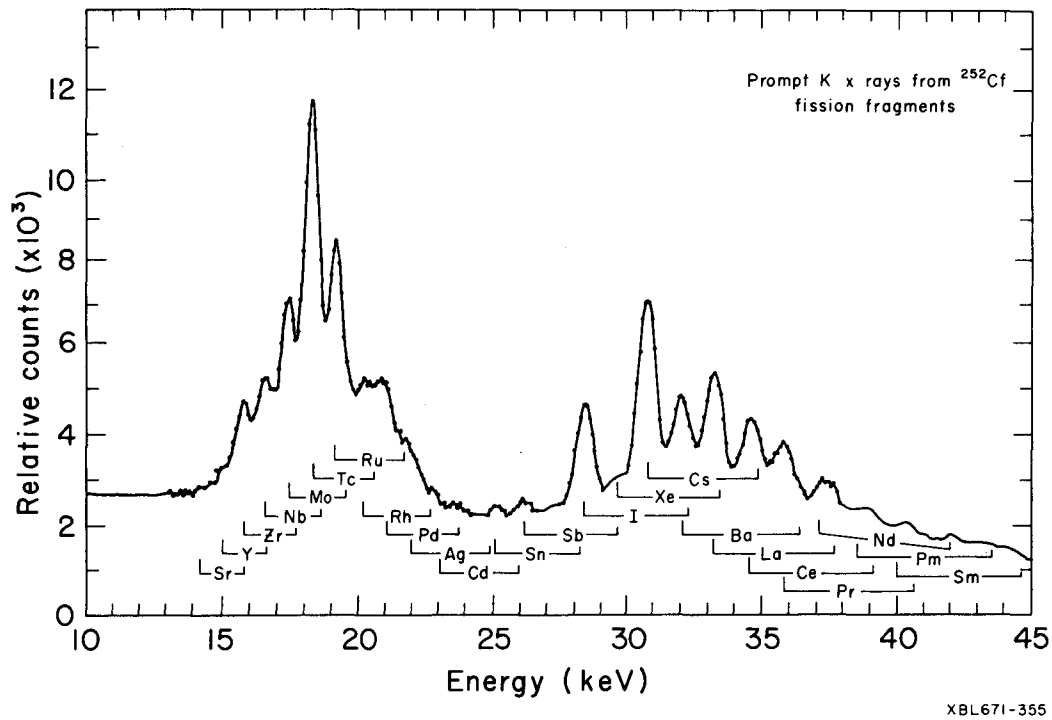

Fig. D.2-1. The energy spectrum of K x rays emitted by primary ^{252}Cf fission products in coincidence with fission. The locations of the Kα- and Kβ-x-ray groups are indicated for most fission-product elements by brackets.

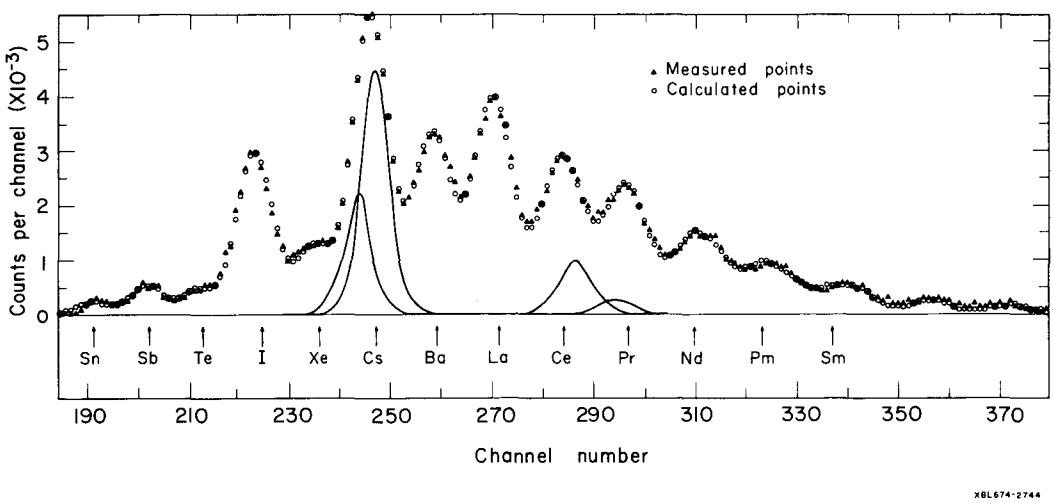

Fig. D.2-2. The measured and calculated K x-ray distributions associated with the primary heavy fission products (Sn through Sm) formed in the spontaneous fission of ^{252}Cf. The Gaussian fitting functions for the element cesium are shown by the solid curves, and the locations of the centroids of the Kα_1-x-ray components belonging to the other elements are indicated by arrows.

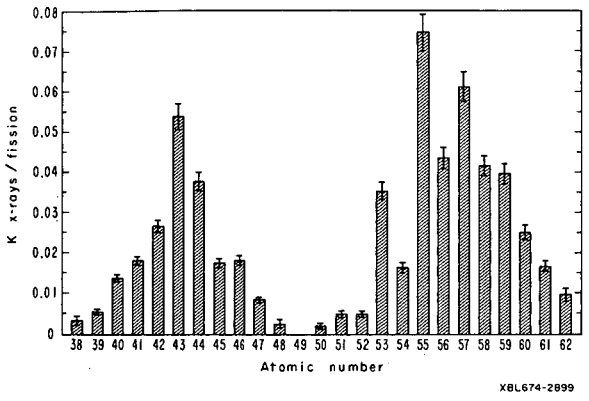

Fig. D.2-3. The observed yields of K x rays per fission arising from primary ^{252}Cf fission products within 93 nsec after fission.

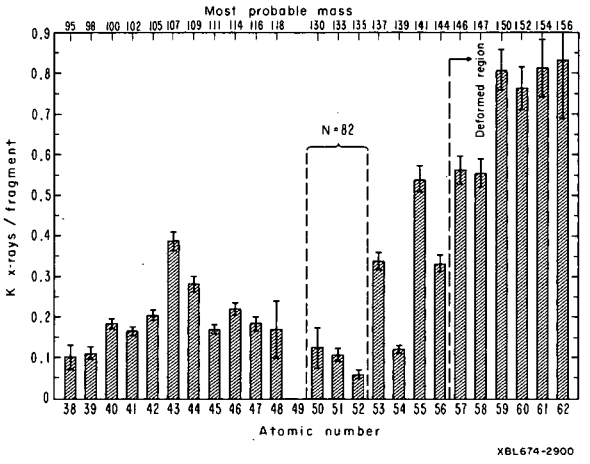

Fig. D.2-4. Estimates of the yields of K x rays per fragment arising from primary ^{252}Cf fission products. The indicated errors reflect only the uncertainty in the x-ray intensity measurements. Atomic numbers for which N = 82 closed-shell fission products are expected to occur are denoted, and the approximate boundary of the deformed region is shown. The top scale indicates the calculated most probable fragment mass associated with each atomic number.

Fig. D.2-5. The observed yields of K x rays per fragment emitted within 50 nsec after fission from primary ^{252}Cf fission products, versus the final masses (M_f^*) of the fragments. The top scale indicates the average atomic number associated with each fragment mass (taken from Kapoor et al., Ref. 2).

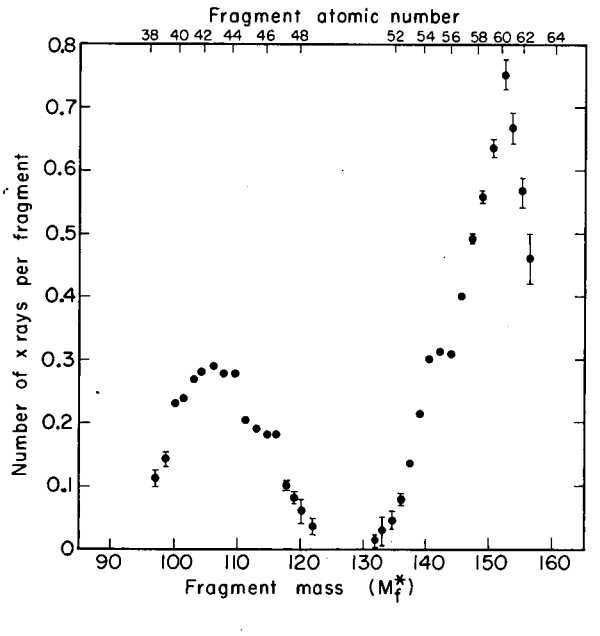

3. x-RAY-γ-RAY COINCIDENCE MEASUREMENTS ON SHORT-LIVED FISSION PRODUCTS

J. B. Wilhelmy, S. G. Thompson, and J. O. Rasmussen

X-ray-γ-ray coincidence measurements have been performed on short-lived fission products produced in the spontaneous fission of ^{252}Cf. With the aid of the high-resolution solid-state detectors now available, it has become possible to resolve the K x-ray groups for the individual elements produced in fission. By performing x-ray-γ-ray coincidence measurements the element from which the γ ray was emitted can be identified. For the study of short-lived fission products this technique eliminates the necessity of performing the time-consuming radiochemical separations which have been the limiting factor in obtaining spectroscopic information on these isotopes. The fundamental limitation of this method is that not all γ rays are in coincidence with K x rays. If the nucleus is decaying by β^- emission, the requirement for the coincidence is that there be a prompt γ-ray cascade with at least one of the members undergoing internal conversion in the K-electron shell.

By use of this technique, measurements were made on the fission products from the spontaneous fission of ^{252}Cf. A 10-μg source of ^{252}Cf ($\approx 3.7 \times 10^8$ fissions/min) was electroplated onto a platinum foil. The source was covered with a gold foil of approximately 1 mg/cm^2 thickness and placed in the center of a 2-ft^3 Lucite box. A continuously moving belt was passed under the source, allowing the fission products to become embedded into the belt. The products were then transported to the counting position where x-ray-γ-ray coincidence measurements were performed by use of a standard fast-slow coincidence arrangement. The x rays were detected with a lithium-drifted silicon detector (2 cm^2 × 0.3 cm), and a lithium-drifted germanium detector (8 cm^2 × 0.8 cm) was used to detect the γ rays. The coincident analog signals were stored event by event on a multiparameter pulse-height analyzer and then transferred onto magnetic tape. The magnetic tape was subsequently processed by a CDC 6600 computer to give γ-ray spectra with respect to x-ray energy intervals. Positive assignment of γ rays to specific elements could then be obtained by using the computer to sort out and identify the x-ray spectrum which was in coincidence with the γ-ray line. The requirements for assignment are that both the Kα and Kβ x-ray groups be observed in coincidence with the γ ray and that they have the correct energies and relative intensities. Half-life information was obtained for the isotopes by varying the transit time between the source and the detectors. Since the fission rate was a constant, the density of fission fragments on the belt decreased as the velocity past the source increased. Therefore, in the analysis of the half-life data, the observed counting rate was normalized to a constant density.

Coincidence information was taken at 19 different transit times from as long as 135 minutes to as short as 0.27 second. Half-life information was obtained on about 350 γ-ray lines in the energy interval from 60 to 650 keV. These have been tentatively assigned to approximately 75 isotopes. Figure D.3-1 is an example of the computer-processed data and shows the γ-ray spectrum obtained upon sorting on an x-ray energy interval containing the Kα x rays of neodymium. The indicated γ rays have been assigned to transitions arising after the beta decay of ^{147}Pr. The numbers above the peaks are the energies in keV, and the numbers in parentheses are the observed half-lives for these lines. This spectrum was chosen as an example because it has a relatively large number of γ rays of varying intensities and is therefore indicative of the type of accuracy that is obtainable by this method. The literature value for the half-life of this isotope is 12 min,[1] and the values obtained experimentally were between 11.7 and 15.9 min, with both extremes being on low-intensity peaks.

To complement the coincidence measurements high-resolution x-ray and γ-ray singles are now being taken. This allows the utilization of the much higher efficiency of singles measurements to obtain better intensities for the γ-ray lines observed in the coincidence experiment, and it also permits the observation of γ-ray lines which, due to the decay scheme, were not seen in the coincidence experiment. An interesting feature which can be seen readily in the γ-ray singles measurements is the rapid rate at which the activity decreases when the transit time becomes faster than 1 sec. Figure D.3-2 shows four high-resolution γ-ray singles spectra with times of transit between 2.7 and 0.27 sec. The two main features that can be noted are first, the complexity of the singles spectra, and second, the rapid decrease of γ-ray intensity as a function of time. It can be seen that there are no γ rays with half-lives shorter than about 1 sec. This rapid falloff of γ-ray intensity at short times is presumed to be consistent with beta decay theory, which predicts that there should not be beta decay shorter than on the order of 1 sec.

Figure D.3-3 is an example of a useful technique which becomes apparent upon study of the shorter-lived isotopes. This figure is a plot of counting rate versus time for a 258-keV γ-ray line observed in the high-resolution singles run. From the coincidence measurements it is known that this γ ray is associated with a lanthanum K x ray. It is therefore assigned to a nuclear transition following the beta decay of a barium isotope. At short times the decay curve breaks away from the straight line and begins to turn over. This is because the barium isotope is being fed by its cesium precursor. The values of the ordinate intercepts of the two curves are then seen to be important. The bottom intercept is related to the independent fission yield of the barium isotope, and the top intercept is related to the cumulative yield of this isotope. The ratio of the independent to the cumulative yield depends on the mass number of the isotope. Using experimental values for the most probable charge of a mass chain $(Z_p)^2$ and assuming a Gaussian distribution about this Z_p,[3] one can calculate the independent-to-cumulative yield ratio for various masses of barium isotopes produced in the spontaneous fission of ^{252}Cf. These ratios are shown on the figure, and are quite sensitive to the mass number. The experimental value obtained in this preliminary run is 0.67 ± 0.07, which is closest to mass 143.

This example demonstrates the method by which the coincidence and singles measurements can be used in a complementary manner. Improvements are being made in this technique to give more precise determination of these numbers. It is hoped that they will be useful not only in making mass assignments but also for giving information about irregularities in mass yields about the Z_p.

The coincidence measurements have produced large amounts of data which give preliminary points of knowledge throughout the fission product region. With high-resolution singles it is possible to go back and follow more accurately the properties of these identified lines. Then, knowing the characteristics, it is possible to identify lines that were not seen in the coincidence experiment because of their decay scheme. This, then, is a method of obtaining information on essentially all the short-lived isotopes produced in fission.

References

1. C. M. Lederer, J. M. Hollander, and I. Perlman, Table of Isotopes (John Wiley and Sons, New York, 1967).
2. S. S. Kapoor, H. R. Bowman, and S. G. Thompson, Phys. Rev. 140, B1310 (1965).
3. A. C. Wahl, R. L. Ferguson, D. R. Nethaway, D. E. Troutner, and K. Wolfsberg, Phys. Rev. 126, 1112 (1962).

Fig. D.3-1. γ-Ray spectrum in coincidence with Kα x rays of neodymium. The unbracketed numbers are the energies of the peaks in keV, and the numbers in parentheses are the measured half-lives of the lines in min.

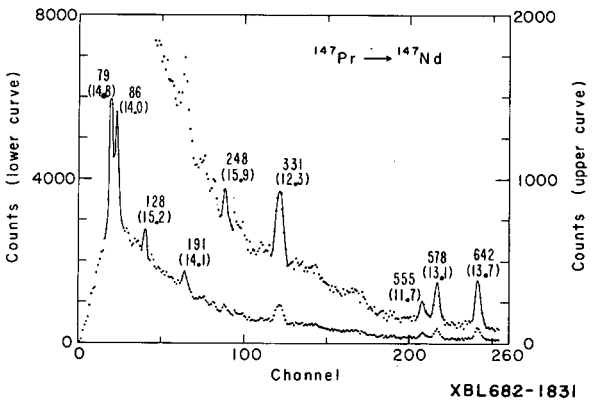

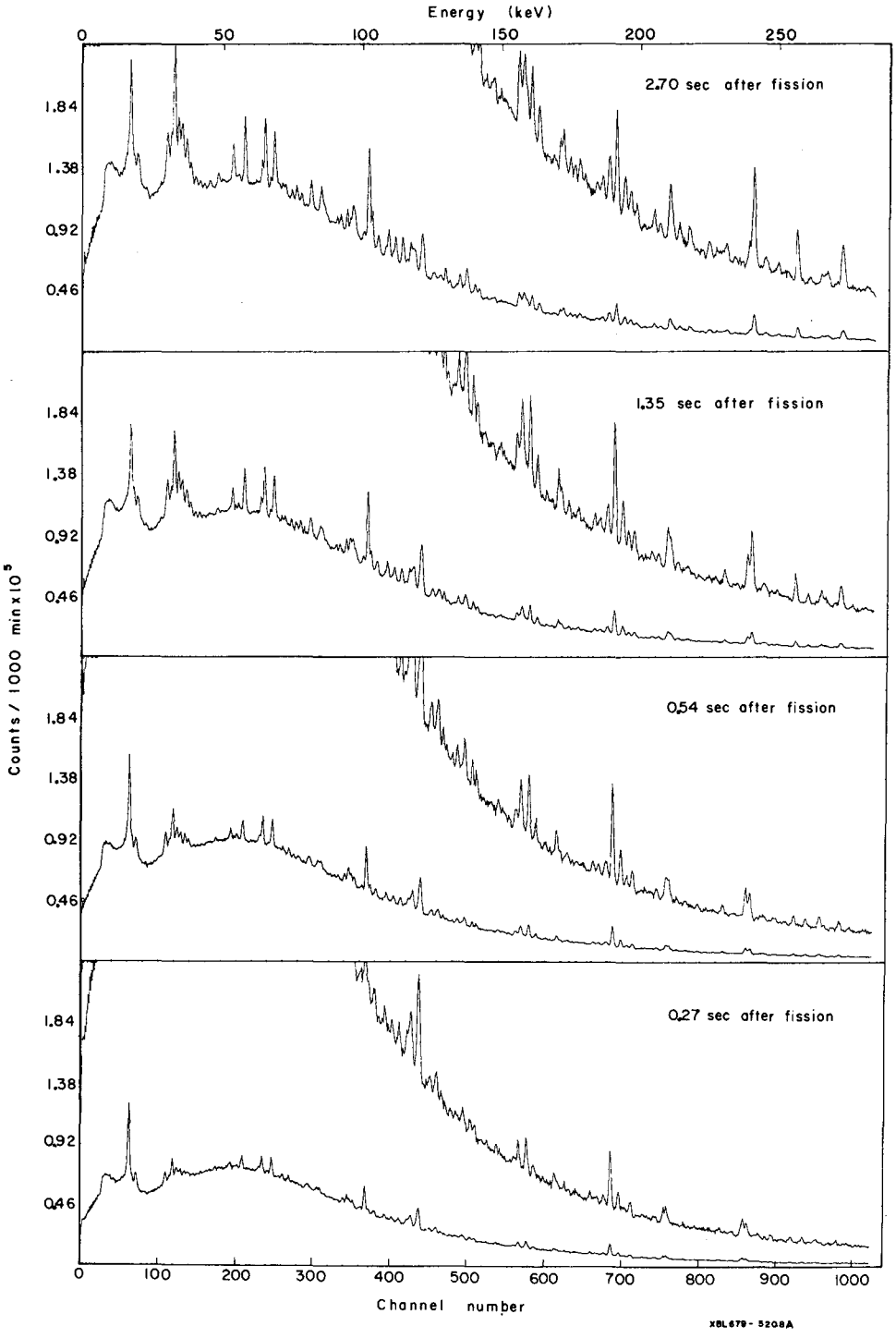

Fig. D.3-2. γ-Ray singles spectra recorded from a continuously moving belt with transit time from source to detector of 2.70, 1.35, 0.54, and 0.27 sec.

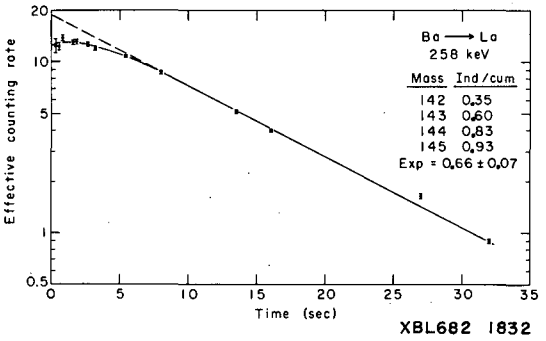

Fig. D.3-3. A plot of the effective counting rate (the counting rate normalized to a constant density of fission fragments on the moving belt) versus time for a 258-keV γ-ray line. This line was known from coincidence measurements to be associated with lanthanum K x rays. The time-equals-zero intercepts are related to the independent and cumulative fission yield of the decaying barium isotope. The ratio of these yields is dependent on the mass of the isotope.

4. INVESTIGATIONS OF THE RELATIVE STABILITY OF SUPERHEAVY NUCLEI

Heiner Meldner†

The fissilities of nuclei below the uranium region depend primarily on rather smooth average nuclear properties, even though in principle they should be determined from a highly complicated many-fermion system. Therefore, for such nuclei the fissilities can be expressed with reasonable accuracy as a simple function of charge and mass numbers, as is done, for example, in the framework of the liquid-drop model.

The stabilities (or lifetimes) are usually described in terms of fission-barrier heights. For medium and heavy nuclei, barrier heights decrease on the average with increasing mass number, although they do show some interesting fluctuations. In particular, barrier heights are systematically larger at closed shells (magic nucleon numbers).

It turns out that the contribution to the barrier height due to shell closures (i.e., structure-dependent tendencies to prefer spherical shapes) is negligible for the proton number Z = 50 and is about 30% of the total for Z around 82 near the beta stability line. In the region beyond Z = 110 the average value or liquid-drop-model barrier becomes practically negligible, since it is quite small compared with the uncertainties in our knowledge of the structure-dependent contributions there.

However, it is just this fact that makes experimental and theoretical research in the superheavy-element region so very hard and challenging. Since the nuclear stability there depends so sensitively on details of the shell structure, any information gained in this region can considerably improve our understanding of the nucleus.

Theoretically the problem is to find a way to describe on the same footing the known gross nuclear properties, like total binding energies (masses), and small-structure effects or responses of the full system, like shell effects and isotope shifts. The region Z = 114, for example, is then investigated by extrapolation. Naturally our confidence in such phenomenology increases when, with a very small number of fixed parameters, more independent nuclear structure data are reproduced and the region of nuclei where this works is enlarged. This means that only an extremely good nuclear shell model calculation can be of help here. One such attempt is reported in Papers C.7 and C.8. Mathematically, the problem there is to solve numerically an integro-differential equation.

Footnote

†NATO Fellow. On leave from Freie Universität Berlin, West Berlin, Germany.

5. SHELL EFFECTS IN NUCLEAR LEVEL DENSITIES

A. Gilbert†

In most nuclear theories it is assumed, at least as a first approximation, that there is an average nuclear potential, whose single-particle states are occupied by the nucleons as independent particles. The total energy is just the sum of the nucleon energies. Calculating the nuclear level density is reduced to a combinatorial problem: in how many ways can the nucleons be distributed among the single-particle states so as to get a given total energy?

In the past, such calculations have assumed that the single-particle spectrum was a slowly varying function of energy. But the outstanding feature of the shell model is the presence of gaps in the spectrum, corresponding to closed-shell configurations. The work presented here incorporates this feature of the shell model.

The single-particle spectrum that we consider is shown in Fig. D.5-1. The spectrum is periodic in energy; d gives the distance between gaps and δ the size of the gap. Between gaps the density of single-particle states is $g = c A$; g is written in this manner to facilitate the correspondence with the Fermi gas model.

This representation has been used to calculate expected densities of neutron resonances for nuclei in the vicinity of closed shells. Odd-even effects were taken into account simply by subtracting from the excitation energy the pairing energy (for odd-A nuclei) or twice the pairing energy (for even-even nuclei). Pairing energies were obtained from the work of Myers and Swiatecki on nuclear masses.[1]

Table D.5-I shows a comparison between experimental and calculated values of ρ_n, the density of neutron resonances, for nuclei in the vicinity of ^{208}Pb. The parameter d was taken to be 7 MeV; however, the results are not sensitive to this quantity. The parameter c is fixed by considering nuclei like ^{195}Pt and ^{197}Au; these nuclei are relatively far from closed shells, so that calculated resonance densities are not critically dependent on the size of the shell gap. A value of $c = 0.067$ MeV^{-1} seems appropriate.

Once c is determined, the shell gap δ is determined from the nuclei closest to the closed-shell configuration (^{206}Pb and ^{207}Pb). This gives a value of δ between 2.0 and 2.4 MeV.

The results of such comparisons indicate that, with appropriate values of the parameters, this single-particle spectrum can be used to calculate neutron resonance densities. But the scheme has its limitations. The parameters that give the best fits to experimental data vary from one closed-shell region to another. There is some question about the significance of these parameters, in relation to actual shell-model spectra. The logical continuation of this work would be to redo the calculations with such spectra. This would probably require a more careful consideration of pairing; some adaptation of the superconductor theory of the nucleus would be necessary.

Footnote and Reference

† Present address: Lawrence Radiation Laboratory, Livermore, California.

1. William D. Myers and Wladyslaw J. Swiatecki, Nuclear Masses and Deformations, UCRL-11980, May 1965.

Table D.5-I. A comparison of experimental and calculated level densities. The experimental values of ρ_n are obtained from the data on neutron resonances compiled by the Brookhaven group.

Target nucleus	ρ_n (experimental) (MeV^{-1})	ρ_n (calculated) (MeV^{-1}) c = 0.065 δ = 2.0 (MeV)	c = 0.067 δ = 2.0 (MeV)	c = 0.067 δ = 2.2 (MeV)	c = 0.067 δ = 2.4 (MeV)
^{195}Pt	58 000 ± 10 000	34 000	48 000	47 000	46 000
^{197}Au	62 000 ± 4000	47 000	66 000	62 000	60 000
^{206}Pb	22 ± 10	37	43	31	23
^{207}Pb	18 ± 10	21	24	16	11

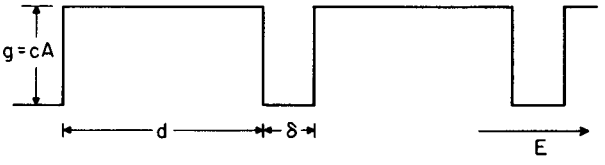

XBL682-1833

Fig. D.5-1. The assumed single-particle level density g as a function of the single-particle energy E.

6. A FOUR-DIMENSIONAL STUDY OF CONVERSION ELECTRONS AND K x RAYS FROM PRIMARY FISSION FRAGMENTS OF SPECIFIC MASS AND ATOMIC NUMBER

R. L. Watson,† R. C. Jared, S. G. Thompson, and J. O. Rasmussen

In a continuing program of investigation dealing with the prompt radiations emitted in the spontaneous fission of ^{252}Cf, an experiment has been performed in which the conversion-electron, the K x-ray, and the fission-fragment energies associated with specific fission events were all measured simultaneously. The value of such a study stems from the fact that the fission fragment energies may be used to determine the average fragment masses, and the x-ray energies specify the fragment atomic numbers. Hence, measuring these energies along with the energies of conversion electrons in a fourfold coincidence experiment allows one to correlate conversion-electron spectra and x-ray intensities with fragment mass and atomic number.

The experimental arrangement used is shown in Fig. D.6-1. A weightless source of ^{252}Cf was located between two fission-fragment detectors in a highly convergent fringing field produced by a large electromagnet. The magnetic field was used to steer electrons emitted from fragments near the magnet symmetry plane 90 deg around the circular pole tips to a lithium-drifted silicon electron detector shielded from other radiations emitted at the source.[1] (Energy resolution ≈ 2.5 keV FWHM at 600 keV.) The fission source was positioned 1 cm from the magnet symmetry plane, and therefore only electrons emitted approximately 1 nsec after fission (the average time of flight for a fragment to travel to the magnet symmetry plane) were detected. Directly below the fragment detector—source axis was mounted a lithium-drifted silicon x-ray spectrometer having an energy resolution of 0.70 keV (FWHM) at an energy of 14 keV.

The energy pulses from each detector (electron, fragment 1, fragment 2, and x ray) were analyzed by a Nuclear Data, Inc. multidimensional pulse-height analyzer, and recorded on magnetic tape event by event. The coincidence system was arranged in such a way as to allow the simultaneous analysis of the following event types:

Type 1. Fragment 1—fragment 2—electron coincidences.
Type 2. Fragment 1—fragment 2—x-ray coincidences.
Type 3. Fragment 1—fragment 2—electron—x-ray coincidences.
Type 4-9. Digital gain stabilizer coincidences for all detectors.

Five dimensions of the multidimensional system were required--one dimension for the output of each detector and one dimension for the identification of each coincidence event as one of the nine possible event types.

The data obtained in the experiment are currently being analyzed. A large amount of rather complicated sorting on the CDC 6600 computer is required in order to extract the desired correlations. Among the primary objectives of the analysis are:

(i) Analysis of the electron spectra resulting from a sort of type 1 events with respect to fragment mass.

(ii) Analysis of the x-ray spectra resulting from a sort of type 2 events with respect to fragment mass. From these spectra, it should be possible to determine the K x-ray yields as a function of both mass and atomic number.[2]

(iii) Analysis of the electron spectra resulting from a sort of type 3 events with respect to both fragment mass and atomic number. These spectra should be considerably simplified from those sorted only with respect to fragment mass--not only because the x-ray energy sort fixes the atomic number of nuclides contributing to each mass-sorted spectrum, but also because the K x-ray coincidence requirement eliminates all electron lines other than K conversion lines (including Auger lines).

As a preliminary example of the gross x-ray spectra measured in this investigation, we present in Fig. D.6-2 a comparison between the (unsorted) x-ray spectrum arising from a collection of type 2 events and the corresponding (unsorted) x-ray spectrum arising from a collection of type 3 events.

Footnote and References

† Present address: Department of Chemistry, Texas A & M University, College Station, Texas.

1. R. L. Watson, J. O. Rasmussen, S. G. Thompson, and H. R. Bowman, Rev. Sci. Instr. 38, 905 (1967).
2. R. L. Watson, H. R. Bowman, and S. G. Thompson, Phys. Rev. 162, 1169 (1967).

Fig. D.6-1. Experimental arrangement for electron—fragment 1—fragment 2—x-ray fourfold coincidence experiment.

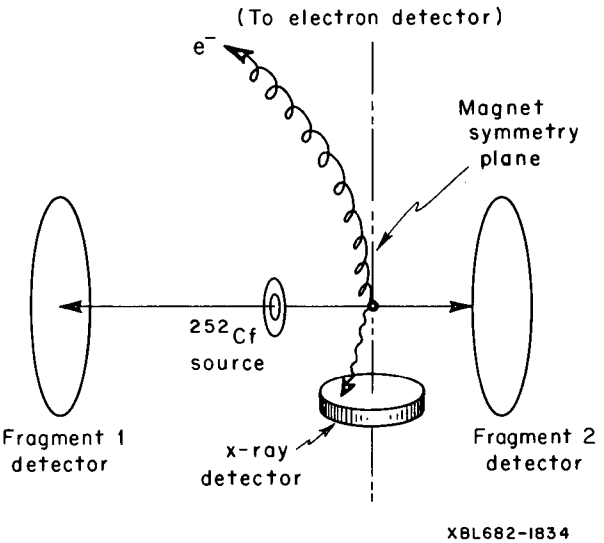

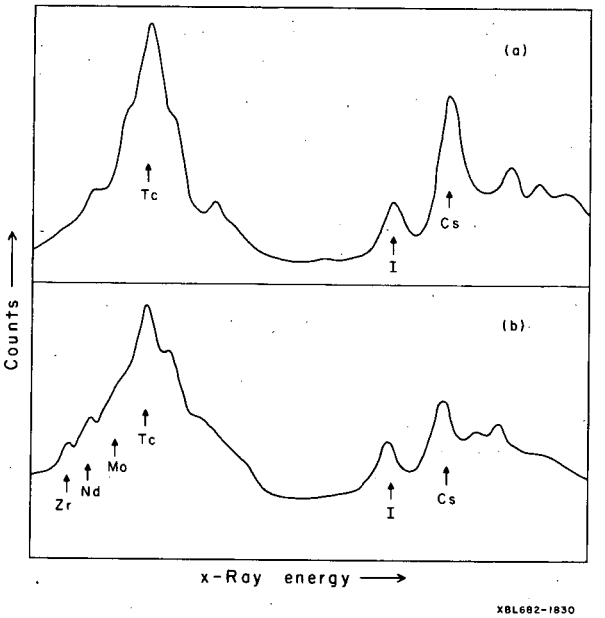

Fig. D.6-2. A comparison between (a) the unsorted x-ray spectrum in coincidence with both fission fragments and (b) the unsorted x-ray spectrum in coincidence with both fission fragments and a conversion electron.

7. FIRST-CHANCE FISSION PROBABILITIES FOR ^{188}Os AND ^{187}Os

Luciano G. Moretto,† Raymond C. Gatti, and Stanley G. Thompson

The dominant modes of decay in intermediate and heavy nuclei at moderate excitation energies are fission and neutron emission; the total decay width Γ_{total} can therefore be expressed as the sum of the fission width Γ_f and neutron width Γ_n. Fission does not occur only for the produced compound nucleus, but competes also at every stage of neutron evaporation. Fission occurring for the original compound nucleus is called first-chance fission, that occurring after the emission of one neutron, second-chance fission, and so on. It follows that the fission cross section is not simply related to the fission decay width Γ_f or to the first-chance fission probability Γ_f/Γ_{total}, which are the quantities of interest for comparison with theoretical calculations. A simple way to evaluate the first-chance fission probability is to determine the total fission probability as a function of excitation energy for two isotopes differing only by a neutron. Let us call $P^{A}_{f,total}(E)$ the total fission probability of a compound nucleus of mass A and excitation energy E, and $P^{A-1}_{f,total}(E)$ the same quantity for the isotope of mass A-1. Neglecting angular momentum effects, we have

$$P^{A}_{f,total}(E) = \frac{\Gamma_f}{\Gamma_{total}}(E) + \left(1 - \frac{\Gamma_f}{\Gamma_{total}}(E)\right)\int_0^{E-B_n} P^{A-1}_{f,total}(E - B_n - \epsilon)\, g(\epsilon)\, d\epsilon, \qquad (1)$$

where B_n = neutron binding energy, ϵ = neutron kinetic energy,

$g(\epsilon)$ = normalized distribution in neutron kinetic energy.

The quantities $P^{A}_{f,total}$ and $P^{A-1}_{f,total}$ can be obtained by dividing the experimental fission cross sections by the total reaction cross section.

The first-chance fission probability has been determined for ^{188}Os and ^{187}Os. The He^4-induced fission cross sections of ^{182}W, ^{183}W, and ^{184}W have been measured from 35 to 120 MeV bombarding energy.

The experimental equipment consists of a fission chamber that allows the measurement of the fission fragment angular distribution; mica was used as a fission detector. From 55 to 120 MeV bombarding energy, a fission chamber of 6.35 cm radius was used; the targets were about

300-$\mu g/cm^2$ thick WO_3 on a 300-$\mu g/cm^2$ Al backing. For the lower energies, because of the very small fission cross section, a chamber of 2.84 cm radius was used; the targets consisted of a water-cooled copper block covered with more than 20 mg/cm^2 high-purity silver (to prevent fissions occurring on the copper impurities escaping from the target) on which ≈ 1 mg/cm^2 tungsten oxide was evaporated. Enough overlapping between the two sets of measurements was obtained in order to allow for internormalization.

The fission cross section curves as a function of excitation energy are shown in Fig. D.7-1. To transform these quantities to total fission probabilities it is necessary to evaluate the total reaction cross section; this has been determined here by an optical model calculation. The total fission probabilities are shown in Fig. D.7-2. These three curves can be used to evaluate, through Eq. 1, the first-chance fission probability for ^{188}Os and ^{187}Os. This calculation depends on the choice of $g(\epsilon)$; we have chosen the traditional Maxwellian form, $g(\epsilon) = k\epsilon e^{-\epsilon/T}$, where T is the nuclear temperature, related to the excitation energy by the relation $E = a_n T^2$. The quantity a_n is a level-density parameter which, for a Fermi gas, is proportional to A; we have used the relation $a_n = A/10$, which has been found reasonably successful in fitting neutron resonance data. A more refined way would be to determine a_n by fitting the lower-energy data where only first-chance fission occurs with a theoretical expression for Γ_f/Γ_{total}. The first-chance fission probabilities together with the total-chance fission probabilities for ^{187}Os and ^{188}Os are shown in Figs. D.7-3 and D.7-4.

It is possible to see that at excitation energies higher than 50 MeV the higher-chance fission probabilities start being a relevant fraction of the total fission probability until, at very high energies, they become of the same order of magnitude as first-chance fission.

An attempt will be made to fit the first-chance fission probabilities with theoretical expressions based on the Fermi gas level-density formula. Because both the ground and saddle-point level densities are required, this will be an important test for the Fermi gas model over a wide range of excitation energies and for two different nuclear deformations. Furthermore, the two isotopes ^{188}Os and ^{187}Os are sufficiently far away from closed shells that shell effects should be unimportant, making the test even more significant.

Footnote

† Visitor from the Laboratorio di Radiochimica, Università di Pavia, Pavia, Italy.

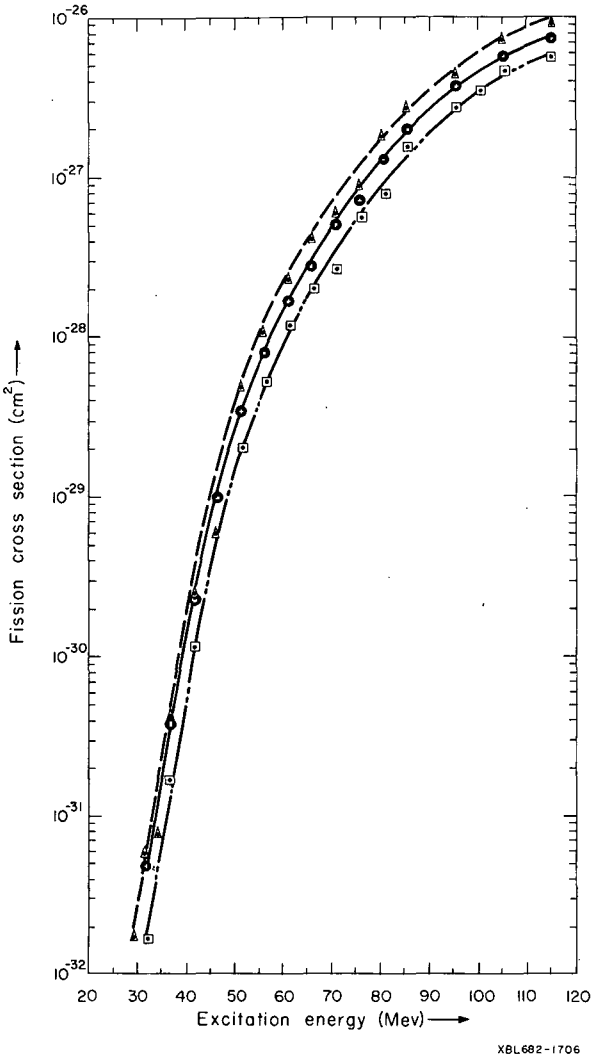

Fig. D.7-1. ^{4}He-induced fission cross sections for ^{182}W, ^{183}W, and ^{184}W.

-- △ -- $^{182}_{74}W + ^{4}_{2}He \rightarrow ^{186*}_{76}Os \rightarrow$ Fission

—○— $^{183}_{74}W + ^{4}_{2}He \rightarrow ^{187*}_{76}Os \rightarrow$ Fission

---⊡--- $^{184}_{74}W + ^{4}_{2}He \rightarrow ^{188*}_{76}Os \rightarrow$ Fission

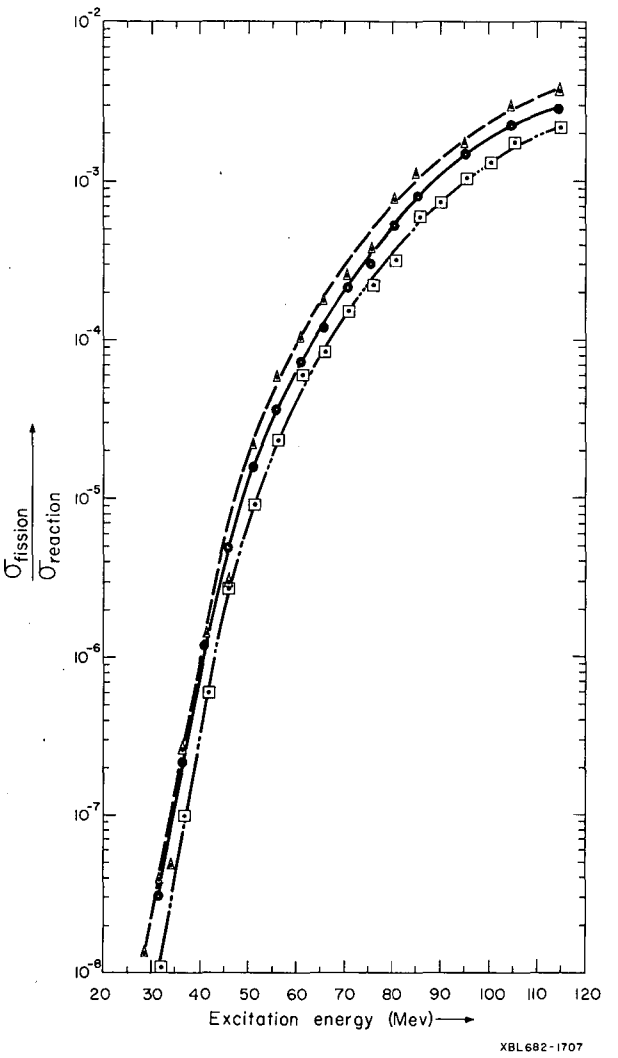

Fig. D.7-2. Total fission probabilities for ^{186}Os, ^{187}Os, and ^{188}Os.

-- △ -- $^{182}_{74}W + ^{4}_{2}He \rightarrow ^{186*}_{76}Os \rightarrow$ Fission

—○— $^{183}_{74}W + ^{4}_{2}He \rightarrow ^{187*}_{76}Os \rightarrow$ Fission

---⊡--- $^{184}_{74}W + ^{4}_{2}He \rightarrow ^{188*}_{76}Os \rightarrow$ Fission

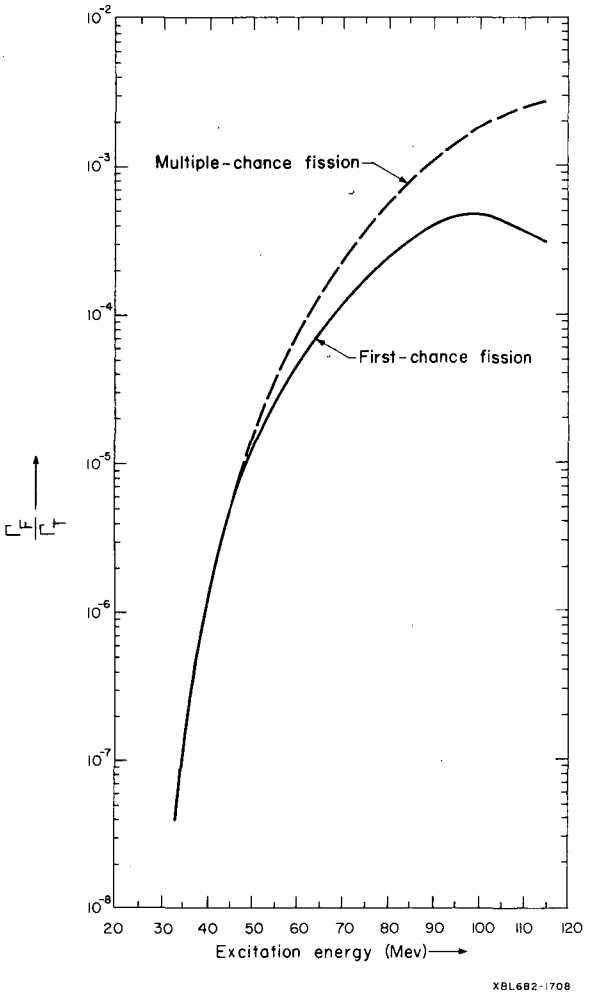

Fig. D.7-3. First-chance fission probabilities for ^{187}Os.
$^{183}_{74}W + ^{4}_{2}He \rightarrow ^{187*}_{76}Os \rightarrow$ Fission

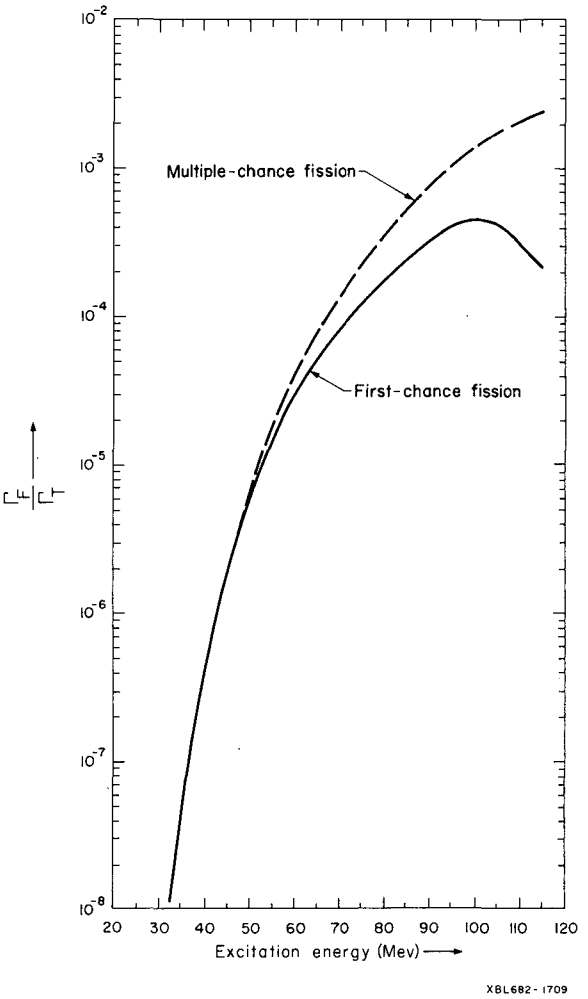

Fig. D.7-4. First-chance fission probabilities for ^{188}Os.
$^{184}_{74}W + ^{4}_{2}He \rightarrow ^{188*}_{76}Os \rightarrow$ Fission

8. POSSIBLE EVIDENCE OF LARGE PAIRING EFFECTS AT THE FISSION SADDLE POINT OF SOME POLONIUM ISOTOPES

Luciano G. Moretto,† Raymond C. Gatti, Stanley G. Thompson, John R. Huizenga,* and John O. Rasmussen‡

The fission saddle point represents a quasi-stationary state that can be studied within the unified model.[1] Therefore, it would be interesting to compare physical quantities, measured at the saddle and ground-state deformations, in order to determine the effects of large deformations in nuclei. Some recent experiments[2, 3] on ^{240}Pu seem to indicate that the pairing effects are larger at the saddle point than in the ground state. To determine the relation of this effect with the increase of deformation, the nuclei ^{210}Po and ^{211}Po, which are highly deformed at the saddle point, were studied.

Fission-fragment angular distributions were measured for helium-ion-induced fission of ^{206}Pb and ^{207}Pb, starting at an energy of ≈ 3 MeV over the fission barrier. Since the fission cross section is small in the energy region of interest, mica was used to detect fission fragments. A schematic diagram of the fission chamber is shown in Fig. D.8-1. The radius of the chamber is 28.40 mm, the diameter of the collimator is 1.59 mm, and its length is 22.35 mm. The position of the beam on the target is determined by the low convergence of the incoming beam, controlled by a quadrupole focusing lens positioned about 7 meters away from the collimator. The ^{4}He beam was provided by the 88-inch variable-frequency cyclotron.

The target consists of a water-cooled copper block on which more than 20 mg/cm^2 of high-purity silver has been evaporated in order to stop any possible fission fragments coming from impurities in the copper. The target material is deposited over the silver by partial (fractional) evaporation to minimize the amount of impurities.

Theoretical angular distributions can be calculated on the basis of symmetrical-top wave functions at the saddle point. The relevant angular momentum quantum numbers of an (assumed) axially symmetric nucleus at the saddle point (see Fig. D.8-2) are the total angular momentum I, its projection M on the space-fixed Z axis, and its projection K on the body-fixed symmetry axis. If the axial symmetry is preserved from the saddle to the scission point, then K is a good quantum number and the angular distribution will be

$$W(\theta) = \frac{2I+1}{4\pi} \left| D^I_{M,K} \right|^2 \qquad (1)$$

where $D^I_{M,K}$ are the symmetrical-top wave functions. Since we choose the Z axis to lie along the beam direction, the quantum number M is for our cases either exactly zero (for ^{206}Pb + ^{4}He, since both are spinless) or approximately zero (for ^{207}Pb + ^{4}He, which has M = ± $\frac{1}{2}$, since the spin of ^{207}Pb is $\frac{1}{2}$).

For large I and M = 0, a good approximation to Eq. 1 is

$$W(\theta) = \frac{2I}{4\pi^2} \left(I^2 \sin^2\theta - K^2\right)^{-\frac{1}{2}}.$$

To reproduce the actual angular distribution, an average must be taken over the distributions of K and I. From statistical considerations, the K distribution is expected to be of the form $\exp(-K^2/2K_0^2)$, K_0^2 being the square of the standard deviation of the K distribution.[4] The I distribution is determined by the reaction used to produce the compound nucleus, and is calculated here by using optical-model transmission coefficients. The final angular distribution is given by

$$W(\theta) \propto \sum_{I=0}^{\infty} (2I+1)T_I \quad I\left[\operatorname{erf}\left(I/\sqrt{2K_0^2}\right)\right]^{-1} \exp(-I^2 \sin^2\theta/4K_0^2) \times J_0\left(iI^2 \sin^2\theta/4K_0^2\right), \qquad (2)$$

where erf denotes an error function and J_0 a zeroth-order Bessel function. The experimental angular distributions are transformed to the center-of-mass system, and a least-squares fit is made with expression 2 in order to deduce K_0^2. The K_0^2 curves as a function of energy for ^{210}Po and ^{211}Po are shown in Figs. D.8-3 and D.8-4.

For ^{210}Po, at about 3 MeV over the top of the barrier, K_0^2 = 2.3, far too small to be accounted for in terms of intrinsic excitations. In other words, this point should lie within the pairing gap. On the other hand, at about the same energy above the saddle point ^{211}Po presents at K_0^2 value large enough to justify intrinsic excitations, as one would expect because of the odd-unpaired particle. The ^{211}Po curve follows the trend of the ^{210}Po curve remarkably well, but lies about 7 units of K_0^2 higher. If this is interpreted as an odd-even effect, then the contribution of one quasi-particle to K_0^2 will be 7 units. As a qualitative check, we have calculated from a Nilsson diagram the average of the square of the Ω values about the Fermi level. At the maximum deformation for which Nilsson results are available (ϵ = 0.6) we find for ^{210}Po and ^{211}Po about 8 units for neutrons and 5 for protons (average over 16 levels), giving an over-all average of 6.5.

Along the same line, one should look for structures corresponding to the onset of two and four quasi-particle states in ^{210}Po, and three and five quasi-particle states in ^{211}Po. Actually in both cases the K_0^2 curves present two flattenings that could correspond to the structures looked for. In ^{210}Po the flattenings occur at $K_0^2 \approx 15$ and $K_0^2 \approx 27.5$; these values are very close to two and four times the contribution of 7 units found for one quasi-particle. On the other hand, in ^{211}Po the flattenings occur at $K_0^2 \approx 21$ and $K_0^2 \approx 35$, again very near to three and five times the one-quasi-particle contribution.

This interpretation seems to be consistent with the experimental data, and allows one to estimate the value of the gap parameter Δ at the saddle point of these two isotopes. The position of the lowest point in ^{210}Po with respect to the barrier sets a lower limit of ≈ 3 MeV for 2Δ, and the position of K_0^2 structures due to the onset of different numbers of quasi-particle states suggests $2\Delta \gtrsim 4$ MeV. More work is in progress on ^{212}Po, ^{208}Po, ^{213}At, and ^{201}Tl compound nuclei to compare with the ^{210}Po and ^{211}Po data.

Footnotes and References

†Visitor from the Laboratorio di Radiochimica, Università di Pavia, Pavia, Italy.
*Present address: Department of Chemistry, University of Rochester, Rochester, New York.
‡Present address: Department of Chemistry and Physics, University of California, Berkeley, California.

1. A. Bohr, in Proceedings of the International Conference on the Peaceful Uses of Atomic Energy, Geneva, 1955, Vol. 2 (United Nations, New York, 1956), Paper No. P/911, p. 151.
2. James J. Griffin, Phys. Rev. 132, 2204 (1963).
3. H. C. Britt, R. Stokes, W. Gibbs, and J. Griffin, Phys. Rev. Letters 11, 393 (1963).
4. I. Halpern and V. M. Strutinskii, in Proceedings of the Second International Conference on the Peaceful Uses of Atomic Energy, Geneva, 1958, Vol. 15 (United Nations, Geneva, 1958), Paper No. P/1513, p. 408.

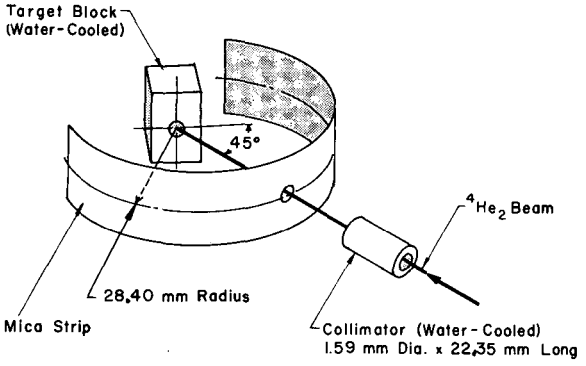

Fig. D.8-1. Schematic drawing of the apparatus used in measuring angular distributions of fission fragments.

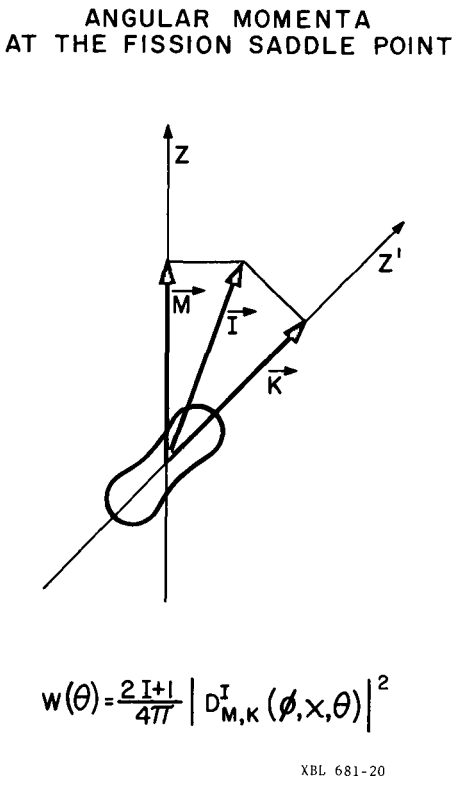

Fig. D.8-2. Angular momentum quantum numbers at the fission saddle point.

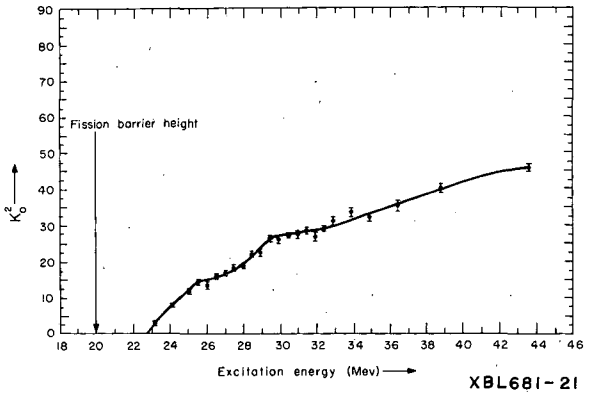

Fig. D.8-3. K_0^2 versus excitation energy for ^{210}Po at the saddle point.
$^{206}_{82}Pb + ^{4}_{2}He \rightarrow ^{210*}_{84}Po \rightarrow$ Fission

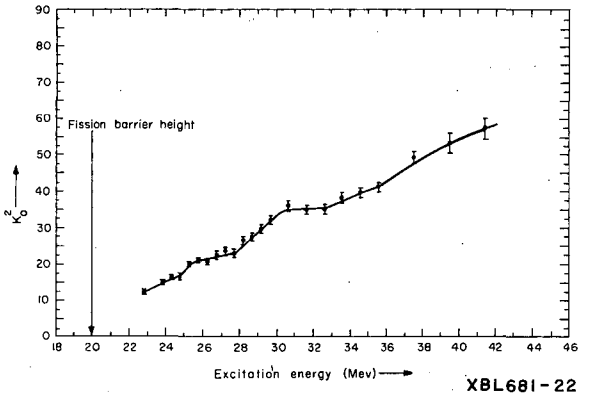

Fig. D.8-4. K_0^2 versus excitation energy for ^{211}Po at the saddle point
$^{207}_{82}Pb + ^{4}_{2}He \rightarrow ^{211*}_{84}Po \rightarrow$ Fission

9. SEARCH FOR NUCLEI OF ATOMIC NUMBER 114

H. R. Bowman, R. C. Gatti, R. C. Jared, L. G. Moretto,† W. J. Swiatecki, and S. G. Thompson

Several theoretical investigations of the stability of nuclei which might exist above the region of presently known elements ($Z > 105$) have suggested the following:
(i) Fission barriers predicted from liquid-drop theory are approaching zero in the region $Z = 114$. Thus the existence of nuclei with half-lives long enough to permit detection could come about only through the influence of special stability due to shells.[1]
(ii) Several recent calculations[2-6] seem to agree that $Z = 114$ is a strong magic number and that neutron numbers near 180 give additional stability. This may result in fission barriers in that neighborhood as high as 5 to 10 MeV. Estimates of half-lives for spontaneous fission, alpha decay, and electron capture indicate that total half-lives for such nuclei could be rather long, in which case detection should be easily accomplished if targets and projectiles for producing them with reasonable cross sections were available.

Beams of ^{40}A ions of energies up to 415 MeV are available at the LRL Hilac, and as a preliminary step in a systematic search for elements near $Z = 114$ we have bombarded targets of ^{244}Cm (300 $\mu g/cm^2$) and ^{248}Cm (150 $\mu g/cm^2$) with argon in the attempt to observe products from reactions of the type

$$^{248}_{96}Cm + ^{40}_{18}A \rightarrow ^{284}114 \text{ (170 neutrons)} + 4n.$$

The Coulomb barrier for this reaction is calculated to be about 216 MeV, and the peak yield of the (^{40}A, 4n) reaction should be in the region between 216 and 220 MeV. The width (FWHM) of the energy distribution of ^{40}A ions is ≈ 10 MeV.

We have used two methods in the attempt to detect nuclei in the region of $Z = 114$. The first involves a technique described by Ghiorso et al.[7] in which the reaction products are collected on a rotating drum and fission fragments from the decay of these products are detected by using mica. In the second method the recoil products are collected on a recoil catcher, and fission fragments are detected in mica (facing the catcher but shielded from the beam).

The efficiency of the second method for collecting products undergoing decay on the recoil catcher was tested by bombarding ^{164}Dy with ^{40}A and observing the α decay of ^{199}Po ($E_\alpha = 6.06$; $T_{1/2} \approx 4$ min). The efficiency of collection was found to be greater than 95%. The transit time

for a Z = 114 nucleus from target to catcher is $\approx 10^{-8}$ sec, and nuclei having longer half-lives should be detectable. If the products undergo a rapid sequence of alpha or electron-capture decays on the recoil catcher, at some stage a daughter in the highly unstable intermediate region of atomic numbers between Z = 105 and Z = 114 having a large branching in favor of spontaneous fission should occur and be detected. In order to be able to detect very long as well as very short half-lives the recoil catcher, in most of the experiments, was counted at the end of the bombardment for α particles and spontaneous fissions. In no case were any significant events observed in times of the order 1000 min.

The experimental arrangement is shown schematically in Fig. D.9-1. If the recoil products undergo binary fission after being stopped the fission fragments have their full energies in the direction of the mica (i.e., 130 MeV est.), while the (prompt) fission of impurities in the catcher occurs while the compound nucleus is in motion and therefore the fission fragments have much lower energies ($\approx$ 50. MeV) in the backward direction. This makes it possible to increase the sensitivity for detecting Z $\approx$ 114 by covering the mica with ≈ 1.8 mg/cm^2 of aluminum foil. (The average range of the recoiling Z = 114 nucleus should be about 1.5 mg/cm^2 Al, while the range of its fission fragments should be 4.0 mg/cm^2 in aluminum. In making these estimates we used Ref. 8.)

The result of the preliminary runs made to date is that we have not detected any events that could with confidence be assigned to Z = 114. Table D.9-I lists some of the upper limits we have deduced. We have seen varying numbers of fission tracks on the mica detectors, but as far as we can tell they may well be due to background events. We are now developing an improved system aimed at reducing these uncertainties and increasing the sensitivity of detection, we hope by factors of 10 to 1000.

One conclusion of this work so far is that for a compound system with Z = 114 and 170 neutrons the cross sections cannot be larger than about a microbarn: the production of the relatively lighter isotopes of 114 will not be easy. On the other hand the calculations (in particular those of Nilsson and Nix) indicate that 170 neutrons, rather than the optimum N $\approx$ 180, may indeed not give sufficient stability, but that the addition of a few more neutrons would have a large stabilizing effect. (Predicted spontaneous fission half-lives increase by several powers of ten per added neutron.)

We expect to increase the sensitivity of our detection system in the coming months, but the crucial factor in increasing the chances of making element 114 would seem to be the development of ion sources for neutron-rich projectiles, especially ^{48}Ca.

Footnote and References

† Visitor from the Laboratorio di Radiochimica, Università di Pavia, Pavia, Italy.

1. W. D. Myers and W. J. Swiatecki, Nucl. Phys. 81, 1 (1966).
2. Heiner Meldner, Arkiv Fysik 36, 593 (1967).
3. V. M. Strutinskii, Arkiv Fysik 36, 629 (1967) and Nucl. Phys. A95, 420 (1967).
4. C. Gustafson, I. L. Lamm, B. Nilsson, and S. G. Nilsson, Arkiv Fysik 36, 613 (1967).
5. Philip A. Seeger, A Model-Based Mass Law, and the r-Process as a Mass-Law Test, Los Alamos Scientific Laboratory Report LA-DC-8950, 1967.
6. S. G. Nilsson and J. R. Nix (Lawrence Radiation Laboratory), private communication.
7. M. Nurmia, T. Sikkeland, R. Silva, and A. Ghiorso, Phys. Letters 26B, 78 (1967).
8. Palmer G. Steward and Roger Wallace, Calculations of Stopping Power and Range-Energy Values for Any Heavy Ion in Nongaseous Media, UCRL-17314, Dec. 1966.

Table D.9-I. Measured cross sections as upper limits.

^{40}A Energy (MeV)	Cross sections (upper limits) (10^{-30} cm^2) Without Al cover	With Al cover
215	1.0 ± 0.2	
216	1.1 ± 0.2	
223.5	6.6 ± 0.6	
224	10.5 ± 0.7	0.6 ± 0.2
229	1.6 ± 0.16	0.08 ± 0.04
238	5.7 ± 1.0	2.9 ± 0.7
241	1.1 ± 0.15	0.17 ± 0.07
246	0.6 ± 0.2	
216 (Rotating-drum technique)	0.046 ± 0.008	
	Background runs	
226	6.9 ± 0.5	
232	0.8 ± 0.3	

Fig. D.9-1. Schematic diagram of experimental apparatus.

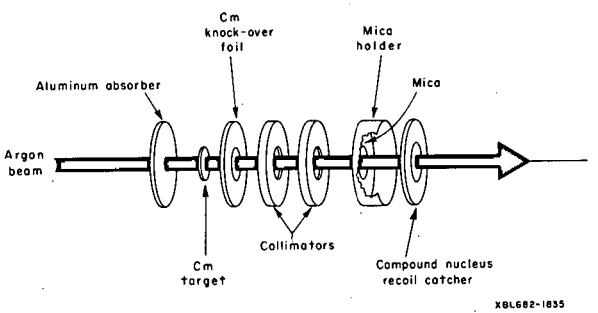

10. SPONTANEOUS FISSION OF LIGHT FERMIUM ISOTOPES; NEW NUCLIDES ^{244}Fm AND ^{245}Fm †

Matti Nurmia, Torbjorn Sikkeland, Robert Silva, and Albert Ghiorso

We have observed spontaneous-fission branching in the decay of ^{248}Fm and ^{246}Fm, using mica to scan a rotating-drum recoil-collection device. These nuclides were produced by bombarding targets of ^{233}U, ^{235}U, and ^{236}U with beams of ^{16}O ions and targets of ^{239}Pu and ^{240}Pu with ^{12}C ions. The targets were about 500 μg/cm^2 and the beam intensities about 2 μA over an area of 0.2 cm^2. The assignment of the fission activities to the above nuclides was made by comparing the half-lives and excitation functions with those of the known alpha activities of ^{248}Fm and ^{246}Fm. The latter were obtained with semiconductor detectors in a conveyor-gas recoil-collection system. In the case of ^{246}Fm the fission branching was large enough to allow simultaneous measurement of the alpha spectrum and the fission events in the conveyor-gas system.

In the course of these experiments, a new alpha activity of 8.15 MeV energy was observed in the bombardments of ^{233}U and ^{234}U with ^{16}O and of ^{239}Pu with ^{12}C. Figure D.10-1 shows the decay curve and half-life obtained for this alpha activity. A comparison of the experimentally observed excitation function with that computed for the $^{233}U(^{16}O, 4n)$ reaction from compound-nucleus theory[1] is shown in Fig. D.10-2. The activity was assigned to ^{245}Fm on the basis of its production in the cross-bombardments with the expected excitation functions and from alpha-decay systematics.[2]

Bombardments of ^{239}Pu and ^{240}Pu with ^{12}C ions and ^{235}U and ^{236}U with ^{16}O ions showed the presence of two distinct alpha activities of 8.18 and 7.87 MeV energy with half-lives of approximately 5 and 30 sec. These activities were assignable to ^{247}Fm, as recently reported by the Dubna group.[3]

Finally, a short-lived fission activity was observed in bombardments of ^{233}U with ^{16}O ions. A decay curve and half-life for this activity are shown in Fig. D.10-1. The cross section for production had the energy dependence expected for the $(^{16}O, 5n)$ reaction as shown in Fig. D.10-2. The activity was not produced in bombardments of the same target with ^{14}N ions. This was taken as indicating the activity is unlikely due to an isotope or isomeric state of an element other than fermium. The above evidence suggests the assignment of ^{244}Fm to this activity.

A summary of the observed properties of these nuclides is given in Table D.10-I. Also shown is a comparison of the maximum values in the production cross sections with those calculated according to Ref. 1. Included are the energies at which the maxima occurred. In all cases, the experimental data are in reasonably good agreement with the calculated values. It should be pointed out that an excitation function is only a necessary and not a sufficient condition for the correct mass assignment of spontaneous fission activities, and that further experimental work is being carried out.

The systematics of the spontaneous-fission half-lives of the heaviest elements, in the light of the results presented here, is shown in Fig. D.10-3. The new data on the fermium isotopes clearly provide further support to the recent reassignment of the 2.3-sec fission activity from ^{254}No (Refs. 4, 5) to ^{252}No (Refs. 2, 6). They also serve to illustrate the dramatic effect of the 152-neutron subshell on the fission half-lives of the isotopes of the heaviest elements.

Footnotes and References

†Condensation of article in Phys. Letters, 26B[2], 78 (1967).

1. Torbjorn Sikkeland, in Proceedings of the Lysekil Symposium, 1966 (to be published in Arkiv Fysik).
2. A. Ghiorso and T. Sikkeland, Physics Today 20, No. 19, 25 (1967).
3. G. N. Flerov, S. M. Polikanov, V. L. Mikheev, V. J. Plyuschenko, M. B. Miller, and V. A. Shechegolev, At. Energ. (USSR) 22, 342 (1967).
4. Albert Ghiorso, in Proceedings of the Second Conference on Reaction Between Complex Nuclei, Eds. A. Zucker, E. C. Halbert, and F. T. Howard (John Wiley and Sons, New York, 1960).
5. Albert Ghiorso, At. Energ. (USSR) 7, 338 (1959).
6. A. Ghiorso, T. Sikkeland, and M. J. Nurmia, Phys. Rev. Letters 18, 401 (1967).

Table D.10-I. Summary of observed decay properties and production conditions.

Nuclide	Total half-life	Alpha-decay energy (MeV)	Partial S. F. half-life	Method of production	σ (max.) (μb) Exp.	σ (max.) (μb) Calc.	Energy at σ (max.) (MeV) Exp.	Energy at σ (max.) (MeV) Calc.
^{244}Fm	3.3 ± 0.5 msec	- - - - -	3.3 ± 0.5 msec [a]	^{233}U(^{16}O, 5n)	0.013	0.015	97	97
^{245}Fm	4.2 ± 1.3 sec	8.15 ± 0.02	- - - - - - - -	^{233}U(^{16}O, 4n)	0.20	0.11	93	91
^{246}Fm	1.2 ± 0.2 sec	8.24 ± 0.02	15 ± 5 sec	^{239}Pu(^{12}C, 5n)	0.33	0.40	78	80
^{248}Fm	38 ± 4 sec	{7.87 ± 0.02 (80%) 7.83 ± 0.02 (20%)}	10 ± 5 h	^{240}Pu(^{12}C, 4n)	1.3	3.8	71	72

a. Assuming negligible alpha branching as predicted by systematics.

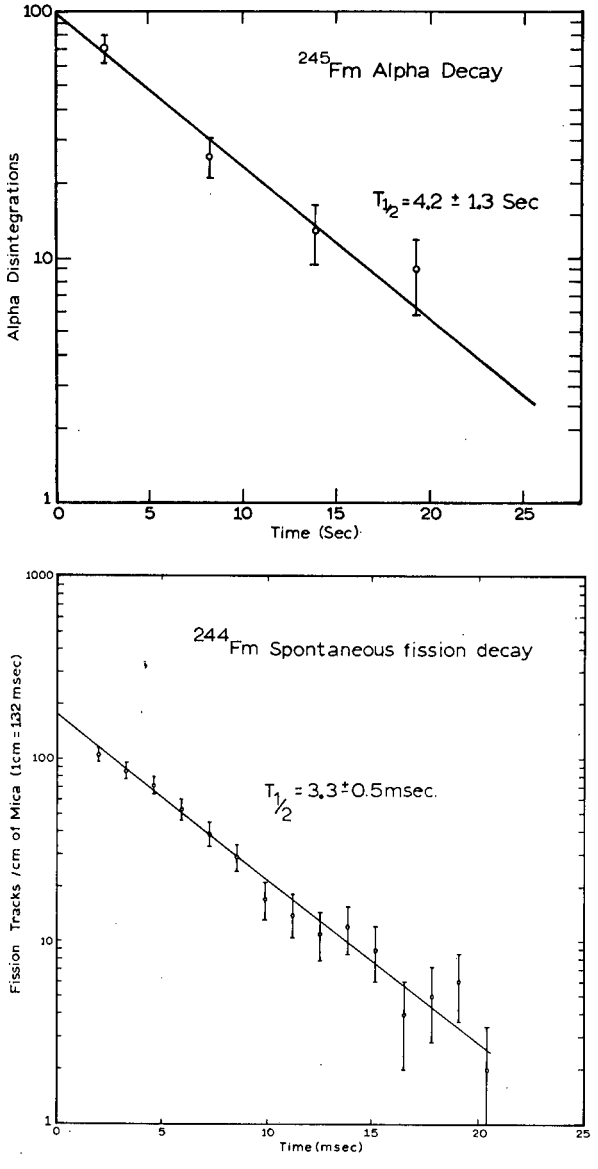

XBL 6710-2185

← Fig. D.10-1. Decay curves for spontaneous fission of ^{244}Fm and alpha decay of ^{245}Fm.

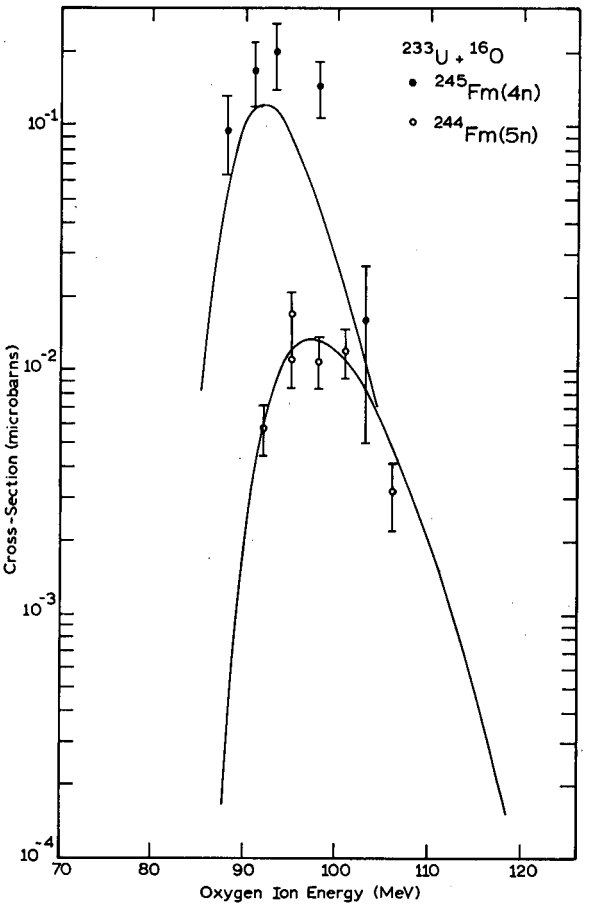

XBL6710 2105

Fig. D.10-2. Experimental (points) and calculated (solid lines) excitation functions for production of ^{244}Fm and ^{245}Fm from bombardment of ^{233}U with ^{16}O ions.

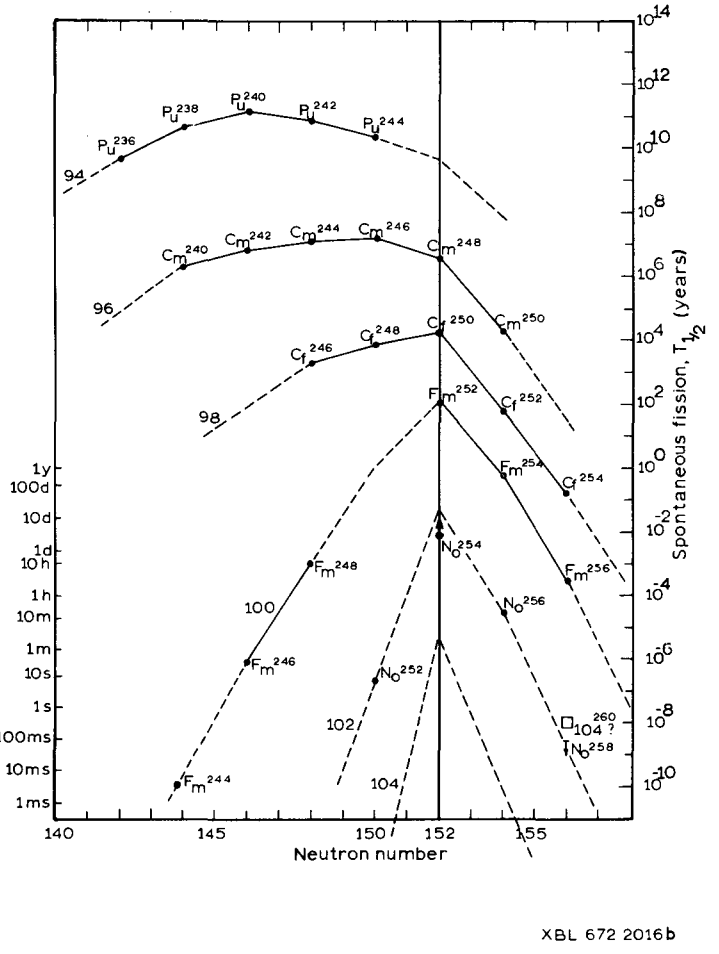

XBL 672 2016b

Fig. D.10-3. Systematics of the spontaneous-fission half-lives of the heaviest elements.

11. DYNAMICAL CALCULATIONS OF THE DIVISION OF IDEALIZED NUCLEI†

James Rayford Nix

We study the dynamics of the division of nuclei idealized as incompressible uniformly charged liquid drops with constant surface tension and nonviscous irrotational hydrodynamical flow. The shape of the nuclear surface is specified with six degrees of freedom, in terms of three smoothly joined portions of quadratic surfaces of revolution (e.g., two spheroids connected by a hyperboloidal neck). Figure D.11-1 illustrates for three values of the fissility parameter x the sequences of shapes from the saddle point to scission, for initial conditions at the saddle point corresponding to 1 MeV of kinetic energy in the fission mode and 1 MeV in the mass-asymmetry mode. The parameter x is defined as $\frac{1}{2}E_c^{(0)}/E_s^{(0)}$, where $E_s^{(0)}$ and $E_c^{(0)}$ denote respectively the surface and Coulomb energies of the original spherical drop (with a sharp surface); the nuclei that correspond approximately to these values of x are indicated in parentheses.[1] We observe that: (i) the time from saddle to scission increases substantially with increasing x; (ii) for small values of x the motion consists primarily of a constriction of the drop's neck, whereas for large x the drop also elongates substantially; (iii) the mass-asymmetric component of motion is not

amplified into a large mass asymmetry during the descent as proposed by Hill[2] and by Hill and Wheeler,[3] but instead represents stable oscillations about a symmetrical division. This means that within the limitation of a parameterization that permits only binary division, the liquid-drop model does not suggest an explanation of the observed mass asymmetry in fission.

In Fig. D.11-2 we compare as a function of x the calculated (solid curve) and experimental most-probable total translational kinetic energies of fission fragments at infinity. The dashed curve represents approximately the translational kinetic energy acquired by the fragments from their Coulomb repulsion after scission, and the dot-dashed curve gives the translational kinetic energy acquired by the fragments prior to scission. The increase in this quantity as x increases above ≈ 0.7 reflects the increased distance from saddle to scission and the greater prescission elongation at larger values of x. The experimental prescission kinetic energies were deduced from experimental data on long-range α particles emitted during fission (open triangle[4] and open octagon[5]). The experimental total kinetic energies are most-probable (open symbols) and average (solid symbols) fragment kinetic energies from a variety of sources, but include only cases in which the mass distribution is symmetrical. The calculations (with no adjustable parameters[1]) reproduce both the correct order of magnitude and the correct trend with x of the kinetic energies, but a systematic difference of about 5% is evident.

Footnotes and References

†Resumé of UCRL-17540, Contribution No. 7.21 to International Conference on Nuclear Structure, September 7-13, 1967, Tokyo, Japan. Figure D.11-2 has been updated.

1. In converting from natural liquid-drop units to conventional units, and vice versa, we use the latest semiempirical mass-formula constants of W. D. Myers and W. J. Swiatecki, Arkiv Fysik 36, 343 (1967).
2. D. L. Hill, Ph. D. dissertation, Princeton University, April 1951.
3. D. L. Hill and J. A. Wheeler, Phys. Rev. 89, 1102 (1953).
4. I. Halpern, Alpha Particle Emission in Fission, preprint.
5. Y. Boneh, Z. Fraenkel, and I. Nebenzahl, Phys. Rev. 156, 1305 (1967).

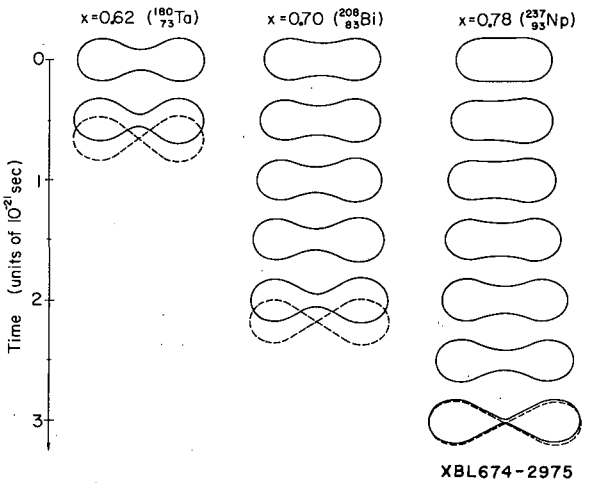

Fig. D.11-1. Illustrations of the descent from saddle to scission.

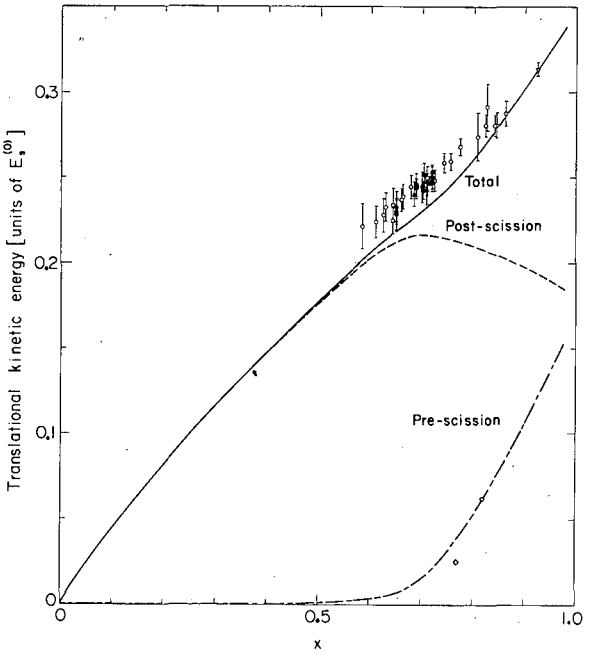

Fig. D.11-2. Calculated and experimental fission-fragment kinetic energies.

12. FURTHER STUDIES IN THE LIQUID-DROP THEORY OF NUCLEAR FISSION†

James Rayford Nix

In a recent simplified treatment[1] of the liquid-drop theory of nuclear fission, a certain approximation was employed to calculate the properties of the fission of nuclei lighter than about radium. For such elements the calculations were found to reproduce, without the use of adjustable parameters, certain, but not all, of the properties of the experimental distributions in the masses and kinetic energies of the fragments at infinity. Because of the outcome of this study it was decided to perform analogous calculations with a more realistic parameterization of the nuclear shape, so that the predictions of the liquid-drop model would be known for the fission of the heavy elements as well as the light. Such calculations are described here for a parameterization in terms of three smoothly joined portions of quadratic surfaces of revolution (e.g., two spheroids connected by a hyperboloidal neck).

The properties of the fission process that we calculate are the distributions in mass and kinetic energies of the fragments at infinity. The general procedure that we use for calculating these distributions is analogous to that employed in Ref. 1, and consists of several distinct steps:
(i) The potential energy, which is the sum of the surface energy and the Coulomb energy, is calculated as a function of the deformation coordinates, and the saddle point is located and its properties studied. The more important known saddle-point properties[2] are reproduced with amazing accuracy in the three-quadratic-surface parameterization over the entire range of the fissility parameter x from 0 to 1. The fissility parameter is defined as one-half the ratio of the Coulomb energy of the spherical drop (with a sharp surface) to the surface energy of the spherical drop. For values of $x < 0.51$ the parameterization is in fact more accurate than expanding the drop's radius vector in a series of 18 Legendre polynomials.[2]
(ii) The kinetic energy is calculated as a function of the coordinates and their time derivatives. This has been done both exactly (by solving Laplace's equation for the velocity potential) and by use of the Werner-Wheeler method,[3] which consists of approximating the internal hydrodynamical flow by the flow of circular layers of fluid. The Werner-Wheeler method was found to be sufficiently accurate for the distortions of primary interest in fission, and this method was used for most of the calculations.
(iii) The frequencies and eigendisplacements of the normal modes of oscillation of the system about its saddle-point shape are determined.
(iv) The transition-state method is used to calculate the probability for finding the system in a given state of motion as it passes through the vicinity of the saddle point.
(v) The solution of Hamilton's classical equations of motion determines the motion of the system from the saddle point on, for a given set of initial conditions near the saddle point. This final step converts the probability distributions for the states of motion near the saddle point into the desired probability distributions for the observable characteristics of the fission fragments, namely their masses and kinetic energies.

In this way we find that the most probable mass division is a division into two equal parts. Thus, within the limitations of our parameterization and the Werner-Wheeler approximation for the kinetic energy, the liquid-drop model does not reproduce the observed mass asymmetry in the fission of the heavy elements at low excitation energy, as had been suggested by the calculations of Hill[4] and Hill and Wheeler.[5]

We present in Fig. D.12-1 the calculated most probable energies. The figure shows how the available energy, which consists of the sum of the energy release E_{rel} and the fission-barrier height B_f, is divided among the fragments at infinity. The division is into kinetic energy of translation E^{∞}_{trans} and vibrational energy E^{∞}_{vib}. The translational kinetic energy at infinity is shown further divided into the energy E^{scis}_{trans} acquired prior to scission and the energy $E^{postscis}_{trans}$ after scission. The prescission translational kinetic energy is seen to increase rapidly as x increases above ≈ 0.7. Similarly, the vibrational energy is shown further divided into the energy $E^{scis}_{vib\,kin}$ acquired prior to scission and the energy $E^{postscis}_{vib}$ acquired after scission. The sum of E^{scis}_{trans} and $E^{scis}_{vib\,kin}$, which is denoted by E^{scis}_{kin}, represents the system's total kinetic energy at scission, and hence gives the most probable decrease in potential energy in going from the saddle point to scission. These calculations reproduce, without the use of adjustable parameters, both the correct order of magnitude and the correct trend with x of experimental kinetic energies, but a systematic discrepancy of about 5% exists. (We use the values of Myers and Swiatecki[6] for the constants of the semiempirical mass formula. Our first three figures refer to the fission of

nuclei along Green's approximation[7] to the line of beta stability.)

The predicted distributions in both the masses and kinetic energies of the fragments are to lowest order Gaussian in shape. The full widths at half maximum of the mass distributions for various values of the nuclear temperature Θ at the saddle point are shown as functions of x in Fig. D.12-2. The predicted distributions are seen to become infinitely broad for values of $x \leq x_{BG} = 0.396$, where the drops become unstable with respect to mass-asymmetric distortions.[8] Figure D.12-3 is a similar plot of the full widths at half maximum of the translational kinetic-energy distributions.

The predicted widths of the distributions in mass and kinetic energy are compared with the experimental data of Plasil, Burnett, Britt, and Thompson[9] in Figs. D.12-4 and D.12-5, respectively. The variances of the distributions (which are proportional to the squares of the widths) are plotted as functions of the nuclear temperature Θ at the saddle point. The theoretical and experimental curves have not been normalized in any way. We observe that the theory accounts approximately for the magnitudes and slopes of the experimental points, but certain deviations are apparent: The experimental points are consistently higher than the theoretical curves, the experimental $^{198}_{82}Pb$ slopes for both distributions are too large, and the experimental slopes for the remaining kinetic-energy distributions are too small.

The general conclusion reached from all comparisons that have been made is that the liquid-drop model yields an approximate description of the distributions in mass and kinetic energy for the fission of the light elements at all excitation energies and the heavy elements at high excitation energy, but that, within the limitation of a parameterization that permits only binary division, it does not reproduce the observed properties of the fission of the heavy elements at low excitation energy.

Footnotes and References

† Resumé of UCRL-17958, to be submitted to Nucl. Phys.

1. J. R. Nix and W. J. Swiatecki, Nucl. Phys. 71, 1 (1965).
2. S. Cohen and W. J. Swiatecki, Ann. Phys. (N. Y.) 22, 406 (1963).
3. F. G. Werner and J. A. Wheeler, unpublished manuscript.
4. D. L. Hill, Ph. D. dissertation, Princeton University, April 1951.
5. D. L. Hill and J. A. Wheeler, Phys. Rev. 89, 1102 (1953).
6. W. D. Myers and W. J. Swiatecki, Arkiv Fysik 36, 343 (1967).
7. A. E. S. Green, Nuclear Physics (McGraw-Hill Book Co., New York, 1955), pp. 185, 250.
8. U. L. Businaro and S. Gallone, Nuovo Cimento 5, 315 (1957).
9. F. Plasil, D. S. Burnett, H. C. Britt, and S. G. Thompson, Phys. Rev. 142, 696 (1966).

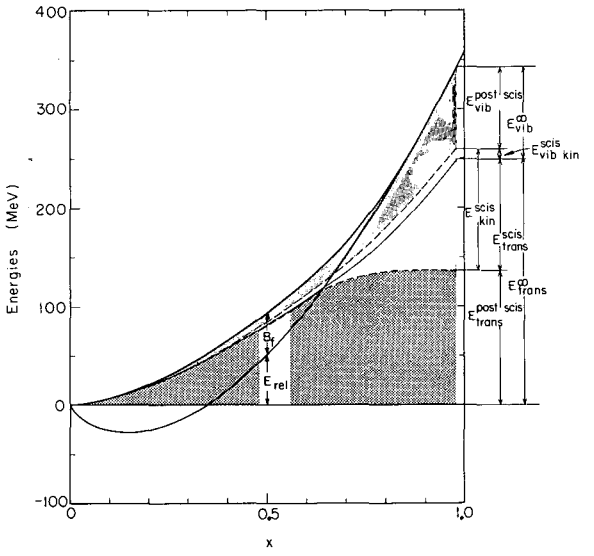

XBL675-3022

Fig. D.12-1. The most probable fission-fragment energies as functions of the fissility parameter x.

Fig. D.12-2. The full widths at half maximum of fission-fragment mass distributions as functions of the fissility parameter x, for various values of the nuclear temperature Θ at the saddle point. The critical Businaro-Gallone[8] value of x is indicated by the dashed line.

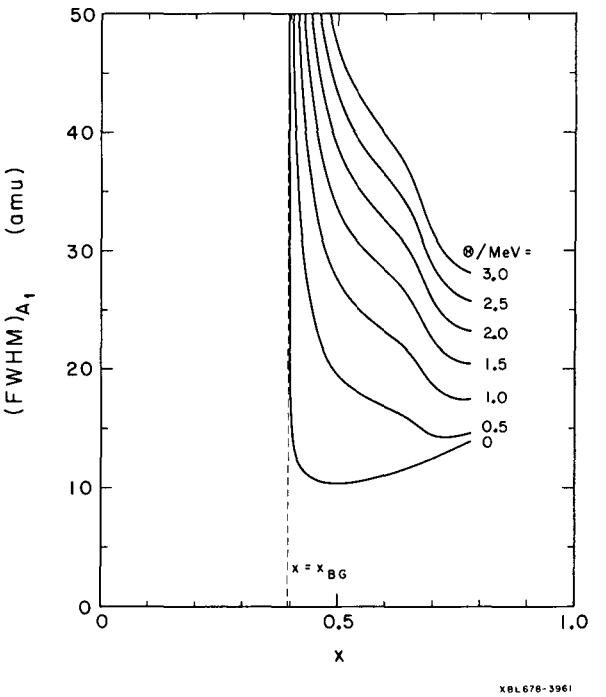

XBL678-3961

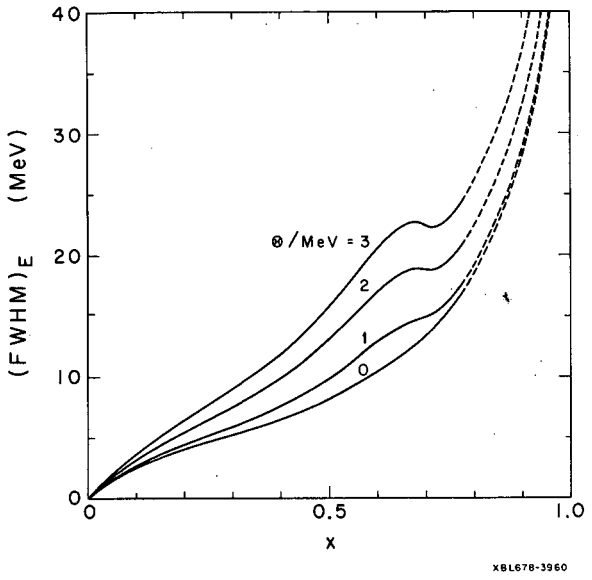

Fig. D.12-3. The full widths at half maximum of fission-fragment translational kinetic-energy distributions as functions of the fissility parameter x, for various values of the nuclear temperature Θ at the saddle point. The portions of the curves indicated by the dashed lines are of reduced accuracy.

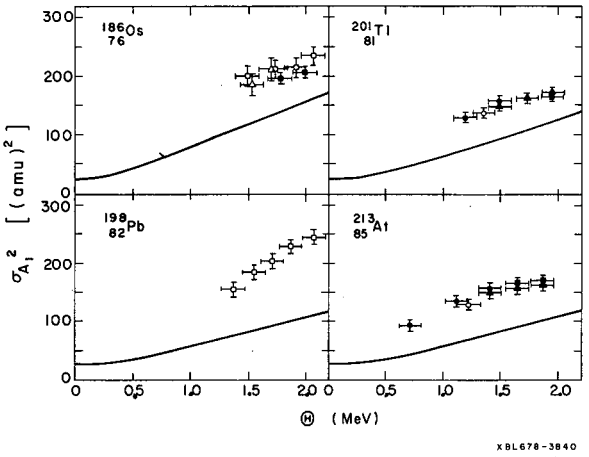

Fig. D.12-4. Comparisons of theoretical and experimental[9] variances of fission-fragment mass distributions, as functions of the nuclear temperature Θ at the saddle point, for four compound nuclei.

Fig. D.12-5. Comparisons of theoretical and experimental[9] variances of fission-fragment kinetic-energy distributions, as functions of the nuclear temperature Θ at the saddle point, for four compound nuclei.

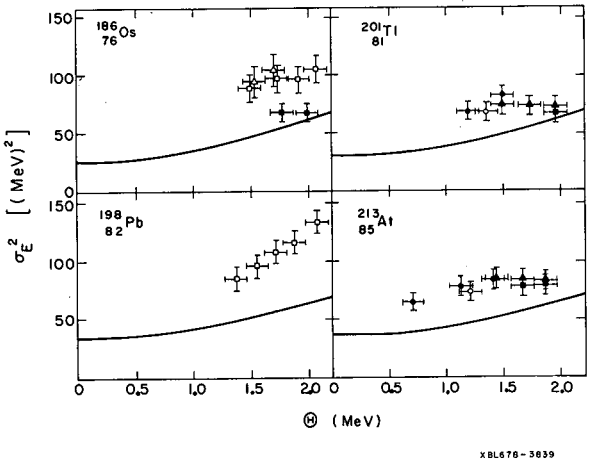

This value is in good agreement with the value obtained by conventional optical spectroscopy.[2]

A similar situation pertains when the atomic beam consists of radioactive ^{134m}Cs. Here, though, the hfs of both $6^2S_{1/2}$ and $6^2P_{1/2}$ are smaller than for ^{133}Cs, so that Stark tuning can bring about only one overlap of the beam-absorption lines with the lamp-emission lines. However, there are four possible overlap positions of the Stark-shifted energy levels of ^{134m}Cs beam atoms with the unshifted levels of ^{133}Cs atoms in the absorption cell. As seen in Fig. E.1-3 these overlap positions correspond to minima in the observed intensity pattern. From the energy-level diagram it is clear that the separation between the minima α and β and between γ and δ corresponds to the hfs of the $6^2P_{1/2}$ state of ^{134m}Cs. These are experimentally seen to be equal. Moreover, the separations between α and γ and between β and δ should correspond to the hfs of the $6^2P_{1/2}$ state of ^{133}Cs. This also agrees with our observations. From the observed separations we infer

$$\Delta\nu^{134m}(6^2P_{1/2}) = 473 \pm 60 \text{ MHz}.$$

In addition, from the position of the minima we obtain a new precision value for the ^{134m}Cs-^{133}Cs isotope shift. We find

$$\text{isotope shift} = +\ 1.4(2.0) \times 10^{-3}\ \text{cm}^{-1},$$

where the positive sign indicates that the shift is in the direction predicted by the normal-volume effect. This value is substantially smaller than that reported in Ref. 1, where apparently an overly optimistic assessment of the error was made.

Footnote and References

†Condensed from Phys. Rev. Letters 19, 1(1967).

1. R. Marrus and D. McColm, Phys. Rev. Letters 15, 813 (1965).
2. H. Kleiman, J. Opt. Soc. Am. 52, 441 (1962).

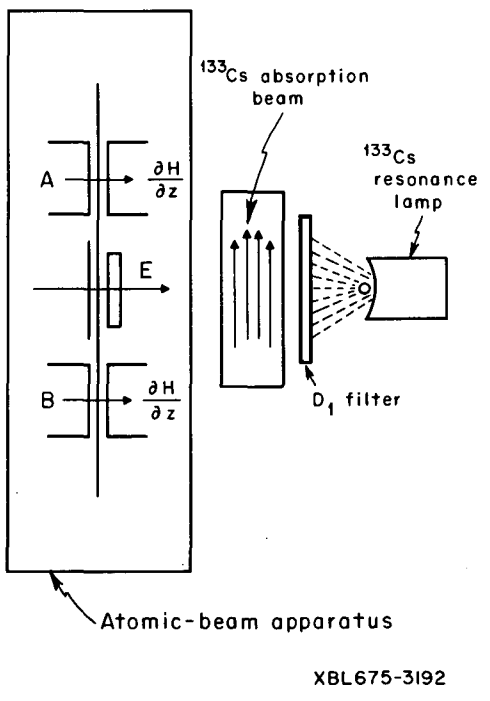

Fig. E.1-1. Schematic diagram of apparatus.

E. HYPERFINE INTERACTIONS

1. MEASUREMENT OF THE HYPERFINE STRUCTURE OF OPTICALLY EXCITED STATES OF RADIOACTIVE ISOTOPES†

Richard Marrus, Edmond Wang, and Joseph Yellin

It has been shown recently[1] that the atomic-beam method can be extended to the study of isotope shifts and the optical Stark effect in radioactive isotopes. We describe a way in which this method can be modified to obtain a substantial improvement in resolution. With this improvement, details of the hfs of the $6^2P_{1/2}$ states of the cesium isotopes are revealed to a precision within about 50 MHz. It is felt that this method should be generally applicable to the study of the hfs of optically excited states in any isotope (radioactive or stable) that can be deflected in an atomic-beam apparatus, and we report here as a demonstration the measurement of the hfs in the $6^2P_{1/2}$ state of ^{134m}Cs ($\tau_{1/2}$ = 2.9 h).

The basic apparatus (see Fig. E. 1-1) is identical to that of Ref. 1 except for the addition of an atomic-beam absorption cell. An atomic-beam flop-in apparatus is employed whose C region consists of a pair of electric field plates with a gap of 0.035 in. The homogeneity of the electric field produced is estimated to be about 0.5% and is sufficiently good so that it does not contribute appreciably to the line width. Light from a cesium-resonance lamp illuminates the region in the gap. The light is filtered so that only the D_1 transition ($6^2P_{1/2} \rightarrow 6^2S_{1/2}$) is passed. In the lamp line, the hfs of the $6^2P_{1/2}$ state is not completely resolved, and the lamp line consists of a doublet, the components of which are separated by the hfs of the ground state. With this apparatus, the precision is limited by the width of the lamp line, about 1500 MHz. However, the precision may be substantially improved by passing the filtered light through an optically dense cesium absorption beam. The effect of the absorption beam is to remove a doublet from each of the lamp lines. The two components of the doublet are separated by the hfs of the $6^2P_{1/2}$ state, and each component has a width of about 150 MHz (see the energy-level diagram in Fig. E. 1-2). In principle, this width can be made as low as the natural line width, which for the cesium resonance line is about 10 MHz. However, such high precision would demand an electric field that is homogeneous and reproducible to better than 0.5×10^{-3} at fields of almost 0.5×10^{6} V/cm. This is presently beyond our capability, and accordingly, we have designed our absorption beam to achieve a width of about 150 MHz.

The Cs atoms in the atomic-beam apparatus are state-selected by the narrow gap between the electric-field plates so that essentially we can refocus only atoms in the lowest hyperfine state (F = 3 for ^{133}Cs and F = 15/2 for ^{134m}Cs). The observed ^{133}Cs intensity pattern is shown in Fig. E. 1-2 and can be understood with reference to the inserted energy-level diagram. Indicated directly above each of the observed intensity minima is the position of the Stark-shifted energy levels of ^{133}Cs-beam atoms relative to the unshifted levels of atoms in the absorption cell. At zero electric field the absorption lines of the Cs atomic beam overlap the absorption lines of the Cs absorption beam, and a minimum in the intensity curve is observed. However, as the electric field is turned on, the Stark effect decreases the frequency of the absorption lines of the atoms in the beam apparatus, and the observed signal increases. When the electric field is sufficient to shift the frequency by an amount equal to the hfs of the excited ($6^2P_{1/2}$) state, a second intensity minimum is observed. At higher electric fields the frequency is shifted by an amount equal to the ground-state hfs, and the beam-absorption line is brought into resonance with the second lamp-emission line. Here three intensity minima can be observed corresponding to the overlap positions indicated in the energy-level diagram. These three minima are equally spaced, and correspond to a shift by an amount equal to the hfs of $6^2P_{1/2}$. The unlabeled minima correspond to structure present in the lamp line.

As can be seen from the energy-level diagram, the separation between the two minimum points labeled α and δ corresponds to a Stark shift of the energy levels equal to 9192 MHz, the hfs of the ^{133}Cs ground state. Using this as a calibration, and taking the separations α-β, γ-δ, and δ-ϵ as equal to the hfs of the $6^2P_{1/2}$ state, we obtain

$$\Delta\nu^{133}(6^2P_{1/2}) = 1167 \pm 40 \text{ MHz}.$$

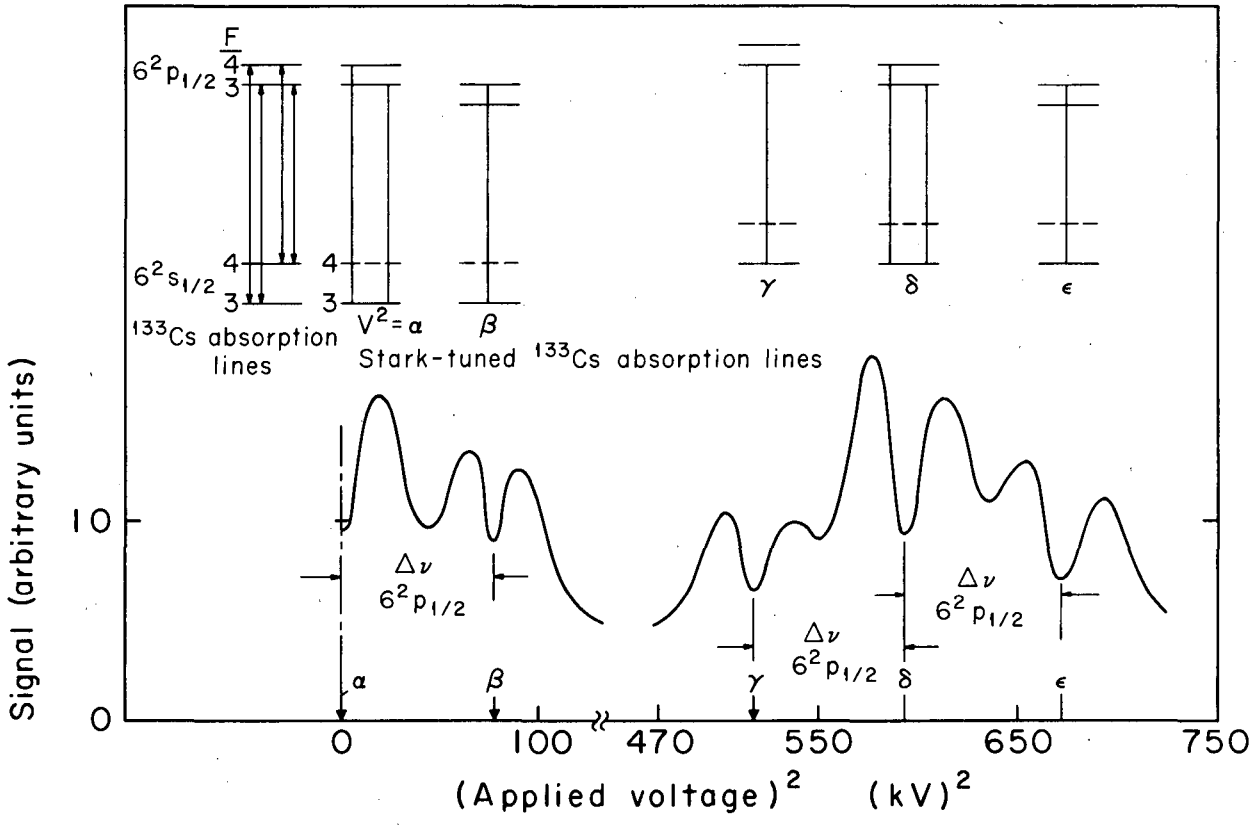

XBL675-3193

Fig. E.1-2. Observed ^{133}Cs signal versus square of applied voltage. The position of the Stark-shifted absorption lines relative to those in the absorption cell for each of the observed minima is indicated directly above the minima. The separation between α and δ corresponds to a shift equal to the ground-state hyperfine separation, and serves as a calibration.

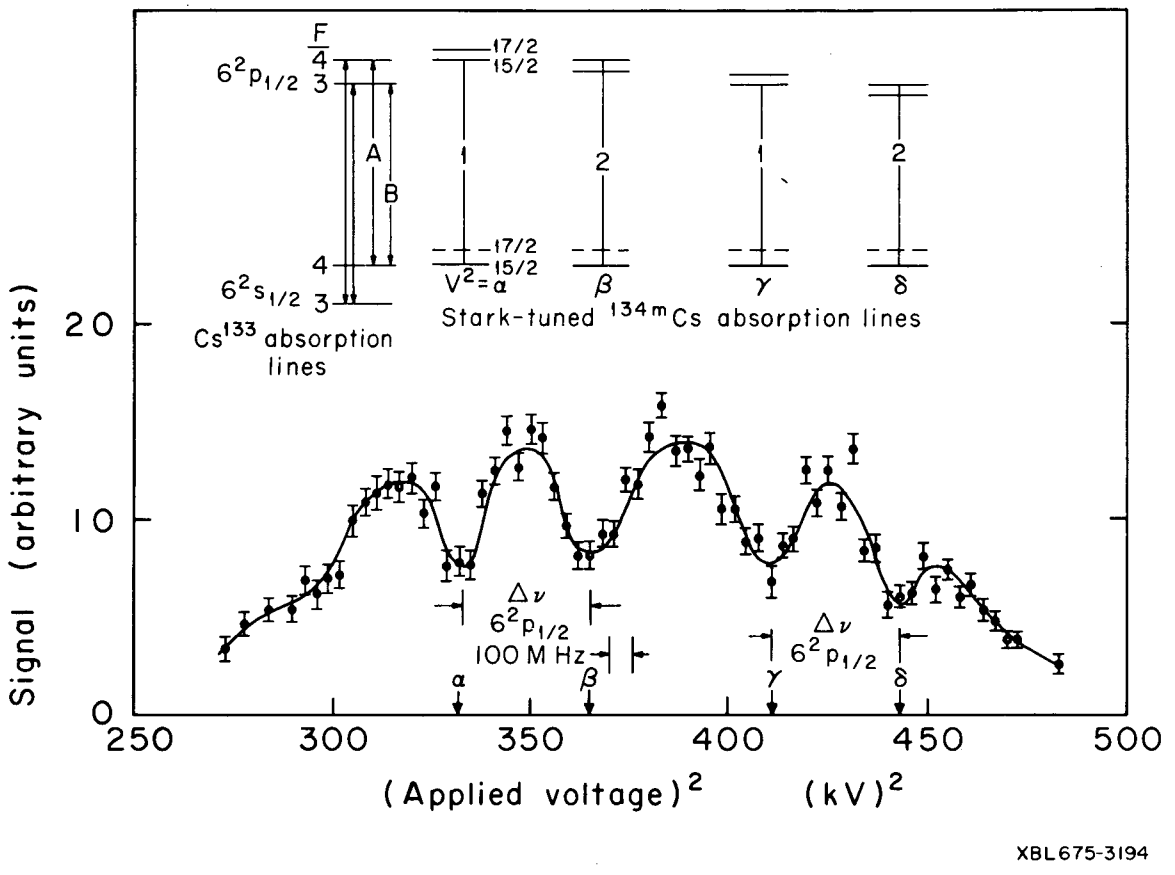

XBL675-3194

Fig. E. 1-3. Observed ^{134m}Cs signal versus square of applied voltage. The minimum α occurs when beam-absorption line 1 coincides with ^{133}Cs absorption line A; β occurs when line 2 coincides with A; γ occurs when 1 coincides with B; and δ occurs when 2 coincides with B.

2. SPINS AND ATTENUATION COEFFICIENTS OF THE 86.5- AND 105.3-keV STATES IN ^{155}Gd†

A. J. Soinski, E. Karlsson,* and D. A. Shirley

Despite several experimental investigations,[1-8] the spins of the 86.5- and 105.3-states in ^{155}Gd had not been determined with certainty. The E1 nature of both the 86.5- and 105.3- keV transitions to the 3/2-ground state,[9] together with the log ft values for the beta decay of ^{155}Eu,[10] establish both states as having positive parity and spins of 3/2 or 5/2. From a measurement of the angular distribution of these two γ rays following the decay of oriented ^{155}Eu, we have been able to make unequivocal spin assignments of 3/2 to the 105.3-keV state and 5/2 to the 86.5-keV state. In addition, we have derived values for the attenuation coefficients G_2 for both γ rays. These values, $G_2(86.5) = 0.26(8)$ for the decay through the 6.35-nsec, 86.5-keV state, and $G_2(105.3) = 0.80(9)$ for the decay through the 1.14-nsec 105.3-keV state, constitute the first evidence for a time-dependent attenuation following the decay of oriented nuclei.

Europium-155 was oriented in the neodymium ethylsulfate (NES) lattice into which Eu^{3+} grows substitutionally. The angular distribution of γ rays following the decay of oriented europium nuclei in NES is given by

$$W(\theta) = 1 + g_2\, G_2\, U_2\, F_2\, P_2\,(\cos\theta) + \cdots, \qquad (1)$$

where g_2 is a solid-angle factor, and the other terms have their usual meanings.[12] The spin Hamiltonian governing orientation is pure quadrupolar, and for low degrees of orientation the orientation tensor B_2 is given by[13]

$$B_2 \approx -\frac{P}{3kT}\left(\frac{1}{5}I(I+1)(2I-1)(2I+3)\right)^{1/2}, \qquad (2)$$

where P is the quadrupole coupling constant, given by $P = -(3eQ/4I(I-1))\partial E/\partial z$. We have used ^{154}Eu in the same sample as a nuclear thermometer. Its nuclear orientation characteristics have been studied,[14] and $B_2^{(154)}(T)$ was obtained from the angular distribution of the 1277-keV γ ray following the decay of ^{154}Eu. For a given lattice the electric field gradient at the nucleus is independent of A. Thus $B_2^{(155)} = 1/2(14/3)^{1/2}(Q_{155}/Q_{154})\, B_2^{(154)}$, where $B_2^{(154)}$ is known to be positive.

The angular-momentum factors U_2F_2 have different signs for E1 decays through 3/2+ and 5/2+ states, but their magnitudes depend on the spin of ^{155}Eu (which we take as 5/2) and, in the case of the decay through the 5/2+ state, on the Fermi-to-Gamow-Teller mixing ratio in the allowed beta decay. For decay through a 3/2+ state, $U_2F_2 = -0.2944$; and for decay through a 5/2+ state, $U_2F_2 = +0.2458$ or $+0.3742$ for pure Gamow-Teller or pure Fermi decay, respectively. Since the Gamow-Teller-to-Fermi ratio is not known, we average the latter values to +0.310(64). Clearly a positive U_2F_2 indicates spin 5/2, while a negative U_2F_2 requires a spin of 3/2. We found $G_2B_2U_2F_2(86.5) = +0.014(3)$ and $G_2B_2U_2F_2(105.3) = -0.041(4)$ at $T = 0.011°K$. These values are obtained directly from the difference between the cold and warm count rate (see Fig. E.2-1). If $Q_{155}/Q_{154} > 0$ and $G_2 > 0$ for both states (both very good assumptions), then $B_2^{(155)} > 0$, and I(86.5) = 5/2 and I(105.3) = 3/2. The pertinent decay scheme with these assignments is shown in Fig. E.2-2.

Having determined the spins, we can now make a more quantitative interpretation of the data. Of particular interest is the time dependence of G_2 in intermediate states following beta decay of oriented nuclei. Relatively little is known about reorientation effects in ionic crystals. Earlier experiments in this Laboratory had indicated that substantial attenuation could occur in a few nsec, but not in < 1 nsec. The ^{155}Gd results are thus of special interest because we might expect substantial attenuation in the 6.4-nsec 86.5-keV level but little attenuation in the 1.1-nsec 105.3-keV level. Using $Q = Q_0\, I(2I-1)/(I+1)(2I+3)$, and assuming $Q_0(154) \approx Q_0(155)$, we can compare our results with theory to obtain $G_2(86.5) = 0.26(8)$ and $G_2(105.3) = 0.80(9)$, in excellent confirmation of these expectations. If we have made a systematic error in the analysis and if $G_2(105.3)$ is, in fact, 1, the derived value of $G_2(86.5)$ is 0.33(10). Thus the orientation in the 86.5-keV state is strongly attenuated. None of the proposed theoretical models[15] accounts for this much attenuation.

Footnotes and References

†UCRL-17970, Dec. 1967, submitted to Phys. Letters.

*Summer visitor, 1967. Permanent address: University of Uppsala, Institute of Physics, Uppsala, Sweden.

1. B. I. Deutsch, R. F. Metzger, and F. J. Wilhelm, Nucl. Phys. 16, 81 (1960).
2. B. N. Subba Rao, Nucl. Phys. 28, 503 (1961).
3. A. Z. Hrynkiewicz, S. Ogaza, J. Styczeń, B. Hrastnik, B. Pudlowska, and R. Kulessa, Nucl. Phys. 80, 608 (1966).
4. N. Y. Delyagin, Hussein El Sayes, and V. S. Shpinel, Zh. Eksperim, i Theo. Fiz. 51, 95 (1966) [English transl. Soviet Phys. JETP 24, 64 (1967)].
5. R. R. Stevens, Jr., Y. K. Lee, and J. C. Walker, Phys. Letters 21, 401 (1966).
6. R. R. Stevens, Jr., J. S. Eck, E. T. Ritter, Y. K. Lee, and J. C. Walker, Phys. Rev. 158, 1118 (1967).
7. F. F. Tomblin and P. H. Barrett, in Proceedings of the International Conference on Hyperfine Interactions Detected by Nuclear Radiation, Asilomar, 1967, to be published.
8. M. Blumberg, B. Persson, and M. Bent, Ibid.
9. B. N. Subba Rao, Nuovo Cimento 16, 283 (1960).
10. P. H. Blichert-Toft, E. G. Funk, and J. W. Mihelich, Nucl. Phys. A96, 190 (1967).
11. A. Krusche, D. Bloess, and F. Münnich, Z. Physik 192, 490 (1966).
12. David A. Shirley, Ann. Rev. Nucl. Sci. 16, 89 (1966).
13. R. J. Blin-Stoyle and M. A. Grace, Handbuch der Physik 42, 555 (1957).
14. J. Blok and D. A. Shirley, Phys. Rev. 143, 911 (1966).
15. J. M. Daniels and Sushil K. Misra, Can. J. Phys. 44, 1965 (1966).

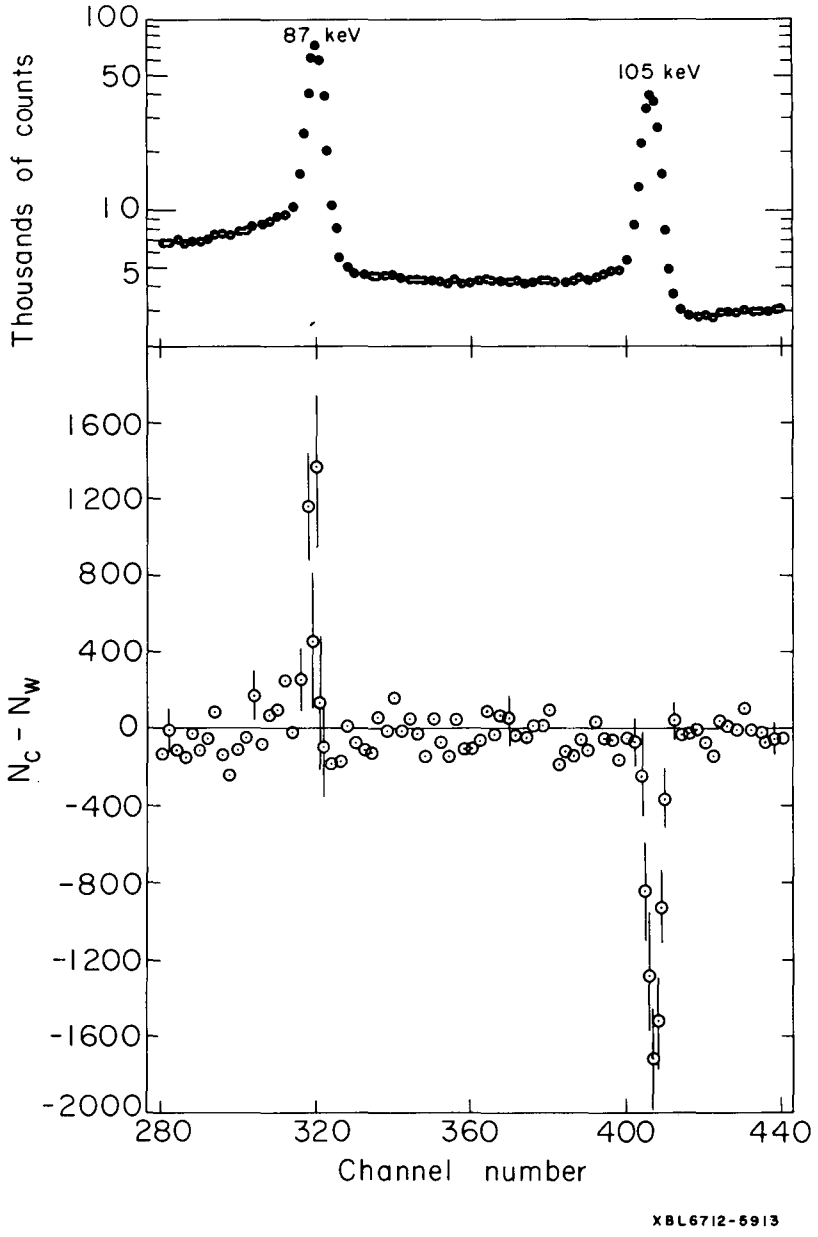

Fig. E.2-1. Upper: Summation of cold counts at 0.011°K following 16 adiabatic demagnetizations. Lower: Difference between the total cold counts (aligned nuclei) and the total warm counts (nuclei randomaly oriented at 1°K) for the same series of demagnetizations. The spin assignments I(86.5) = 5/2 and I(105.3) = 3/2 depend on the signs of these energies.

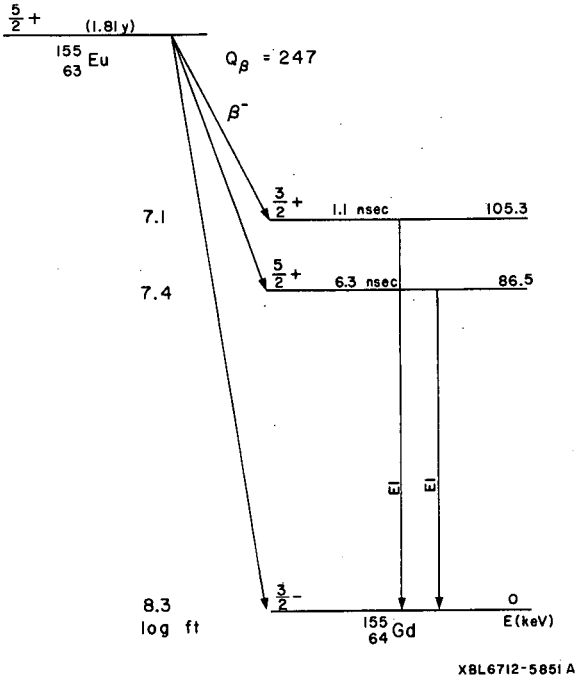

Fig. E.2-2. Partial decay scheme of ^{155}Gd; adapted from Ref. 10.

3. HYPERFINE STRUCTURE IN THE ^{253}Es EMISSION SPECTRUM†

Earl F. Worden,* Ralph G. Gutmacher,* Ronald W. Lougheed,*
James E. Evans,* and John G. Conway

We have photographed some ^{253}Es emission lines at high resolution and have determined the hyperfine structure (hfs) present. A total of six lines was observed; one line showed completely resolved hfs, three showed partially resolved hfs, and two were unresolved flag patterns. The line at 3498.10 Å has eight well-resolved components. The 3555.34-Å line has only five resolved hfs components, but their spacing and the total width of the line indicate the presence of eight components.

The Es emission lines were obtained by using an electrodeless lamp containing 0.6 μg of Es and 100 μg of Gd as anhydrous iodides. The emission lines were photographed with a 3.4-m Ebert spectrograph with a 300-lines/mm grating, blazed for use at angles near 60 deg. The reciprocal dispersion was about 0.3 Å/mm for the region investigated.

The lamp performance was very poor, and its useful lifetime was about 10 minutes. For this reason, only a limited region of the spectrum from 3420 to 3805 Å was photographed. The wavelengths and character of the Es lines observed are given in Table E.3-I. Because of the nature of the source used, these lines are probably the most sensitive first-spectrum lines of Es in this spectral region.

The ^{253}Es was obtained from the beta decay of ^{253}Cf and is isotopically pure.

Footnotes

†Submitted to J. Opt. Soc. Am.
*Lawrence Radiation Laboratory, Livermore, California.

Table E.3-I. Einsteinium-253 lines observed from an electrodeless lamp.

Wavelength (Å)	Width		Character
	Å	cm^{-1}	
3428.4540	0.055	0.47	Unresolved flag pattern degraded to the violet. Weak.
3498.1085	0.2198	1.795	Eight well-resolved components degraded to the violet. Strong.
3555.3414	0.072	0.56	Partially resolved flag pattern degraded to the red. Five resolved components. Medium.
3563.397	≈0.065	≈0.52	Unresolved pattern too weak to determine direction of degradation. Very weak.
3792.9662	0.055	0.38	Partially resolved pattern. Four resolved components. Weak.
3801.5204	0.067	0.46	Partially resolved pattern degraded to the red. Four resolved components. Weak.

F. MASS SPECTROSCOPY

1. AUTOIONIZATION OF HIGHLY EXCITED Ar^+ IONS PRODUCED BY ELECTRON IMPACT†

Amos S. Newton, A. F. Sciamanna, and R. Clampitt

It was previously shown that electron impact on argon produces long-lived highly excited states of Ar^+ which undergo a transition to Ar^{++} near a metal surface.[1] At the time we found no evidence for the existence of a long-lived autoionizing state of Ar^+ which Daly declared he had observed.[2,3] Further experimental work with a modified ion source has shown that both autoionization and surface-induced transitions from the last slit contribute to the $(M/q)^* = 10$ peak. In the experimental arrangement used, the Ar^{++} ions arising from surface-induced transitions at the last slit were about equal in number to the Ar^{++} ions resulting from autoionization after the last slit.

The Isatron ion source in a Dempster-type mass spectrometer (C. E. C. Model 21-103B) was modified as shown in Fig. F.1-I. The last normal slit, S_2, was insulated from ground and supplied various fractions of the ion accelerating voltage, V_A, from taps in the high-voltage dropping resistor network. Slit S_3 was added, and operated at ground potential. The slit S_3 was modified to be (i) 0.76 mm thick and 0.76 mm wide, (ii) 0.76 mm thick and 1.0 mm wide, and (iii) 0.76 mm thick and 1.5 mm wide, covered on the side facing slit S_2 with a gold screen of 82% transparency. The recording system was increased in sensitivity by a factor of 40 by use of a Loeneo Model 21B electrometer with a 10^{12}-ohm grid resistor in place of the CEC electrometer. The scan rate was reduced by a factor of 100 to accommodate the longer time constant of this electrometer. A 50-liter inlet volume was used (rather than the original 3 liters) to decrease the leak rate from the inlet system from the normal value of about 20% per hour to about 1% per hour.

For a transition involving a change of charge at some point in the ion-accelerating region, if an ion of mass M with a charge q is accelerated through a potential V_1, and after the transition the ion, with a charge q_2, is accelerated through a potential V_2, then the apparent mass, $(M/q)^*$, at which the peak appears is given by

$$\left(\frac{M}{q}\right)^* = \frac{M\,(q_1 V_1 + q_2 V_2)}{q_2^{\,2}\,(V_1 + V_2)} \quad . \tag{1}$$

For the autoionization of Ar^+ or the transition of Ar^+ to Ar^{++} at the last slit, S_3,

$$Ar^+ \xrightarrow{\text{autoionization}} Ar^{++} + e^- \tag{2}$$

or

$$Ar^+ \xrightarrow{\text{surface}} Ar^{++} + e^-; \tag{3}$$

according to Eq. 1 the peak will appear at $(M/q)^* = 10.00$. If, however, the transition occurs at S_2 (Eq. 3) and S_2 is at a potential V_2, then the peak appears at a mass greater than 10.00, according to Eq. 1.

In Fig. F.1-2, the peaks at $(M/q)^*$ near 10 are shown with $V_{S_2} = 0.058\ V_A$ for S_3 the gold screen (A), for S_3 an open slit (B), and for $V_{S_2} = 0$ (C). In Fig. F.1-3 the positions of these peaks with increasing V_{S_2} are shown to follow Eq. 1 except for the intermediate peak in Fig. F.1-2A and B. The interpretation of Fig. F.1-2A is that the peak at 10.00 is from surface-induced transitions at slit S_3 (gold screen), the peak at $(M/q)^* = 10.58$ is from surface-induced transitions at slit S_2, and the peak at $(M/q)^* = 10.10$ is due to autoionization beyond slit S_3. The rising base line between $(M/q)^* = 10.10$ and 10.58 is due to autoionization in the space between S_2 and S_3. The position of the autoionization peak [$(M/q)^* = 10.10$ in Fig. F.1-2A and B], which should be at

$(M/q)^* = 10.00$, can be qualitatively explained on the basis of the ion optics of the product ion of a gas-phase transition after slit S_3, i.e., the position on the mass scale increases with increase in V_{S_2} as shown in curve B of Fig. F.1-3.

Proof that the peak at $(M/q)^* = 10.58$ in Fig. F.1-2A and B arises from surface-induced transitions at S_2 and the peak at $(M/q)^* = 10.10$ arises after the slits is shown in Fig. F.1-4, where the ion beam in the Isatron is scanned across slit S_2 by varying the inner-focus voltage. At the best focus on S_2 (Fig. F.1-4D) the peak at $(M/q)^* = 10.58$ shows a double maximum: the first where the beam strikes one edge of the slit, then a minimum where the beam is passing through the slit, and a second maximum when it strikes the other edge. In contrast, the $(M/q)^* = 10.10$ peak shows a single maximum where the beam of Ar^+ ions is passing through the slit, this maximum being at the same point as the minimum for the $(M/q)^* = 10.58$ peak.

Ionization efficiency curves of the three peaks in Fig. F.1-2A are shown in Fig. F.1-5. It is seen that the peaks at $(M/q)^* = 10.00$ and 10.58 follow one curve and that of $(M/q)^* = 10.10$ follows another curve. Although both peaks are at a maximum at an electron energy of about 57 eV, the curve for $(M/q)^* = 10.10$ shows a sharper maximum, falls off more rapidly at higher energies, and crosses over the other curve at lower energies to yield an appearance potential, AP which is greater by about 0.5 eV. It is concluded that different states are involved in the two processes. The autoionizing state must be a state of total energy slightly greater than the AP of Ar^{++}. We had previously concluded that the states undergoing transition by surface induction were the higher Rydberg levels of Ar^+.[1] The present data are consistent with this conclusion.

In explaining the movement of the mass position of the peak due to autoionization with changes of V_{S_2} (Curve B, Fig. F.1-3), two considerations are involved. First is the difference in focus conditions when $(M/q)^* = 10.00$ is collected but $M/q = 40$ must pass through slit S_2. Since the Isatron is itself a mass spectrometer of low resolution (it is in the magnetic field), when V_A and H, the magnetic field, are set to collect $M/q = 10$, to get $M/q = 40$ through S_2 the beam must be deflected by changing the relative voltages on the focus slits, hence the beam does not pass through S_2 in a normal (perpendicular) direction. Second, the slit system S_2-S_3 is a divergent lens system, and increases the divergence by an amount proportional to the voltage applied.

Coggeshall[4] and Newton[5] have derived the equations for the collection of metastable ions in Dempster-type instruments. These derivations implicitly implied normal trajectories of the parent ion through slit S_2. Figure F.1-6 is a schematic representation of the situation for collecting the product ion if the angle of divergence from normal is ϕ.

The equation for the apparent radius, r^*, at which the product ion is collected as a function of R, the radius of the parent ion; r, the radius of a normal ion; ϕ, the angle of emergence from S_2; and θ, the angle traversed before transition is

$$r^* = \frac{R^2 + 2r^2 - R^2\cos\theta + 2Rr\cos(\theta+\phi) - 2Rr\cos\phi}{R + 2r\cos(\theta+\phi) - R\cos\theta}, \qquad (4)$$

and g, the displacement of the new center of r^* from the normal magnet center, is

$$g = (R-r^*)^2 + R^2 + r^2 - 2Rr\cos\phi - 2r(R-r^*)\cos(\theta+\phi) - 2R(R-r^*)\cos\theta. \qquad (5)$$

The peak cutoff occurs when $r^* + g$ is equal to the outer radius of the analyzer tube or when $r^* - g$ is equal to the inner radius of the analyzer tube.

In Fig. F.1-7 the field of collectible orbits for the autoionization of Ar^{+*} to Ar^{++} is shown as a function of ϕ and θ, the upper and lower solid lines being the outer and inner analyzer-tube cutoffs. The intensity of the peak is proportional to θ, the distance of travel in a collectible orbit, hence the time allowed for transition to occur.

As ϕ increases, both the apparent mass and the intensity (θ values) of the peak increase. Therefore as the beam is diverged by increasing the voltage on S_2, the center of mass of the resulting peak due to autoionization should increase, as is observed.

Footnote and References

† Short version of J. Chem. Phys. 47, 4843 (1967).

1. A. S. Newton, A. F. Sciamanna, and R. Clampitt, J. Chem. Phys. 46, 1779 (1967).

2. A. S. Newton, A. F. Sciamanna, and R. Clampitt, in Nuclear Chemistry Annual Report, 1966, UCRL-17299, Jan. 1967, p. 222.
3. N. R. Daly, Proc. Phys. Soc. (London) 85, 897 (1965).
4. N. D. Coggeshall, J. Chem. Phys. 37, 2167 (1962).
5. A. S. Newton, J. Chem. Phys. 44, 4015 (1966).

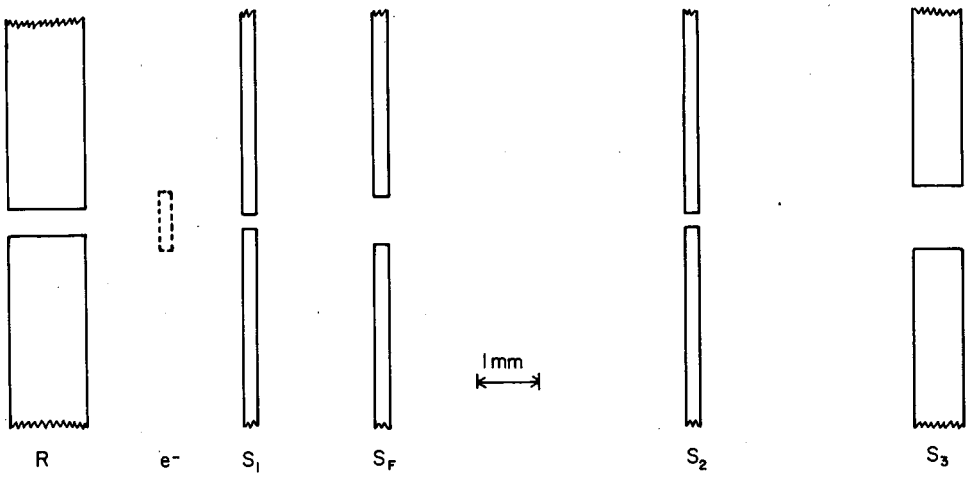

Fig. F.1-1. Modified Isatron ion source. R = repellers, normally run at $\approx 1.01\ V_A$; S_1 = ion-source first slit, run at V_A; S_F = ion-source focus slits, normally run at $\approx 0.92\ V_A$; S_2 = ion-source last slit, normally grounded but now insulated from ground and run at V_{S_2}; S_3 = added slit, run at ground potential. All work reported here was done with a magnetic field equal to 984 gauss, at which $(M/q)\ V_A = 7540$; i.e., $(M/q)^* = 10$ was scanned at $V_A = 754$ volts.

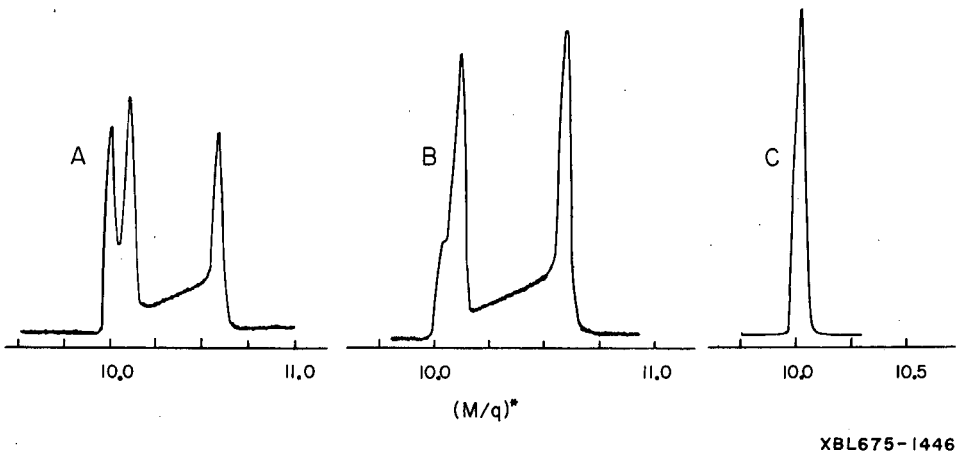

Fig. F.1-2. Peak profiles of $(M/q)^* = 10$ peaks in argon obtained by using modified Isatron ion source.
(A) Slit S_3 = gold screen, $V_{S_2} = 0.058\ V_A$.
(B) Slit S_3 = 1.0-mm slit, $V_{S_2} = 0.058\ V_A$.
(C) Slit S_3 = 1.0-mm slit, $V_{S_2} = 0$.
Conditions: inlet pressure = 1000 μ, I_{e^-} = 75 μA, V_{e^-} = 57.5 eV
Peak intensities are on an arbitrary scale.

Fig. F.1-3. Shift in apparent mass of $(M/q)^* = 10$ peaks in argon with potential on slit S_2.
——— calculated for surface-induced transitions at slits S_2 and S_3 respectively,
○ slit S_3 = 0.76-mm slit,
○ slit S_3 = gold screen.

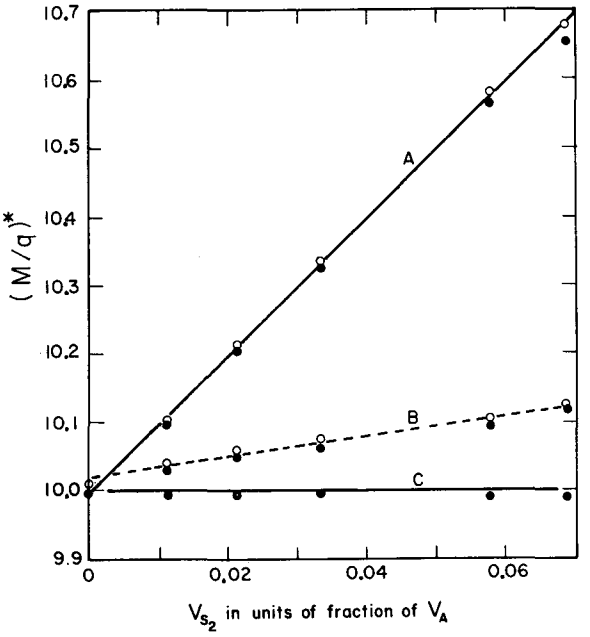

XBL 675-1447

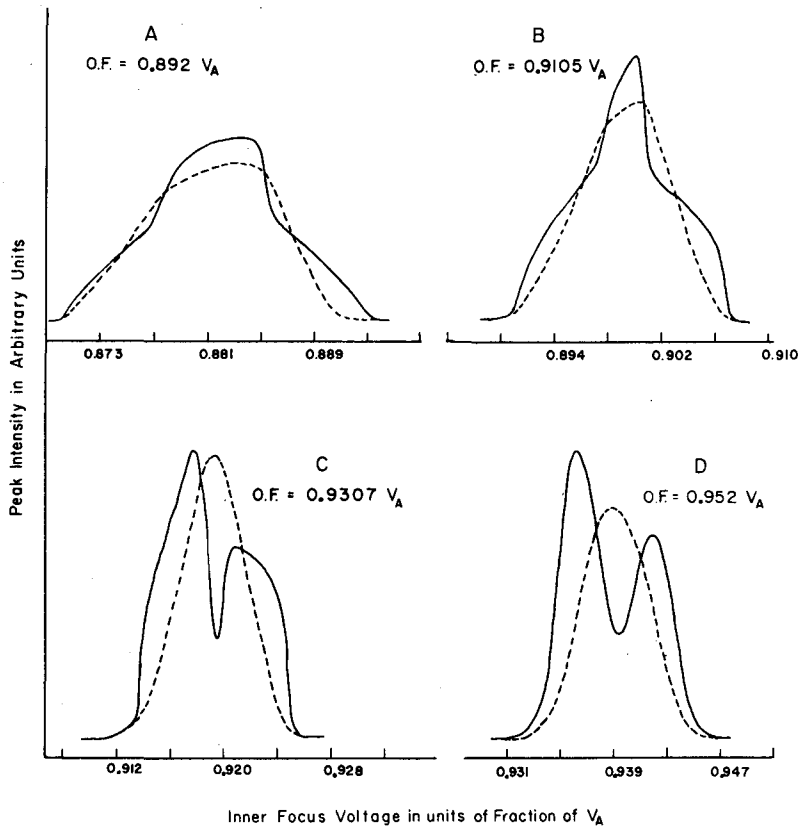

XBL675-1449

Fig. F.1-4. Variation in peak intensities of the autoionizing $(Ar^+)^*$ peak [$(M/q)^* = 10.12$] (----), and the S_2 surface-induced transition peak [$(M/q)^* = 10.69$] (———), as observed when the Ar^+ is scanned across slit S_2 by varying the inner-focus potential at selected values of the outer-focus potential (O. F.).
Conditions: $V_{S_2} = 0.069$ V_A, inlet pressure = 1000 μ, $I_{e^-} = 75\,\mu A$, $V_{e^-} = 57.5$ eV, S_3 = 1.0-mm slit.

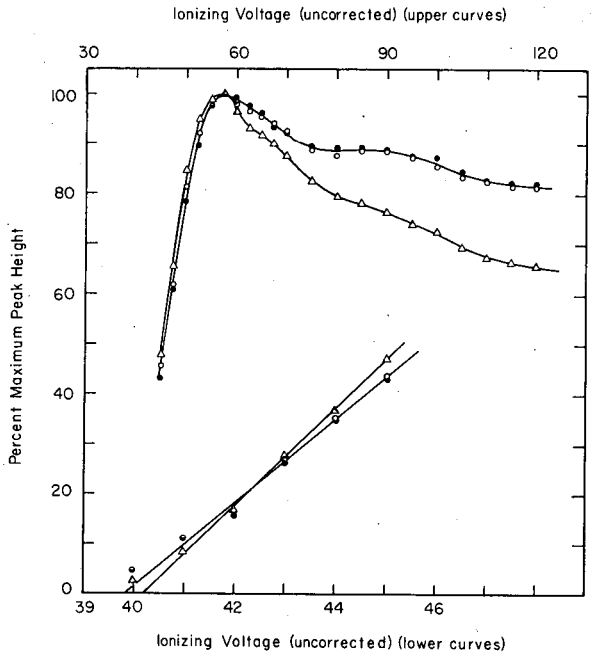

Fig. F.1-5. Ionization efficiency curves for various components of the $(M/q)^*$ = 10 peak in argon.
○ $(M/q)^*$ = 10.00 peak from surface-induced transitions at slit S_3;
○ $(M/q)^*$ = 10.58 peak from surface-induced transitions at slit S_2; and
△ $(M/q)^*$ = 10.10 peak from auto-ionization of $(Ar^+)^*$ beyond slit S_3.
Conditions: Slit S_3 - gold screen, V_{S_2} = 0.058 V_A;
inlet pressure = 1000 μ, I_{e^-} = 75 μA, repellers = 1.011 V_A.

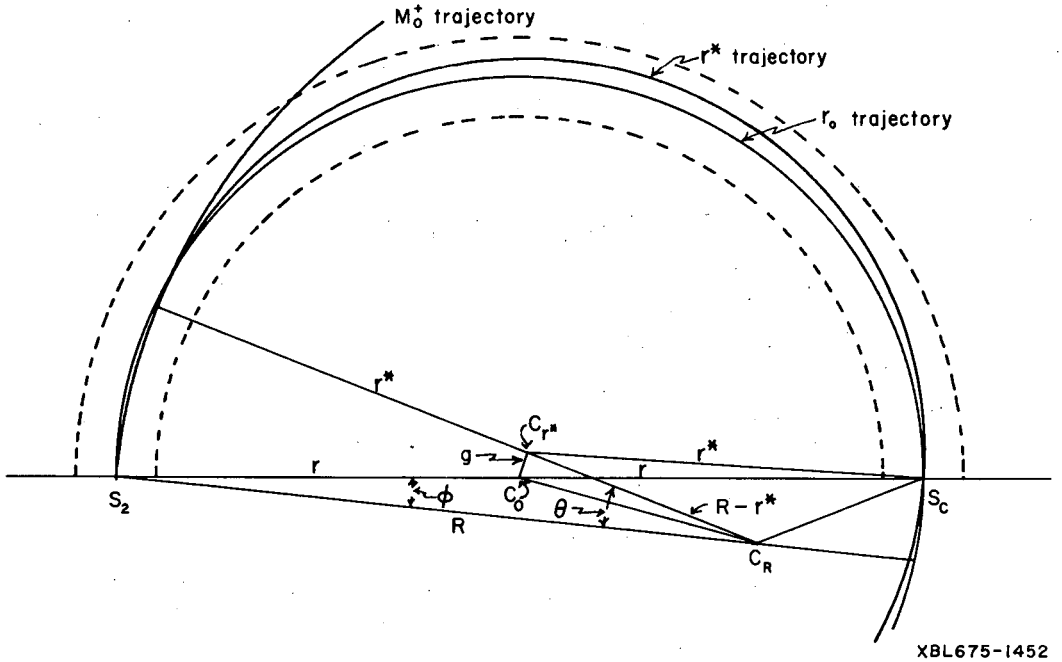

Fig. F.1-6. Schematic construction for deriving r^* and g as a function of R, r, θ, and ϕ.
R = radius of parent ion; r^* = apparent radius of daughter ion; r = normal radius of ions; S_2 = Isatron last slit; S_c = collector slit; g = displacement of new center, C_r^* from normal center, C_0; θ = angle of travel of parent ion, M_0, in trajector of radius R before transition; ϕ = deflection of ion beam M_0^+ from perpendicular at slit S_2. Construction shown is for deflections of ϕ toward the magnet center.

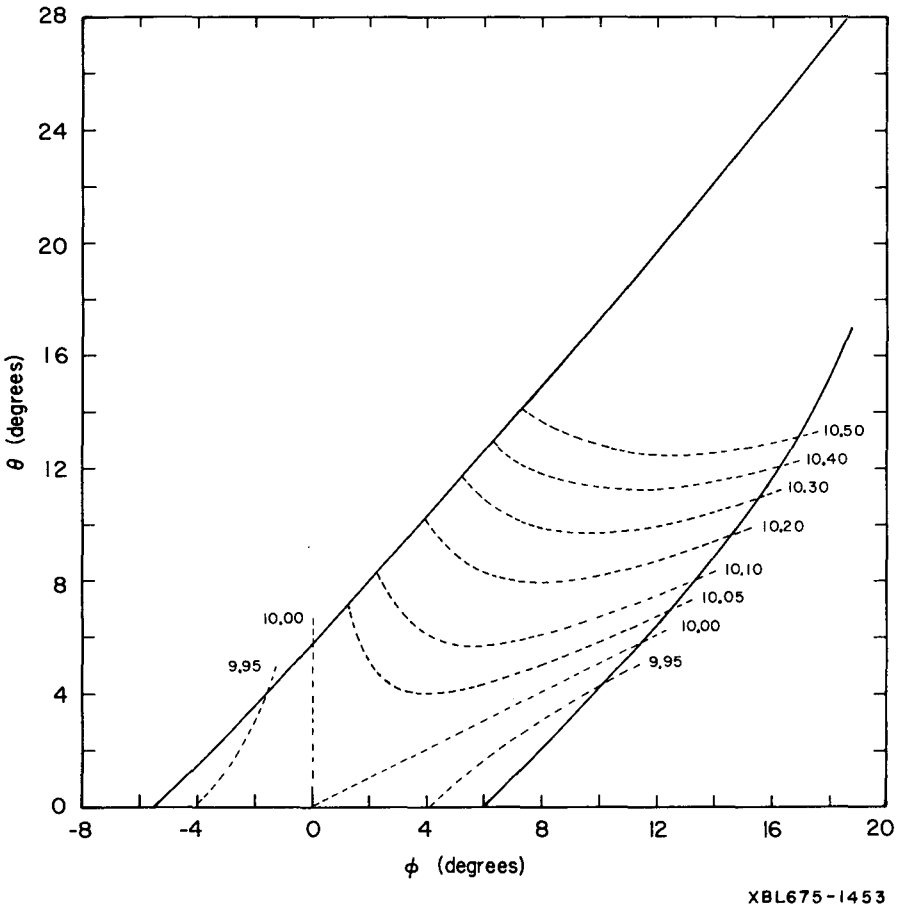

Fig. F.1-7. Field of collectible orbits for the autoionization $(Ar^+)^* \rightarrow Ar^{++} + e^-$ as a function of the angle ϕ of emergence of $(Ar^+)^*$ through slit S_2 and the angle θ of travel on the Ar^+ orbit before transition. Upper solid line is the outer cutoff by the analyzer tube, lower solid line the inner cutoff by the analyzer tube. Dotted lines are isobars of apparent mass $(M/q)^*$ of the daughter (Ar^{++}) ions. Positive ϕ is for deflections toward magnet center; negative ϕ is for deflections away from magnet center.

2. OPERATION OF AN ULTRAHIGH-VACUUM MOLECULAR BEAM APPARATUS FOR STUDIES ON EXCITED STATES OF MOLECULES

R. Clampitt† and Amos S. Newton

A brief report was previously given[1] on the design of a molecular beam apparatus operating at pressures in the ultrahigh-vacuum region. We now report on its performance over a period of several months.

In order to detect low-lying electronically excited states of molecules by electron ejection from a surface, and to detect efficiently states above 5 eV, it is desirable to use a surface of low work function. Previous workers, using common vacuum techniques, succeeded in maintaining an active alkali metal deposit on the detector for periods of from one-half hour to several hours.[3] In our apparatus cesium-coated particle multipliers can be used for several months without loss of

activity by contamination; the lifetime of the cesium is not limited by background contaminants but solely by the chemical nature of the molecular beam.

Vacuum Level

The excitation chamber, pumped by a trapped diffusion pump (an ion pump was used originally but this was found to produce many high-velocity excited neutral molecules that reached the detector), and the detection chamber, pumped by a liquid helium-cooled surface, can be baked to 450°C. After 20 hours' baking at about 250°C the pressure in the detection chamber lies between 6×10^{-11} and 1×10^{-10} torr, depending upon the previous history of the apparatus. The major gases contributing to the pressure are H_2, CO, and CH_4. In the presence of molecular beams such as H_2, N_2O, C_2H_4, and C_3H_6 ($\approx 10^{13}$ mols/sec) the equilibrium pressure in the detection chamber is about 4×10^{-9} torr. Hence contamination of the cesium even by a chemically reactive gas is minimal. The pumping speed of the helium-cooled surface for H_2 at 1×10^{-8} torr is ≈ 1000 liters sec^{-1}.

More than 50 hr of operational time with N_2 as the gas load has been achieved without significant deterioration in cesium activity or vacuum level. With more readily condensible molecular beams significantly longer operational periods should be possible.

Detectors

Two types of multiplier have been used: one is a 16-stage windowless electron multiplier, the first dynode of which was coated with a film of antimony followed by cesium in the hope of producing cesium antimonide. An increase of about 100 in the photoelectric sensitivity of the cesium-coated surface over the antimony surface was observed by using light from a tungsten filament at 1200 to 1500°C. A similar increase was observed in the sensitivity to metastable N_2 molecules. Figure F.2-1 shows the first differential of the excitation curve for the production of N_2 by electron impact with an antimony surface used as the detector. Figure F.2-2 shows the excitation function and its first differential after deposition of cesium. It is seen that the efficiency of detecting the peak at 11.0 eV (presumed to be $A^3\Sigma_u^+$ and $B^3\pi_g$) and the peak at 14.7 eV ($C^3\pi_u$) has increased relative to that for the peak at 12.7 eV ($E^3\Sigma_g^+$). Therefore it appears that the efficiency of detecting excited molecules depends both on the level of excitation and on the nature of the surface. The spectral response of the photoemissive surface was not measured and so its composition is unknown.

The other multiplier used was a 931A photomultiplier manufactured by RCA (almost identical to the 1P21). The composition of the dynodes is known to be Cs_3Sb, which exhibits a characteristic spectral response curve. No light was detected at the photomultiplier when a N_2 beam was excited, so the photon contribution to the N_2^* excitation curve is negligible. Excited N_2 molecules were then detected by remote removal of the vacuum envelope of the multiplier (see following paper). Figure F.2-3 shows the resultant excitation curve produced by electrons of ≈ 0.1 eV energy spread. The $E^3\Sigma_g^+$ state peaks at $\approx$12.2 eV, in agreement with previous results.[4] This curve differs considerably from that in Fig. F.2-2 for a cesium-coated surface of unknown composition and work function.

More work is necessary on the effects of surface composition on the detection of electronically excited molecules. It will be particularly instructive to study the metastable excitation function during deposition of cesium metal on the surface and at the same time to monitor the spectral response of the surface.

Acknowledgments

The authors thank C. E. Minor and R. E. Parsons for considerable help in the engineering aspects of the design of the apparatus.

References

† Present address: The Culham Laboratory. Abingdon, Berkshire, England

1. R. Clampitt and Amos S. Newton, in Nuclear Chemistry Annual Report, UCRL-17299, Jan. 1967, p. 221.
2. R. Freund and W. Klemperer, J. Chem. Phys. 47, 2897 (1967).
3. W. Lichten, Phys. Rev. 109, 1191 (1958).
4. J. Olmsted, Amos S. Newton, and K. Street, J. Chem. Phys. 42, 2321 (1965).

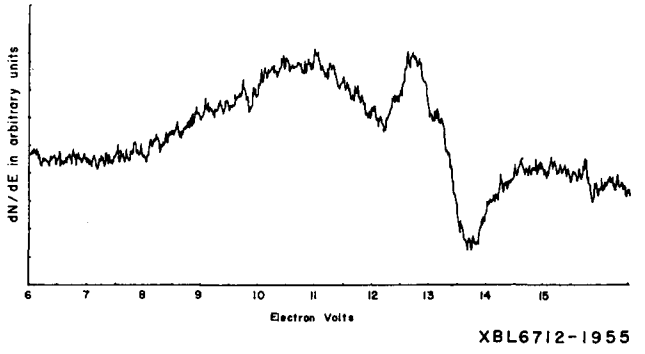

Fig. F.2-1. First differential of the N_2^* excitation curve before cesium deposition. Ordinate = detector current

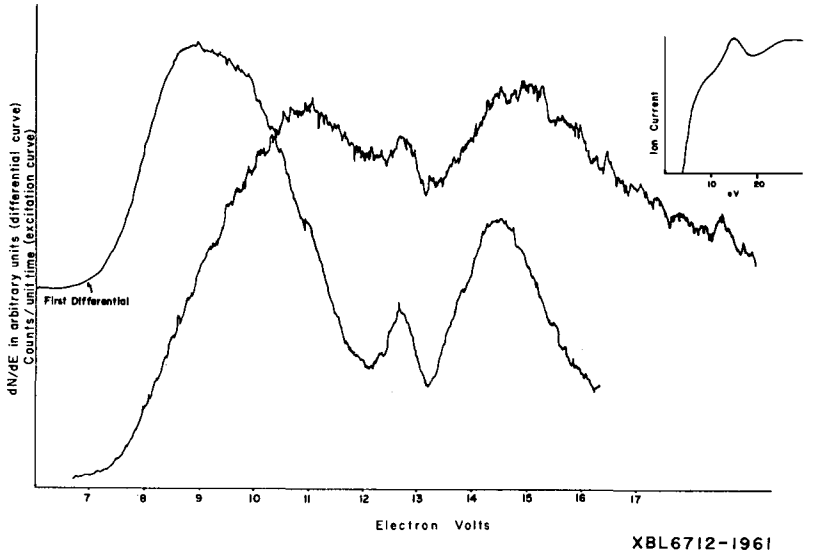

Fig. F.2-2. Excitation function for N_2^* following cesium depositions. Ordinate = detector current.

Fig. F.2-3. N_2^* excitation curve measured with 931A photomultiplier. Ordinate = detector current

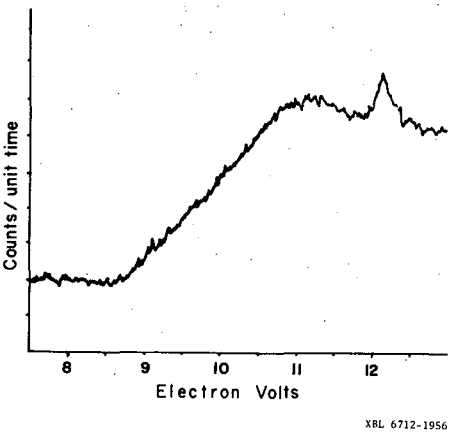

3. A PHOTOMULTIPLIER FOR THE DETECTION OF METASTABLE ELECTRONICALLY EXCITED MOLECULES

R. Clampitt† and Amos S. Newton

Introduction

In the course of some work on the detection of long-lived excited states of molecules by electron ejection from the first dynode of an electron multiplier, we wanted to use a dynode surface of very low work function. A standard RCA nine-stage 931A photomultiplier (almost identical to the 1P21) has Cs_3Sb-coated dynodes and exhibits a spectral response peak in the visible region. The photocathode of the 931A is not deposited on the glass envelope, as it is with most photomultipliers, and so it should make a very sensitive detector of metastable molecules if its vacuum envelope can be removed in a vacuum. This has been carried out in the detection chamber of the apparatus described in the preceding paper.

Experimental Technique

Figure F.3-1 shows the photomultiplier in position. The spectral response curve (S-4) is measured by using modulated light from a monochromator at the quartz window, H. The light signal is detected with a lock-in amplifier. The monochromator serves also to study the stability of the Cs_3Sb photocathode, A, during the impingement of a molecular beam. The glass envelope is not removed until the pressure is down to $\leq 2\times10^{-10}$ torr in the detection chamber; a quadrupole mass filter is used to monitor the residual gases (mainly H_2, CO, and CH_4). A copper weight, D, of 500 g is suspended from the envelope by means of several steel wires C. The multiplier is clamped in a holder near its base. A nichrome wire, previously outgassed, and which is in contact with a diamond-etched mark on the glass, is heated rapidly, whereupon the envelope breaks and falls with the copper weight into a bucket above the liquid helium pump. The envelope will not fall without the encouragement of a weight, partly because it is held to the multiplier by sprung metal spacers.

The support F is a hollow tube that can be filled with liquid nitrogen to cool the multiplier. A shield E surrounds the multiplier and is operated at a potential selected for minimum noise current; it can also be used to prevent ions from reaching the multiplier. The spectral response curve for the windowless photomultiplier was unchanged in the visible region, and it was found that the glass envelope transmitted 65% of light at 550 mμ. The spectral sensitivity of the Cs_3Sb is unaffected by the impingement of such molecular beams as N_2, H_2, CO, N_2O, C_2H_4, and C_3H_6; it was used to obtain all the time-of-flight data presented in the following paper.

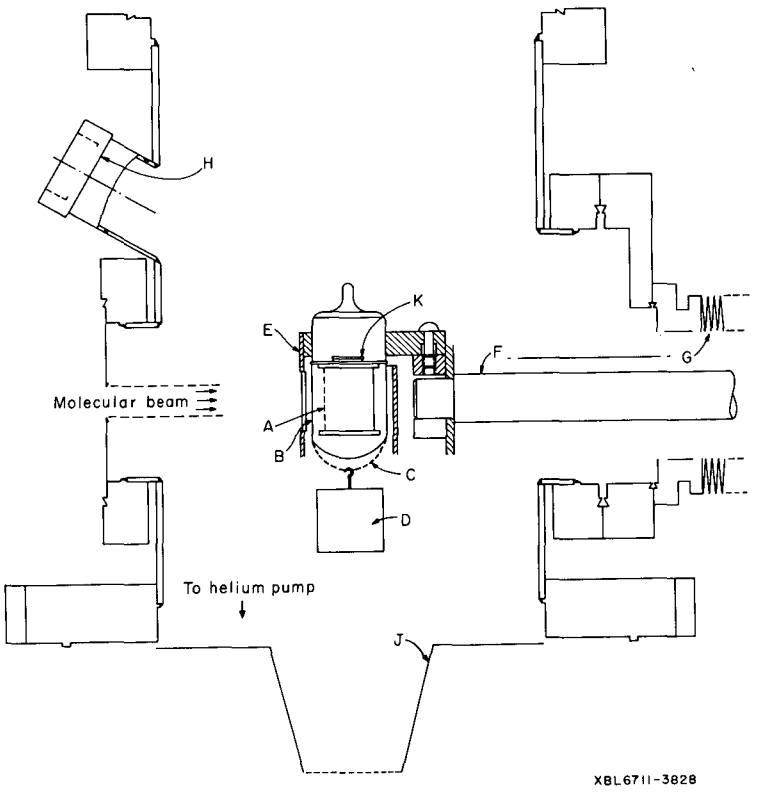

Fig. F.3-1. Removal of the glass envelope of a 931A photomultiplier in an ultrahigh vacuum.

4. TIME-OF-FLIGHT RESOLUTION OF ELECTRONICALLY EXCITED MOLECULES

R. Clampitt† and Amos S. Newton

Some preliminary studies on excited states of molecules have been made with the apparatus described in a previous paper. There are several methods of operating the apparatus, and the use of time-of-flight techniques is described here.

It is desirable to know the photon contribution to the measured excitation function for a metastable molecule and also to determine whether the excited species is the parent molecule or a neutral fragment. The resolution of an excited fragment can be achieved in the present apparatus only if it is formed with kinetic energy of dissociation, in which case it becomes resolvable by its time of flight in the following way. The electron beam, usually 0.5 to 1 μA, is pulsed on for 10 μsec, and this pulse starts the time sweep on a multichannel analyzer operated in the multiscaler mode. If one uses 10 μsec channel residence time, and allows for a dead time per channel of about 12 μsec, one complete sweep of 100 channels can be made in ≈ 220 μsec. The first channel registers photons resulting from optically allowed transitions, but the metastable molecules arrive at the detector much later. Figure F.4-1 shows the velocity distribution of krypton. The photon contribution is insignificant. Figure F.4-2 shows the H_2^* velocity distribution obtained with 15-eV electrons; the photon contribution is considerable. It has been supposed that the photon contribution to the excitation functions of metastable molecules, obtained by molecular beam methods, is negligible due to the extremely small solid angle subtended by the detector to photons emitted in the excitation chamber. For hydrogen, at least, this is not so. The excitation curve for photon emission can be separated from the excitation curve for excited molecules by a method of delayed coincidence,

described below.

Figure F.4-3 shows the velocity distribution of the excited species produced by electron impact on N_2O. The peak of the distribution corresponds to a mass of about two, and so the excited species cannot be N_2O^* but must be a kinetically energetic fragment.[3]

Delayed Coincidence Measurements

To obtain the excitation function for the production of H_2^* by electron impact, without interference from photons, the scheme shown in Fig. F.4-4 was used. The electron beam is pulsed on for 10 μsec at a repetition rate of 3300 Hz. This pulse triggers a ramp sweep of the electron energy and also starts the multichannel analyzer. The total scan time for a hundred channels on the analyzer is chosen to equal the sweep rate of the ramp, typically 40 msec. The excitation function so obtained consists of both photons and metastable molecules. If now a square-wave pulse, synchronized with the electron beam pulse but delayed by 10 μsec, is used to gate on the pulse amplifier, the analyzer registers only the signal from metastable molecules. Conversely, if the pulse amplifiers are allowed to count only during the 10-μsec duration of the electron beam pulse, the photon excitation curve is obtained. The sweep rate of the ramp is very slow compared with the electron beam pulsing rate, so that several pulses occur for each 0.2 V increase in electron energy. Figure F.4-5 shows the photon excitation curve for H_2. Figure F.4-6 shows the metastable excitation curve; this exhibits the characteristic feature of resonance excitation of a triplet state, and is very similar to that reported previously by Lichten,[1] using a molecular beam magnetic resonance method. The present measurement has resolved the discrepancy between Lichten's curve and that obtained a few years ago in this Laboratory.[2] The latter included no correction for the photon contribution.

Acknowledgments

The authors thank F. Vogelsberg for enthusiastic support during the course of this work.

Footnote and References

† Present address: The Culham Laboratory, Abingdon, Berkshire, England.

1. W. Lichten, Phys. Rev. 120, 848 (1960).
2. J. Olmsted, Amos S. Newton, and K. Street, J. Chem. Phys. 42, 2321 (1965).
3. Also recently observed by R. Freund and W. Klemperer, J. Chem. Phys. 47, 2897, (1967).

Fig. F.4-1. Velocity distribution of metastable Kr atoms at 17 eV electron impact energy; 500 Hz pulse repetition rate. Full scale along the abscissa equals 3 msec.

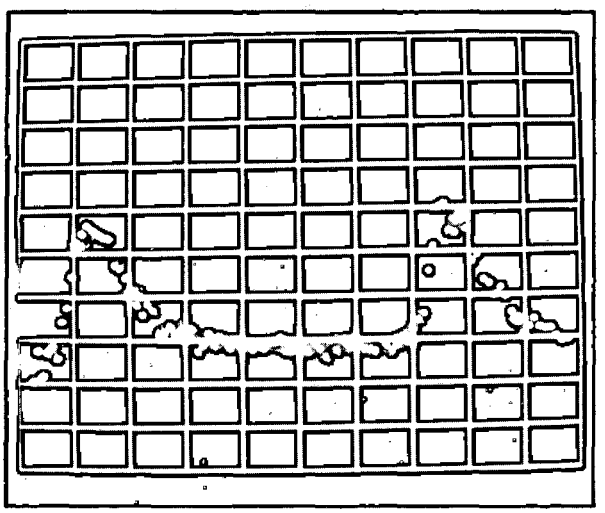

XBB6711-6579

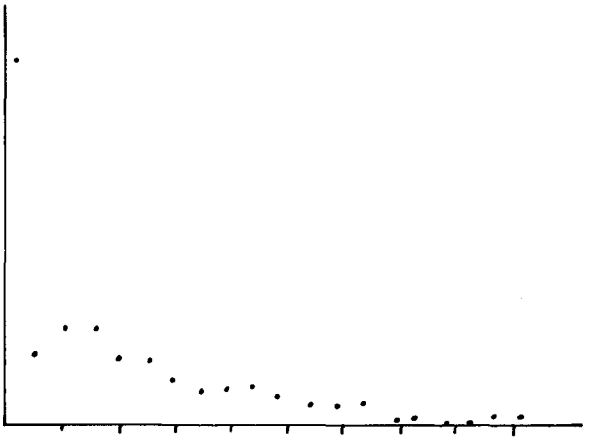

XBL 6712-1957

Fig. F.4-2. Velocity distribution of H_2^* at 15 eV electron energy; one division along the abscissa equals 2.2 msec.

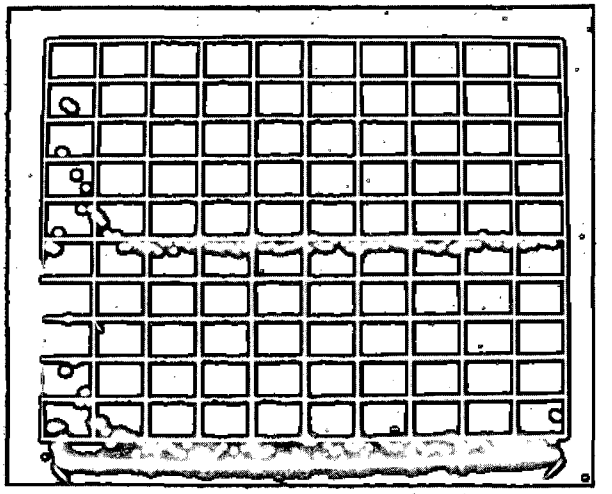

XBB6711-6583

Fig. F.4-3. Velocity distribution of excited fragment from N_2O; top curve 20-eV electrons, bottom curve 18-eV electrons. Full scale along abscissa equals 2.2 msec.

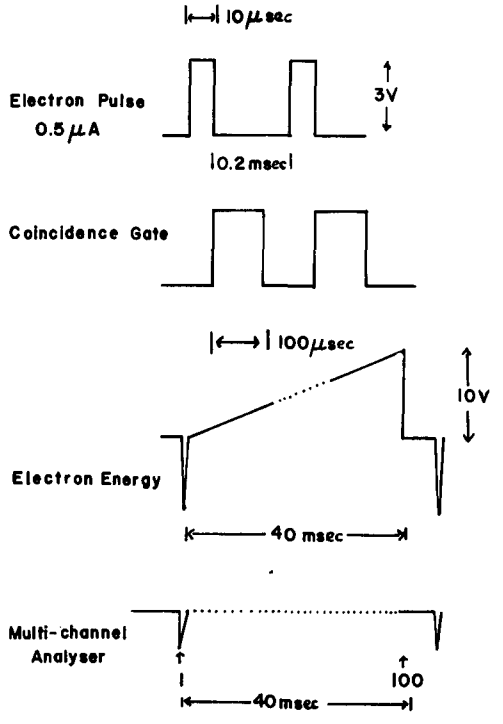

XBL 6712-1958-A

Fig. F.4-4. Scheme of delayed coincidence for the resolution of photons from metastable molecules.

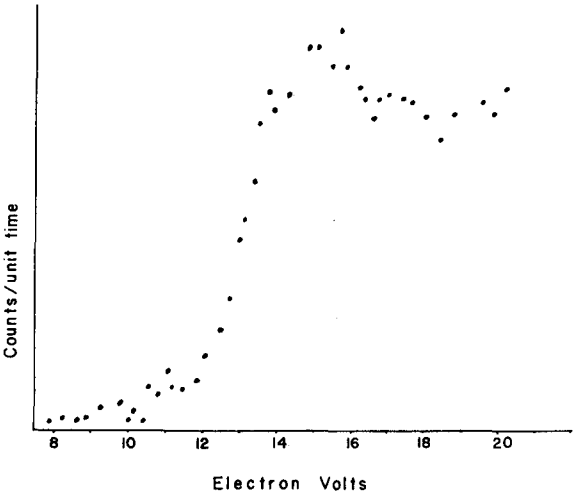

XBL 6712-1959

Fig. F.4-5. Excitation function for production of photons from H_2.

Fig. F.4-6. Excitation function for production of metastable H_2.

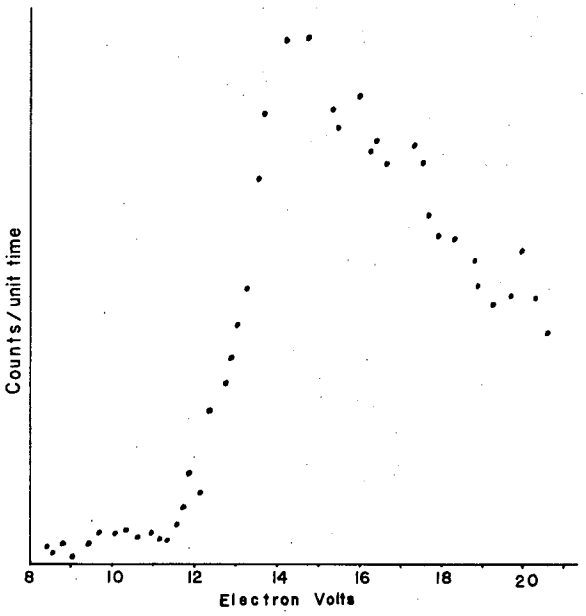

XBL 6712-1960

G. CHEMISTRY

1. DIPOLE MOMENTS OF SOME ALKALI HALIDE MOLECULES BY THE MOLECULAR BEAM ELECTRIC RESONANCE METHOD†

A. J. Hebert, F. J. Lovas, C. A. Melendres, C. D. Hollowell,
T. L. Story, Jr., and K. Street, Jr.

We have made rather accurate measurements of the dipole moments of a number of alkali halide molecules by the molecular beam electric resonance method. Our particular interest in these measurements was largely motivated by attempts to improve[1,2] the simple ionic model of the gaseous alkali halide molecules; however, they may be of some interest for other reasons also.

A description of the apparatus used, the method of reducing the data, and some results for other alkali halides have been published previously;[3-5] in the interests of economy of space only the results are given here. More detailed accounts of these measurements are available in a series of unpublished Lawrence Radiation Laboratory reports, reference to which is given in Table G. 1-I.

Dipole moments for some of the molecules (NaBr, NaI, and RbCl) have not been reported previously, others represent only some improvement in the accuracy of measurement. Since the principal source of disagreement between dipole measurements made in different laboratories is likely to arise from uncertainties in the value of the Stark field used, we have included in Table G. 1-I our measurements on LiF and KCl. LiF has been previously measured at Harvard[6] and KCl has been recently measured at Nijmegen.[7] A comparison of these results indicates that independent Stark-field measurements at Harvard, Nijmegen, and Berkeley are in excellent agreement.

Footnote and References

†UCRL-17962, Nov. 1967.

1. K. Street, Jr., The Simple Ionic Model of the Alkali Halide Molecules.
2. K. Street, C. D. Hollowell, and F. J. Lovas, An Extended Ionic Model of the Alkali Halide Molecules.
3. A. J. Hebert, F. W. Breivogel, Jr., and K. Street, Jr., J. Chem. Phys. 41, 2368 (1964).
4. C. D. Hollowell, A. J. Hebert, and K. Street, Jr., J. Chem. Phys. 41, 3540 (1964).
5. F. W. Breivogel, Jr., A. J. Hebert, and K. Street, Jr., J. Chem. Phys. 42, 1555 (1965).
6. L. Wharton, W. Klemperer, L. P. Gold, R. Strauch, J. J. Gallagher, and V. E. Derr, J. Chem. Phys. 38(5), 1203 (1963).
7. R. van Wachem and A. Dymanus, J. Chem. Phys. 46 (10), 3749 (1967).

Table G. 1-I. Dipole moments.

Molecule†	Vibrational state, v			Dipole moment function $u_v = u_e + u_I(v+\frac{1}{2}) + u_{II}(v+\frac{1}{2})^2$		
	v = 0	v = 1	v = 2	u_e	u_I	u_{II}
$^6Li^{19}F$ [a]	6.32736(20)	6.41472(20)	6.50317(20)	6.28409(25)	0.08627(5)	0.00054(2)
[b]	6.32764(100)	6.41211(100)	6.50341(100)	6.28446(100)	0.08612(3)	0.00060(2)
$^7Li^{19}F$ [a]	6.3248(10)	6.4072(10)	6.4905(10)	6.2839(12)	0.08153(30)	0.00044(12)
$^6Li^{35}Cl$ [a]	7.1289(10)*	7.2168(10)*	7.3059(10)*	7.0853(13)	0.0868(4)	0.00056(14)
[c]	7.1195(22)*	7.2069(22)*	7.2964(22)*			
$^6Li^{37}Cl$ [a]	7.1287(10)*	7.2163(10)*	7.3052(10)*	7.0853(13)	0.0864(5)	0.00064(16)
[c]	7.1192(22)*	7.2071(22)*	7.2972(22)*			
$^{39}K^{35}Cl$ [a]	10.2688(10)	10.3288(15)	10.3877(22)	10.2384(12)	0.0610(9)	0.00055(40)
[d]	10.26900(100)	10.32900(100)	10.38945(100)	10.23911(100)	0.05966(14)	0.00019(3)
$^{23}Na^{35}Cl$ [e]	9.0020(5)	9.0619(5)	9.1223(5)	8.9721(6)	0.05963(20)	0.00017(10)
[f]	9.000(4)	9.061(4)	9.122(4)			
$^{23}Na^{37}Cl$ [e]	9.0017(7)	9.0610(7)		8.9721(13)	0.0593(6)	
$^{23}Na^{79}Br$ [e]	9.1183(6)	9.1715(6)	9.2246(6)	9.0918(13)	0.0531(7)	
$^{23}Na^{127}I$ [g]	9.2357(30)	9.2865(30)	9.3368(30)	9.2103(30)	0.0507(8)	
$^{85}Rb^{19}F$ [g]	8.5465(5)	8.6134(7)	8.6809(9)	8.5131(7)	0.06650(28)	0.00026(12)
[h]	8.5464(7)	8.6127(17)				
$^{85}Rb^{35}Cl$ [g]	10.510(5)	10.564(5)	10.618(5)	10.483(6)	0.054(3)	
$^{133}Cs^{19}F$ [g]	7.8839(9)	7.9546(10)*	8.0257(10)*	7.8486(13)	0.0704(3)	0.00018(20)
[i]	7.875(6)	7.9472(63)*	8.0194(66)*	7.839(6)*	0.0722(3)	
[j]	7.878(3)	7.950(3)		7.842(3)*	0.07229(12)	
$^{133}Cs^{35}Cl$ [g]	10.387(4)	10.445(4)	10.503(4)	10.358(5)	0.058(1)	
[i]	10.42(2)	10.476(22)*	10.532(24)*	10.392(20)*	0.056(2)	

*These values were calculated here from data in the reference cited.
†Values for NaI, KCl, RbCl, and CsCl were determined from J = 2 spectra, while all the others are from J = 1 spectra. All values are in Debye units.

a. A. J. Hebert, C. D. Hollowell, T. L. Story, and K. Street, Jr., UCRL-17256, March 1967.
b. Reference 6.
c. D. T. F. Marple and J. W. Trischka, Phys. Rev. 103, 597 (1956).
d. Reference 7.
e. Carlos A. Melendres, A. J. Hebert, and K. Street, Jr., UCRL-17916, Nov. 1967.
f. Lewis P. Gold (Ph. D. Thesis), Harvard University, Cambridge, Mass., November 1961.
g. Frank J. Lovas, Radio-Frequency Stark Spectra of RbF, RbCl, CsF, CsCl, and NaI (Ph. D. Thesis), UCRL-17909, Nov. 1967.
h. G. Gräff, R. Schönwasser, and M. Tonutiti, S. Physik 199, 157 (1967).
i. J. W. Trischka, J. Chem. Phys. 25, 784 (1956).
j. G. Gräff and O. Runolfsson, Z. Physik 187, 140 (1965).

2. SPECTROSCOPIC INVESTIGATIONS OF EINSTEINIUM IODIDE†

R. G. Gutmacher,* E. F. Worden,* and J. G. Conway

An electrodeless lamp containing 0.6 μg of ^{253}Es and 100 μg GdI_3 was prepared to observe the hyperfine structure of Es. The material in the lamp exhibited a bright self-luminescence which was activated by the radioactive decay of the Es. The lamp was used to photograph the self-luminescence of Es^{3+}. At room temperature, the glow was green; at 77°K, it was bright orange. The low-temperature spectrum showed a broad band centered at 4700 Å and three groups of lines in the red and near infrared. A group of five lines around 6700 Å was the strongest feature. At room temperature, additional groups in the blue and green appeared. The data will be compared with theoretical calculations of the energy levels for the $5f^{11}$ configuration of Es IV.

Footnotes

†Presented at the Atomic Spectroscopy Symposium, National Bureau of Standards, Gaithersburg, Maryland, Sept. 11-14, 1967.

*Lawrence Radiation Laboratory, Livermore, California.

3. EXTENSION OF THE ANALYSIS OF THE CmI AND CmII SPECTRA†

E. F. Worden and J. G. Conway

The ground configurations of CmI and CmII $5f^7\,6d\,7s^2$ and $5f^7\,7s^2$, respectively, and the low odd configuration $5f^7\,6d\,7s$ of CmII have been discussed previously.[1,2] The levels of the lowest terms from the even configurations $5f^8\,7s^2$ and $5f^8\,7s$ of CmI and CmII have now been determined. These configurations lie unexpectedly low. The lowest level of $5f^8\,7s$, $^8F_{6.5}$, is 2093.88 cm^{-1} above the ground level in CmII and the lowest level of $5f^8\,7s^2$ in CmI, $^7F_6$, is only 1214.18 cm^{-1} above the ground level. The analagous separation in GdI is about 10 000 cm^{-1}. This indicates that in the adjacent heavier actinides the configuration $f^n s^2$ may lie considerably lower than $f^{n-1} ds^2$, the separation being about 10 000 cm^{-1} greater than in the corresponding lanthanide.

Footnote and References

†Presented at the Atomic Spectroscopy Symposium, National Bureau of Standards, Gaithersburg, Maryland, Sept. 11-14, 1967.

1. E. F. Worden, R. G. Gutmacher, E. K. Hulet, J. G. Conway, and M. Fred, J. Opt. Soc. Am. 52, 1311 (1962).
2. E. F. Worden, and J. Conway, Physica 33, 274 (1967).

4. AIRBORNE SPECTROGRAPHIC OBSERVATIONS OF THE SOLAR ECLIPSE OF NOVEMBER 12, 1966†

John G. Conway, William F. Morris, and C. Frederick Andrews*

On November 12, 1966, a total eclipse of the sun was observed from a C135 "flying laboratory" instrumented by the Lawrence Radiation Laboratory, Mid-totality occurred at 14 hr 18 min U. T. off the coast of Rio Grande, Brazil, at 35° 35′ south and 49° 40′ west. The aircraft, flying at an altitude of 33 000 feet and at a ground speed of 550 knots, remained in the eclipse shadow for 3 min 22 sec.

During totality, the spectrum of the solar corona was photographed over a wavelength region extending from 3000 to 6750 Å. Two spectrographs were employed in the airborne experiment.

The primary spectrograph, a Czerny-Turner F/6.3, was shock-mounted in the aircraft and illuminated with the coronal image by means of an automatic tracker. The instrument, equipped with a 1200 g/mm grating blazed at 5000 Å, gave a linear dispersion of 9 Å/mm. Two settings of the grating were required to cover the spectrum wavelength range of 3800 to 6750 Å, which was photographed on Kodak type 103aF plates.

The second instrument, a Hilger F/4 prism spectrograph, was mounted in a special carriage which allowed manual alignment of the instrument with the sun. During totality six exposures were taken in the wavelength region 3000 to 5400 Å. The spectra were photographed on Kodak 103aO plates.

In general, the objectives of the spectrographic observations were realized. It should be noted, however, that the intensity of the coronal light incident on the Czerny-Turner spectrograph was weaker than anticipated due, in part, to optical losses. Also there were solar prominences in the region observed. As a result, only two coronal lines, 5303 and 6374 Å, were recorded in the high-resolution spectrum along with prominence emission lines due to H, He, and CaII. The widths of the two coronal lines were measured to yield the calculated coronal temperatures listed in Table G. 4-I. Limb-to-corona intensity profiles of the observed lines have been recorded. These are shown in Fig. 1. The unusual spatial profile of the CaII lines in which CaII reappears at a point 1 solar radius above the limb is not explained. The presence of CaII in the middle corona is not consistent with the temperature prevalent in that region.

Of the six spectra photographed on the Hilger F/4 spectrograph, five show coronal lines superimposed on chromospheric and prominence lines due to TiII, CrII, CaII, He, and H. One spectrum displays predominantly coronal lines with the exception of CaII and HeI lines. The coronal lines observed were 5303 Å, 4231 Å, 3987 Å, 3801 Å, 3643 Å, 3601 Å, 3454 Å, 3388 Å, 3327 Å, 3170 Å, 3073 Å, 3021 Å.

Footnotes

†Condensation from Astrophys. J. 150, 229 (1967).
*LRL, Livermore, California.

Table G. 4-I. Coronal temperature calculated from coronal line widths.

Line Wavelength (Å)	Identification	Half-width	Temperature (°K)
5303	Fe XIV	0.80±0.08	2.5×10^6
6374	Fe X	0.81±0.08	1.8×10^6

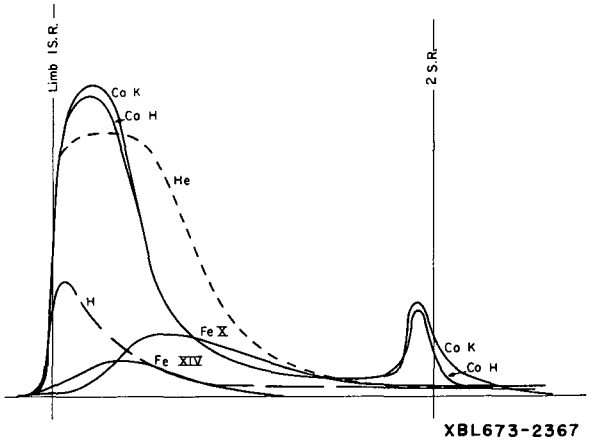

Fig. G. 4-1. Limb-to-corona intensity profiles for H at 4340 Å, HeI at 5875 Å, HeI at Å, Fe x at 6374 Å, Ca H at 3968 Å, and Ca K at 3933 Å.

5. SUPERCONDUCTING MAGNETS FOR SPECTROSCOPY†

John G. Conway, Sumner P. Davis,* and Richard J. Wolff*

One of the most powerful tools used for the analysis of complex spectra is the Zeeman effect. It is generally accepted that higher magnetic fields than can be produced by conventional electromagnets are needed. In recent years the magnetic fields achieved by superconducting magnets indicate that spectroscopy can expect some help. We have taken spectra of rare earths in a superconducting magnet at fields of 50 000 G, using microwave excitation and a high-dispersion spectrograph. The spectra of Pm and Er have been photographed and improvements are quite noticeable. The problems we have found are mostly with the storage of liquid helium and with changes in the current, which cause the magnet to go conducting. These are mainly our experimental techniques and will have to be worked out.

Footnotes

†J. Opt. Soc. Am. 57, 583 (1967).
*Department of Physics, University of California, Berkeley, California.

6. TETRAVALENT Np INDUCED IN CaF_2 BY γ IRRADIATION

J. J. Stacy, R. D. McLaughlin, N. M. Edelstein, and J. G. Conway

The divalent state of all of the lanthanides can be stabilized in CaF_2 by γ irradiation.[1] Recently we have shown that divalent Am can likewise be stabilized in CaF_2. However, extension of this work to include Pu and Cm showed that the tetravalent state is formed when the tripositive ion is irradiated.[3,4] We present here our results for Np in CaF_2.

Single crystals of CaF_2 doped with 0.1 to 0.2 wt % of ^{237}Np (half-life, 2.16×10^6 years) were grown as described previously.[2] The absorption data for these crystals were obtained with a Jarrell-Ash Model 75, f/6 spectrograph and a Cary Model 14 spectrophotometer. From a comparison of our data with Krupke's data for Np^{3+} in $LaBr_3$,[5] we conclude that our Np is initially in the 3+ state. From Fig. G.6-1 it can be seen that in $LaBr_3$ the spectrum consists of definite groups of sharp lines, whereas in CaF_2 it is considerably more complex. This is due to (i) a larger crystal field splitting in CaF_2, and (ii) the existence of different site symmetries in the charge-compensated CaF_2.

When our crystal was γ-irradiated for 15 hours with a ^{60}Co source (7800 curies), it turned from its original light green color to a deep blue. In addition to the Np^{3+} peaks, an intense broad absorption appeared throughout the visible region and three new groups of sharp lines appeared. In Fig. G.6-1 it is shown that these three groups agree extremely well with the most intense Np^{4+} peaks reported by Waggener in D_2O.[6] We were not able to observe the Np^{4+} peaks at $\approx1.2\,\mu$ because the 3+ absorption was so intense in that region. Table G.6-I lists the Np^{4+}:CaF_2 wavelengths and their corresponding J values as calculated by Conway.[7] The assignment of the 0.7-μ group is not straightforward because of the calculation of four J levels in that region. The broad absorption in the visible region has been tentatively assigned to color centers. There still exists the possibility that this absorption is characteristic of divalent Np; however, we have no evidence to support this conclusion.

When a trivalent ion is incorporated into the CaF_2 lattice, the extra positive charge must be compensated. Different charge-compensating mechanisms give rise to spectra characteristic of the particular site symmetry about the dopant ion. We investigated the high-resolution absorption spectra of Np^{3+}: CaF_2 in the region 9400 to 10 000 Å and found that only certain peaks decreased in intensity upon γ irradiation. Of 12 peaks studied, 8 remained unchanged but 4 decreased to 1/3 their original intensity. From this we conclude that there is a selective oxidation of Np^{3+}; that is, only certain symmetry sites can be oxidized by γ irradiation. Such a phenomenon has been reported for the reduction of trivalent rare earths in CaF_2,[8] but never for their oxidation.

The Np^{4+} is not completely stable and decreases slightly in intensity over a period of a few months at room temperature. When the crystals are heated at 400°C for 20 minutes the color centers are bleached out and the Np^{4+} structure is completely destroyed. This behavior can be accounted for by the model offered by Makovsky,[9] in which electron traps become localized at the vicinity of the 4+ ions. Reconversion occurs when these trapped electrons are released by thermal agitation and recombine with the 4+ ion.

Further work is in progress.

References

1. Z. J. Kiss in Lasers and Applications, W. S. C. Chang, Ed. (Ohio State University Press, Columbus, 1963).
2. N. Edelstein, W. Easley, and R. McLaughlin, J. Chem. Phys. 44, 3130 (1966).
3. R. McLaughlin, R. White, N. Edelstein, and John G. Conway, Optical Spectra of Pu in CaF_2, J. Chem. Phys. (in press).
4. N. Edelstein, W. Easley, and R. McLaughlin, Optical and Electron Paramagnetic Resonance Spectroscopy of Actinide Ions in Single Crystals, UCRL-17183, Oct. 1966.
5. W. F. Krupke and J. B. Gruber, J. Chem. Phys. 46, 542 (1967).
6. W. C. Waggener, J. Chem. Phys. 62, 382 (1958).
7. J. Conway, J. Chem. Phys. 41, 904 (1964).
8. J. L. Merz and P. S. Pershan, Phys. Rev. 162, 217 (1967), and references contained therein.
9. J. Makovsky, Phys. Rev. Letters 15, 953 (1965).

Table G.6-I. Lines that grow into $Ca(Np)F_2$ crystal γ irradiation.

Wavelength (Å)	Wave number (Cm^{-1})	J value
7257	13777	
7282	13728	
7313	13671	$\frac{15}{2}, \frac{7}{2}, \frac{5}{2}, \frac{3}{2}$
7328	13643	
7333	13633	
7347	13608	
9672	10336	$\frac{3}{2}$
9694	10313	
9816	10185	
9870	10128	
9951	10046	
16630	6010	
16750	5967	
16810	5948	
16950	5897	$\frac{11}{2}$
16970	5890	
17010	5876	
17040	5868	
17290	5780	

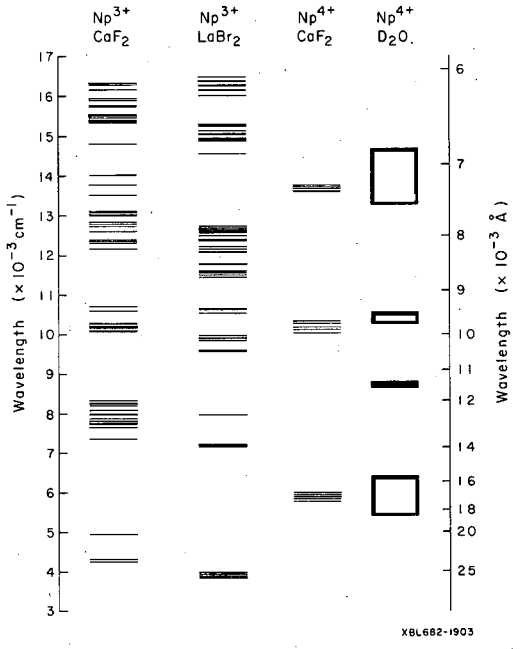

Fig. G. 6-1. Comparison of Cm spectra in various matrices.

7. ZERO-FIELD SPLITTINGS OF Am^{2+} AND Cm^{3+} IN CUBIC SYMMETRY SITES IN CaF_2†

N. Edelstein and W. Easley

I. Introduction

The lanthanide series has been extensively investigated in crystals of the fluorite type by electron paramagnetic resonance (epr) and optical spectroscopy. The trivalent ions in these crystals may be found in various symmetry sites, depending upon the conditions under which the crystals were grown.[1] The divalent ions are found in sites of cubic symmetry. Two of the most studied lanthanide ions are Gd^{3+} and Eu^{2+}, the half-filled shell ($4f^7$, $^8S_{7/2}$) configuration. For these ions in cubic symmetry the crystal field splittings are readily measured, although the mechanisms causing these splittings are not well understood.[2]

We have previously reported the spin Hamiltonian parameters for Am^{2+} and Cm^{3+}, the $5f^7$ actinide analogs for Eu^{2+} and Gd^{3+}.[3] The earlier epr measurements were done at 9.2 GHz and temperatures of 4° and 1° K, and were obtained for these actinide ions doped in CaF_2 in sites of cubic symmetry. No resonance lines due to actinide ions were seen at 77° K. In this paper we report epr measurements made at 35 GHz on Am^{2+} and Cm^{3+} in cubic crystal field sites in the CaF_2 lattice. The larger magnetic field mixes into the ground crystal field state (Γ_6) the next highest crystal field state (Γ_8), which causes the measured g values to be anisotropic. From the anisotropy of the g value we have determined the zero-field splitting in these two ions. We also show that the simple point-charge model qualitatively explains the magnitude of the effects.

Discussion and Results

A free ion placed in a crystalline electric field undergoes a splitting of its total angular momentum J which is dependent upon the symmetry of the electrostatic field. We are interested in the case of a $J = 7/2$ state placed in a cubic symmetry site in the CaF_2 lattice. From group

theoretical arguments, the J = 7/2 state in zero magnetic field will split into two doubly degenerate states, Γ_6 and Γ_7, and one quartet state, Γ_8. The Hamiltonian for this problem, including the Zeeman effect caused by an external magnetic field, may be written

$$\mathcal{H} = g_J \beta \vec{H} \cdot \vec{J} + B_4(O_4^0 + 5\,O_4^4) + \beta_6(O_6^0 - 21\,O_6^4). \quad (1)$$

The first term represents the Zeeman interaction, where g_J is the Landé g value for the lowest free ion level, β is the Bohr magneton, and $\vec{H}$ is the external magnetic field. The last two terms represent the effect of the cubic crystalline field on the J = 7/2 manifold, where we consider B_4 and B_6 as adjustable parameters related to the strength of the crystalline field. The O_n^m terms are angular momentum operators of the appropriate symmetry.[4]

For zero magnetic field we find an exact solution for this Hamiltonian applied to the J = 7/2 manifold, the energies of the levels being given in terms of $b_4 = 60B_4$ and $b_6 = 1260B_6$. The energy-level diagram is shown in Fig. G. 7-1. If we choose the energy of the Γ_6 state to equal zero, the second column in Fig. G. 7-1 shows the relative energies. If the crystal field splitting is much greater than the Zeeman interaction, then the zero field wave functions will be an accurate representation and can be used to calculate g values of the crystal field energy levels.

At higher magnetic fields the Zeeman term becomes important, and causes an anisotropy in the epr spectrum of the Γ_6 state, since this interaction mixes the Γ_8 with the Γ_6 state. From the magnitude of the anisotropy we can determine the splitting of the $\Gamma_6 - \Gamma_8$ levels. The experimental data are shown as circles in Fig. G. 7-2. We have plotted the g value of the Γ_6 state for both Cm^{3+} and Am^{2+} as a function of the angle of the magnetic field with respect to the unit cell axis of the CaF_2 lattice. The magnetic field was rotated in the [110] plane of CaF_2. In order to determine the values of the parameters b_4, b_6, and g_J which would reproduce the experimental data, the Hamiltonian (Eq. 1) was applied to the J = 7/2 manifold, which resulted in an 8×8 matrix with elements in terms of the above parameters, the magnetic field H, and the direction cosines of H relative to the cubic axes of CaF_2. A computer program was written which diagonalized the 8×8 matrix and calculated the g values for the ground Kramers doublet state.[5] The values of b_4, b_6, and g_J were varied until the best fit to the experimental data was found. The calculated fits for Am^{2+} and Cm^{3+} are shown in Fig. G. 7-2 along with the values for the parameters. The solid line is the calculated g value for Am^{2+}, the dotted line is for Cm^{3+}.

Unique values of b_4 and b_6 could not be determined from this analysis, as the anisotropy depended only on the $\Gamma_6 - \Gamma_8$ splitting. Therefore, there are any number of values of b_4 and b_6 which can give the same splitting. The Γ_7 level is so relatively high in energy that our data are not sensitive to its position. We have determined the magnitude of the $\Gamma_6 - \Gamma_8$ splitting as $13.4 \pm 0.5\ cm^{-1}$ for Cm^{3+}:CaF_2 and $18.6 \pm 0.5\ cm^{-1}$ for Am^{2+}:CaF_2. The g_J values were found to be 1.9261 ± 0.001 and 1.9258 ± 0.001 for Cm^{3+} and Am^{2+}, respectively. The absolute values of g_J are measured to the accuracy shown; however, the relative measurement of the two g_J values is about one order of magnitude better.

In the lanthanide series a recent survey has shown that for trivalent rare earth ions in cubic sites in the CaF_2 lattice, the fourth-order term b_4 is about an order of magnitude larger than the sixth-order term b_6.[1] This ratio also prevails for Eu^{2+} in the CaF_2 lattice. We have made this assumption, $b_6 < b_4$, for Cm^{3+} and Am^{2+} and show in Fig. G. 7-3 the energy-level diagrams for the crystal field levels with the values of $b_6 = 0$, and $-0.1\ cm^{-1}$. For the purpose of comparison, we show the energy diagram of Gd^{3+} and Eu^{2+} doped in CaF_2 in Fig. G. 7-4.

Our experimental results show that the crystal field splittings of the nominally $^8S_{7/2}$ actinide ions are approximately 250 times the values for the corresponding lanthanides. Clearly such a large effect must arise from the differences of the electronic structures of the two sets of ions. Such differences are quite significant, and arise because of the intermediate coupling effects induced by the relatively large spin-orbit coupling energies of the actinide ions. The spin-orbit interaction matrix elements are diagonal in J but are not diagonal in L and S, so states of the same J but different L and S will be mixed.[6] For example, the leading terms of the ground-state wave function of Gd^{3+} have been given by Wybourne as[7]

$$\psi(Gd^{3+},\ J = 7/2) = 0.987|^8S\rangle + 0.162|^6P\rangle - 0.012|^6D\rangle + \cdots, \quad (2)$$

which shows that for Gd^{3+} the ground state is approximately 98% pure $^8S_{7/2}$. Recent work on the optical spectra of Cm^{3+} has shown that the leading terms for the Cm^{3+} ground state wavefunction are[8]

$$\psi\,(Cm^{3+},\ J = 7/2) = 0.891|^8S\rangle + 0.414|^6P\rangle - 0.090|^6D\rangle + \cdots, \tag{3}$$

so that it is only 79% pure $^8S_{7/2}$. However, the fourth-order crystal field operator will not split any of the three terms listed above, nor will there be any nonzero matrix elements between any combination of them. Therefore, the contribution to the zero field splitting from the intermediate coupled wavefunction will come from a large number of small terms. We have calculated the zero field splitting caused by these terms, using the electrostatic point charge model, and the results for Cm^{3+} and Gd^{3+} are

$$b_4(Cm^{3+}) = 60B_4(Cm^{3+}) = -0.24\ Cm^{-1} \tag{6}$$

and

$$b_4(Gd^{3+}) = 60B_4(Gd^{3+}) = -4.7\times10^{-4}\ cm^{-1}. \tag{7}$$

These numbers can be compared with the experimental values,

$$b_4(Cm^{3+})_{expt} \approx -1.12\ cm^{-1}, \tag{8}$$

$$b_4(Gd^{3+})_{expt} = -46\times10^{-4}\ cm^{-1}. \tag{8b}$$

We may also take the ratio of the calculated parameters and compare them with the ratio of the experimental parameters. We find

$$\frac{b_4(Cm^{3+})_{exp}}{b_4(Gd^{3+})_{exp}} = 243 \tag{9}$$

and

$$\frac{b_4(Cm^{3+})_{calc}}{b_4(Gd^{3+})_{calc}} = 511. \tag{10}$$

The signs of the calculated b_4 parameters agree with experiment but the magnitudes are off. However, it has been shown that the lattice summation term (A_4^0) in the simple point-charge model is not a good approximation, and one must consider the extended nature of the induced moments. For this reason comparison of the ratio of the calculated b_4 terms with the ratio of the experimental b_4 terms is a more valid criterion. We find that these ratios differ by approximately a factor of two. Considering the uncertainties in the parameters used, this agreement shows the intermediate coupling mechanism accounts qualitatively in a very satisfactory manner for the difference in the crystal field splittings between the half-filled shell configurations of the lanthanide and actinide ions.

Footnote and References

†Shortened version of UCRL-17855, Sept. 1967, to be published in J. Chem. Phys.

1. M. J. Weber and R. W. Bierig, Phys. Rev. 134, A1492 (1964), and references contained therein.
2. M. M. Abraham, L. A. Boatner, C. B. Finch, E. J. Lee, and R. A. Weeks, J. Phys. Chem. Solids 28, 81 (1967), and references contained therein.
3. N. Edelstein, W. Easley, and R. McLaughlin, J. Chem. Phys. 44, 3130 (1966).
4. K. R. Lea, M. J. M. Leask, and W. P. Wolf, J. Phys. Chem. Solids 23, 1381 (1962).

5. We are indebted to Miss Ruth Hinkins of the LRL Mathematics and Computing Group for writing the program for this computation.
6. B. G. Wybourne, Spectroscopic Properties of Rare Earths (Interscience Publishers, New York, 1965).
7. B. G. Wybourne, Phys. Rev. 148, 317 (1966).
8. J. B. Gruber, W. R. Cochron, J. G. Conway, and A. J. Nicol, J. Chem. Phys. 45, 1423 (1966).

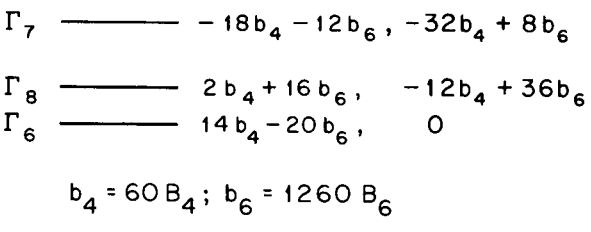

Fig. G. 7-1. The zero-field splittings of a $J = 7/2$ manifold in cubic symmetry.

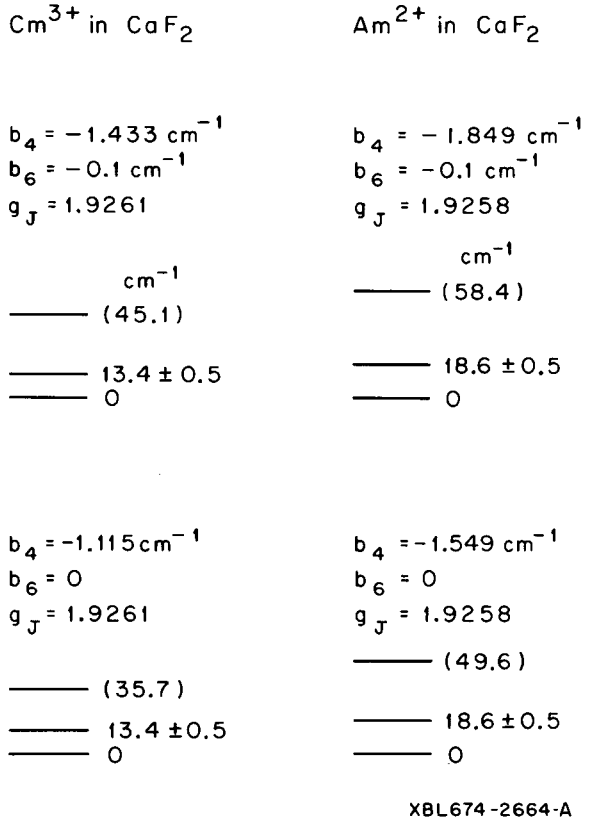

Fig. G. 7-3. The zero-field splittings for the ions Cm^{3+} and Am^{2+} for the values of the fourth- and sixth-degree parameters shown.

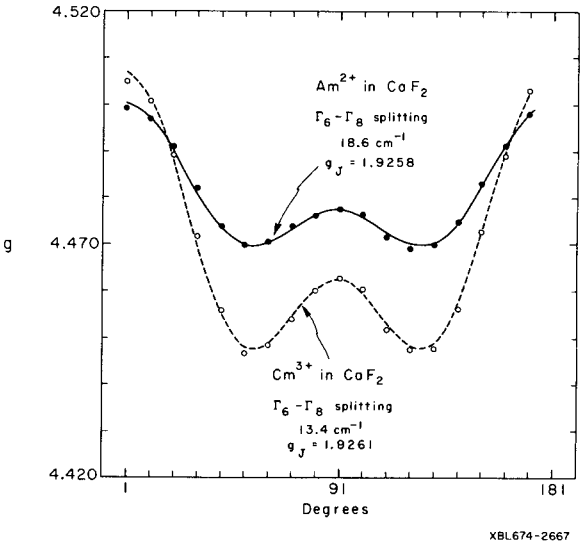

Fig. G. 7-2. The measured g value as a function of the rotation of the dc magnetic field in the 110 plane of CaF_2. The angle 0 deg corresponds to the 100 direction.

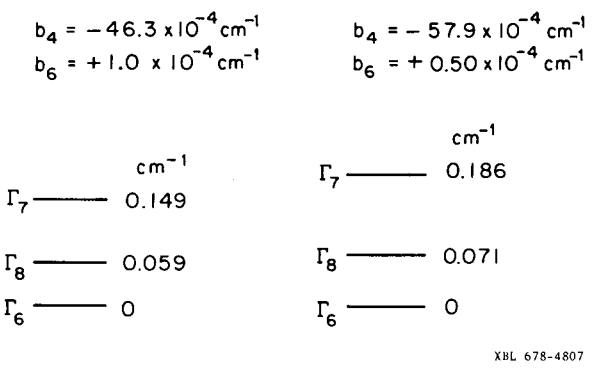

Fig. G. 7-4. The zero-field splittings for the lanthanide ions Gd^{3+} and Eu^{2+} in cubic symmetry. The data are taken from Table II in Ref. 2.

8. THE AMALGAMATION BEHAVIOR OF HEAVY ELEMENTS. I. OBSERVATION OF ANOMALOUS PREFERENCE IN FORMATION OF AMALGAMS OF CALIFORNIUM, EINSTEINUM, AND FERMIUM

Jaromír Maly†

The extraction of rare earths which have a somewhat stable 2+ valence (like Eu, Sm, Yb), in alkali-metal amalgams is well known.[1-6] Related methods which transfer these rare earth elements into amalgams by the electrolysis of water solutions containing alkali metals, acetates, and citrates are also well described in a number of papers.[1, 7-11]

Some of these papers demonstrate methods for the purification of Yb or Sm and Eu from neighboring elements by means of sodium amalgam extraction. Eu, Sm, and Yb may preferentially replace Na in amalgams, often with a yield of more than 50% in one extraction, when other rare earths (which do not have +2 valence) are extracted[1-4, 6, 13, 14] or electrolyzed[8-10, 15, 16] with a yield of about only one-tenth the amount of Eu.

The first application of these methods to the actinide family, by use of a lithium-amalgamated cathode during electrolysis of actinium[17, 18] or lithium-amalgam extraction of some actinides from citrate solution,[19] was reported recently. Some experiments were performed that demonstrate the possibility of using the sodium-amalgam method of separation of some transuranium elements from others. Described below are some typical experiments, which show the possibility of high preferential extraction of Cf, Es, and Fm in sodium amalgam, or the possibility of electrolytic separation of Cf, Es, and Fm on a mercury cathode, while Pu, Am, Cm, and Bk remain mostly in the original solution.

Table G. 8-I presents a summary of the sodium amalgam extraction experiments. The elements were subjected to four successive 1-min extractions from a solution of 150 λ 7 M sodium acetate, by using 60 λ of sodium amalgam (3.5 milliequivalents Na/ml) mixed with the solution by sucking in and out of a pipette. The amount of HCl added to the sodium acetate solution is given in the last column. The amount extracted was determined by α-pulse-height analysis and by β counting of sources prepared from the amalgam phase by treating with HCl and electroplating.

The data of Table G. 8-I clearly show that Cf, Es, and Fm are extracted with sodium amalgam very similarly to Yb (and the other lanthanides which can exhibit 2+ valency). The actinide homologs of Sm and Eu--Pu and Am--are extracted poorly ($< 10\%$) relative to Yb and Cf, but comparably to the light lanthanides, like La, Ce, Pr, and Nd.[14]

Berkelium is the least extracted of the actinides tested. In this respect it resembles terbium, which shows very low extraction. However, dysprosium, the lanthanide analog of Cf, shows very low extraction in the same experiment in which Cf shows high extraction, $\approx$ 1000 times better than Dy, and close to Sm or Eu in the lanthanide family.

The results of four electrolytic experiments are shown in Table G. 8-II below. Experiments 1 and 2 were performed with the addition of 5 λ or 0.5 N tertiary sodium citrate; 3 and 4 were done with the addition of 50 λ of 3 M HCl to the original mixture.

Electrolyses were performed for 30 min with a current density of 30 mA/cm^2. The separated mercury phase was treated as in the extraction case.

The results in Tables G. 8-I and G. 8-II show that Cf, Es, and Fm could be extracted or separated by electrolysis about 10 to 30 times as efficiently as the lighter actinides.

Both kinds of experiments described above gave extraction yields similar to those reported for the preferential extraction into sodium amalgam[2-5] or preferential electrolytic separation on a mercury cathode of Sm, Eu, and Yb, which exhibit +2 valency in the lanthanide series.[15, 16]

Several authors[15-16] explain this preference in electrolysis by a mechanism in which they suppose that the Yb, Eu, and Sm are first reduced to the 2+ state, before amalgamation or electrodeposition. It seems logical to expect therefore that in the family of actinides, Fm, Es, or Cf may form a 2+ valence.

Footnote and References

†On leave from Institute of Nuclear Research, Řež near Prague, Czechoslovakia.

1. H. N. McCoy, J. Am. Chem. Soc. 63, 1622 (1942).
2. J. K. Marsh, J. Chem. Soc. 398 (1942).
3. J. K. Marsh, J. Chem. Soc. 523 (1942)
4. J. K. Marsh, J. Chem. Soc. 8 (1943).
5. J. K. Marsh, J. Chem. Soc. 531 (1943).
6. T. Moeller and H. E. Kremers, Analytical Chem. 17 [12], 798 (1945).
7. H. N. McCoy, J. Am. Chem. Soc. 63, 3423 (1942).
8. E. I. Onstott, J. Am. Chem. Soc. 77, 2129 (1955).
9. E. I. Onstott, J. Am. Chem. Soc. 78, 2070 (1956).
10. E. I. Onstott, J. Am. Chem. Soc. 81, 4451 (1959).
11. D. I. Ryabchikov, YU. S. Sklyarenko, and N. S. Stroganova, Zh. Neorg. Khim. (USSR) 9, 1954 (1956).
12. J. K. Marsh, Inorg. Syn. 5, 22 (1957).
13. M. F. Barrett, D. Sweasey, and N. E. Topp, J. Inorg. Nucl. Chem. 24, 571 (1962).
14. M. F. Barrett, D. Sweasey, and N. E. Topp, J. Inorg. Nucl. Chem. 25, 1286 (1963).
15. V. P. Shvedov and Fu I-Bei, Radiokhim. 2 [1], 57 (1960).
16. V. P. Shvedov and Fu I-Bei, Radiokhim. 2 [2], 231 (1960).
17. G. Bouissières, M. Haissinski, and Y. Legoux, Bull. Soc. Chim. France 1028 (1961).
18. F. David and G. Bouissières, Bull. Soc. Chim. France 1001 (1965).
19. G. Bouissières and Y. Legoux, Bull. Soc. Chim. France 386 (1965).

Table G.8-I. Sodium amalgam extraction of lanthanide and actinide elements.

% Extracted and ratio to Cf extracted	Element										
	^{149}Tb	^{151}Dy	^{169}Yb	^{239}Pu	^{241}Am	^{244}Cm	^{249}Bk	^{252}Cf	^{252}Es	^{252}Fm	HCl added
1 %	---	---	29	4.9	3.3	1.5	---	40	---	---	---
Ratio to Cf			0.725	0.125	0.082	0.037		1.000			---
2 %	---	---	33	2.3	2.1	1.8	---	45	---	90	---
Ratio to Cf	---	---	0.732	0.051	0.047	0.040		1.00		2.00	---
3 %	---	---	---	2.7	2.3	2.2	0.5	39	---	57	---
Ratio to Cf				0.047	0.040	0.039	0.013	1.00		1.46	---
4 %	---	---	---	5.6	3.3	3.3	0.9	51	50	---	50λ, 3M
Ratio to Cf				0.11	0.065	0.065	0.018	1.00	0.98		
5 %	---	---	---	6.7	5.4	4.1	1.4	60	61	---	50λ, 3M
Ratio to Cf				0.112	0.090	0.068	0.023	1.00	0.98		
6 %	0.15	---	62	5.1	3.0	2.6	---	68	---	---	75λ, 2M
Ratio to Cf	0.0022		0.912	0.075	0.044	0.038		1.00			
7 %	0.14	---	53	2.7	1.5	2.3	---	50	---	---	75λ, 2M
Ratio to Cf	0.0028		1.06	0.054	0.030	0.046		1.00			
8 %	---	0.06	50	16.9	7.9	5.7	---	95	---	---	75λ, 3M
Ratio to Cf		0.0006	0.526	0.179	0.083	0.060		1.000			
9 %	---	0.06	53	16.3	7.7	5.3	---	≈100	---	---	75λ, 3M
Ratio to Cf		0.0006	0.530	0.163	0.077	0.053		1.000			

Table G.8-II. Electrolysis of lanthanide and actinide elements.

Yield of electrolyzed elements	Element ^{169}Yb	^{239}Pu	^{241}Am	^{244}Cm	^{249}Bk	^{252}Cf	^{252}Es	^{252}Fm	Added to electrolysis solution
1 %	27	4.7	2.2	2.1	---	49	---	80	5 λ 0.5 N
Ratio to Cf	0.55	0.096	0.045	0.043		1.00		1.63	Na citrate
2 %	---	3.6	1.8	4.8	0.3	38	---	67	5 λ 0.5 N
Ratio to Cf		0.095	0.097	0.126	0.008	1.00		1.76	Na citrate
3 %	---	5.1	3.2	5.2	1.6	71	75	---	50λ 3M HCl
Ratio to Cf		0.072	0.045	0.073	0.022	1.00	1.056		
4 %	---	5.3	2.8	4.8	0.6	55	60		50λ 3M HCl
Ratio to Cf		0.096	0.051	0.087	0.011	1.00	1.091		

9. THE AMALGAMATION BEHAVIOR OF HEAVY ELEMENTS. II. DIPOSITIVE STATE OF MENDELEVIUM

Jaromír Malý and Burris B. Cunningham

Mendelevium-256 was produced by irradiation with 41-MeV helium ions of an einsteinium target consisting of ≈5 μg of ^{253}Es mounted on a 4-mg/cm^2 Be foil. Irradiation for 30 to 60 min at a beam current of 50 to 100 μA/cm^2 (10 to 20 μA through the target) yielded approximately 10^5 atoms of ^{256}Md, which were collected on a Be catcher foil, along with 10^6 to 10^7 alpha d/m of ^{253}Es knocked out of the target. The catcher foil was dissolved in 6 M HCl containing ≈500 μg La^{3+} and precipitated as $La(OH)_3$. This precipitate, containing the isotopes of Md and Es, was washed with 6 M KOH and water. The washed precipitate usually was dissolved in 200 λ of 1 to 3 M HCl to form a "stock Md" solution.

The extraction experiments usually were carried out from a mixture of about 1/5 of the "stock Md" solution in 1 M HCl, 100 λ of 7 M sodium acetate, 5 λ of 8 M ammonium acetate, and selected amounts of HCl, as shown in Table G.9-I. The extractions were performed in a 3-ml cone, with 250 λ of sodium amalgam, containing ≈3.5 milliequivalent Na/ml. The extracted actinide elements were back-extracted from the mercury phase with 6 M HCl, neutralized by NH_4OH, and then electroplated from NH_4Cl solution onto a Pt disk.

The compositions of the solutions used in electrolysis were similar to those used for amalgam extractions.

The electrolyses were carried out for 35 min, with periodic interruption at 5-min intervals for sampling the mercury phase. Current densities are given in Table G.9-II. Following any 5-min period of electrolysis, the current was stopped, and after 1 min of mixing of both phases, 5 λ of mercury was withdrawn by pipetting.

The results are summarized in Table G.9-II.

The results presented in Table G.9-I indicated that Md is extracted by sodium amalgam somewhat more readily than is einsteinium, and on comparison with results presented previously,[1] it appears that Md is extracted more readily than californium. This suggests that Md^{2+} is more stable than Cf^{2+} or Es^{2+}. The data presented in Table G.8-II demonstrates a very substantial separation of Md from Es by electrolysis.

The expected analogy between Tm and Md led Seaborg[2] to predict the relatively stable Md^{2+} state in 1949.

Accordingly, we sought direct evidence for a dipositive state of mendelevium, and have attempted to establish rough limits for the potential of the $Md^{3+} + e = Md^{2+}$ couple. To this end, various reducing agents were added to the "stock Md" solution, and $BaSO_4$ or $EuSO_4$ precipitated

from the mixture. The distribution of Es, ^{256}Fm, and ^{256}Md activities between the precipitate and supernatant solution was then determined.

The results of these experiments are summarized in Table G. 9-III.

Details of the counting data obtained in an experiment with V^{2+} used as a reducing agent are given in Fig. G. 9-1.

The growth of spontaneous fission (SF) activity in the $BaSO_4$ fraction from V^{2+} reduction is clearly evident and indicates enrichment of Md by a factor of 10 to 15. The deviation of the SF decay curve in the precipitate from the Ti^{3+} solution in comparison with the decay curve of the input solution is also evident, and shows an enrichment of Md by a factor of only 2 to 3. From this last experiment it would appear that the standard reduction potential of the $Md^{3+} + e = Md^{2+}$ couple is about -0.1 volt.

The results suggest that the +2 state of mendelevium is more stable than the dipositive state of ytterbium, and even of europium.

References

1. J. Malý, The Amalgamation Behavior of Heavy Elements. I. Observation of Anomalic Amalgamation of Californium, Einsteinium, and Fermium, UCRL-17526, May 1967.

2. G. T. Seaborg, J. J. Katz, and W. M. Manning, The Transuranium Elements, Part II, National Nuclear Energy Series, Vol. 14B, Paper 21.1 (McGraw-Hill Book Company, Inc., New York, 1949).

Table G. 9-I. Extraction of Md and Es by sodium amalgam.

Experiment number	% Es extracted	% Md extracted	Amount 1 M HCl added
1	89	90-100	15 µl
2	≈ 100	90-100	75 µl

Table G. 9-II. Separation of mendelevium from einsteinium by electrolysis.

Experiment number	Current density ($mA\ cm^{-2}$)	Ratio of spontaneous fission activity to alpha activity		Maximum enrichment factor $^{256}Fm + ^{256}Md$ relative to Es
		Original solution	In mercury	
1	10	$\frac{1}{3150}$	$\frac{1}{100}$	31.5
2	5	$\frac{1}{9600}$	$\frac{1}{305}$	31.5

Table G. 9-III. Results of reduction of Md.

Reducing ion	Precipitate	Reduction potential (volts)	Corresponding reaction	Observed enrichment factor $^{256}Md/^{256}Fm$
Yb^{2+}	$EuSO_4$	-1.15	$Yb^{3+} + e \rightarrow Yb^{2+}$	≈ 10
$Zn + Eu^{2+}$	$EuSO_4$	-0.763	$Zn^{2+} + 2e \rightarrow Zn$	≈ 10
Eu^{2+}	$EuSO_4$	-0.43	$Eu^{3+} + e \rightarrow Eu^{2+}$	≈ 10
Cr^{2+}	$BaSO_4$	-0.41	$Cr^{3+} + e \rightarrow Cr^{2+}$	≈ 10
V^{2+}	$BaSO_4$	-0.255	$V^{3+} + e \rightarrow V^{2+}$	≈ 10
Ti^{3+}	$BaSO_4$	-0.1	$TiO^{2+} + 2H + e \rightarrow Ti^{3+} + H_2O$	≈ 2-3

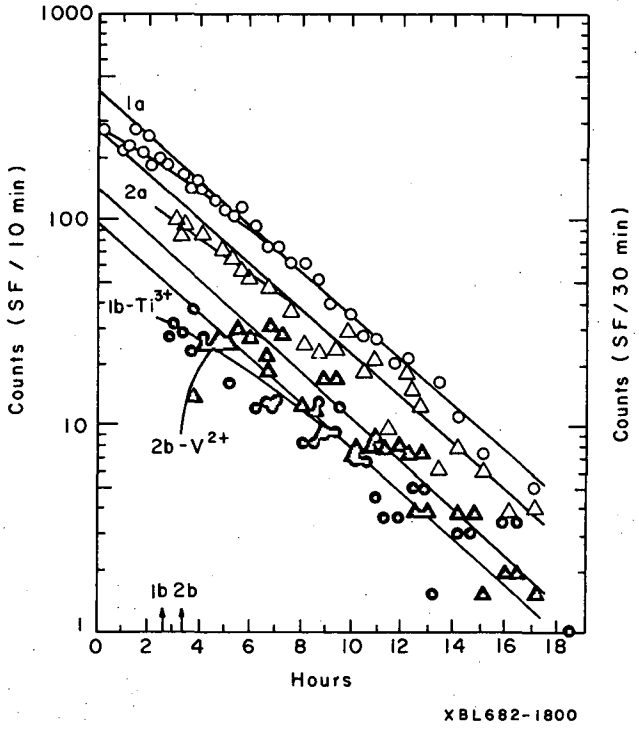

Fig. G. 9-1. Spontaneous-fission decay of $BaSO_4$ fractions after reduction with Ti^{3+} and V^{2+}. Curves 1a and 1b: decay curves of "stock Md" solutions (left scale, SF/30 min) used for reduction with Ti^{3+} (1a, 22% of input) and V^{3+} (2a, 34% of input). Curves 2a and 2b: decay curves of $BaSO_4$ fraction after reduction (right scale, SF/10 min) with Ti^{3+} (1b) and V^{2+} (2b). The arrows 1b and 2b show the separation time (precipitation of $BaSO_4$) in the case of V^{2+} or Ti^{3+} reduction.

10. THE RADIATION-INDUCED "HYDROLYSIS" OF THE PEPTIDE BOND†

Michael A. J. Rodgers, Harvey A. Sokol, and Warren M. Garrison

We find that the γ radiolysis of oxygen-free solutions of model peptides such as the N-acetyl-amino acids leads to liberation of the free amino acid as a major reaction product. As a specific example, the alanine[1] yield from N-acetylalanine in evacuated solution at pH 7 increases abruptly with increasing solute concentration over the range 0.05 M to 0.25 M and then levels off to a limiting value of G(alanine) ≈ 1 at acetylalanine concentrations above 0.5 M.

This radiation-induced liberation of free amino acid is quenched by second solutes such as hydronium ion, molecular oxygen, and chloracetate ion, all of which are known to be effective scavengers of the hydrated electron, e^-_{aq}, formed in the radiation-induced step[2]

$$H_2O \rightsquigarrow H_2O_2, H_2, OH, H^+, e^-_{aq}. \quad (1)$$

A reciprocal-yield plot of G(alanine) as a function of chloracetate concentration is given in Fig. G. 10-1, insert.

The evidence is then that the reducing species, e^-_{aq}, is specifically involved in the chemistry that leads to liberation of free alanine. Previous work has established that the oxidizing species, OH, is removed preferentially through H abstraction at the α-carbon position of acetylalanine,[3,4]

$$OH + RCONHCHR_2 \rightarrow RCONHC\dot{R}_2 + H_2O.$$

Addition of OH scavengers such as formate ion has no effect on G(alanine).

Now, if the removal of e^-_{aq} leads to reduction of the peptide linkage, e.g.,

$$(RCONHCHR_2)^- + H_2O \rightarrow R\dot{C}(OH)NHCHR_2 + OH^-$$

then it is clear that combination of $R\dot{C}(OH)NHCHR_2$ with like species or with the α-carbon radical $RCONHC\dot{R}_2$ would lead to formation of Schiff-base derivatives of the type $R(R')C(OH)NHCHR_2$, which compounds are labile and decompose $R(R')C(OH)NHCHR_2 \rightarrow R(R')CO + NH_2CHR_2$ to yield a carbonyl products and the free amino group.

However, we find experimentally that the yield of carbonyl products is negligible, $G \leq 0.2$, and we conclude that reductive cleavage of the peptide bond cannot account for the appearance of free alanine in the present system.

The concept that appears to provide a clue to the interpretation of the chemistry of present system is that the radical products of e^-_{aq} and OH attack are ultimately removed not by dimerization (combination) but by disproportionation. Of course, disproportionation involving $R\dot{C}(OH)NHCHR_2$ and the α-carbon radical would lead simply to a reconstitution of the parent peptide,

$$R\dot{C}(OH)NHCHR_2 + RCONHC\dot{R}_2 \rightarrow 2\ RCONHCHR_2. \quad (2)$$

However, since the reduced radical $R\dot{C}(OH)NHCHR_2$ is an amine species, it is likely to be in an adduct form in the presence of high concentrations of the peptide,

$$R\dot{C}(OH)NHCHR_2 + RCONHCHR_2 \rightleftharpoons \begin{matrix} RC(OH)NCHR_2 \\ | \\ RC(OH)NHCHR_2 \\ \dot{} \end{matrix}$$
(I)

Removal of the adduct radical (I) via the analog of reaction 2 leads to formation of a Schiff-base (I), which, as shown in Eq. 3, can rearrange to give alanine and diacetylalanine,[5]

$$\underset{\text{(I)}}{\begin{array}{l}\text{RCONCHR}_2\\ \quad\vert\\ \text{RC(OH)NHCHR}_2\end{array}} \rightarrow (R_2CO)_2NCHR_2 + NH_2CHR_2, \qquad (3)$$

$$(R_2CO)_2\,NHCHR_2 + H_2O \rightarrow RCOOH + RCONHCHR_2.$$

Our measurements of G(acetic) are in good agreement with this formulation. We find that the yield of free acetic acid is low, $G \leq 0.3$, and we also find that on mild differential hydrolysis of the irradiated solution additional acid is liberated to give $G(\text{acetic}) \approx 1.5 \approx G(\text{alanine})$.

Footnotes and References

†Based on UCRL-17930, Nov. 1967, submitted to J. Am. Chem. Soc.

1. Alanine was identified chromatographically and assayed by the ninhydrin method; since ammonia is produced as a minor product and is "ninhydrin-positive," a correction was made on the basis of a standard ammonia assay after the method of Conway.

2. C. J. Hochanadel and R. Casey [Radiation Res. 25, 198 (1965)] report the following 100-eV yield for reaction 1: $G_{OH} = 2.59$, $G_{e^-_{aq}} = 2.58$, $G_H = 0.55$, $G_{H_2} = 0.45$, $G_{H_2O_2} = 0.72$.

3. H. L. Atkins, W. Bennett-Corniea, and W. M. Garrison, J. Phys. Chem. 71, 772 (1967).

4. W. M. Garrison and B. M. Weeks, Radiation Res. Suppl. 4, 54 (1964).

5. Product I could, of course, be formed through combination of $RC(OH)NHCHR_2$ with nitrogen radicals of the type RCONCHR. The latter are not produced through OH attack, but we cannot rule out the possibility that such species may be formed through "direct-action" processes at high solute concentrations.

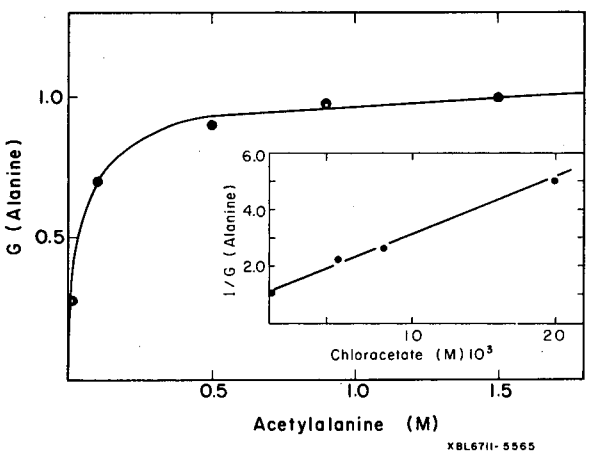

Fig. G. 10-1. G(alanine) as a function of acetylalanine concentration in oxygen-free solution at pH 7 under γ rays. Insert: Reciprocal yield plot of G(alanine) as a function of chloracetate concentration in 1 M acetylalanine.

12. MECHANISM AND STOICHIOMETRY IN THE RADIOLYTIC OXIDATION OF PURINES AND AMINOPURINES IN AQUEOUS SOLUTION†

John Holian and Warren M. Garrison

We have recently shown that a principal action of γ rays on the typical purine bases xanthine, hypoxanthine, and uric acid in oxygenated solution results in a preferential oxidation at the 4, 5 carbon-carbon double bond.[1] Oxidation of the base, B, may be represented in terms of OH addition to the 4, 5 position, $B + OH \rightarrow \dot{B}(OH)$, followed by $\dot{B}(OH) + O_2 \rightarrow B(OH)\dot{O}_2$, $HO_2 + B(OH)\dot{O}_2 \rightarrow B(OH)OOH + O_2$, where B(OH)OOH represents a labile hydroxy-hydroperoxide intermediate which undergoes hydrolytic degradation to yield characteristic carbonyl products; the overall stoichiometry for the radiolytic oxidation of xanthine, for example, is given by

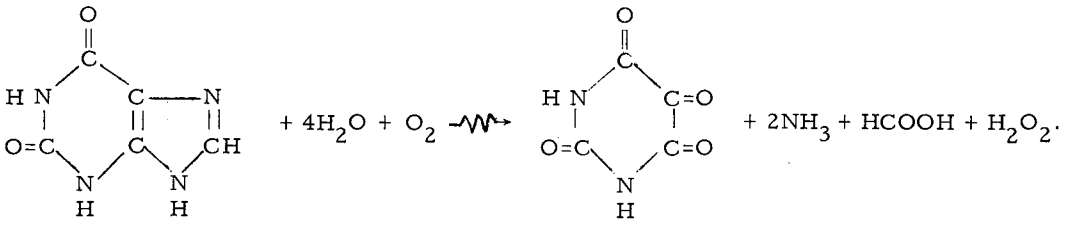

The 100-eV yield (G value) for carbonyl production in these systems depends on the chemical composition of the purine in question. With xanthine, the addition of OH at the 4, 5 position is essentially quantitative, i.e., G(alloxan) ≈ 2, which value approximates the 100-eV yield of OH radicals formed in water under γ rays, $G_{OH} = 2.5$.[2] With the amino purine, adenine, the carbonyl yield is quite low, G(mesoxalic acid) = 0.45; other purine bases give intermediate G(carbonyl) values. It is clear that there is an alternative path for oxidation of the purine nucleus that does not yield carbonyl products.

We have just completed a quantitative study of reaction stoichiometry in the γ radiolysis of oxygenated solutions of hypoxanthine and adenine, and find in these systems that a second mode of oxidation at the 4, 5 position yields oxalic acid and urea as characteristic products. The irradiated solutions were subjected to mild acid hydrolysis (2 N HCl, 90°C, 2 hr) to effect the quantitative release of the various product species. Oxalic acid was identified and determined by colorimetric[3] and by gas-chromatographic[4,5] methods. Urea was assayed colorimetrically;[6] preliminary identification and assay involved the use of urease.[7] Ammonia was measured after Conway.[7] Methods used in the identification and determination of carbonyl products have been described.[1] Typical data are summarized in Table G. 12-I.

The formation of these observed products in the indicated yields is consistent with a formulation in which all reaction is initiated by OH attack at the 4, 5 position. That is, the hydrolytic degradation of B(OH)OOH as represented in Eq. 1 occurs in parallel and in competition with a more extensive overall degradation which is typified as follows for hypoxanthine:

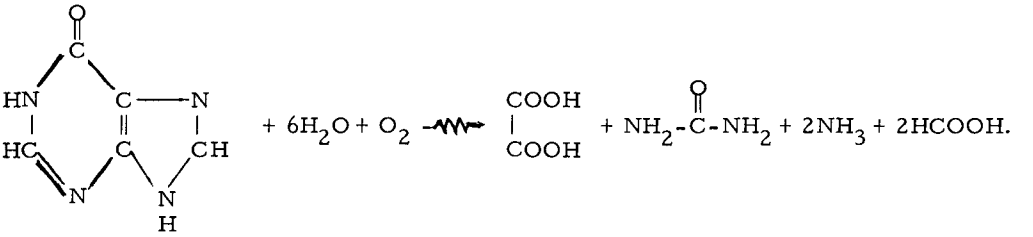

For both hypoxanthine and adenine, the data of Table G. 12-I give the value $G(-B) - [G(\text{oxalic}) + G(\text{mesoxalic})] \approx 0.5$ which represents an upper limit for the yield of OH reaction at sites other than the 4, 5 position.

Footnotes and References

†Chem. Commun. 676 (1967).

1. J. Holian and W. M. Garrison, J. Phys. Chem. 71, 462 (1967).
2. C. J. Hochanadel and R. Casey, Radiation Res. 25, 198 (1965).
3. M. Paget and R. Berger, Bull. Biol. Pharm. 70 (1938).
4. E. T. Oakley, L. Weissbecker, and F. E. Resnick, Anal. Chem. 37, 380 (1965).
5. We are indebted to Mr. H. A. Sokol for the gas-chromatographic determinations.
6. R. M. Archibald, J. Biol. Chem. 157, 507 (1945).
7. E. J. Conway, Microdiffusion Analysis and Volumetric Error (Crosby Lockwood and Son, Ltd., London, 1962.
8. Although the radiolytic oxidation of the purine bases can be satisfactorily represented in terms of the degradations of the labile product $B(OH)OOH$, it is to be noted that stoichiometrically equivalent reactions of the radical intermediate $B(OH)\dot{O}_2$ may also be involved.

Table G. 12-I. Product yields in the γ-ray-induced oxidation of hypoxanthine and adenine in oxygenated solution.[a]

	G(mol/100 eV)	
Product	Hypoxanthine	Adenine
-base	2.4[b]	2.1[c]
ammonia	8.8	9.6
urea	0.4	0.5
oxalic acid	0.75	1.2
mesoxalic acid	1.1	0.45[d]

a. 10^{-3} M, pH 1.2 (adjusted with H_2SO_4).
b. Independent of hydrogen ion concentration over the range pH 1 to 7.
c. Decreases to G(-B) = 1.2 at pH 7.
d. Represents a combined yield of mesoxalic acid plus a lesser amount of glyoxylic acid.

13. RADIATION CHEMISTRY OF ORGANO-NITROGEN COMPOUNDS†

Warren M. Garrison

The radiation chemistry of the organic compounds of nitrogen in their various ionic forms is of considerable intrinsic interest from the strictly physicochemical standpoint, and also has important applications in numerous other areas of radiation research. Among these, for example, are the radiation-chemical synthesis and modification of nitrogenous chemicals and fibers, the radiation preservation and sterilization of foods and drugs, and, of course, the elucidation of the basic and elementary processes of radiobiology.

This paper treats some of the more recent investigations of reaction mechanism in the radiolysis of certain bio-organic derivatives of nitrogen. Included are studies of amino acids, amines, peptides, polypeptides, pyrimidines, and purines. The emphasis here is primarily on reactions in irradiated aqueous solution. Consideration is also given to a few solid-state systems for which specific and detailed reaction mechanisms have been outlined.

Summary

Oxidative deamination of amines and amino acids is induced by attack by OH radicals at the C-H linkage α to the amino group. The characteristic products are ammonia and a carbonyl.

Amino compounds containing the grouping $NH_3^+CH(R)COX$, where X represents O^-, OH, OR, NHR, etc., undergo reductive deamination on reaction with e^-_{aq} to give the corresponding fatty acid derivative. If more than one carbon unit separates the amino and carbonyl groups, reductive deamination does not occur.

The chemistry of reductive deamination indicates that e^-_{aq} adds to the carbonyl double bond and that cleavage of the N-C linkage ensues on rearrangement of the reduced intermediate. Observed correlation between pK of the NH_3^+ group and the velocity constant for the e^-_{aq} reaction are in accord with this formulation.

Oxidative degradation of substituted amines, including peptides, is initiated by OH attack at the C-H linkage of the α-carbon atom.

The hydrated electron adds to the peptide bond but N-C cleavage does not ensue.

The reactions of OH and e^-_{aq} with the pyrimidine and purine bases occur almost exclusively at the carbon-carbon double bond.

The actions of ionizing radiations on solid glycine and alanine in the absence of oxygen indicate that the electron escapes the parent ion and is subsequently removed through addition to adjacent-C=O groups. The reduced intermediate looses ammonia on rearrangement. There is a marked similarity in the radiation chemistry of the difunctional amino acids in the solid state and in aqueous solution (oxygen-free). This analogy does not hold in the case of certain trifunctional amino acids, e.g., cysteine and cystine.

A major chemical effect of ionizing radiations on solid peptide derivatives of the aliphatic α-amino acids leads to the formation of amide and fatty acid through main-chain scission at the NH-CH(R) linkage. There is evidence that main-chain scission also occurs at the CHR-CO linkage.

Footnote

†Summary of paper (UCRL-17440, March 1967), to appear in Current Topics Radiation Res.

14. EXTRACTION OF $HClO_4$ AND $HReO_4$ BY DILUTE SOLUTIONS OF TRIBUTYL PHOSPHATE IN CCl_4, ISOOCTANE, AND 1,2-DICHLOROETHANE

J. J. Bucher and R. M. Diamond

A previous study of $HClO_4$ extraction by dilute solutions of tributyl phosphate (TBP) in CCl_4[1] indicated a three-TBP-coordinated acid complex was formed in the organic phase. This study also showed at least one water molecule was always coextracted. By combining these two results a model for the acid complex structure was suggested: The complex has a hydronium ion core around which the maximum number of three TBP molecules are coordinated. It was also suggested this model could have general application as a guide for understanding acid extraction by other dilute solutions of organic extractants as well as by other TBP-diluent systems.

To test the validity of this proposed model the extraction of $HClO_4$ by TBP in other diluents was investigated. For this paper, the first of a two-part study, $HClO_4$ extraction by TBP-isooctane and -1,2-dichloroethane was studied. Instead of using acid-base titration methods for determining the amount of extracted acid, as was done in the previous TBP-CCl_4 system study, radioactive perrhenate (ReO_4^-) tracer was employed. Since the molecular structure and charge distribution of ReO_4^- is similar to that of ClO_4^-, it is found that this tracer anion can be used successfully as a marker for ClO_4^- although it is not identical in behavior. Because this radioactive tracer technique allows accurate determination of much lower organic phase acid concentrations than previously obtained, the TBP-HCl_4($HReO_4$)-CCl_4 system was also reexamined over a greater range of dilute TBP concentrations.

The extraction may be expressed as

$$H^+ + X^- + xH_2O + nTBP\,(org.) = H^+ \cdot nTBP \cdot xH_2O \cdots X^-(org.) \quad (1)$$

$$= H^+ \cdot nTBP \cdot xH_2O\,(org.) + X^-\,(org.), \quad (1')$$

with the corresponding equilibrium constants

$$K^a = (H^+ \cdot nTBP \cdot xH_2O \cdots X^-)_0/(TBP)_0^n\,(H_2O)^x(H^+X^-), \quad (2)$$

$$K^d = [H^+ \cdot nTBP \cdot xH_2O]_0[X^-]_0 y_\pm^{\,2}/(TBP)_0^n(H_2O)^x(H^+X^-), \quad (2')$$

where [ ] denote concentration, ( ) signify activities, $y_\pm$ is a mean molar activity coefficient, and subscript 0 means the quantity is in the organic phase.

From log-log plots of the organic acid concentration vs the aqueous acid activity, with the TBP concentration and water activity held constant, it can be determined whether the extracting species is an ion pair or a pair of dissociated ions. Such plots are shown in Figs. G. 14-1 and G. 14-2 for the tracer $HReO_4$ out of $HClO_4$ or $HReO_4$, and the slope of 1.0 for the TBP-CCl_4 and TBP-isooctane systems indicates an ion pair; the slope of one-half for the TBP-1, 2-dichloroethane system indicates a pair of dissociated ions.

The value of n can be determined from log-log plots of the organic acid vs the equilibrium TBP concentration at a fixed aqueous acid activity. Such plots are shown in Figs. G. 14-3, G. 14-4, and G. 14-5 for the above TBP-diluent systems, and yield resolved values of n = 2 or 3 for TBP-CCl_4 and TBP-isooctane and a slope of 1.5 for TBP-1, 2, -dichloroethane. The slope of 1.5 results from plotting the square root of the organic acid activity, and indicates n = 3 for TBP-1, 2-dichloroethane system. The molar activity coefficients used in this system were calculated by the Mayer-Poirier method.[2]

A number of approximations have been made to calculate the constants quoted below. Mainly, activities have been replaced by molar concentrations. However, since the constants are evaluated at dilute concentrations this approximation is probably permissible. Nonetheless, these constants are not true-equilibrium constants and consequently a different symbol, K_n, will be used to signify them. The subscript n will serve to identify which TBP coordination complex is included in the constant.

Diluent	Acid	K_2^a	K_3^a
isooctane	$HClO_4$	1.8×10^{-3}	9×10^{-2}
CCl_4	$HReO_4$	2.0×10^{-3}	4×10^{-2}
			K_3^d
1, 2-dichloroethane	$HReO_4$	---	2.4×10^{-4}

In the previous study of $HClO_4$ extraction by TBP-CCl_4 only a three-TBP coordinated complex was found. Obviously, this result is in disagreement with the finding of a 2TBP complex, in addition to a 3TBP complex, in the present study. This previous result, however, can be attributed to the experimental circumstance of using TBP concentrations only ≥ 0.037 M. The present data, with that restriction, would yield a good fit to a value of n = 3 alone. It is only when more dilute TBP solutions are examined that the existence of a 2TBP complex is clearly evident.

However, in view of this new evidence, the question arises whether the previously suggested extraction model is appropriate for interpreting acid extraction data. It is suggested that the hydronium-core model is still necessary to explain the present data. In each of the three diluent systems, over some range of dilute TBP concentrations, 3TBP complexes were found. Without the existence of a hydronium ion, with its three positive charge sites, it is difficult to conceive how TBP coordination numbers of three could be obtained. It is suggested that the appearance of a 2TBP complex at lower TBP concentrations is more a natural consequence of the stepwise

formation of coordination complexes than an indication of the breakdown of the proposed model. Obtaining lower-coordination-number complexes may be viewed as being analogous to the behavior found in metal complexes, where lower complexes can result in more dilute solutions of the complexing reagent. Unfortunately, we cannot determine the water coextracted by the 2TBP complex, at the low concentration where this species predominates, to prove that at least one water molecule is indeed involved.

A further interesting result, graphically displayed in this study, is the difference of range over which a 2TBP complex is stable. In isooctane, the lower coordination complex predominates only to TBP concentrations of 0.0075 M; it is the major species up to 0.1 M in CCl_4. When one uses the results of isooctane as a measure of the intrinsic tendency for forming mixed complexes, it is clear that some additional factor is present to stabilize the 2TBP complex in CCl_4. It is probable that this factor is the CCl_4 molecule itself, providing, by means of dispersion forces, better solvation of the hydronium ion and thus reducing the need for adding a third TBP molecule.

Another factor that may be important in the extraction process is the role of the anion. A comparison of extraction data between 1,2-dichloroethane and isooctane shows only 3TBP complexes in 1,2-dichloroethane at TBP concentrations equal to or lower than those which in isooctane show evidence for a 2TBP complex. It would surely be expected that 1,2-dichloroethane would provide the extracted complex with "chemical" solvation equal to that of isooctane, and thus a turnover to a lower complex should be observed with the former diluent at a TBP concentration equal to or higher than with isooctane. However, the two systems have a major difference. The ClO_4^- or ReO_4^- anion is free of the cation complex in 1,2-dichloroethane, while in isooctane the anion is electrostatically bound to it. It may be that the oppositely charged anion gives enough electrostatic solvation to the hydronium complex to tend to displace one of the coordinating TBP molecules. That is, the presence of the anion may help stabilize a complex of lower coordination number.

Part two of this study will consider the effects of still other diluents upon the extraction, and in later work the role of the anion, with use of more strongly interacting anions such as Br^- and Cl^-, will be discussed.

Footnote and References

1. D. C. Whitney, and R. M. Diamond, J. Phys. Chem. 67, 209 (1963).
2. J. C. Poirier, J. Chem. Phys. 21, 965 (1953).

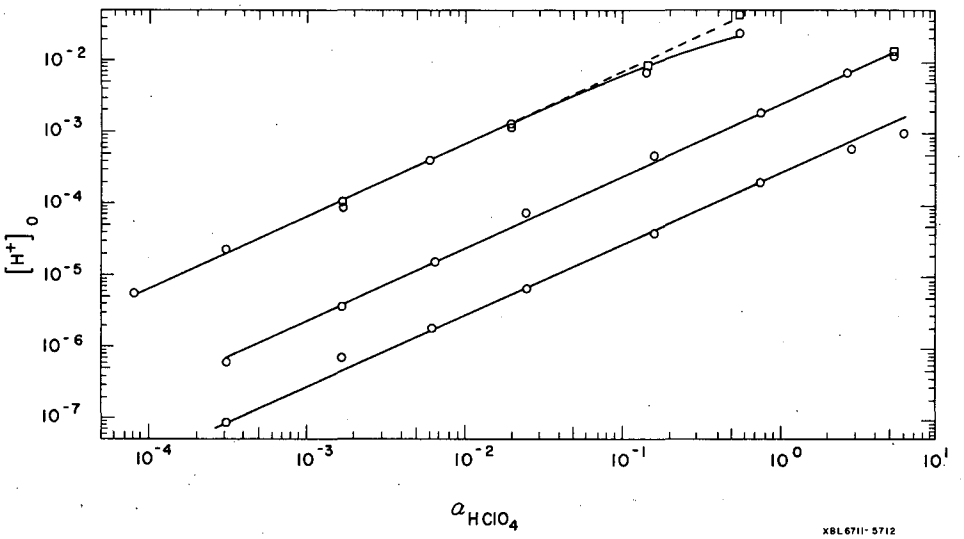

Fig. G. 14-1. Variation of acid content of organic phase with aqueous $HClO_4$ activity for TBP-isooctane concentrations of 0.073 M (lower line) and 0.367 M (upper line); and for TBP-CCl_4 concentration of 0.367 M (middle line). O, uncorrected data; □, data corrected for used-up TBP.

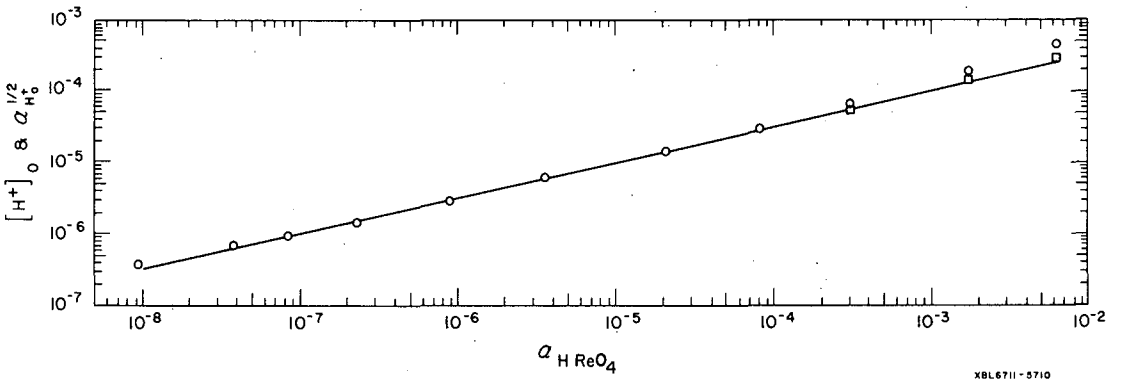

Fig. G. 14-2. Variation of acid content of organic phase with aqueous $HReO_4$ activity for TBP-1,2-dichloroethane concentration of 0.367 M. O, uncorrected data; □, data corrected for activity coefficients.

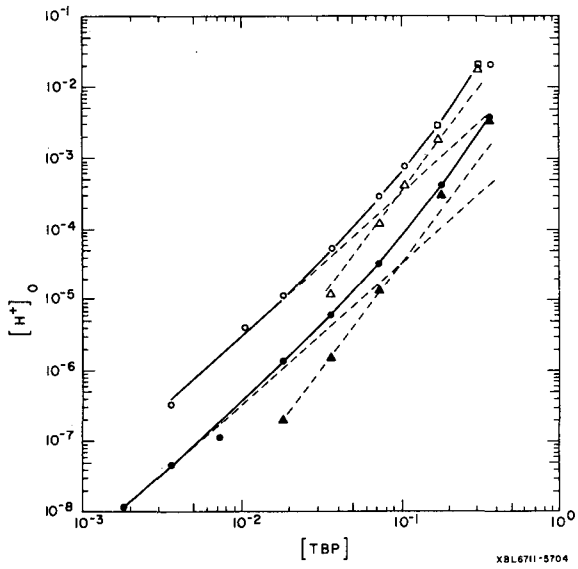

Fig. G. 14-3. Variation of acid content of organic phase with TBP in CCl_4 for aqueous $HReO_4$ concentrations of 1.60 M (●) and of 2.91 M (○), uncorrected, unresolved data; △, ▲, resolved n = 3 lines; other dashed lines, n = 2; □, data corrected for used-up TBP.

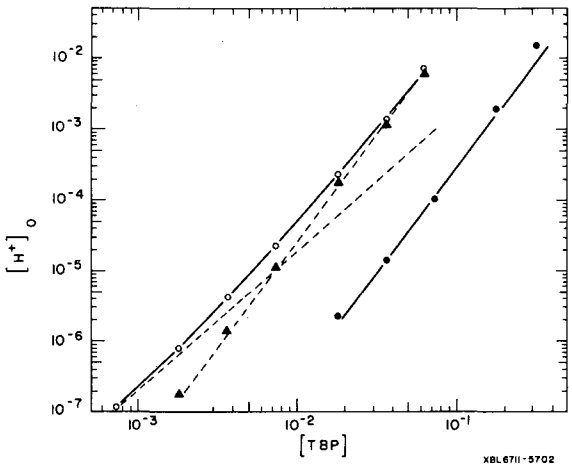

Fig. G. 14-4. Variation of acid content of organic phase with TBP in isooctane for aqueous $HReO_4$ concentration of 0.870 M (●), and for aqueous $HClO_4$ concentration of 4.00 M (○), uncorrected data; △, resolved n = 3 line; other dashed line, n = 2.

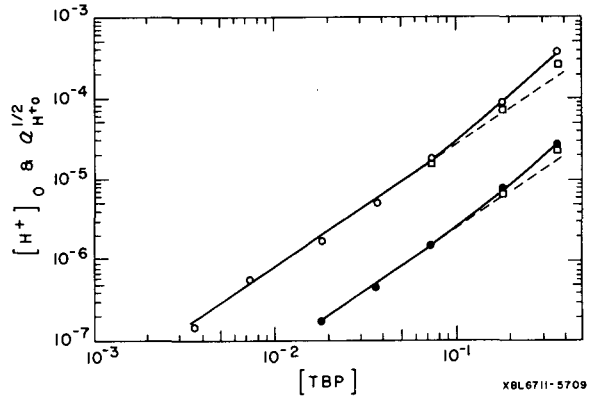

Fig. G. 14-5. Variation of acid content of organic phase with TBP in 1, 3-dichloroethane for aqueous $HReO_4$ concentrations of 0.0100 M (●), and of 0.100 M (○), uncorrected data; □, data corrected for activity coefficients.

15. EXTRACTION OF $HClO_4$ AND $HReO_4$ BY DILUTE SOLUTIONS OF TRIBUTYL PHOSPHATE IN BENZENE, 1,3,5-TRIETHYL BENZENE, AND $CHCl_3$

J. J. Bucher and R. M. Diamond

In the first part of this study dealing with $HClO_4$ or $HReO_4$ extraction by tributyl phosphate (TBP), three types of diluents were used; isooctane, an example of a relatively inert hydrocarbon; CCl_4, a halogenated diluent capable of moderate dispersion-force interactions; and 1,2-dichloroethane, a solvent of relatively high dielectric constant. It was demonstrated that stepwise complexing was occurring in two of these diluents and that CCl_4 showed a solvent effect by stabilizing a lower TBP coordination complex. It was also shown that the interpretation of the extraction data was consistent with a model for the acid complex which has a hydronium ion as a core around which a maximum of three TBP molecules could coordinate.

In this study the extraction of $HClO_4$ or $HReO_4$ with dilute TBP is examined in two more types of diluents: benzene and 1,3,5-triethylbenzene, representing basic aromatic diluents, and $CHCl_3$, an acidic solvent. The data are presented, as in part one, in the form of log-log plots with the aim of determining n, the TBP coordination number. As before, ReO_4 tracer was used to determine the organic-phase acid concentrations.

A log-log plot (not shown) of organic acid vs aqueous acid activity at a constant TBP concentration in benzene gave a slope of one, indicating the acid complex is ion-paired. Since the dielectric constants of the other diluents used herein are also low, it will be assumed they also form ion-paired extraction complexes. Thus the ion-pair equations and equilibrium constants, as outlined in part one, apply to these TBP-diluent systems too.

In Figs. G. 15-1 and G. 15-2 the log-log plots of organic acid vs equilibrium TBP at a constant aqueous acid concentration are shown, and indicate $n = 2$ for TBP-benzene and TBP-$CHCl_3$, while $n = 2$ and 3 for TBP-triethyl benzene. Thus, only 2TBP complexes are formed in benzene and $CHCl_3$ and a mixture of 2TBP and 3TBP complexes is extracted by triethyl benzene. The slight upturn of the extraction curve at TBP concentrations above 0.15 M in benzene may indicate that a 3TBP complex is forming; however, the more likely explanation for this upturn, is the breakdown of the dilute solution behavior (constant organic-phase activity coefficients) upon which the analysis is based. Thus, data from TBP concentration > 0.15 M will be considered suspect.

The constants, within the limitation noted in part one, are

Diluent	Acid	K_2	K_3
benzene	$HClO_4$	1.6×10^{-2}	---
triethyl benzene	$HClO_4$	4.1×10^{-3}	1.2×10^{-1}
$CHCl_3$	$HReO_4$	9×10^{-4}	---

The range of 2TBP complexes in each of these diluents is greater than that found previously for the standard system: TBP-isooctane. It is suggested that the aromatic diluents are playing an active role, stabilizing the 2TBP complex. Both benzene and triethyl benzene have π-electron systems that could solvate the complex. That is, the π electrons allow the aromatic molecules to act as weak bases in coordination with the extracted hydronium ion, and so tend to displace TBP molecules from the complex. Providing a more adequate solvating medium also means better extraction (relative to isooctane). Furthermore, a comparison between benzene and triethyl benzene indicates that the degree of interaction is in the right direction. Triethyl benzene has a π-electron density of only one-half that of benzene, per unit volume, and the π electrons, due to the attached ethyl groups, are probably not so accessible. Consequently a lesser range of 2TBP complex is expected than with benzene, as is observed, and the extraction is poorer.

$CHCl_3$, like the above diluents, allows a long range of 2TBP complex, but for a different reason. The predominant feature of $CHCl_3$ is its acidic hydrogen, which can readily coordinate with TBP to form a molecular adduct: $CCl_3H\cdots$ TBP. Thus, although the data for TBP-$CHCl_3$ are plotted against the stoichiometric TBP concentration, the actual effective TBP concentration

(activity) is considerably less. This means the extraction is being examined, in effect, at more dilute TBP, where $2TBP/H^+$ complexes are favored in the usual stepwise equilibrium. Another result should be a lowering in the observed value of K^a. As can be seen by comparing the constants for benzene and $CHCl_3$, the overall extraction is clearly depressed in $CHCl_3$, even though it has a dielectric constant nearly twice as large as that for benzene.

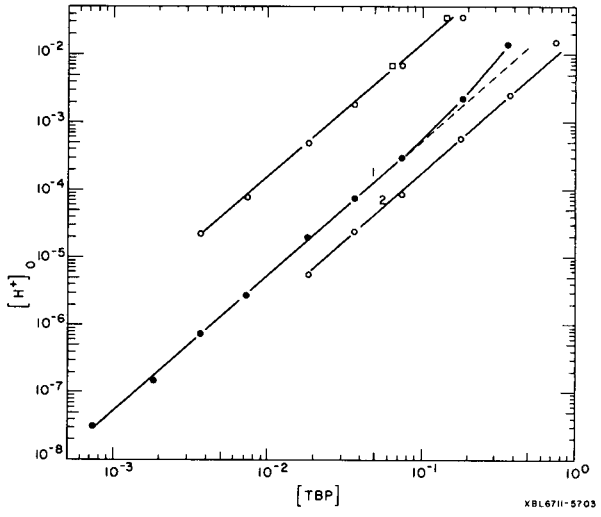

Fig. G. 15-1. Variation of acid content of organic phase with TBP in benzene for aqueous $HClO_4$ concentrations of 4.00 M (upper curve) and of 1.60 M (middle curve); in $CHCl_3$ for aqueous $HReO_4$ concentration of 2.91 M (lower curve). O, ●, uncorrected data: □, data corrected for used-up TBP.

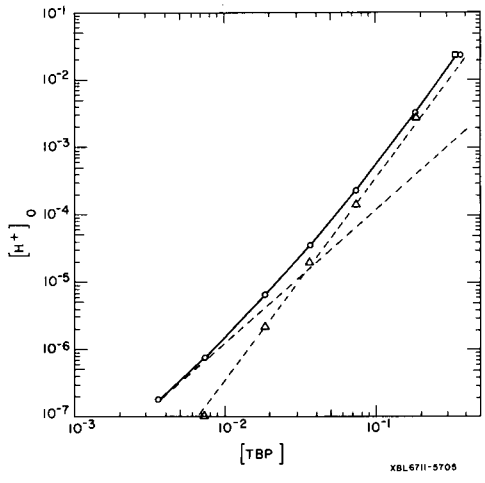

Fig. G. 15-2. Variation of acid content of organic phase with TBP in 1, 3, 5-triethyl benzene for aqueous $HClO_4$ concentration of 1.60 M. O, unresolved data; △, resolved n = 3 line; other dashed line, n = 2.

16. THE SOLVENT EXTRACTION OF PERCHLORIC ACID AND THE SOLVATION OF THE PROTON

D. J. Turner and R. M. Diamond

The extraction of a monobasic acid from water into a dilute solution of a basic extractant in an organic diluent is largely determined by the balance of a competition between the extractant, the water, and the acid anion to solvate the proton in the organic phase. The role assigned to the diluent in such a model is a secondary one which is, no doubt, justified when a nonpolarizable, nonpolar diluent is used. However, additional, though small, cation solvation effects appear when diluents with polarizable π electrons, such as benzene, are chosen, while the use of diluents with a large permanent dipole moment and higher dielectric constant may have a pronounced influence on the extraction.

In this work the relatively weak base 1-decanol has been used as extractant, and the effect of using, on the one hand, isooctane (ϵ = 1.92, 25°), and on the other, 1, 2-dichloroethane (ϵ = 10.4, 25°)

as diluent has been studied.

The equilibrium for the extraction of water alone into the organic phase is maintained independently of other equilibria in the system,

$$H_2O + nROH(org) = H_2O \cdot nROH(org),$$

and a mixed concentration quotient may be written

$$K = \frac{[H_2O \cdot nROH]_0}{(H_2O)[ROH]_0^n} . \quad (1)$$

A log-log plot (Fig. G. 16-1) of organic-phase water concentration vs equilibrium concentration of alcohol for the systems 1-decanol in isooctane (0.05 to 0.3 M) and in 1, 2-dichloroethane (0.02 to 0.5 M) gives, for the former, a slope n = 2.0 (K = 0.25), i. e., a 2:1 complex, $H_2O \cdot 2ROH$, while the latter has unit slope (K = 0.2), which is consistent with the formation of a 1:1 complex.

Beyond the water concentrations required by the above equilibria, the excess of water in the organic phase after equilibrating with aq. $HClO_4$ (2 to 10 M) is a measure of the proton hydration in that phase. Data obtained from such investigations, and corrected for the extraction of water by the alcohol alone at the appropriate water activity in the aqueous phase, allow an estimate to be made of the proton hydration number at a particular organic-phase acid concentration. Dependent on the latter concentrations, the hydration number ranges from 2 to 2.5 for both diluent systems.

A mixed concentration quotient for the partition of $HClO_4$ between the two phases can be expressed

$$K^a = \frac{[H^+ \cdot xH_2O \cdot yROH \ldots ClO_4^-]_0}{(H^+)(ClO_4^-)(H_2O)^x[ROH]_0^y} \quad (2a)$$

if the extracted species is ion-paired, or

$$K^d = \frac{[H^+ \cdot xH_2O \cdot yROH][ClO_4^-]_0}{(H^+)(ClO_4^-)(H_2O)^x[ROH]_0^y} \quad (2b)$$

if the species is dissociated in the organic phase. Which case obtains is largely determined by the dielectric properties of the diluent. At a constant concentration of alcohol, a log-log plot of organic-phase acid concentration vs the product of the aqueous activity of acid and the water activity raised to the power x (where x is the hydration number at a given organic-phase concentration of acid) should generate a line of slope 1 if case (2a) obtains, or of slope 0.5 if the extracted species is dissociated. Figure G. 16-1, where data are presented for the alcohol-isooctane system, shows that the former result is realized and the extracted species is ion-paired. However, in Fig. G. 16-2 the similar treatment of data obtained from the alcohol-1, 2-dichloroethane system yields a curve whose gradient is 0.5 at the lowest concentrations and rises to a value between 0.5 and 1.0 at higher activities. Such behavior strongly suggests that the extracted species is dissociated and, consequently, organic-phase activity coefficients must be applied to the data at higher concentrations, where the curvature becomes pronounced. Activity coefficients were computed from the Mayer-Poirier expression, using as many terms as were necessary for convergence. Their introduction then lowers the points onto the line of slope 0.5, as shown in Fig. G.16-2.

Figure G. 16-3 shows the log-log dependence of the organic-phase acid concentration on the alcohol concentration in isooctane at a fixed concentration of aqueous acid. Expression 2a indicates that the slope of this line should yield a value y, the number of alcohol molecules which solvate the proton. After correction to equilibrium concentrations, the gradient of the line that passes through the points is y = 3.0.

For 1,2-dichloroethane systems, the formalism shows that, since the extracted species is dissociated, the gradient of the line generated by the above plot will be y/2. In Fig. G. 16-4 the lines at two fixed aqueous concentrations of acid are of slope 1.5, which, as before, indicates a trialcoholated extracted species.

In both systems it is probable that the primary solvation unit is a hydronium ion, H_3O^+, with three molecules of 1-decanol coordinated at the three sites of formal positive charge on the hydrogen atoms. The presence of a trisolvated hydronium ion has been similarly inferred from studies of the extraction of $HClO_4$ by tributyl phosphate[1] and by trioctylphosphine oxide[2] in CCl_4 as diluent.

Additional water in the proton solvation unit either bridges between the hydronium ion and the alcohol molecules, or, less likely, is hydrogen-bonded to the hydroxyl proton of the alcohol.

The change in diluent from isooctane to 1,2-dichloroethane is not expected to lead to serious changes in the solvation number of the proton, and it was found that the extracted cationic species was similar in the two diluents. The diluents are distinguished, however, by their influence on the interionic forces in the organic phase. In dichloroethane, where the dielectric constant is moderately high, the organic-phase species is dissociated at low concentrations, while at similar concentrations in isooctane the acid is predominantly associated, and extraction is poorer.

References

1. D. C. Whitney and R. M. Diamond, J. Phys. Chem. 67, 209 (1963).
2. T. J. Conocchioli, M. I. Tocher, and R. M. Diamond, ibid 69, 1106 (1965).

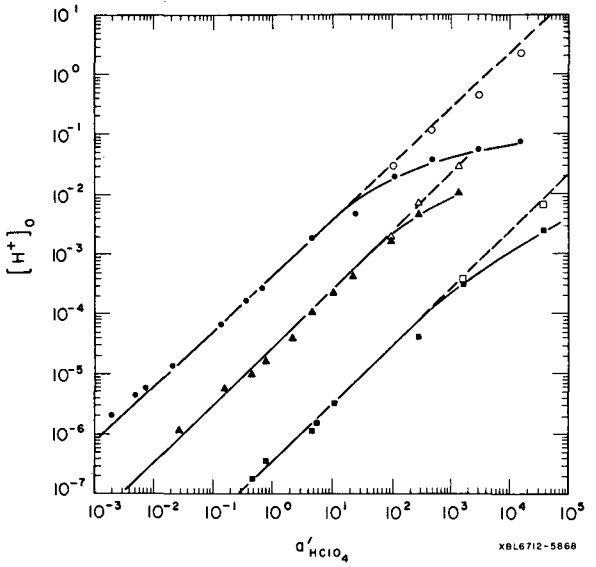

Fig. G. 16-1. Dependence of acid extraction on aqueous acid and water activities at fixed concentrations of 1-decanol in isooctane: ●, 0.314 M, ▲, 0.105 M, ■, 0.0262 M 1-decanol; O, △, □, data corrected to equilibrium concentrations of alcohol.

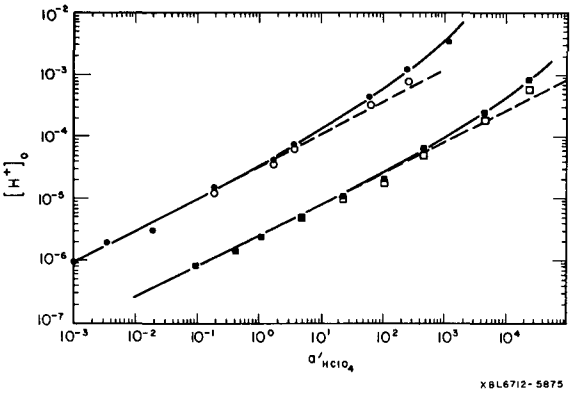

Fig. G. 16-2. Dependence of acid extraction on aqueous acid and water activities at fixed concentrations of 1-decanol in dichloroethane: ●, 0.105 M, and ■, 0.0209 M 1-decanol; O, □, data corrected for organic-phase activity coefficient of extracted acid.

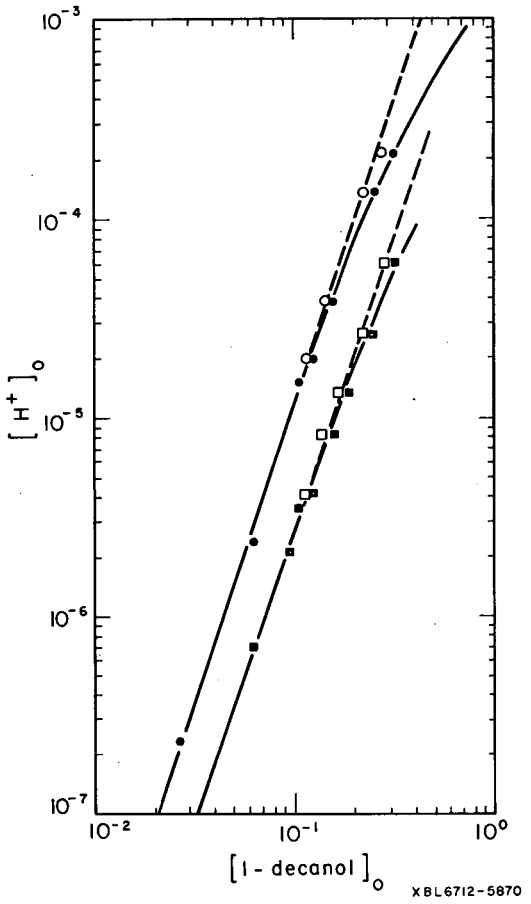

Fig. G. 16-3. Dependence of acid extraction on alcohol concentration in isooctane at constant equilibrium aqueous concentrations of acid: ●, 0.950 M, ■, 0.473 M; ○, □, data corrected to equilibrium concentrations of alcohol.

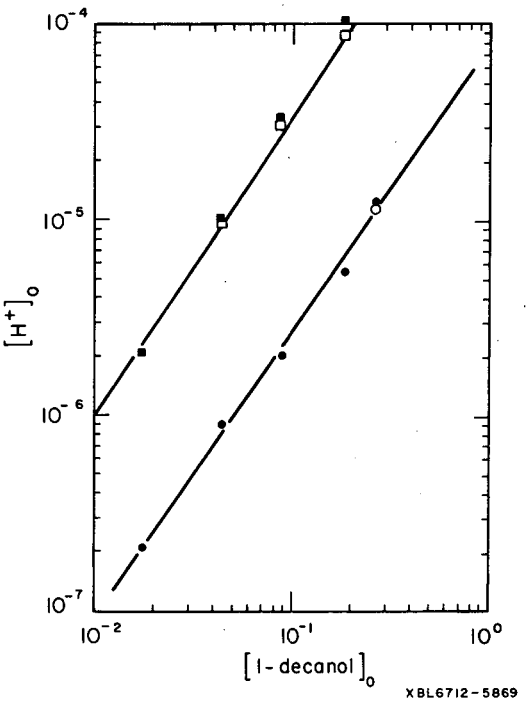

Fig. G. 16-4. Dependence of acid extraction on alcohol concentration in dichloroethane at constant equilibrium aqueous concentrations of acid; ●, 0.105 M, and ■, 0.983 M; ○, □, data corrected for organic-phase activity coefficient of extracted acid.

17. SOLVENT EXTRACTION OF TETRABUTYLAMMONIUM NITRATE AND THE SOLVATION OF THE NITRATE ION

D. J. Turner and R. M. Diamond

The solvation number of the nitrate ion in a nonaqueous medium has been determined by investigating the partition of tetrabutylammonium nitrate between its aqueous solution and dilute solutions of 1-decanol in 1,2-dichloroethane. The effect of a polar diluent of moderate dielectric constant ($\epsilon_{25} \approx 10.2$) is to disfavor less strongly the transfer into it of a pair of oppositely charged ions from the aqueous phase than would diluents with a lower dielectric contant, like benzene or cyclohexane. Although, to this extent, the diluent does influence the partition by electrostatically solvating the extracted salt, the transfer is determined largely by the short-range acid-base interactions between the anion and the more acidic molecules (water, alcohol) in the two phases. Furthermore, specific interactions between the basic centers of either organic-phase component and the cation $(C_4H_9)_4N^+$ are unlikely because of the structure and size of the latter. Solvation of the extracted salt means, therefore, a coordination to the nitrate ion.

Solutions of 1-decanol in 1,2-dichloroethane (0.2 M and 0.5 M), were equilibrated with aqueous solutions of tetrabutylammonium nitrate (TBAN) over the range of concentrations 0.003 to 0.14 M. At equilibrium, samples from the organic phase were transferred to a large, measured excess of water and back-extracted. The resultant aqueous concentration—and hence, the equilibrium organic-phase concentration—of TBAN was determined by a spectrophotometric method.

Assuming for the moment that the extracted salt is an ion pair, the reaction for the equilibrium may be written $Bu_4N^+ + NO_3^- + n\ ROH(org) + mH_2O = Bu_4N^+ \ldots NO_3^- \cdot nROH \cdot mH_2O(org)$, for which the mixed concentration quotient is

$$K = \frac{[Bu_4N^+ \ldots NO_3^- \cdot nROH \cdot mH_2O]_0}{(Bu_4N^+)(NO_3^-)(H_2O)^m [ROH]_0^n} \quad . \qquad (1)$$

At the low aqueous concentrations of TBAN considered here, the water activity will remain very close to unity, so Eq. 1 suggests that a log-log plot of organic-phase concentration of TBAN vs the equilibrium aqueous activity of TBAN at a constant concentration of alcohol should generate a line of unit slope if the salt is ion-paired in the organic phase. The plots so constructed in Fig. G. 17-1 for 0.2 M and 0.5 M 1-decanol do, indeed, satisfy this requirement.

Equation 1 then further suggests that a value for n, the number of alcohol molecules complexed to each molecule of organic-phase nitrate salt, can be determined by measuring the dependence of the latter concentration on the equilibrium concentration of alcohol at a fixed aqueous activity of TBAN. Figure G. 17-2 shows the appropriate log-log plot for an initial aqueous salt concentration of 0.014 M. The line has a unit slope, which suggests that in this system only one alcohol molecule solvates the nitrate ion.

Further importance then attaches to the problem of determining m, the hydration number of the extracted species. The presence or absence of coextracted water is the resultant of several factors. Water is more acidic then 1-decanol and may well be able to approach the site of anionic charge more closely than can an alcohol. Although these factors would tend to favor coextraction of water, there are considerations which oppose it. Various evidences suggest that the nitrate ion is not highly hydrated in the aqueous phase and that it is, indeed, a pronounced structure breaker in water. As with its co-ion, Bu_4N^+, the water structure tends to push the nitrate out into the less structured organic diluent, and so requires less extensive specific solvation by alcohol or water in the organic phase to overcome the positive electrostatic free energy change opposing the transfer. For this reason, TBAN gives significant extraction into 1,2-dichloroethane even in the absence of alcohol. This nonalcoholated TBAN coextracts somewhat more than one molecule of water with it, and combined with the high blank for water distributing into the 1,2-dichloroethane diluent itself (≈ 0.1 M), makes very difficult the determination of the water coextracted by the $Bu_4N^+ \ldots NO_3^- \cdot ROH$ complex. Our data seem to indicate that the latter has ≈ 1 molecule of water associated with it, although the accuracy is poor enough so that we cannot completely rule out an anhydrous species. Apparently the free energy recovered by ion-pairing and by the coordination of one alcohol per TBAN is almost sufficient to stabilize the organic-phase species $[Bu_4N^+ \ldots NO_3^- \cdot ROH]$ over the concentration ranges considered here.

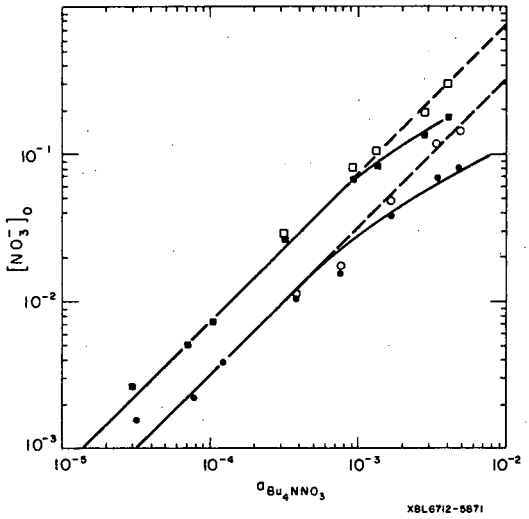

Fig. G. 17-1. Dependence of nitrate extraction on aqueous activity of TBAN at a fixed concentration of 1-decanol: ◘, 0.524 M, ●, 0.209 M 1-decanol; □, O, data corrected to constant equilibrium concentrations of 1-decanol.

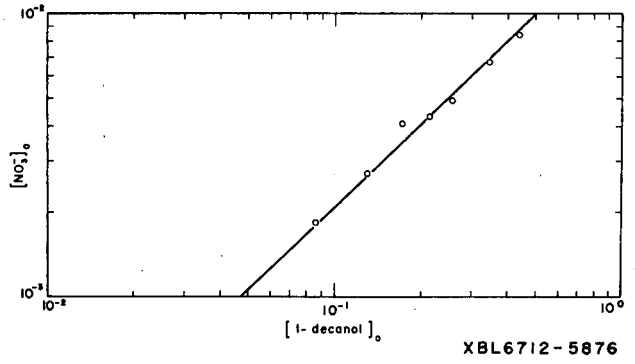

Fig. G. 17-2. Dependence of nitrate extraction on concentration of 1-decanol at a constant equilibrium aqueous TBAN activity of 1.34×10^{-4} (0.0129 M); ●, initial concentration of 1-decanol; O, equilibrium concentration.

18. SOLVENT EXTRACTION OF TETRAHEPTYLAMMONIUM FLUORIDE AND THE SOLVATION OF THE FLUORIDE ION

D. J. Turner, A. Beck, and R. M. Diamond

A previous paper treated the solvation of the hydroxide ion and showed that a solvent extraction method was suitable for the experimental determination of the alcoholation of this ion in various organic diluents.[1] The work presented here provides an extension of the method to the fluoride ion, which is isoelectronic with the hydroxide ion, but is not expected to show trisolvation as did the latter. By using extractants of widely differing acidity one might expect changes in the solvation number. Furthermore, an increase in the acidity constant should favor the coordination of the extractant rather than water to the anion, and may be expected to displace water entirely from the anion solvation sheath if the extractant is sufficiently acidic. In this work, the partition of tetraheptylammonium fluoride (THAF) between dilute solutions of benzyl and of decyl alcohol in toluene, and between dilute solutions of 1-naphthal and p-phenylphenol in toluene, was investigated.

Aqueous concentrations of THAF (0.0005 to 0.05 M) containing a small amount of ^{18}F tracer were equilibrated with solutions of alcohol over the concentration range 0.07 to 0.5 M. If the extracted salt is ion-paired in the organic phase, then a mixed concentration quotient for the partition can be written

$$K = \frac{[R_4N^+ \cdots F^- \cdot mH_2O \cdot mROH]_0}{(R_4N^+)(F^-)(H_2O)^m [ROH]_0^n} . \qquad (1)$$

At the low concentrations considered here the water activity is close to unity, as are the aqueous ionic activity coefficients, and Eq. 1 can be simplified to

$$K' = \frac{[F^-]_0}{[R_4N^+][F^-][ROH]_0^n} , \qquad (2)$$

where $[F^-]_0$ refers to the organic-phase salt concentration. A log-log plot of $[F^-]_0$ vs $[R_4N^+][F^-]^0$ for extractions by 0.193 M benzyl alcohol and by 0.433 M 1-decanol in toluene has, in both cases, unit slope, which is consistent with the assumption that the extracted salt is ion-paired.

Equation 2 then suggests that a value for n, the alcoholation number, can be recovered if the extraction is studied as a function of alcohol concentration at a fixed aqueous concentration of THAF. Figure G. 18-1 shows such a log-log relationship wherein the line that passes through the points, corrected to equilibrium concentrations of benzyl alcohol, has a slope m = 4.0. An identical result holds also for extractions into 1-decanol.

Data plotted for the extraction of THAF by a constant concentration of the more acidic extractants, p-phenylphenol (7.39×10^{-3} M) and 1-naphthol (6.4×10^{-3} M) in toluene, give a log-log slope of 1, indicating that in both cases the organic species is again an ion pair. However, the dependence of the extraction at a fixed aqueous concentration of THAF, 2.74×10^{-4} M, on the concentration of 1-naphthol shows a discontinuity in gradient at a naphthol concentration of about 3×10^{-3} M. A line of slope 2 drawn through the lower points and extended to higher concentrations may tentatively be identified as evidence of a disolvated species. Subtraction of these concentrations from the total experimental concentration $[F^-]_0$ allows a division of the measured concentration into a disolvate and a higher component. The line which passes through the latter (shown in Fig. G. 18-2 after correction to equilibrium naphthol concentrations) then has a slope 3.5, suggesting the presence of a tetrasolvate. The extraction from an aqueous concentration of 2.74×10^{-3} M THAF (Fig. G. 18-3) shows, unambiguously, a discontinuity at the same order of phenol concentration with a disolvated species below 3×10^{-3} p-phenylphenol and a tetrasolvated species above this concentration.

Studies of water coextracted into the organic phase show that (a little over) two molecules of water accompany the transfer of each fluoride ion into solutions of alcohol in toluene. That is, the organic-phase species $[R_4N^+ \ldots F^-]$ requires four molecules of alcohol to stabilize the extracted anion in the low dielectric medium, but since the acidity constants of water and the alcohols are not widely different, water is still able to compete with the alcohol molecules for solvating the fluoride ion, possibly bridging the position between the anion and an alcohol molecule, and two waters per anion are coextracted.

However, the acidity constants of the phenols used are probably seven or eight orders of magnitude larger than those for the alcohols, and are greater by 10^6 than that for water. The first consequence of this is that over a wide concentration range a smaller number of hydrogen bonds of superior strength are sufficient to meet the solvation requirements of the anion in phenolic media. Secondly, the water-anion interactions are relatively so much weaker than the anion-phenol interactions that the solvation competition is shifted completely in favor of the extractant. Investigation of the water behavior showed that the extracted salt is anhydrous; the phenols have completely displaced water from the solvation sheath of the fluoride ion.

Reference

1. B. Argawal and R. M. Diamond, J. Phys. Chem. 67, 2785 (1963).

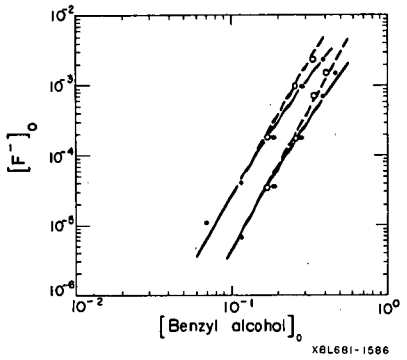

Fig. G. 18-1. Dependence of fluoride extraction on benzyl alcohol concentration at a constant equilibrium aqueous fluoride concentration of 0.0116 M (upper) and 0.00463 M (lower): ●, initial alcohol concentrations; O, equilibrium alcohol concentrations. Dashed lines drawn with slope of 4.0.

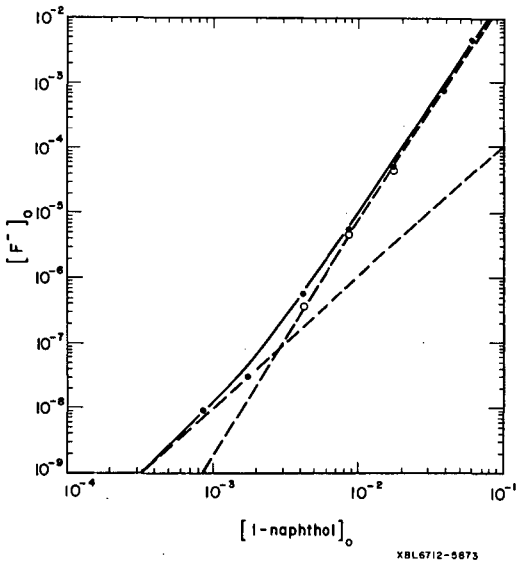

Fig. G. 18-2. Dependence of fluoride extraction on equilibrium concentrations of 1-naphthol in toluene at a constant equilibrium aqueous fluoride concentration of 2.74×10^{-4} M; ●, total organic-phase fluoride concentration; O, total organic-phase fluoride concentration less concentration of disolvated species.

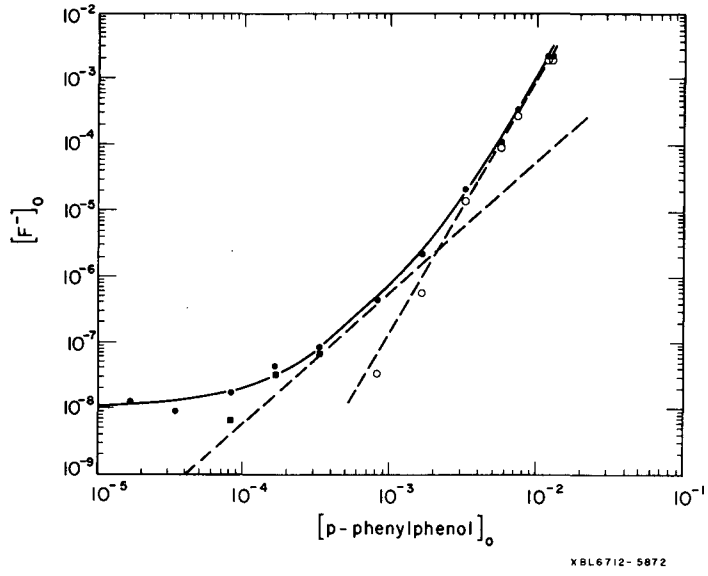

Fig. G. 18-3. Dependence of fluoride extraction on equilibrium concentrations of p-phenylphenol in toluene at a constant equilibrium aqueous fluoride concentration of 2.74×10^{-3} M; ●, total organic-phase fluoride concentration; ◘, data corrected for extraction into toluene alone; ○, total organic-phase fluoride concentration less concentration of disolvated species.

19. CRYSTAL STRUCTURES AND LATTICE PARAMETERS OF THE COMPOUNDS OF BERKELIUM. I. BERKELIUM DIOXIDE AND CUBIC BERKELIUM SESQUIOXIDE†

J. R. Peterson* and B. B. Cunningham

The first structure determination of a compound of berkelium was carried out in 1962 by x-ray diffraction of 0.004 μg of BkO_2.[1] A cubic lattice parameter of 5.33 ± 0.02 Å was derived from the indexing of four lines. With the present availability of microgram quantities of berkelium, a systematic study of the compounds of berkelium was undertaken.

The berkelium used in this work was purified by solvent extraction and ion exchange. Mass analysis determined cerium and neodymium contents to be 0.27 and 0.06 at. %, respectively.

This purified material was sorbed to saturation in single beads of cation-exchange resin for air calcination at ≈ 1200°C to form BkO_2. Hydrogen reduction of BkO_2 at 600°C leads to the body-centered cubic, Mn_2O_3-type Bk_2O_3. Reoxidation in air or oxygen at 600°C converts the sesquioxide back to the dioxide. The techniques used in this air calcination and subsequent hydrogen reduction have been published previously.[1-3] All samples were examined by standard x-ray powder techniques.

Most probable lattice parameters were computer-determined, according to a least-squares fit of the differences between observed and calculated $\sin^2\theta$ values.[4] Theoretical line intensities were calculated,[5] assuming the fluorite structure for BkO_2 and the bixbyite structure for Bk_2O_3. In both cases all lines could be indexed on the basis of the assumed structures, and the agreement between observed and calculated line intensities was considered satisfactory.

The observed lattice parameters for a few of the individual compound preparations along with their ^{249}Cf content are listed in Table G. 19-I. The dioxide parameter increases with time (increasing Cf content), while the sesquioxide parameter decreases with time. This is attributed to the relative sizes of the Bk^{4+}, Bk^{3+}, and Cf^{3+} ions.

A plot of the actinide dioxide lattice parameters is shown in Fig. G. 19-1. The data clearly show the "actinide contraction," but the cusp at Cm has no immediate explanation. Perhaps the evident cusp is caused by some of the parameters being derived from nonstoichiometric dioxides.

A plot of the cubic lattice parameters of the lanthanide and actinide Mn_2O_3-type sesquioxides is shown in Fig. G. 19-2. Both series of sesquioxides show the characteristic 4f and 5f contractions, as well as the cusp at the point of the half-filled electron subshell.

This series of isomorphic compounds lends itself to calculation of the corresponding cationic radii. That calculated for sixfold coordinated Bk^{3+} is 0.954 Å. Although such radii values should be regarded with caution and considered only as relative values, they are often very useful for predicting actinide crystal chemistry on the basis of radius ratios and known lanthanide crystal chemistry.

Footnotes and References

†Inorg. Nucl. Chem. Letters 3, 327 (1967).

*Present address: Department of Chemistry, The University of Tennessee, Knoxville, Tennessee 37916.

1. B. B. Cunningham, in Proceedings of the Robert A. Welch Foundation Conference on Chemical Research, VI, Topics in Modern Inorganic Chemistry, 1962.

2. B. B. Cunningham, Microchemical Journal, Symposium, 1961.

3. J. L. Green, The Absorption Spectrum of Cf^{3+} and Crystallography of Californium Sesquioxide and Californium Trichloride (Ph. D. Thesis), UCRL-16516, Nov. 1965.

4. D. E. Williams, Ames Laboratory Report IS-1052, 1964.

5. D. K. Smith, A Fortran Program for Calculating x-Ray Powder Diffraction Patterns, UCRL-7196, April 1963.

Table G. 19-I. Crystallographic properties of the berkelium oxides.

Sample number	Film number	Compound[a]	^{249}Cf content[b] (atom %)	Observed[c] a_0 (Å)	$\pm 2\sigma$[d]	Method of preparation
JRP-VIII	2560A	BkO_2	0.88	5.334	0.001	air ignition at 1200°C
JRP-X	2564A	BkO_2	1.10	5.335	0.001	$Bk_2O_3 + O_2$ at 600°C for 61 min
JRP-XVII	2596A	BkO_2	3.68	5.336	0.001	air-fired BkO_2 + HF at 500°C for 62 min
JRP-X	2568A	Bk_2O_3	1.53	10.889	0.003	low-temp. $BkO_2 + H_2$ at 600°C for 60 min
JRP-IX	2572A	Bk_2O_3	1.75	10.887	0.001	H_2 reduction of higher oxide at 600°C for 64 min
JRP-XV	2590A	Bk_2O_3	3.26	10.885	0.001	air-fired $BkO_2 + H_2$ at 600°C for 60 min

a. The stoichiometries of both berkelium oxides were assumed. Direct determination was deemed impossible on the 0.2-μg samples.

b. Calculated by assuming ^{249}Bk half-life is 314 days. Other known contaminants: 0.27 at. % Ce, 0.06 at. % Nd.

c. Calculated least-squares value using the LCR-2 program (Ref. 4).

d. This represents the 95% confidence range reflecting only the internal consistency of the data for the individual preparation.

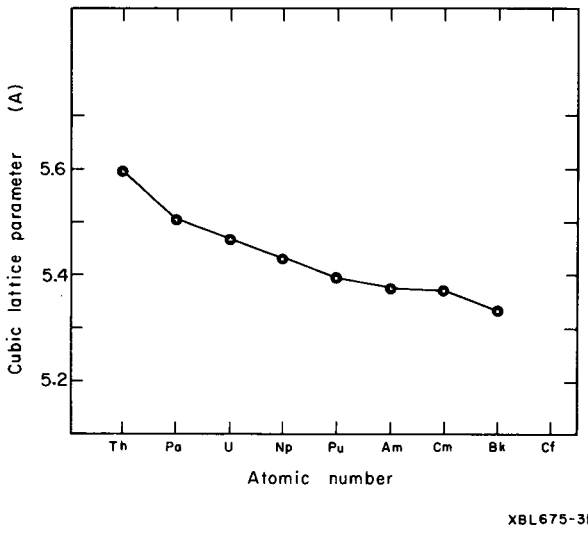

Fig. G. 19-1. Actinide dioxide lattice parameters.

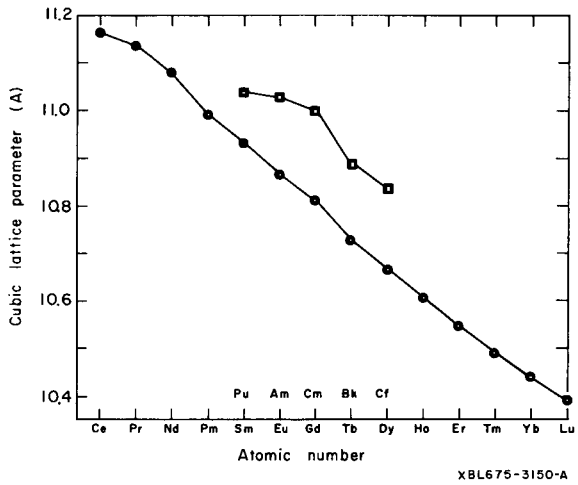

Fig. G. 19-2. Cubic lattice parameters of the lanthanide and actinide Mn_3O_3-type sesquioxides.

20. CRYSTAL STRUCTURES AND LATTICE PARAMETERS OF THE COMPOUNDS OF BERKELIUM II. BERKELIUM TRICHLORIDE †

J. R. Peterson* and B. B. Cunningham

As part of a continuing program to investigate the crystallographic properties of berkelium, we report here our results for the UCl_3-type hexagonal berkelium trichloride.

The source of berkelium was the same as reported previously.[1] The line-green trichloride samples were prepared by treatment of the berkelium oxides with anhydrous HCl gas at ≈ 520° C for three 10- to 12-min periods interrupted by cooling, evacuation, and admission of fresh HCl gas. The techniques employed in this hydrochlorination have been published previously.[2,3]

All $BkCl_3$ samples exhibited the UCl_3-type hexagonal structure. Powder data were treated as before,[1] and theoretical intensity calculations were carried out with the atomic coordinates of UCl_3[4] assumed for $BkCl_3$.

The observed lattice parameters of the individual trichloride preparations along with their ^{249}Cf content are listed in Table G. 20-I. Film 2652A was a second exposure of sample number JRP-XVI (Film 2598A) after a time lapse. This was to see if the lattice parameters would shift noticeably toward those of $CfCl_3$, as the californium content in the $BkCl_3$ increased. The parameters clearly show the expected expansion in the a_0 parameter and shrinkage in the c_0 parameter.

The observed lattice parameters were corrected for the known Cf and Ce contents in accordance with Vegard's Law, and then averaged to obtain $a_0 = 7.382 \pm 0.002$ Å and $c_0 = 4.127 \pm 0.003$ Å. The error limits reported here were computed by using the 95% confidence level equal to $(4.30/\sqrt{N})\sqrt{\Sigma d_i^2/(N-1)}$, where d_i is the deviation of the individual lattice parameters from the average value, N is the number of observations, and the factor 4.30 is the 95% confidence Student t value for three observations.

Plots of the a_0 and c_0 lattice parameters of the UCl_3-type hexagonal actinide trichlorides are given in Fig. G. 20-1. An anisotropic "actinide contraction" is clearly evident. Because of the anisotropics in this trichloride series, the concept of ionic radius should be regarded with considerable caution. Calculations of interatomic distances and sixfold-coordinated trivalent ionic radii derived from the UCl_3-type lanthanide trichlorides show a similar anisotropic contraction. Comparison of similarly calculated trivalent ionic radii shows almost identical values for the following lanthanide-actinide pairs: Gd-Cf, Eu-Bk, Sm-Cm, Pm-Am, Nd-Pu, Pr-Np, and Ce-U.

By comparison of radius ratios and by analogy with known lanthanide trichloride crystal chemistry, one is led to the prediction that there will be a crystal structure change noted in the actinide trichlorides heavier than $CfCl_3$. The confirmation of this prediction will have to wait until $EsCl_3$ is prepared and its crystal structure is determined.

Footnotes and References

†J. Inorg. Nucl. Chem. (to be published in Feb. 1968 issue).

*Present address: Department of Chemistry, The University of Tennessee, Knoxville, Tennessee 37916.

1. J. R. Peterson and B. B. Cunningham, Inorg. Nucl. Chem. Letters 3, 327 (1967).
2. B. B. Cunningham, Microchemical J. Symposium, 1961.
3. J. L. Green, The Absorption Spectrum of Cf^{3+} and Crystallography of Californium Sesquioxide and Californium Trichloride (Ph. D. Thesis), UCRL-16516, Nov. 1965.
4. W. H. Zachariasen, The Transuranium Elements, Part II, National Nuclear Energy Series, Vol. 14B (McGraw-Hill Book Company, Inc., New York, 1949), Paper 20.6, pp. 1473-85.

Table G. 20-I. Berkelium trichloride lattice parameters (UCl_3-type hexagonal).

Sample number	Film number	^{249}Cf[a] content (atom %)	Observed lattice parameters[b] (A) $a_0 \pm 2\sigma$	$c_0 \pm 2\sigma$
JRP-XIV	2587 A	3.04	7.382 ± 0.001	4.127 ± 0.001
JRP-XVI	2598 A	3.68	7.384 ± 0.001	4.127 ± 0.001
JRP-XVII	2600 A	3.90	7.383 ± 0.001	4.125 ± 0.001
JRP-XVI	2652 A	20.17	7.387 ± 0.001	4.122 ± 0.001

a. Calculated on the assumption ^{249}Bk half-life is 314 days. Other known contaminants: 0.27 at. % Ce, 0.06 at. % Nd.

b. Lattice parameters are the least-square values. The 2σ error limits represent the 95% confidence range reflecting only the internal consistency of the data for the individual preparation.

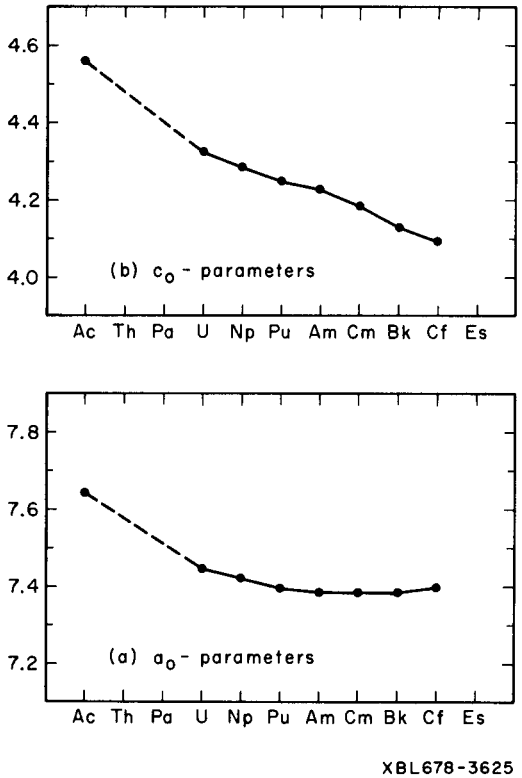

Fig. G. 20-1. Lattice parameters (in angstroms) of the UCl_3-type hexagonal actinide trichlorides.

21. CRYSTAL STRUCTURES AND LATTICE PARAMETERS OF THE COMPOUNDS OF BERKELIUM. III. BERKELIUM OXYCHLORIDE†

J. R. Peterson* and B. B. Cunningham

The preparation and crystallographic characterization of berkelium oxychloride are discussed in this paper. The source of berkelium was the same as reported previously.[1] Anhydrous berkelium trichloride samples[2] were treated at ≈ 500°C with an $HCl_{(g)}$ - $H_2O_{(g)}$ mixture to produce the very pale green BkOCl samples.

From the work of Koch[3] on the thermodynamics of the reaction, $AmCl_{3(s)} + H_2O_{(g)} \rightleftharpoons AmOCl_{(s)} + 2HCl_{(g)}$, it was calculated that the vapor in equilibrium with a 9.5 to 10 M HCl solution should contain the proper HCl/H_2O ratio to drive the corresponding berkelium reaction to the right at 500°C. Dry nitrogen gas was used as an inert carrier gas for the $HCl_{(g)}$ - $H_2O_{(g)}$ mixture. The N_2 was bubbled through the HCl solution at room temperature, passed through a quartz-wool plug to remove spray, then through the quartz x-ray capillary containing the berkelium sample held at ≈ 500°C, and finally through an H_2SO_4 bubbler. Since the equilibrium constant favors trichloride formation at low temperature, the oxychloride samples were cooled in vacuum or in a dry $N_{2(g)}$ atmosphere.

Unlike berkelium trichloride,[4] BkOCl is not hygroscopic. All BkOCl samples exhibited the PbFCl-type tetragonal structure.[4] The BkOCl powder patterns were of poorer quality than those obtained from other berkelium compounds, in that the high-angle lines were often light and diffuse. The powder data were treated as before,[1] with the atomic coordinates of AmOCl (Ref. 5) being assumed for those of BkOCl.

The observed lattice parameters for three individual oxychloride preparations along with their ^{249}Cf content are listed in Table G. 21-I. The three sets of lattice parameters were corrected for the known Ce and Cf contents, by assuming that the impurities formed ideal solid oxychloride solutions with the berkelium (Vegards' Law). These "corrected" BkOCl parameters were then averaged to obtain $a_0 = 3.966 \pm 0.004$ Å and $c_0 = 6.710 \pm 0.009$ Å, where the lattice parameter error limits are the 95% confidence interval calculated by using the standard statistical method for the average of three independent determinations.

A plot of the molecular volumes of the PbFCl-type lanthanide and actinide oxychlorides is shown in Fig. G. 21-1. With the exception of UOCl (Ref. 7) the correlation is good, showing the familiar contractions in the lanthanide and actinide series.

Similar to the UCl_3-type actinide trichlorides,[2] the anion crowding is very severe in this PbFCl-type tetragonal structure. In BkOCl the oxygen-oxygen distance is 2.80 Å, the chlorine-chlorine distance, 3.34 Å. The Bk-O distance is 2.32 Å, whereas the Bk-Cl distances are 3.07 Å and 3.05 Å. Both anion-anion distances are considerably smaller than twice the crystal radii given by Zachariasen for O^{2-} (1.46 Å) and Cl^- (1.81 Å).[8] Different values are obtained for the Bk^{3+} radius from the Bk-Cl and Bk-O distances. These calculations clearly illustrate the limitations of the ionic radius concept.

Footnotes and References

†UCRL-17766; submitted to Inorg. Nucl. Chem. Letters.

*Present address: Department of Chemistry, The University of Tennessee, Knoxville, Tennessee 37916.

1. J. R. Peterson and B. B. Cunningham, Inorg. Nucl. Chem. Letters 3, 327 (1967).
2. J. R. Peterson and B. B. Cunningham, Crystal Structure and Lattice Parameters of the Compounds of Berkelium. II. Berkelium Trichloride, to be published in J. Inorg. Nucl. Chem., Feb. 1968.
3. C. W. Koch, Thermodynamics of the Trichlorides and Oxychlorides of Some of the Lanthanide and Actinide Elements (Ph. D. Thesis), UCRL-2286, Sept. 1953.
4. W. Nieuwenkamp and J. M. Bijuoet, Z. Krist. 81, 469 (1931).
5. D. H. Templeton and C. H. Dauben, J. Am. Chem. Soc. 75, 4560 (1953).
6. D. E. Williams, Ames Laboratory Report IS-1052, 1964.
7. S. A. Shchukarev and A. I. Efimov, Zh. Neorg. Khim. 2, 2303 (1957).

8. W. H. Zachariasen, The Actinide Elements, National Nuclear Energy Series, Vol. 14A (McGraw-Hill Book Company, Inc., New York, 1954), Chapter 18, pp. 769-96.

Table G. 21-I. Berkelium oxychloride lattice parameters (PbFCl-type tetragonal).

Sample number	Film number	^{249}Cf Content[a] (atom %)	Observed lattice parameters[b] (A)	
			$a_0 \pm 2\sigma$	$c_0 \pm 2\sigma$
JRP-XVII	2600 A	3.90	3.964 ± 0.003	6.709 ± 0.005
JRP-XVII	2610 A	4.95	3.967 ± 0.001	6.711 ± 0.003
JRP-XX	2612 A	5.16	3.965 ± 0.001	6.704 ± 0.003

a. Calculated assuming ^{249}Bk half-life is 314 days. Other known contaminants: 0.27 at. % Ce, 0.06 at. % Nd.
b. Lattice parameters are the least squares value (Ref. 6). The 2σ error limits represent the 95% confidence range reflecting only the internal consistency of the data for the individual preparation.

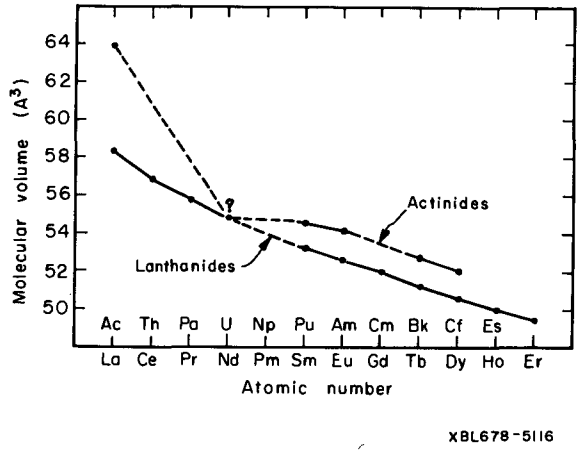

Fig. G. 21-1. Molecular volumes of the PbFCl-type lanthanide and actinide oxychlorides.

22. CRYSTAL STRUCTURES AND LATTICE PARAMETERS OF THE COMPOUNDS OF BERKELIUM. IV. BERKELIUM TRIFLUORIDE†

J. R. Peterson* and B. B. Cunningham

The preparation and crystallographic characterization of two structural forms of berkelium trifluoride are discussed in this paper. The berkelium used in this work was derived from two separate purification cycles, both carried out as described previously.[1] Mass analyses of the two berkelium solutions showed the Ce and Nd contents to be 0.27 at. % Ce and 0.06 at. % Nd in one Bk solution, as contrasted with 9.53 at. % Ce and 0.03 atom percent Nd in the other. The presence of the Ce and Cf (from Bk decay) contaminants prevented the determination of accurate lattice parameters for BkF_3.

Berkelium trifluoride samples were prepared by treatment of the oxides with a $H_{2(g)}$ - $HF_{(g)}$ mixture at 600°C for 1 hr. The trifluoride samples were either cooled rapidly to obtain the high-temperature, trigonal modification, or cooled slowly to obtain the low-temperature, orthorhombic modification. The very pale yellow-green samples were sealed in evacuated quartz capillaries for x-ray examination. Further details of the hydrofluorination techniques can be found in Ref. 2.

Berkelium trifluoride was found to exist in both the LaF_3-type trigonal structure,[3] characteristic of the lanthanide trifluorides of La through Pm and the YF_3-type orthorhombic structure,[4] characteristic of the lanthanide trifluorides of Sm through Lu.

The observed lattice parameters of the individual trifluoride preparations along with their ^{249}Cf and Ce contents are listed in Table G. 22-I. Since CeF_3 does not exhibit an orthorhombic modification, the YF_3-type berkelium trifluoride lattice parameters were initially corrected for the known Cf content of the Bk sample in accordance with Vegard's Law.[5] These "corrected-for-Cf" orthorhombic BkF_3 lattice parameters were then plotted versus the Ce content of the berkelium sample and extrapolated to zero Ce content to obtain "best estimates" for the lattice parameters of orthorhombic BkF_3: $a_0 = 6.70 \pm 0.01$ Å, $b_0 = 7.09 \pm 0.01$ Å, and $c_0 = 4.41 \pm 0.01$ Å, where the error limits reflect the uncertainties in the derivation of the lattice parameters.

Similarly for LaF_3-type trigonal berkelium trifluoride, since the trigonal modification of CfF_3 is unknown, the lattice parameters were corrected for the known Ce content of the Bk sample. These "corrected-for-Ce" trigonal BkF_3 lattice parameters did not vary in any regular fashion as the Cf content of the berkelium sample increased, so they were just averaged to obtain "best estimates" for the lattice parameters of trigonal BkF_3: $a_0 = 6.97 \pm 0.01$ Å and $c_0 = 7.14 \pm 0.01$ Å, where again the lattice parameters are rounded off to the nearest hundreth and the error limits reflect the uncertainties in the derivation of the lattice parameters.

Orthorhombic BkF_3 samples were easily converted to the trigonal form by annealing at 600°C. The inversion temperature of BkF_3 lies between 350 and 600°C, but could not be determined more precisely, since long-term annealings of trigonal BkF_3 samples failed to produce significant transformations to the orthorhombic form.

The trifluorides of Bk and Cf (Ref. 6) are the first of the actinide trifluorides to be prepared in the YF_3-type orthorhombic modification. The calculated Bk^{3+} radii are consistent with a crystal structure change, as expected by analogy with the lanthanide trifluorides.

The calculated densities (x-ray) of the two berkelium trifluoride modifications reflect the general trend noted in the lanthanide trifluorides that the high-temperature trigonal modification is the more dense one.

Footnotes and References

†UCRL-17912; submitted to J. Inorg. Nucl. Chem.

*Present address: Department of Chemistry, The University of Tennessee, Knoxville, Tennessee 37916.

1. J. R. Peterson and B. B. Cunningham, Inorg. Nucl. Chem. Letters 3, 327 (1967).

2. Joseph R. Peterson, The Solution Absorption Spectrum of Bk^{3+} and the Crystallography of Berkelium Dioxide, Sesquioxide, Trichloride, Oxychloride, and Trifluoride (Ph. D. Thesis), UCRL-17875, Oct. 1967.

3. Allan Zalkin, David H. Templeton, and Ted E. Hopkins, Inorg. Chem. 5, 1466 (1966).

4. Allan Zalkin and D. H. Templton, J. Am. Chem. Soc. 75, 1453 (1953).

5. A. F. Wells, Structural Inorganic Chemistry, Chapter XXVII (Oxford University Press, London, 1962), pages 971-1028.

6. J. R. Peterson, J. C. Copeland, and David Temple (Lawrence Radiation Laboratory), unpublished results, 1967.

Table G.22-I. Berkelium trifluoride lattice parameters.

Sample number	Film number	Structure type	^{249}Cf[a] content (atom %)	Total Ce content[b] (atom %)	Observed lattice parameters[c] (Å) $a_0 \pm 2\sigma$	$b_0 \pm 2\sigma$	$c_0 \pm 2\sigma$
JRP-XXIII	2624 A	YF_3	7.03	0.27	6.695±0.004	7.086±0.004	4.407±0.003
JP-VII	2691 A	YF_3	1.53	9.53	6.717±0.015	7.114±0.011	4.409±0.005[d]
JP-X	2713 A	YF_3	5.16	9.53	6.716±0.001	7.103±0.001	4.408±0.001
JRP-XXI	2614 A	LaF_3	5.26	0.27	6.973±0.002		7.143±0.003
JRP-XXII	2619 A	LaF_3	6.20	0.27	6.965±0.003		7.140±0.003
JP-VII	2691 A	LaF_3	1.53	9.53	6.990±0.001		7.157±0.001
JP-X	2716 A	LaF_3	5.79	9.53	6.990±0.001		7.158±0.002
JP-X	2734 A	LaF_3	8.05	9.53	6.988±0.001		7.156±0.002

a. Calculated[b] assuming ^{249}Bk half-life is 314 days.
b. Determined by mass analysis. See text.
c. Lattice parameters are the least-squares value. The 2σ error limits represent the 95% confidence range reflecting only the internal consistency of the data for the individual preparation.
d. The second phase in a predominantly trigonal BkF_3 powder pattern.

23. THE CRYSTAL AND MOLECULAR STRUCTURE OF CEMBRENE †

Michael G. B. Drew, David H. Templeton, and Allan Zalkin

A crystalline diterpene ($C_{20}H_{32}$) called cembrene[1] or thunbergene[2] has been isolated from the turpentine oil of Pinus albicaulus, Punus thunbergii, and several other species of pine trees. Two independent investigations by Dauben, Thiessen, and Resnick[3,4] and by Kobayashi and Akiyoshi[5,6] have shown by systematic degradation and spectroscopic evidence that this hydrocarbon is 1-isopropyl-4, 8, 12-trimethyl-2, 4, 7, 11-cyclotetradecatetraene, but failed to establish the stereochemistry of the double bonds. We have determined the crystal structure of this compound by x-ray diffraction, confirming the molecular structure and showing that the ring is trans at three double bonds and cis only at the 4-ene:

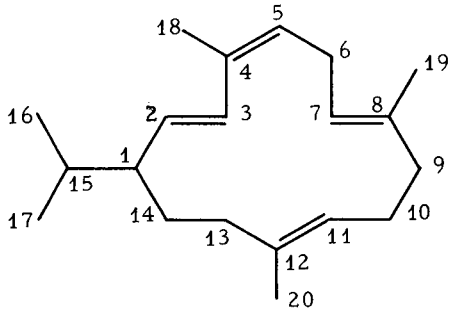

Crystals were kindly provided by Prof. W. G. Dauben of this University. Two crystals of approximately the same size (0.1×0.3×0.2 mm) were used in the experiment, each mounted on the a axis. Preliminary photographs by the Weissenberg technique showed an orthorhombic lattice. The cell dimensions are

$$\underline{a} = 6.224(4),\ \underline{b} = 21.517(8),\ \underline{c} = 13.794(6)\ \text{Å}.$$

These dimensions agree with those reported by Ibers.[7] With $\underline{Z} = 4$, the calculated density 0.980 g cm^{-3} agrees with the value observed by flotation, 0.98 g cm^{-3}, again in accord with Ibers.[7] Reflections are absent for h00 if h = 2n+1, for 0k0 if k = 2n+1, and for 00ℓ if ℓ = 2n+1. These rules are characteristic of space group $P2_12_12_1$, and this choice is confirmed by the structure determination. All atoms are in the general set of positions:

$$4(a)\ x, y, z;\ 1/2-x, -y, 1/2+z;\ 1/2+x, 1/2-y, -z;\ -x, 1/2+y, 1/2-z.$$

Intensities were measured for 2045 independent reflections, of which 217 were recorded as zero, with CuKα radiation filtered through Ni by a θ, 2 θ scan technique. The first crystal was used to collect data for reflections for which 2 θ < 110 deg; however, the intensity of the four standard reflections had uniformly dropped by approximately 15% and the crystal was discarded. A second crystal was used for data in the range 100 to 140 deg, and here too the standard reflections for this crystal dropped by 15%. No correction was made for absorption.

The structure of cembrene was solved by a statistical method using the general principles laid down for noncentrosymmetric structures.[8,9] Ninety-eight reflections with |E| values greater than 1.67 were used in this calculation. An E map (Fourier) was calculated by using the phases of only 98 reflections. A least-squares refinement confirmed that, of the top 20 peaks in this map, 19 were carbon atoms. The final carbon atom was located by a difference Fourier using all reflections. In the subsequent least-squares refinement, we gave zero weight to each reflection whose observed structure factor was less than twice the calculated standard deviation. A difference Fourier revealed the location of all the hydrogen atoms. All 309 parameters (carbon anisotropic, hydrogen isotropic) by full-matrix least squares for three cycles gave an R value of 0.063 (0.088 for all data). The final coordinates and thermal parameters for the carbon atoms in cembrene are given in Table G.23-I.

Discussion of the Structure

The a projection of the structure is shown in Fig. G.23-1, together with the C-C bond distances. This figure shows the enantiomorph which is consistent with the absolute configuration determined by Dauben, Thiessen, and Resnick[4] and Kobayashi and Akiyoshi.[6] Our x-ray data gave no evidence concerning this configuration. The fourteen-membered ring in the structure contains four double bonds. The conjugated diene is transoid, with one double bond, C(2)-C(3), trans and the other, C(4)-C(5), cis. The other two double bonds, C(7)-C(8) and C(11)-C(12), are both trans. After the inclusion of the hydrogen atoms in the refinement, the C-C bond distances altered considerably, the maximum change being 0.05 Å. The four categories of angles in the ring follow a similar pattern: the C-C-C angles are larger when the central carbon atom is bonded to hydrogen(s) than when it is bonded to carbon(s). The average bond distance for the C-H bonds is 1.01Å (maximum deviation 0.07 Å) for the nonmethyl hydrogen atoms and 0.98 (maximum deviation 0.18 Å) for the methyl hydrogen atoms. These values are somewhat shorter than the standard C-H bond lengths, as is typical for x-ray diffraction work. The consistency of the C-H bond distances for the nonmethyl hydrogen atoms agrees well with the standard deviations of the bonds (≈0.05 Å) calculated from the least-squares refinement. All angles C-C-H and H-C-H for the internal ring atoms fall within the range 102 to 124 deg. Figure G.23-2 shows the a projection of cembrene and the mode of packing in the unit cell.

Hydroxylated derivatives of cembrene have been found in tobacco leaves and cigaret smoke.[10-14] Most of these various compounds have been related to 12-isopropyl-1, 5, 9-trimethyl-4, 8, 13-cyclotetradecatriene-1, 3-diol. NMR and degradation studies,[10, 14] have shown that all three double bonds in the diol are probably trans. This structure determination of cembrene has confirmed the close similarity between these two compounds, for in cembrene, the same double bonds are also trans. Such a configuration for both compounds is compatible with the proposed biosyntheses from geranylgeraniol.[3, 11, 14]

Footnote and References

†Condensation of article submitted to Acta Crystallographica.

1. N. T. Mirov, U. S. Dept. Agr. Tech. Bull. No. 1239 (1961).
2. S. Akiyoshi, Osaka Kogyo Gijutsu Shikensho Hokoku (Rept. Osaka Ind. Res. Inst.) 17, No. 10 (1937).
3. W. G. Dauben, W. E. Thiessen, and P. R. Resnick, J. Am. Chem. Soc. 84, 201 (1962).
4. W. G. Dauben, W. E. Thiessen, and P. R. Resnick, J. Org. Chem. 30, 1693 (1965).
5. H. Kobayashi and S. Akiyoshi, Bull. Chem. Soc. Japan 35, 1044 (1962).
6. H. Kobayashi and S. Akiyoshi, Bull. Chem. Soc. Japan 36, 823 (1963).
7. J. A. Ibers, Acta Cryst. 14, 1001 (1961).
8. J. Karle and H. Hauptmann, Acta Cryst. 9, 635 (1956).
9. J. Karle and I. L. Karle, Acta Cryst. 21, 849 (1966).
10. D. L. Roberts and R. L. Rowland, J. Org. Chem. 27, 1797 (1962).
11. R. L. Rowland and D. L. Roberts, J. Org. Chem. 28, 1165 (1963).
12. R. L. Rowland, A. Rodgman, J. N. Schmacher, D. L. Roberts, L. C. Cook, and W. Waller, J. Org. Chem. 29, 16 (1964).
13. G. W. Kinzer, T. F. Page, and R. R. Johnson, J. Org. Chem. 31, 1797 (1966).
14. J. L. Courtney and S. Macdonald, Tetrahedron Letters 459 (1967).

Table G. 23-I. Final coordinates ($\times 10^4$) and thermal parameters ($\times 10^2$) for the carbon atoms in cembrene.[a]

Atom	x	y	z	B_{11}	B_{22}	B_{33}	B_{12}	B_{13}	B_{23}
C(1)	1958(6)	4701(2)	8296(2)	461(18)	351(13)	350(14)	37(15)	01(13)	-33(12)
C(2)	0792(6)	4548(2)	7371(3)	423(18)	367(14)	383(15)	71(14)	09(14)	-29(12)
C(3)	1356(6)	4100(2)	6765(3)	443(17)	359(14)	325(13)	48(14)	-00(14)	-02(12)
C(4)	0186(7)	3924(2)	5876(3)	557(20)	415(16)	327(14)	-09(16)	-29(15)	46(13)
C(5)	0893(9)	3445(2)	5330(3)	719(28)	512(20)	327(15)	-40(20)	-59(17)	-11(15)
C(6)	2746(9)	3034(2)	5519(3)	718(27)	512(19)	385(16)	54(22)	70(19)	-105(15)
C(7)	2452(8)	2620(2)	6396(3)	535(21)	363(16)	472(17)	55(17)	10(17)	-113(14)
C(8)	3808(7)	2531(2)	7121(3)	431(18)	376(14)	535(19)	79(15)	15(16)	-97(14)
C(9)	3149(10)	2130(2)	7972(3)	715(29)	327(15)	590(21)	112(19)	-77(21)	03(15)
C(10)	3044(10)	2501(2)	8929(3)	696(28)	489(20)	461(19)	69(21)	-67(20)	65(15)
C(11)	1441(8)	3018(2)	8891(3)	533(21)	458(18)	383(16)	44(17)	-13(17)	73(13)
C(12)	1347(8)	3504(2)	9466(3)	661(23)	439(17)	349(14)	-27(18)	81(16)	58(13)
C(13)	-0366(8)	3983(2)	9361(4)	562(23)	507(20)	505(20)	18(18)	207(20)	01(17)
C(14)	0459(9)	4646(2)	9173(3)	718(28)	460(18)	395(18)	52(21)	133(20)	-40(16)
C(15)	3041(8)	5351(2)	8264(3)	606(23)	370(16)	515(19)	-33(17)	-104(19)	-21(15)
C(16)	1505(12)	5884(2)	8076(4)	893(40)	366(18)	693(29)	91(23)	109(30)	03(19)
C(17)	4877(11)	5349(3)	7527(6)	570(25)	586(26)	995(39)	-57(24)	100(28)	162(28)
C(18)	-1733(10)	4296(3)	5601(4)	738(32)	598(25)	516(22)	36(23)	-200(25)	16(20)
C(19)	5943(10)	2826(3)	7187(5)	499(27)	912(37)	757(34)	39(26)	-62(26)	40(31)
C(20)	2920(17)	3600(3)	10281(4)	957(48)	790(33)	457(23)	76(36)	-142(29)	-81(23)

a. Standard deviations estimated by least squares for the least significant digit are given in parentheses.

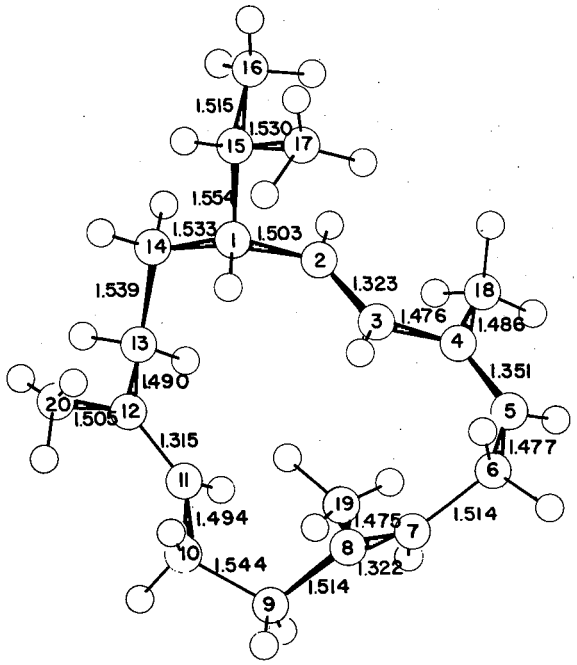

Fig. G. 23-1. Bond distances in cembrene.

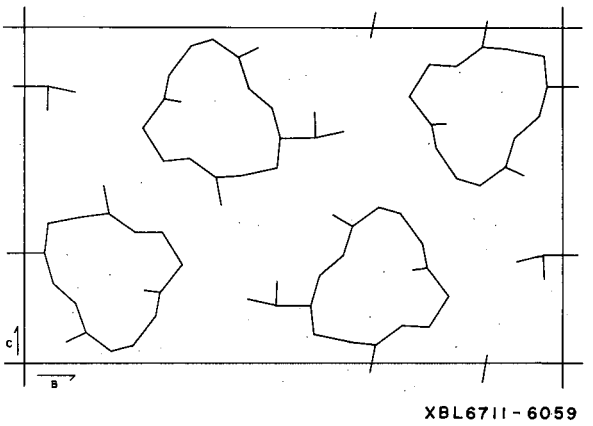

Fig. G. 23-2. The a projection of cembrene.

24. CRYSTAL AND MOLECULAR STRUCTURE OF 1-BROMOTRIPTYCENE, $Br\text{-}C_{20}H_{13}$ †

K. J. Palmer* and David H. Templeton

Electric dipole moments of isomeric triptycene derivatives[1] and the infrared spectrum of triptycene[2,3] support the conclusion that triptycene is a highly symmetrical and rigid molecule. The ultraviolet spectra of triptycene and a number of its derivatives led Bartlett and Lewis[4] to conclude that inter-ring resonance occurs. On the other hand, Wilcox[5,6] concluded on the basis of quantum mechanical calculations that interaction between benzene rings is negligible. The investigation presented here was undertaken to determine the length of the bridge bonds and thereby evaluate their bond character. In addition, 1-bromotriptycene, shown in Fig. G. 24-1, cannot form without considerable deviation from normal values of one or more of the angles made by the bridge bonds. This study shows which bonds are strained and by what amount.

The 1-bromotriptycene used in this investigation was obtained from Prof. A. Streitwieser, who had received it from Prof. L. Friedman. It was synthesized by the method of Friedman and Logullo.[7] Dr. E. Ziegler checked the purity of this material by passing it through a gas-liquid chromatographic column. He found only one peak. Crystals of 1-bromotriptycene suitable for x-ray analysis were prepared by sublimation at approximately 250°. The crystals were rhombohedral in shape. In polarized light the extinction is symmetrical and the birefringence is high; c-axis views showed a uniaxial interference figure of positive character.

Multiple-level Weissenberg and precession photographs were taken. The precession photographs are compatible with a Laue symmetry of $\bar{3}$. Reflections were indexed on a hexagonal lattice and were found to obey the rule $(-h + k + l) = 3n$. The primitive lattice is therefore rhombohedral, and the orientation of the rhombohedral lattice in the hexagonal lattice is obverse. The observed

density of 1.52 g cm^{-3} requires six molecules per hexagonal cell or two per rhombohedral cell. The most probable space group, therefore, is $\underline{R}\bar{3}$, and the asymmetric unit is $C_6H_4\text{-}(C_2HBr)_{1/3}$. Two-theta scans at 1 deg takeoff angle led to the following hexagonal unit cell: $\underline{a}$ = 11.852(5) Å, $\underline{c}$ = 17.574(9) Å, V = 2,138.0 $Å^3$, Z = 6, ρ_{calc} = 1.54 g cm^{-3}, ρ_{obs} = 1.52 g cm^{-3}. Estimated standard deviations ($\times 10^3$) are given in parenthesis. Intensity data were collected by counting for 10 sec with a stationary crystal and stationary counter at a takeoff angle of 4 deg. A total of 1050 independent reflections was measured (maximum 2θ = 150 deg), 35 of which were assigned zero intensity. Cu Kα x rays (λ = 1.5418 Å) filtered with Ni foil were used. The crystal used for intensity measurements had dimensions of 0.088 × 0.088 mm × 0.118 mm. The absorption factor for this crystal is 35.0 cm^{-1}, and μR is about 0.21 or less, making the absorption quite low. No corrections were applied to the data for either absorption or extinction.

The three-dimensional Patterson function showed many well-resolved peaks. Since the 1-bromotriptycene molecule has threefold symmetry and there are six molecules in the hexagonal cell, the bromine and the two aliphatic carbon atoms were assumed to occupy the special positions $\underline{c}$ with parameters (0, 0, ± z), (2/3, 1/3, 1/3 ± z), and (1/3, 2/3, 2/3 ± z). A straightforward interpretation of the Patterson function led to the z coordinates of the bromine atom and the carbon atom bonded to it. A three-dimensional electron density map was then calculated by use of signs determined by the carbon and bromine atoms. The resulting map permitted evaluation of the parameters of the remaining seven carbon atoms in the asymmetric unit. The positions of the five hydrogen atoms were calculated.

Fourier calculations of the electron density showed a peak at 0, 0, 0.46 about half as high as a carbon atom. Because of space limitations this position is impossible for any plausible chemical impurity that we have been able to invent. Attempts to identify an error in the data which would produce the peak also failed. We suggest that this peak is the result of disorder of some kind, but we have failed to find a satisfactory model of the details of the disorder. Least-squares calculations with one-tenth of a bromine atom or with a carbon atom at that position improved the agreement slightly and at the same time shifted other atoms by small amounts. The differences in coordinate found in these refinements suggest that standard deviations of positions should be stated as about 0.02 Å, rather than the values given in Table G. 24-I, to include the uncertainty introduced by our ignorance of the nature of the disorder.

The positional and thermal parameters and their calculated standard deviations are listed in Tables G. 24-I and G. 24-II respectively for all atoms except hydrogen. These parameters were obtained by using all data, not refining the positional parameters of the hydrogens, and holding the temperature parameter of the hydrogens equal, but allowing it to be refined. The R value of this refinement was 0.123.

The structure consists of three nonpolar molecular doublets arranged on the three threefold inversion axes of the hexagonal cell. The two molecules of each doublet are related by a center of symmetry. The orientation of the benzene rings is shown schematically in Fig. G. 24-2a. The heavy lines in Fig. G. 24-2b represent the benzene rings of one molecule and the dashed lines the benzene rings of the molecule related to it by the center of symmetry. The solid circle represents bromine.

The interatomic distances and bond angles are given in Tables G. 24-III and G. 24-IV, respectively. It is interesting to compare the value of the bond angles at C(1) and C(2) because these angles cannot all have their normal value in triptycene. The angles about C(1) are within 2 deg of the tetrahedral value whereas the angles at C(2) are: C(1)-C(2)-C(7) = 110.7 deg; C(1)-C(2)-C(3) = 128.5 deg; and C(3)-C(2)-C(7) = 120.7 deg. The two angles external to the benzene ring are distorted approximately 9 deg from the usual value of 120 deg which can be interpreted as evidence that these bond angles are more easily distorted than are the sp^3 tetrahedral bonds at C(1).

The variation in the observed bond angles and distances in the benzene ring may be due to the strain caused by the distortion of the C(1)-C(2)-C(3) bond angle, but is more likely a result of the molecular disorder mentioned above.

The C-Br bond distance (1.97 Å) is in excellent agreement with that determined by Robertson and Sheldrick[8] in α-methyl D-galactoside 6-bromohydrin of 1.974 Å. In both cases bromine is bonded to an aliphatic carbon atom. The C(1)-C(2) and C(7)-C(20) distances of 1.53 and 1.51 Å, respectively, are in good agreement with the expected value of 1.515 Å for an sp^2-sp^3 carbon bond.[9] It is concluded, therefore, that there is no interaction between benzene rings in 1-bromotriptycene. Since the bond angles and interatomic distances are the same for both bridges (within the accuracy of this investigation), it appears that the bromine atom has a negligible effect

on adjacent bond angles and bond distances.

We thank Professor A. Streitwieser for suggesting this problem, Dr. E. Ziegler for checking the purity, Dr. F. T. Jones for the determination of the optical properties, Mrs. Kay S. Lee for taking the Weissenberg photographs, Professor A. Pabst for the precession photographs, and Dr. A. Zalkin for many helpful suggestions and the use of his computer programs.

Footnotes and References

†Condensed from article submitted to Acta Crystallographica.

*Western Regional Research Laboratory, Agricultural Research Service, U. S. Department of Agriculture, Albany, California.

1. F. Ogura, K. Toshiyasu, K. Kimura, R. Fujishiro, and M. Nakagawa, Bull. Chem. Soc., Japan, 37, 757 (1964).
2. P. D. Bartlett and F. D. Greene, J. Amer. Chem. Soc. 76, 1088 (1954).
3. W. Theilacker, K. Albrecht, and H. Uffmann, Chem. Ber. 98, 428 (1965).
4. P. D. Bartlett and E. S. Lewis, J. Amer. Chem. Soc. 72, 1005 (1950).
5. C. F. Wilcox, Jr., J. Chem. Phys. 33, 1874 (1960).
6. C. F. Wilcox, Jr. and A. C. Craig, J. Org. Chem. 26, 2491 (1961).
7. L. Friedman and S. M. Logullo, J. Amer. Chem. Soc. 85, 1549 (1963).
8. J. H. Robertson and B. Scheldrick, Acta Cryst. 19, 820 (1965).
9. M. J. S. Dewar and H. N. Schmeising, Tetrahedron 11, 96 (1960).

Table G. 24-I. Final positional parameters and standard deviations[a] in parentheses $\times 10^4$.

Atom	x	y	z
Br	0.0	0.0	0.1052(1)
C(1)	0.0	0.0	0.2173(7)
C(20)	0.0	0.0	0.3595(8)
C(2)	0.1212(7)	0.1184(7)	0.2490(5)
C(3)	0.2241(8)	0.2153(9)	0.2099(6)
C(4)	0.3275(9)	0.3147(8)	0.2525(7)
C(5)	0.3249(8)	0.3146(8)	0.3291(6)
C(6)	0.2207(8)	0.2154(9)	0.3679(6)
C(7)	0.1198(7)	0.1170(7)	0.3282(5)
H(20)[b]	0.0	0.0	0.420
H(3)[b]	0.225	0.215	0.150
H(4)[b]	0.405	0.395	0.220
H(5)[b]	0.400	0.390	0.360
H(6)[b]	0.225	0.215	0.430

a. The standard deviations listed are those estimated by least squares. Because of disorder, as described in the text, the uncertainty is judged to be about twice as great as indicated by these values.
b. These parameters are not refined.

Table G. 24-II. Anisotropic thermal parameters[a] and standard deviations in parentheses $\times 10^2$.

Atom	B11	B22	B33	B12	B13	B23
Br	4.78(7)	B11	3.73(9)	B11/2	0.0	0.0
C(1)	1.72(31)	B11	2.38(53)	B11/2	0.0	0.0
C(20)	1.58(30)	B11	2.94(58)	B11/2	0.0	0.0
C(2)	1.31(27)	1.46(29)	3.78(38)	0.74(23)	-0.16(25)	-0.12(26)
C(3)	2.32(35)	2.51(36)	4.48(46)	1.33(30)	-0.08(32)	-0.53(32)
C(4)	2.31(36)	1.63(32)	6.80(61)	1.16(29)	0.36(37)	-0.39(35)
C(5)	1.95(34)	2.09(34)	4.97(47)	1.07(29)	0.42(32)	0.91(32)
C(6)	1.62(22)	2.97(25)	4.51(33)	1.38(20)	0.17(21)	0.88(23)
C(7)	1.17(27)	1.48(29)	3.53(36)	0.46(23)	-0.15(25)	0.18(25)

a. Units are in $Å^2$. The temperature factors are in the form exp- $\Sigma\beta_{ij}h_ih_j$, so that $\beta_{ij} = B_{ij}b_ib_j/4$, where b_ib_j are reciprocal cell length.

Table G. 24-III. Interatomic distances (in Å) with standard deviations ($\times 10^2$) for 1-bromotriptycene.

Br - C(1)	1.97(20)
C(1) - C(2)	1.53(1)
C(2) - C(3)	1.37(2)
C(2) - C(7)	1.39(2)
C(3) - C(4)	1.42(2)
C(4) - C(5)	1.35(2)
C(5) - C(6)	1.39(2)
C(6) - C(7)	1.37(2)
C(7) - C(20)	1.51(2)

Table G. 24-IV. Interatomic bond angles (deg) with standard deviations ($\times 10^1$) for 1-bromotriptycene.

Br - C(1) - C(2)	111.4(6)
H(20) - C(20) - C(7)	111.4(6)
C(1) - C(2) - C(3)	128.5(9)
C(20) - C(7) - C(6)	128.0(9)
C(2) - C(1) - C(2)	107.5(6)
C(7) - C(20) - C(7)	107.4(6)
C(1) - C(2) - C(7)	110.7(8)
C(20) - C(7) - C(2)	112.2(8)
C(2) - C(3) - C(4)	118.1(9)
C(7) - C(6) - C(5)	120.0(9)
C(3) - C(4) - C(5)	121.1(9)
C(2) - C(7) - C(6)	119.9(7)
C(4) - C(5) - C(6)	120.2(8)
C(3) - C(2) - C(7)	120.7(7)
C(2) - C(3) - H(3)	120.2(8)
C(3) - C(4) - H(4)	116.7(10)
C(4) - C(5) - H(5)	120.6(8)
C(5) - C(6) - H(6)	118.1(8)

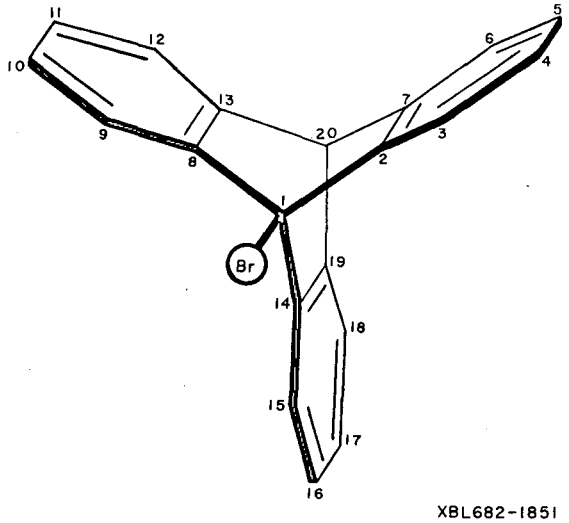

Fig. G. 24-1. 1-Bromotriptycene molecule with numbering system used in this investigation. The asymmetric unit is $(BrC_2)_{1/3}C_6$.

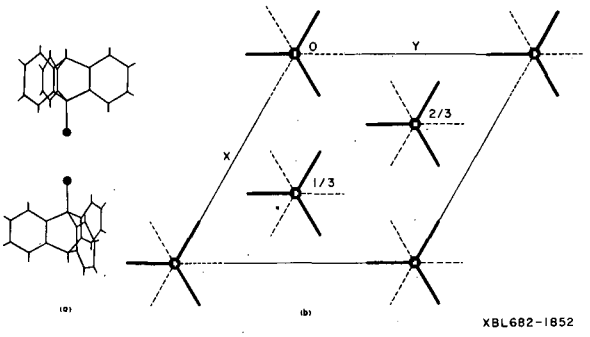

Fig. G. 24-2. (a) The stacking arrangement of two 1-bromotriptycene molecules about a center of symmetry. (b) The packing arrangement as viewed down the c axes. The numbers refer to the z coordinate of the inversion center.

25. CRYSTAL AND MOLECULAR STRUCTURE OF BIS(2,4-PENTANEDIONATO)BIS(PYRIDINE N-OXIDE)NICKEL(II), $Ni(C_5H_7O_2)_2(C_5H_5NO)_2$†*

William DeW. Horrocks, Jr.,‡ David H. Templeton, and Allan Zalkin

Introduction

Heterocyclic amine N-oxides act as oxygen donor ligands in a variety of transition metal coordination compounds.[1] Very recently structural studies have been reported for compounds which involve pyridine N-oxide acting as a bridging ligand between copper atoms;[2-4] however, no other structural work dealing with complexes of this class of ligand appears to have been done. Not long ago Kluiber and Horrocks[5,6] synthesized and studied complexes of the type bis(2,4-pentanedionato)bis(heterocyclic amine N-oxide)metal(III), hereafter referred to as $M(AA)_2(ligand)_2$, where M = Co, Ni. These complexes belong to the class of neutral donor adducts of $M(AA)_2$ of which the dihydrates,[7,8] $M(AA)_2(H_2O)_2$, and dipyridinates,[9] $M(AA)_2(C_5H_5N)_2$, are known and which involve trans octahedral coordination of the metal in the solid state. On the basis of an analysis of the dipolar (pseudocontact) contribution to the isotropic proton magnetic resonance shifts in solution in the complexes $M(AA)_2(L)_2$, M = Co, Ni, L = pyridine N-oxide or γ-picoline N-oxide, Kluiber and Horrocks[5] estimated an average M-O-N angle in the range 115 to 130 deg for the coordinated heterocyclic amine N-oxides.[10] These results were based on a trans octahedral model for coordination which was suggested by the known solid-state structures[7-9] for the compounds with L = H_2O, C_5H_5N. Clearly the detailed geometry of the coordination of heterocyclic amine N-oxides in general and the stereochemistry of $M(AA)_2(C_5H_5NO)_2$ in particular are of interest. This article reports the results of the crystal and molecular structure determination of $Ni(AA)_2(C_5H_5NO)_2$. Earlier powder x-ray work[5] showed the analogous cobalt complex to crystallize in two modifications, one of which was isomorphous and presumably isostructural with the nickel compound.

Crystals of bis(2,4-pentanedionato)bis(pyridine N-oxide)nickel(II), $Ni(C_5H_7O_2)_2(C_5H_5NO)_2$, were prepared by the method of Kluiber and Horrocks.[5] A crystal of approximate dimensions 0.16×0.15×0.08 mm was chosen for intensity measurements and was mounted on a quartz fiber with the b axis (unique) of the monoclinic cell parallel to the spindle axis of the instrument. The

unit cell dimensions are a = 14.653 ± 0.005 Å, b = 16.972 ± 0.005 Å, c = 18.344 ± 0.005 Å, and β = 100.74 ± 0.05. Systematic absences for reflections suggested space groups Cc or C2/c. The density measured by flotation in a carbontetrachloride-methylcyclohexane mixture was 1.32 ± 0.01 g/cm^3, which compares favorably with the calculated density of 1.324 for Z = 8. With eight molecules per unit cell and the appearance of 2x, 2y, 2z peaks for nickel in the Patterson function, the centric space group C2/c was chosen, and this choice was confirmed by the subsequent refinement of the structure. All atoms occupy general positions, and no molecular symmetry conditions are imposed by crystallographic symmetry. Intensity data for the final refinement reported here were recorded on an automated GE XRD-5 diffractometer. Nickel-filtered copper radiation (λ = 1.54051 for Kα_1) and a θ - 2θ scan technique were used. Of the 2319 nonequivalent reflections measured, 2113 were observed to be nonzero.

A Patterson synthesis located the nickel and several of the adjacent oxygens. A least-squares refinement and subsequent Fourier synthesis disclosed the remaining atoms. Least-squares refinement proceeded with all 29 atoms, with only the nickel atom treated anisotropically, to a conventional R value of 0.117, where $R = \Sigma \| F_o | - | F_c \| / \Sigma | F_o |$. A difference synthesis disclosed all but one of the 24 hydrogens. When the hydrogens were included and refined, R dropped to a final value of 0.097 for all reflections. The isotropic thermal parameters have the form $\exp(-B \sin^2\theta/\lambda^2)$, and the anisotropic temperature factor was

$$\exp[-0.25(B_{11}b_1^2\underline{h}^2 + B_{22}b_2^2\underline{k}^2 + B_{33}b_3^2\underline{\ell}^2 + 2B_{12}b_1b_2\underline{hk} + 2B_{13}b_1b_3\underline{h\ell} + B_{23}b_2b_3\underline{k\ell})],$$

where b_i is the $\underline{i}$th reciprocal axis. In some instances considerable displacement of the hydrogen from the position expected on the basis of the heavy-atom structure was noted. Since the hydrogen positions in the present structure are of no particular chemical interest, no further consideration is given to them here. The final heavy-atom parameters are given in Table G. 25-I.

The crystal is composed of discrete molecules, $Ni(AA)_2(C_5H_5NO)_2$, in which the six oxygens are coordinated to the nickel in a very nearly regular octahedral array. In Fig. G. 25-1 the overall molecular geometry is illustrated along with the atom labeling, and average values of chemically equivalent bond distances are given. A pair of stereoscopic representations is provided in Fig. G. 25-2 to permit the reader to appreciate the details of the geometry. The closest Ni-Ni approach is 6.882 Å, which occurs within the unit cell for molecules related by x, y, z, and 1/2-x, 1/2-y, -z. This juxtaposition is achieved by efficient molecular packing and no specific intermolecular interactions are indicated.

The two pyridine N-oxide molecules occupy positions cis to each other in the coordination sphere of the nickel. This contrasts with the solid-state structures of $M(AA)_2(H_2O)_2$ (Refs. 7, 8) and $M(AA)_2(C_5H_5N)_2$,[9] M = Co, Ni, in which the neutral monodentate ligands occupy trans positions. However, precedents for a cis coordination geometry in divalent metal acetylacetonate compounds are provided by the crystal structures of $[Ni(AA)_2]_3$,[11] $[Co(AA)_2]_4$,[12] and $[Co(AA)_2H_2O]_2$.[13] These polymeric complexes involve a cis octahedral arrangement of the terminal chelate rings. Also, complex anions of the type $[M(AA)_3^-]$ (Refs. 14-18) necessarily involve coordination of this sort. These findings, taken together, suggest that there is very little energy difference between cis and trans structures of this type. Crystal packing forces may very well determine the solid-state conformation in any particular example.

The nickel–to–ligand atom distances appear normal. The average Ni-acetylacetonate oxygen distance found here (2.02 Å) is in excellent agreement with those found for trans $Ni(AA)_2(H_2O)_2$ (2.02 Å),[8] and for the terminal chelate oxygens of $[Ni(AA)_2]_3$ (2.01 Å).[11] The average distance from the nickel to the pyridine N-oxide oxygen found here is 2.10 Å. This is slightly, but perhaps significantly, shorter than the nickel-to-water oxygen distance of 2.14 Å in $Ni(AA)_2(H_2O)_2$.[8] This indicates that of the two neutral oxygen donor ligands, pyridine N-oxide is the more strongly coordinating.

In the structure dealt with here the two independent pyridine-N-oxide molecules, P1 and P2, coordinate with Ni-O-N angles of 119.2 and 122.4 deg respectively. This angular coordination is to be expected from a consideration of the directional properties of the lone pair electrons on the oxygen, which form the coordinate bond to the nickel. The angle of approximately 120 deg suggests that a reasonable description of the bonding in pyridine N-oxide involves $\underline{sp}^2$ hybridization on the oxygen (two lone pairs and the N-O bond pair), with the third lone in a pure $\underline{p}$ orbital.

The internal distances and angles of the pyridine N-oxide ligand, in particular the average N-O bond distance of 1.33 Å, agree well with those recently reported[3] for the bridging ligand in

$[CuCl_2(C_5H_5NO)]_2$. The pyridine N-oxide oxygens P10 and P20 are respectively 0.06 and 0.07 Å out of the least-squares planes through the pyridine rings.

The bond lengths and angles of the acetylacetonate chelate rings appear normal and compare well with those in the literature. The methyl carbons fall within 0.15 Å of the least-squares planes defined by the oxygens and carbons 2, 3, and 4 of the chelate rings. As has been noted in other acetylacetonate complexes,[8] the central metal does not lie exactly in the plane of the chelate ring. In the present structure the nickel atom falls 0.17 and 0.46 Å from the least-squares planes of rings R1 and R2 respectively.

One of us (W. DeW. H., Jr.) thanks the Lawrence Radiation Laboratory for its hospitality during the course of this work. We are indebted to Mr. B. G. DeBoer, Dr. M. G. B. Drew, and Mrs. H. Ruben for considerable help and useful discussion involving all aspects of this work.

Footnotes and References

†Condensed from UCRL-17666, July 1967, to be submitted to Inorg. Chem.

*This work was supported in part by the National Science Foundation through Grant GP 6321, Princeton University.

‡Frick Chemical Laboratory, Princeton University, Princeton, New Jersey 08540.

1. See, for example, D. W. Herlocker, R. S. Drago, and V. I. Meek, Inorg. Chem. 5, 2009 (1966); M. R. Kidd, R. S. Sager, and W. H. Watson, Jr., Inorg. Chem. 6, 946 (1967); P. D. Kaplan and M. Orchin, Inorg. Chem. 6, 1096 (1967); F. E. Dirkson, E. W. Gowling, and F. F. Bentley, Inorg. Chem. 6, 1099 (1967); and references therein.
2. S. Scávnicar and B. Matković, Chem. Comm. 297 (1967).
3. R. S. Sager, R. J. Williams, and W. H. Watson, Jr., Inorg. Chem. 6, 951 (1967).
4. H. L. Schafer, J. C. Morrow, and H. M. Smith, J. Chem. Phys. 42, 504 (1965).
5. R. W. Kluiber and W. D. Horrocks, Jr., J. Am. Chem. Soc. 87, 5350 (1965).
6. R. W. Kluiber and W. D. Horrocks, Jr., J. Am. Chem. Soc. 88, 1399 (1966).
7. G. J. Bullen, Acta Cryst. 12, 703 (1959).
8. H. Montgomery and E. C. Lingafelter, Acta Cryst. 17, 1481 (1964).
9. J. T. Hashagen and J. P. Fackler, Jr., J. Am. Chem. Soc. 87, 2821 (1965).
10. A similar estimate was later, but apparently independently, made for the same systems: E. E. Zaev and U. N. Molin, J. Struct. Chem. USSR 7, 680 (1966).
11. G. J. Bullen, R. Mason, and P. Pauling, Inorg. Chem. 4, 456 (1965).
12. F. A. Cotton and R. C. Elder, Inorg. Chem. 4, 1145 (1965).
13. F. A. Cotton and R. C. Elder, Inorg. Chem. 5, 423 (1966).
14. F. P. Dwyer and A. M. Sargeson, Proc. Roy. Soc., New South Wales, 90, 29 (1956).
15. M. Peter, Phys. Rev. 116, 1432 (1959).
16. W. H. Watson, Jr., and C.-T. Liu, Inorg. Chem. 5, 1074 (1966).
17. W. D. Horrocks, Jr., R. H. Fischer, J. R. Hutchinson, and G. N. LaMar, J. Am. Chem. Soc. 88, 2436 (1966).
18. B. Granoff, Ph. D. Thesis, Princeton University, 1966.

Table G. 25-I. Final positional and thermal parameters for $Ni(AA)_2(C_5H_5NO)_2$.[a]

	x	y	z	B
Ni	0.2180(1)	0.0537(1)	-0.0443(1)	b
R1O1	0.2769(3)	-0.0262(2)	0.0311(2)	3.3(1)
R1O2	0.1454(3)	-0.0321(2)	-0.1040(2)	3.4(1)
R1C1	0.2933(11)	-0.1409(6)	0.1043(6)	5.0(2)
R1C2	0.2517(5)	-0.0987(4)	0.0340(4)	3.3(1)
R1C3	0.1900(6)	-0.1354(4)	-0.0208(4)	3.4(2)
R1C4	0.1417(5)	-0.1037(4)	-0.0856(4)	3.7(1)
R1C5	0.0766(9)	-0.1547(6)	-0.1392(7)	5.2(2)
R2O1	0.3239(4)	0.0460(2)	-0.1017(2)	4.1(1)
R2O2	0.1535(3)	-0.1340(2)	-0.1184(2)	3.3(1)
R2C1	0.4329(11)	0.0913(9)	-0.1724(8)	9.1(3)
R2C2	0.3399(7)	0.0997(5)	-0.1457(4)	5.2(2)
R2C3	0.2837(8)	0.1616(5)	-0.1725(5)	4.6(2)
R2C4	0.1946(6)	0.1740(4)	-0.1602(4)	3.7(1)
R2C5	0.1391(10)	0.2433(6)	-0.1991(5)	5.3(2)
P1O	0.1104(3)	0.0723(2)	0.0155(2)	3.2(1)
P1N	0.1198(4)	0.0447(3)	0.0848(3)	2.9(1)
P1C1	0.0668(6)	-0.0142(4)	0.0997(4)	3.4(2)
P1C2	0.0730(7)	-0.0408(4)	0.1712(4)	4.0(2)
P1C3	0.1344(7)	-0.0098(5)	0.2262(5)	4.8(2)
P1C4	0.1918(7)	0.0476(5)	0.2111(5)	5.2(2)
C1C5	0.1851(7)	0.0754(5)	0.1387(5)	4.5(2)
P2O	0.2851(4)	0.1457(2)	0.0199(2)	3.7(1)
P2N	0.3754(5)	0.1582(3)	0.0272(3)	3.1(1)
P2C1	0.4022(7)	0.2318(4)	0.0176(4)	3.7(2)
P2C2	0.4955(9)	0.2487(6)	0.0314(5)	5.2(2)
P2C3	0.5628(9)	0.1919(6)	0.0480(6)	5.6(3)
P2C4	0.5305(12)	0.1144(7)	0.0570(7)	5.5(3)
P2C5	0.4379(9)	0.0996(5)	0.0466(5)	4.4(2)

a. Standard deviations indicated in parentheses refer to the least significant digit(s). The atom labeling conforms to Fig. G. 25-1. The carbon (C), nitrogen (N), and oxygen (O) atoms are numbered serially within their respective organic moieties. R1 and R2 designate chelate rings 1 and 2, while P1 and P2 refer to pyridine N-oxide ligands 1 and 2. These group designations precede the individual atom element symbols and numbers.

b. Components of the anisotropic thermal tensor for Ni defined as in the text are: B_{11} = 5.30(10), B_{22} = 4.30(5), B_{33} = 4.62(5), B_{12} = -0.17(5), B_{13} = 1.13(5), B_{23} = 0.24(4).

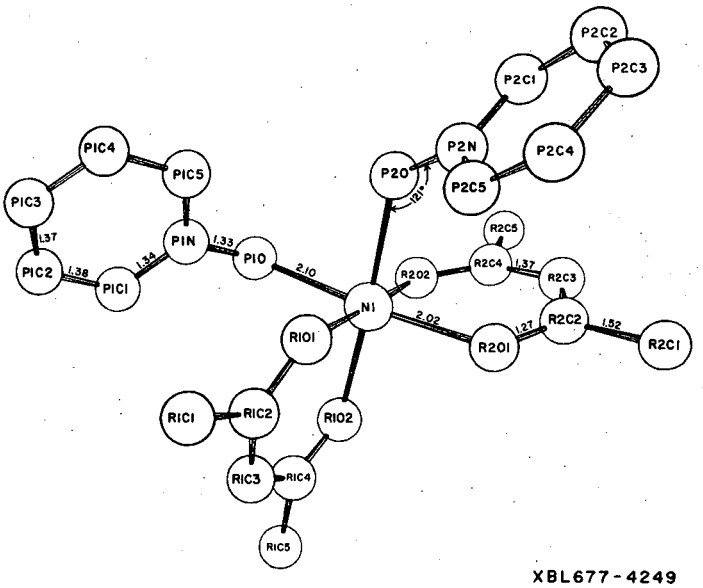

Fig. G. 25-1. Geometry of $Ni(AA)_2(C_5H_5NO)_2$ with the average values of chemically equivalent bond lengths indicated.

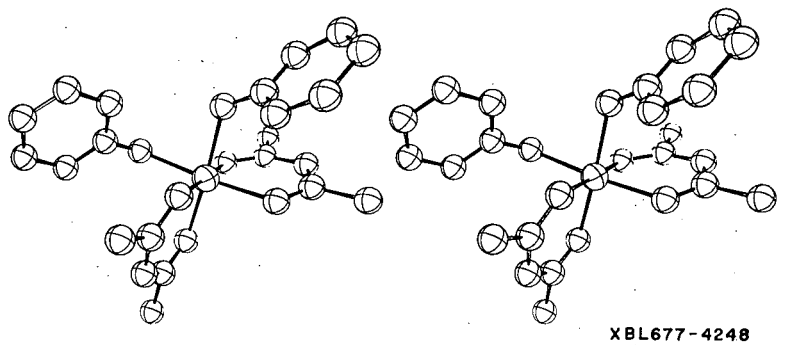

Fig. G. 25-2. Stereoscopic pair of $Ni(AA)_2(C_5H_5NO)_2$ molecules. The labeling of the atoms may be determined by a comparison with Fig. G. 25-1.

26. CRYSTAL AND MOLECULAR STRUCTURE OF SULFUR NITRIDE—BORON TRIFLUORIDE†

Michael G. B. Drew, David H. Templeton, and Allan Zalkin

In a recent study of the reaction of sulfur nitride, S_4N_4, with the boron trihalides, Wynne and Jolly[1] isolated compounds of the composition $S_4N_4 \cdot BF_3$ and $S_4N_4 \cdot BCl_3$. Several other adducts of S_4N_4 with Lewis acids have been prepared in the past,[2] and Neubauer and Weiss[3] have published a crystal structure determination, by x-ray diffraction methods, of $S_4N_4 \cdot SbCl_5$. In this report an analysis of the crystal structure of $S_4N_4 \cdot BF_3$ confirms that the boron atom is bonded to nitrogen. The molecular shape is very similar to that of the antimony chloride adduct, with the sulfur atoms nearly planar. This conformation differs from that of S_4N_4, in which the nitrogen atoms are planar.[4]

Crystals of $S_4N_4 \cdot BF_3$ were obtained from Dr. K. Wynne of this University. The diffraction data were obtained from a crystal of approximate dimensions $0.15 \times 0.4 \times 0.15$ mm mounted with b parallel to the instrument axis. The crystal was stuck to the inside of a glass capillary with the ends sealed. The stationary-crystal stationary-counter method was used to measure 1393 independent reflections ($2\theta < 50$ deg) of which 174 were recorded as zero. During the course of the experiment, no significant change in intensity was detected.

$S_4N_4 \cdot BF_3$ is monoclinic with $a = 7.114 \pm 0.005$ Å, $b = 10.418 \pm 0.007$ Å, $c = 10.754 \pm 0.008$ Å, $\beta = 95.40 \pm 0.06$ deg, $Z = 4$, $D_x = 2.11$ g cm^{-3}, $D_m = 2.0$ g cm^{-3} (by flotation[2]). Space group $P2_1/n$ (C_{2h}^5), with $hO\ell$ absent if $h + \ell = 2n + 1$, OkO absent if $k = 2n + 1$. All atoms are in general positions

$$4(e): \pm(x, y, z; \quad 1/2 - x, \quad 1/2 + y, \quad 1/2 - z).$$

The structure was solved by use of the symbolic addition procedure[5] to determine the phases. We used only the Σ_2 relation, $s\, E_h \sim s \sum_k E_k E_{h-k}$, where s means "sign of," and E is the normalized structure factor. It was found that for this data set 69 independent reflections had $|E|$ values greater than 2.0. An E map (Fourier synthesis) was computed, using the 69 reflections with signs based on this procedure. The four highest peaks in this map, near the corners of a square, were correctly assigned as the sulfur atoms, and a nitrogen and a fluorine atom were also found. A Fourier synthesis of ΔF, based on the six atoms, was calculated, and the rest of the structure of $S_4N_4 \cdot BF_3$ was immediately discernible. With individual anisotropic thermal parameters there were 109 parameters. The final R was 0.069 for 1391 reflections (or 0.072 including the two of zero weight). It was noted that the signs derived from the Σ_2 relation were all correct. The final values of the parameters are listed in Table G. 26-I.

The structure consists of an eight-membered sulfur-nitrogen ring, with a BF_3 group bonded to one of the nitrogen atoms through the boron. The B-N bond length (1.577 Å) is similar to that found in NN-dimethylaminodiborane[6] and in trimethylamine-borontrifluoride[7] (1.55 ± 0.02 Å, 1.58 Å). The configuration of the NBF_3 entity is unremarkable: the four atoms around the boron are approximately tetrahedral, and the bond distances are as expected.

The conformation adopted by the ring can be compared with those determined in two previous studies: that of S_4N_4 itself[4] and that of the $S_4N_4 \cdot SbCl_5$ adduct.[3] The crystal structure of sulfur nitride shows a molecule containing a slightly elongated tetrahedron of sulfur atoms with nitrogen atoms added out from four of the edges. The four nitrogen atoms are planar to less than 0.01 Å. Figure G. 26-1a shows a projection of this molecule onto the plane of the four nitrogen atoms; the sulfur atoms are approximately 1.0 Å above and below this plane. The average S-N bond distance in S_4N_4 is 1.616 ± 0.010 Å, and the average angles at S and N are 105 and 113 deg. The distances between sulfur atoms on the same side of the nitrogen plane are 2.58 and 2.59 Å, and the existence of $p\sigma$ bonds between these atoms has been suggested.[8,9]

In this structure, and in the $SbCl_5$ adduct, it is the sulfur atoms which form the square and the nitrogen atoms, the tetrahedron. In Fig. G. 26-1 b, c are shown the projections of these two structures upon the least-squares planes of the sulfur atoms. For clarity, the chlorine atoms in c have been omitted. The two configurations are remarkably similar. In the BF_3 adduct, the dimensions correspond closely to mirror symmetry across the ring (disregarding the fluorine atoms). The dimensions for the $SbCl_5$ adduct deviate from this mirror symmetry by as much as 0.07 Å, but this structure was not refined, and high accuracy is not claimed. We interpret the

lack of symmetry as an indication of the accuracy of the bond distances. According to this estimate of the accuracy, there is no significance to the discrepancies of distances and angles between the two substances.

In both cases the addition reaction has increased the short S-S distance across the ring from 2.58 Å to more than 3.8 Å, clearly destroying whatever bonding exists between these pairs of atoms. The distances listed in Table G.26-II reveal how nearly planar the nitrogen and sulfur atoms, respectively, are in the three structures, and how similar the two adducts are. In each adduct, the nitrogen atom (N1) which is bonded to the adduct is much more out of the plane than are the others.

The environment of N1 in this structure may be compared to that of nitrogen in $S_4N_4H_4$.[10] The S-N distances average 1.66 Å in our compound, compared to 1.67 Å in $S_4N_4H_4$, and they are significantly longer than the other bonds in the ring (1.54 to 1.59 Å). Planar trigonal bonding was suggested[10] for $S_4N_4H_4$, and we find N1 to be within 0.03 Å of the plane of its three neighbors. The bond angles S-N-S are not so similar (113 deg in our adduct, 122 deg in $S_4N_4H_4$).

The arrangement of the molecules in the lattice is shown in Fig. 26-2. The molecular packing is determined by several sulfur-fluorine contacts near the sum of the van der Waals radii, 3.2 Å, and there is no indication of any exceptional interaction between molecules.

We have made no detailed analysis of the anisotropic thermal parameters, but inspection reveals that the largest amplitudes correspond approximately to torsional motion of the fluorine atoms around the axis of the B-N bond. None of the distances listed in this paper have been corrected for thermal motion.

Footnote and References

†Condensed from Inorg. Chem. 6, 1906 (1967).

1. K. J. Wynne and W. L. Jolly, Inorg. Chem. 6, 107 (1967).
2. See citations listed in Ref. 1.
3. D. Neubauer and J. Weiss, Z. Anorg. Allgem. Chem. 303, 28 (1960).
4. B. D. Sharma and J. Donohue, Acta Cryst. 16, 891 (1963).
5. I. L. Karle and J. Karle, Acta Cryst. 16, 969 (1963).
6. K. Hedberg and A. J. Stosick, J. Am. Chem. Soc. 74, 954 (1952).
7. S. Geller and J. L. Hoard, Acta Cryst. 4, 399 (1951).
8. I. Lindqvist, J. Inorg. Nuclear Chem. 6, 159 (1958).
9. A. G. Turner and F. S. Mortimer, Inorg. Chem. 5, 906 (1966).
10. R. L. Sass and J. Donohue, Acta Cryst. 11, 497 (1958).

Table G. 26-I. Final coordinates ($\times 10^4$) and thermal parameters ($\times 10^2$) for $S_4N_4 \cdot BF_3$.[a]

Atom	x	y	z	B_{11}	B_{22}	B_{33}	B_{12}	B_{13}	B_{23}
S1	4576(2)	6733(1)	2968(2)	350(7)	281(6)	481(8)	75(5)	98(6)	-3(6)
S2	6066(3)	6640(2)	0526(2)	516(9)	446(8)	311(7)	11(7)	-67(6)	72(6)
S3	9549(2)	5453(2)	1731(2)	348(7)	426(8)	495(8)	68(6)	119(6)	35(6)
S4	7877(2)	5697(2)	4103(1)	382(7)	397(7)	299(6)	-38(6)	-68(5)	-4(5)
N1	5751(6)	5407(4)	3369(4)	278(19)	249(19)	323(20)	39(16)	34(15)	10(16)
N2	4842(7)	7097(5)	1559(5)	319(22)	337(23)	493(27)	26(18)	-50(19)	37(20)
N3	7697(8)	5611(5)	0811(5)	465(26)	419(26)	339(23)	-1(21)	99(19)	-38(20)
N4	9461(7)	5577(5)	3153(5)	280(21)	371(24)	511(27)	13(18)	-41(19)	70(21)
B1	5087(9)	3995(6)	3032(6)	315(27)	257(26)	327(28)	14(22)	68(22)	2(22)
F1	4931(7)	3327(4)	4117(4)	1005(31)	368(18)	395(18)	-60(19)	248(19)	38(15)
F2	6421(5)	3402(3)	2393(4)	456(18)	325(16)	561(20)	8(14)	180(15)	-88(14)
F3	3388(5)	4085(4)	2309(4)	366(17)	476(20)	794(26)	-17(15)	-149(17)	-135(19)

[a]Standard deviations estimated by least squares for the least significant digit are given in parentheses.

Table G. 26-II. Distances of atoms from least-squares planes, in Å.

	Sulfurs	Nitrogens
S_4N_4[ab]	1.01, -0.98, 0.98, -0.99	0.00, 0.00, 0.00, 0.00
$S_4N_4 \cdot SbCl_5$[cd]	-0.01, 0.01, -0.01, 0.01	-0.94, 0.35, -0.34, 0.21
$S_4N_4 \cdot BF_3$[d]	-0.02, 0.02, -0.02, 0.02	-0.92, 0.24, -0.48, 0.23

a. Least-squares plane calculated through the four nitrogen atoms.
b. Coordinates taken from Ref. 4.
c. Coordinates taken from Ref. 3.
d. Least-squares plane calculated through the four sulfur atoms.

FIGURE 1

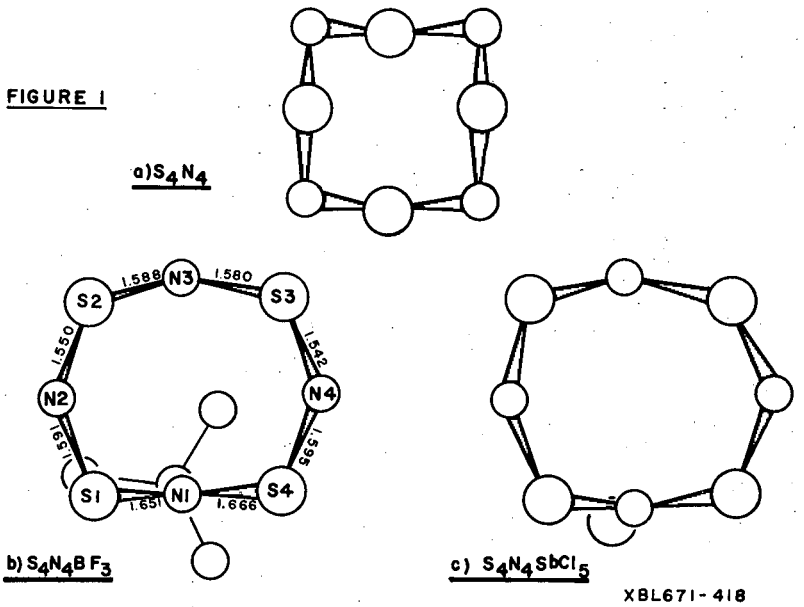

Fig. G.26-1. Projections of the three molecules S_4N_4, $S_4N_4 \cdot BF_3$, and $S_4N_4 \cdot SbCl_5$. In S_4N_4, the four nitrogen atoms are in a plane; in the other two, the sulfur atoms are in a plane.

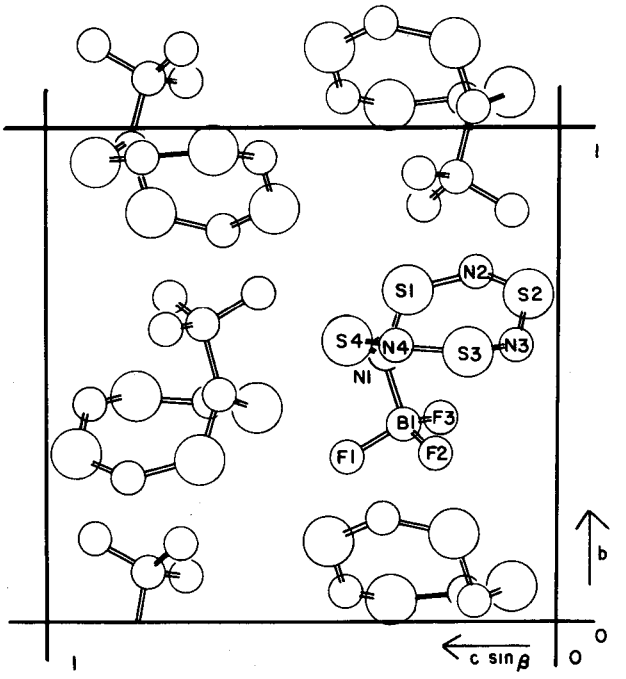

XBL 676-4127

Fig. G. 26-2. Projection of $S_4N_4 \cdot BF_3$ down [100].

27. CRYSTAL STRUCTURE OF $Cs(B_9C_2H_{11})_2Co$ †

Allan Zalkin, Ted E. Hopkins, and David H. Templeton

The salt $Cs(B_9C_2H_{11})_2$ Co was synthesized in the laboratory of Professor M. F. Hawthorne[1] at the University of California at Riverside. A crystal structure study was undertaken to confirm the proposed structure of two icosahedra joined at the cobalt apex; this we proved to be true. The synthesizers of this material had hoped they had produced a compound in which the carbon atoms were not adjacent to each other; unfortunately, we found the carbon atoms to be disordered and therefore could neither affirm nor deny this hypothesis.

A light brown parallelopiped-shaped crystal of dimensions ≈0.15×0.15×0.30 mm was selected and glued to the end of a Pyrex fiber in air. A total of 2051 independent intensities was measured, of which 144 were recoreded as zero. A stationary-crystal stationary-counter technique using a 10-sec count for every reflection was used.

Four formula units of $(B_9C_2H_{11})_2$ CoCs are in the monoclinic C-centered unit cell whose dimensions are $a = 11.698 \pm 0.005$ Å, $b = 7.381 \pm 0.004$ Å, $c = 21.207 \pm 0.006$ Å, and $\beta = 101.73 \pm 0.05$ deg. The calculated x-ray density is 1.692 g/cm^3. The density measured by flotation is 1.69 g/cm^3. The observed extinctions correspond to C2/c or Cc, and good agreement of observed and calculated structure factors was achieved in the centric space group, C2/c. The Cs and Co atoms were located by the Patterson function.

The cesium occupies the special fourfold position on the twofold axis, and the cobalt is on a center of symmetry at the origin. A difference function phased by these two heavy atoms revealed the positions of the eleven boron and carbon atoms. In attempting to locate the two carbon atoms, we used the two criteria of temperature factors and interatomic distances. No two atoms stand out as carbon atoms on these bases, but the results are consistent with the carbon atoms being distributed in the pentagon adjacent to the cobalt in a disordered manner. Various models using

different ratios of B and C in the disordered positions were tried; temperature factors were affected, but no significant changes in the distances in the icosahedral structure resulted. A difference function was calculated, and it showed the 11 hydrogen atoms among the top 17 peaks. The final least-squares, performed with all 24 atoms of the structure included, resulted in an R of 0.042. The coordinates and isotropic temperature factors for hydrogen were refined, and coordinates and with anisotropic temperature factors for all the other atoms were refined. The real and imaginary components of the anomalous dispersion correction were applied to the Cs and Co atoms. Atoms 2, 3, 5, and 6 in the icosahedron were treated as half boron and half carbon atoms. The B12 and B23 temperature factors of Cs were restrained to zero as required by the symmetry of the special position. The last shift in the parameter in each case was less than 0.001 of the estimated standard deviation of that parameter. The final set of parameters is shown in Table G.27-I. The sets of positions are

Cs in 4(e): $\pm(0, y, 1/4; 1/2, 1/2 + y, 1/4)$;

Co in 4(a): $(0,0,0; 0,0,1/2; 1/2, 1/2, 0; 1/2, 1/2, 1/2)$;

B and C in 8(f): $\pm(x, y, z; x, \bar{y}, 1/2+z; 1/2+x, 1/2+y, z; 1/2+x, 1/2-y, 1/2+z)$.

The anisotropic temperature-factor refinements were carried out primarily for the purpose of looking for hydrogen atoms. It has been our experience that it is often necessary to remove the anisotropies of the bonding atom in order to see the hydrogens in the difference Fouriers. With the exception of Cs, all the temperature factors appear to be fairly isotropic.

The structure consists of a Cs^+ cation and a $(B_9C_2H_{11})_2Co^-$ anion. The cesium ion is surrounded by ten hydrogen atoms at distances from 3.00 to 3.34 Å; the next nearest neighbors to the cesium atom are two boron atoms, at 3.67 Å.

The framework of the $(B_9C_2H_{11})_2Co^-$ group is shown in Fig. G.27-1. The structure consists of two icosahedra in a staggered configuration joined at a common apex, which is the cobalt atom. The two carbon atoms are shown in disordered positions in the pentagon of atoms adjacent to the cobalt, occupying mainly positions 2, 3, 5, and 6. The interatomic distances in the framework are shown in Fig. G.27-2. Each atom with the exception of cobalt in the framework shown in Fig. G.27-1 has bonded to it a hydrogen atom.

The above icosahedral structure is very similar to that found in $(B_9C_2H_{11})Fe(C_5H_5)$[2] and in $(B_9C_2H_{11})Re(CO)_3$,[3] where there is no disorder of the carbon atoms. Because of the disorder in $(B_9C_2H_{11})_2CoCs$, we cannot say if the carbon atoms are adjacent or not in each molecule, nor indeed if the crystal contains a single isomer or more than one isomer.

We thank Professor M. F. Hawthorne and Dr. T. D. Andrews for providing us with the interest and the crystals that made this work possible.

Footnote and References

†Condensed from Inorg. Chem. 6, 1911 (1967).

1. M. F. Hawthorne and T. D. Andrews, Chemical Commun. 19, 443 (1965).
2. A. Zalkin, T. E. Hopkins, and D. H. Templeton, J. Am. Chem. Soc. 87, 3988 (1965).
3. A. Zalkin, T. E. Hopkins, and D. H. Templeton, Inorg. Chem. 5, 1189 (1966).

Table G. 27-I. Atomic[a] and Thermal Parameters[b] in $(B_9C_2H_{11})_2$ CoCs.

Atom	x	y	z	B11	B22	B33	B12	B13	B23
Cs	0[c]	0.4060	1/4[c]	7.46	3.05	4.30	0[c]	-1.11	0[c]
Co(1)	0[c]	0[c]	0[c]	1.75	2.30	2.13	-0.17	0.35	-0.13
BC(2)[d]	0.1224	-0.1774	0.0476	2.5	3.3	2.9	0.3	0.3	0.0
BC(3)[d]	0.1415	0.0369	0.0743	2.5	3.3	3.0	-0.4	-0.1	0.0
B(4)	0.0121	0.1172	0.0904	3.0	2.7	2.2	-0.2	0.4	-0.2
BC(5)[d]	0.4146	0.4396	0.0744	2.9	2.8	2.6	-0.2	1.0	0.0
BC(6)[d]	0.4823	0.2579	0.0470	2.8	2.7	2.7	-0.3	0.5	0.2
B(7)	0.1959	-0.1381	0.1256	2.4	4.0	3.3	-0.1	-0.1	0.5
B(8)	0.1267	0.4838	0.1538	3.5	3.5	2.5	-0.8	-0.1	-0.3
B(9)	0.4810	0.4845	0.1537	3.4	3.2	2.4	-0.4	0.8	-0.2
B(10)	0.4613	0.2594	0.1260	2.8	3.3	2.5	-0.6	0.4	0.2
B(11)	0.0949	-0.3173	0.1087	3.1	3.0	3.4	0.0	0.2	0.3
B(12)	0.0962	-0.1757	0.1761	3.3	3.3	2.8	-0.2	0.0	0.2
H(2)	0.173	-0.233	0.015	2.2[e]					
H(3)	0.197	0.111	0.062	2.5					
H(4)	0.490	-0.262	0.085	1.9					
H(5)	0.319	0.456	0.061	3.0					
H(6)	0.436	0.152	0.019	2.0					
H(7)	0.281	-0.165	0.139	2.1					
H(8)	0.177	0.139	0.186	0.6					
H(9)	0.432	-0.458	0.191	0.4					
H(10)	0.397	0.170	0.142	2.6					
H(11)	0.128	-0.455	0.113	1.1					
H(12)	0.128	-0.227	0.221	0.9					

a. Estimated standard deviations on the atomic positions for Co, B or BC, and H are ±0.0005 Å, ±0.005 Å, and ±0.05 Å respectively.
b. The thermal parameters have the units A^2. The estimated standard deviations on the thermal parameters of Co or Cs, B or BC, and H are ±0.04 $Å^2$, ±0.2 $Å^2$, and ±1.4 $Å^2$ respectively.
c. Parameter fixed by the space-group symmetry.
d. Half boron and half carbon.
e. Isotropic B in the case for hydrogen.

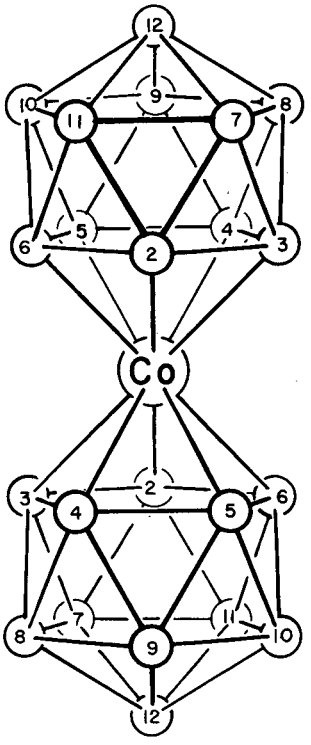

$(B_9C_2H_{11})_2Co^-$

MUB-14180

Fig. G.27-1. Framework of the $(B_9C_2H_{11})_2Co^-$ ion. Hydrogen atoms, which are on each of the atoms with the exception of cobalt, are not shown.

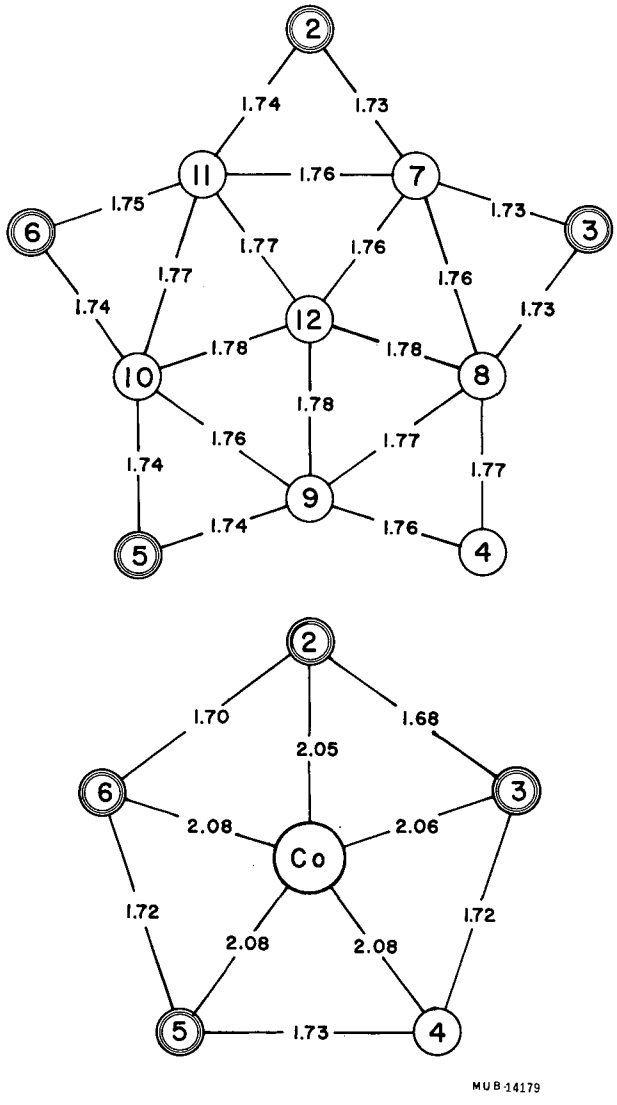

Fig. G. 27-2. Interatomic distances in the $(B_9C_2H_{11})_2Co$ icosahedra. Multiple circles indicate the disordered positions containing half boron–half carbon atoms. Single circles represent borons. The estimated standard deviations on these bond lengths are ±0.01 Å.

28. CRYSTAL STRUCTURE OF THE RUBIDIUM SALT OF AN OCTADECAHYDROEICOSABORATE(2-) PHOTOISOMER†

Barry G. DeBoer,* Allan Zalkin, and David H. Templeton

In the last few years, there has been considerable interest in the reactions of the $B_{20}H_{18}^{2-}$ ion and proposals have been made for the probable structures of the products.[1-8] The structure of the parent ion has been established[4,5] as a pair of capped-square-antiprismatic polyhedra, of 10 borons, connected by a pair of three-center bonds which join the 1-2 edge of one polyhedron to the 2' position of the other and the 1'-2' edge of the second to the 2 position of the first.[9] Recently, Hawthorne and Pilling[1] observed the isomerization of $B_{20}H_{18}^{2-}$ in acetonitrile solution when exposed to light from a mercury lamp. They predicted that the photoisomer was one of the two possible structures which result when two polyhedra, consisting of 10 borons each, are joined by a pair of B-H-B bridges, one between each pair of equatorial four-rings. This work was undertaken to determine the geometry of the photoisomerization product. The results prove that the geometry is the centrosymmetric (2/m or C_{2h}) alternative of the pair suggested by Hawthorne and Pilling.

Crystals of the rubidium salt were sent to us by Professor M. F. Hawthorne of the University of California, Riverside. Part of this material was recrystallized from water by slow evaporation. A colorless crystal about 0.11×0.06×0.05 mm in size was secured to a Pyrex glass fiber for intensity measurements. As the material appears to be radiation-sensitive, a shutter excluded the x rays from the crystal except during the actual counting time. The measurements included 1175 Laue-independent reflections, of which 240 recorded as zero. The intensities of several reflections that were measured at frequent intervals showed only small, random fluctuations. Pyroelectricity was indicated by attraction of a crystal to the side of the glass Dewar after the crystal was quickly dipped into liquid nitrogen.

Four formula units of $Rb_2B_{20}H_{18}$ are contained in the orthorhombic unit cell with dimensions $a = 12.344 \pm .007$ Å, $b = 19.014 \pm .010$ Å, $c = 7.260 \pm .005$ Å. The calculated density of 1.58 g/cm^3 agrees with the value ($1.57 \pm .01$ g/cm^3) obtained by flotation in a mixture of carbon tetrachloride and dibromoethane. The Laue symmetry and observed extinction rules correspond to both the centric Pnma and the noncentric $Pn2_1a$. The positive test for pyroelectricity and the violations of Friedel's rule indicate the noncentric $Pn2_1a$, and this choice leads to a successful structure.

The Patterson function calculated from the first data set was consistent with either one rubidium ion in the eightfold Pnma or a pair of nearly centric rubidium ions in the fourfold $Pn2_1a$. The latter was chosen because of the observed pyroelectric effect and the broadening of the Patterson peaks in the a and c directions. The zero coordinate of the y axis in the polar space group $Pn2_1a$ was defined by requiring the two rubidium ions to have equal and opposite y coordinates in this and all subsequent refinements. A Fourier synthesis phased on the rubidiums was calculated and sixteen boron atoms were found. A difference Fourier was calculated on the basis of the 2 rubidium ions and 16 borons, and the remaining 4 borons were located.

Seventeen reflections were selected and examined for anomalous dispersion effects. These data showed that the wrong alternative had been chosen for the polarity. When the structure was inverted as required, a refinement of two anisotropic rubidium ions and twenty borons, including anomalous dispersion, gave an R of 0.136 on the 1175 data. Another difference Fourier showed, for all eighteen hydrogens, peaks ranging from 0.78 to 0.46 electrons/A^3 in reasonable positions. Many attempts at refining the hydrogen positions under various restrictions produced various degrees of agreement, various unacceptable temperature factors and boron-hydrogen distances, and much frustration. The structure was finally refined with each hydrogen in a calculated position 1.2 Å from its boron (≈ 1.3 Å in the case of the two bridging hydrogens) and constrained to "ride" on its boron. All hydrogens were also required to have the same temperature factor. The final R was 0.127 on all 1175 data and 0.073 on the 935 nonzero data. The final positional and thermal parameters are presented in Table G. 28-I. Observed and calculated values of 17 selected anomalous dispersion data ($hk\ell$, $h\bar{k}\ell$) clearly establish the noncentric space group, and are strong evidence of the correctness of the structure.

The structure of the photoisomeric $B_{20}H_{18}^{2-}$ anion found in this study is shown in Fig. G.28-1. This structure is the more symmetric one of the two possibilities postulated by Hawthorne and Pilling.[1] The anion has an approximate 2/m (C_{2h}) point symmetry. A calculation of the anion's deviations from perfect 2/m symmetry gave a root-mean-square deviation of 0.07 Å (excluding B5'; see below). We feel that this is within the accuracy of the determination. Thus the non-

centric nature of the space group is a result of an unsymmetrical arrangement (Fig. G. 28-2) of symmetric pieces.

There is no significance to the handedness found for the particular sample from which the data were obtained, and we would expect another crystal to have an equal chance of having either handedness.

An examination of the boron-boron distances given in Table G. 28-II shows that B5' is apparently mislocated in a position too far from the apex and too close to the opposite equatorial ring. We do not understand how this effect arises, but did exclude B5' from the calculation of the deviations of the anion from 2/m symmetry and from the calculations of average boron-boron distances. The average of 15 apical-equatorial distances (excluding B1'-B5') is $1.68 \pm .04$ Å, and the average of 28 equatorial-equatorial distances (excluding B5'-B8', B5'-B9', and the interbridging-boron distances) is $1.82 \pm .05$ Å. The shortened interbridging-boron distances average $1.685 \pm .05$ Å and the B-B distances across the B-H-B bridges average $2.04 \pm .09$ Å. The errors quoted are root-mean-square deviations. The increase in calculated bond distances due to thermal motion is estimated to be ≈ 0.02 Å, or about half a standard deviation. These averages may be compared with those found[10] for the cuprous salt of $B_{10}H_{10}^{2-}$, which are $1.73 \pm .02$ Å for apical-equatorial distances, $1.86 \pm .03$ Å for distances within the equatorial rings, and $1.815 \pm .015$ Å for distances between equatorial rings.

The two rubidium ions are nearly centrically located, as can be seen from the table of atomic coordinates. The distance between one rubidium ion and the invert ($\bar{1}$) of the other's position is $0.062 \pm .008$ Å. The rubidiums' nearest neighbors are hydrogens, none closer than 2.6 Å. There are no borons nearer than 3.3 Å.

The $B_{20}H_{18}^{2-}$ ion described above is not the only one that might be constructed by joining two B_{10} polyhedra with two B-H-B bridges involving adjacent borons in each B_{10} unit. There are thirteen isomers which may be so constructed, five of which are symmetric and the remaining eight of which form four enantiomorphic pairs. Other isomers involving bridging to nonadjacent atoms were not considered because of the drastic crowding of the pair of B-H groups that lie between any such nonadjacent pair. Hawthorne and Pilling mention[1] "the formation of unidentified metastable intermediates" in the thermal reversion of the photoisomer studied here to the parent ion. Thus it may be that some or all of the isomers also exist.

We thank Professor M. F. Hawthorne of the University of California, Riverside, for helpful discussions and for providing the crystals which made this work possible.

Footnotes and References

†Condensed from UCRL-17125, Sept. 1967.

*National Science Foundation Graduate Fellow.

1. M. F. Hawthorne and R. L. Pilling, J. Am. Chem. Soc. 88, 3873 (1966).
2. M. F. Hawthorne, R. L. Pilling, and P. M. Garrett, ibid. 87, 4740 (1965).
3. M. F. Hawthorne, R. L. Pilling, and P. F. Stokely, ibid. 87, 1893 (1965).
4. R. L. Pilling, M. F. Hawthorne, and E. A. Pier, ibid. 86, 3568 (1964).
5. B. L. Chamberland and E. L. Muetterties, Inorg. Chem. 3, 1450 (1964).
6. M. F. Hawthorne, R. L. Pilling, P. F. Stokely, and P. M. Garrett, J. Am. Chem. Soc. 85, 3704 (1963).
7. A. R. Pitochelli, W. N. Lipscomb, and M. F. Hawthorne, ibid. 84, 3026 (1962).
8. A. Kaczmarczyk, R. Dobrott, and W. N. Lipscomb, Proc. Natl. Acad. Sci. U. S. 48, 729 (1962).
9. Numbering according to: R. Adams, Inorg. Chem. 2, 1087 (1963); see Fig. G. 28-1.
10. R. Dobrott and W. N. Lipscomb, J. Chem. Phys. 37, 1779 (1962).

Table G. 28-I. Final positional and thermal parameters in $Rb_2B_{20}H_{18}$.

Atom	x	y	z	B[a]
Rb(1)	-0.3714(2)[b]	-0.0801(1)	0.3225(4)	(c)
Rb(2)	0.3688(2)	0.0801(1)	-0.3299(4)	(c)
B(1)	0.039(2)	0.176(1)	0.566(4)	4.4(6)
B(2)	0.052(1)	0.219(1)	0.369(3)	1.1(4)
B(3)	0.158(2)	0.167(1)	0.457(3)	2.7(5)
B(4)	0.069(2)	0.092(1)	0.499(3)	3.0(5)
B(5)	-0.044(1)	0.146(1)	0.407(2)	0.8(3)
B(6)	0.140(2)	0.181(1)	0.218(3)	1.8(4)
B(7)	0.162(2)	0.091(1)	0.315(4)	3.2(5)
B(8)	0.022(2)	0.075(2)	0.275(4)	4.8(7)
B(9)	0.000(2)	0.160(1)	0.174(3)	2.3(4)
B(10)	0.096(2)	0.111(1)	0.110(4)	3.0(5)
B(1')	0.138(2)	0.389(1)	0.400(3)	2.9(4)
B(2')	0 095(2)	0.316(1)	0.293(3)	2.8(5)
B(3')	0.077(2)	0.405(1)	0.195(3)	2.3(5)
B(4')	0.229(1)	0.421(1)	0.239(2)	0.9(4)
B(5')	0.241(2)	0.329(1)	0.312(3)	2.4(4)
B(6')	0.081(2)	0.330(1)	0.048(3)	2.8(5)
B(7')	0.172(2)	0.403(1)	0.005(4)	3.1(5)
B(8')	0.287(2)	0.350(1)	0.104(3)	3.1(5)
B(9')	0.188(2)	0.284(1)	0.153(3)	4.0(5)
B(10')	0.204(2)	0.318(1)	-0.062(3)	3.2(5)

a. The units are $Å^2$.
b. The number in parentheses is the standard deviation in the least significant digit as derived from the least-squares matrix.
c. The anisotropic temperature factors for Rb(1) are: $\underline{B}_{11}$, 4.1(2); $\underline{B}_{22}$, 2.5(2); $\underline{B}_{33}$, 5.6(2); $\underline{B}_{12}$, 0.7(1); $\underline{B}_{13}$, 1.4(1); $\underline{B}_{23}$, 0.3(1); and for Rb(2): $\underline{B}_{11}$, 4.3(2); $\underline{B}_{22}$, 3.1(2); $\underline{B}_{33}$, 3.8(2); $\underline{B}_{12}$, -0.7(1); $\underline{B}_{13}$, -1.1(1); $\underline{B}_{23}$, 1.1(1), where the units are $Å^2$.

Table G. 28-II. Distances[a] (in Å) in $Rb_2B_{20}H_{18}$.

Apex-ring	Distance	Intra-ring	Distance	Inter-ring	Distance
B(1) - B(2)	1.66(3)	B(2) - B(3)	1.77(3)	B(2) - B(6)[c]	1.72(3)
- B(3)	1.67(3)	B(3) - B(4)	1.82(3)	B(6) - B(3)	1.78(3)
- B(4)	1.70(3)	B(4) - B(5)	1.87(3)	B(3) - B(7)	1.77(3)
- B(5)	1.64(3)	B(5) - B(2)	1.85(3)	B(7) - B(4)	1.76(3)
B(10) - B(6)	1.64(3)	B(6) - B(7)	1.86(3)	B(4) - B(8)	1.76(4)
- B(7)	1.73(4)	B(7) - B(8)	1.78(3)	B(8) - B(5)	1.85(4)
- B(8)	1.65(4)	B(8) - B(9)	1.80(4)	B(5) - B(9)	1.80(3)
- B(9)	1.58(3)	B(9) - B(6)	1.80(3)	B(9) - B(2)	1.91(3)
B(1') - B(2')	1.68(3)	B(2')- B(3')	1.86(3)	B(2')- B(6')	1.80(3)
- B(3')	1.70(3)	B(3')- B(4')	1.93(3)	B(6')- B(3')	1.79(3)
- B(4')	1.73(3)	B(4')- B(5')	1.83(3)	B(3')- B(7')	1.82(3)
- B(5')[b]	1.82(3)	B(5')- B(2')	1.83(3)	B(7')- B(4')	1.88(3)
B(10')- B(6')	1.73(3)	B(6')- B(7')	1.82(3)	B(4')- B(8')	1.82(3)
- B(7')	1.73(3)	B(7')- B(8')	1.88(3)	B(8')- B(5')[b]	1.66(3)
- B(8')	1.70(3)	B(8')- B(9')	1.79(3)	B(5')- B(9')[b]	1.58(3)
- B(9')	1.70(4)	B(9')- B(6')	1.76(3)	B(9')- B(2')[c]	1.65(3)

across bridges	
B(2) - B(2')	1.98(3)
B(6) - B(9')	2.10(3)

a. These distances are not corrected for thermal motion. The terminal digits in parentheses are the standard deviations as estimated from the least-squares matrix in units of .01 Å. However, we feel that the root-mean-square deviations from the averages given in the text of ≈ .05 Å are a better measure of the accuracy of these distances.
b. Evidence that B(5') is displaced from its "true" position.
c. Pairs of borons in the same B_{10} unit which are involved in hydrogen bridges.

Fig. G. 28-1. $B_{20}H_{18}^{2-}$ photoisomer (terminal hydrogens omitted for clarity).

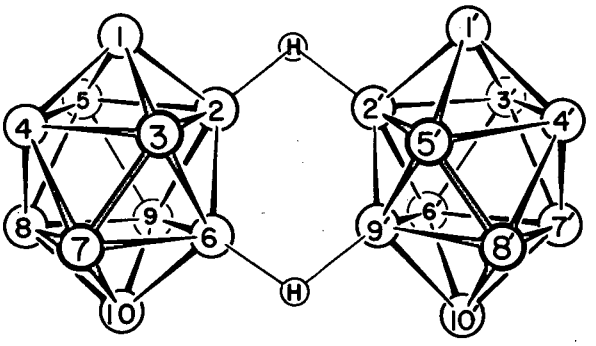

XBL 678-4463

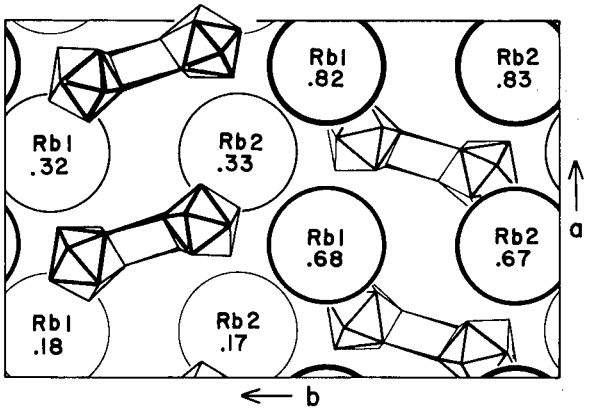

XBL678-4462

Fig. G. 28-2. One unit cell of $Rb_2B_{20}H_{18}$ seen down c axis (hydrogens omitted). Numbers on Rb ions are z coordinates as decimal fractions of c; the centers of the B_{20} units are approximately at z = 1/4 and z = 3/4.

29. AMPEROMETRIC TITRATION OF PALLADIUM(II) BY OXIDATION WITH HYPOCHLORITE†

Ray G. Clem and E. H. Huffman

Although the principal oxidation states of palladium are 2+ and 4+, there has apparently been no analytical procedure reported for the oxidimetric determination of palladium(II). That such a method is lacking is probably because no medium has been found in which there is a favorable difference in the oxidation potentials of palladium and an oxidant. For example, in a chloride medium the potentials for the Pd(IV)/Pd(II) and Ce(IV)/Ce(III) couples are about the same,[1,2] and permanganate cannot be used because it readily oxidizes chloride. The alkali metal and ammonium salts of hexachloropalladium(IV) react with hot water to generate chlorine, and with aqueous ammonia to liberate nitrogen.[3] These facts would not lead one to expect oxidimetry to be a fruitful method for determining palladium(II) unless the oxidation potential of the palladium couple could be lowered considerably.

A method has been found which utilizes, for the first time, the oxidation of palladium(II) to palladium(IV) with hypochlorite. The titration has been made feasible through the stabilizing influence of a 0.5 M chloride—0.05 M azide supporting electrolyte at pH 2 to 3 on the palladium(IV) species. The titration end point is detected with a rotated platinum electrode at 0.5 V versus a saturated calomel electrode. The method is most useful in the range (0.5 to 2.1 mg Pd; 0.01 M hypochlorite) slightly above that covered by spectrophotometry and below that conveniently amenable to gravimetry, with a precision of about 0.5%. Formal potential measurements of the Pd(IV)/Pd(II) couple in the recommended electrolyte gave values from 0.64 to 0.53 V on changing the pH from 2 to 3, with an attendant tenfold increase in azide ion concentration; the standard potential in a chloride medium is 1.288 V.[1]

Figure G.29-1 shows polarographic scans of the supporting electrolyte, supporting electrolyte plus palladium(II), and supporting electrolyte plus hypochlorite, and Fig. G.29-2 shows titration curves for 0.525 mg of palladium at different pH values. Deviations from the expected ratio of 2:1 hypochlorite to palladium were found while developing the procedure, but these deviations are of no consequence when the titrant is standardized against palladium. In addition to pH, the following variables were studied: chloride concentration, azide concentration, temperature, time of titration, photoreduction of palladium(IV), and concentration of palladium.

Table G.29-I shows the recovery of 0.525 mg of palladium in the presence of large amounts of diverse ions, and Fig. G.29-3 (XBL678-3895) shows the cation interferences giving waves at potentials greater than 0.0 V vs SCE. By polarographic comparison (Figs. G.29-1 and G.29-3), iridium(IV) is as strong an oxidizing agent as is hypochlorite. The potential selected is sufficiently positive that most of the possible interfering ions do not give waves, yet sufficiently negative that excess hypochlorite is sensitively detected.

Footnote and References

†Presented at 11th Conference on Analytical Chemistry in Nuclear Technology, Gatlinburg, Tennessee, October 10-12, 1967; Anal. Chem., in press.

1. W. M. Latimer, Oxidation Potentials, 2nd ed. (Prentice-Hall, Englewood Cliffs, N. J., 1952), p. 203.
2. G. F. Smith, Cerate Oxidimetry (G. Frederick Smith Chemical Co., Columbus, Ohio, 1942), p. 22.
3. A. F. Cotton and G. Wilkinson, Advanced Inorganic Chemistry, 2nd ed. (Interscience Publishers, New York, 1966), p. 1035.

Table G.29-I. Tolerance for foreign ions (0.525 mg Pd in each).

Foreign ion	Amount added (mg)	Pd found (mg) (average duplicates)	Error (%)
Cr^{3+}	100	0.512	-2.5
Fe^{3+}	100	0.527	+0.4
Co^{2+}	111	0.515	-1.9
Ni^{2+}	116	0.526	+0.2
Cu^{2+}	103	0.510	-2.9
Zn^{2+}	108	0.530	+1.0
Rh^{3+}	30	0.532	+1.3
Ir^{4+}	2	0	-100
Pt^{4+}	118	0.526	+0.2
Au^{3+}	20	0.526	+0.2
Pb^{2+}	108	0.511	-2.7
Na_2SO_4	1000	0.521	-0.8
$NaNO_3$	1000	0.518	-1.5

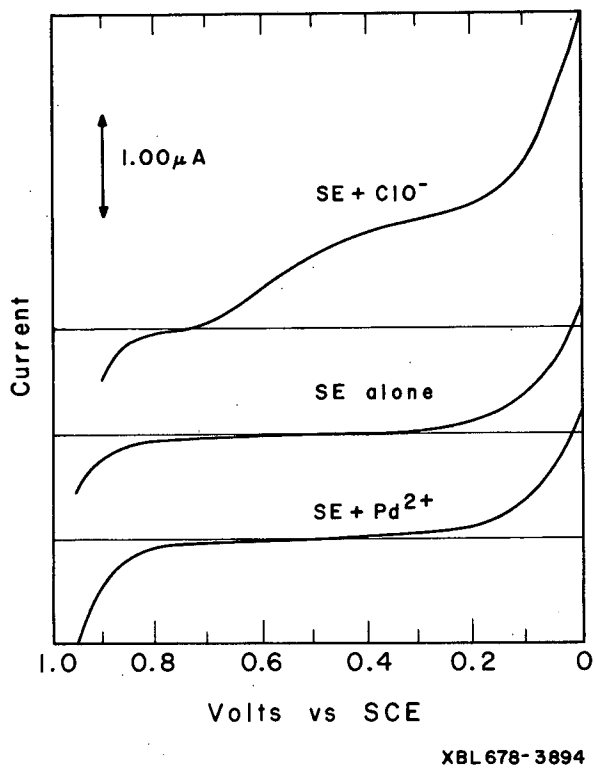

Fig. G.29-1. Polarograms of supporting electrolyte (SE) and reactants.

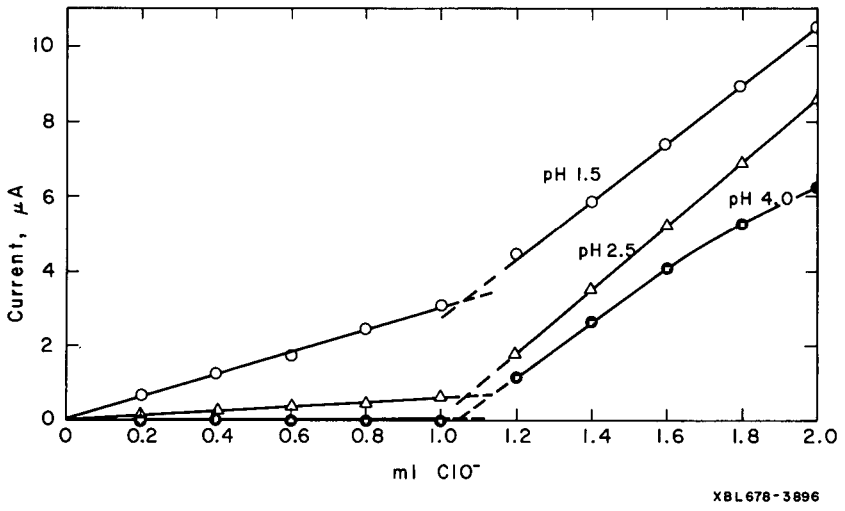

Fig. G. 29-2. Amperometric titration of palladium(II) with 9.61×10^{-3} M hypochlorite at various pH values.

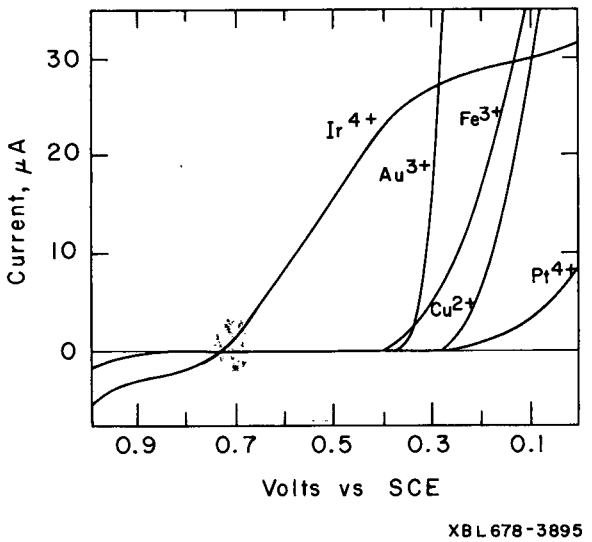

Fig. G. 29-3. Polarograms of diverse ions giving waves at positive potentials.

H. CHEMICAL ENGINEERING

1. MATHEMATICAL REPRESENTATION OF BATCH CULTURE DATA†

Victor H. Edwards* and Charles R. Wilke

A generalized logistic equation is proposed for the mathematical representation of batch culture kinetic data for bacterial growth and associated phenomena,

$$y = \frac{K}{1 + \exp[F(t_1)]} ,$$

where $F(t_1)$ = some function of time, K = numerical constant, $t_1 = t - t_L$, t_L = length of lag phase, $t > t_L$, y = dependent variable, i.e., concentration of cells, product, or substrate. Introduction of the time scale, t_1, permits better modeling of the lag phase. An equation of this form retains a number of advantages, even for fairly complex $F(t_1)$. These advantages include ease of use, physical meaning for at least some parameters, and constant limiting values of y at small and large values of t_1.

Although better choices of F(t) may exist, a simple polynomial was selected, giving the equation

$$F(t) = a_0 + a_1 t + a_2 t^2 + \cdots a_n t^n .$$

As pointed out by Dewitt, [1] this particular form of the generalized logistic equation can fit many types of data of sigmoidal form. It is also easy to make initial estimates of the values of the parameters, simplifying its use. An additional advantage of this equation for modeling kinetic data is that at low values of y/K, exponential growth is well approximated, gradually going over to product-inhibited growth at large time values. The dependence of the specific growth rate on values of Y and t_1 is shown by

$$\frac{1}{y}\frac{dy}{dt} = -(1 - y/K)(+ a_1 + 2a_2 t_1 + 3a_3 t_1^2 + \cdots + n a_n t_1^{n-1}) .$$

The generalized logistic equation thus meets the need for flexibility, being especially adaptable to systems with product inhibition.

To reduce the labor of fitting the equation to the data, a computer program in Chippewa Fortran was written for use with a Control Data 6600 computer. A method of nonlinear least-squares curve fitting was used to fit the equation to the data. A linear least-squares method does not work because the generalized logistic equation is nonlinear in the parameters to be computed. The nonlinear method consists of making initial guesses for the values of the coefficients and correcting these initial guesses by repeated iteration until a desired degree of convergence is obtained. The method and a detailed outline of the computer program are given elsewhere. [2] Many groups of data may be analyzed in sequence by the program. The program fits succeedingly complex forms of the generalized logistic equation to the data, statistically testing each succeeding equation until a fit is obtained that satisfies a χ^2 test. The computer program also tabulates observed and calculated values of the data, tabulates values of the calculated parameters, and prepares graphs comparing calculated and observed data.

Results

Both artificial and real batch culture kinetic data were supplied to the computer program to test its performance. Two examples of the results are described here. Further applications are reported elsewhere. [2]

One test of the equation was made by using data from an imaginary culture showing an exponential increase of cell concentration followed by a phase of constant cell concentration. For

convenience, these data are referred to as the exponential model.

The artifical data values are listed in the second column of Table H.1-I and are shown as open circles in Fig. H.1-1. The exponential data were taken from a table of exponentials.[3] If the imaginary data are plotted on semilog graph paper, the data representing the exponential growth period fall on one straight line of positive slope and the points representing the stationary period fall on a second, intersecting, horizontal straight line. The slope discontinuity prevented the continuous function from fitting the curve perfectly and provided a stress on the model. These hypothetical results would never be achieved in practice, but a close approximation might be made by a culture growing on a synthetic medium limited by a carbon source if the inoculum were a young, adapted, and exponentially growing culture that would continue growing exponentially upon inoculation. Cell mass versus time would most likely follow a course well approximated by an exponential and a resting phase, although cell number might not, there being a tendency for cell division to continue for a short period even after exhaustion of the carbon source. Figure H.1-2 and Table H.1-II compare the exponential model with the curves fitted by the computer for the first-degree polynomial (which is equivalent to the simple logistic equation) and for a fifth degree polynomial in the generalized form of the equation. The first-degree equation is satisfactory in the low values of cell concentration, but it is inadequate at high cell concentrations, giving an average relative error of 6.9%. For the fifth-degree polynomial, the fit is good throughout, with an average relative error of less than 2%. The equations fitted to the data are, respectively,

$$N = \frac{239.966}{1 + \exp(5.5530 - 0.5389\, t)} \qquad \text{and} \qquad (1)$$

$$N = \frac{151.473}{1 + \exp(5.01945 - 0.60037\, t + 0.10757\, t^2 - 0.040219\, t^3 + 0.0059485\, t^4 - 0.00031375\, t^5)}. \qquad (2)$$

Use of Eq. 1 is clearly inconvenient without a computer or desk calculator. The fit of the specific growth rates calculated by computer is compared to the exponential model in Fig. H. 1-3. As can be seen, the first-degree equation again fails, particularly at high values of time and cell concentration, but the fifth-degree equation does a good job of representing a general form of the variation of the specific growth rate with time. Average relative errors in calculated specific growth rates were 9.6% and 5.4% for the first- and fifth-degree cases; better results could be obtained by smoothing of the specific growth-rate data obtained by computer.

A second test was made using the batch culture kinetic data of Luedeking.[4] Luedeking studied the lactic-acid-producing bacteria, Lactobacillus delbruckii. His data were especially useful as a test because he also tabulated graphically measured growth rates.

The generalized logistic equation fitted to the cell-concentration data of Luedeking's run number 13 has the form

$$N = \frac{9.4906}{1 + \exp(4.6029 - 0.4622t + 0.10374t^2 - 0.03135t^3 + 0.003279t^4 - 1.192\times10^{-4}\, t^5)}. \qquad (3)$$

The actual data are compared with the values calculated with Eq. 3 in Fig. H. 1-3. An average relative error of 4.1% resulted, with very good agreement between calculated and observed data over the entire range of values. Growth rates determined from the data by graphical differentiation by Luedeking are compared with values calculated by analytical differentiation of Eq. 3 as shown in Fig. H. 1-4.

Adequate representation of simple batch culture kinetic data may be obtained by using the generalized logistic equation. This is borne out both by the results discussed here and by a considerable body of other results presented elsewhere.[2] The generalized logistic equation can be used to describe the decrease of substrate concentration with time in a batch culture, although only the description of cell and product concentrations was attempted in this study.

For more complicated data, such as those obtained with the penicillin fermentation, the generalized logistic equation can be used only when adequate data are available over the entire range of interest. Convergence difficulties may also arise in fitting complex data with the method used here to compute parameters. By using a more sophisticated technique to determine the best values of the fittable parameters, the generalized logistic equation should be able to describe the more complex data, also. With the present approach, good results may be obtained[2] by dividing complex data into two or more regions, as was done with the diauxie data of Monod, but this decreases the convenience of the method somewhat. The representation of the lag phase could be improved, because use of the present method results in a discontinuity at the end of the lag phase. However, this disadvantage is not serious because the rate of product formation at the end of the lag is not generally significant anyway.

By using a computer program to perform the analysis, the data may be reduced quickly to an equation. The equation may be used to perform manipulations of the data (e.g., differentiation or interpolation), and physical meaning can be derived from the values of some of the parameters in the equation. The equation is a method of storing data concisely. The computer can also be used to prepare graphs comparing the observed data and the fitted curve.

References

1. C. C. Dewitt, Ind. Eng. Chem. 35, 695 (1943).
2. Victor Henry Edwards and C. R. Wilke, Analytical Methods in Bacterial Kinetics UCRL-16398, Jan. 1967.
3. Charles D. Hodgman, Robert C. Weast, and Samuel M. Selby, in Handbook of Chemistry and Physics, 40th Ed. (Chemical Rubber Publishing Co., Cleveland, 1958).
4. R. L. Luedeking, The Lactic Acid Fermentation at Controlled pH: Kinetics of the Batch Process and Continuous Flow Theory and Experiment (Ph. D. Thesis), University of Minnesota, Minneapolis, Minnesota, 1956.

Table H.1-I. Test of data-fitting with exponential model.

Independent variable	Dependent variable		
	Given	Calculated F(t) first degree	Calculated F(t) fifth degree
0	1.0000	1.0000	1.0000
1	1.6487	1.5838	1.6773
2	2.7183	2.7022	2.6915
3	4.4817	4.5952	4.4136
4	7.3891	7.7706	7.4159
5	12.182	13.019	12.406
6	20.086	21.485	20.194
7	33.115	34.615	32.395
8	54.598	53.794	53.921
9	90.017	79.486	93.892
10	148.41	110.19	138.12
11	148.41	142.24	150.88
12	148.41	171.30	151.47

Table H.1-II. Specific growth rates, exponential model.

Independent variable	Time derivative of dependent variable		
	Given	Calculated F(t) first degree	Calculated F(t) fifth degree
0	0.5	--	--
1	0.5	0.535	0.478
2	0.5	0.533	0.479
3	0.5	0.529	0.510
4	0.5	0.521	0.522
5	0.5	0.510	0.503
6	0.5	0.491	0.474
7	0.5	0.461	0.481
8	0.5	0.418	0.544
9	0.5	0.360	0.526
10	--	0.291	0.212
11	0	0.219	0.0162
12	0	0.154	0.00012

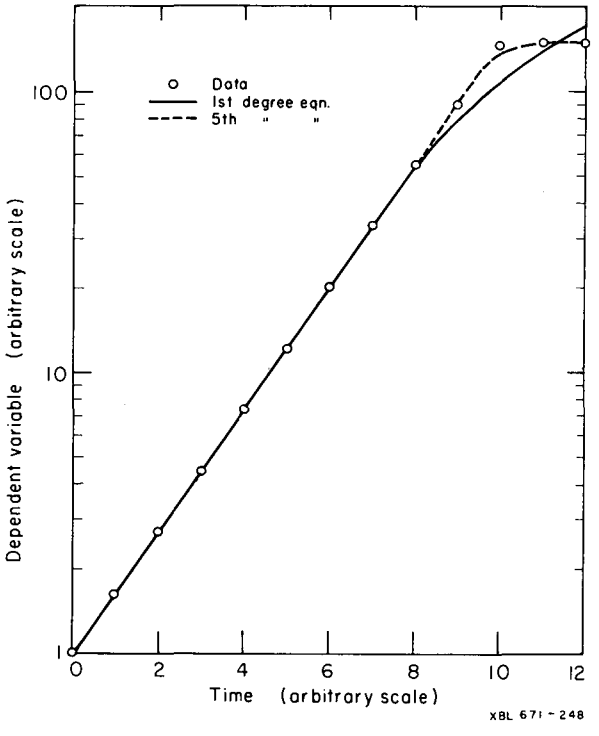

Fig. H.1-1. A comparison of exponential test data with first- and fifth-degree fitted curves.
O Data; ——— first-degree equation; ---- fifth-degree equation.

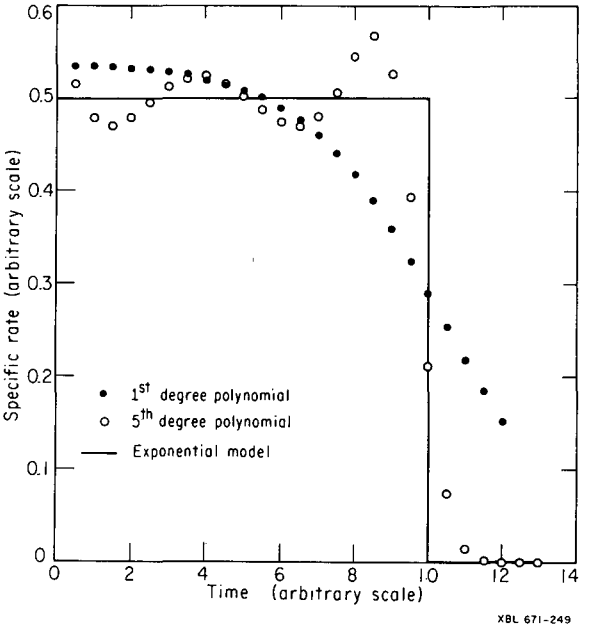

Fig. H.1-2. A comparison of the specific growth rates of the exponential model with values calculated from the first- and fifth-degree fitted equations.
O First-degree polynomial; O fifth-degree polynomial; ——— exponential model.

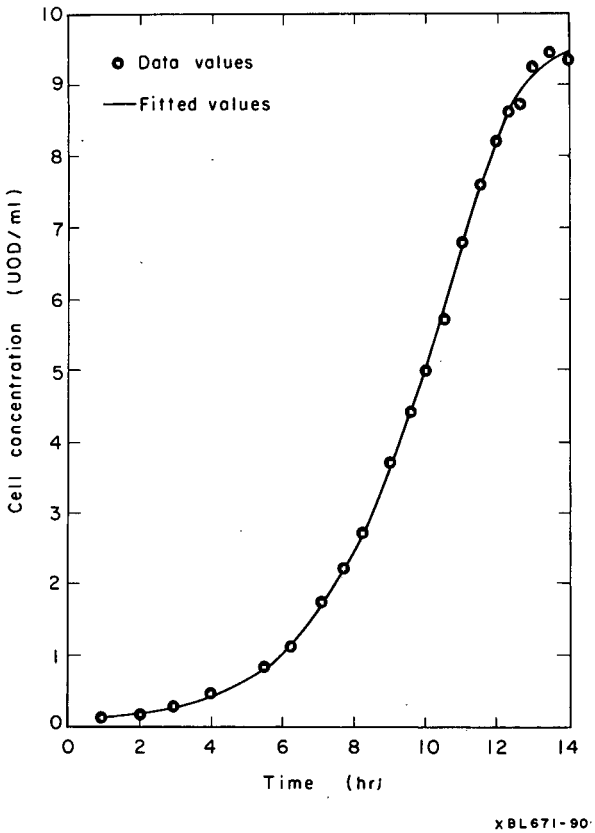

Fig. H.1-3. Comparison of cell concentration data (run 13) of Luedeking (Ref. 4) with fitted fifth degree curve.
Data; ——— fitted values.

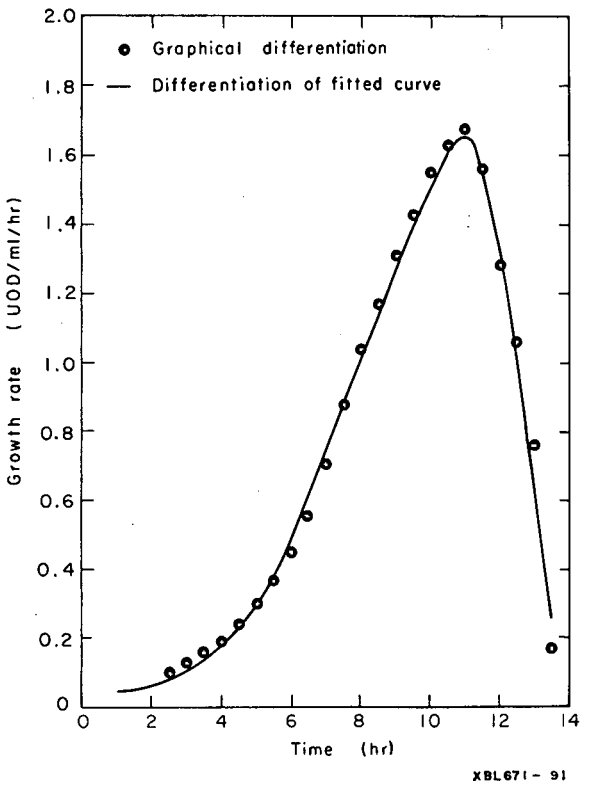

Fig. H.1-4. Comparison of graphically measured growth rate of Luedeking (Ref.4) with values calculated as derivatives of the fitted curve.
○ Graphical differentiation; ——— differentiation of fitted curve.

2. HEAT AND MASS TRANSFER BETWEEN FLUID PHASES

Michael W. Clark,† William H. Brown, and C. Judson King

This project involves studies of interphase heat and mass transfer between flowing gas and liquid phases. The apparatus employed is a closed horizontal rectangular channel, 3 in. wide, 1 in. high, and 18 in. long in the direction of flow. Gas and liquid streams pass through in stratified cocurrent or countercurrent flow. The channel is constructed of transparent polycarbonate, and is equipped with inlet and exit divider plates and with thermocouple probes and hypodermic tubing sample probes at the liquid exit and halfway along the flow path. The height of these probes above or below the liquid surface is adjustable, so that profiles of temperature and composition normal to the gas-liquid interface can be measured. The channel assembly is shown in Figs. H.2-1 and H.2-2.

During 1967 studies were made of the evaporation of highly volatile pure liquids and the evaporation of a highly volatile component from liquid mixtures. A number of publications concerning the project appeared during the year.[1-5]

A theoretical basis was developed for analyzing gas-phase mass transfer in the channel device under high-flux high-concentration-level conditions.[3,4] A necessary part of this development was the computer solution under high-flux conditions of the Leveque equation representing mass transfer into a fluid with a linear velocity gradient and zero surface velocity.

Experimental measurements were made of the rates of evaporation of pure n-pentane and isopentane into flowing nitrogen.[3,4] The results are in reasonable agreement with theoretical predictions made by incorporating the high-concentration and high-flux correction factors. These correction factors are substantial, as can be seen from the comparison of predicted vs experimental values of the high-flux correction factor in Fig. H.2-3. In this figure θ_{AB} is the high-flux correction factor, and x_{A_0} is the mole fraction of solute at the interface. Evaporation was carried out under conditions such that the liquid vapor pressure ranged up to 70% of the total pressure.

Measurements were also made of evaporation rates of carbon disulfide, n-pentane, cyclopentane, and ethyl ether from a nonvolatile n-tridecane solvent into flowing nitrogen.[3,5] These all represent situations in which the anticipated resistance to mass transfer is distributed more or less evenly between the gas and liquid phases. Figure H.2-4 shows results for one of these systems, that of nitrogen—cyclopentane—n-tridecane. In this figure F_s is the fraction of saturation attained by the gas phase in the channel, and XL_A is the mole fraction of cyclopentane in the bulk liquid. The lower curve represents the theoretical prediction based upon the application of convective diffusion theory to both phases. The upper curve represents the prediction if the liquid phase resistance to mass transfer is somehow eliminated completely.

At low concentration levels the agreement of experiment with theory was good in all systems. At the higher concentration levels a series of different tests showed that the liquid-phase mass-transfer coefficient was increased above the value to be expected from simple convective diffusion theory. This behavior was, in turn, traced to the occurrence of interfacial mixing cells. An investigation of various stability criteria revealed that this interfacial cellular motion was most likely caused by gradients in surface tension brought about by concentration gradients resulting from the mass transfer. The cellular motion was found to arise at values of the Thompson group,

$$Th = \frac{\left(\frac{\partial \gamma}{\partial C_A}\right)\left(\frac{\partial C_A}{\partial y}\right) h^2}{D_{AB}\mu},$$

above 8000. In the Thompson group γ is surface tension, C_A is the concentration of one of the species present, y is distance normal to the interface, h is the depth of the zone over which the concentration gradient occurs, D_{AB} is diffusivity, and μ is viscosity; $(\partial C_A/\partial y)$ and $\underline{h}$ were taken by analogy to the simple penetration model, ignoring the presence of cells.

Critical values of XL_A, above which mixing cells occurred, were

	XL_A
Ethyl ether—tridecane	0.014
n-Pentane—tridecane	0.029
cyclopentane—tridecane	0.071

At XL_A above 0.35, the gas-phase resistance became completely controlling for the ethyl ether system. The carbon disulfide system showed no influence of surface-tension-driven cells, since the surface tension of carbon disulfide is higher than that of n-tridecane.

A unique correlation of the % increase in liquid-phase mass-transfer coefficient vs the ratio of the Thompson number to the critical Thompson number (8000) was obtained for the three systems showing instability. For Thompson numbers between 8000 and 24 000, the factor by which the liquid-phase mass-transfer coefficient is increased varies as the $\frac{1}{4}$ power of the Thompson number. This behavior is similar to experimental results found for heat transfer due to natural convection driven by density gradients.

Footnote and References

† Present address: Dow Chemical Company, Walnut Creek, California.

1. C. H. Byers and C. J. King, Gas-Liquid Mass Transfer with a Tangentially Moving Interface: I. Theory, A. I. Ch. E. J. 13, 628 (1967).

2. C. H. Byers and C. J. King, Gas-Liquid Mass Transfer with a Tangentially Moving Interface: II. Experimental, A. I. Ch. E. J. 13, 637 (1967).

3. M. W. Clark and C. J. King, Mass and Heat Transfer Processes in Laminar, Two-Phase Flow, UCRL-17527, June 1967.

4. M. W. Clark and C. J. King, Evaporation Rates of Volatile Liquids in a Laminar Flow System. Part I. Pure Liquids, UCRL-17655, Dec. 1967.
5. M. W. Clark and C. J. King, Evaporation Rates of Volatile Liquids in a Laminar Flow System. Part II. Liquid Mixtures, UCRL-17656, Dec. 1967.

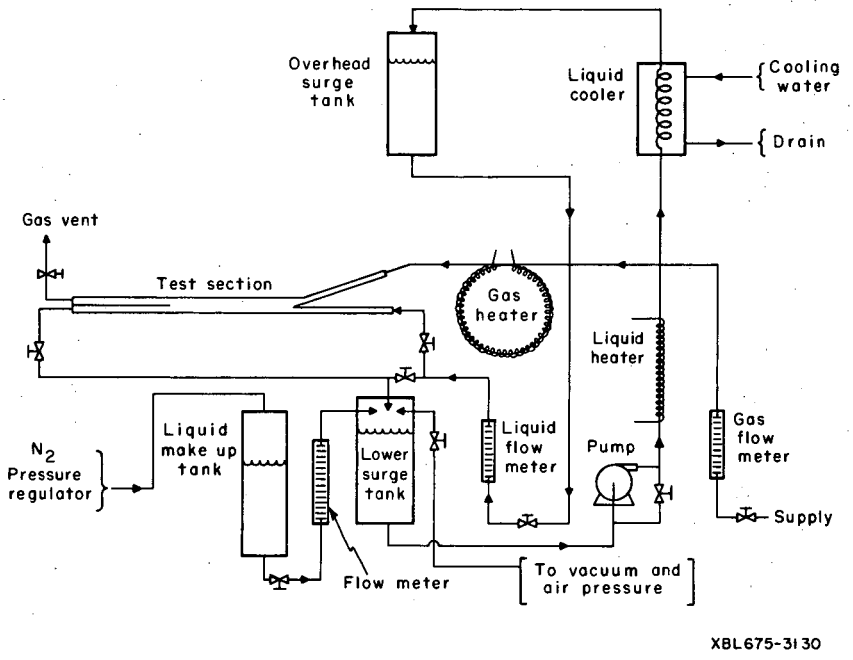

Fig. H.2-1. Schematic view of experimental apparatus, showing liquid and gas flow geometries.

Fig. H.2-2. Test section, with overall dimensions and placement of the temperature and concentration probes indicated.

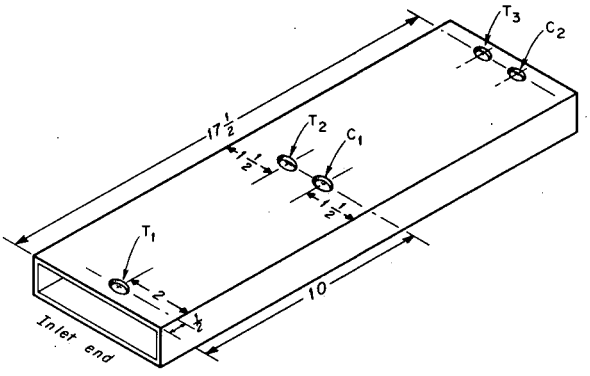

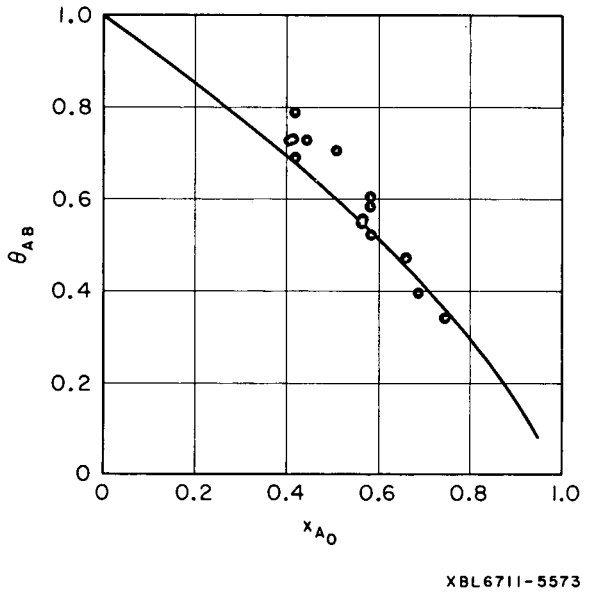

Fig. H.2-3. Comparison of predicted and experimental high-flux correction factors for the evaporation of pure n-pentane and pure isopentane.

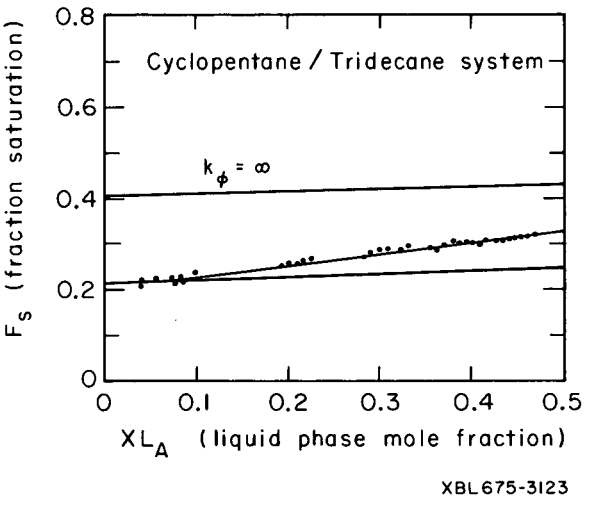

Fig. H.2-4. Gas phase fraction saturation (cup mixing) as a function of liquid phase mole fraction (bulk), for the system; cyclopentane/tridecane evaporating into nitrogen. **O** ··· indicates experimental data, the lower solid line represents the predicted behavior using the high flux addition of resistances approach. Interfacial temperature = 25 ± 0.1°C.

I. INSTRUMENTATION

1. DIFFERENTIAL CIRCLE DIVIDERS

Herman P. Robinson

Two devices have been constructed for accurate angular settings (see Figs. I. 1-1 and I. 1-2). The first can be used as an attachment to a milling machine dividing head to produce virtually any number of divisions of a circle. The second is a table to be used in a horizontal position (axis vertical) which can be set to any of 129 240 positions. The principle of these devices has been discussed in the literature.[1,2] Precision dividing tables are available commercially, but are generally limited to 360 positions in the smaller sizes.[3] The two devices herein described consist essentially of two tables, with different numbers of teeth. The smallest angular setting possible is the difference between the minimum angular settings of the two sets, hence the name differential divider.

If two toothed wheels resembling bevel gears are meshed face to face, the position of one wheel with respect to the other assumes some average position. If the wheels are disengaged, and moved a number of teeth, the new position is again an average. Errors in tooth positions tend to be distributed, hence the angle through which the wheels are moved is much more accurately fixed than would be expected from the absolute positional error of each tooth. Commercial dividers are constructed of steel, and the teeth are lapped together by a tedious process, resulting in an expensive device, but one giving extremely accurate angle settings. Maximum errors of 0.25 arc second are obtainable.

For many purposes this accuracy is not needed, and more conventional machining techniques can be used. The milling machine attachment is constructed mainly of brass. A "top" wheel contains 128 teeth on one face. A matching wheel ("vernier") contains 128 teeth on one face and 135 teeth on the opposite face. The "bottom" wheel has 135 teeth. A better choice would have been 144 and 145 teeth, since the smallest division would be obtained by separating the wheels and moving the vernier one tooth, then meshing the wheels. However, tables are easily prepared for settings to obtain any specified number of divisions. The total number of divisions possible is $128 \times 135 = 17\,280$. This is entirely adequate for most work on an ordinary milling machine, since the setting error need be no larger than 1/34 560 revolution, or 38 arc seconds. The top wheel is graduated every 2 deg, the vernier contains 135 graduations, and the bottom wheel has attached to it a glass plate and scribed line (indicator) for aligning the wheels to a desired setting. In addition, a bubble level is attached to the bottom wheel. The vernier contains two small magnets, and the other two wheels each have an iron plate inside acting as armatures. The magnets serve to hold the assembly together. A central loose-fitting shaft guides the wheels when they are separated, but otherwise does not contribute to the positioning of the wheels. Shown also in Fig. I. 1-1 is a mirror which can replace the bubble level so that the divider can be used with an autocollimator.

In use the device is mounted on the dividing head with work attached, and the dividing head turned until the bubble is level. This is the initial position. The wheels are separated and turned to the desired positions, then the teeth are engaged. The dividing head is now moved until the bubble is again level. In this way the work has been turned precisely through the desired angle.

After constructing the divider, it was found that the wheels rocked slightly on some slightly irregular teeth. This was corrected by pressing the assembly together in an arbor press for all possible tooth positions. An estimated pressure of 1000 pounds was used. After this treatment, spot checks were made on the accuracy by comparing with a Griswold astronomical dividing head. The errors indicated were not more than 10 arc seconds, which was the limit of accuracy of the Griswold divider. The setting of the differential device is very much faster, since only relatively coarse readings of wheel positions have to be made. Also there is no backlash.

The dividing table is also made of brass, and has a diameter of 5 inches. The top wheel contains 360 teeth, and the bottom one 359. The top wheel is calibrated every degree, and the vernier wheel is divided into 100 parts, so that angles are read directly to 0.01 deg and can be

estimated to 0.002 deg. Since the exact position must match the teeth, a table of actual angles possible can be consulted if greater accuracy is justified. The "pressing" of the teeth was done with too much pressure, which work-hardened the teeth in the first few pressings, and resulted in a device with a periodic error of ±23 arc seconds, or 0.006 deg.

After calibration, the divider proved to be extremely useful in aligning the pole face sectors on a 27-inch ^{3}He cyclotron. It is planned eventually to anneal the brass wheels and press them together with less pressure in order to improve the setting accuracy.

References

1. W. L. Bond, Differential Circle Dividing Machines, Rev. Sci. Instr. 37, 1401 (1966).
2. P. L. Garrett, High Performance Indexing Fixtures, ASME Conference Paper 64-Mech-42, October 1964.
3. "Ultradex" by A. A. Industries and "Millichex" by Michigan Tool Company.

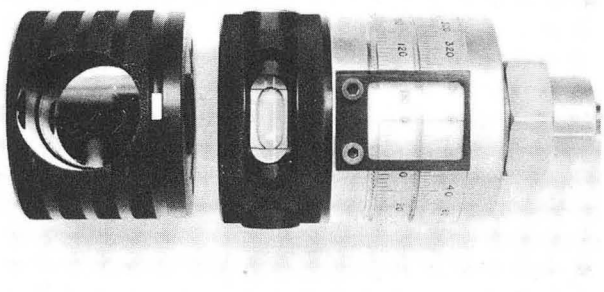

XBB682-536

Fig. I. 1-1. Dividing head attachment.

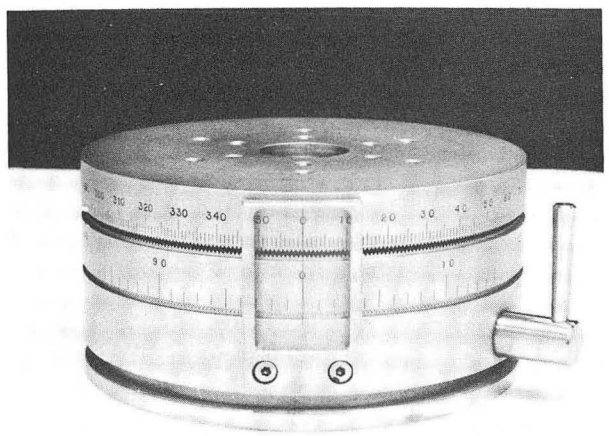

XBB682-537

Fig. I. 1-2. Differential dividing table.

2. TIME CODE GENERATOR†

Herman P. Robinson

To facilitate the transmission of precise time information within the Laboratory, a time code generator has been constructed (see Fig. I. 2-1). It differs from commercial generators in that the time is given in terms of a continuous day count dating from any desired epoch, together with the decimal part of a day elapsed since 0 hours Universal Time (UT). The decimal information is transmitted to a millionth of a day, and updated every microday (86.4 milliseconds). However, the display is in units of ten microdays. Conventional time code generators provide time in hours, minutes, and seconds, and the day count from the beginning of the year.

The time code is shown in Fig. I. 2-2. It is patterned after the IRIG standard Format A, but conveys more information because of the use of a decimal system.

The day count presently being used is the Modified Julian Day (MJD), having as its epoch 0 hours UT, 17 November 1858. It was chosen simply because convenient calendars are available for converting between MJD and the conventional date. The use of the continuous day count and decimal day is a convenience in calculations involving elapsed time as well as exact dating.

The time code is transmitted over ordinary intercom circuits between buildings in the form of a dc level shift of about 6 volts. Receivers for the time code are described in the report following this one.

The input to the generator is at 2.5 MHz, obtained directly from a frequency standard operating at the "atomic" frequency. Division by 216 produces 10^9 pulses per day, which is the starting point for generating the code. Provision is made for offsetting the frequency by any amount from 0 to 1000×10^{-10} in steps of 1×10^{-10}, permitting conversion to UTC or UT2. The setting of the time is accomplished by using an external reset pulse to set the four least significant digits, and internal pulses to advance the remaining digits to the time desired. Power is supplied from the line, but if a line power failure occurs, a 12-volt storage battery takes over without interruption of the signal. Signals from a second clock can be compared with those in the generator. An alarm sounds if a disagreement develops, and a bit marker is added to the last position on the time code before the P_0 marker. This alerts the receiver to the fact that an error in time may be present.

In the future it is planned to use most of the remaining space in the time code to transmit the time in hours, minutes, and seconds for those users who want time information in this form.

Footnote

†From UCRL-17884.

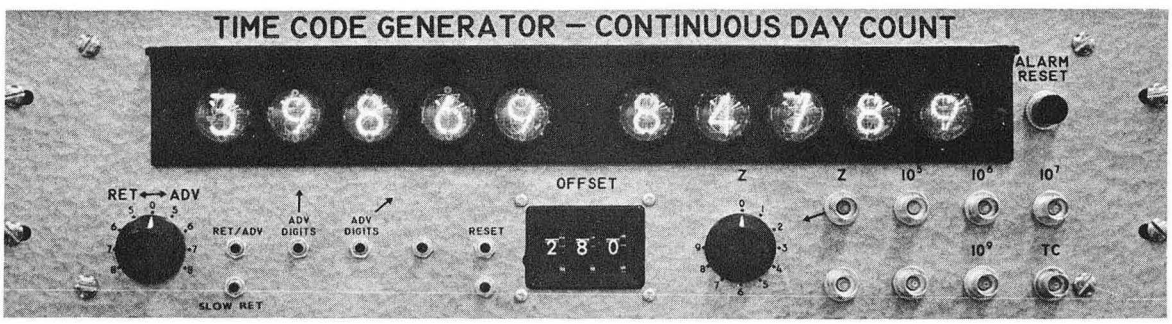

XBB682-538

Fig. I. 2-1. Time code generator.

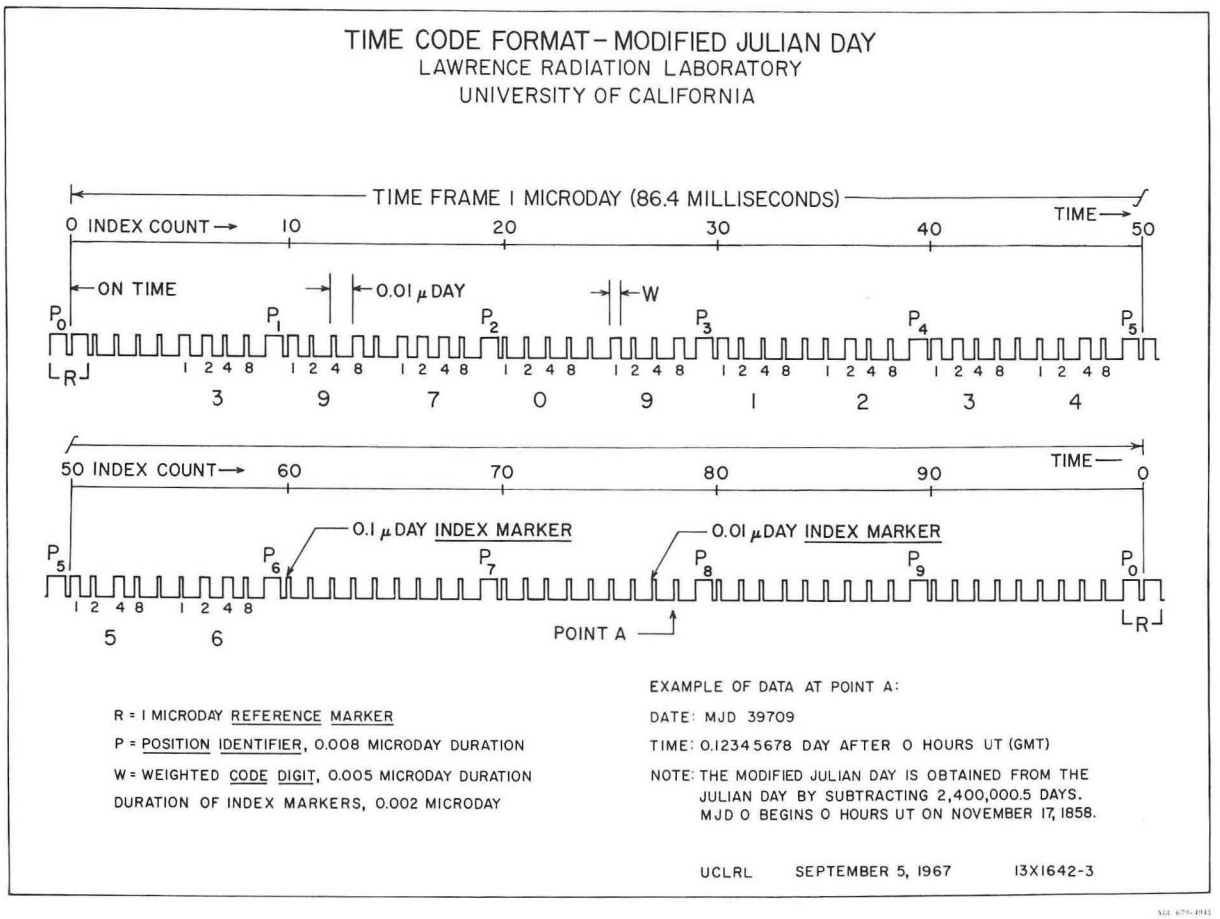

Fig. I. 2-2. Time code format.

3. A RECEIVER FOR CONTINUOUS DAY COUNTING

J. E. Arnold

The ability of the experimenter to record the beginning and ending of a nuclear experiment and having these times and dates recorded with the data has been a difficult situation in the past at best. With the beginning of transmission of timing code for continuous day counting (UCRL-17884) the experimenter has, with a telephone line or intercom wire pair and the receiver, the ability to enter the information along with the data obtained in the experiment on a magnetic tape ready for computer data reduction.

A prototype receiver has been constructed having two 12-decade memories: one for START time and one for current or STOP time. A 12-decade buffer storage is used to provide parallel output capabilities. Ten decades of NIXIE display are employed.

In use, the START and STOP time memories are at the current time until the beginning of the experiment, then only the STOP time memory continues at the current time. The display and its buffer storage are tracking the current time unless the user pushes a switch to display the START time. This switch is disabled during the read-out process. Output can be either serial or parallel 1-2-4-8 code. The first installation is planned to have the receiver controlled by a Victoreen 1600-channel analyzer using a Kennedy magnetic tape deck as the read-out device.

Flexibility has been kept in mind in the construction of the prototype, since one proposal in the transmission of the time code has been to include the normal civil time in the unused portion of the microday frame of transmission. The 12-decade memory occupies less than 4 by 6 inches of printed circuit board space, using only six integrated circuit modules. Future models can easily be tailored to the user's desires by adding or subtracting the number of plug-in printed circuit boards.

The unit was constructed in an AEC NIM bin of a four-unit width.

A general block diagram (Fig. I. 3-1) is included to show the overall view of the system.

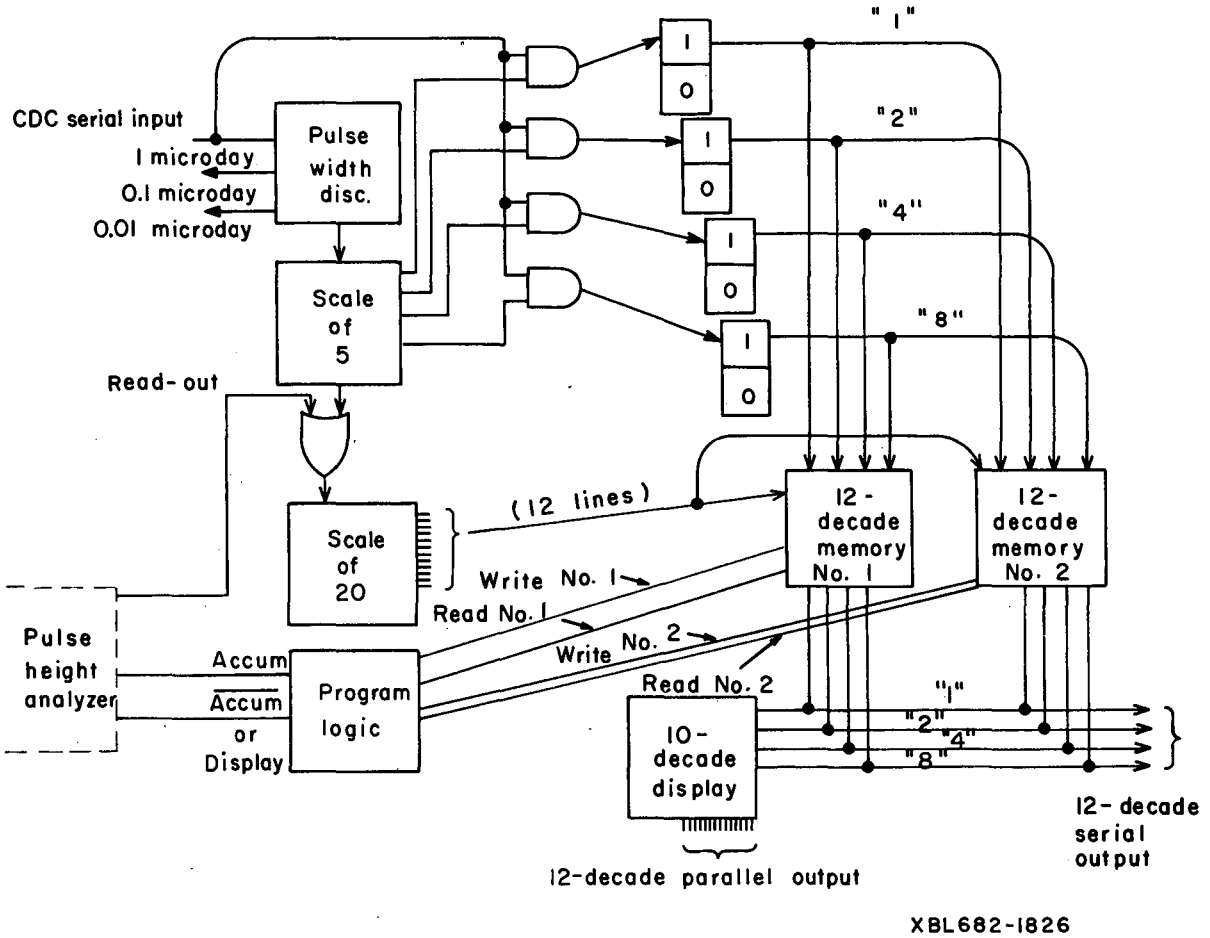

Fig. I. 3-1. A receiver for continuous day counting.

4. GERMANIUM FET's POINT THE WAY TO LOWER-NOISE PREAMPLIFIERS†

E. Elad and M. Nakamura

A novel low-noise preamplifier for use with semiconductor radiation detectors is described. The preamplifier utilizes the low-noise characteristics of a cooled germanium junction field-effect transistor (JFET).

Preamplifiers based on silicon JFET's are currently used in most high resolution spectrometers.[1] The advantages of the germanium FET over its silicon counterpart are closely related to the properties of the two materials at cryogenic temperatures. Germanium has inherently higher mobility than silicon and with lattice scattering being the dominant scattering mechanism down to liquid helium temperatures, the optimum mobility of germanium is much higher than that of silicon and is attained at much lower temperatures. Also, due to lower ionization energies of impurities in germanium, the density of free carriers in this material at low temperatures is higher than that in silicon. These two factors combine in germanium FET's to give high transconductance (g_m) at very low temperatures.

It is well known that the main noise source of JFET's is the thermal noise of the channel. Thus it could be expected that lowering the temperature will result in reduced noise of the device.

The described preamplifier employs germanium FET's operated at 4.2°K to attain their high-gain low-noise characteristics. The input stage consists of two p-channel JFET's type TIXM12 in cascode. The g_m of these transistors at liquid helium temperature is around 25 000 micromhos and the input resistance is in the region of 10^{10} - $10^{11}\Omega$. Input capacitance is approximately 20 pF. The rest of the preamplifier is a conventional type amplifier using bipolar transistors, which was described elsewhere.[1]

Pulse generator resolution of the preamplifier for zero external capacitance is 0.3 keV FWHM (Ge) with a slope of 0.018 keV/pF. The very low sensitivity to external capacitance (detector) is a result of the relatively high input capacitance of the FET's, which on the other hand prevents the achievement of higher signal-to-noise ratio.

The preamplifier was used with a low-capacitance silicon detector, and the obtained low-energy spectra of ^{55}Mn and ^{241}Am are shown in Figs. I. 4-1 and I. 4-2. The K_α and K_β lines of ^{55}Mn, only 0.6 keV apart, are resolved and measured with 0.37-keV resolution. The spectrum of ^{241}Am shows the fine structure of this source with some of the very weak lines (L_η, L_{β_6}, L_{γ_4}) being resolved from the background noise. The L_α line (L_{α_1} = 13.96 keV, L_{α_2} = 13.78 keV) was measured with 0.42-keV resolution and the L_{γ_1}, and L_{γ_6} lines (0.68 keV apart) were resolved. The L_{β_1} and L_{β_2} lines (0.81 keV apart) previously barely resolved now show a 2:1 peak-to-valley ratio.

Footnote and Reference

†Short version of reports in Nucl. Instr. Methods 54, 308 (1967), and "Germanium FET-A Novel Low Noise Active Device" (UCRL-17818, Sept. 1967), presented at the 14th Nuclear Science Symposium, IEEE, Oct. 31-Nov. 2, 1967, Los Angeles, California.

1. E. Elad and M. Nakamura, "High Resolution Beta- and Gamma-Ray Spectrometer," IEEE, Trans. on NS-14, No. 1, pp. 523-532 (February 1967), 13th Nuclear Science Symposium, Boston, Mass., 1966.

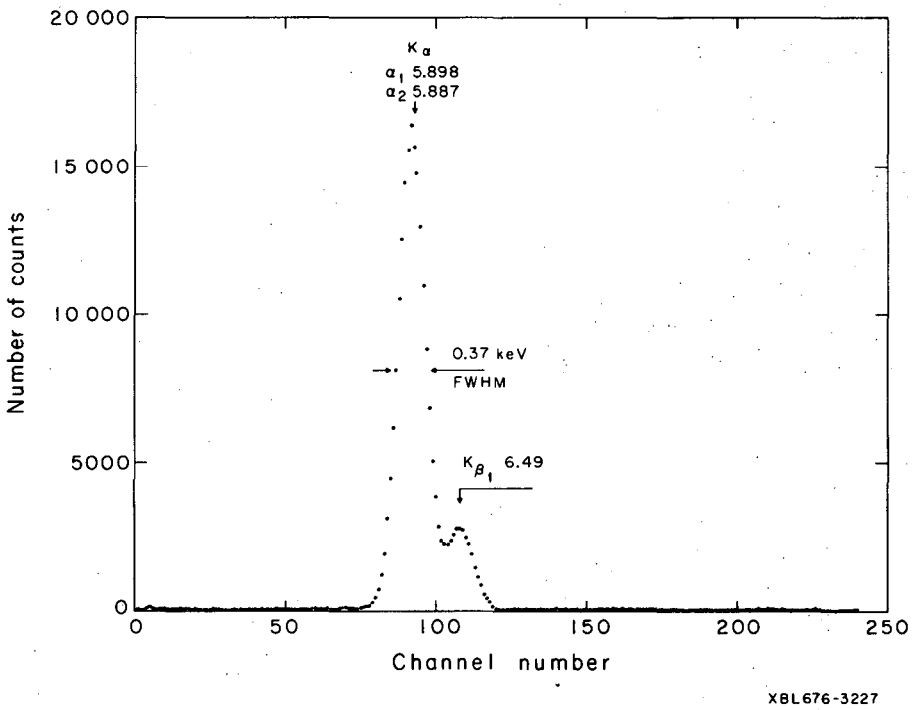

Fig. I. 4-1. Spectrum of ^{55}Mn x rays. Energy in keV.

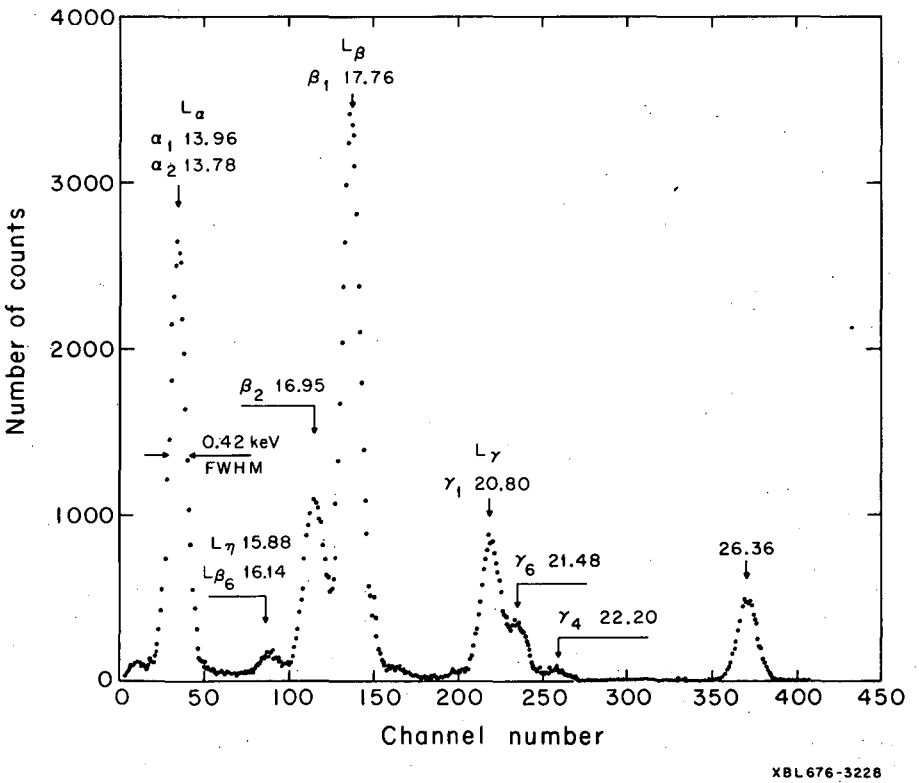

Fig. I. 4-2. Spectrum of ^{241}Am x rays. Energy in keV.

5. RAPID x-RAY FLUORESCENCE ANALYSIS OF ARCHAEOLOGICAL MATERIALS†

H. R. Bowman, R. D. Giauque, and I. Perlman

A number of early (predynastic and dynastic) Egyptian artifacts were borrowed from the Robert H. Lowie Museum of Anthropology at the University of California at Berkeley to evaluate the usefulness of the recently developed x-ray fluorescence spectrometer in the identification of the chemical composition of archaeological materials. Over one hundred separate items were analyzed and recorded. Many times the analysis was made by simply holding the article in front of the spectrometer for one or two minutes.

In brief, x-ray fluorescence analysis involves the measurement of characteristic x-rays excited in a sample by a primary source of radiation. In our system we used a small radioactive source of gamma radiation (^{125}I or ^{241}Am) for the primary radiation. The secondary radiation or characteristic x rays from the sample were detected with high-resolution solid-state detectors (either lithium-drifted silicon or germanium) which are described in more detail elsewhere. [1]

The results of this investigation indicate that the x-ray fluorescence spectrometer does have a potential use in the field of archaeology although it is not clear yet what problems are more suited to it. The main features that may appeal to the archaeological investigator are:

(1) The equipment is relatively easy to operate.
(2) It provides a rapid means of identifying the elemental materials in a large number of articles.
(3) It is portable and can be moved into a museum or into the field.
(4) It can be used for quantitative results.

An example of the rapid determination of chemical composition is shown in Fig. I. 5-1, where the two sides of an early dynastic Egyptian mirror were analyzed. In the photograph we see side "A". The x-ray analysis on the right indicates that side "A" has a much higher tin content than side "B". These results suggest that side "A" was plated with a thin layer of tin, perhaps to increase its reflectivity, although one cannot rule out the selective corrosion of one of the mirror surfaces. The point to be made here is not that the problem has been solved, but that a very rapid scan (≈30 sec on each side) did turn up a problem of potential archaeological interest.

In many cases the primary gamma rays can be focused onto a particular part of the object. The article in Fig. I. 5-2 (labeled late dynastic bronze clamp) reveals exceptionally intense iron x-rays coming from the labeled locations. This iron may suggest the use of iron pins, nails, or rivets. The appearance of iron on this particular object sheds considerable doubt as to whether it belongs in such an early context.

Preliminary measurements indicate that the x-ray fluorescence technique can be used for more quantitative results if one is willing to sacrifice a small amount of the material to be tested. About 100 mg of material can be taken and ground into a powder, incorporated into a cellulose matrix, and pressed into a wafer. The wafer is then placed in a standard sample holder and attached to what is called a source-target assembly. This assembly is shown schematically in Fig. I. 5-3. The gamma rays from the source impinge upon the target material, which can be made of any element and excite target x rays characteristic of that element. The target x rays then impinge on the sample and excite sample x rays which are then detected by the x-ray detector. The target material can be varied for maximum analytical sensitivity. This source-target technique was originally developed by Rhodes[2] and in general reduces or eliminates many of the difficulties encountered in x-ray fluorescence analysis.

A number of early sub-Saharan African glass beads from Mapumgubwe were used to evaluate this technique. We are indebted to Professor J. Desmond Clark for placing these beads at our disposal and informing us of their significance. The initial results (Table I.5-I show that quite aside from the coloring matter of the beads, a number of different types of glasses appear. The "A" series all contain lead, and in all except one, antimony was present (presumably added for opacity). All but two of the "D" series contain lead and tin, but none antimony. There is a report that the use of tin in place of antimony occurred at a particular time. If so, the "A" and the "D" series fall on either side of this magic date. The two in the "D" series containing neither lead nor tin are very similar to the "C" series. Of special significance for an archaeologist is the fact that the "D" series from Skeleton #14 at Mapumgubwe has beads of two quite different chemical compositions. This fact suggests that the beads which were traded up the Limpopo River to Mapumgubwe came from at least two different sites.

We would like to emphasize that the instrument and the techniques are new and will no doubt be improved with further application. There is certainly a potential use for it in the field of archaeology, but it will probably take the archaeologist himself, using the instrument either in the laboratory, museum, or in the field, to determine the manner in which the instrument can be best applied to his problems.

Footnote and References

†Resumé of UCRL-17968 presented at the conference: Applications of Science to Medieval Archaeology, Los Angeles, California, October 26-28, 1967.

1. Harry R. Bowman, Earl K. Hyde, Stanley G. Thompson, and Richard C. Jared, Science 151, 562 (1966).
2. J. R. Rhodes, The Analyst 91, 683 (1966).

Table I.5-I. The analysis of sub-Saharan African beads (Iron Age) using the source-target x-ray fluorescence asssembly.

Sample No.	Sample	Sample origination	Fe (%)	Cu (%)	Zn (%)	As (%)	Sn (%)	Sb (%)	Pb (%)
A-1	Brownish red beads	Mapumgubwe S. Limpopo, rockshelter	1.3	1.7				0.5	4.3
A-2	Pink beads					1.6		0.5	25.5
A-3	Light-blue beads					3.7		0.1	21.9
A-5	Blue beads					2.1		<0.05	27.4
A-6	Long light-green beads			1.1				1.2	32.5
A-7	Dark-blue beads			2.2				1.8	9.8
A-8	Long dark-blue beads			2.8				0.5	10.8
A-10	Bluish-green beads			1.2				2.1	12.7
A-12	White beads					4.2		0.1	13.6
C-1	Black beads	Mapumgubwe skeleton #23	0.9						0.1
C-2	Light-blue beads		1.5						<0.1
D-1	Yellow beads	Mapumgubwe, eastern area Ex. 7, No. 1, skeleton #14	1.0				1.0		5.9
D-2	Amber beads		0.7		0.4		1.5		9.5
D-3	Turquoise beads		1.1	1.5			1.4		0.3
D-4	Apple-green beads		0.8	1.5			1.2		6.9
D-5	Blue beads		1.5						<0.1
D-6	Black beads		1.0						
Maximum metal content if none reported.			<0.2	<0.2	<0.1	<0.1[a]	<0.1	<0.1	<0.1

a. <0.3% if more than 5% Pb is present.

XBB6710-6034

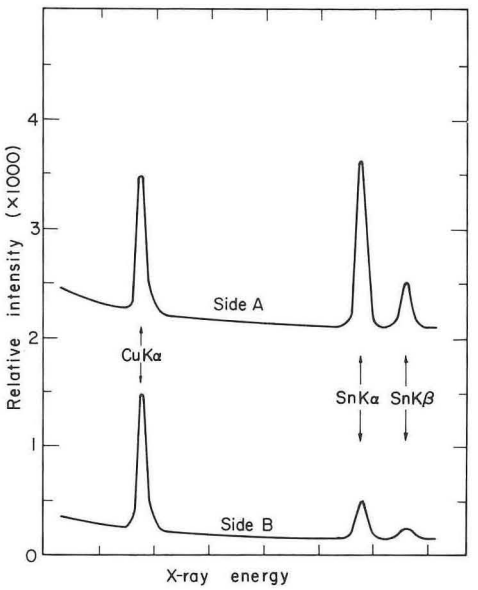

Fig. I. 5-1. The x-ray energy spectra obtained from the two sides of an early dynastic Egyptian bronze mirror. Side "A" is shown in the photograph.

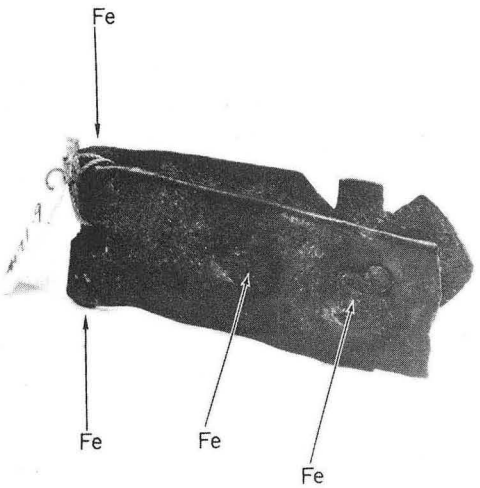

XBB6710-6021

Fig. L 5-2. A late dynastic Egyptian bronze clamp. Iron was detected at the labeled locations.

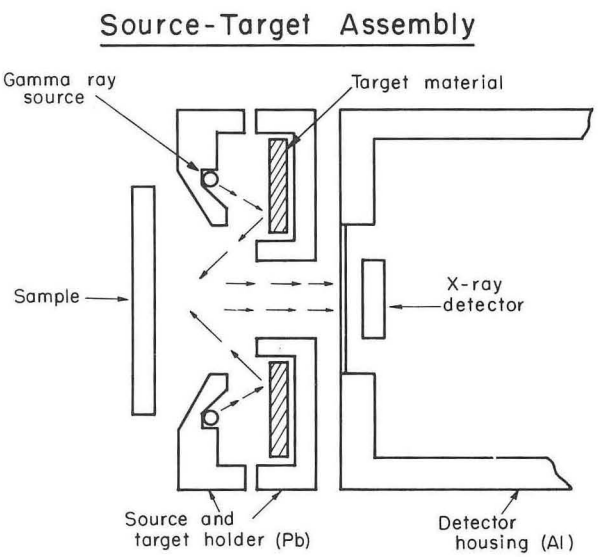

Fig. L 5-3. Schematic arrangement of the source-target assembly.

6. AN IMPROVED LIQUID-INK PEN ASSEMBLY FOR THE CALCOMP DIGITAL PLOTTER

R. L. LaPierre, M. Nakamura, and R. Zane

During the early part of 1967 we experienced difficulty in obtaining usable CalComp liquid-ink plots from our computer center. Close examination of the plots revealed that the problems were due mainly to poor performance of the ink-pen assembly. The faulty plots were sometimes due to the failure of the plotter to hold the pen in the pen-up position while moving between two nonconnecting points. It was also found that the pen-down operation of the assembly was marginal.

A simplified sketch of the assembly is shown in Fig. I. 6-1. Once the pen has been raised by current surge, a small holding current in the solenoid keeps the plunger assembly in the pen-up position. The force of gravity and the restoring spring return the plunger to the surface of the paper when the holding current is interrupted by a pen-down command. The mica spacer prevents having a magnetic latch in the up position and consequently little force is required to restore the pen to the down position.

It was found that under some conditions the air gap introduced by the mica spacer can be too large to maintain the pen in the up position. The carriage assembly on older plotters is exposed to severe vibrations when the carriage and drum stepping motors are operated. In addition, the air gap is often much larger than the original design value because the mica spacer is deformed by exposure to ink spills and to cleaning agents. We found that it was best to remove the mica spacer and use a magnetic latch for the pen-up condition. Because of the latch it is necessary to use a stronger spring in the cap assembly. We use seven turns of 0.016-in. spring steel wound with a pitch of 0.125 in. for a restoring spring. It requires a force of about 65 g to compress the spring to a height of 0.250 in., compared with a force of less than 20 g for the original spring.

The spring-loaded pin that is used to keep the pen from rotating was replaced with stainless steel. The original pins become permanently magnetized and are a restraining force on the downward movement of the pen.

With the modifications mentioned above, there is positive pen-up and pen-down action over 90% of the pen travel adjustment range. It should be noted that because of the wide dynamic range of pen travel available it is preferable to use pens that have a damping spring on the cleaning rod. Without the spring, the range of the pen travel adjustment is more limited because bounce of the cleaning rod will interrupt the flow of ink to the pen.

Of course it is extremely necessary that the pens be kept clean to insure proper ink flow and that care be taken to protect the polished surface of the plunger, but with the positive action of the modified assembly the problems of liquid-ink plots have been minimized.

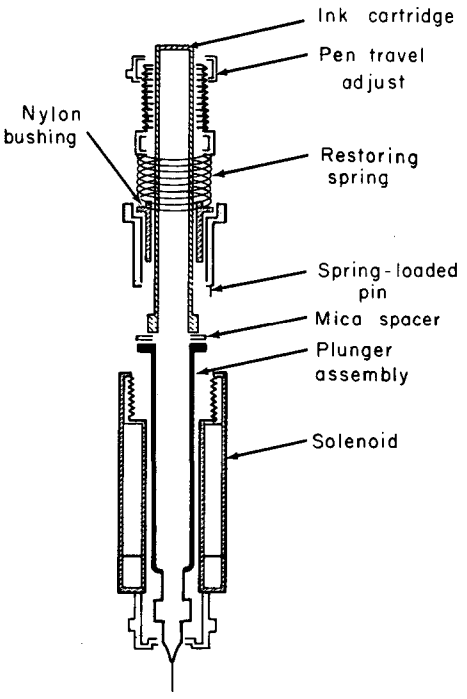

XBL6712-5974

Fig. I. 6-1. CalComp liquid-ink-pen assembly.

7. COMPUTER CONTROL SYSTEM FOR THE FIELD-FREE SPECTROMETER

Ron Zane

A Digital Equipment Corporation PDP-8 computer is being incorporated into a system to collect data from the Field-Free Spectrometer while at the same time controlling the operation of the spectrometer. The system will be capable of running a preprogrammed series of experiments without the need for operator intervention.

The system hardware is almost completely designed and is presently being assembled and "debugged" (Fig. I. 7-1). The system software is in the early stages of development. In its final form the system will not only acquire the data from a series of experiments but will perform a limited amount of on-line analysis. High quality graphic output will be available through incorporation of a CalComp model 565 plotter in the system.

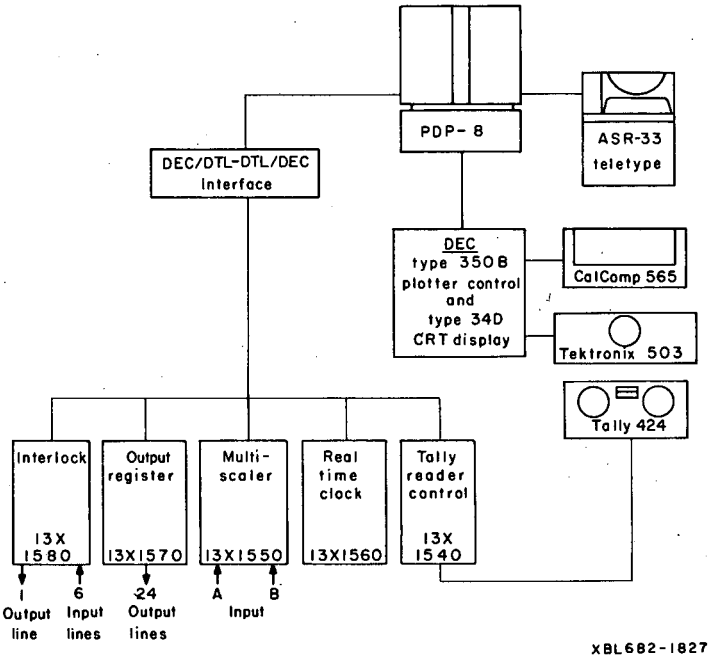

Fig. I. 7-1. PDP-8 data acquisition and control system.

8. A MODULAR 1- TO 1.2-kV POWER SUPPLY (13X1520)

Ron Zane

A high-voltage power supply of novel design has been added to the variety of general-purpose modules within the Nuclear Instrumentation Bin concept. The supply is intended to fill the need for a simple low-cost low-noise supply capable of operating a scintillation detector or other photomultiplier tube device.

The supply is passively regulated with a 1200-V zener diode string. It is protected by an overload circuit which will turn the primary supply off in the event that loads of approximately 3 mA are drawn. The overload circuit not only protects the supply from the effects of overcurrent but also greatly reduces the shock hazard to personnel using the equipment.

The output voltage may be set for 1000, 1100, or 1200 V by a front panel switch. It is anticipated that the majority of uses will involve a positive output polarity. It is possible to build the units with a negative output polarity by reversing all diodes, substituting a PNP transistor for the NPN overcurrent protection transistor, and reversing the polarity of all tantalum filter capacitors.

Line voltage variation over the range of 105 to 125 V ac produces an output voltage variation of less than 15 V dc. A variation in load current from no load to 2 mA produces an output voltage variation of less than 25 V dc. Output ripple is less than 20 mV rms at 2 mA load current.

9. GERMANIUM DETECTOR SYSTEM DEVELOPMENT

R. H. Pehl, F. S. Goulding, W. L. Hansen, D. A. Landis, D. F. Malone, R. C. Cordi, and G. I. Saucedo

Progress in the development of germanium detectors continues to be largely determined by the quality of germanium crystals that can be obtained. Only Hoboken crystals have been bought during this year.

The variation of the quality of detectors that can be made from different crystals is quite large, and there is a definite tendency for the detector quality to become worse as the crystal diameter becomes larger. In fact, we have not succeeded in making a high-quality detector (<2.5-keV resolution at ^{60}Co) from crystals of greater than 4.0 cm diam.

Because of the recognition that development of consistently good crystals of various sizes is the most important step that can be made in this program, work has begun on pulling single crystals in our laboratory. Early results have been very promising; detectors approximately equal to the very best that we have made from Hoboken material have been made from crystals pulled in our laboratory.

During the calendar year 1967, 36 detector systems were put into service. Many of these incorporated some degree of mechanical isolation from the cold finger to reduce the microphonic noise generated by the boiling liquid nitrogen. A new high-resolution high-rate preamp amplifier system[1] was used with most of these detectors.

Reference

1. F. S. Goulding, D. A. Landis, and R. H. Pehl, UCRL-17560, May 1967.

10. THE ENERGY-RESOLUTION CAPABILITIES OF SEMICONDUCTOR DETECTORS FOR PARTICLES IN THE 10- TO 100-MeV RANGE†

F. S. Goulding, D. A. Landis, and R. H. Pehl

Recent advances in accelerators have resulted in the possibility of carrying out experiments with energy resolutions of about 0.02% FWHM. To fully utilize the energy-resolution capabilities of these machines, the system analyzing the reaction products must exhibit inherent fluctuations in the 0.02% FWHM region. Since existing semiconductor detector systems have not demonstrated this performance, we are driven to consider the use of very expensive magnetic analysis systems. In view of this we have attempted to make a serious estimate of the performance we can ultimately expect to realize with semiconductor detectors.

Several factors determine the energy resolution of detector systems, and their relative importance changes as a function of particle energy. We will deal with each of these factors in turn.

Detector Noise

The relative magnitude of the two components that contribute to detector noise depends upon such factors as temperature, applied voltage, amplifier pulse-shaping network time constants, etc. The first component, due to bulk leakage current, behaves in a reasonably predictable fashion, the leakage and its associated noise becoming smaller as the temperature is reduced and the mean-square noise voltage increasing linearly with increasing amplifier time constant. The second component, due to surface effects, is more difficult to predict; however, one can say that its value increases with increase in applied voltage, is dependent on the surface treatment of the detector, and that its mean-square value increases very rapidly with increasing amplifier time constant. Obviously, the common factor strongly influencing these two noise sources is the amplifier time constant, and from this point of view, the shorter the time constant, the better will be the

noise performance. Decreasing the detector temperature decreases the bulk leakage current and also reduces the charge-collection time in the detector. This is advantageous in that it permits use of shorter amplifier time constants.

Using a shaping network of about 0.5 μsec time constant in the amplifier, and a detector at -75°C, we can realize a total detector noise contribution to energy resolution of << 5 keV with no difficulty. Further reduction of the temperature is only possible if silicon exhibiting very little charge trapping is available.

Input-Amplifying-Stage Noise

Here we can use results obtained in work on high-resolution detector systems for lower-energy applications and make some reasonable extrapolations to higher energies. The detectors used in high-resolution nuclear reaction experiments exhibit capacities smaller than 5 pF. For high-energy applications, the feedback capacitor in the charge-sensitive loop must be increased from the small value used in low-energy applications--5 pF is a good general-purpose value. Therefore, the total input capacity will be about 10 pF.

A typical FET preamplifier using an optimally cooled UC250 will exhibit a FWHM energy resolution of (2+0.1C) keV for a Gaussian shaping network peaking at 0.5 μsec (where C is the added input capacity measured in pF). Therefore an input-stage noise contribution of 3 keV can be expected, and together with the detector noise, the total front-end noise should not exceed 5 keV.

Noise Due to Later Stages of Amplification

This is frequently a major source of noise in high-energy applications because of the use of general-purpose amplifiers designed for use with all types of radiation from 20-keV x rays to 100-MeV particles. However, it is a simple matter to design an amplifier especially for the 10-100 MeV range. Moreover, since the number of stages of amplification required is much smaller than in general-purpose amplifiers, the gain stability is also much improved.

Gain Stability

By use of low-temperature-coefficient resistors and air-conditioned equipment racks we are already achieving gain stabilities that are almost adequate. However, servo stabilization of gain will probably be required for long experiments.

Statistics of Charge Production in the Detector

The statistical nature of the sharing of energy between ionizing and other processes results in a spread in the signal. The mean-square fluctuation in the number of hole-electron pairs is given by $N^2 = F N$, where F is the Fano factor and N is the number of hole-electron pairs produced. Recent measurements indicate that the Fano factor in silicon is smaller than 0.15. Converted into energy, the FWHM spread due to this source is given by $E_{stat} = 2.35\sqrt{FE\epsilon}$. Since $\epsilon = 3.70$ eV for silicon at -75°C, we have $E_{stat} = 1.75\sqrt{E}$ keV, where E is the particle energy in MeV. The values given in Table I. 10-I and I. 10-II are calculated from this relationship.

Nuclear Collisions

When heavy particles pass through an absorbing medium, part of their energy is lost by collisions with the nuclei of the absorbing medium. This energy appears in the form of recoiling atoms of the absorber which knock out further atoms, producing virtually no ionization. Since only a small number of nuclear collisions occur in the track of particle, and the energy exchanges at these collisions are rather high, this causes rather a large statistical fluctuation in the output signal.

This effect has been analyzed by Lindhard and Nielsen,[1] who show that the dominant result is due to the very-low-energy portion of the particle's track.

For alpha particles:	E_{nucl} = 6.4 keV FWHM.
For protons:	E_{nucl} = 0.7 keV FWHM.

Trapping Effects in Detector

We have demonstrated that trapping effects are very significant in determining resolution at high energies, as the charge trapped is proportional to the energy of the incoming particle. Although insufficient data exist on this problem it seems reasonable to assume that the spread in signal resulting from trapping is proportional to $\sqrt{E}$. The effect varies a great deal with the quality of silicon used in the detector, but the use of good quality silicon at -75°C should result in no serious resolution degradation due to trapping for particles up to 100 MeV.

Background γ Pile-Up

Recent work indicates that slight tailing on peaks observed in nuclear reaction experiments in this energy range may be due to γ rays from the target producing signals at a high rate in the detector. These superimpose on the signals and can cause loss of resolution and tailing. No simple method of eliminating this effect has been found, but use of a bending magnet combined with shielding is an obvious (though fairly complex and expensive) solution if it is necessary. The use of a short amplifier time constant is also desirable to reduce these pile-up effects.

Detector Temperature Variations

The energy required to produce a hole-electron pair is a function of temperature. Measurements indicate a change of between 0.01 and 0.02%/°C. We note that this could easily be a major limitation, and to make its effect negligible, the detector temperature should be controlled to ±0.25°C.

Summary of Results

These various factors will be added together in quadrature since they are almost uncorrelated. The results are summarized in Tables I.10-I and I.10-II. The final two columns of these tables show the predicted experimental energy resolution allowing 0.075 and 0.02% respectively for beam spread (FWHM).

Footnote and Reference

†UCRL-17556; submitted to Gatlinburg Conference on Semiconductor Detectors and Associated Circuits, May 1967.

1. J. Lindhard and V. Nielsen, Phys. Letters 2, No. 5, 209 (1962).

Table I. 10-I. Anticipated energy resolution for protons.

ENERGY MeV	ELECTRONIC keV	DETECTOR STATISTICS keV	NUCLEAR COLLISIONS keV	BEAM .075% keV	BEAM .02% keV	TOTAL FOR .075% BEAM	TOTAL FOR .02% BEAM
10	5	5.5	0.7	7.5		10.5	
					2		7.7
20	5	7.8	0.7	15		17.6	
					4		10
30	5	9.6	0.7	22.5		25.0	
					6		12.4
40	5	11.1	0.7	30		32.3	
					8		14.6
50	5	12.4	0.7	37.5		39.8	
					10		16.7
60	5	13.6	0.7	45		47.0	
					12		18.7
70	5	14.7	0.7	52.5		54.8	
					14		20.9
80	5	15.7	0.7	60		60.2	
					16		23.0
90	5	16.6	0.7	67.5		67.5	
					18		25.0
100	5	17.5	0.7	75		75.0	
					20		27.0

XBL 675-1463

Table I. 10-II. Anticipated energy resolution for alphas.

ENERGY MeV	ELECTRONIC keV	DETECTOR STATISTICS keV	NUCLEAR COLLISIONS keV	BEAM .075% keV	BEAM .02% keV	TOTAL FOR .075% BEAM	TOTAL FOR .02% BEAM
10	5	5.5	6.4	7.5		12.3	
					2		10.0
20	5	7.8	6.4	15		18.8	
					4		11.9
30	5	9.6	6.4	22.5		25.8	
					6		14.0
40	5	11.7	6.4	30		33.2	
					8		15.9
50	5	12.4	6.4	37.5		40.3	
					10		17.8
60	5	13.6	6.4	45		47.3	
					12		19.8
70	5	14.7	6.4	52.5		55.0	
					14		21.8
80	5	15.7	6.4	60		60.2	
					16		23.9
90	5	16.6	6.4	67.5		67.5	
					18		25.8
100	5	17.5	6.4	75		75	
					20		28.3

XBL 675-1464

11. THE DESIGN AND PERFORMANCE OF A HIGH-RESOLUTION, HIGH-RATE AMPLIFIER SYSTEM FOR NUCLEAR SPECTROMETRY†

F. S. Goulding, D. A. Landis, and R. H. Pehl

Introduction

Improvements in electronic noise in preamplifiers, and the availability of germanium exhibiting a Fano factor of about 0.1, have made possible the achievement of an energy resolution of 2 keV or smaller in germanium γ-ray spectroscopy in the 1-MeV energy region. This has resulted in increasing emphasis on other factors such as the effect of counting-rate and rise-time sensitivity of pulse-shaping networks upon resolution.

Description of System

The linear amplifier part of the system (shown in Fig. I. 11-1) is designed to develop unipolar pulses with a single short differentiator (1 μsec) while all other unavoidable differentiating time constants are made very long (>0.1 sec). For the integrator, required to improve the signal-to-noise ratio, we have chosen to use a modified version of the active integrator.[1] We thereby obtain the almost Gaussian-shaped pulse shown in Fig. I. 11-2(a)--a shape which experience has shown to be very nearly optimum from the point of view of resolution with all practical detector-FET preamplifier combinations. A fast-output pulse is also provided [Fig. I. 11-2(b)] by the amplifier for use in timing and coincidence experiments, and for pile-up rejection purposes.

The major design problem in the main amplifier is the removal of the 120~ power supply ripple from the output. Since all the later stages are capable of passing frequencies as low as about 1 Hz, power supply ripple is a more serious problem than in more conventional amplifiers. It is avoided by careful attention to decoupling in the constant-current sources used as transistor loads in the operational amplifier stages which form the basis of the amplifier.

The single unwanted differentiating time constant, which cannot be avoided in the system, is due to the feedback network R_1C_F in the charge-sensitive preamplifier. To correct this pole-zero cancellation[2] is used, the amount being adjustable with a preset control mounted on the front panel.

The following points on the preamplifier-detector combination are also worthy of note:
(a) The detector is dc-coupled to the FET. This permits the use of the feedback voltage to monitor detector leakage. It also reduces stray capacities on the FET gate as compared with ac coupled systems.
(b) A delay time-constant box is inserted in the detector voltage supply line. Also included in this box is provision to inject a test pulse through the detector capacity. By matching the pulser peak height at the amplifier output to that of a known γ-ray peak, a direct measure of detector capacity can be made and its variation with voltage determined.
(c) The FET is mounted together with a power Zener diode on a high thermal resistance (≈200°C/W) post which mounts onto the liquid-nitrogen-cooled part of the system. Adjustment of the Zener current allows optimization of the FET temperature.

With correct adjustment of the pole-zero preamplifier decay correction, excellent results like those shown in Fig. I.11-3, I.11-4, and I.11-5 are realized by using the amplifier to drive a pulse-height analyzer. This is a vast improvement in performance as compared with earlier systems used in our laboratory. However, as is evident in Fig. I.11-5, trash between peaks is very significant at high counting rates. In order to produce a significant improvement in these results, the pile-up rejector system shown in block form in Fig. I.11-6 has been designed. The slow-output signal from the amplifier, used for pulse-height analysis, passes through a linear gate to the analyzer only when the pile-up rejector signifies that the pulse is "uncontaminated" by the other pulses. The pile-up rejector makes the decision based on examination of the fast-output pulse from the amplifier. Its logic circuits perform three tests on a pulse before allowing it to be regarded as valid:
(a) The pulse being considered must not have been preceded by another in a time interval shorter than an adjustable inspection time (variable from 5 to 25 μsec).
(b) No pulse must occur during the rise time and for 0.5 μsec after the peak of the pulse being considered.
(c) The pulse being considered must not contain a significant slow component. Since detectors vary in rise time the allowable "slowness" of a pulse is adjustable by the user.

Only if these three conditions are met is the pulse allowed to pass through the linear gate

into the analyzer.

Experimental Results

Experimental results demonstrating the performance of the system used with three different detectors are given in Figs. I.11-7 – I.11-10. The following characteristics were measured on a 5-cc planar detector using the complete amplifier and pile-up rejector system:

(a) γ-resolution at low rates on 1.33-MeV line: 1.90 keV. Pulser resolution: 1.35 keV. Fano factor F: 0.08.

(b) Resolution change at high rates (with complete system):

Rate	Resolution
1 kHz	2.0 keV
10 kHz	2.1 keV
50 kHz	2.35 keV

Figures I.11-7 and I.11-8 should be compared with Figs. I.11-3 and I.11-5. They illustrate that, while causing no degradation in the spectrum at low rates, the pile-up rejector cleans up the spectrum considerably at high counting rates. The background between the 1.16- and 1.33-MeV lines in Figs. I.11-8 and I.11-5 shows this very clearly. The next two figures are illustrations of the peak-to-Compton ratios achieved with different types of detectors. The best measured resolutions on the 1.33-MeV line were:

5-cc planar (capacity 8 pF): 1.8 keV; 15-cc double drift (capacity 13 pF): 2.1 keV; 40-cc coaxial (capacity 45 pF): 2.7 keV.

Although one might expect some degradation in resolution at low energies due to the effect of noise on the base-line corrector, very little indication of this effect is present at the energy of ^{57}Co. For lower energies there is little justification for using the pile-up system.

Footnote and References

†UCRL-17560; submitted to Gatlinburg Conference on Semiconductor Detectors and Associated Circuits, May 1967.

1. E. Fairstein and J. Hahn, Nucleonics 24, 54 (1966).
2. C. N. Nowlin and J. L. Blankenship, Rev. Sci. Instr. 36, 1830 (1965).

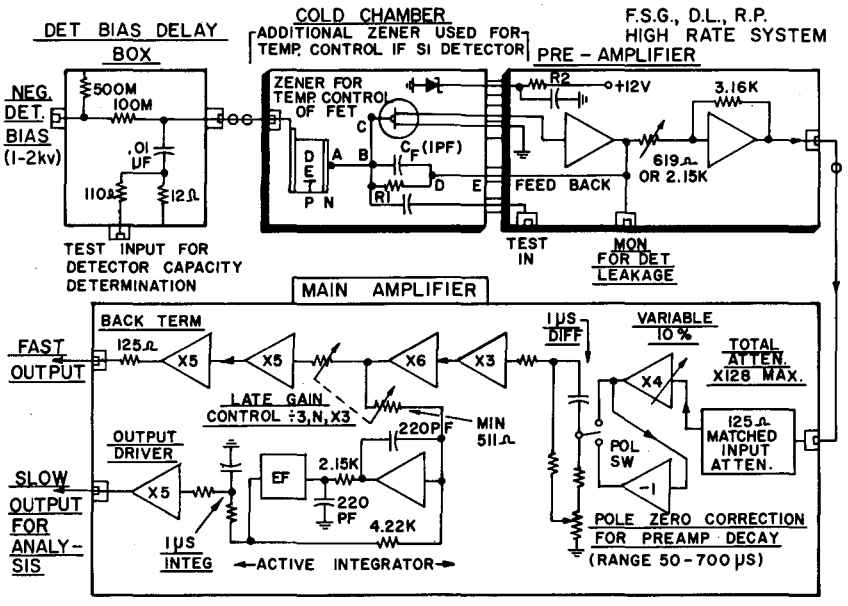

XBL 675-1468

Fig. I. 11-1. Essential features of high-rate system.

Fig. I. 11-2. Amplifier output pulse shapes.

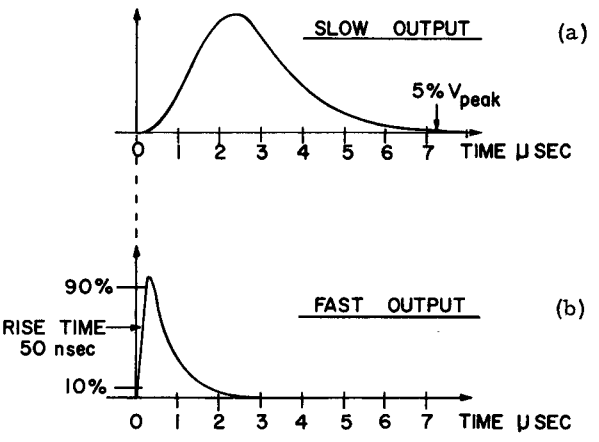

XBL 675-1470

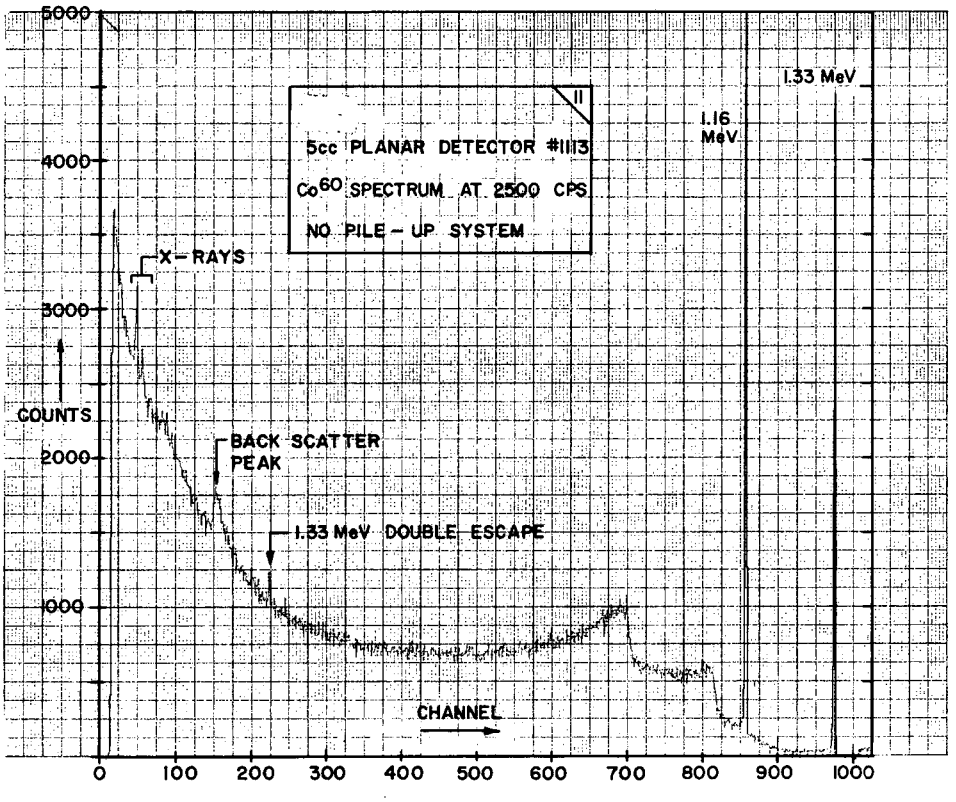

XBL 675-1471

Fig. I. 11-3. 5-cc planar detector; ^{60}Co spectrum at 2500 Hz (no pile-up system).

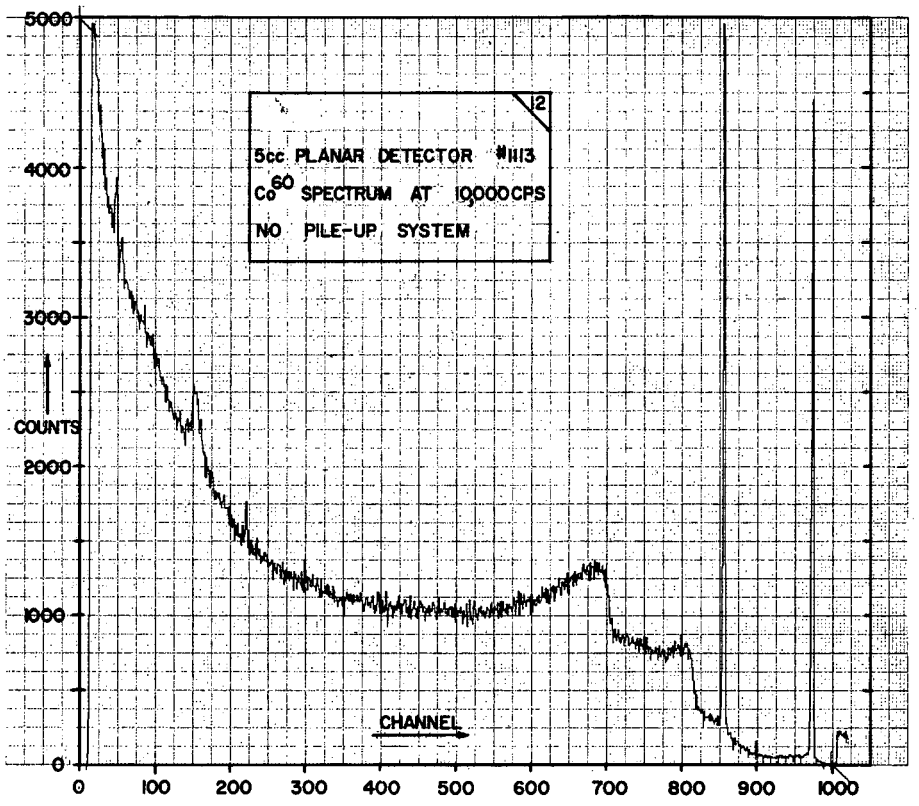

XBL 675-1472

Fig. I. 11-4. As Fig. I. 11-3 but at 10 000 Hz.

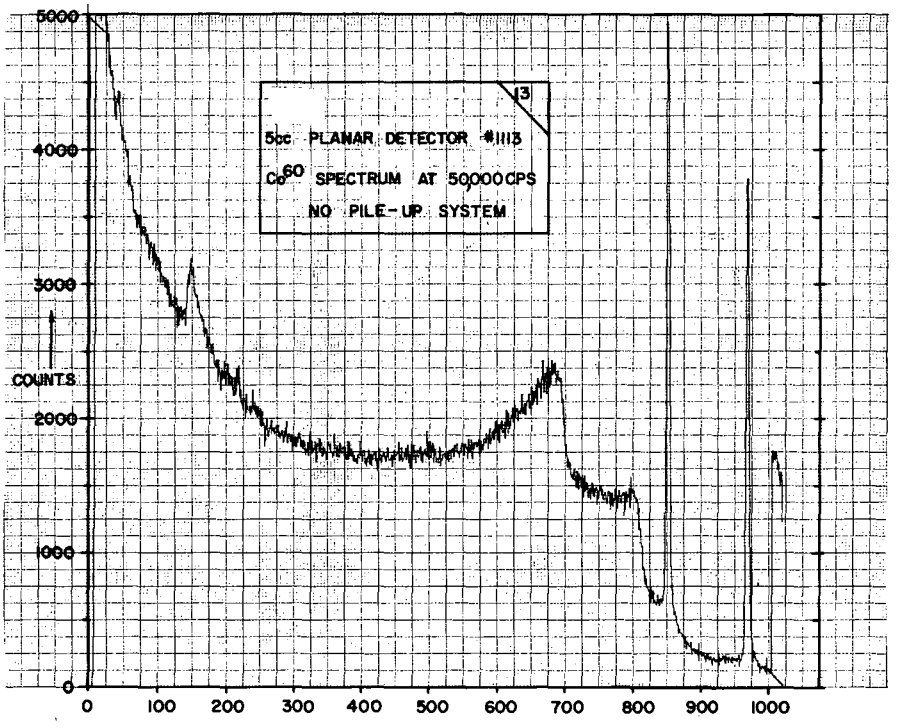

XBL 675-1473

Fig. I. 11-5. As Fig. I. 11-3 but at 50 000 Hz.

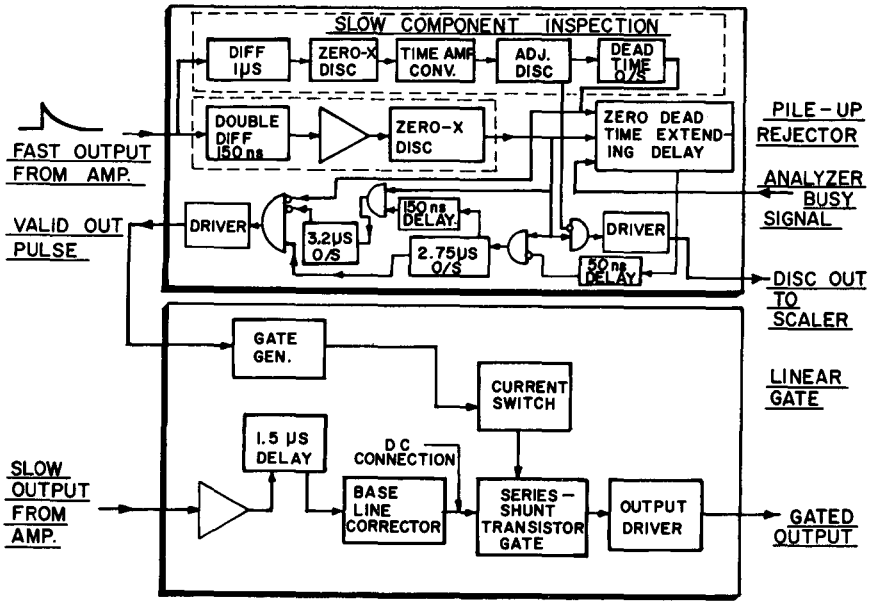

XBL 675-1474

Fig. I. 11-6. Block diagram of pile-up rejector and gate.

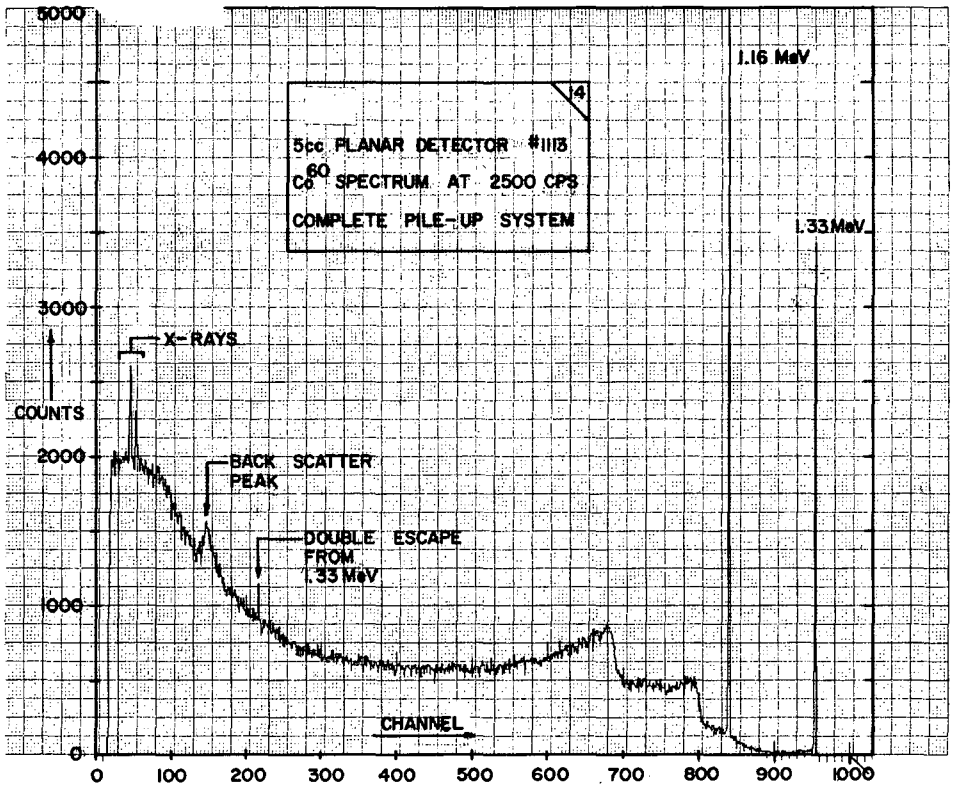

XBL 675-1476

Fig. I. 11-7. 5-cc planar detector; ^{60}Co spectrum at 2500 Hz (with pile-up rejector system).

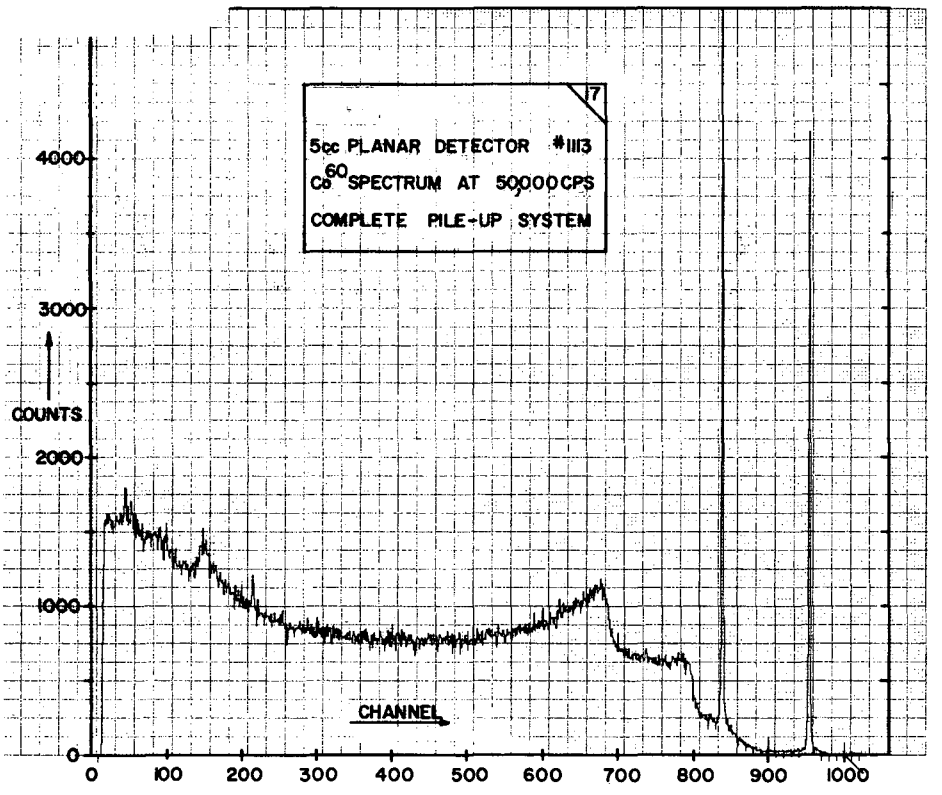

XBL 675-1478

Fig. I. 11-8. As Fig. I. 11-9 but 50 000 Hz.

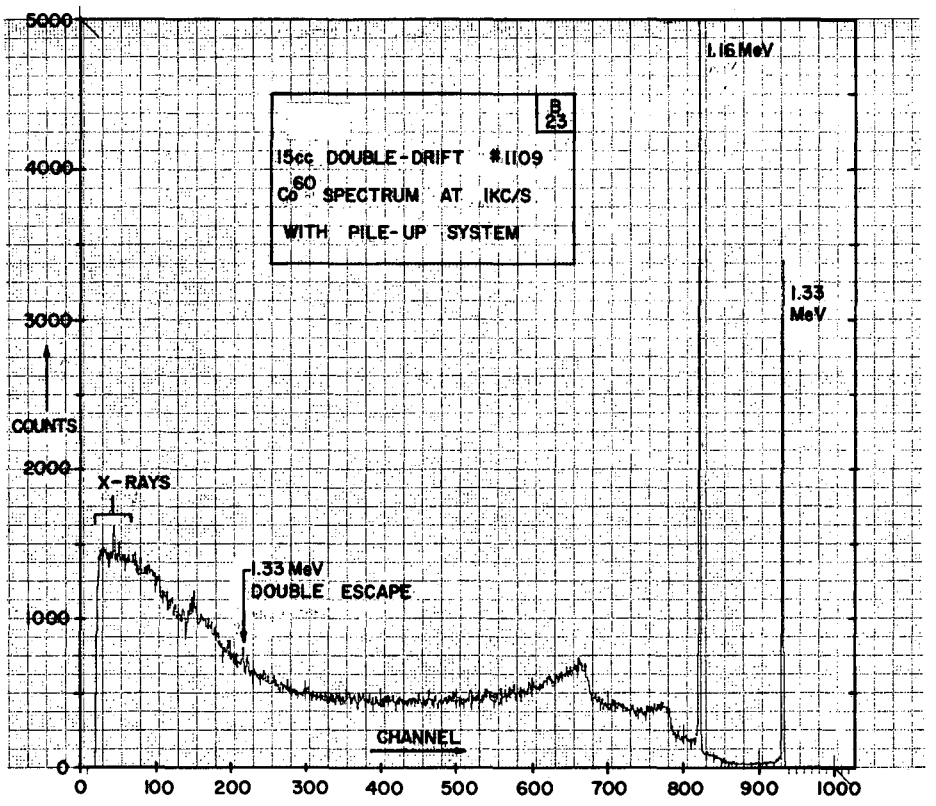

XBL 675-1481

Fig. I. 11-9. 15-cc double-drift detector; ^{60}Co at 1 kHz (with pile-up rejector system).

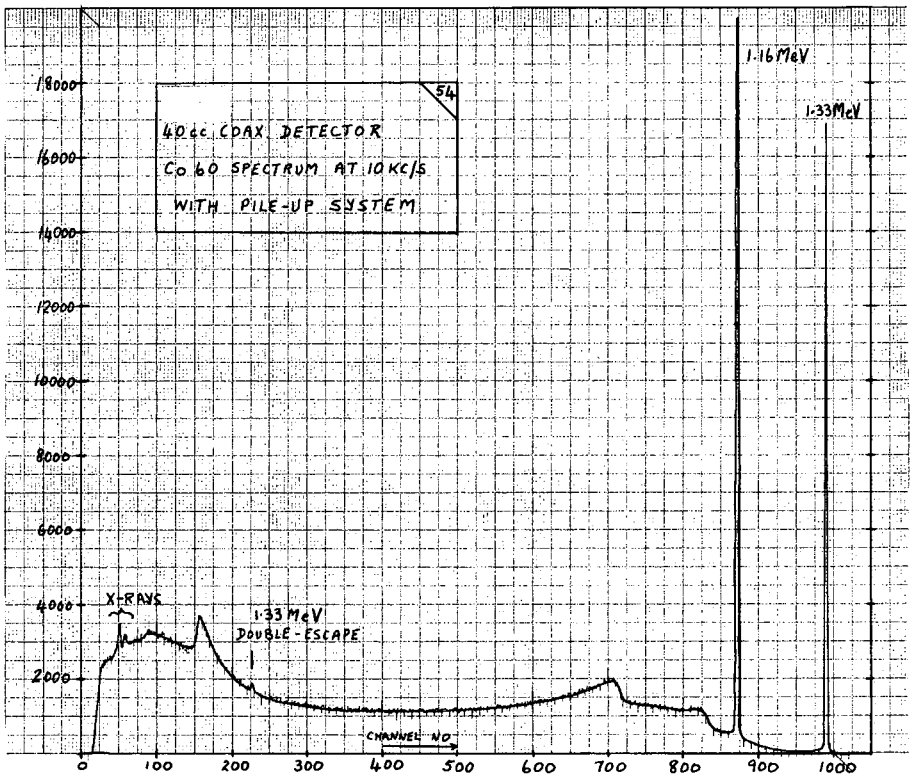

XBL 675-1482

Fig. I. 11-10. 40-cc coaxial detector; ^{60}Co at 10 kHz (with pile-up rejector system).

12. ACCURATE DETERMINATION OF THE IONIZATION ENERGY IN SEMICONDUCTOR DETECTORS†

Richard H. Pehl, Fred S. Goulding, Donald A. Landis, and Martin Lenzlinger

Several groups[1, 2] have reported a rather large difference in the value of ϵ, the average energy required to produce an electron-hole pair, for alpha particles relative to electrons in silicon. They found values of $\epsilon_\alpha = 3.61 \pm 0.01$ eV and $\epsilon_{e^-} = 3.79 \pm 0.01$ eV at a temperature of 300°K. Since we felt it was rather difficult to account for such a large difference we have undertaken an extensive program of determining ϵ, either to convince ourselves that such a large difference really exists, or to obtain counter information.

Figures I. 12-1 and I. 12-2 summarize our results on Si. Over the temperature range studied, ϵ appears to be a linear function of the temperature. Since the variation of the forbidden energy gap, E_g, with temperature is not a linear function,[3] if our ϵ data are plotted vs E_g (see Fig. I. 12-3)[g] one does not obtain a linear relationship as would be expected from a simple model. Making a short linear extrapolation to 300°K, we obtain $\epsilon_\alpha = 3.625 \pm 0.02$ eV, in excellent agreement with the published values.[1, 2, 4, 5] This value does not include any "window" correction, but such a correction is less than 0.02 eV.

However, the same extrapolation to 300°K results in $\epsilon_{e^-} = 3.67 \pm 0.02$ eV, considerably lower than the published values.[1, 2] The errors placed on our values are based on an estimate of

systematic errors; since the same system was used for determining ϵ_α and ϵ_{e^-}, the difference between these values should be determined very accurately. Thus, although there may be a slight difference between ϵ_α and ϵ_{e^-}, this difference now appears to be of the order of 1% instead of 5%. Why our data exhibit much less difference has not been resolved. However, preferential hole trapping could account for the observed difference. When an alpha particle source is used the holes do not have to travel as far as they do when an electron source is used, consequently there is more chance of the holes being trapped in the latter case. This would decrease the amount of charge collected for the incident electrons, and the apparent value of ϵ that is measured would increase.

Figure I. 12-4 compares our ϵ_{e^-} data against the published values[2] as a function of temperature. Note that not only are the ϵ_{e^-} values we have measured lower, but the rate of change of ϵ_{e^-} is less. This difference is more marked at colder temperatures, indicating that an appreciable amount of charge may have been trapped in the previous work. As can be seen from Figs. I. 12-1, I. 12-2, and I. 12-3, we find that the rate of change of ϵ as a function of temperature is the same for electrons and alpha particles, whereas the previous work[2] gave a considerably greater rate of change for electrons than for alpha particles. In fact, for ϵ_α we not only agree in absolute value but also in rate of change with the previous work.

In the second part of this experiment, one of our "thin window" Ge detectors[6] was studied over a temperature range from 90 to 180°K.

Figures I. 12-5 and I. 12-6 summarize our results on Ge. Over the temperature range studied, ϵ in Ge does not appear to be a linear function of temperature as was the case for Si. In fact, the degree of nonlinearity results in a linear relationship between ϵ and the published[3] variation of E_g for Ge within the accuracy of our data as illustrated in Fig. I. 12-7. Making a short extrapolation to 77°K, we obtain $\epsilon = 2.97 \pm 0.02$ eV for both electrons and gamma rays, in excellent agreement with the published values.[2,7] For alpha particles we find the same ϵ value as for electrons although the additional "window" problem makes these data less precise. To reduce the window problem, and to further the general investigation, ϵ in Ge will soon be measured by using long-range particles at the cyclotron.

Since our initial measurements on Ge indicate that $\epsilon_\alpha \approx \epsilon_{e^-}$, one is led to suspect that $\epsilon_\alpha \approx \epsilon_{e^-}$ in Si also, and that the differences that have been observed are not fundamental. However, the data for Ge are not precise enough at present to use as a conclusive point against the Si results. The fact that the relationship between ϵ and E_g apparently is linear for Ge whereas it is not linear for Si is rather surprising, and certainly worthy of more study.

Footnote and References

†To be published in Nuclear Instruments and Methods, and in the proceedings of the May 1967 Gatlinburg Conference that will be published in book form.

1. C. Bussolati, A. Fiorentini, and G. Fabri, Phys. Rev. 136, A1756 (1964).
2. F. E. Emery and T. A. Rabson, Phys. Rev. 140, A2089 (1965).
3. R. A. Smith, Semiconductors (Cambridge University Press, New York, 1959), pp. 351-352.
4. E. Baldinger, J. Gutmann, and G. Matile, Z. Angew. Math. Phys. 15, 90 (1964).
5. G. Fabri, E. Gatti, and V. Svelto, Phys. Rev. 131, 134 (1963).
6. F. S. Goulding and B. V. Jarrett, A Method of Making Thin-Window Germanium Detectors, UCRL-16480, January 1966.
7. S. O. W. Antman, D. A. Landis, and R. H. Pehl, Nucl. Instr. Methods 40, 272 (1966).

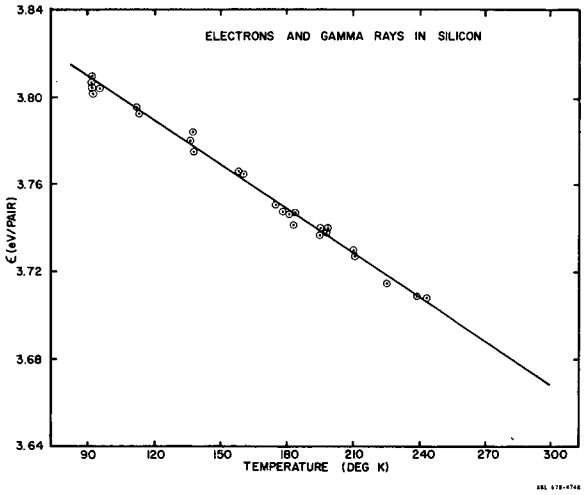

Fig. I. 12-1. Ionization energy for electrons and gamma rays in Si as a function of temperature.

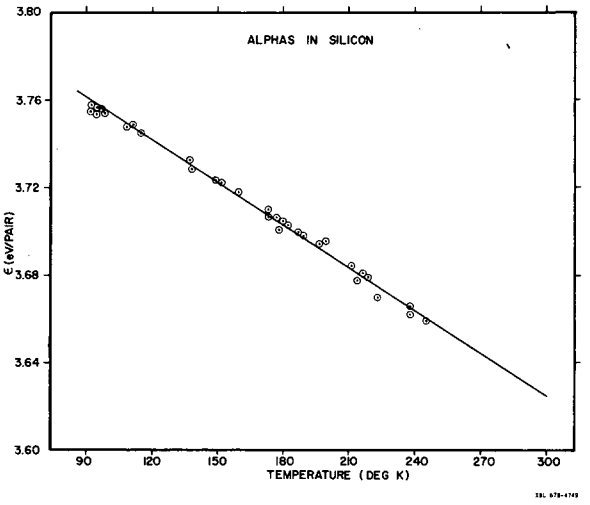

Fig. I. 12-2. Ionization energy for alpha particles in Si as a function of temperature.

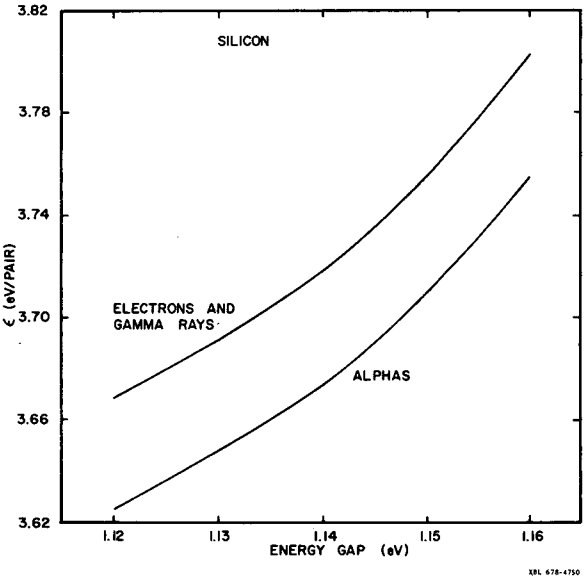

Fig. I. 12-3. Ionization energy in Si as a function of the forbidden energy gap.

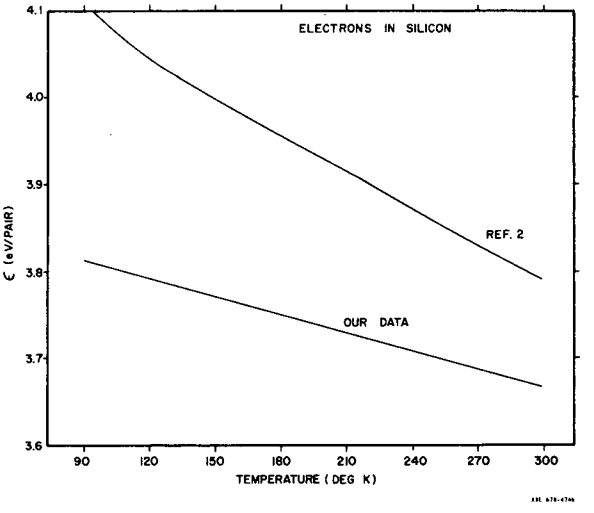

Fig. I. 12-4. Comparison of our ionization energy data for electrons in Si against the published values.

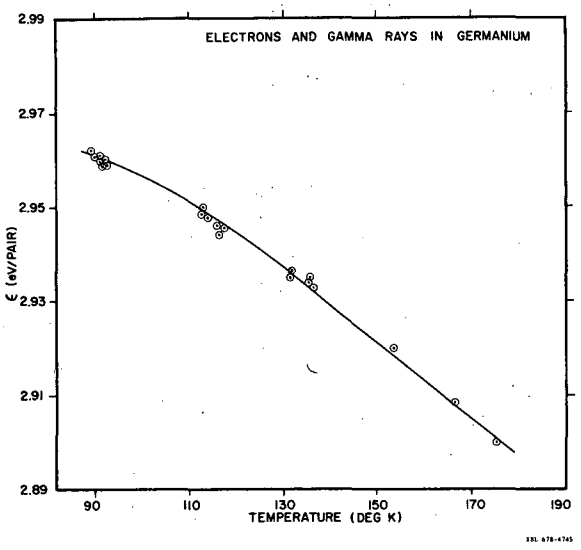

Fig. I. 12-5. Ionization energy for electrons and gamma rays in Ge as a function of temperature.

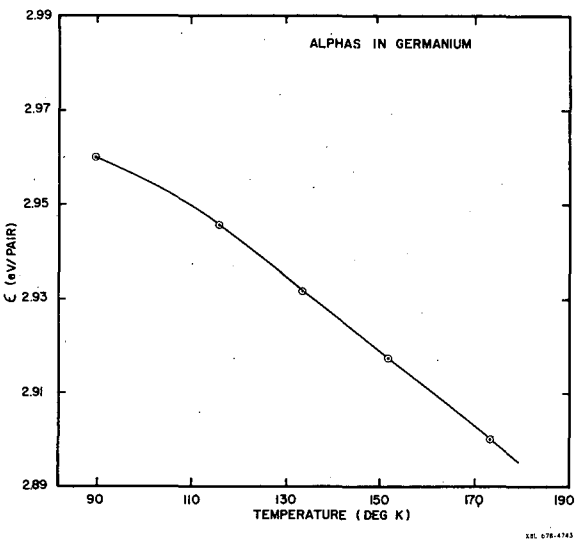

Fig. I. 12-6. Ionization energy for alpha particles in Ge as a function of temperature. A window correction of 0.02 eV has been included.

Fig. I. 12-7. Ionization energy in Ge as a function of the forbidden energy gap.

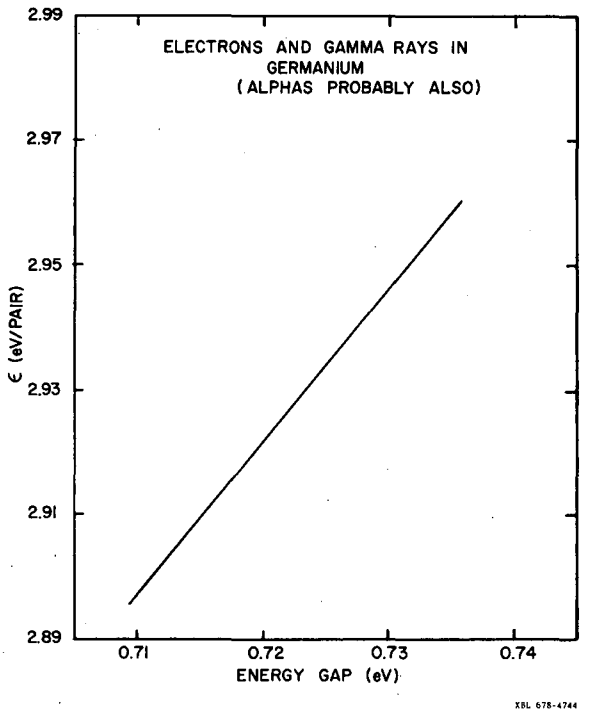

13. DIRECT VOLTAGE CALIBRATION OF THE IRON-FREE β SPECTROMETER

C. S. Fadley, G. L. Geoffroy, S. B. M. Hagström, and J. M. Hollander

The calibration of any magnetic β spectrometer requires the accurate determination of a constant connecting electron kinetic energy (T) to the quantity measured experimentally, by means of the characteristic equation of the spectrometer. This equation is derived from the relation

$$T = [(m_0c^2)^2 (\frac{e}{m_0c})^2 (B\rho)^2 + (m_0c^2)^2]^{1/2} - m_0c^2 , \quad (1)$$

where $B\rho$ = electron magnetic rigidity,
m_0 = electron rest mass,
c = velocity of light,
e = electronic charge.

For an iron-free spectrometer the magnetic field B should be strictly proportional to coil current (I) and ρ is fixed, so the characteristic equation becomes

$$T = [A(CI)^2 + D^2]^{1/2} - D, \quad (2)$$

with obvious replacement of constants.

The simplest technique for determining C is to measure the current corresponding to some primary $B\rho$ standard.[1,2] Another method is to measure the current ratios of two conversion electron lines whose energy difference is very accurately known.[3] These two techniques have been applied to the Berkeley iron-free spectrometer and have given consistent results.[4] A third technique involves measuring the current corresponding to electrons emitted from an electron gun with precisely known accelerating voltage.[5] The method described below combines the principles of the last two and gives a determination of C dependent only on current and voltage measurements.

With the aid of an apparatus designed for x-ray photoelectron spectroscopic work,[6] the current of a certain photoelectron line (I_0) is measured. A retarding field is then applied to the photoelectron source by means of an accurately measured voltage ΔT_-. The current of the shifted photoelectron line (I_-) is then measured. The same is done for ΔT_+ (= ΔT_-) and I_+. The three equivalent equations for T are then

$$T_1 = [A(CI_+)^2 + D^2]^{1/2} - D - \Delta T, \quad (3)$$

$$T_2 = [A(CI_0)^2 + D^2]^{1/2} - D, \quad (4)$$

$$T_3 = [A(CI_-)^2 + D^2]^{1/2} - D + \Delta T. \quad (5)$$

These equations are solved self-consistently for C and T by means of a trial-and-error computer program. The self-consistency or error parameter is

$$\alpha = |T_1 - T_2| + |T_3 - T_2|; \quad (6)$$

α is minimized by varying C in steps of 0.0001 G-cm/A about a previously determined calibration constant for the spectrometer. Defining α in this way gives a cusp at the minimum and therefore permits very accurate determination of C (and thus T). The method could in principle be applied to radioactive electron sources and/or electron spectrometers with different characteristic equations.

The photoelectron line used for calibration was that from carbon 1s electrons expelled from a powdered graphite sample by aluminum Kα radiation [denoted C1s, graphite (AlKα)]. This line has an energy of about 1200 eV. ΔT was varied from 100 to 600 eV with no systematic change in the C values obtained. Variation of the x-ray flux by a factor of 20 also did not change C significantly. The average values from nine measurements are C = 78.6949 ± 0.0057 G-cm/A, T = 1197.80 eV, and α = 0.05 eV. The error quoted on C includes both random and systematic contributions.

Unfortunately, there appear to be limitations on the type of sample that can be used for this calibration procedure. Attempts to use lines from two ionic crystals [Na1s, NaCl(AlKα) and Na1s, $Na_2S_2O_3$ (AlKα)] were unsuccessful, apparently because of a screening of the accelerating or retarding potential. The effective potential was found to be 0.2-0.9 ΔT and strongly dependent on x-ray flux. Such screening has been observed[7] previously in NaCl but the exact cause is as yet unclear. A slight screening effect could even be present with the line C1s, graphite (AlKα) but the constancy of C with variation in x-ray flux indicates the magnitude of any such effect is probably less than $3:10^4$.

As an independent check, calibrations were made by using the Mg1s, MgO(CrKα_1) line as a primary standard.[2] This line has an energy of about 4100 eV. The measured energy of this line was found to vary systematically with x-ray flux, causing a corresponding change in C. This effect is shown in Fig. I. 13-1, where we use counts at peak intensity as an indicator of total x-ray flux. This shift in line position could be due to charging of the sample by the photoelectric emission. Such charging was investigated in the original Bρ measurement of this line[2] by comparing the energies of the two lines: Al1s, Al deposited on Al(CuKα_1) and Al1s, Al deposited on insulating Mylar (CuKα_1). No shift was found between these lines[1], indicating negligible charging for this metallic sample even when it is insulated from the spectrometer. Our results, on the other hand, indicate that the effect of charging could introduce an absolute error of up to $3:10^4$ in the Bρ value assigned to the line Mg1s, MgO(CrKα_1). Further investigation will be necessary, however, to determine the exact cause of the shift in Fig. I. 13-1. The C value obtained from eight measurements on MgO at ≈12 000 peak counts/12 sec is C = 78.7058 ± 0.0047 G-cm/A. Charging and/or slight screening effects can thus easily explain the $1:10^4$ discrepancy between the two calibration techniques.

References

1. K. Siegbahn, in Alpha-, Beta-, and Gamma-Ray Spectroscopy, Ed. by K. Siegbahn (North-Holland Publishing Co., Amsterdam, 1965), p. 193.
2. S. B. M. Hagström and S.-E. Karlsson, Ark. Fysik 26, 451 (1964).
3. K. Siegbahn, Ark. Mat. Astr. Fys. 28B, No. 6 (1941).
4. T. Yamazaki and J. M. Hollander, Nucl. Phys. 84, 505 (1966).
5. D. I. Meyer and F. W. Schmidt, Phys. Rev. 94, 927 (1954).
6. C. S. Fadley, S. B. M. Hagström, M. P. Klein, and D. A. Shirley, UCRL-17005, August 1967.
7. K. Siegbahn, private communication.

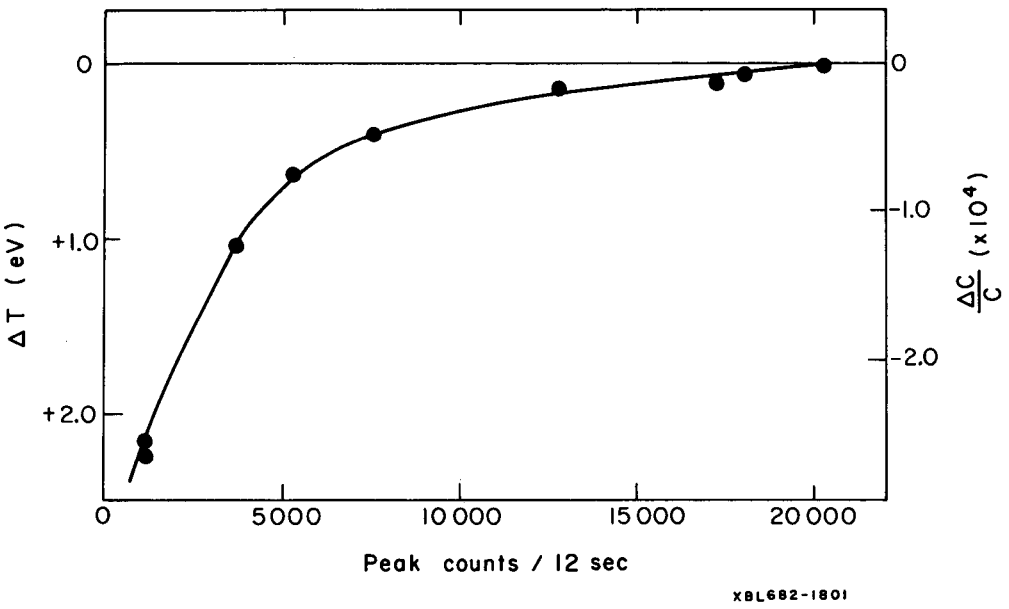

Fig. I. 13-1. The effect of x-ray flux variation (as indicated by peak counts) on the location of the photoelectron line Mg1s, MgO($CrK\alpha_1$). Both the shift in line kinetic energy and the fractional change in calibration constant are shown.

14. 88-INCH-CYCLOTRON DEVELOPMENT

D. J. Clark, P. Frazier, A. Luccio, D. Morris, and F. Resmini

The improvements made to the 88-inch cyclotron during 1967 included a number of new components in the cyclotron and beam handling system, and some cave rearrangement.

Internal Beam Region

During a shutdown in January the normal ion source was moved from the top of the magnet yoke to the bottom. This provides space on top for the permanent installation of the axial injection system and polarized-ion source. The axial injection system of electric quadrupoles was redesigned with a larger aperture using triplets instead of doublets. Studies of the beam optics were made through the section of increasing magnetic field in the 8-in. plug to optimize beam transport.

In the acceleration region, the original "defining slits" in the dee were modified to be used at radii of 5-10 inches. An additional "half-turn" slit was installed to define the beam phase about 180 deg after the ion source on the first particle revolution. This slit retracts behind the ion source when not being used. A new C probe was built with several separate sections for beam monitoring from 15-39 in. radius. A ^{3}He ion source gas recovery system was installed. This system recovers over 90% of the ^{3}He gas, giving a large saving in ^{3}He costs. A 10-in. oil diffusion pump was installed on the dee tank with liquid nitrogen baffle. This gives a factor of 2 lower pressure in the acceleration region. Another test was made on the new regenerative deflection system with H. Kim of the University of Maryland. This test verified the previous result that the extraction efficiency was 50-70%, about the same as with the old deflector. However, there were still some problems in holding deflector voltage for the highest energies, so the old deflector was installed again.

External Beam Region

In the external beam region, the switching magnet regulation was improved by using a nuclear magnetic resonance probe in the magnet gap, to feed the regulator. Fast vacuum valve development was done. By using gunpowder with a Teflon gate, a closing time of 2 msec was obtained.

Two new small scattering chambers were built for Cave 1, and a third beam line added there. In Cave 3 the Biomed line was moved to make space for the high-resolution line to Cave 4. Cave 4 line was designed and the cave built. The two 110-deg magnets are fabricated and being installed. A 1000-A transistor bank regulator was built for them and is being tested.

Beam Development

Beam development work in recent months has been mainly devoted to the investigation of a possible single-turn operation for the 88-inch cyclotron. That mode of operation consists in achieving a definite separation between all successive turns in the cyclotron, thus providing a spatially well-defined beam at the extraction radius. Single-turn extraction can only be attained if both the phase width of the beam and the amplitude of radial oscillations are severely restricted, e.g., by means of suitable defining slits in the center of the machine. Typical figures for the 88-inch cyclotron should be 6-8 deg for the phase width and about 1 mm for the oscillation amplitude.

Although these restrictions are likely to limit the amount of accelerated beam, single-turn extraction presents some interesting features, which can be summarized as follows: higher extraction efficiencies (in principle up to 100%) can be reached, thus much reducing septum problems. The energy resolution of the beam produced by the cyclotron is improved and could be, for the phase widths given above, of the order of 0.15%. Higher transmission efficiencies and lower overall background are in turn obtained when external energy analyzing magnets are used. Emittance of the external beam is improved, giving better beam transport.

Present single-turn extraction studies are carried out on the 30-MeV α beam (15-MeV deuterons). That choice has been determined by the actual ripple of the rf voltage (0.8%), which limits the number of turns that can, one hopes, be separated to about 120. This is approximately the case of 30-MeV α's accelerated with 50-kV peak dee voltage (150 turns). The phase width of the beam is defined by a collimator set on the first half-turn of the accelerated particles. A width of 6 deg is commonly used, which corresponds to a gap of about 1.5 mm. The radial width of the beam is successively restricted to 2 mm by a defining slit having a gap of the same order and positioned at a radius of 6.5 in., where the beam energy is approximately 0.85 MeV.

Experimental work on this beam is still in a preliminary stage. However, some results are already available. A typical turn pattern of the internal beam, as given by a wire probe driven along a machine radius, is shown in Fig. I. 14-1. Turns are completely resolved for 10 revolutions. Then the pattern smears out, an effect due to the remaining radial oscillation amplitude and the rf ripple. The turns are, however, still partially separated up to the extraction.

The extraction efficiency reached to date is about 80%, depending on the tuning accuracy. This high efficiency indicates that the cyclotron operates, at least partially, with single-turn extraction. External currents of 1 μA have been obtained. However, no attempts have been made so far in order to establish the upper limit of the extracted beam intensity, which is mostly a problem of source limits.

Measurements of the phase width, quality, and energy resolution of the external beam, which are of course needed in order to evaluate the possible advantages of single-turn extraction, are now in progress.

Polarized-Ion Source

The design of the polarized proton and deuteron source for the 88-inch cyclotron has been completed, and the construction of the various parts is in progress. After a careful consideration of the possibility of purchasing the entire system or components from industrial firms, we decided to build the source ourselves at LRL, with the exception of the ionizer system, which has been ordered from the ORTEC Company. Completion schedule of the source is for June 1968.

The scheme we decided to use resembles closely the successful source at Saclay, France. We have chosen, however, a different set of rf transitions, which appeared to us more simple, while leading to the same final resulting values of the proton and deuteron polarization. The injection scheme into the cyclotron is axial, through a hole in the upper pole and yoke. Studies to improve the axial injection transport system are in progress.

Figure I. 14-2 shows the mechanical design of the source, mounted with its axis vertical above the cyclotron vault shielding. Atomic hydrogen or deuterium is produced from molecules in the discharge tube (D), of the conventional "hairpin" design, driven by an rf power supply. An atomic beam is then formed by effusion from a nozzle and successive collimation through two holes in the walls of the "beam" (B) and "collimation" (C) chambers. B is evacuated by means of a 1600-cfm Roots pump and C by two 10-in. Hg diffusion pumps.

Next, the beam is split into its magnetic components by a sextupole magnetic lens 50 cm long, with longitudinally tapered pole pieces (M). A set of two rf transitions, by the adiabatic passage method, operate the following interchanges of the population of sublevels (labeled according to their decreasing energies as "1", "2", ...):

Element	Transition	Frequency (MHz)	Polarization
S	"3" - "5"	331	P_{zz} = -1 deuterons
S	"2" - "6"	458	P_{zz} = +1 deuterons
W	"1" - "4"	7.5	P_{z} = -2/3 deuterons
W	"1" - "3"	7.5	P = -1 protons

The vacuum box containing M, S, W is evacuated by means of a 10-in. oil diffusion pump.

As a last stage, the ionizer (I) provides the ionization of the atomic beam by electrons confined in a longitudinal magnetic field of about 2000 G. By reversing the sign of the field, it is possible to reverse the sign of vector polarization for protons or deuterons. In order to keep the background as low as possible in the ionizer region, its vacuum box has liquid-nitrogen-cooled baffles and is evacuated by an electro-ion pump.

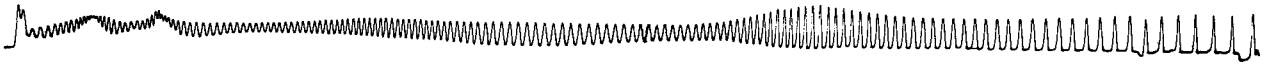

XBL 682-105

Fig. I. 14-1. Internal beam pattern with wire probe from 39 to 5 in. radius (from left to right). The beam is 15-MeV deuterons. The phase width is 7 deg with 50 kV on the dee. Both half-turn and defining slits were used.

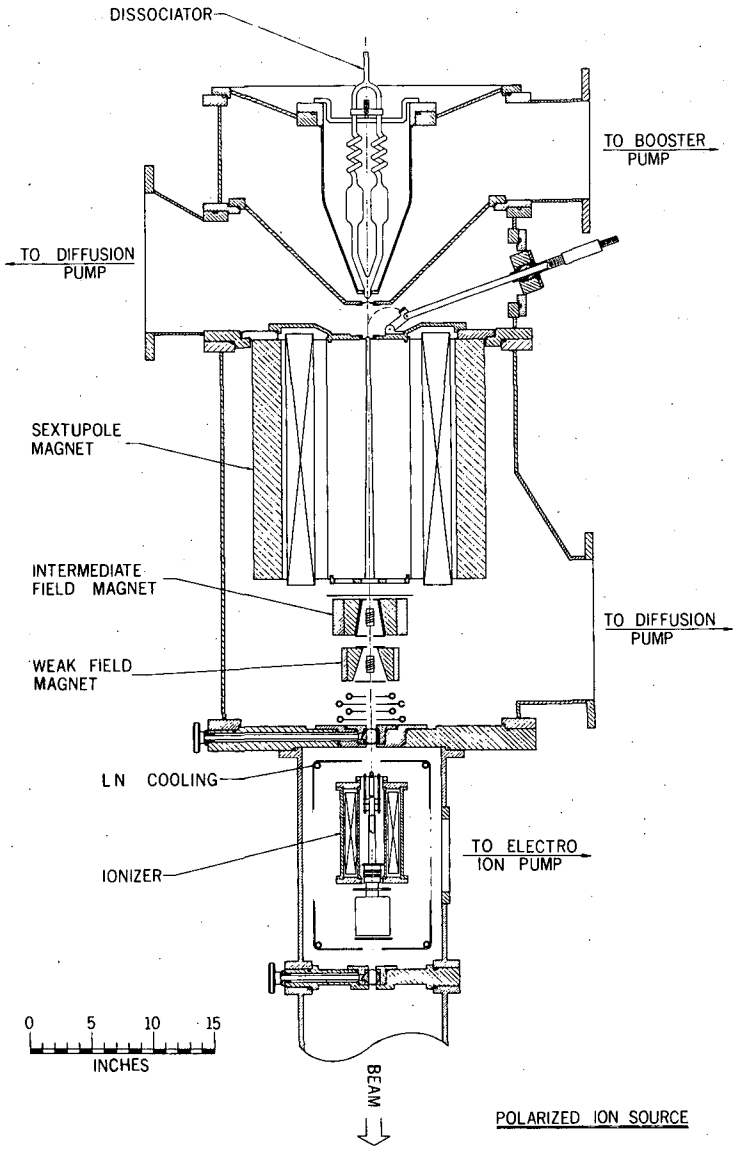

Fig. I. 14-2. Polarized-ion source design now under construction. Atomic hydrogen or deuterium is produced by the dissociator, separated magnetically by the sextupole. Transitions take place in the following section,and a polarized-ion beam is given by the ionizer.

J. THESIS ABSTRACTS

On the following pages the abstracts of theses issued in 1967 are given as they appeared in the original documents.

1. MASS AND SPECTROSCOPIC MEASUREMENTS OF COMPLETE ISOSPIN QUARTETS IN THE LIGHT NUCLEI

Gilbert W. Butler
(Ph. D. Thesis)

(From UCRL-17783)

The mass 13, 21, and 37 isospin T = 3/2 quartets have been completed through a series of nuclear reaction investigations. A standard particle identifier was used to measure the mass of the $T_z = -3/2$ nuclide ^{13}O via the $^{16}O(^3He, ^6He)^{13}O$ reaction at 65 MeV. An improved particle-identification system, which employed two transmission (dE/dx) and one stopping (E) detector, was used to determine the masses of the $T_z = -3/2$ nuclei ^{21}Mg and ^{37}Ca via the $^{24}Mg(^3He, ^6He)^{21}Mg$ and $^{40}Ca(^3He, ^6He)^{37}Ca$ reactions at 56 MeV. The first three T = 3/2 levels in ^{21}Ne were established by a simultaneous study of the $^{22}Ne(d, t)^{21}Ne$ and $^{22}Ne(d, ^3He)^{21}F$ reactions at 39.6 MeV, while the $^{23}Na(p, t)^{21}Na$ reaction at 42 MeV was utilized to observe the lowest T = 3/2 level in ^{21}Na. Excitation energies of the lowest T = 3/2 levels in ^{37}K and ^{37}Ar were determined via the $^{39}K(p, t)^{37}K$ and $^{39}K(p, ^3He)^{37}Ar$ reactions induced by 45-MeV protons. Data from the complete isospin quartets were used to test the isobaric multiplet mass equation and the various predictions of masses of neutron-deficient nuclei. Preliminary studies of the angular distributions of the $^{16}O(^3He, ^6He)^{13}O$, $^{16}O(^3He, ^6Li)^{13}N$, $^{16}O(^3He, ^7Li)^{12}N$, and $^{16}O(^3He ^7Be)^{12}C$ reactions at 70 MeV are also presented.

2. MASS AND HEAT TRANSFER PROCESSES IN LAMINAR, TWO-PHASE FLOW

Michael W. Clark
(Ph. D. Thesis)

(From UCRL-17527)

High flux and high concentration level heat and mass transfer experiments have been carried out for several gas-liquid systems which exhibited resistance to transfer in both the liquid and gaseous phases. These experiments were carried out in a horizontal, rectangular duct of high aspect ratio, in which the gaseous and liquid phases were contacted while moving in stratified, laminar cocurrent flow. A calculational method, which utilizes the principle of addition of the individual phase resistances in a trial and error manner, was developed and utilized to predict the interphase high flux, high concentration level mass transfer behavior of the system. In order to ascertain the gas phase resistance for this model accurately, the equation of convective diffusion was solved numerically for the case of a finite interfacial mass flux (high flux) combined with a linear velocity profile away from the mass transfer interface (the Leveque model). The flux level correction factor obtained from this solution, which differed only slightly from the penetration model correction factor, was confirmed experimentally be evaporating isopentane and n-pentate into a flowing nitrogen stream.

During the course of the interphase mass transfer experiments a large reduction in the liquid phase resistance to mass transfer was observed at higher concentration levels of the

volatile components. This reduction was ultimately traced to a form of cellular convection in the liquid phase which appeared to be driven by surface tension variations brought about by the concentration gradients existing in the system. The effect of this type of cellular convection upon the experimentally observed, liquid-phase mass transfer coefficients for several systems was well represented by a single correlation involving the Thompson number.

3. PREPARATION AND CRYSTALLOGRAPHIC ANALYSIS OF CALIFORNIUM SESQUIOXIDE AND CALIFORNIUM OXYCHLORIDE

J. C. Copeland
(M. S. Thesis)

(From UCRL-17718)

This study was undertaken to extend the knowledge of the physical and chemical properties of californium. The preparation and crystallographic analysis of a low-temperature californium oxide of near-sesquioxide stoichiometry and of californium oxychloride have been carried out.

In an earlier study, 6 μg of Cf^{249} were purified. The purification techniques and analytical methods used for analysis of purity are summarized. Results of the purity evaluation indicated that the samples were adequately pure with respect to lanthanides and other actinides, but that impurities such as Ca or Al were potentially present. Because of the reasonably long half-life of Cf^{249}, the self-contamination of the sample since the time of purification was small.

Three samples of the low-temperature, cubic, Mn_2O_3-type californium "sesquioxide" were prepared. Two of these samples, prepared by the hydrolysis of other californium compounds, gave the same lattice parameters, within the error limits with the average lattice parameter being $a = 10.838 \pm 0.02$ Å. The third sample, reacted in oxygen, had the lattice parameter $a = 10.809 \pm 0.003$ Å. In an earlier study, the lattice parameter of an air-ignited oxide sample was significantly smaller than the parameter of the same sample after heating in hydrogen. If these differences in lattice parameter reflect varying stoichiometries, then this might be evidence for higher and/or lower oxidation states of californium. The exact stoichiometries of the oxide samples prepared in this study are not known.

Three samples of californium oxychloride were prepared and were studied by x-ray diffraction techniques. The CfOCl had the tetragonal PbFCl-type structure and gave the average lattice parameters $a = 3.956 \pm 0.002$ Å and $c = 6.662 \pm 0.009$ Å.

The error limits reported for the lattice parameters of CfOCl and "Cf_2O_3" from the hydrolysis reactions are based on a statistical analysis of the consistency of the group of measurements. The limits placed on the lattice parameter of the "Cf_2O_3" sample from the reaction with oxygen represent the 95% confidence level and reflect the internal consistency of the data for that particular sample.

4. ELECTRON PARAMAGNETIC RESONANCE STUDIES OF RADIOACTIVE TRANSITION-METAL IONS

Warren Cliett Easley
(Ph. D. Thesis)

(From UCRL-17699)

Electron paramagnetic resonance (EPR) was observed in 253d Ag^{110m}, present as Ag^{2+} in the $[(iso\text{-}C_3H_7)_2NCS_2]_2Ag$ complex. Eleven hfs (hyperfine structure) lines were observed, the positions of the other two lines being obscured by other absorptions present in the sample, and

the nuclear spin of 6 was confirmed. A hfs constant $a_{110m} = (7.108 \pm 0.02) \times 10^{-3}$ cm^{-1} was determined. A hyperfine anomaly of $\Delta_{107,109} = -0.40\% \pm 0.1\%$ was observed for stable Ag^{2+} in this complex, indicating that the hfs arises from contact interaction. A nuclear moment of $\mu_{110m} = +3.55 \pm 0.04$ nm was derived after a 3.7% hyperfine-anomaly correction. The nuclear moment does not agree with shell-model predictions using empirical g factors, being low by 1 nm. It is suggested that the $(g_{9/2})^7$ proton configuration might be coupled to spin 7/2. This yields a moment of +3.54 nm.

EPR experiments on yttrium ethylsulfate single crystals containing terbium isotopes in the ratios $Tb^{158}/Tb^{157}/Tb^{158} = 2.5/1.6/1$ were carried out at Q-band frequencies (35 GHz). The nuclear spin of Tb^{158} was found to be 3 and by comparison with the observed hyperfine structure of Tb^{159} and its known nuclear moment, a magnetic moment $\mu^{158} = 1.740 \pm 0.007$ nm was calculated. Transitions due to Tb^{157} were not observed, presumably because they were obscured by the stronger Tb^{159} lines. Assuming $I^{159} = I^{157} = 3/2$, the following limits were set on the value of μ^{157}: $1.88 \leq \mu^{157} \leq 2.10$. Tb^{160} lines were also observed in YES single crystals. They gave $\mu^{160} = 1.685 \pm 0.008$ nm. Nuclear alignment experiments on Tb^{158} in a single crystal of neodymium ethylsulfate were also carried out in order to determine a relationship between the quadrupole coupling constant and the magnetic hyperfine structure constant. This information, as well as existing nuclear orientation results on Tb^{160}, was combined with the EPR data to obtain quadrupole coupling constants. Quadrupole moments calculated from the coupling constants were found to be:

$$Q^{158} = 2.7 \pm 0.5 \text{ barns and } Q^{160} = 3.0 \pm 0.5 \text{ barns.}$$

The first well-verified divalent actinide ion, Am^{2+} ($5f^7$, nominal $^8S_{7/2}$), was stabilized in a calcium fluoride single crystal and characterized by EPR and optical spectroscopy. Reduction of the trivalent ion was obtained by solid-state electrolysis and/or as a result of the emission of ionizing α-radiation during the americium nuclear decay. The radiation-reduced crystals were observed to thermoluminesce at 500°C; emitting radiation characteristic of the Am^{3+} ion. The electrolytically-reduced crystals did not thermoluminesce. EPR measurements at liquid helium temperatures showed the Γ_6 crystal-field state to be lowest in energy. The X-band EPR spectra were fitted with the following spin Hamiltonian parameters:

$$|g| = 4.490 \pm 0.002, \quad |A|\ (Am^{243}) = (1.821 \pm 0.002) \times 10^{-2} \text{ cm}^{-1},$$

$$|A|\ (Am^{241}) = (1.837 \pm 0.002) \times 10^{-2} \text{ cm}^{-1}, \quad I^{241} = I^{243} = 5/2 \ .$$

Analysis of the americium hfs allowed the determination of a contact hfs constant (corrected for the effect of the crystal field) $a_c = (-)\ 9.01 \times 10^{-3}$ cm^{-1}. This is equivalent to a hyperfine magnetic field per unpaired 5f electron of (-)285 kilogauss. Measurements on isoelectronic $^{244}Cm^{3+}$ ($I = 0$) at sites of cubic symmetry were also carried out, yielding an isotropic g value which agreed within experimental error with that of Am^{2+}. Two charge-compensated sites with trigonal symmetry about the [111] axes of the cube were also observed. The components of the g tensors were found to be:

$$g_{\parallel}\text{(site I)} = 3.41 \pm 0.02, \quad g_{\perp}\text{(site I)} = 6.88 \pm 0.02$$

$$g_{\parallel}\text{(site II)} = 2.69 \pm 0.02, \quad g_{\perp}\text{(site II)} = 5.91 \pm 0.02.$$

Subsequent studies at Q-band frequencies allowed the cubic crystal-field splittings to be determined. The splitting between the ground Γ_6 state and the first excited Γ_8 state was found to be 13.4 ± 0.5 cm^{-1} and 18.6 ± 0.5 cm^{-1} for Cm^{3+} and Am^{2+} at cubic sites in CaF_2, respectively. The splittings are shown to be due primarily to the effects of intermediate couplings on the ground state wave function.

5. ANALYTICAL METHODS IN BACTERIAL KINETICS

Victor Henry Edwards
(Ph. D. Thesis)

(From UCRL-16398)

This three part thesis is mainly concerned with the development of methods useful in the study of the kinetics of bacterial growth and metabolism. In the first part of this work, a comprehensive review of the literature of mathematical models for bacterial growth is given. A computerized method for the analysis of batch culture kinetic data is presented that fits a generalized logistic equation to the data. The fitted equations are useful for interpolation, integration, differentiation, and other manipulations of the data.

In the second part of this work, experimental data obtained with a salt tolerant strain of sulfate-reducing bacteria grown in both batch and continuous culture is presented and a novel continuous culture apparatus is described. The data, which were taken for use in evaluation of the feasibility of projects using these bacteria, are analyzed using the computer program developed in the first part of this work. The results are correlated and discussed in relation to some of the proposed models discussed in the first part of this work.

In the third part of this work, a sophisticated apparatus for measuring bacterial cell-size concentration distributions is described. The technique, based on a resistance principle, is shown to differentiate between normal cells and heat-killed cells, a result that should be of considerable use in the study of bacterial sterilization kinetics. The apparatus is calibrated and used in obtaining information on the cell size under a variety of experimental conditions. A computer program for the analysis of the computer-coupled output is presented. The system described will provide a powerful tool in the study of microbial kinetics.

6. THE MAGNETIC MOMENT OF PLUTONIUM-239

John Faust
(Ph. D. Thesis)

(From UCRL-16999)

The triple-loop technique of atomic-beam magnetic resonance has been used to determine the magnetic moment of plutonium-239 directly. The final measurement was carried out at a magnetic field of 720 gauss and the magnetic moment was found to be

$$\mu_I = +0.200(4) \text{ nm (corrected)} ,$$

where the sign is measured to be positive.

Hyperfine-structure measurements on plutonium-241 and tungsten-185 and tungsten-187 were attempted. These experiments involved the observation of four- and six-quantum transitions because of the inverted level ordering which was caused by the unusually large values of the quadrupole moments of all of these isotopes.

7. A COMPARATIVE STUDY OF (p, t) AND (p, ^{3}He) REACTIONS ON LIGHT NUCLEI

Donald George Fleming
(Ph. D. Thesis)

(From UCRL-17790)

The (p, t) and (p, ^{3}He) reactions on ^{15}N and ^{13}C targets have been investigated. Transitions to mirror final states in the mass 13 and mass 11 final nuclei were studied over 15 and 12.5 MeV of excitation, respectively. Several new spin and parity assignments are made. In particular, the lowest 1p shell $T = 3/2$ states in these nuclei have been identified.

The DWBA predictions of the angular distributions arising from these (p, t) and (p, ^{3}He) transitions were generally found to well reproduce experiment. For the ^{15}N(p, t)^{13}N and ^{15}N(p, ^{3}He)^{13}C reactions, these calculations were carried out using intermediate coupling wave functions to describe the final state; for the ^{13}C(p, t)^{11}C and ^{13}C(p, ^{3}He)^{11}B reactions, pure jj configurations were assumed. In addition to giving a good account of the observed angular distributions, the DWBA calculations of relative cross sections for the (p, t) transitions were also found to be in good agreement with experiment.

Comparative measurements of these (p, t) and (p, ^{3}He) reactions populating mirror final states has been used to test some of the assumptions made in current theories of direct two-nucleon transfer reactions. The agreement in cross section ratios of mirror (p, t) to (p, ^{3}He) transitions is found to improve in every case with the inclusion of a strongly spin-dependent force in the nucleon-nucleon interaction, but overall satisfactory agreement is not obtained. The (p, t) transitions are found to be generally stronger than expected relative to their mirror (p, ^{3}He) transitions and three cases are discussed where the experimental ratios of these cross sections exceed the theoretical upper limit. Interference terms arising either through the spin-orbit interaction in the optical potential or through a core-excitation mechanism are suggested as accounting for this result.

8. POLARIZATION OF INDIUM NUCLEI IN FERROMAGNETS AND NUCLEAR MAGNETIC RESONANCE OF POLARIZED COBALT IN IRON

Rondel James Holliday
(M. S. Thesis)

(From UCRL-17536)

The hyperfine magnetic fields at In nuclei dissolved in iron and nickel were determined by low temperature nuclear orientation of ^{114m}In in iron and nickel. ^{57}Co was used as the thermometer. The results are: H_{int}(In in Fe) = -295 ± 10 kG, H_{int}(In in Ni) = 42 ± 6 kG.

Nuclear magnetic resonance was observed in ^{60}Co nuclei polarized in iron at low temperatures. The resonance frequency if 165.75 ± 0.15 MHz.

9. RADIO FREQUENCY STARK SPECTRA OF RbF, RbCl, CsF, CsCl, AND NaI

Francis John Lovas
(Ph. D. Thesis)

(From UCRL-17909)

The molecular beam electric resonance method was used to measure the radio frequency Stark spectra of ^{85}RbF, ^{87}RbF, $^{85}Rb^{35}Cl$, CsF, $Cs^{35}Cl$, and NaI. Weak field measurements were made on RbF to obtain accurate hyperfine structure constants. Intermediate to strong field measurements were made on all the above molecules to obtain dipole moment values for the three lowest vibrational states of the J = 1 or 2 rotational state.

Work on a polarizable ion model of the alkali halides which computes dipole moments, the molecular dissociation energy and the second coefficient of the Dunham expansion of the potential energy is also presented. Good agreement with experimental values is obtained.

10. THE (^{3}He, p) AND (α, d), TWO-NUCLEON STRIPPING REACTIONS ON ^{12}C AND ^{16}O: MECHANISM AND NUCLEAR SPECTROSCOPY

Nolan Farrin Mangelson
(Ph. D. Thesis)

(From UCRL-17732)

Spectra and angular distributions were obtained for the reactions and conditions listed: $^{12}C(^3He, p)^{14}N$ at $E(^3He) = 20.1$ MeV, from $\theta_{lab} = 8^o$ to 170^o for ^{14}N excited states below 13 MeV excitation; $^{12}C(^3He, ^3He)^{12}C$ at $E(^3He) = 20.1$ MeV, from $\theta_{lab} = 8.5^o$ to 62.5^o for the ground state and 4.433-MeV state of ^{12}C; $^{16}O(^3He, p)^{18}F$ at $E(^3He) = 19.8$ MeV, from $\theta_{lab} = 9^o$ to 170^o for ^{18}F excited states below 11.3 MeV excitation; $^{16}O(\alpha, d)^{18}F$ at $E(\alpha) = 40.3$ MeV, from $\theta_{lab} = 8^o$ to 80^o for ^{18}F excited states below 12.7 MeV excitation.

Distorted-wave calculations of angular distributions and relative cross sections for the two (^{3}He, p) reactions were compared to experimental values. Agreement was found when a spin-independent interaction potential was used. Nuclear wave functions used in the calculations were discussed.

Spectroscopic and configuration assignments were made or confirmed on the basis of excitation energy, angular distribution, comparison of (α, d) and (^{3}He, p) results, relative total cross section, and comparison of experimental quantities to the DW calculations. The following assignments were made for ^{14}N. A spin and parity assignment of 2^- and a tentative assignment of 4^+ were made for the 9.388- and 10.85-MeV, T = 0 levels respectively. Suggested configurations were made for the 8.979-, 10.213-, and 10.85-MeV levels.

Configurations and J^π values of 3^+ and 4^+ were suggested for ^{18}F levels at 3.358 and 5.504 MeV respectively. Configurations and $J^\pi T$ values were confirmed for some levels and T = 0 assignments were made for a large number of levels. A new ^{18}F level at an excitation energy of 8.596 MeV was identified.

11. THE SOLUTION ABSORPTION SPECTRUM OF Bk^{3+} AND THE CRYSTALLOGRAPHY OF BERKELIUM DIOXIDE, SESQUIOXIDE, TRICHLORIDE, OXYCHLORIDE, AND TRIFLUORIDE

Joseph Richard Peterson
(Ph. D. Thesis)

(From UCRL-17875)

The work reported here is the beginning of a systematic study of the physical and chemical properties of berkelium and its compounds. A total of ~30 μg Bk^{249} was made available for use in this study. The procedures used to purify the Bk^{249} solution are discussed in detail, as are the analytical techniques used to evaluate the purity of the Bk sample following each purification cycle. Repeated purifications were necessary to maintain the Bk samples in a state of high purity, since Bk^{249} decays to Cf^{249} at the rate of ~0.2% per day.

The experimental techniques used to study the Bk^{3+} solution absorption spectrum are discussed. One of these techniques, using a newly developed, light-pipe, microabsorption cell, marks a significant advancement in the further development of experimental techniques suitable for heavy-actinide-element research. The composite results of the observed spectra yielded 16 Bk^{3+} absorption peaks in the wavelength region 320 to 700 mμ. The two most intense peaks observed were at 418 and 474 mμ. The experimentally determined, electronic energy levels of Bk^{3+} are compared with theoretically derived values; however, no attempt to fit the observed data to the theoretical energy level scheme is made. Mention is made of an unsuccessful attempt to observe the Bk^{4+} solution absorption spectrum.

A discussion of the techniques to prepare a series of compounds on a single, submicrogram sample of material is given. These techniques were employed to prepare five compounds of berkelium. The conditions used to prepare these five Bk compounds are given, along with a discussion of the treatment of the data obtained from x-ray examination of the compound samples.

All samples of BkO_2 exhibited the fluorite-type, face-centered cubic structure with the "purest" sample yielding a lattice parameter $a_o = 5.334 \pm 0.001$ A. The dioxide stoichiometry was assumed, as was that of the Mn_2O_3-type cubic sesquioxide. The "purest" sample of Bk_2O_3 yielded a cubic lattice parameter $a_o = 10.889 \pm 0.003$ A. The effect of time on both of these lattice parameters is noted. These lattice parameter error limits represent the 95% confidence interval reflecting only the internal consistency of the data for these particular preparations.

The structure exhibited by $BkCl_3$ samples was the UCl_3-type hexagonal structure having lattice parameters $a_o = 7.382 \pm 0.002$ A and $c_o = 4.127 \pm 0.003$ A. Samples of BkOCl exhibited the PbFCl-type tetragonal structure having lattice parameters $a_o = 3.966 \pm 0.004$ A and $c_o = 6.710 \pm 0.009$ A. The lattice parameter error limits reported for $BkCl_3$ and BkOCl are the 95% confidence interval calculated using the standard statistical method for the average of three independent determinations.

BkF_3 samples exhibited two crystal structures, a low-temperature, YF_3-type orthorhombic structure and a high-temperature, LaF_3-type trigonal structure. "Best estimates" for the lattice parameters of these two BkF_3 modifications are: $a_o = 6.70 \pm 0.01$ A, $b_o = 7.09 \pm 0.01$ A, $c_o = 4.41 \pm 0.01$ A (orthorhombic) and $a_o = 6.97 \pm 0.01$ A, $c_o = 7.14 \pm 0.01$ A (trigonal). The lattice parameter error limits reported here are empirical, reflecting the uncertainties in the derivation of the lattice parameters.

Comparisons of the lattice parameters of these berkelium compounds with those of similar actinide compounds consistently showed evidence of the "actinide contraction". Calculations of the Bk^{3+} radius from the crystallographic data of Bk_2O_3, $BkCl_3$, and BkF_3 are tabulated. With reference to these calculations the limitations of the concept of ionic radius are discussed.

12. STATISTICAL THERMODYNAMICS OF PARTICULATE FLUIDIZATION

James A. Saxton, Jr.
(Ph. D. Thesis)

(From UCRL-11216)

In this investigation a statistical-thermodynamic theory of fluidization has been postulated, and an experimental assessment of its validity made. A literature survey of liquid theory and fluidization properties led to the choice of the smoothed-potential cell model of liquids for use in interpreting fluidization phenomena. Experimental measurements were made of expansion, viscosity, miscibility, and surface-tension behavior in water-fluidized glass-sphere systems.

Both rotating-spindle and moving-sphere viscosity measurements were made. The agreement between the results of the two techniques was found to be quite good. The data were analyzed in terms of our cell model using the hard-sphere viscosity expression of Collins and Raffel. By this analysis, the fluidized-bed parameter equivalent to thermodynamic temperature was found to be a function only of fluid properties, and to be proportional to the square of the fluidizing velocity.

A 3/4-inch-diameter sampling tube was utilized for the investigation of miscibility in two-phase beds. Sampling confirmed the visually-observed interface, and indicated uniformity of concentration within each phase. The mutual solubility of different-diameter particles was found to diminish with increasing fluidizing velocity. Our cell-model analysis could be extended to two-phase systems due to the lack of dependence upon particle properties of the "nominal-temperature" function. Results that lay within an order of magnitude of our experimental observation were achieved.

Measurements were made by visual observation of waves created at the interface by a dropping cylinder. From the surface-wave data, the particle free volume at the surface was found to be less than in the bulk phase.

K. AUTHOR INDEX

1. PAPERS PUBLISHED AND UCRL REPORTS ISSUED, 1967

BICHSEL, H.
A FORTRAN program for the calculation of the energy loss of heavy charged particles
UCRL-17538, May 1967

BICHSEL, H., and C. Tschalaer
A range energy table for heavy particles in silicon
UCRL-17663, July 1967
Nuclear Data

BICHSEL, H. (See Slobodrian, R. J., UCRL-17507 Abstract)

BICHSEL, H. (See Slobodrian, R. J., UCRL-17669)

BOWMAN, H. R., R. C. Gatti, R. C. Jared, G. Kilian, L. G. Moretto, S. G. Thompson, M. R. Croissiaux, J. H. Heisenberg, R. Hofstadter, L. M. Middleman, and M. R. Yearian
Electron induced fission in U^{238}, Bi^{209}, and Ta^{181}
UCRL-17864, October 1967
Phys. Rev. Letters

BOWMAN, H. R. (See Watson, R. L., UCRL-17289)

BOWMAN, H. R. (See Watson, R. L., UCRL-17358)

BREWER, W. D. (See Barclay, J. A., UCRL-17716)

BRUNNADER, H. (See Cosper, S. W., UCRL-17709)

BUTLER, G. W.
Mass and spectroscopic measurements of complete isospin quartets in the light nuclei
UCRL-17783, August 1967
Ph. D. Thesis

BUTLER, G. W., J. Cerny, S. W. Cosper, and R. L. McGrath
Mass and spectroscopic measurements in the completed mass 21 and 37 isospin quartets
UCRL-17693, July 1967
Phys. Rev.

CAO-X. -C.
The quasi-elastic stopping cross-section for very low energy ions
UCRL-17717, August 1967

CAO-X. -C.
The stopping cross-section for low energy ions
UCRL-17747 Abstract, August 1967
Meeting of the American Physical Society, Pasadena, California, December 18-20, 1967

CERNY, J. (See Ball, G. C., UCRL-17888 Abstract)

CERNY, J. (See Butler, G. W., UCRL-17693)

CERNY, J. (See Cosper, S. W., UCRL-17709)

CERNY, J. (See Fleming, D. G., UCRL-17731)

CERNY, J. (See Fleming, D. G., UCRL-17840)

CERNY, J. (See Goulding, F. S., UCRL-16711)

CERNY, J. (See McGrath, R. L., UCRL-17777)

CERNY, J. (See McGrath, R. L., UCRL-17885 Abstract)

CERNY, J. (See McGrath, R. L., UCRL-17927)

CLAMPITT, R. (See Newton, A. S., UCRL-17546)

CLARK, D. J. (See McKee, J. S. C., UCRL-17320)

CLARK, D. J. (See Slobodrian, R. J., UCRL-17421)

CLARK, D. J. (See Slobodrian, R. J., UCRL-17422)

CLARK, M. W., and C. J. King
Mass and heat transfer processes in laminar, two-phase flow
UCRL-17527, June 1967

CLEM, R. G., and E. H. Huffman
Amperometric titration of palladium(II) by oxidation with hypochlorite
UCRL-17824, September 1967
Eleventh Conference on Analytical Chemistry in Nuclear Technology, Gatlinburg, Tennessee, October 10-12, 1967)

CONWAY, J. G., W. F. Morris, and C. F. Andrews
Airborne spectrographic observations of the solar eclipse of November 12, 1966
UCRL-17506, April 1967
Astrophys. J. 150, 299 (1967)

CONWAY, J. G. (See McLaughlin, R., UCRL-17630)

COOPER, J. A., J. M. Hollander, and J. O. Rasmussen
Energy levels of ^{90}Nb populated by the decay of ^{90}Mo
UCRL-17104, October 1967
Nucl. Phys.

COPELAND, J. C.
Preparation and crystallographic analysis of californium sesquioxide and californium oxychloride
UCRL-17718, August 1967
M. S. Thesis

CORNIEA-BENNETT, W. (See Garrison, W. M., UCRL-17307)

CORNIEA-BENNETT, W. (See Garrison, W. M., UCRL-17967)

COSPER, S. W., H. Brunnader, J. Cerny, and R. L. McGrath
Energy dependence of ^{26}Mg(p, t)^{24}Mg and ^{12}C(p, t)^{10}C L= 0 and L= 2 angular distribution shapes
UCRL-17709, August 1967
Phys. Letters 25B, 324 (1967)

COSPER, S. W. (See Butler, G. W., UCRL-17693)

COSPER, S. W. (See McGrath, R. L., UCRL-17777)

CROISSIAUX, M. R. (See Bowman, H. R., UCRL-17864)

CUMMING, J. B. (See Poskanzer, A. M., UCRL-17759)

CUNNINGHAM, B. B., J. R. Peterson, R. D. Baybarz, and T. C. Parsons
The absorption spectrum of Es^{3+} in hydrochloric acid solutions
UCRL-17692, August 1967
Inorg. Nucl. Chem. Letters

CUNNINGHAM, B. B.
Compounds of the actinides
"Preparative Inorganic Reactions," Vol. 3, ed. by William L. Jolly, (Interscience Publishers, a division of John Wiley and Sons, New York, 1966), p. 79

CUNNINGHAM, B. B. (See Green, J. L., UCRL-17539)

CUNNINGHAM, B. B. (See Maly, J., UCRL-17679)

CUNNINGHAM, B. B. (See Peterson, J. R., UCRL-17337)

CUNNINGHAM, B. B. (See Peterson, J. R., UCRL-17576)

CUNNINGHAM, B. B. (See Peterson, J. R., UCRL-17710)

CUNNINGHAM, B. B. (See Peterson, J. R., UCRL-17766)

CUNNINGHAM, B. B. (See Peterson, J. R., UCRL-17912)

CURTIS, M. R. (See Main, R. M., UCRL-17274)

DeBOER, B. G., A. Zalkin, and D. H. Templeton
The crystal structure of the rubidium salt of an octadecahydroeicosaborate(2-) photoisomer
UCRL-17125, August 1967
Inorg. Chem.

DIAMOND, R. M.
Heavy-ion in-beam spectroscopy
UCRL-17762 Abstract, August 1967
Meeting of the American Physical Society, Madison, Wisconsin, October 23-25, 1967

DIAMOND, R. M., E. Matthias, J. O. Newton, and F. S. Stephens
Nuclear alignment in heavy-ion reactions
UCRL-16889, May 1966
Phys. Rev. Letters 16, 1205 (1966)

DIAMOND, R. M. (See Turner, D. J., UCRL-17581 Abstract)

DREW, M. G. B., D. H. Templeton, and A. Zalkin
The crystal and molecular structure of sulfur nitride-boron trifluoride
Inorg. Chem. 6, 1906 (1967)

DUHM, H. H., D. L. Hendrie, and B. G. Harvey
Scattering and bound state potentials in DWBA calculations
UCRL-17883, October 1967
Phys. Letters

DUHM, H. H. (See Hendrie, D. L., UCRL-17547)

DUHM, H. H. (See Hendrie, D. L., UCRL-17890)

EASLEY, W. C.
Electron paramagnetic resonance studies of radioactive transition-metal ions
UCRL-17699, August 1967
Ph. D. Thesis

EASLEY, W. C., J. A. Barclay, and D. A. Shirley
Nuclear moments of Tb^{157}, Tb^{158}, and Tb^{160} by electron paramagnetic resonance and nuclear alignment
UCRL-17578, August 1967
Phys. Rev.

EASLEY, W. (See Edelstein, N., UCRL-17855)

EDELSTEIN, N., and W. Easley
Zero field splittings of Am^{2+} and Cm^{3+} in cubic symmetry sites in CaF_2
UCRL-17855, September 1967
J. Chem. Phys.

EDELSTEIN, N. (See Matthias, E., UCRL-17509)

EDELSTEIN, N. (See McLaughlin, R., UCRL-17630)

EDWARDS, V. H., and C. R. Wilke
Mathematical representation of batch culture data
UCRL-17953, November 1967
Biotech. Bioeng.

EWAN, G. T. (See Yamazaki, T., UCRL-17226)

FADLEY, C. S., S. B. M. Hagstrom, J. M. Hollander, M. P. Klein, and D. A. Shirley
Chemical bonding information from photoelectron spectroscopy
UCRL-17426 Rev, May 1967
Science 157, 1571 (1967)

FADLEY, C. S., S. B. M. Hagstrom, M. P. Klein, and D. A. Shirley
Chemical effects on core electron binding energies in iodine and europium
UCRL-17005, July 1966
J. Chem. Phys.

FAESSLER, A., N. K. Glendenning, and A. Plastino
Surface delta interaction model for nuclear structure analyzed by proton inelastic scattering
UCRL-16976, December 1966
Phys. Rev. 159, 846 (1967)

FLEMING, D. G.
A comparative study of (p, t) and (p, ^{3}He) reactions on light nuclei
UCRL-17790, September 1967
Ph. D. Thesis

FLEMING, D. G., J. Cerny, and N. K. Glendenning
Inadequacy of the simple DWBA treatment of comparative (p, t) and (p, ^{3}He) transitions
UCRL-17731, July 1967
Phys. Rev.

FLEMING, D. G., J. Cerny, C. C. Maples, and N. K. Glendenning
The $^{15}N(p, t)^{13}N$ and $^{15}N(p, ^3He)^{13}C$ reactions and the spectroscopy of levels
UCRL-17840, September 1967
Phys. Rev.

FRANCO, V.
On the possible non-additivity of quark amplitudes in high-energy cross sections
UCRL-17510, April 1967
Phys. Rev. Letters 18, 1159 (1967)

FUGER, J.
Thermal expansion coefficients of the anhydrous trichlorides of cerium, plutonium, and americium
UCRL-16352, August 1965
J. Inorg. Nucl. Chem. 28, 3066 (1966)

GARRISON, W. M., M. E. Jayko, B. M. Weeks, H. A. Sokol, and W. Bennett-Corniea
Chemical evidence for main-chain scission as a major decomposition mode in the radiolysis of peptides
UCRL-17307, December 1966
J. Phys. Chem. 71, 1546 (1967)

GARRISON, W. M., M. E. Jayko, M. A. J. Rodgers, H. A. Sokol, and W. Bennett-Corniea
Ionization and excitation in peptide radiolysis
UCRL-17967, November 1967
Advances in Chemistry Series

GARRISON, W. M.
Radiation chemistry of organo-nitrogen compounds
UCRL-17440, March 1967
Chapter in "Current Topics in Radiation Research, " (North-Holland Publishing Co., Amsterdam, 1967)

GARRISON, W. M. (See Holian, J., UCRL-17575)

GARRISON, W. M. (See Rodgers, M. A. J., UCRL-17886)

GARRISON, W. M. (See Rodgers, M. A. J., UCRL-17930)

GARRISON, W. M. (See Willix, R. L. S., UCRL-17285)

GATTI, R. C. (See Bowman, H. R., UCRL-17864)

GATTI, R. C. (See Moretto, L. G., UCRL-17349)

GHIORSO, A., T. Sikkeland, and M. J. Nurmia
Isotopes of element-102 with mass 251 to 258
UCRL-17369, February 1967
Phys. Rev. Letters 18, 401 (1967)

GHIORSO, A.
New accelerators for very heavy ions - Production of super-elements
UCRL-17295, March 1967
U. S. National Particle Accelerator Conference, Washington, D. C., March 1-3, 1967

GHIORSO, A., and T. Sikkeland
The search for element 102
UCRL-17427, March 1967
Physics Today 20, 25 (1967)

GHIORSO, A. (See Maly, J., UCRL-17995)

GHIORSO, A. (See Nurmia, M., UCRL-17891)

GHIORSO, A. (See Sikkeland, T., UCRL-17362)

GHIORSO, A. (See Sikkeland, T., UCRL-17363)

GLENDENNING, N. K.
Inelastic scattering and nuclear structure
UCRL-17503, August 1967
International School of Physics "Enrico Fermi", Course XL, Varenna (Como), Italy, June 26-July 15, 1957

GLENDENNING, N. K., D. L. Hendrie, and O. N. Jarvis
Relation between the optical potential for spherical and deformed nuclei
UCRL-17935, November 1967
Phys. Letters

GLENDENNING, N. K. (See Faessler, A., UCRL-16976)

GLENDENNING, N. K. (See Fleming, D. G., UCRL-17731)

GLENDENNING, N. K. (See Fleming, D. G., UCRL-17840)

GLENDENNING, N. K. (See Hendrie, D. L., UCRL-17547)

GLENDENNING, N. K. (See Hendrie, D. L., UCRL-17890)

GOODMAN, A. L., G. L. Struble, and A. Goswami
Restoration of axial symmetry of the equilibrium shape of Mg^{24} by pairing correlations
UCRL-17900, October 1967
Phys. Letters

GOSWAMI, A. (See Goodman, A. L., UCRL-17900)

GOTH, G. W. (See McGrath, R. L., UCRL-17885 Abstract)

GOULDING, F. S., D. A. Landis, J. Cerny, and R. H. Pehl
An improved particle identifier for studies of low-yield nuclear reactions
UCRL-16711, February 1966
IEEE Trans. Nucl. Sci. 13, 514 (1966)

GRAZIER, R. (See Main, R. M., UCRL-17274)

GREEN, J. L., and B. B. Cunningham
Crystallography of the compounds of californium. I. Crystal structure and lattice parameters of californium sesquioxide and californium trichloride
UCRL-17539, May 1967
Inorg. Nucl. Chem. Letters 3, 343 (1967)

GREEN, J. L. (See Ryan, V. A., UCRL-11618)

HAGSTROM, S. B. M. (See Fadley, C. S., UCRL-17005)

HAGSTROM, S. B. M. (See Fadley, C. S., UCRL-17426 Rev)

HALBACH, K.
A program for inversion of system analysis and its application to the design of magnets
UCRL-17436, April 1967
Second International Conference on Magnet Technology, Oxford University, Oxford, England, July 10-14, 1967

HARVEY, B. G. (See Duhm, H. H., UCRL-17883)

HARVEY, B. G. (See Hendrie, D. L., UCRL-17547)

HARVEY, B. G. (See Hendrie, D. L., UCRL-17890)

HARVEY, B. G. (See Jarvis, O. N., UCRL-17352)

HEBERT, A. J., F. J. Lovas, C. A. Melendres, C. D. Hollowell, T. L. Story, Jr., and K. Street, Jr.
Dipole moments of some alkali halide molecules by the molecular beam electric resonance method
UCRL-17962, November 1967
J. Chem. Phys.

HEBERT, A. J., C. D. Hollowell, T. L. Story, and K. Street, Jr.
The molecular-beam electric-resonance spectra of LiF, LiCl, and KCl
UCRL-17256, March 1967

HEISENBERG, J. H. (See Bowman, H. R., UCRL-17864)

HENDRIE, D. L., N. K. Glendenning, B. G. Harvey, O. N. Jarvis, H. H. Duhm, J. Mahoney, and J. Saudinos
Determination of Y_4 deformations in the rare earth region by inelastic alpha particle scattering
UCRL-17547, August 1967
International Conference on Nuclear Structure, Tokyo, September 7-13, 1967

HENDRIE, D. L., N. K. Glendenning, B. G. Harvey, O. N. Jarvis, H. H. Duhm, J. Saudinos, and J. Mahoney
Determination of Y_{40} and Y_{60} components in the shapes of rare earth nuclei
UCRL-17890, October 1967
Phys. Letters

HENDRIE, D. L.
Higher order collective deformations in the rare earth nuclei
UCRL-17908 Abstract, November 1967
Meeting of the American Physical Society, Madison, Wisconsin, October 23-25, 1967

HENDRIE, D. L. (See Duhm, H. H., UCRL-17883)

HENDRIE, D. L. (See Glendenning, N. K., UCRL-17935)

HENDRIE, D. L. (See Jarvis, O. N., UCRL-17352)

HOFSTADTER, R. (See Bowman, H. R., UCRL-17864)

HOLIAN, J., and W. M. Garrison
Mechanism and stoichiometry in the radiolytic oxidation of purines and aminopurines in aqueous solution
UCRL-17575, May 1967
Chemical Communications, 676 (1967)

HOLLANDER, J. M. (See Bergkvist, K.-E., UCRL-17338)

HOLLANDER, J. M. (See Cooper, J. A., UCRL-17104)

HOLLANDER, J. M. (See Fadley, C. S., UCRL-17426 Rev)

HOLLANDER, J. M. (See Prussin, S. G., UCRL-17843)

HOLLANDER, J. M. (See Sakai, M., UCRL-16548)

HOLLIDAY, R. J.
Polarization of indium nuclei in ferromagnets and nuclear magnetic resonance cobalt in iron
UCRL-17536, May 1967
M. S. Thesis

HOLLOWELL, C. D. (See Hebert, A. J., UCRL-17256)

HOLLOWELL, C. D. (See Hebert, A. J., UCRL-17962)

HOPKINS, T. E., A. Zalkin, D. H. Templeton, and M. G. Adamson
The crystal and molecular structure of tetraphenylarsonium cis-diaquotetrachloro ruthenate monohydrate
UCRL-16758, March 1966
Inorg. Chem. 5, 1427 (1966)

HOPKINS, T. E., A. Zalkin, D. H. Templeton, and M. G. Adamson
The crystal structure of cesium aquopentachlororuthenate
UCRL-16759, March 1966
Inorg. Chem. 5, 1431 (1966)

HOPKINS, T. E. (See Zalkin, A., UCRL-17371)

HOPKINS, T. E. (See Zalkin, A., UCRL-16752)

HORROCKS, W. D., Jr., D. H. Templeton, and A. Zalkin
The crystal and molecular structure of bis(2, 4-pentanedionato) bis(pyridine n-oxide) nickel(II) $Ni(C_5H_7O_2)_2(C_5H_5NO)_2$
UCRL-17666, July 1967
Inorg. Chem.

HUFFMAN, E. H. (See Clem, R. G., UCRL-17824)

HUIZENGA, J. R. (See Moretto, L. G., UCRL-17349)

HYDE, E. K.
Nuclear models
Chemistry 40, 12 (1967)

HYDE, E. K. (See Treytl, W., UCRL-17405)

HYDE, E. K. (See Valli, K., UCRL-16735 Rev)

HYDE, E. K. (See Valli, K., UCRL-17272)

HYDE, E. K. (See Valli, K., UCRL-17322)

JARED, R. C. (See Bowman, H. R., UCRL-17864)

JARVIS, O. N., B. G. Harvey, D. L. Hendrie, and J. Mahoney
The inelastic scattering of 17.8 MeV protons from ^{58}Ni, ^{60}Ni, and ^{120}Sn, and the determination of spin and parity assignments for ^{58}Ni from α-particle scattering
UCRL-17352, January 1967
Nucl. Phys.

JARVIS, O. N. (See Glendenning, N. K., UCRL-17035)

JARVIS, O. N. (See Hendrie, D. L., UCRL-17547)

JARVIS, O. N. (See Hendrie, D. L., UCRL-17890)

JAYKO, M. E. (See Garrison, W. M., UCRL-17307)

JAYKO, M. E. (See Garrison, W. M., UCRL-17967)

KENNEDY, P. B. (See Main, R. M., UCRL-17274)

KILIAN, G. (See Bowman, H. R., UCRL-17864)

KING, C. J. (See Clark, M. W., UCRL-17527)

KLECKA, J. F.
Analysis for yttrium with a semiconductor x-ray emission spectrograph and I^{125} source
UCRL-17144, October 3, 1966

KLECKA, J. F.
Quantitative analysis of uranium and thorium solutions with a semiconductor x-ray emission spectrometer
UCRL-17166 Rev, October 3, 1966

KLEIN, M. P. (See Fadley, C. S., UCRL-17005)

KLEIN, M. P. (See Fadley, C. S., UCRL-17426 Rev)

KÖRNER, H. J. (See Matthias, E., UCRL-17509)

KRUPKE, W. F. (See Rajnak, K., J. Chem. Phys. 46, 3532 (1967))

LAMB, J., D. M. Lee, and S. S. Markowitz
Simultaneous determination of O^{18} and O^{16} isotopes by He^3 activation analysis
UCRL-17812, August 1967
Second Meeting on Practical Aspects of Activation Analysis with Charged Particles, Liege, Belgium, 21-22 September 1967

LANDIS, D. A. (See Goulding, F. S., UCRL-16711)

LATIMER, R. M. (See Aly, H. F., UCRL-17409)

LEBECK, D. F. (See Sikkeland, T., UCRL-17588 Rev)

LEE, D. M. (See Lamb, J. F., UCRL-17812)

LOVAS, F. J.
Radio frequency stark spectra of RbF, RbCl, CsF, CsCl, and NaI
UCRL-17909, November 1967
Ph. D. Thesis

LOVAS, F. J. (See Hebert, A. J., UCRL-17962)

LOWENHAUPT, E. H. (See Ryan, V. A., UCRL-11618)

LUCCIO, A. U. (See McKee, J. S. C., UCRL-17755)

MA, C. W. (See Rasmussen, J. O., Z. Physik 202, 182 (1967))

MAHONEY, J. (See Hendrie, D. L., UCRL-17547)

MAHONEY, J. (See Hendrie, D. L., UCRL-17890)

MAHONEY, J. (See Jarvis, O. N., UCRL-17352)

MAIN, R. M., M. R. Curtis, R. Grazier, P. B. Kennedy, B. H. Smith, and D. A. Spence
A small helium-3 cyclotron
UCRL-17274, March 1967
U. S. National Particle Accelerator Conference, Washington, D. C., March 1-3, 1967

MALY, J.
The amalgamation behavior of heavy elements. 1. Observation of anomalous preference in formation of amalgams of californium, einsteinium, and fermium
UCRL-17524, May 1967
Inorg. Nucl. Chem. Letters 3, 373 (1967)

MALY, J., and B. B. Cunningham
The amalgamation behavior of heavy elements. 2. Dipositive state of mendelevium
UCRL-17679, July 1967
Inorg. Nucl. Chem. Letters

MALY, J., and J. R. Nix
Calculations of the flattening of idealized nuclei during head-on collisions
UCRL-17541, May 1967
International Conference on Nuclear Structure, Tokyo, September 7-13, 1967

MALY, J., T. Sikkeland, R. Silva, and A. Ghiorso
Studies of the tracer chemistry of element 102
UCRL-17995, December 1967
Science

MALY, J. (See Sikkeland, T., UCRL-17363)

MALY, J. (See Sikkeland, T., UCRL-17588 Rev)

MANGELSON, N. F.
The (^{3}He, p) and (α, d) two-nucleon stripping reactions on ^{12}C and ^{16}O: Mechanism and nuclear spectroscopy
UCRL-17732, August 1967
Ph. D. Thesis

MAPLES, C. C. (See Fleming, D. G., UCRL-17840)

MARKOWITZ, S. S. (See Lamb, J. F., UCRL-17812)

MATTHIAS, E.
Angular correlation- and Mössbauer-NMR
UCRL-17877, October 1967
International Conference on Hyperfine Interactions Detected by Nuclear Radiation, Asilomar, Pacific Grove, California, August 25-30, 1967

NURMIA, M., T. Sikkeland, R. Silva, and A. Ghiorso
Spontaneous fission of light fermium isotopes; new nuclides ^{244}Fm and ^{245}Fm
UCRL-17891, October 1967
Phys. Letters

NURMIA, M. J. (See Ghiorso, A., UCRL-17369)

NURMIA, M. J. (See Sikkeland, T., UCRL-17363)

NURMIA, M. J. (See Valli, K., UCRL-16735 Rev)

OLSEN, B. A. (See Matthias, E., UCRL-17509)

PARSONS, T. C. (See Cunningham, B. B., UCRL-17692)

PEHL, R. H. (See Goulding, F. S., UCRL-16711)

PERLMAN, I. (See Asaro, F., UCRL-16738)

PETERSON, J. R.
The solution absorption spectrum of Bk^{3+} and the crystallography of berkelium dioxide, sesquioxide, trichloride, oxychloride, and trifluoride
UCRL-17875, October 1967
Ph. D. Thesis

PETERSON, J. R., and B. B. Cunningham
Crystal structures and lattice parameters of the compounds of berkelium. I. Berkelium dioxide and cubic berkelium sesquioxide
UCRL-17576, May 1967
Inorg. Nucl. Chem. Letters 3, 327 (1967)

PETERSON, J. R., and B. B. Cunningham
Crystal structures and lattice parameters of the compounds of berkelium. II. Berkelium trichloride
UCRL-17710, August 1967
Inorg. Nucl. Chem. Letters

PETERSON, J. R., and B. B. Cunningham
Crystal structures and lattice parameters of the compounds of berkelium. III. Berkelium oxychloride
UCRL-17766, August 1967
Inorg. Nucl. Chem. Letters 3, 579 (1967)

PETERSON, J. R., and B. B. Cunningham
Crystal structures and lattice parameters of the compounds of berkelium. IV. Berkelium trifluoride
UCRL-17912, November 1967
J. Inorg. Nucl. Chem.

PETERSON, J. R., and B. B. Cunningham
Some chemical properties of element 97
UCRL-17337, January 1967
Meeting of the American Nuclear Society, San Diego, California, June 11-14, 1967

PETERSON, J. R. (See Cunningham, B. B., UCRL-17692)

PLASTINO, A. (See Faessler, A., UCRL-16976)

POSKANZER, A. M., J. B. Cumming, and L. P. Remsberg
The $Al^{27}(p, p\pi^+)Mg^{27}$ reaction
UCRL-17759, August 1967
Phys. Rev.

PRUSSIN, S. G., and J. M. Hollander
Energy levels of $^{210}_{84}Po$ populated by the decay of $^{210}_{85}At$
UCRL-17843, September 1967
Nucl. Phys.

RAJNAK, K., and W. F. Krupke
Energy levels of Ho^{3+} in LaCl
J. Chem. Phys. 46, 3532 (1967)

RASMUSSEN, J. O.
Closing remarks
UCRL-17951, November 1967
International Conference on Hyperfine Interactions Detected by Nuclear Radiation, Asilomar, Pacific Grove, California, August 25-30, 1967

RASMUSSEN, J. O., and C. W. Ma
On the influence of shell structure and matrix element fluctuations on the pairing correlation in nuclei
Z. Physik 202, 182 (1967)

RASMUSSEN, J. O. (See Bernthal, F. M., UCRL-17504)

RASMUSSEN, J. O. (See Cooper, J. A., UCRL-17104)

RASMUSSEN, J. O. (See Moretto, L. G., UCRL-17349)

RASMUSSEN, J. O. (See Watson, R. L., UCRL-17289)

RASMUSSEN, J. O. (See Watson, R. L., UCRL-17290)

RASMUSSEN, J. O. (See Watson, R. L., UCRL-17358)

REMSBERG, L. P. (See Poskanzer, A. M., UCRL-17759)

ROBINSON, H. P.
A timing code for continuous day counting
UCRL-17884, October 17, 1967
Tele-Communications Working Group, Inter-Range Instrumentation Group, Range Commanders Council, White Sands Missile Range, October 24-26, 1967

RODGERS, M. A. J., and W. M. Garrison
Excited-molecule reactions in the radiolysis of peptides in concentrated aqueous solution
UCRL-17886, October 1967
J. Phys. Chem.

RODGERS, M. A., H. A. Sokol, and W. M. Garrison
The radiation-induced "hydrolysis" of the peptide bond
UCRL-17930, November 1967
J. Am. Chem. Soc.

RODGERS, M. A. J. (See Garrison, W. M., UCRL-17967)

ROSENBLUM, S. S. (See Shirley, D. A., UCRL-17701)

ROSENBLUM, S. S. (See Shirley, D. A., UCRL-18028)

RYAN, V. A., J. L. Green, and E. H. Lowenhaupt
Oxygen content of lanthanide and actinide metals obtained by reduction of "wet" and "dry" produced trifluorides
UCRL-11618, August 1964
J. Inorg. Nucl. Chem. 29, 581 (1967)

SAKAI, M., T. Yamazaki, and J. M. Hollander
New weak beta transition from ^{88}Y
UCRL-16548, January 1966
Nucl. Phys. 84, 302 (1966)

SAUDINOS, J. (See Hendrie, D. L., UCRL-17547)

SAUDINOS, J. (See Hendrie, D. L., UCRL-17890)

SCIAMANNA, A. F. (See Newton, A. S., UCRL-17546)

SHIRLEY, D. A., S. S. Rosenblum, and E. Matthias
Angular correlation studies of cadmium and ruthenium in nickel
UCRL-17701, July 1967
International Conference on Hyperfine Interactions Detected by Nuclear Radiation, Asilomar, Pacific Grove, California, August 25-30, 1967

SHIRLEY, D. A., S. S. Rosenblum, and E. Matthias
Hyperfine fields at solutes in ferromagnets: cadmium and ruthenium in nickel
UCRL-18028, December 1967
Phys. Rev.

SHIRLEY, D. A.
Magnetic resonance in oriented nuclei
UCRL-17854, September 1967
International Conference on Hyperfine Interactions Detected by Nuclear Radiation, Asilomar, Pacific Grove, California, August 25-30, 1967

SHIRLEY, D. A.
On transferred hyperfine structure in ferromagnets
Phys. Letters 25A, 129 (1967)

SHIRLEY, D. A. (See Barclay, J. A., UCRL-17716)

SHIRLEY, D. A. (See Easley, W. C., UCRL-17578)

SHIRLEY, D. A. (See Fadley, C. S., UCRL-17005)

SHIRLEY, D. A. (See Fadley, C. S., UCRL-17426 Rev)

SHIRLEY, D. A. (See Matthias, E., UCRL-17509)

SHIRLEY, V. S.
Table of nuclear moments
UCRL-17990, October 1967
Proceedings of International Conference on Hyperfine Interactions Detected by Nuclear Radiation, Asilomar, Pacific Grove, California, August 25-30, 1967

SIIVOLA, A.
Alpha active platinum isotopes
UCRL-16673, January 1966
Nucl. Phys. 84, 385 (1966)

SIKKELAND, T., A. Ghiorso, J. Maly, and M. Nurmia
Decay properties of new isotopes ^{243}Cf and ^{244}Cf
UCRL-17363, February 1967
Phys. Letters 24B, 333 (1967)

SIKKELAND, T., J. Maly, and D. F. Lebeck
Evaporation of 3 to 8 neutrons in reactions between ^{12}C and various uranium nuclides
UCRL-17588 Rev, November 1967
Phys. Rev.

SIKKELAND, T., and A. Ghiorso
A new californium isotope ^{242}Cf
UCRL-17362, February 1967
Phys. Letters 24B, 331 (1967)

SIKKELAND, T. (See Ghiorso, A., UCRL-17369)

SIKKELAND, T. (See Ghiorso, A., UCRL-17427)

SIKKELAND, T. (See Maly, J., UCRL-17995)

SIKKELAND, T. (See Nurmia, M., UCRL-17891)

SILVA, R. (See Maly, J., UCRL-17995)

SILVA, R. (See Nurmia, M., UCRL-17891)

SLOBODRIAN, R. J., J. S. C. McKee, H. Bichsel, and W. F. Tivol
High precision measurement of proton-proton polarization between 10 and 20 MeV
UCRL-17669, July 1967
Phys. Rev. Letters 19, 704 (1967)

SLOBODRIAN, R. J., H. Bichsel, J. S. C. McKee, and W. F. Tivol
High resolution fast neutron spectroscopy of the reaction $^{9}Be(p, n)^{9}B$ at 20 MeV
UCRL-17507, June 1967
Phys. Rev. Letters 19, 595 (1967)

SLOBODRIAN, R. J.
Possible observation of vacuum polarization effects in the $^{1}S_0$ p-p state
UCRL-17627, June 1967
Phys. Letters 25B, 89 (1967)

SLOBODRIAN, R. J., J. S. C. McKee, D. J. Clark, W. F. Tivol, and T. A. Tombrello
A search for excited states of ^{3}He
UCRL-17422, March 1967
Nucl. Phys. A101, 109 (1967)

SLOBODRIAN, R. J., J. S. C. McKee, W. F. Tivol, D. J. Clark, and T. A. Tombrello
The 2p final-state interaction in the $^{3}He(^{3}He, \alpha)2p$ reaction
UCRL-17421, March 1967
Phys. Letters 25B, 19 (1967)

SLOBODRIAN, R. J. (See McKee, J. S. C., UCRL-17320)

SLOBODRIAN, R. J. (See McKee, J. S. C., UCRL-17755)

SMITH, B. H. (See Main, R. M., UCRL-17274)

SOKOL, H. A. (See Garrison, W. M., UCRL-17307)

SOKOL, H. A. (See Garrison, W. M., UCRL-17967)

SOKOL, H. A. (See Rodgers, M. A., UCRL-17930)

SORENSEN, R.
Nuclear moments
UCRL-17729, August 1967
International Conference on Hyperfine Interactions Detected by Nuclear Radiation, Asilomar, Pacific Grove, California, August 25-30, 1967

SPENCE, D. A. (See Main, R. M., UCRL-17274)

STEPHENS, F. S., D. Ward, and J. O. Newton
Nuclear spectroscopy following ^{40}Ar reactions
UCRL-17568, May 1967
International Conference on Nuclear Structure, Tokyo, September 7-13, 1967

STEPHENS, F. S. (See Diamond, R. M., UCRL-16889)

STEPHENS, F. S. (See Ward, D., UCRL-17537)

STORY, T. L. (See Hebert, A. J., UCRL-17256)

STORY, T. L. (See Hebert, A. J., UCRL-17962)

STREET, K. (See Hebert, A. J., UCRL-17256)

STREET, K. (See Hebert, A. J., UCRL-17962)

STRUBLE, G. L. (See Goodman, A. L., UCRL-17900)

TEMPLETON, D. H. (See DeBoer, B. G., UCRL-17125)

TEMPLETON, D. H. (See Drew, M. G. B., Inorg. Chem. 6, 1906 (1967))

TEMPLETON, D. H. (See Hopkins, T. E., UCRL-16758)

TEMPLETON, D. H. (See Hopkins, T. E., UCRL-16759)

TEMPLETON, D. H. (See Horrocks, W. D., UCRL-17666)

TEMPLETON, D. H. (See Zalkin, A., UCRL-16752)

TEMPLETON, D. H. (See Zalkin, A., UCRL-17371)

THOMPSON, S. G.
Some aspects of the study of fission
Arkiv Fysik 36, 267 (1967)

THOMPSON, S. G. (See Bowman, H. R., UCRL-17864)

THOMPSON, S. G. (See Watson, R. L., UCRL-17289)

THOMPSON, S. G. (See Watson, R. L., UCRL-17358)

TIVOL, W. F. (See McKee, J. S. C., UCRL-17320)

TIVOL, W. F. (See McKee, J. S. C., UCRL-17755)

TIVOL, W. F. (See Slobodrian, R. J., UCRL-17421)

TIVOL, W. F. (See Slobodrian, R. J., UCRL-17422)

TIVOL, W. F. (See Slobodrian, R. J., UCRL-17507 Abstract)

TIVOL, W. F. (See Slobodrian, R. J., UCRL-17669)

TOBOCMAN, W.
Use of the projection operator method in nuclear reaction theory
UCRL-17784, August 1967
Phys. Rev.

TOMBRELLO, T. A. (See Slobodrian, R. J., UCRL-17421)

TOMBRELLO, T. A. (See Slobodrian, R. J., UCRL-17422)

TREYTL, W. J., and E. Matthias
g factor of the 243-keV level in ^{86}Y
UCRL-17636, June 1967
International Conference on Hyperfine Interactions Detected by Nuclear Radiation, Asilomar, Pacific Grove, California, August 25-30, 1967

TREYTL, W., E. K. Hyde, and K. Valli
On-line α spectroscopy of neutron-deficient actinium isotopes
UCRL-17405, February 1967
Phys. Rev.

TREYTL, W. (See Valli, K., UCRL-17272)

TREYTL, W. (See Valli, K., UCRL-17322)

TSCHALAER, C. (See Bichsel, H., UCRL-17663)

TURNER, D. J., and R. M. Diamond
The extraction of tetraheptyl ammonium fluoride and the solvation of the fluoride ion
UCRL-17581 Abstract, June 1967
154th National Meeting of the American Chemical Society, Chicago, September 10-15, 1967

VALLI, K., E. K. Hyde, and W. Treytl
Alpha decay of neutron deficient francium isotopes
UCRL-17272, November 11, 1966
J. Inorg. Nucl. Chem. 29, 2503 (1967)

VALLI, K., M. J. Nurmia, and E. K. Hyde
Alpha decay properties of neutron deficient isotopes of emanation
UCRL-16735 Rev, May 1966
Phys. Rev. 159, 1013 (1967)

VALLI, K.
Compilation of experimental E_α values in the region above Z = 81 and below N = 128
UCRL-17723, August 1967
Third International Conference on Atomic Masses, Winnipeg, Canada, August 28-September 1, 1967

VALLI, K., W. J. Treytl, and E. K. Hyde
On-line α spectroscopy of neutron-deficient radium isotopes
UCRL-17322, December 1966
Phys. Rev. 161, 1284 (1967)

VALLI, K. (See Treytl, W., UCRL-17405)

WARD, D., F. S. Stephens, and J. O. Newton
Gamma rays following ^{40}Ar induced reactions
UCRL-17537, October 1967
Phys. Rev. Letters

WARD, D. (See Stephens, F. S., UCRL-17568)

WANG, C. C.
Automatic control system for detection of nuclear magnetic resonance
UCRL-17715, August 1967

WATSON, R. L., H. R. Bowman, S. G. Thompson, and J. O. Rasmussen
Gamma-ray and conversion electron spectra from primary ^{252}Cf fission fragments
UCRL-17289, January 9, 1967
Nuclear Data

WATSON, R. L., and J. O. Rasmussen
Electron binding energies for highly ionized fission fragments atoms
UCRL-17290, January 10, 1967
J. Chem. Phys. 47, 778 (1967)

WATSON, R. L.
K x-ray yields of primary ^{252}Cf fission products
UCRL-17518, May 1, 1967
Phys. Rev. 162, 1169 (1967)

WATSON, R. L., J. O. Rasmussen, H. R. Bowman, and S. G. Thompson
A magnetic steering device for electron coincidence experiments
UCRL-17358, January 27, 1967
Rev. Sci. Instr. 38, 905 (1967)

WEEKS, B. M. (See Garrison, W. M., UCRL-17307)

WHITE, R. (See McLaughlin, R., UCRL-17630)

WILKE, C. R. (See Edwards, V. H., UCRL-17953)

WILLIX, R. L. S., and W. M. Garrison
Chemistry of the hydrated electron in oxygen-free solutions of amino acids, peptides, and related compounds
UCRL-17285, November 18, 1966
Radiation Res. 32, 452 (1967)

YAMAZAKI, T., and G. T. Ewan
Isomeric states in the 3 to 500 nanosecond range populated by (α, xn)-reactions
UCRL-17226, February 1967
Phys. Letters 24B, 278 (1967)

YAMAZAKI, T. (See Sakai, M., UCRL-16548)

YEARIAN, M. R. (See Bowman, H. R., UCRL-17864)

ZALKIN, A., D. H. Templeton, and T. E. Hopkins
The atomic parameters in the lanthanum trifluoride structure
UCRL-16752, March 1966
Inorg. Chem. 5, 1466 (1966)

ZALKIN, A., T. E. Hopkins, and D. H. Templeton
The crystal structure of $Cs(B_9C_2H_{11})_2Co$
UCRL-17371, February 1967
Inorg. Chem. 6. 1911 (1967)

ZALKIN, A. (See DeBoer, B. G., UCRL-17125)

ZALKIN, A. (See Drew, M. G. B., Inorg. Chem. 6, 1906 (1967))

ZALKIN, A. (See Hopkins, T. E., UCRL-16758)

ZALKIN, A. (See Hopkins, T. E., UCRL-16759)

ZALKIN, A. (See Horrocks, W. D., UCRL-17666)

2. CONTRIBUTIONS TO THIS REPORT

ANDREWS, C. F.
G. 4

ARNOLD, J. E.
I. 3

ASARO, F.
A. 1

BECK, A.
G. 18

BERNTHAL, F. M.
A. 2

BICHSEL, H.
B. 16, 19

BOWMAN, H. R.
D. 1, 2, 9
I. 5

BROWN, W. H.
H. 2

BROWNE, E.
A. 1

BRUNNADER, H.
B. 15

BUCHER, J. J.
G. 14, 15

BUTLER, G. W.
B. 10

CERNY, J.
B. 9, 10, 11, 12, 13, 14, 15
C. 3

CHENEVERT, G.
B. 1

CLAMPITT, R.
F. 1, 2, 3, 4

CLARK, D. J.
B. 17, 18
I. 14

CLARK, M. W.
H. 2

CLEM, R. G.
G. 29

CONWAY, J. G.
E. 3
G. 2, 3, 4, 5, 6

CONZETT, H. E.
C. 2

CORDI, R. C.
I. 9

COSPER, S. W.
B. 10, 11, 12, 13, 15

CROISSIAUX, M. R.
D. 1

CUNNINGHAM, B. B.
G. 8, 19, 20, 21, 22

DAVIS, S. P.
G. 5

DeBOER, B. G.
G. 28

DIAMOND, R. M.
A. 8, 11, 12, 13
G. 14, 15, 16, 17, 18

DREW, M. G. B.
B. 23, 26

DUHM, H. H.
B. 2, 3. 7

EASLEY, W.
G. 7

EDELSTEIN, N.
G. 6, 7

EDWARDS, V. H.
H. 1

ELAD, E.
I. 4

EVANS, J. E.
E. 3

FADLEY, C. S.
I. 13

FAESSLER, A.
C. 4

FLEMING, D. G.
B. 12, 14
C. 3

FRAZIER, P.
I. 14

GARRISON, W. M.
G. 10, 11, 12, 13

GATTI, R. C.
D. 1, 7, 8, 9

GEOFFROY, G. L.
I. 13

GHIORSO, A.
D. 10

GIAUQUE, R. D.
I. 5

GILBERT, A.
D. 5

GLASSHAUSER, C.
B. 4

GLENDENNING, N. K.
B. 2, 6, 14
C. 3, 4, 5

GOTH, G. W.
B. 12

GOULDING, F. S.
I. 9, 10, 11, 12

GUTMACHER, R. G.
E. 3
G. 2

HAGSTRÖM, S. B. M.
I. 13

HALPERN, I.
B. 1

2. CONTRIBUTIONS TO THIS REPORT

ANDREWS, C. F.
G.4

ARNOLD, J. E.
I.3

ASARO, F.
A.1

BECK, A.
G.18

BERNTHAL, F. M.
A.2

BICHSEL, H.
B.16, B.19

BOWMAN, H. R.
D.1, D.2, D.9
I.5

BROWN, W. H.
H.2

BROWNE, E.
A.1

BRUNNADER, H.
B.15

BUCHER, J. J.
G.14, G.15

BUTLER, G. W.
B.10

CERNY, J.
B.9, B.10, B.11, B.12

CHENEVERT, G.
B.1

CLAMPITT, R.
F.1, F.2, F.3, F.4

CLARK, D. J.
B.17, B.18
I.14

CLARK, M. W.
H.2

CLEM, R. G.
G.29

CONWAY, J. G.
E.4
G.2, G.3, G.4, G.5,

CONZETT, H. E.,
C.2

CORDI, R. C.
I.9

COSPER, S. W.
B.10, 11, 12, 13, 15

CROISSIAUX, M. R.
D.1

CUNNINGHAM, B. B.
G.8, 19, 20, 21, 22

DAVIS, S. P.
G.5

EASLEY, W. C.
G.7

EDELSTEIN, N.
G.6, 7

EDWARDS, V. H.
H.1

ELAD, E.
I.4

EVANS, J. E.
E.4

This report was done with support from the Department of Energy. Any conclusions or opinions expressed in this report represent solely those of the author(s) and not necessarily those of The Regents of the University of California, the Lawrence Berkeley Laboratory or the Department of Energy.

TECHNICAL INFORMATION DEPARTMENT
LAWRENCE BERKELEY LABORATORY
UNIVERSITY OF CALIFORNIA
BERKELEY, CALIFORNIA 94720